PROCEEDINGS OF SPIE

SPIE—The International Society for Optical Engineering

Optical Storage and Optical Information Processing

Han-Ping D. Shieh
Tom D. Milster
Chairs/Editors

26-27 July 2000
Taipei, Taiwan

P
PROCEEDINGS
SERIES

Volume 4081

PROCEEDINGS OF SPIE

SPIE—The International Society for Optical Engineering

Optical Storage and Optical Information Processing

Han-Ping D. Shieh
Tom D. Milster
Chairs/Editors

26-27 July 2000
Taipei, Taiwan

20011130 082

Volume 4081

SPIE is an international technical society dedicated to advancing engineering and scientific
applications of optical , photonic, imaging, electronic, and optoelectronic technologies.

AQ F02-02-03 01

Please use the following format to cite material from this book:

Author(s), "Title of paper," in *Optical Storage and Optical Information Processing*, Han-Ping D. Shieh, Tom D. Milster, Editors, Proceedings of SPIE Vol. 4081, page numbers (2000).

Printed in the United States of America.

REPORT DOCUMENTATION PAGE

Form Approved OMB No. 0704-0188

1. AGENCY USE ONLY (Leave blank)	2. REPORT DATE July 2000	3. REPORT TYPE AND DATES COVERED 26-27 July 2001 Conference Proceedings - Final Report

4. TITLE AND SUBTITLE

Optical Storage and Optical Information Held in Taipei, Taiwan on 26-27 July 2000.

5. FUNDING NUMBERS

6. AUTHOR(S)

Han-Ping D. Shieh and Tom D. Milster, Editors

7. PERFORMING ORGANIZATION NAME(S) AND ADDRESS(ES)
Industrial Technology Research Institute
Taipei, Taiwan

8. PERFORMING ORGANIZATION REPORT NUMBER

ISSN 0277-786X

9. SPONSORING/MONITORING AGENCY NAME(S) AND ADDRESS(ES)
US Department of the Air Force
Asian Office of Aerospace Research and Development (AOARD)
Unit 45002
APO AP 96337-5002

10. SPONSORING/MONITORING AGENCY REPORT NUMBER

11. SUPPLEMENTARY NOTES

12a. DISTRIBUTION/AVAILABILITY STATEMENT

Approved for Public Release. U.S. Government Rights License. All other rights reserved by the copyright holder. (Code 1, 20)

12b. DISTRIBUTION CODE

A

12. ABSTRACT (Maximum 200 words)

This conference on Optical Data Storage and Optical Information Processing was part of the International Optoelectronics Symposium Held in Taipei, Taiwan on 26-28 July 200 in conjunction with Photonics Taiwan 2000 (See http://www.spie.org/web/meetings/programs/pt00/pt00_home.html.). The conference objective is to serve as a forum for presenting and discussing the latest technical issues, results and applications. In the area of data storage, topics include devices to improve the performance of optical heads, measurement of optical media parameters, new superresolution techniques, three-dimensional memory, and near-field devices. For optical signal processing, some of the topics are: Chinese seal recognition, optical infinite impulse response filters, all-optical logic devices, and a fast fingerprint identification method.

13. SUBJECT TERMS
AOARD, Foreign reports, Optical signal processing, Optical data storage, international standards, DVD-RAM, Holographic Storage

15. NUMBER OF PAGES

16. PRICE CODE

17. SECURITY CLASSIFICATION OF REPORT UNCLASSIFIED	18. SECURITY CLASSIFICATION OF THIS PAGE UNCLASSIFIED	19, SECURITY CLASSIFICATION OF ABSTRACT UNCLASSIFIED	20. LIMITATION OF ABSTRACT UL

Contents

PLENARY PAPER

SESSION 1   DISK AND MATERIALS

SESSION 2   DVD AND DRIVE

Conference Committee

Conference Chairs

       Han-Ping D. Shieh, National Chiao Tung University (Taiwan)
       Tom D. Milster, Optical Sciences Center/University of Arizona (USA)

Program Committee

       Di Chen, Chen and Associates Consulting (USA)
       Chong Two Chong, Data Storage Institute (Singapore)
       Fu-Xi Gan, Shanghai Institute of Optics and Fine Mechanics (China)
       Kenya Goto, Tokai University (Japan)
       Ken Yuh Hsu, National Chiao Tung University (Taiwan)
       Der-Ray Huang, Industrial Technology Research Institute (Taiwan)
       Akito Iwamoto, Toshiba Corporation (Japan)
       Soon Gwang Kim, Korea Institute of Science and Technology
       Takashi Kurokawa, Tokyo University of Agriculture and Technology (Japan)
       Sing H. Lee, University of California/San Diego (USA) and NIPT Inc. (USA)
       Takeshi Maeda, Hitachi Central Research Laboratory (Japan)
       Sung-Chul Shin, Korea Advanced Institute of Science and Technology
       Glenn T. Sincerbox, University of Arizona (USA)
       Jun Tanida, Osaka University (Japan)
       Junji Tominaga, National Institute for Advanced Interdisciplinary
         Research (Japan)
       Henk Van Houten, Philips Research Laboratories (Netherlands)
       Wai William Wang, Acer Peripherals, Inc. (Taiwan)

Session Chairs

    1   Disk and Materials
        Tom D. Milster, Optical Sciences Center/University of Arizona (USA)

    2   DVD and Drive
        Di Chen, Chen and Associates Consulting (USA)

    3   High Density and Superresolution
        Takeshi Maeda, Hitachi Central Research Laboratory (Japan)

    4   Optical Information Processing I
        Yoshimasa Kawata, Shizuoka University (Japan)

    5   Near-Field Recording
        Han-Ping D. Shieh, National Chiao Tung University (Taiwan)

    6   Optical Information Processing II
        Ken Yuh Hsu, National Chiao Tung University (Taiwan)

Introduction

Optical data storage and optical information processing are key technologies in the new information age. With the introduction of the digital versatile disk (DVD) and soon the digital video recorder (DVR), the capacity and speed of consumer-level optical data storage products are dramatically increasing. However, the need for increased capacity and data rate is never satisfied. This fact is especially true when one considers the tremendous bandwidths that are now being implemented in business-class and consumer-class communication technologies. New storage and information processing equipment must be designed to meet these demands. A variety of ideas and technology is available, but there is no single technology that will clearly meet all future requirements. Therefore, regular meetings, conferences, and symposia are necessary to communicate the latest findings in this exciting field.

This volume presents the collected works from a majority of the authors in the conference on Optical Storage and Optical Information Processing, which is part of SPIE's International Optoelectronics Symposium, Photonics Taiwan. The objective of this conference is to provide a forum for presenting and discussing the latest technical issues, results, and applications in the fields of optical data storage and optical information processing. For data storage, a variety of topics is included in the presentations, such as devices to improve the performance of optical heads, measurement of optical media parameters, new superresolution techniques, three-dimensional memory, and near-field devices. For optical signal processing, some of the topics are: Chinese seal recognition, optical infinite impulse response filters, all-optical logic devices, and a fast fingerprint identification method.

Han-Ping D. Shieh
Tom D. Milster

Plenary Paper

Photonic Technologies in the 21st Century : Creation of New Industries[*]

Teruo Hiruma

Hamamatsu Photonics KK

Hamamatsu, Japan

ABSTRACT

As we approach the new millennium, the ongoing aim of human society is not only for promoting scientific technology but also creating new industries. To achieve this goal, each person in industry must recognize anew that the real meaning of science is to explore the absolute truth. It is also important that people recognize that there are unlimited matters which we humans do now yet know.

1. INTRODUCTION

The 20th century was one that witnessed many great discoveries and our knowledge increased many times during the last one hundred years. Yet even with such an explosion of knowledge and information there is much more that we do not yet understand. Our present knowledge represents only a fraction of what there is to know. For example, there have been major breakthroughs in understanding cell structure by studying individual components or systems such as the role of calcium ions in signal transduction. However very little is known about how all of these components work in concert. It is very much like trying to understand an orchestra by studying the individual instruments. In the future we will develop methods to study the function of the entire cell not just individual systems. On the molecular level we are just beginning to study the details of molecular dynamics during a chemical reaction. The work of this year's Nobel Prize winner in chemistry, Dr Zewail shows how it is possible to use photonics to study the intimate detail of a chemical reaction. Once we gain such detailed information about more complex systems it will be possible to more efficiently produce the chemicals we need and to destroy those that we no longer require.

At Hamamatsu Photonics it is our corporate mission to provide photonics technology that will help us to gain new knowledge of the world we live in. Photonic technologies are very unique in that they let us observe the parts of the world that are very far away (thousands of light years), very small (nanometers) or happen very quickly (in femtoseconds). The roots of our company can be found in the pioneering spirit of Professor Kenjiro Takayanagi who independently developed the technology of television despite the fact those around believed it could not be done because it had never been done. Professor Takayanagi hoped to develop a new way for people to experience the world. We inherited his spirit and continue this idea by using photonics to gain knowledge as well as improve the quality of life for all people.

In the twenty first century it will be possible that we could make all of mankind healthy. Not just in a physical sense but in the definition of the World Health Organization where "Health is a state of complete physical, mental and social well-being and not merely the absence of disease or infirmity." Photonics has the potential for creating the knowledge and industry that could make this possible. It is our hope that this new century sees the beginning of a new economic cycle shown in Figure 1. While industry is designed to generate profit, the purpose of industrialization is for all of mankind to share a common understanding of the New Life Style and to benefit from the New Standard of value, namely Health as defined above.

Figure 1:

New Science → **New Scientific Knowledge** → **New Technology**
↑   ↓
New Standard of Value   **New Application**
↑   ↓
New Style of Life   ←   **New Industry**   ←   **New Market**
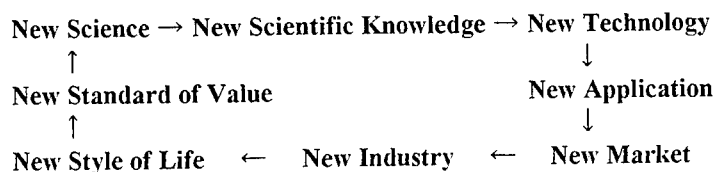
[*]Also published in Proceedings of SPIE Volumes 4078, 4079, 4080, and 4082

Through the application of photonics we are now beginning to develop the New Science that will lead to the cycle illustrated in Figure 1. In this cycle, mankind is constantly improving its status by using new technologies to discover new knowledge. The application of this new knowledge leads first to new industries and then to a change in the social fabric of society. We understand that this is a very long-term goal. But mankind needs to dream in order to progress. Only by trying to see over the horizon can we discover something that will radically improve all of our lives. Thus while Hamamatsu Photonics' short-term goal is to generate profits, these profits are to be used in the quest for new knowledge which is our long-term target.

2. TECHNOLOGIES

This paper will discuss several technologies that are key to the development of new knowledge which will eventually produce new industries. Application of these technologies will be also discussed.

A.   The Ultimate Laser Photon (Photon Factory)

The light emitted by a laser is unique in that it is monochromatic, coherent and directional. These properties have made laser-generated photons vital to all types of research ranging from biology to high-energy physics. We need to obtain a better understanding of exactly what is a photon and how it interacts with the world. By better understanding the photon on a fundamental level we will be able to use it more effectively. Phenomena such as the particle wave duality and teleportation must be better understood through a study of the photon.

The development of very small terawatt and pedawatt laser systems give many researchers access to inexpensive ultra high power. New physical phenomena are being discovered when such intense laser beams interact with matter because these lasers create electric fields much greater than those seen in any other experiment do.

B.   Ultra Fast Measurement Technology

By continuing to push the speed at which we make measurements we will discover greater detail of how our world operates. We now have lasers that are capable of measuring the individual motion of atoms in molecules. Newer and faster methods will help get even greater detail of how molecules react. Even faster methods will allow us to follow the motion of electrons during important chemical reactions such as photosynthesis or vision.

C.   Optical Correlation Technology

Even though we have discovered only a small fraction of our knowledge, we are severely limited in using it because even this limited amount of knowledge is to great to process with conventional computer systems. We must learn how to process information in parallel with optical processors such as spatial light modulators. Ultimately our goal is to process information in 3 or more dimensions using technology that must still be invented.

D. Forecast Simulators

With time not only has our information become too complex, but also the questions we need to answer become more difficult. As our planet' s population increases and our technology becomes more complex, the risk of answering a question incorrectly grows exponentially. For example, the consequences of incorrectly predicting the outcome of global warming will be severe if we either under estimate or over estimate the significance of burning fossil fuels. Premature curtailing of fossil fuels will severely curtail the growth of developing countries leading to unnecessary pain and suffering. Failure to prevent global

3

warming will have even worse consequences. We need better methods to simulate events or conditions so we can better guide environmental, economic, technical, political, and military decisions.

Ultimately nations will never again fight a war on the battlefield but instead will use simulations to replace them. The simulations will simultaneously decide the output as well as convince the parties that physical conflict is too costly.

E. High Power Lasers

Photons are capable of doing many important things such as curing cancer, printing this manuscript or repairing an integrated circuit. At very high photon densities there are many new things that photons can do. At present, it is expensive to generate a lot of photons because the photon sources are expensive. Semiconductor laser diodes hold the promise of being able to reliably and inexpensively generate photons for many new and exciting applications. Just like the replacement of the vacuum tube with the transistor and then to the integrated circuit, so too will the semiconductor laser evolve and result in important technologies and new industries that we cannot even imagine today.

F. New Photochemistry

Much of our planet's energy is wasted in creating chemicals that we need to live or to improve our lives. Lasers are capable of creating specific excited states. Finding ways to selectively excite molecules so that they can be moved along specific reaction pathways will lead to huge savings in cost, energy and pollution. New knowledge on how to perform pathway specific photochemistry is vital to the goal of making everyone healthy according to the World Health Organization's definition of health.

3. APPLICATIONS

We can only speculate on what the full effect of such new photonic technologies will have in the long term. However over a short period of time we can easily imagine some of the benefits we might enjoy from these as well as other photonic technologies. Some of these benefits are discussed below.

A. Measurement of Physiological Functions

The pulse oximeter has already found an important role in guaranteeing that the oxygen concentration of the blood is maintained at as close to optimum as possible. Countless lives have been saved and others have had severe injury prevented by this simple optical device. Not very far away are devices that will permit rapid and painless screening for diabetes. Noninvasive cancer diagnosis is already being tested in clinical trials.

Ultimately a device will be available that checks your body's functions on a daily basis. It screens for potential problems before they cause disease. Adjustments to exercise, diet or even administration of drugs can be performed before the individual is aware of a problem. Such an advanced detection system would save costs, pain and anxiety. It would go as long way to attaining the goal of making people truly healthy.

B. Optical Medicine

In the past few years, photodynamic therapy has been shown to be a valuable treatment for some forms of cancer. In some cases it is far more useful than other techniques such as surgery because it leaves the effected organ in tact. Therefore for young women, cancer of the cervix no longer means that it is the end of their dream to have a family. For older people suffering from the wet form of macula degeneration, photodynamic therapy will soon be used to prevent the blindness caused by this disease.

4

New chemicals are being developed that are absorbed faster by the cancer cells and discharged more rapidly by the body. This will make treatment simpler and more effective. Patients may not even need to stay overnight in a hospital. Presently PDT can only be used on cancers that are found on a surface. Techniques are being developed that will be used in the treatment of cancers that are deep inside an organ.

Cosmetic uses of photons for hair removal, port wine stain removal or tattoo removal make it easier for a person to be accepted by society. These applications are far from superficial since they greatly improve the quality of life for those that need them.

Other applications of photonics to medical practice will certainly emerge in the near future for things such as the treatment of stroke, heart disease, healing of wounds and reducing or relieving pain.

C. Early Detection of Disease

Cancer screening using Positron Emission Tomography (PET) holds the promise of early detection and cure of this terrible affliction. Injection of fluorodeoxyglucose into the blood stream is current used to uncover cells that are metabolizing at rates faster than those of their neighbors. These cells are then analyzed to determine if they are malignant. Such a screening method could in the near future make an entire city cancer death free.

Light CT uses nonionizing infrared photons to take a three dimensional image of the body. Work is under way in many places around the world to use light CT as a method for detecting breast cancer. This technique could be less expensive than x-ray methods and used safely on all individuals including pregnant women. Other uses of the light CT would be to quickly determine if a stroke is caused by ischemia or a hematoma. Such information is vital in determining the correct treatment. Rapid treatment of stroke can greatly reduce the damage to the brain resulting in a patient that can lead a normal life even after such a severe trauma.

In the future we hope to quantify the health of a person, not just the presence of disease.

D. Fiberless Optical Communication

Information is the most important commodity in our society. We are constructing very large and expensive infrastructures to move information from one location to the other. Fiber optics is one of the key technologies for information transport because of the very high capacity available due to wavelength division multiplexing. This technique suffers from the fact that fibers must be placed between locations. At Hamamatsu Photonics we have developed a series of fiberless optical communications systems. These operate by transmitting the optical signals through air. They have the capability to send data, or video without the need for government licenses or owning a right of way. One such a fiberless system is used at sporting events such as golf

tournaments to transmit the video camera output to the broadcaster's trailer or even back to a studio. Such a system was used at the Atlanta Olympics and is now being tested in Hamamatsu City. In our hometown it is being used to connect elementary schools with the city hall. It could also be used to connect remote clinics with the medical school for telemedicine.

E. Health Industry for Successful Aging

Many countries will soon suffer from an increase in their average age. In the past such an increase in age would greatly burden society in terms of medical expenses and the cost of financially supporting an aging population. We believe that it is possible to completely eliminate the impact of a graying population by finding ways to reduce the pace and effect of the aging process. At Hamamatsu Photonics we are using photonic technology to understand how locomotion is effected as a person ages. We hope to develop exercises that will prevent the loss of mobility and greatly reduce the probability of an older person falling. While just a small step, it will have a big impact on the quality of life of our seniors.

F. Disposal of Industrial Waste

High power lasers and controlled photochemistry hold the promise of being able to safely dispose of dangerous waste products. It will do this by selective destruction of the dangerous ingredients into less danger or even harmless smaller molecules. These smaller molecules can then be recycled into new products.

G. Search for New Energy Sources

Perhaps the biggest impact that photonics can have on mankind is the development of clean and inexpensive energy. For once this is available; the quality of life of the entire world can be improved without damaging the plant. We must continue our search for a way to harness laser fusion and solar energy for they are needed to make the world a better place to live for all of us.

Photonics holds the promise of creating New Science and New Technology which will lead to New Industrial and of course to a world population that is truly healthy.

SESSION 1

Disk and Materials

Status of Optical Disk Standards and Copy Protection Technology

Di Chen*, President, Chen and Associates Consulting, Mound, MN 55364

ABSTRACT

Optical data storage is now well into the second decade of continuing market and technology expansion. Media removability, whish is the main attribute of this technology, presented the optical recording industry with unmatched opportunities and also new challenges. On the one hand, data interchange between the media and drives from different sources becomes a major concern, which can only be solved if international standards for all optical recording disk/cartridge are available. Many standards organizations, with the help of world wide industrial support, took up the challenge, and numerous international standards were established which are now being adapted. One the other hand, copy protection technology must be developed to prevent illegal copying and distribution of contents using this removable media. This need is accentuated by the proliferation of low cost CD and now DVD disks replication means and the availability of recordable and rewritable CD and DVD devices. This paper provides an update of the brief summary of the current status of the international optical disk standards published ealier[1] and a breif review of the copy protection technology.

Keyword: Optical recording, international standards, copy protection

I. INTRODUCTION

Research and development in optical data storage started more than three decades ago. Product introduction however was not realized until early 1980's. Initial devices were mainly read only or write-once-read mostly (WORM) types. The very first attempt to offer a guideline of a WORM disk standard was presented by T. A. Olson [2] at the Optical Data Storage Topical Meeting in 1983. Subsequently, the National Bureau of Standards (now NIST) took on the task to promote optical disks international standards and held numerous meetings on the standards development. Participation of ANSI in developing the optical disk standards started in 1984 and the X3 B11 committee was created. The first B11 Chairman was Mike Deese, who held the first International Standardization Organization (ISO) SC23 meeting in Japan. In the ensuring years, B11 committee was chaired by Joe Zajaeczkowski, Ken Hallam, Pat Sandell and now John Neumann. The B11 committee is now organized under National Committee for Information Technology Standards (NCITS). Concurrently, the European Computer Manufacturers Association (ECMA) added the optical disk standards to their standards activities and formed a Technical Committee TC31 in 1984. These activities are now coordinated by the joint technical committee (JTC1) under joint effort of ISO and the International Electrotechnical Commission (IEC). All industrial nations, with US, Japan and some European countries as the major contributors, joined this effort and resulted in numerous international standards, including read only, WORM, recordable (Dye polymer or ablative media) and rewritable disks, (magneto optic or phase change media) with disk diameters ranging from 80 mm to 356 mm. The most popular read only Compact Disc (CD-ROM), started with a de-facto standard by Philips and Sony, are now also embraced by the international standards. More recently, Digital Versatile Disc (DVD) technology was introduced. The standards work on this type of disks is on Fast Track and the first group of DVD disc standards have been completed.

The ease of copying information to a recordable or rewritable CD or DVD optical disc brought about the need for copy protection. The work was started over four years ago. The three industrial concerns, namely the Information Technology (IT), the Consumer Electronics (CE) and the Content Providers such as the Motion Picture Association (MPA) and Secure Digital Music Initiative (SDMI), realizing the importance of copy protection, agreed to join force to develop the required

* Correspondence: Email dichen2127@cs.com

technology. The work is coordinated under the Copy Protection Technology Working Group (CPT-WG), with Allen Bell of IBM as the Chairman. CPT-WG meets monthly, participated by all industrial concerns, with the support of the DVD Forum WG-9, Mt. Fuji, DVD-CCA, MPA, SDMI, and many other organizations. The technologies developed to date includes the proprietary Content Scrambling System administrated by DVD-CCA, the use of Watermark in the content. More recently, the proprietary Copy Protection techniques for Recordable Media and Prerecorded Media (CPRM and CPPM) were developed which will be available for licensing.

In this paper, we will review the activities of of ISO/IEC JTC1, ANSI, ECMA and other organizations including OSTA, and DVD-Forum. The status of copy protection technologies developed to date will then be discussed.

II. ANSI NCITS B11 STANDARDS ACTIVITIES

The American National Standards Institute started the pioneering effort in optical disk standards and established the X3 B11 (now NCITS B11) committee in 1984. Much of the early work was in the WORM disks using ablative recording media with 300 mm and 130 mm disk diameters. By late 1980 and early 1990. recordable and rewritable disks was introduced. 90 mm, 120 mm (CD) and 130 mm disk sizes standards were advancing rapidly. Test and measurement standards were also introduced. In the mid 1990, DVD discs were developed. DVD-ROM, DVD-recordable and DVD-rewritable disc standards are currently under intense development. The ANSI NCITS B11 activities and accomplishments over the past fifteen years are monumental indeed. This is a tribute to the world wide contributions and cooperation from all national bodies, companies, and individuals in this field.

Over the years, developers of optical recording media and drive have generated a set of important parameters which collectively defines a disk standard. Nearly all disk and cartridge standards, irrespective to the size and usage, have included detailed values and margins of these parameters to insure data interchange. These essential disk parameters are:
           (1) Environmental: Operating, transportation and storage
           (2) Mechanical and Physical:
           (3) Optical:
           (4) Reference Drive:
           (5) Track Format:
           (6) Data Format:
           (7) Read /Write/Erase Laser Power and power control
           (8) Data Coding: Modulation Code, Error Correction Code
           (9) Defect management
           (10) Test and measurement:
           (11) Annexes: Optional features as permitted
Besides these, there are many variations and additions which may be required for a specific case.

With this many parameters which must be defined in detail for each disk standard, and be agreed by all concerns, the task to establish a standard is indeed overwhelming. From the start of the acceptance of project proposal, going through a number of versions of draft standards for review and comments with letter ballots, and eventually resolving all objections and reach the final publication of an international standard, typically takes years of work. The projects developed under B11 committee and the resulting standards published are summarized in Table I.

As the optical disk standards activities gravitated into the international arena in the past two years, the work under NCITS B11 has now dropped from an active to a maintenance mode.

III. ISO/IEC JTC1 STANDARDS ACTIVITIES

The members of the International Organization of Standardization and International Electrotechnical Commission participate in the development of International Standards through the joint technical committees established by the respective organization to deal with particular fields of technical activity. ISO and IEC technical committees collaborate in fields of mutual interest. Other international organizations in liaison with ISO and IEC, also take part in the work. ISO/IEC information technology technical committee JTC1 was established to work on the standards in the information industry including the optical disks. Within JTC1, there are a number of subcommittees (SC) each addressing a specific area of work. Working groups (WG) within the SC are where the most significant work being conducted to address the technical issues, and to resolve differences. All National Bodies (country members of ISO and IEC) can participate in this standards work. Under the standard 5-stage development procedure, any standards project must first be approved, and editor(s) assigned to prepare the working draft international standard (WD). The draft is then reviewed and modified by all National Bodies. The working group is the venue where the National Bodies participate in resolving technical issues. The standards so prepared then go through several letter ballots: Committee Draft (CD) and Final Committee Draft (FCD) at the SC level, and Final Draft International Standard (FDIS) at the JTC1 level. This balloting procedure can be as short as 6 months, or as long as 18 months, depending on the technical maturity of the WD when it is first balloted. At long last, an international standard will be published.. JTC1 has also offered an additional method of producing an International Standard known as the Fast Track procedure. In this case, after the approval of the standards project, and assignment of the editor(s), a draft international standard (DIS)will be prepared. The draft is reviewed and modified by all national bodies and the working groups will participate in resolving technical issues. The standards so prepared will go through one of more letter ballot procedure..

IV. ECMA STANDARDS ACTIVITIES

The European Computer Manufacturers Association (ECMA) was formed in 1961. In 1987, a technical committee TC 97 became part of ISO/IEC JTC1, ECMA became A-liaison member of JTC1, thereby accelerating the process by which ECMA standards can be adapted as an International Standard. Mr. Dora Hekimi held the position of Secretary General from 1961 to 1991. This position is now taken over by Mr. J. van den Beld. The ECMA optical disk/cartridge standards activities are organized under TC 31. From 1987 to 1991, the work has been in the development of 130 mm WORM and R/W disk standards, 90 mm R/W and CD-ROM. From 1992-1996, 90 mm and 130 mm disks of different applications were included, together with SSF and CCS servo methods, and CD and PD format disks. Since 1997, 120mm and 80mm DVD disk standards have been the center of action. The classification of Optical Disk Case/cartridge Standards defined by ECMA and ISO/IEC is summarized in Table II[4].

V. OTHER STANDARDS ACTIVITIES

Much of the ANSI and ECMA standards work are in coordination with the Japanese standards organizations. In fact, much of the recent technical work on optical disk/cartridge was developed in Japan. DVD-Forum, chaired by Koli Hase of Toshiba was founded in 1995 by 10 companies (Hitachi, Matsushita, Mitsubishi, Philips, Pioneer, Sony, Thomson Multimedia, Time Warner, Toshiba and Victor Company of Japan), with purpose of maintanence and development of DVD specifications.. Currently there are 100 members who take part in the Forum activities, promoting and developing products based on DVD Specifications, and receive information.. to One of the main contribution of DVD Forum to DVD disc standards is through the publication of DVD books. The DVD books published to date is listed in Table III[5]. There are many verification laboratories established world wide, inlcuding Philips in Europe; Hitachi, JVC, MEI, Pioneer, Sony, and Toshiba in Japan; ITRI in Taiwan, and Warner in US, to serve as the clearing house for disc or drive conformation to the standards set by the books.

With respect to rewritable DVD discs, there is the Mount Fuji working group which deals with all aspects of the issues related to Content Protection, Real Time recording, and Access Control. On audio recording, Secure Digital Music Initiative (SDMI) is leading the effort.

Besides these organizations, a world wide trade association named OSTA (Optical Storage Technology Association) was organized by Ray Freeman in 1992, consisting of members from optical product manufacturers from three continents. The purpose is to promote the use of writeable optical technologies and products for storage of computer data and images. In the past, OSTA has been working on the migration path for the 130 mm and 90 mm writeable drives, to insure that technology advances will not cause premature obsolicence. More recently, OSTA has been working on the Universal Data Format (UDF), and compatibility issues for CD and DVD discs. A MutiRead technology was advanced which defined the requirements for the readablility of CD-ROM, CD-R and CD-RW discs by all CD devices. This technology is being extended for DVD drives.

There are many other standards activities world wide which will have an direct impact to Optical Disk standards. The data format such as UDF as mentioned above, and the Multi Media Command Set Standards proposal under NCITS T10 for example, can directly affect the ability for data interchange of optical disks. These activities should be taken into consideration carefully in the development of disk/drives comforming to the specified International Standards.

VI. COPY PROTECTION TECHNOLOGY

In the US, there is a concerted effort to address the Content Protection Technology. The future market development in DVD recordable technology depends on the availability of acceptable Content Protection standards. Development of the technologies for the protection of intellectual properties has been in progress since the mid 1990's. This effort involves many complex issues such as the technology development, the legal reminification, the business interests, and the consumer acceptance. To be acceptable to all concerns, this work has a goal to prevent illegal copying of contents, to be invisible to users, to be compatible to existing architecture, to require minimum management, to be low cost, to encourage voluntary compliant, to be robust and to allow technology growth.

There are many organizations currently involved in the development and administration of the copy protection technologies. The Copy Protection Technology Working Group (CPT-WG) is the coordinating orgainzation which ia working with the Information Technology Inductry Association (ITI), the Content Providers such as the Motion Picture Association of America (MPAA) and the Recording Industry Association of America (RIAA), and the Consumer Electronic Manufacturers Association (CEMA) together to develop the required technology.. There is a monthly meeting to review progresses and resolve issues. The DVD Forum has the WG-9 working group to addresses the DVD copy protection in total systems. The Technical Working Groups such as the ad hoc group AhO-3 within TC-31 which deals with the DVD-R devices. To address the copy protection as data is transmitted, there is the Data Transmission Group which deals with protection in the data interface. For the read only media such as DVD-ROM, a proprietory Content Scrambling System (CSS) has been developed. This system is now implemented and available for licensing through DVD-CCA. An earlier version of CSS unfortunately was broken by a hacker late last year, resulting in much legal and technological debate. The other technique is the use of Water Mark which is embedded in the content and provides a way for tracking and control of the stored information. This system is however still under development and not yet implemented for a number of reasons. One is related the selection of the two proposed Water Mark techniques namely the Millennium system and the Galaxy system. Decision has yet to be made as to which one to use. Also there has been much debates on the location where the Water Mark detection should take place. It could reside in the drive or in the data processing system.

IBM, Intel, Toshiba and Matsushita (4C) have advance a general guide line of the architectural aspects of copy protection, (copy protection systems achitectural CPSA). 4C also introduced copy protection techniques in two proposals, one for recordable media (CPRM) and one for prerecorded media (CPPM). The system is based on three technical elements: (1) Key management for interchangable media, (2) Content encryption and (3) Media Based renewability. Deteail of these proposal can be accessed through 4C web site[5]. These proposals are currently under discussion and the technologies are expected to be available for licensing in the near future.

The above mentioned technologies are media and drive related. There is also some interest to develop copy protection in the data transmission between PC (video traqnsmission) and the display device (video receiver). A Digital Visual Interface

(DVI) specification has been proposed by Intel, in corporation with Silicon Image. Information may be obtained from DVI web site[6].

Copy Protection technology is still at the stage of rapid development. It appears that all currently available techniques are privately developed and details are not in the public domain. However, for the protection of content providers, disc and drive manufacturers are urged to participate and endorse the copy protection technologies, for the benefit and health of the entire industry.

VII. CONCLUSION

The creation of the international standards of optical data storage disks and cartridges is a major endeavor of this industry.. Earlier effort, with the exception of CD, was initiated in the US. Earlier US participants includes major companies such as 3M, DEC, IBM, Kodak, HP, Verbatim, and start-up companies such as ISI, MaxOptix, and Optotech. The critical parameters and other pioneering work for optical disk standards were developed during this period. By 1990's, the effort in the development of optical data storage devices and media in US decreases drastically. Associated with the reduced US drive and media industrial participation, the standards work started to migrated from US to Europe and Japan. At present, ANSI NCITS B11 committee has reduced its work from the active to a maintenance mode. ECMA is now leading the optical disk standards activities, and many of the hard technology and engineering work in standards are being carried out in Japan. For the DVD disc standards work, major companies in Japan, such as Hitachi, MCC, Matsushita, Pioneer, Ricoh, Sony, Toshiba, Yamaha, together with Philips in Europe, and HP in US, are now the main driving forces.

As the optical recording technology advances, the optical standards activities will continue to expand. Although it is important to encourage new development, we must not loss sight in the ability to recover information stored in optical disks. Studies have shown that most optical disks will have a data retention life of over 50 years. The main concern is whether there will be a drive which can recover the data stored on the disk at that time. This may be the ultimate test of Data Interchange that we should be addressing.

The ease of record data on optical disks brought about a concern for copy protection. The Information Industry, the Content Provider and the Consumer Electronics Industry are joining force to develop user friendly, low cost solution to the copy protection technology. Many approaches advanced to date are either being implemented or will be implemented in the near future. It is however important to realize that any protection technology are susceptible to tempering, and in time could be broken. Any copy protection technology must establish a clear path for migration to higher level of protection as the need arises. This may be the best strategy to insure a long term solution for this complex problem

ACKNOWLEDGMENTS

The authors wish to a acknowledge helpful discussions with John Neumann and Paul Wehrenberg.

REFERENCE

1. Di Chen, John Neumann, "Status of International Optical Disk Status", *Proc. SPIE* vol. 3806, pp 94-102, 1999
2   Olson, T. A. , Optical Data Storage, Ed. D. Chen, SPIE Vol 382, pp 164, 1983
3. ECMA Standardizing Information and Communication Systems, 1999, www.ecma.ch
4. After DVD-Forum, presented by Koji Hase at the #48 CPT-WG Meeting, March, 2000
5. 4C Entity, LLC web site: http://www.4Centity.com
6. DVI web site: www.digital-cp.com.

Table I. Summary of the Status of Projects Under NCITS B11 Committee:

Project	Disk Dia. (mm)	Read only	Worm	MO	PC	Servo	Cap. (MB)	Publication	Yr Pub.	Note
408-L	300		X			SSF		ISO 13614	95	
483-L	300		X			CCS		ISO 13403	95	
480-L	120	X					650	ISO 10149	89	CD-ROM
456-M	356		X					ISO 10885	93	
457-M	130		X			CCS	325/s	X3 211	92	Unrecorded
481-M	130		X			CCS	325/s	X3 211	92	Recordable
659-M	130		X			SSF	325/s	X3 214	92	4/15 mod.
655-M	130		X			Di-bit	650/s	X3 191	91	RZ modulation
607-M	130			X		CCS	325/s	X3 212	92	
736-L	86			X		CCS	128	ISO 10090		
760-M	86			X		DBF	113	X3 214	94	
679-M	356		X					X3 191	91	Test method
879-M	130		X	X		CCS		ISO 10089		CCW Tech.
883-D	90					CCS				Test method
884-M	130					CCS		X3 234	93	Test Method
893-M	130			X		CSS	2000	ISO 13842	95	MCAV
915-M	90			X				ISO 15041		Extended Cap
950-M	90					CCS		X3 244	95	Test Method
953-M	90					DBF		X3 246	94	Test Method
985-D	130				X		2000	B11 94/154	94	
1000-L	130			X			1000	ISO 13481	93	
1001-L	130			X			1300	ISO 13549	93	
1004-M	130			X			2600	ISO 14517		
1029-D	356				X			DIS 15882		

13

Project	Disk Dia. (mm)	Read only	Worm	MO	PC	Servo	Cap. (MB)	Publication	Yr Pub	Note
763/4-L								ISO 13364	95	Rewritable VF
1055-L								ISO 13800	95	Vol. File Stru.
1066-L	130		X					TR 10091	95	Tech. Aspects
1068-L	90									Measurement
1158-M	90				X		1300	ISO 14760		
1159-I	130	X		X			5200	DIS 15286	99	
1184-M	90				X		230	ISO 13963	95	
1188-L	120	X	X							Vol. File Stru.
1189-L	86			X		CCS	128	TR-13561	94	Tech. Guide
1322-L	120	X						TR 18002	99	DVD File TR3
1323-L	120				X		650	ISO 15485	97	PD format
1324-L	120	X					4700	DIS 16448	99	DVD-ROM
1325-L	120				X		2600-5200	DIS 16824	99	DVD-RAM disk
1326-L	120							DIS-16825	99	DVD-RAM case
1327-L	120				X		3000-6000	DIS 16969	99	+RW format
1328-L	80	X						DIS 16448	99	DVD-ROM
1329-L	90						650	IS 15498	97	HS-1 format
1330-L	130		X	X			2600	IS 15486	99	CCW Tech.

Table II. Classification of Optical Disk and Case/Cartridge Standards (After ECMA) [3]

Size in mm	Maximum Capacity	ECMA Standard	ISO/IEC Standard	Recording Technology		Media Types				
				MO	PC	R/W	WORM	WO	P-ROM	O-ROM
80	5,3 Gbytes **	ECMA-268	ISO/IEC 16449							DVD-ROM
90	128 Mbytes	ECMA-154	ISO/IEC 10090	X		X		X	X	X
90	230 Mbytes	ECMA-201	ISO/IEC 13963	X		X			X	X
90	385 Mbytes	ECMA-223	none	X		X				
90	640 Mbytes	none	ISO/IEC 15041	X		X			X	X
90	650 Mbytes	ECMA-239	ISO/IEC 15498	X		X			X	X
90	1,3 Gbytes	none	ISO/IEC 14760			X			X	X
120	660 Mbytes	ECMA-130	ISO/IEC 10149							CD-ROM
120	650 Mbytes	ECMA-240	ISO/IEC 15485			X	X			
120	17,0 Gbytes **	ECMA-267	ISO/IEC 16448							
120	5,2 Gbytes	ECMA-272	ISO/IEC 16824			DVD-ROM				
120	Case	ECMA-273	ISO/IEC 16825							Case
120	6,0 Gbytes	ECMA-274	ISO/IEC 16969			+RW				
130	650 Mbytes	none	9171				X			
130	650 Mbytes	none	ISO/IEC 10089	X		X				
130	650 Mbytes	ECMA-153	ISO/IEC 11560	X				X		
130	1 Gbyte	ECMA-183	ISO/IEC 13481	X		X		X		
130	1,3 Gbytes	ECMA-184	ISO/IEC 13549	X		X		X	X	X
130	2 Gbytes	ECMA-195	ISO/IEC 13842	X		X		X	X	X
130	2,6 Gbytes	none	ISO/IEC 14517			X		X	X	X
130	2,6 Gbytes	ECMA-238	ISO/IEC 15486	X			X			
130	5,2 Gbytes*	none	CD 15286	X		X		X	X	X
300	12 Gbytes	ECMA-189	ISO/IEC 13614				X			
300	12 Gbytes	ECMA-190	ISO/IEC 13403				X			
356	6,8 Gbytes	none	ISO/IEC 10885				X			
356	14,8 & 25 Gbytes	ECMA-260	ISO/IEC 15898				X			

Legend

X   specified in the standard,   * Double sided,   ** Double sided, double layered

none   no ECMA or ISO/IEC standard in existence for this ODC

Table III. DVD Book Construction (after DVD-Forum)[4]

Book Name	DVD Specification	Version
DVD-ROM Part 1	Physical Specifications	1.0_2
DVD-ROM Part 2	File System Specifications	1.0_2
DVD-Video Part 3	Video Specifications	1.1_1
DVD-Video Part 3	Reference Information-JacketPicture Format	1.0_1
DVD-Video Part 3	Reference Information-IEC958 to convey non-PCM encoded Audio bitstream	1.0_1
DVD-Audio Part 4	Audio Specifications	1.1
DVD-Audio Part 4	Reference Information-Packed PCM: MLP Reference Information	1.0
DVD-R (3.9 G) Part 1	Physical Specifications	1.0
DVD-R (3.9 G) Part 2	File System Specifications	1.0
DVD-R for General (4.7 G) Part 1	Physical Specifications	1.95
DVD-R for General (4.7 G) Part 2	File System Specifications	to be issued
DVD-R for Authoring Part 1	Physical Specifications	2.0
DVD-R for Authoring Part 2	File System Specifications	1.9
DVD-RAM (2.6G) Part 1	Physical Specifications	1.0
DVD-RAM (2.6G) Part 2	File System Specifications	1.0
DVD-RAM (4.7G) Part 1	Physical Specifications	2.1
DVD-RAM (4.7G) Part 2	File System Specifications	2.0
DVD-RW Part 1	Physical Specifications	1.0
DVD-RW Part 2	File System Specifications	1.0
DVD-Video Recording Part 3	Video Recording	1.1

Disk inspection system by two dimensional birefringence distribution measurement

Yukitoshi Otani*,   Natalia Dushkina*,   Toshiyuki Kanno**,   Toru Yoshizawa*

*Tokyo A&T University
(Tokyo Univ. of Agri. and Technology)
Koganei, Tokyo 184-8588, JAPAN
**Fuji Electronic Corporate Research and Development,Ltd.
Matsumoto, Nagano, JAPAN

ABSTRACT

Several kinds of disks, such as DVD, MO and/or CD-R, for the next generation require high quality of plastic surface. Especially their flatness is very important. Here a disk inspection system is proposed using two dimensional birefringence distribution measurement. Small birefringence is a serious problem that is caused by internal strain, and/or residual stress. Moreover it is possible to observe its molecular orientation. The birefringence measurement is necessary to determine the relative retardation and the azimuthal angle of the fast axis in an optical disk. Several images captured by a CCD camera are enough for one birefringence distribution analysis. Experimental procedure and their results of some famous optical disks are discussed.

Keywords: disk inspection,   birefringence measurement, phase shifting technique

1. INTRODUCTION

Recently, a birefringence measurement, especially for optical discs, plastic lenses or glass substrates is important for manufacturing inspection process. Many plastic disks, such as several kinds of CDs, DVDs and next generation hard disks, are used for the data storage system. An injection process is used for manufacturing their plastic disks. A flatness is the most important for a disk manufacturing process. Many researchers suggested the main reason for the defects of flatness is residual stress but there are few reports of its experimental results.

In this report, we propose a disk inspection system by two-dimensional (2-D) birefringence measurement. It is necessary for the birefringence measurement to determine both the relative retardation and the azimuthal angle of the fast axis in a sample. Until now, modulation techniques utilizing a photoelastic modulator or an optical heterodyne method[1,2] have been reported and also commercialized on the market. However, since these 2-D birefringence distribution measurements are single point measurement methods, the sample needs to be moved mechanically. These methods are time cosuming and such systems are apt to be large. Nowadays, there are many papers related to two dimensional birefringence distribution measurement. [3-5].

In this paper we propose an improved method and device for measurement of 2-D retardance and principal plane azimuth distributions from intensity of the polarimeter using a phase shifting technique. In our trial both the phase retardation and the principal axis distribution can be determined without moving or rotating the sample. The basic expressions that describe the operation of the systems are presented. A microscopic birefringence measurement is also proposed to analyze an inside of the disk. Finally, we show some experimental results of disks.

2. PRINCIPLE OF DISK INSPECTION SYSTEM

An optical configuration of a disk inspection system by 2-D birefringence measurement is shown in Fig.1. The system based on a polarimeter using a phase shifting method. A liner polarized beam from He-Ne laser at 632.8nm passed through a Babinet-Soleil compensator (BSC) as a retarder and its phase is changed by the birefringence of the sample. An intensity I at a CCD camera after the polarizer can be easily expressed using Stokes parameters and Mueller matrix, as follows [6-8].

*   Correspondence : Email : otani@cc.tuat.ac.jp, yoshi@tuat.ac.jp; http://www.tuat.ac.jp/~otani/
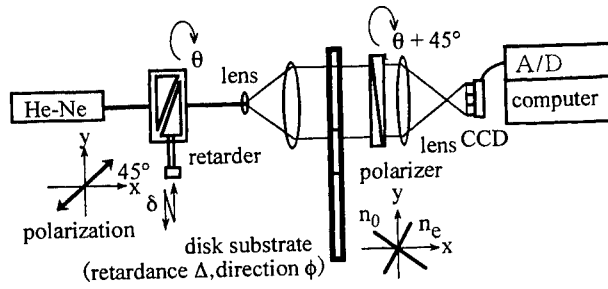   Tel : + 81 42 388 7103 Fax : +81 42 385 7204

Fig. 1 Principle set up for disk inspection by two dimensional birefringence measurement.

$$I = \tfrac{1}{2} \cdot I_0 \cdot [\; 1 \\ - \cos \{ \tan^{-1}(\Delta \cos(2\theta - 2\phi)) + \delta \} \;]$$
(1)

We use twice the phase shifting technique to determine the birefringence parameters Δ and ϕ.

First, the azimuthal angle θ of the BSC is adjusted as 0 deg and a vector Φ can be calculated the intensity $I_0 \sim I_3$ of the polarimeter to change the retardation of BSC δ as 90deg of each time using the phase shifting technique.

$$\Delta \cdot \cos(2\theta - 2\phi) = \frac{I_1 - I_3}{I_0 - I_2} = \Phi$$
(2)

Next, the phase Φ changes sinusoidal as two periods concerning one rotation of the retarder θ. We can easily get the retardance Δ and the azimuthal angle ϕ using 4-step method in case of the rotation angle of θ. As there are two unknown parameters in Eq.(2), six or eight images are enough to analyze birefringence distribution. We analyze birefringence parameters, such as retardance Δ and azimuthal direction ϕ, using 16 images for improving resolution as follows.

$$\phi = \frac{1}{2} \tan^{-1} \frac{\Phi_1 - \Phi_3}{\Phi_0 - \Phi_2}$$
(3).

$$\Delta = \frac{1}{2} \sqrt{(\Phi_2 - \Phi_0)^2 + (\Phi_3 - \Phi_1)^2}$$
(4)

For this analysis, we have checked both retardance and azimuthal direction errors as ±1deg. Its measurement time is expected less than 1 min. using a liquid crystal retardaer and electrical control stage to rotate a polarizer.

The local-sampling phase shifting technique is more powerful method to improve a resolution of the retardance[9].

Figure 2 shows its result compared with a calibrated phase difference known birefringence distribution, a Babinet-Soleil compensator as a specimen, was examined to check sensitivity and accuracy of this system shown in Fig.(3). At first the principal axis direction of a Babinet-Soleil compensator is set to 0 degrees and the variation of the birefringence phase difference is tested. Figure 3(a) shows the result of the measured birefringence phase difference that is given by changing the thickness of the wedge using a micrometer of Babinet-Soleil compensator. The symbols circles indicate the measured results by this method and the straight-line means the calibration line. We archived a retardance as ±0.02deg.
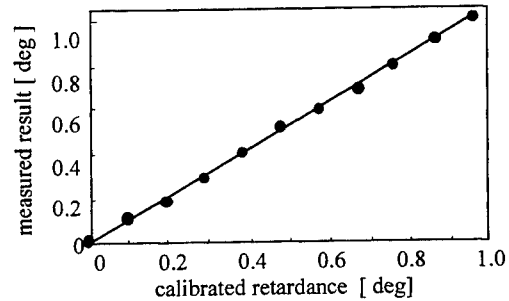
Fig.2 Calibrated result in small birefringence range using a local sampling method

3. EXPERIMENT RESULTS OF OPTICAL DISKS

Figure 3 shows the 2-D birefringence distribution of a DVD-R optical disk both inside and outside. The measurement area is limited to 13x15mm by the optics used in this experimental setup. The retardation is shown in gray scale in the image in Fig.3(a). Fig.3(b) means the vector plot which indicate the azimuthal direction.
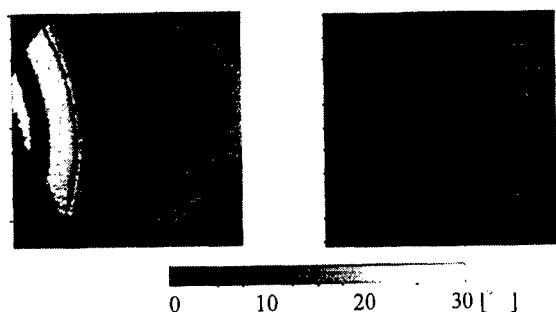
(a) Retardance : measured area 13x15mm

(inside)　　　　　(out side) — 30°

(b) Vector plot
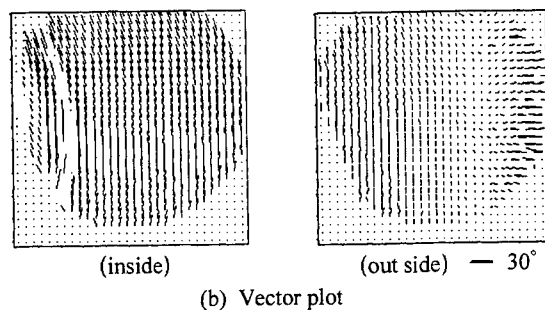
Fig.3　Birefringence distribution of DVD-R

Figure 4 is the results of the optical disks, such as CD-R, CD-ROM, DVD-ROM, and DVD-R. There is an interesting result that the retardance is double even if the thickness of the CD is twice comparing the DVD.

Moreover, we built up a microscopic type of a
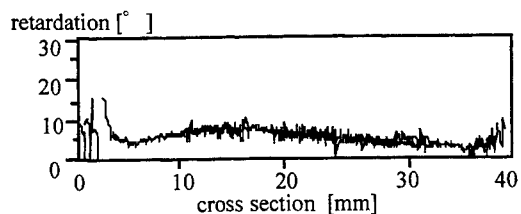
(a)　CD-R
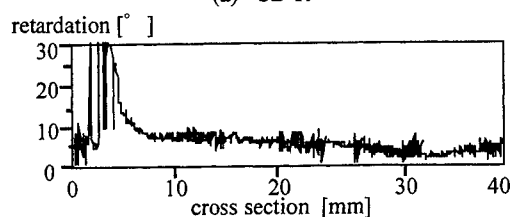
(b)　CD-ROM
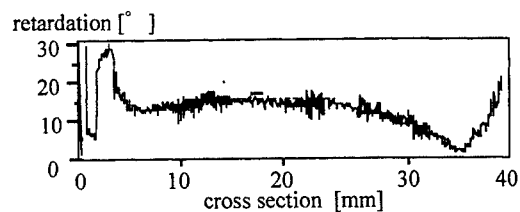
(c)　DVD-ROM
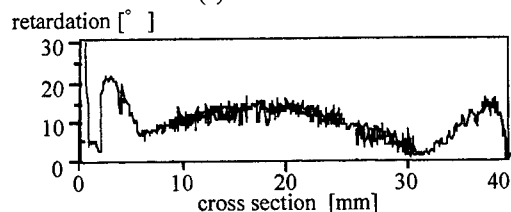
(d)　DVD-R

Fig.4　Measured results of optical disks
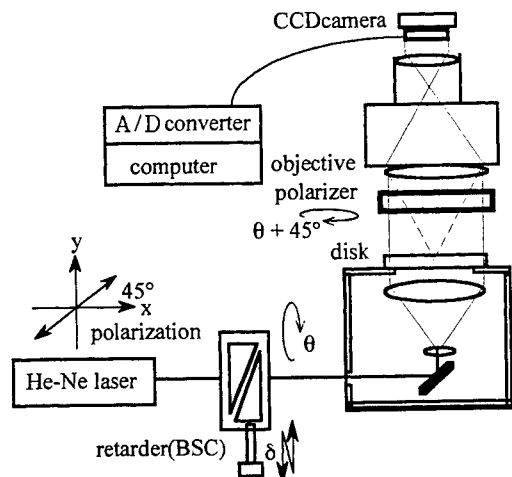
Fig.5　Microscopic measurement system of birefringence distribution inside disk substrate
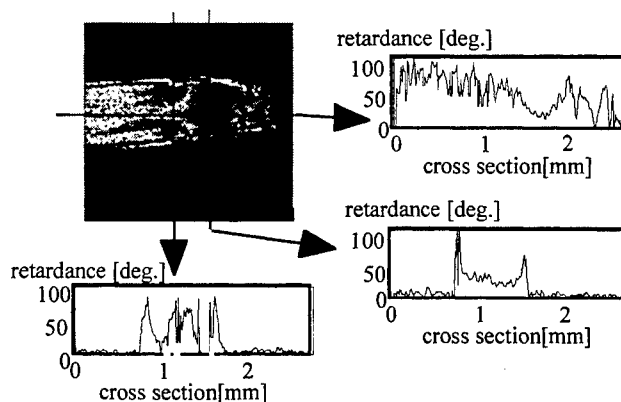
Fig.6　Measurement result of the microscopic distribution of inside disk

birefringence measurement system in Fig.5. This is a transmission type of a microscope. It is possible to detect in a very small area. We tried to make a small sample cut as a sliced piece of the disks to analyze a birefringence distribution of its cross section. Figure 6 shows its result of the cross section of the plastic disk. Its viewing area might be as small as 1x1mm. In the present measurement it is 2.5x2.5mm. We can check an injection process of disks from its birefringence distribution. Although this result seems a little bit noisy, because the light source used is a coherent light (a He-Ne laser), it might be reduce by using a incoherent light source.

4. CONCLUSION

A disk inspection system was proposed using two dimensional birefringence distribution measurement. This system is very powerful that several kinds of disks, such as DVD, MO and/or CD-R, for the next generations require high quality of plastic surface can be applicable. The birefringence measurement is necessary to determine the relative retardation and the azimuthal angle of the fast axis in an optical disk. Several images captured by a CCD camera are enough for one birefringence distribution analysis. We have shown an experimental procedure and the results of some famous optical disks are discussed. This information is useful not only to analyze its flatness, but also to observe its molecular orientation .

5. REFERENCES

1. Y.Mochida : Optical and Eectro-Optical Engineering Contact, 27, 3, pp.127-134 (1989) (in Japanese) .
2. N.Umeda and H.Kohwa: Electronics and Communications in Japan, part 2, 74, 5, pp.21-28, (1991).
3. G.Mei and R.Oldenbourg :, Proc.SPIE 2265, pp.29-39 (1994).
4. Y.Zhu, T.Takada, K.Sakai and D.Tu : J. Phys.D: Appl. Phys.,29, pp.2892-2900 (1996).
5. Y.Otani, T.Shimada, T.Yoshizawa and N.Umeda : Optical Engineering, 33, 5, pp.1604 (1994).
6. P.S.Theocaris, E.E.Gdoutos : Matrix Theory of Photoelasticity (1979, Springer).
7. E.Collett : Polarized light (1993, Marcel Dekker) .
8. R.M.A.Azzam and N.M.Bashara : Ellipsometry and Polarized Light , (North-Holland 1987).
9. Y.Otani, T.Shimada, T.Yoshizawa : The local-sampling phase shifting technique for precise two-dimensional birefringence measurement , Optics Review 1, 1, pp.103-106 (1994)

STATIC TESTER FOR CHARACTERIZATION OF OPTICAL NEAR-FIELD COUPLING PHENOMENA

Ferry Zijp[*), Yourii V. Martynov

Philips Research Laboratories
Prof. Holstlaan 4, 5656AA Eindhoven, The Netherlands

ABSTRACT

We present an experimental set-up for systematical studies of optical near-field coupling phenomena using a solid immersion lens (SIL) to surpass the conventional far field diffraction limit. The set-up incorporates a microscope objective lens with NA=0.80 in combination with a hemispherical SIL manufactured from glass with refractive index $n=1.887$ and a laser with a wavelength of 430 nm. Test samples are positioned within the evanescent decay distance from the bottom surface of the SIL using a closed-loop-controlled piezo actuator. The laser spot can be scanned over the sample enabling a study of the push-pull signal of pregrooved samples on a split photodiode. The intensity distribution and polarisation state of the light reflected from the sample in the exit pupil of the microscope objective lens is studied on a CCD camera. The reflected light can be combined with a reference beam into an interferogram used for alignment purposes. We present measurements of evanescent coupling of light to a glass sample and the push-pull signal of a reflective phase grating with a groove pitch of 300 nm as a function of thickness of the air gap between de SIL and the sample. The evanescent coupling to a glass sample can accurately be described by thin-film optics theory. Experiments show that the push-pull signal amplitude depends on the polarisation state of the irradiating beam.

Keywords: near-field, evanescent field, solid immersion lens

1. INTRODUCTION

Near-field optical recording is a promising new data storage technology. An important part of a near-field optical recording system is a solid immersion lens (SIL) that is used to increase the numerical aperture of the irradiating objective lens by a maximum factor of the refractive index n of the SIL. Such a combination of objective lens and SIL can result in an effective numerical aperture larger than 1. For read-out using the full effective numerical aperture, the medium must be close to the bottom surface of the SIL within the evanescent decay distance of the light (the near-field) that is focussed at an angle larger than the critical angle. This evanescent decay distance is a fraction of the wavelength of the irradiating laser beam. Practical near-field recording systems rely therefore on an air-bearing slider to maintain this distance. Slider technology, however, does not provide sufficient freedom in changing the air gap and the speed of the lateral movement of the medium to allow for a systematic experimental study of the phenomena that are related to near-field coupling and diffraction by grooves and recording layers. Besides the technological challenges of building a fully functional near-field optical recorder system, the system requires thorough theoretical investigation. Whereas conventional far-field optical recording systems such as CD and DVD can quite accurately be described by scalar or quasi-vectorplane wave theory, near-field optics requires a full vector approach.

To improve the understanding of the above phenomena we have built a near-field static tester. In this experimental set up we use a piezo actuator rather than a slider to position a test sample with respect to the bottom surface of the SIL in a reproducible way with nanometer precision.

[*) Correspondence: E-mail: Ferry.Zijp@philips.com
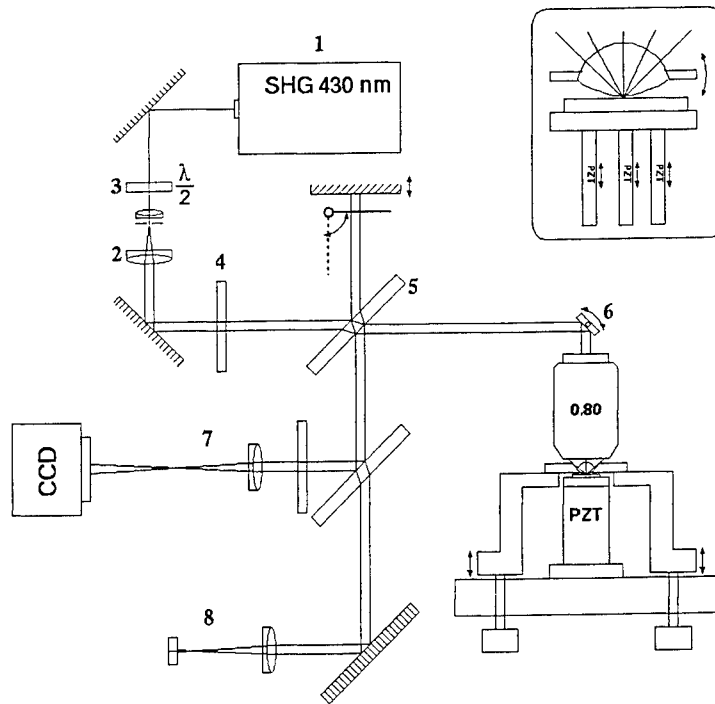
Figure 1. Diagram of the near-field static tester.

2. NEAR-FIELD STATIC TESTER

2.1 Experimental set-up

The experimental set-up is depicted in Figure 1. As a light source we used a continuous-wave frequency-doubled diode laser (1) with a wavelength of 430 nm. The laser beam is expanded by a telescope (2) with spatial filter to reduce aberrations and create a parallel beam with a homogeneous intensity distribution. A half-wave plate (3) is used to select a polarisation state and an additional polariser (4) eliminates any residual ellipticity. A beam splitter plate (5) reflects a portion of the beam towards a reference mirror while the rest of the beam is directed into the optical head. A galvano mirror (6) is used to scan the optical spot over a test sample. Light reflected from the sample is analysed by two detection branches (7) and (8). In the first branch (7) the exit pupil of the microscope objective lens is imaged onto a CCD camera in order to study the intensity distribution and the polarisation state of the reflected light. In the second branch (8) light is detected with a split photo diode generating push-pull signal. In order to suppress parasite signals the lens in this branch is positioned in such a way that the scanning galvano mirror and the photodetector are in its conjugate planes

The set-up incorporates a large-working-distance microscope objective lens with NA=0.80 in combination with a hemispherical SIL manufactured from the LASFN-9 glass sort that has refractive index n=1.887 at 430 nm. The first surface of the SIL was antireflection coated while its bottom is bare. The sample is mounted on top of a piezo actuator. The actuator contains 3 piezo elements that can be controlled in closed loop using built-in strain gauge displacement sensors. The actuator allows adjustment of tip-tilt and translation along the optical axis with accuracy better than 1 nm. The SIL is fixed in a holder in a form of a cap covering the actuator and can be aligned using three micro spindles. The SIL holder is made from the same material as the actuator body (stainless steel) in order to minimise displacements due to thermal expansion. The current set-up does not include a direct measurement of the distance between SIL and the sample. Therefore, we measure the sample displacement relative to the position of mechanical contact which can be determined with an accuracy of approximately 5 nm by observing changes in the CCD image while the sample is moving continuously towards SIL.

2.2 Alignment of the SIL head

We chose a hemispherical SIL instead of the super-spherical SIL because of its more relaxed tolerance on the thickness. The choice of the shape of bottom surface of the SIL was determined by the alignment problem. For a flat bottom the tolerance on angular alignment of the SIL and a flat sample for very small air gaps becomes prohibitively tight. To overcome this problem several solutions have been proposed ranging from conical bottoms with a sharp tip [1], a very small 'nose' [2] to a spherical bottom surface [3]. We have chosen to grind and polish the bottom surface spherically because such a geometry has a contact point at any tilt angle between SIL and test sample. In such a geometry alignment is only necessary to reduce aberrations by making sure that this contact point lies within the field of view of the objective-SIL combination. In order to be able to determine the angle between the SIL and the sample, the SIL was mounted in a small glass disk with its optical axis perpendicular to the disk surface. By irradiating the sample with a parallel laser beam through this disk we could obtain an interference pattern between the light reflected from the test sample and the surface of this small disk facing the test sample (the surface of the disk facing the irradiating laser beam is antireflection coated). By minimising the number of tilt-fringes of the interference pattern the SIL can be aligned with respect to the sample within 0.1 mrad. After aligning the SIL to the sample, the microscope objective lens is put into place. By moving the objective lens in two lateral directions and monitoring the image on the camera the contact point between SIL and the sample can be found. Another way of aligning the optical axis of the objective lens with the optical axis of the SIL is by minimising the astigmatism that is induced by misalignment.

3. EXPERIMENTAL RESULTS

3.1 Evanescent coupling to a glass sample

With the static tester set-up we studied evanescent coupling of light to a bare glass sample with refractive index $n=1.48$ by measuring the amount of reflected light with a single photodiode at the position of the push-pull detector and by analysing the intensity distribution and polarisation state in the image of the exit pupil of the objective lens on the CCD camera. The experimental results were compared with simulations using the classical thin-film matrix formalism. This specific configuration with evanescent coupling to bare dielectric is relevant for the case of lithographic production of optical disk masters using a SIL. Near-field mastering systems have been proposed that control the SIL-to-master-disk distance with an actuator. The total amount of reflected light might serve as the error signal for the air gap servo in such a system [4].

In Figure 2 we show images of the reflected light intensity distribution recorded with the CCD camera for an air gap of 1000 nm and the axis of the analyser parallel (a) and perpendicular (b) to the polarisation direction of the irradiating beam. In Figures 2 (c) and (d) the simulated intensity distributions for the same polarisation states are shown. As can be seen from these images the rays that are focussed at angles larger than the critical angle are totally internal reflected at the bottom of the SIL, hence the bright ring outside NA=1. There is no evanescent coupling to the glass sample for this large air gap, only the rays within NA=1 propagate to the glass sample. The multiple reflections between the glass sample and the bottom of the SIL cause the interference pattern in the reflected light within NA=1. These concentric fringes may be used to align the optical axes of the objective lens and SIL. We also observe that, in agreement with theory, part of the reflected light has changed polarisation state from horizontal to vertical, most notably the parts of the pupil that are focussed at large angles to the bottom of the SIL since for the larger angles the difference between the Fresnel reflection coefficients for s and p polarisation is largest.

In Figure 3 we show images of the reflected light intensity distribution recorded with the CCD for an air gap of 100 nm and the axis of the analyser parallel (a) and perpendicular (b) to the polarisation direction of the irradiating beam. Figures 3 (c) and (d) depict simulated intensity distributions for the same polarisation states. In these images the bright ring at NA>1 has disappeared since the larger part of the light is transmitted into the glass sample by evanescent coupling.

a)   b)

c)   d)
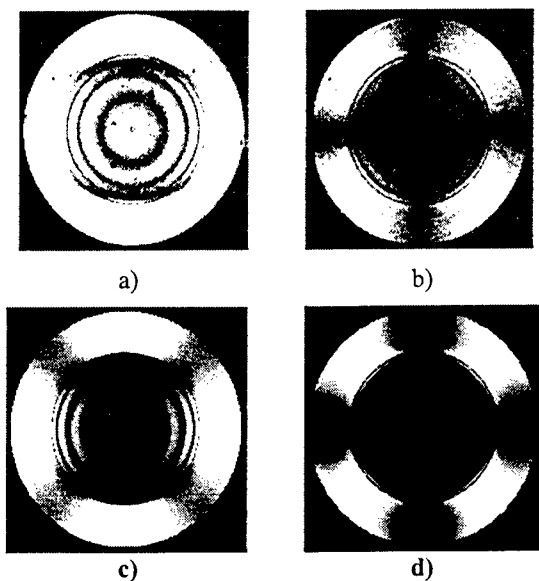
Figure 2. Images of the reflected light intensity distribution for an air gap of 1000 nm and the axis of the analyser parallel (a) and perpendicular (b) to the polarisation of the irradiating beam. In (c) and (d) the simulated intensity distributions are shown for the same polarisation states.

a)   b)

c)   d)
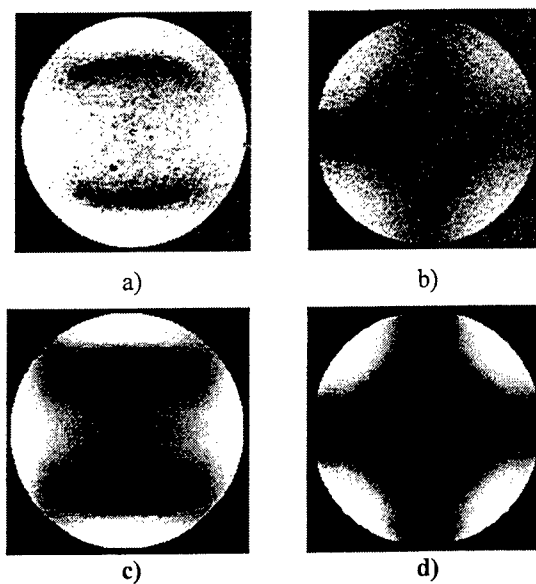
Figure 3. Images of the reflected light intensity distribution for an air gap of 100 nm and the axis of the analyser parallel (a) and perpendicular (b) to the polarisation of the irradiating beam. In (c) and (d) the simulated intensity distributions are shown for the same polarisation states.
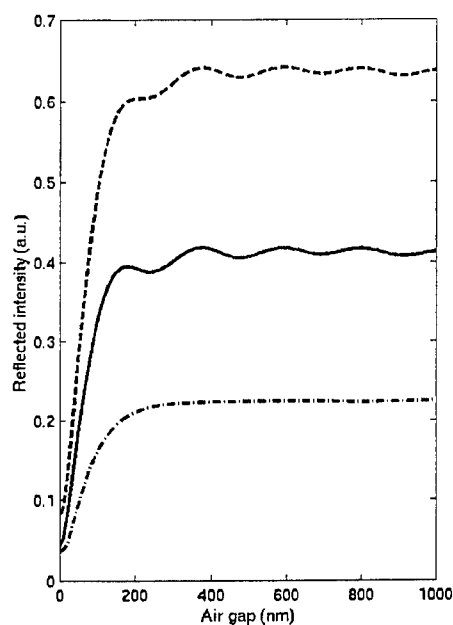
Figure 4. Simulation of the total amounts of the reflected light for the polarisation states parallel (—) and perpendicular (---) to the polarisation state of the irradiating beam, and the sum of both (--).
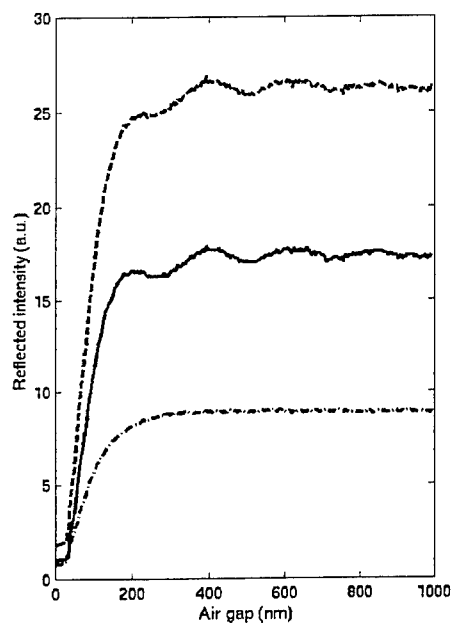
Figure 5. Measurement of the total amounts of the reflected light for the polarisation states parallel (—) and perpendicular (---) to the polarisation state of the irradiating beam, and the sum of both (--).

In Figures 4 and 5 we show the simulation and measurement of the total amounts of the reflected light for both polarisation states and the sum of both. These measurements were corrected for the reflection coefficients of the beam splitter for s and p polarisation. The measurements are in good agreement with theory, the evanescent coupling becomes perceptible below 200 nm and the total reflection drops almost linearly to a minimum at contact. This linear signal may be used as an error signal for a closed loop servo system of the air gap. The oscillations in the horizontal polarisation are caused by the reduction of the number of fringes within NA=1 (see Figure 2) with decreasing of the gap thickness.

3.2 Near-field coupling to a pregrooved disk

In the same setup we also studied reflective phase grating samples resembling portions of a pregrooved disc. The grating was written in a photoresist layer using an UV optical disc mastering machine. A 30 nm layer of aluminium was deposited on top of the grating after development. The resulting sample had a groove pitch of 300 nm, 50% duty cycle and a groove depth of 80 nm. The samples were mounted with the aluminium layer facing SIL.

In Figure 6 the CCD images are shown at air gaps of 750 nm, 250 nm and 40 nm for irradiation with the polarisation perpendicular to the grooves. At the large gap of 750 nm the $+1^{st}$ en -1st diffracted order can bee seen clearly within NA=1. The ring outside NA=1 is due to the total internal reflection at the bottom of the SIL. At an air gap of 250 nm the edges of the diffracted orders appear less sharp because of partial evanescent coupling of light at NA>1. At even smaller air gaps the edges become sharp again since most of the light at NA>1 is coupled to the grooves and, upon diffraction, is returned back into SIL. At a distance of 40 nm the diffracted orders fill the entire pupil, at this distance almost the full effective numerical aperture of 1.51 is reached.

a)   b)   c)
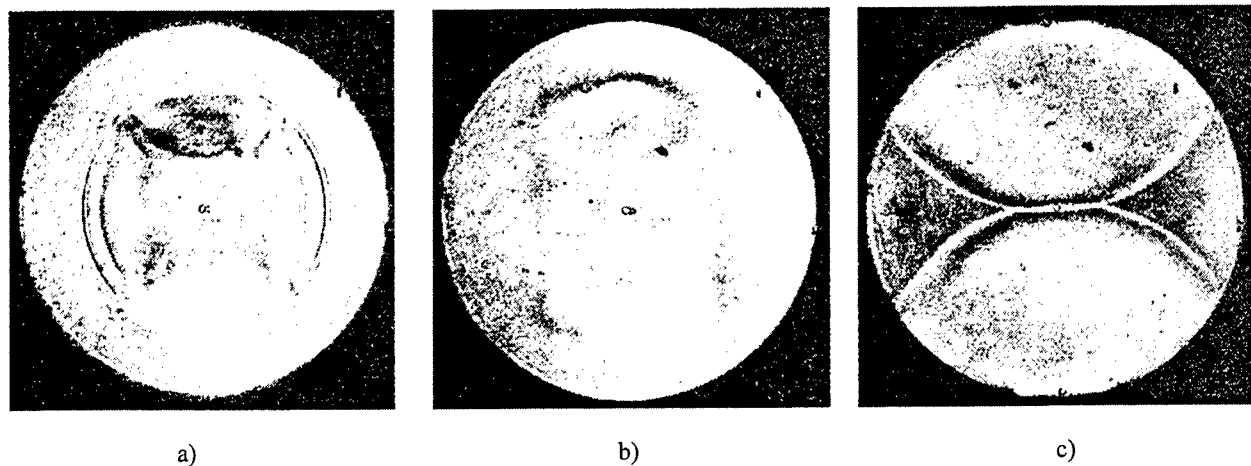
Figure 6. CCD images at an air gap of 750 nm (a), 250 nm (b) and 40 nm (c) for irradiation with the polarisation perpendicular to the grooves.

3.3 Push-pull signals

We measured the amplitude of the push-pull signal from the split photodiode with the focussed spot scanning perpendicular to the grooves of the above described pregrooved sample by driving the galvano mirror with an AC current. The push-pull signal we measured was the difference signal from the two split photodiode signals. The push-pull signal was not normalised to the sum of the signals as is usually done in practical optical storage systems. A sample of the push-pull signal for an air gap thickness equal to 20 nm is shown in Figure 7. In Figure 8 the push-pull signal is plotted versus the air gap with the polarisation of the irradiating beam perpendicular to the grooves and in Figure 9 parallel to the grooves. The procedure we used to determine the maximum push-pull signal was to move the test sample to a defined distance from the SIL and then determine the focus position at which maximum push-pull signal occurs. At larger air gaps we often found a strong push-pull at more than one focus position. A plausible explanation for this phenomenon is that aberrations caused by the objective lens, the SIL and also the air gap can be balanced with some defocus. Apart from the amount of defocus that yields a maximum push-pull signal, there may be other focus positions that result in a local maximum of the push-pull signal. Since the aberrations caused by the objective lens and the SIL and the air gap scale with the effective numerical aperture, and the amount of defocus at a certain focus position scales with the effective numerical aperture, the optimal focus position is not a constant but also varies as the air gap changes. The push-pull amplitude plotted in Figures 7 and 8 is the largest amplitude we found by choosing the optimal focus position at a given air gap. At air gaps larger than 300 nm the push-pull signal became very small so we limited the range of air gaps between 0 and 300 nm.

Both plots show that the push-pull amplitude decreases with increasing air gap size. This is readily understood since the modulation transfer function of the system deteriorates as the air gap thickness increases. There is, however, a difference between both plots. The push-pull signal does not appear to decrease between 100 and 200 nm air gap size when the polarisation of the irradiating beam is perpendicular to the grooves. So far, we do not have an explanation for this behaviour, it may be caused by the polarisation state alone, it might also be caused by aberrations from the objective lens, the SIL and the air gap. More detailed experiments are needed to gain a clearer picture of the influence of polarisation on the push-pull signal in the near-field regime.
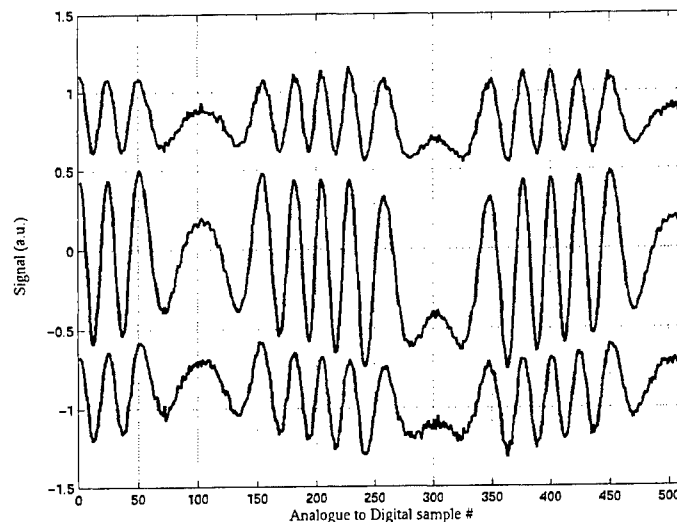
Figure 7. Push-pull signal at an air gap of 20 nm for polarisation of the irradiating beam perpendicular to the grooves. The push-pull signal (middle) is generated from the sum of one part of the split photodiode (upper signal) and the inverted signal of the other part (lower signal).
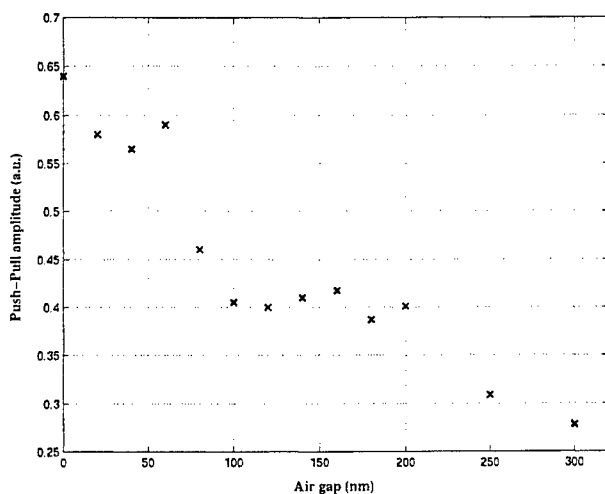
Figure 8. Measured push-pull signal versus the air gap with the polarisation of the irradiating beam perpendicular to the grooves.
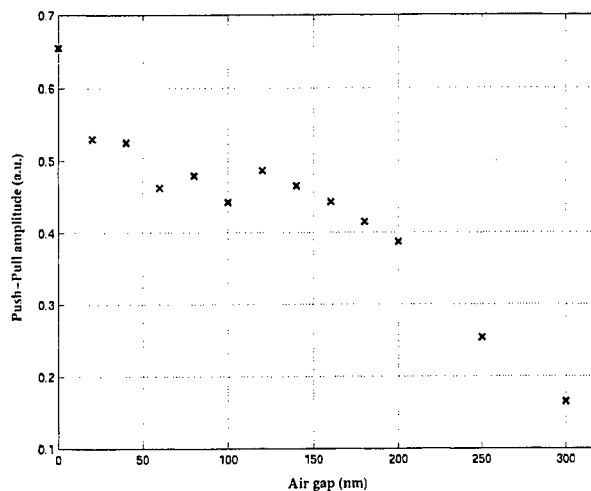
Figure 9. Measured push-pull signal versus the air gap with the polarisation of the irradiating beam parallel to the grooves.

4. CONCLUSION

We have built a near-field static tester set up equipped with a blue, 430 nm wavelength laser, a hemispherical solid immersion lens for systematic analysis of near-field related optical phenomena. In the system an effective numerical aperture of 1.51 can be achieved within a fraction of the evanescent decay length. Experiments show evanescent coupling to a glass sample that can well be described with classical thin-film theory. The push-pull signal from a reflective sample with 300 nm grooves has been measured as a function of air gap thickness. The Push-pull amplitude decreases as the air gap increases due to deterioration of modulation transfer function of the system. The Push-pull amplitude is also a function of the direction of polarisation of incident light.

5. ACKNOWLEDGEMENTS

6. REFERENCES

1. L.P. Ghislain, V.B. Elings, "Near-field scanning solid immersion microscope", *Applied Phyics Letters* **72**, pp. 2779-2781.
2. K. Hirota et.al. , "Nearfield Phase Change Optical Recording Using a GaP Hemispherical Lens*", Technical Digest ISOM/ODS* , 1999, pp. 361-363.
3. J.A.H. Stotz, M.R. Freeman, "A stroboscopic scanning solid immersion lens microscope", *Rev. Sci.Instrum.* **68**, pp. 4468-4477
4. S. Imanishi et.al., "Near Field Optical Head on Disk Mastering Process*", Technical Digest ISOM/ODS,* 1999, pp. 9-11.

Optical and thermal properties of SiN$_x$ for MO disks

Chih-Huang Lai, Cheng-Lin Huang, Chun-Yu Hsu, I-Nan Lin[+] and Jwo-Huei Jou
Department of Materials Science and Engineering, National Tsing Hua University, HsinChu, 300,
Taiwan, R. O. C.
[+]Materials Science Center, National Tsing Hua University, HsinChu, 300, Taiwan, R. O. C.

ABSTRACT

SiN$_x$ films were prepared by rf reactively sputtering. The refractive index of SiN$_x$ films was affected by total pressure and sputtering power. When the total pressure increased, the refractive index decreased. The reduction of sputtering power showed similar effect to raise the total gas pressure. The residual stress and roughness of SiN$_x$ films depended on the total pressure, sputtering power, and the thickness. The thermal cycles may result in irreversible change of residual stress of SiN$_x$ film. The magnetic properties of TbFeCo depended on the residual stress and roughness of SiN$_x$ in the trilayer SiN$_x$/TbFeCo/SiN$_x$ samples. The coercivity of TbFeCo was enhanced in the samples with SiN$_x$ films having low stress and large roughness.

Keywords: SiN$_x$ films, TbFeCo films. refractive index, magnetic properties, residual stress, roughness, MO.

1. INTRODUCTION

Amorphous rare earth-transition metal (RE-TM) films are commercially used for the magneto-optical (MO) recording medium[1,2]. However, the rare earth elements can be easily oxidized. Protecting dielectric films are needed to inhibit the corrosion. Amorphous SiN$_x$ films were commonly used in MO disks[1,2] and their optical properties were studied. Other dielectric films. such as AlSiN. AlSiON and SiO$_2$ were studied for altering the optical properties and for improving the protection capability[2]. Amorphous SiN$_x$ films may have large residual stress under certain deposition conditions[3,4,5] which may accompany with the change of the optical properties. RE-TM films were known to have large magnetostriction coefficients[6,7,8], so the stress state may affect their magnetic properties. As the result, the stress state in dielectric films may affect the magnetic properties of MO films. In this paper, SiN$_x$ dielectric films were deposited by rf reactively sputtering, and the effect of deposition conditions on the index of refraction was studied. In addition, the dependence of stress state and roughness of SiN$_x$ films on the deposition conditions was investigated. The correlation of magnetic properties of MO (TbFeCo) films with the SiN$_x$ properties is reported. Since the writing process of MO recording is of a thermal writing process, the thermal cycles are imposed to MO disks. Due to the difference of thermal expansion coefficient between films and substrates, the thermal stress may be developed during the thermal cycles. The thermal stress and its effect on the magnetic properties of MO films are discussed.

2. EXPERIMENTAL PROCEDURE

SiN$_x$ films, deposited in a planetary sputtering system, were reactively sputtered on Si (100) substrates by using a Si target and a rf power supply. The total working pressure, the sputtering power and the thickness were varied during the deposition to manipulate the optical properties of SiN$_x$. The trilayer of SiN$_x$/TbCoFe/SiN$_x$ was sequentially deposited on Si (100) substrates without breaking vacuum. An alloy target with composition TbFeCo(Tb:20 atomic%,Fe:72 atomic%,Co: 8 atomic%) was used for TbFeCo film. The base pressure before depositions was $3*10^{-7}$ torr. The deposition conditions for the TbFeCo film were the following:dc power=200W and total pressure=5mTorr. After depositions, x-ray diffraction was used for structural characterization, and atomic force microscope (AFM) was used for surface roughness measurement. The composition of films was determined by using Ruthoford backscattering (RBS). The index of refraction n of SiN$_x$ and the film thickness were measured by n & k analyzer with the light wavelength of 680 nm. The bending beam method[9] was carried out to measure thermal stress of SiN$_x$. The temperature was increased from 25 °C to 400 °C, and the thermal stress

was in-situ determined by the curvature of the samples. The residual stress in SiN$_x$ after depositions was measured by using wafer curvature The hysteresis loops of the trilayers were measured by perpendicular magneto-optical Kerr effect (PMOKE) at room temperature.

3. RESULTS AND DISCUSSIONS

In order to reduce noise, SiNx and TbFeCo need to be amorphous. From x-ray θ-2θ scans and grazing angle scans, SiN$_x$ and TbFeCo were verified as amorphous phases, as shown in Fig. 1. After thermal cycles up to 400 °C, both films still maintained their amorphous phases.
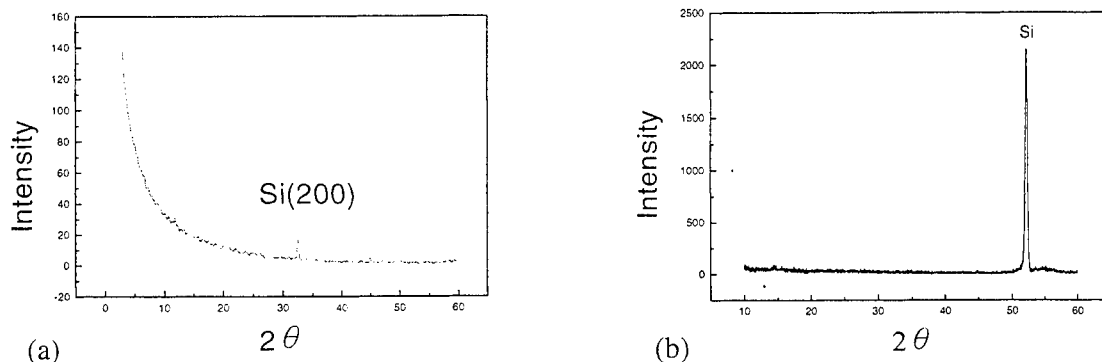
Fig. 1 X-ray scans of 90nm SiN$_x$/ 30nm TbFeCo/90nm SiN$_x$ trilayers. (a) θ-2θ scan (b) grazing angle scan.

The dependence of refractive index n on the total gas pressure is shown in Fig. 2. The n value decreased from 2.6 to 1.6 with increasing total pressure from 3 m torr to 15 m torr. When the total gas pressure increased during depositions, the kinetic energy of sputtered atoms arriving substrate surface decreased due to the scattering with ionized plasma. Consequently, the stacking density of SiN$_x$ films decreased with increasing total pressure. Refractive index is equal to the ratio of the light speed in vacuum to the speed in the medium (n=c/v). The light speed is faster in the less dense medium, and therefore the n value is smaller. In order to confirm the film density, SiN$_x$ was put into H$_3$PO$_4$ (85%, 180℃) solution, and the rate of wet etching is shown in Fig. 3. When the total pressure increased, the etching rate increased, consistent with the decrease in the film density.
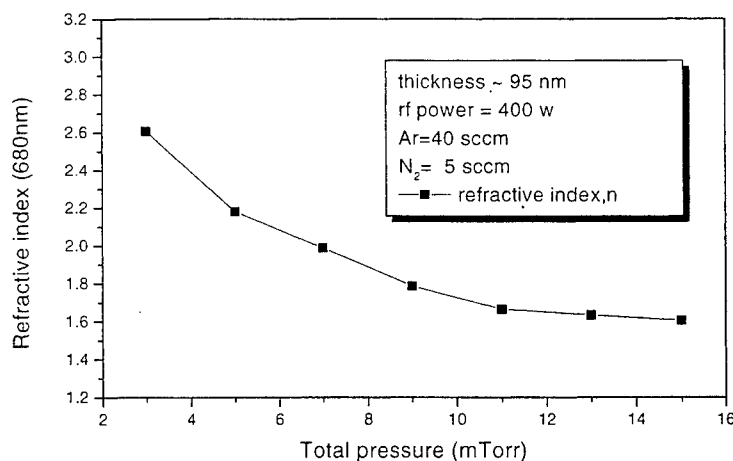
Fig. 2   Dependence of refractive index n of SiN$_x$ films on the total gas pressure. The deposition parameters of SiN$_x$ films are shown in the inset.
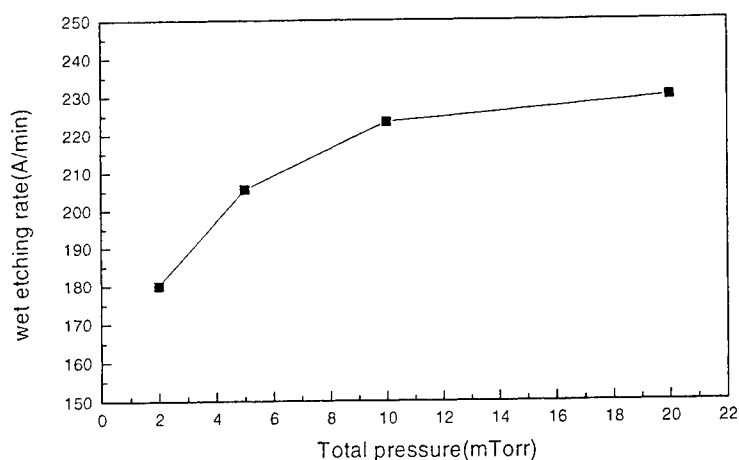
Fig. 3 Dependence of wet etching rate of SiN_x films on the total gas pressure. The etching solution is H_3PO_4 (85%,175℃) .

The dependence of the residual stress on the total pressure is shown in Fig. 4. At low pressure (2 m torr), the atomic pinning effect may be dominated, so the SiN_x film exhibited compressive stress[5]. When the total pressure increase, the atomic pinning effect is suppressed, and hence the compressive stress was reduced. When the total pressure was further increased, the film might become porous and the model of grain boundary relaxation can be applied[5,10,11]. The films deposited at high total pressure showed tensile stress. The surface roughness (root-mean-squre, r.m.s. roughness) was significantly increased with increasing total pressure, shown in Fig. 5. This relationship was commonly observed in other dielectric films. When the total pressure increased, the kinetic energy of sputtered atoms arriving substrates reduced so they could not land on the proper sites to reduce the roughness.
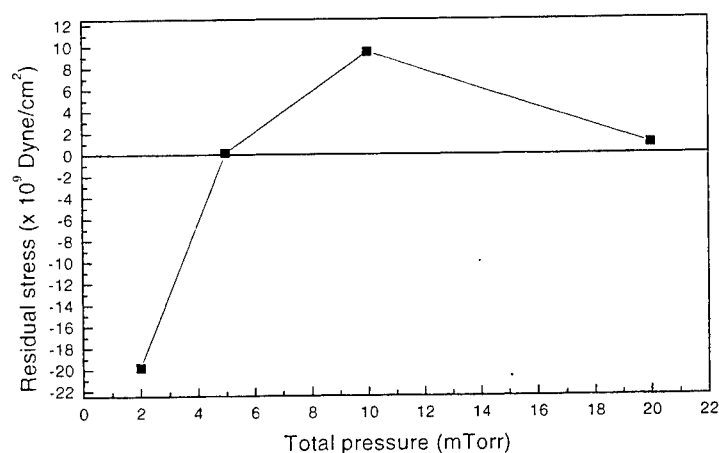
Fig. 4 Variation of residual stress of SiN_x films with the total gas pressure.
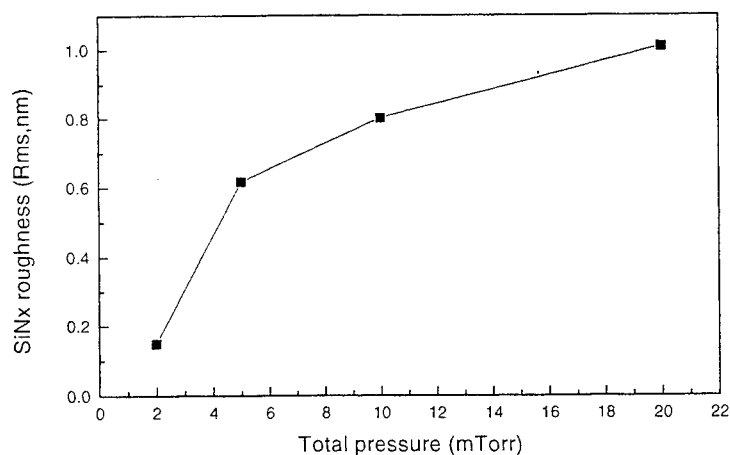
Fig. 5 Variation of root-mean-square (r.m.s.) roughness of SiN$_x$ films on the total gas pressure.

The variation of n with the sputtering power is shown in Fig. 6. The n value was reduced in the films deposited at lower rf power. When sputtering power reduced, the kinetic energy of sputtered atoms arriving the substrate surface was reduced. The effect is similar to the increase in the total pressure, resulting in less dense film, and therefore a lower refractive index. The roughness decreased with increasing sputtering power, shown in Fig.7., which resulted from the increase of kinetic energy of sputtered atoms; therefore, the film was smoother and denser for high sputtering power.
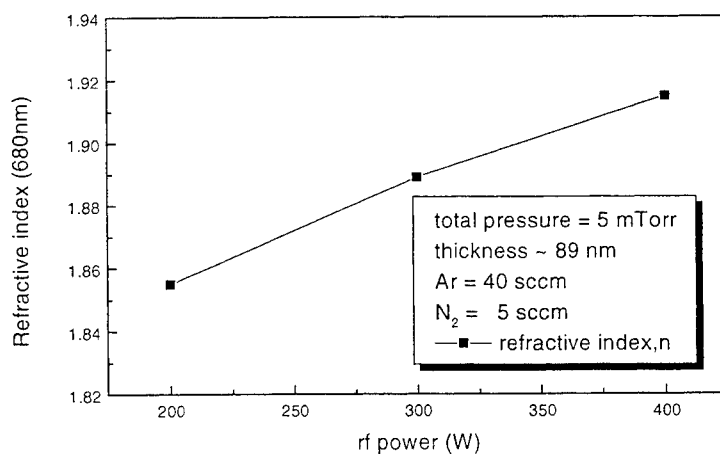
Fig. 6 Variation of refractive index n of SiN$_x$ films with the sputtering power.The deposition conditions are shown in inset.
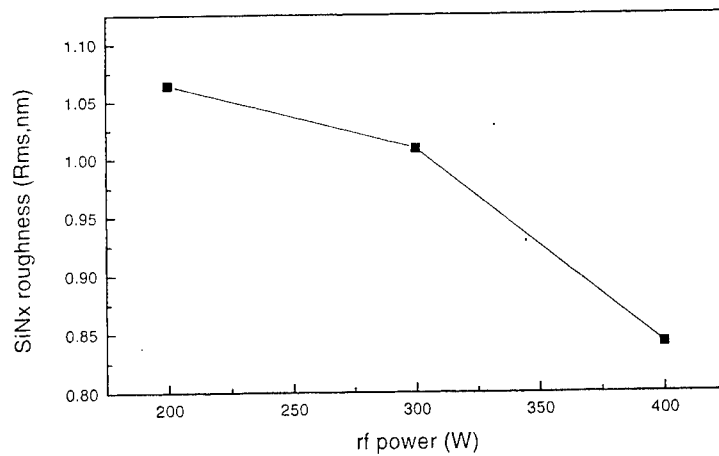
Fig. 7. Dependence of r.m.s. roughness of SiN_x films on the sputtering power.

The refractive index of SiN_x is insensitive to the film thick ranging from 50 nm to 400 nm, as shown in Fig. 8. In contrast, the residual stress and the surface roughness were strong functions of the film thickness. The residual stress and roughness increased significantly with increasing thickness, as shown in Fig. 8. and Fig. 9., consistent with other sputtered dielectric films. The SiN_x developed the columnar structure during the sputtering process, so the stress and roughness can be added up within each column. Consequently, both the stress and roughness increased when the films became thicker.
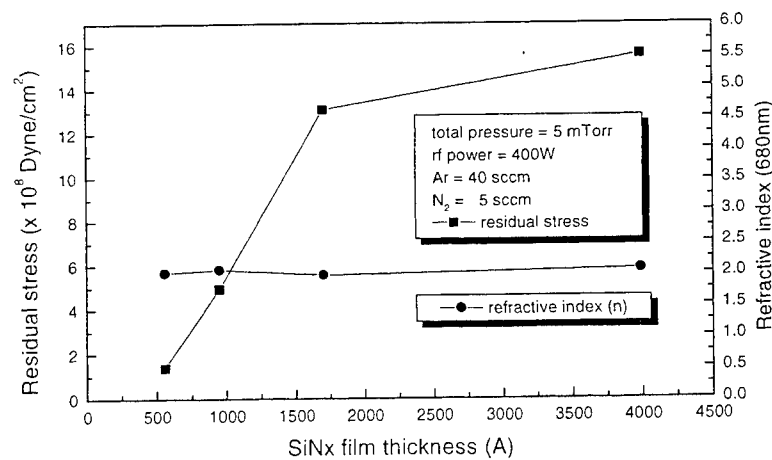
Fig. 8. Dependence of the refractive index and the residual stress and on the SiN_x film thickness.
The deposition conditions are shown in inset.

32
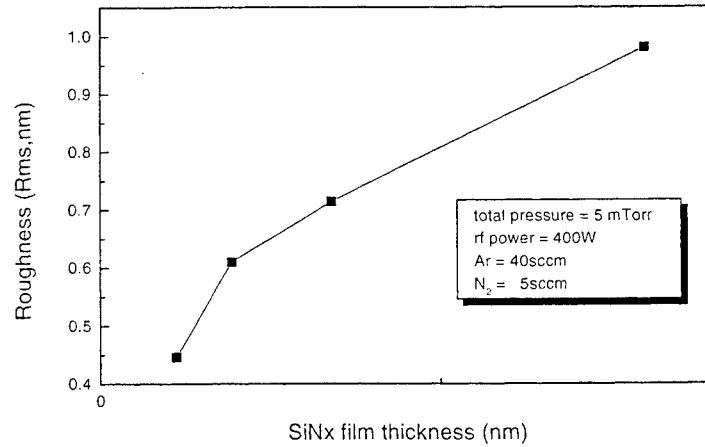
Fig. 9. Dependence of the r.m.s. roughness on the SiN$_x$ film thickness.

The measurement of thermal stress of SiN$_x$ films was carried out at the temperature ranging from 25 °C to 400 °C. During the cooling process, the residual stress became toward tensile stress ,as shown in Fig. 10. During the heating process, the stress almost unchanged. After thermal cycles, residual stress exhibited irreversible change. For the specific sample shown in Fig. 10., after two thermal cycles, the stress changed the sign, from compressive stress to tensile stress. The irreversible change of the stress may result from two reasons: difference of thermal expansion coefficient between the film and subtrate and (or) change of local atomic arrangement. The detailed study of the stress change due to the thermal cycles is currently under investigation.
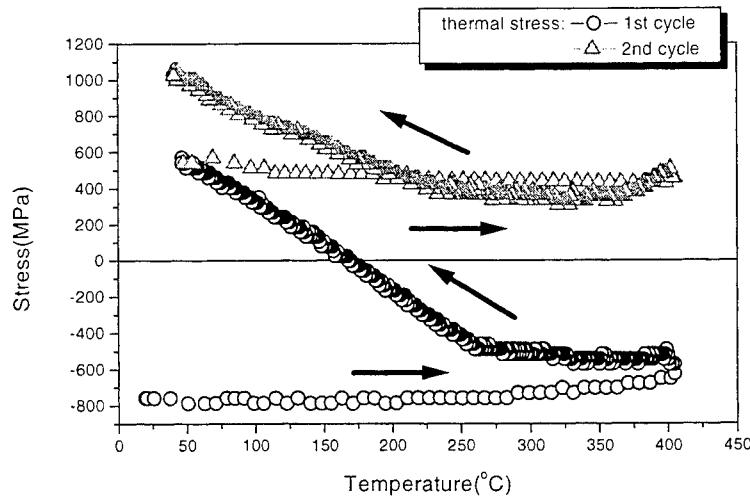
Fig. 10. Relationship between the residual stress of SiN$_x$ films and temperature. Residual stress decreased during the cooling process and almost unchanged in the heating process. After two thermal cycles, the residual stress changed from compressive to tensile.

The hysteresis loop of the trilayer sample 90 nm SiN_x/40 nm $TbFeCo$/90 nm SiN_x is shown in Fig. 11. The perpendicular anisotropy was observed with the coercivity of 11000 Oe. Several deposition parameters were varied to manipulate the stress state and roughness of SiN_x films, but meanwhile the deposition conditions for TeFeCo films were maintained to investigate the effect of SiN_x properties on the magnetic properties of TbFeCo films. The summary of the r.m.s. roughness, residual stress and coercivity of different samples, is shown in Table. 1. The sample A has almost zero residual stress and the highest roughness, showing the highest perpendicular coercivity (~11000 Oe). The hysteresis loop of sample A is shown in Fig. 11. Comparing sample B and C, the magnitude of r.m.s. roughness of SiN_x films is about the same, but the tensile stress in sample B is almost 100 times larger than in sample C. The coercivity of sample B is much less than that of sample C. Sample D and E have similar compressive stress in SiN_x films, but have different r.m.s. roughness. Large roughness in sample D seemed to enhance the coercivity. Based on these results, the roughness and stress in SiN_x may play important roles to determine the magnetic properties of TbFeCo films. It is plausible that the residual stress in SiN_x may affect the stress state in TbFeCo films. Because of high magnetostriction coefficient in TbFeCo films, the stress state can significantly affect the anisotropy of TbFeCo, and hence the coercivity. Roughness in SiN_x films may provide extra pinning sites in TbFeCo films. Consequently, the coercivity is enhanced in the samples with large roughness.
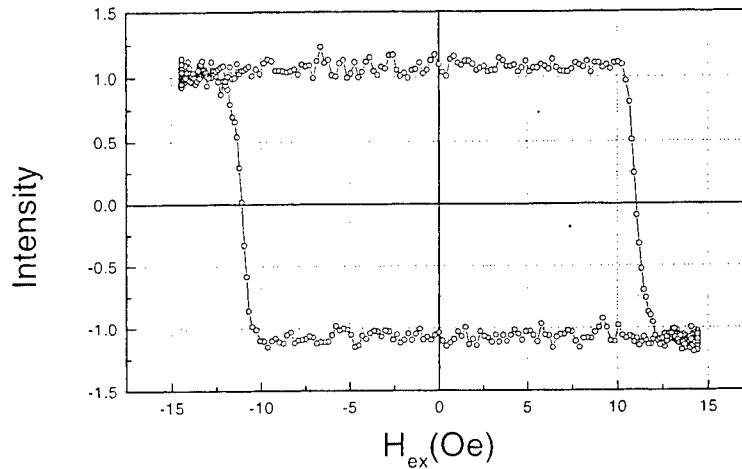
Fig. 11 Hysteresis loop of SiN_x/TbFeCo/SiN_x measured by PMOKE at room temperature. The residual stress of SiN_x in the smaple is almost zero and the r.m.s. roughness of SiN_x is 10 Å.

Table 1 Summary of r.m.s. roughness, residual stress, and coercivity of trilayer SiN_x/TbFeCo/SiN_x samples. The r.m.s. roughness and residual stress are the values in SiN_x films.

	Rms	Residual stress dyne/cm^2	Hc(kOe)
Sample A	10.093Å	~ 0	11.0705
Sample B	8.03Å	9.48E+09	6.63148
Sample C	8.42Å	1.52E+08	10.8095
Sample D	7.508Å	-7.58E+09	10.05418
Sample E	1.5Å	-1.98E+10	3.4227

4. CONCLUSIONS

SiN$_x$ films were prepared by rf reactively sputtering. The refractive index of SiN$_x$ films were affected by total pressure and sputtering power. When the total pressure increased, the kinetic energy of sputtered atoms arriving substrates decreased. Consequently, the films became less dense, so the refractive index decreased. The reduction of sputtering power showed similar effect to raise the total gas pressure. The residual stress and roughness of SiN$_x$ films depended on the total pressure, sputtering power, and the thickness. By adjusting the deposition parameters, the residual stress and roughness of SiN$_x$ films can be manipulated. The thermal cycles may result in irreversible change of residual stress. The magnetic properties of TbFeCo depended on the residual stress and roughness of SiN$_x$ in the trilayer SiN$_x$/TbFeCo/SiN$_x$ samples. The coercivity of TbFeCo was enhanced in the samples with SiN$_x$ films having low stress and large roughness.

REFERENCES

1. Terry W. McDaniel and Randall H. Victora, *Hand Book of Magneto-Optical Data Recording*, Noyes publications, U.S.A., 1997.
2. M. Asano, M. Kobayashi, Y. Maeno, K. Oishi, and K. Kawamura, "Magneto-optical recording media with new protective films ," *IEEE Transactions on Magnetic* Vol. MAG-23, No.5, pp. 2620-2622, September 1987.
3. R. W. Knoll, C. H. Henager, Jr. "Optical and physical properties of sputtered Si:Al:O:N films," *J. Mater. Res.* Vol. 7, No. 5, pp. 1247-1252, May 1992.
4. Joo Han Kim and Ki Woong Chung. "Microstructure and properties of silicon nitride thin films deposited by reactive bias magnetron sputtering ,"*J.Appl. Phys.* vol.83, No.11, pp. 5831-5839,1 June 1998.
5. Henry Windischmann, "Intrinsic stress in sputter-deposited thin film,"*Critical Reviews in Solid State and Materials Sciences,*17(6), pp. 547-596,1992.
6. Clark, A. E., "Magnetostriction and magnetoelastic properties of highly magnetostrictive Rare Earth-Iron laves phase compounds,"*Polymer Preprints, Division of Polymer Chemistry, American Chemical Society Magn and Magn Mater, Conf, 19th, Annu. Proc,* Nov 13-16 1972 Nov 13-16 197 2 1974 *AIP (Conf Proc* n 18 New York pp. 1015-1029.)
7. Clark, Arthur E.; Belson, Henry S., "Magnetostriction of Terbium-Iron and Erbium-Iron alloys," *IEEE Transactions on Magnetics* v MAG-8 n 3 pp. 477-479 ,Sep 1972.
8. Arai, K. I.; Tsuya, N.; Sato, K.; Adachi, K., "Magnetostriction measurements of COS//2 single crystall,"*Journal of Magnetism and Magnetic Materials* v 1 n 1 pp. 55-57, Oct 1975.
9. Min-Yung Han, Jwo-Huei Jou, "Determination of the mechanical properties of r.f.-magnetron-sputtered zinc oxide thin films on substrates, "*Thin Solid Film* 260, pp. 58-64,1995.
10. Jwo-Huei Jou and Min-Yung Han, "Substrate dependent internal stress in sputtered zinc oxide thin films, "*J.Appl. Phys.* 71(9), pp.4333-4336. 1 May 1992.
11. Y. G. Shen, Y. W. Mai, Q. C. Zhang, D. R. McKenzie, W. D. McFall and W. E. McBride, "Residual stress, microstructure, and structure of tungsten thin films deposited by magnetron sputtering," *J. Appl. Phys.* vol.87, No.1, pp.177-187,1 January 2000.

SESSION 2

DVD and Drive

Perspective and future of DVD-RAM

Takeshi Maeda

Central Research Laboratory, Hitachi Ltd.,

1-280 Higashi-Koigakubo, Kokubunji-shi, Tokyo 185-8601 Japan

ABSTRACT

This paper reports the perspective and future of DVD-RAM. The standardization of DVD-RAM and future technologies are described.

Keywords: DVD-RAM, Phase change media, Standardization, Land and Groove format

1. INTRODUCTION

To describe the perspective and future of DVD-RAM, firstly, the standardization of DVD-RAM is reported and secondly, the future technologies is reported.

2. INTERNATIONAL STANDARDIZATION

2.1 Standardization of DVD-RAM in 1999

DVD-RAM disk standard and case standard were proposed as DIS (Draft International Standard) with FTP (Fast Track Procedure) by Japan, and approved as an international

Standard (IS) through a post voting. After that, Annex L (Informative) was eliminated from ECMA standard of DVD-RAM. Then the organization SC23 heard an opinion of each country about a proposal of Annex L elimination, so that the elimination of Annex L was recognized. Based on this, the standardization document was sent ITTF(Information Technology Task Force) by SC23, and it was published as an international standard of ISO/IEC in May, 1999.

The number of international standard is as follows.

ISO/IEC 16824 Information technology - 120 mm DVD rewritable disk (DVD-RAM)

ISO/IEC 16825 Information technology - Case for 120 mm DVD-RAM disks

2.2 Specification and technology of next generation DVD-RAM

The physics specification of DVD-RAM ver.2.0 (4.7 GB / 4.7 GB / side), which is the next generation of DVD-RAM ver.1.0 (2.6 GB / 2.6 GB / side) was published in September, 1999. DVD-RAM ver.1.0, and ver.2.0 prescribe about a disk of 120 mm diameter, but 80 mm diameter disk will adopt the specification of physical format same as ver.2.0.

The specification which includes the specification ver.2.0 of 120 mm diameter and 80 mm diameter disk, is expected to be published in spring, 2000 as standard ver.2.1. The specification / technology outline is reported as follows based on DVD-RAM ver.2.0 specification published already.

(1)Basic specification of DVD-RAM ver.2.0

The most important characteristic of DVD-RAM ver.2.0 is to keep a downward compatibility. Even though recording bit length and track pitch were made narrow so that the recording capacity could increase with approximately 1.8 times from 2.6 GB per one side of ver.1.0 to 4.7 GB per one side, other physical specifications are not changed at all. Furthermore, a important characteristic is to make a data transfer-rate speed up to 22.16 Mbit / sec (Mbps), which is 2 times as fast as DVD-RAM ver.1. Main specifications of DVD-RAM ver.2.0, DVD-RAM ver.1.0 and DVD-ROM ver.1.0 are shown in table 2.2.1.

(2)Technology outline of DVD-RAM ver.2.0

In DVD-RAM ver.2.0, an interchangeability with DVD-ROM is attached importance like DVD-RAM ver.1.0

Thickness of disk substrate, laser wavelength, numerical aperture of object lens, are selected a value same as one of DVD-ROM. As for recording media a phase change media, which has the same read-out principle as DVD-ROM is adopted. Therefore, it is possible to read DVD-RAM by a head of DVD-ROM.

In addition, modulation code and ECC (Error correction code) is adopted same system as DVD-ROM, so that the same signal processing circuit as DVD-ROM is utilized. Recording surface on a disk is divided into 35 zones with the shape such as a doughnut. ZCLV (Zoned Constant Linear Velocity) record system, which changes a rotation between zones and keeps it constant in each zone, is adopted in order to make a recording density and transfer-rate fixed from the inside to the outside of a disk. Here, sector number per a track at the most inner zone is 25.

As for recording format, Land and Groove format, which is able to be superior to cross-talk cancel same as ver.1.0 and make a track pitch narrow, is used. A overview of recording format is shown in figure 2.2.1 (a). Recording track consists of a spiral land and a groove. A land and a groove are connected with each other at one point in turn and the groove replaces automatically to the land (the reverse is also true), so that a single spiral track is formed. This track is wobbled with a single frequency and same phase.

Furthermore, a header part of each sector is arranged as a staggered shape at a boundary part between a groove track and a land track like ver.1.0, as shown in figure 2.2.1 (b). Identification information of each sector (ID, sector number) is formed in 4 folds (ID1, 2 show a sector number of a next land track and ID3, 4 show a sector number of current groove track) so as to decrease the possibility that an address information can't be detected by defects.

The address error rate is restrained even enough to be able to bear computer use by combination of this header construction with above mentioned wobbling of a track. Furthermore, in ver. 2.0, the following new functions are added to ver. 1.0.

(1)A flexible defect management method, to utilize the data volume effectively, was equipped with in Ver2.0, so that DVD-RAM can be applied for real-time AV recording.
(2) the adaptive recording control that recording pulse wave shape is changed according to recording pattern was adopted as shown in Fig.2.2.3. The control information for a adaptive recording control is pre-recorded as a table in a control information part on a disk. A drive system reads the table and uses it at recording, so that a most suitable recording is utilized.
(3)The same BCA as DVD-ROM is equipped with, and all disks are able to identify each other, so that data security is guarded perfectly in DVD-RAM.

As described above, in DVD-RAM ver.2.0, transfer rate of 22.16 Mbps, which is 2 times as fast as ver.1.0 are realized. It is expected that application for DVD-RAM spreads by a higher transfer-rate. For example, when recording a picture of MPEG2, many channel of normal TV quality is able to record simultaneously, and record the most high quality picture of MPEG2 needed transfer-rate of 15 Mbps. About the details of specification of DVD-RAM ver.2.0, refer to DVD forum publication.

3. FUTURE TECHNOLOGY

3.1 Introduction

2.6 GB per one side of DVD-RAM really went to a market last year, and a technology announcement for DVD-RAM of 4.7 GB per one side and DVD-R/W was done as the next product. Furthermore, the technology development that realize a phase change disk of larger capacity is proceeded. So, a trend of a future technology of phase change optical disk was investigated. A high density read/write technology is described in 3.2, media technology is done in 3.3, and other technical is mentioned in 3.4.

3.2 High density read/write technology

In DVD-RAM, a road map to achieve a recording capacity 15 GB / one side as a next generation is announced clearly as shown in Fig.3.2.1, but possibility of the more large capacity is examined because the capacity of more than 20 GB is required in order to record a signal of HD broadcast (HDTV) (TS stream of MPEG2) for more than 2 hours.

As for blue violet semiconductor laser, which is a key component for higher density, a laser of low output power of GaN which is available for a read-only type optical disk went on a market in October, 1999.
The rated output power is 5mW, and maximum power is 10mW. The life time is 10000 hours at room temperature, and 1000 hours at 50 ℃. Other 4 companies reported continuous emission of GaN blue violet laser at room temperature. On the

other hand, a high power laser of the order of 30 m W is needed for recording, but the emission for 400-500 hours with light output 30mW at 60 °C has been already reported [1] and the continuous emission with 30 mW at room temperature is reported by some organizations. [2] The development of high output power laser of blue violet GaN is accelerated.

However, reports about read/write technology using GaN laser are still limited [3),4),5),6)] because it is difficult to get a high output power laser of blue violet GaN. Many reports is related to read only optical disk system. As for a rewritable optical disk system, there are very many reports using Kr ion gas laser instead of blue violet semiconductor laser at present. However, it is thought that reports using a blue violet GaN laser increase.

As for cutting technology of master disk, which is fundamental for higher density, there were two remarkable reports. [7] (1)The technology of Deep-UV cutting using 266nm solid laser has been already reported. In addition, record wave shape is controlled and jitter value is improved. Kr ion laser is used for read-out evaluation, and factors of jitter ingredient is analyzed. This technology needs a special developing process for chemically amplified resist. (2)Near field technology, which uses SIL(NA=1.4), was combined with blue ion gas laser and applied for cutting machine. The method that uses piezo device or air suspension in order to control a narrow gap between SIL and surface on disk is proposed.[8] This technology doesn't need a special process such as a mastering using 266nm laser. So, a current developing process is continued to use even at next generation.

As for increasing a capacity and transfer-rate for the next generation of DVD, there are two flows. One is to attach importance to interchangeability with current DVD, the other is to make NA higher than current optics combined with thin cover layer. The former technology is based on shortening laser wavelength and so on, can reach a capacity of the order of 15 GB. The latter technology doesn't succeed in a current read-out principle that a substrate doubles with a cover layer and separates each other. The aberration caused by high NA is eliminated because light goes through thin cover layer. This technology demonstrated a experimental result of 8 GB using red laser and possibility of 22 GB using blue violet laser.

These are described in detail as follows.
When reaching the capacity of 15 GB combining same substrate and NA as DVD with blue laser, all kinds of margin get narrow. The many means are proposed to solve this problem.[9),10),11),12)] There are cross-talk chancellor for track offset reduction and tilt compensation technology. Four axis lens actuator that has tilt compensation and mechanism for tilt compensation that mirror changes in two axis are proposed.[13]

As for a system using a high NA lens and thin cover layer, a joint research is announced as HD picture recorder system of next generation.[3),5),6)] Element technologies have already reported, but an announcement compromised these as a concept of recorder has never been. A recording layer is formed on substrate of 1.1 mm thickness, and the cover layer of 0.1 mm is formed on it by spin overcoat and laminate sheet, so that the disk is formed. Thickness allowance of a cover layer is $\pm$ less than 3 micron meter. New ECC which reinforces error correction ability against a dust, a fingerprint, and wound because the cover layer is thin is proposed. Modified (1,7) modulation code to improve DC suppression capability is adopted. As for track format, land and groove construction wobbled is adopted same as DVD-RAM and zone CAV to shorten access time is adopted. The format efficiency becomes 79 % between 75 % of DVD-RAM and 84 % of DVD-ROM. The experiment result that uses red laser demonstrated capacity of 9.2 GB, data transfer rate of 33 Mbps were provided, and real-time recording of compressed HD picture. If blue violet laser is used for this system, large capacity of 22 GB is expected.

As another approach for higher density of phase change medium, a experimental result of multi-level recording is reported.[4] By using four level, it is mentioned that CNR reached more than 50dB. Furthermore, as means of other promising approach, there was a great progress in super solution technique. The organic dye which can be made by spattering has a reversible characteristic of transmission and high sensitivity at blue wavelength is provided. The read-out principle are known RAD (Rear-aperture detection) types in magneto-optical disk. The effect of super resolution is proven since this method can read out a signal of 0.2 μ m mark from RW phase change media recorded crescent marks with variable length to 0.15 μ m. It is demonstrated that this method can reach approximately two times as large capacity as RW disk.[5]

3.3 Media technology

(1) medium construction

To record HD picture, not only large capacity but high data transfer-rate are required. Therefore, the media with construction suitable to high speed recording has been developed. The medium construction that Si layer was added to GeSbTe recording layer, its recording layer was put with SiC layers is developed in order to establish heat balance of horizontal and vertical directions and make crystallization velocity fast, so that transfer rate improved to 36 Mbps.[16] Double layer per one side disk added Al layer to this construction is developed, so that capacity of online access increases to 16.8 GB and data transfer rate becomes 27 Mbps.[15] Problems of double layer per one side such as leak to signal from embossed header of under layer and deference of recording power between double layers are pointed out.[17]

Furthermore, in the case of recording method combining high NA and the thin cover layer with blue laser, it is investigated to improve media construction for high date transfer rate, too.
Using SiN instead of SiC raises up crystallization velocity and obtains data transfer rate of 35 Mbps. Jitter of 8 % is provided under the condition of capacity of 22 GB.[17]

(2) recording materials
As for recording materials, GeSbTe have been mainly examined to satisfy the demand of higher data transfer rate and many cycle times such as DVD-RAM. However it has been reported recently that even AgInSbTe are possible.[18] It is assumed that transfer rate becomes fast when mark becomes small by small recording spot depended on difference of erase process in the case of AgInSbTe. It is assumed that a combination of 685nm and NA0.6 makes transfer-rate of more than 41Mbps possible and combination of 400nm and NA0.85 makes transfer-rate of 50 Mbps possible. It is hoped to investigate more in detail from point-view of selecting material.

To eliminate initialization of DVD-RAM, new construction that Sb_2Te_3 was added to recording layer makes crystallization easy at lower temperature and crystallization velocity fast is reported.[19]

3.4 Simulation of phase change mechanism

There are many reports about simulation related to read/write mechanism of phase change media.[20,21,22] One uses a molecule orbitacle model and tries to explain a transition between crystallization and amorphous of phase change media.[20] It is possible to succeed in macro model mentioned next.

The through simulation from recording process to reading process using the macro model has been already reported. This simulation is applied for 4.7GB DVD-RAM. It is proven by comparing a experimental data with a simulation result that an adaptive control method that is introduced for interchangeability is effective.[21]

3.5 other technology

As for near field recording, it is remarkable report that a smaller aperture than wavelength was arranged in an surface of semiconductor laser and marks are directly recorded on a phase change media of GeSbTe without an optics.[23] The aperture is 250nmnm , CNR is obtained 45dB under the condition of line and space of 150 nm, and track pitch of 500nm, recording rate becomes 24 Mbps. It is hoped to make more speed up when narrowing the aperture.

As for super resolution technology, super-RENS has a big progress. Reflection construction is adopted, and SNR can be improved largely using AgOx as
materials.[24] Furthermore, novel super resolution technology that use the beat effect in a spacial frequency with a grating is proposed.

3.6 Summary of future technology

(1) The recording method combining high NA and thin cover has realized higher transfer-rate and larger capacity.
Furthermore, transfer-rate of 35 Mbps is necessary for HD picture but this rate has been limited to 18 Mbps. However, combination of blue violet laser and improvement of media construction rises up transfer rate to 35 Mbps.
(2) The output power of 5mW of blue violet GaN laser has gone on market. As for the high output power laser of 30mW, continuous emission at room temperature for 400-500 hours was reported. The blue violet GaN laser has progressed greatly toward practical use.

(3)There are a proposal of VSAL(very small aperture laser) technology and demonstration of possibility of higher density using this device, report about CNR improvement in super-RENS by reflection construction and so on. The possibility to further high density recording progresses.

Reference:
1. S. Nakamura et al. : Ext. Abstr. (60th meeting1999); Japan Society of Applied Physics and Related Societies, 4p-W-7 [in Japanese]
2. T. Asazuma et al. : Ext. Abstr. (60th meeting1999); Japan Society of Applied Physics and Related Societies, 4p-W-74p-W-6 [in Japanese]
3. T.Narahara, S.Kobayashi, M.Hattori and Y.Shimpuku: ISOM/ODS'99 TECHNICAL DIGEST, MD1(1999)50
4. M.Shinotsuka, N.Onagi, M.Harigaya, YU.Kageyama and M.Umehara: ISOM/ODS'99 TECHNICAL DIGEST, ME-02(1999) Post dead line Paper
5. K.Kurokawa, M.Naito, K.Yasuda, T.Kashiwagi and O.Kawakubo: ISOM/ODS'99 TECHNICAL DIGEST, WA4(1999)197
6. B.Tieke, M.Dekker, N.Pfeffer, R.van Woudenberg, G.F.Zhou and I.P.D.Ubbens: ISOM/ODS'99 TECHNICAL DIGEST, WA5(1999)200
7. M.Takeda, M.Furuki, T.Ishimoto, K.Kondo, M.Yamamoto and S.Kubota: ISOM/ODS'99 TECHNICAL DIGEST, MA1(1999)2
8. S.Imanishi, T.Ishimoto, Y.Aki, T.Kondo and M.Ymamoto: ISOM/ODS'99 TECHNICAL DIGEST, MA4(1999)9
9. S.Yamada, S.Nishiwaki, A.Nakamura, T.Ishida and H.Yamaguchi: ISOM/ODS'99 TECHNICAL DIGEST, MB2(1999)17
10. Y.Motegi, M.Nagasato, Y.Ishibashi, H.Soneya and N.Kikukiri: ISOM/ODS'99 TECHNICAL DIGEST, MB3(1999)20
11. C.Inokuchi, T.Akagi, S.Nishiwaki, K.Nagashima, A.Miyazaki and H.Yamaguchi: ISOM/ODS'99 TECHNICAL DIGEST, MB4(1999)23
12. T.Shihara, K.Watanabe, S.Kadowaki and H.Ishibashi: ISOM/ODS'99 TECHNICAL DIGEST, MB6(1999)29
13. H.-W.Lee: ISOM/ODS'99 TECHNICAL DIGEST, TuD26(1999)184
14. T.Ohta: ISOM/ODS'99 TECHNICAL DIGEST, WA1(1999)188
15. M.Hatakeyama, T.Ando, K.Tsujita, K.Oishi and I.Ueno: Proceedings of PCOS'99(1999)26
16. Y.Kuroda, Y.Kasami, M.Ono, S.Takagawa, K.Seo, M.Yamada and O.Kawakubo: ISOM/ODS'99 TECHNICAL DIGEST, WA3(1999)194
17. K.Kurokawa, Y.Kasami, Y.Kuroda, S.Takagawa, K.Yasuda, K.Seo and O.Kawakubo: Proceedings of PCOS'99(1999)22
18. H.J.Borg, P.W.M.Blom, B.A.J.Jcobs, B.Tieke, A.Wilson, I.P.D.Ubbens and G.F.Zhou: ISOM/ODS'99 TECHNICAL DIGEST, WA2(1999)191
19. X.S.Miao, T.C.Chong, L.P.Shi, P.K.Tan and F.Li: ISOM/ODS'99 TECHNICAL DIGEST, WD15(1999)285
20. T.Uehara and T.Inoue: Proceedings of PCOS'99(1999)6
21. H.Kando, H.Minemura, A.Hirotsune, M.Miyamoto, M.Terao, T.Maeda and R.Imura: Proceedings of PCOS'99(1999)99
22. T.C.Chong, L.P.Shi, Z.R.Li and R.Zhao : Proceedings of PCOS'99(1999)42
23. A.Partovi: ISOM/ODS'99 TECHNICAL DIGEST, ThC1(1999)352
24. J.Tominaga, T.Nakano, M.Kuwabata, T.Fukaya N.Atoda, H.Fuji and H.Katayama: Proceedings of PCOS'99(1999)39

Table 2.2.1 Main specifications of DVD-RAM

Items	DVD-RAM ver. 2. 0	DVD-RAM ver. 1. 0	DVD-ROM ver. 1. 0
Capacity	4. 7 GB／side	2. 6 GB／side	4. 7 GB／side
Transfer-rate	22. 16 Mbps	11. 08 Mbps	11. 08 Mbps
Diameter	120 mm	120 mm	120 mm
Thickness substrate	0. 6 mm×2	0. 6 mm×2	0. 6 mm×2
Recording method	Phase change	Phase change	Embossed pits
Wavelength	650 nm	650 nm	650 nm
NA	0. 6	0. 6	0. 6
Bit length	0. 28 μ m	0. 42 μ m	0. 267 μ m
Track pitch	0. 615 μ m	0. 74 μ m	0. 74 μ m
Track format	Wobbled L&G	Wobbled L&G	Pits line
Physical address	Embossed pits	Embossed pit	Embossed pits
Modulation code	RLL (2, 10) 8-16	RLL (2, 10) 8-16	RLL (2, 10) 8-16
Sector size	2048 B	2048 B	2048 B
ECC	RS Product code	RS product code	RS product code
Block of ECC	16 sector	16 sector	16 sector
Recording(zone)	Z C L V (35 zones)	Z C L V (24 zones)	C L V
Defect management	resent	present	none

DVD-RAM Disc Outline
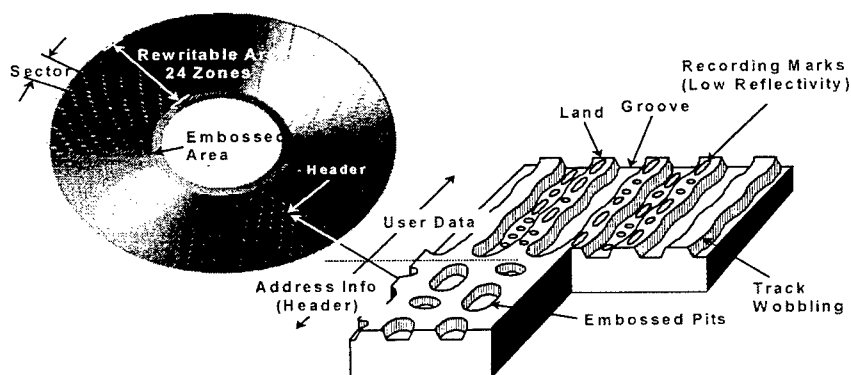
Figure 2.2.1 (a) Outline of DVD RAM format
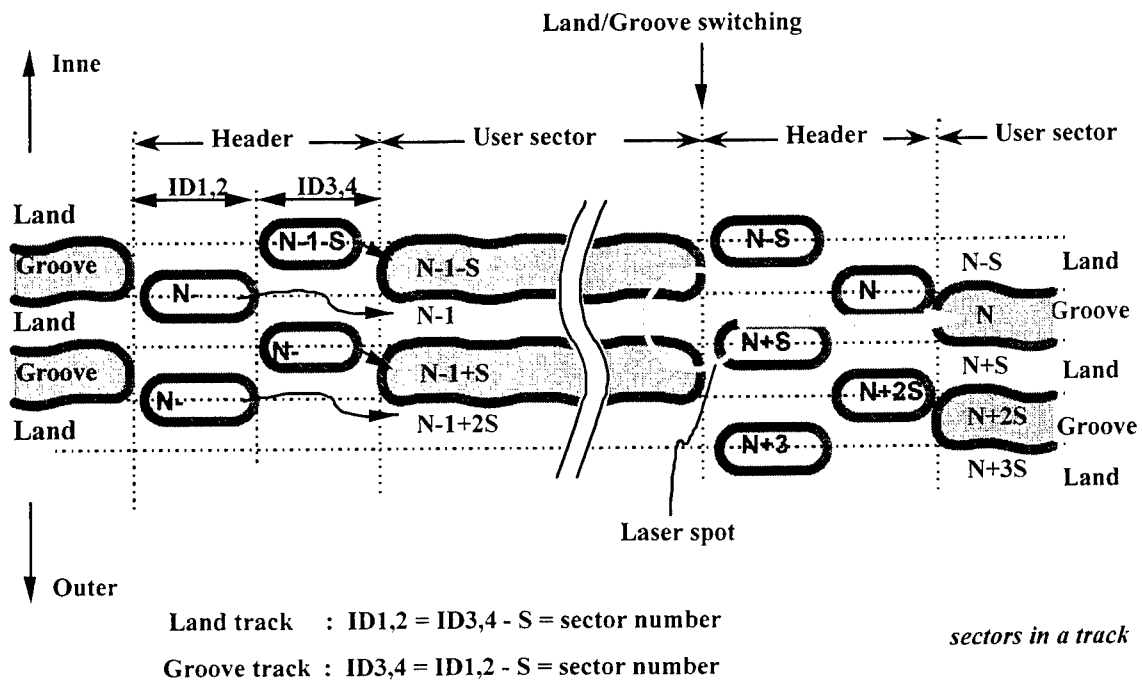
Figure 2.2.1(b) Outline of track format of DVD-RAM

Land track   : ID1,2 = ID3,4 - S = sector number

Groove track : ID3,4 = ID1,2 - S = sector number

sectors in a track

(a)

(b)
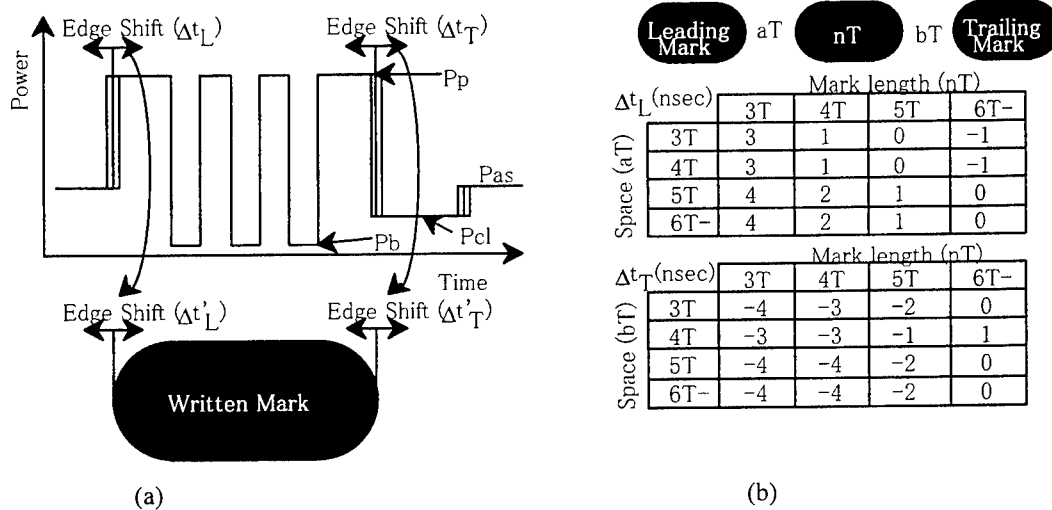
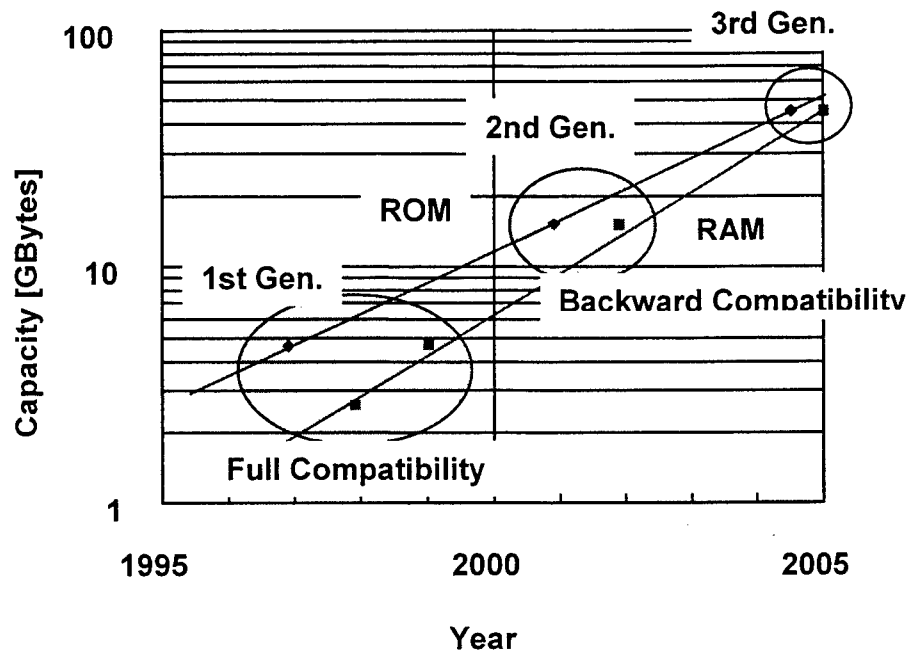Fig.2.2.3 Adaptive Write Compensation (a) Write waveform   (b) Write table

Fig.3.2.1 Road map of DVD

Removal of Hall Sensor Offset To Achieve Stable
Spindle-Motor Loop In A CD System

Chi-Cheng S. Lin, Wai W. Wang, Shun-Yi Tung, Chin-Hong Lin
Storage Devices Division, Acer Peripherals, Inc.
157, San-Ying Road, Kwei-Shan, Taoyuan, Taiwan

I. Introduction

Brushless spindle motor is one of the most important key components used in a CD system. A stable spindle motor control loop is essential to assure reliable data integrity for a high-speed CD drive. However, DC offset is frequently observed on Hall sensors of the spindle motor used in a CD system. This spindle-motor Hall sensor offset also shows large range variation among batches from different motor suppliers. This undesired Hall sensor DC offset can induce unstable spindle-motor control loop and cause malfunction of a CD drive. Being a drive manufacturer to mass produce CD drives over one million unit per month, the problem of Hall sensor offset variation must be overcome to assure smooth operation of the mass production.

As the demand on CD technology continues toward higher data transfer rate, the demand on spin rate stability of a spindle motor continues its advance. The increase of spin rate requires higher power consumption of a spindle motor and excessive heat is generated. This excessive heat aggravates the offset drifting in the Hall sensor and also induces amplitude shrinkage of Hall sensor signals. This undesired offset variation results in timing jitter of spindle-motor timing driving sequence to induce unstable spindle-motor loop in a CD system. In this paper, a practical solution is proposed to remove the offset completely, and thus, to achieve a very stable spindle loop.

II. Experiment result and discussion

The equipment used in this experiment are ACER CD640A CD-ROM drive and ACER CDRW 8432A rewritable drives which writes CD-R disc at 8X, writes CD-RW disc at 4X, and playback at 32X.

Stable spindle-motor control loop is essential to assure a properly functional CD system. To achieve this goal, Hall sensor output free of DC offset and close to 50-50% duty cycle timing sequence of motor driving signal is essential to achieve a stable spindle-motor loop. In reality, most of the spindle motors cannot be free of Hall sensor DC offset due to design and manufacturing process. As shown in Fig. 1, a typical Hall sensor output of a spindle motor shows DC offset. This DC offset results in the timing sequence of the motor driving signal deviated from 50-50% duty cycle. Larger jitter (Fig. 2) on timing sequence of motor drive is also observed. When the DC offset severely deviates out of the design margin of the spindle motor loop, malfunction would occur to knock down the CD system. Fig. 3 shows the Hall sensor DC offset is removed and the duty cycle of motor driving sequence is close to be 50-50%. This is accomplished through the implementation of the technique proposed in this paper. Jitter performance is also improved after the Hall sensor DC offset is removed, as shown in Fig. 4.
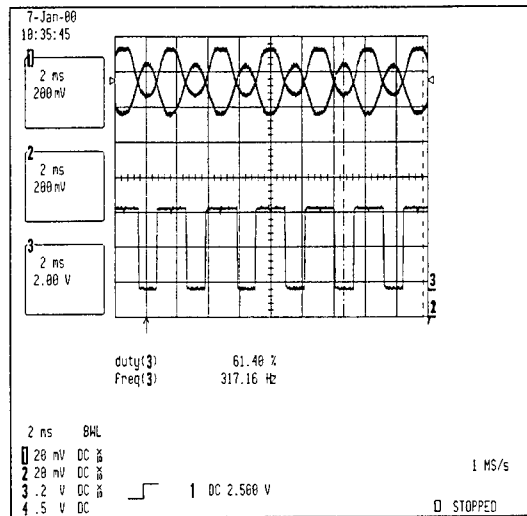
Fig. 1 Hall sensor offset causes
motor drive timing sequence
deviated from 50-50% duty cycle.
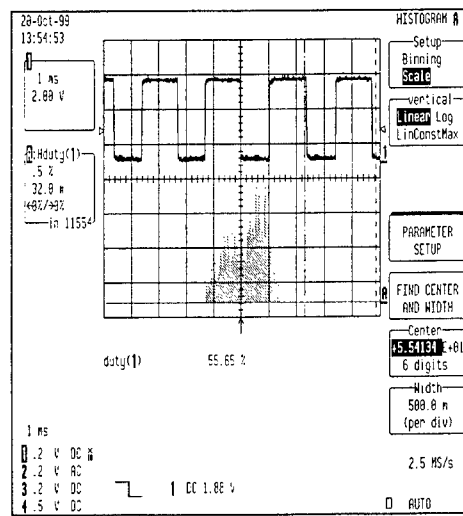
Fig. 2 Jitter is larger with DC offset
existing.
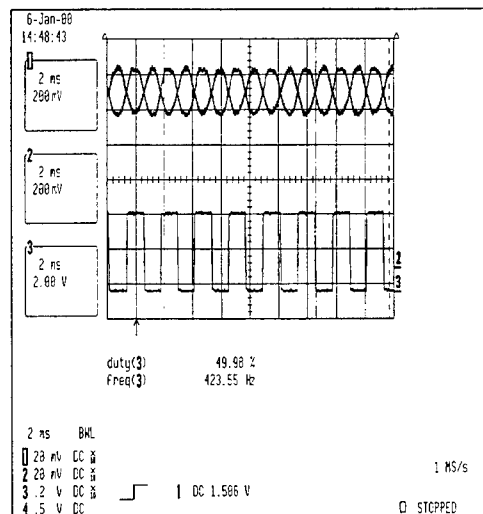
Fig. 3 Hall sensor DC offset is removed
and 50-50% duty cycle is achieved.
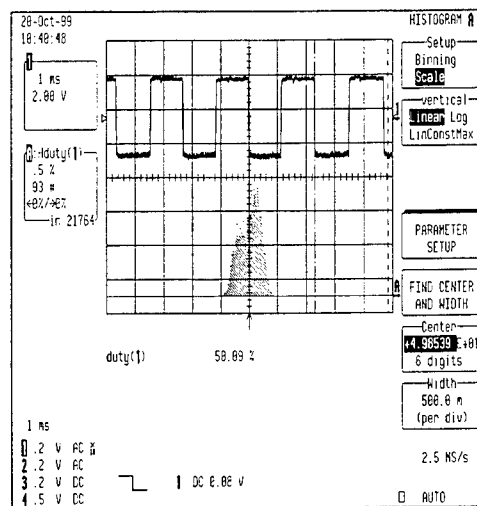
Fig. 4 Jitter spreading is reduced while
Hall offset is removed.

As spindle motor is driven toward higher speed to cause higher power consumption, excessive heat is thus generated to induce higher temperature imposed onto the spindle-motor. Higher temperature not only aggravates the DC offset variation but also causes the shrinkage of Hall sensor output signal. This leads to degradation of signal-to-noise signal of Hall sensor output and worsen the duty cycle balance of motor driving sequence. The technique to overcome the Hall signal shrinkage by using differential comparator is reported before[1]. In this paper, the focus is more on Hall sensor offset removal.

Figure 4 shows the Hall sensor DC offset is removed after the implementation of the technique proposed in this paper and 50-50% duty cycle of motor driving sequence is also achieved. Further, improvement on jitter performance is also observed as shown in Fig. 4. The functional block diagram of the motor control loop with the proposed AC-coupled technique is installed, as shown in Fig. 6. To remove the DC offset of Hall sensor, AC-coupled method is used to filter out the DC portion of Hall sensor signals. This AC-coupled Hall sensor can only be enabled after the spindle-motor is initialized reaching to a desired speed level. At that moment, AC-coupled of Hall sensor can thus be enabled to assure smooth operation of spindle motor (Fig. 6). A timing delay to enable the switch is essential to assure the AC-coupled circuit to function properly.
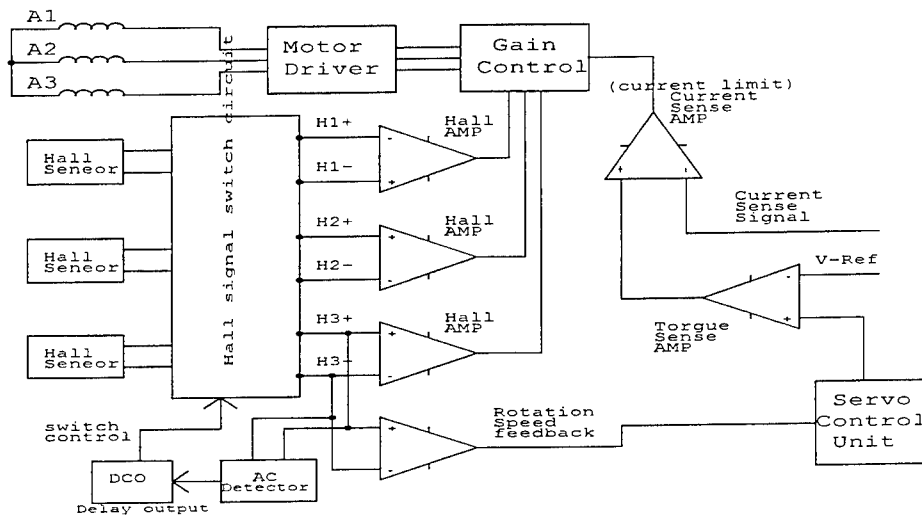
Figure 5 shows the functional block diagram of the motor control loop with AC-coupled Hall sensor.
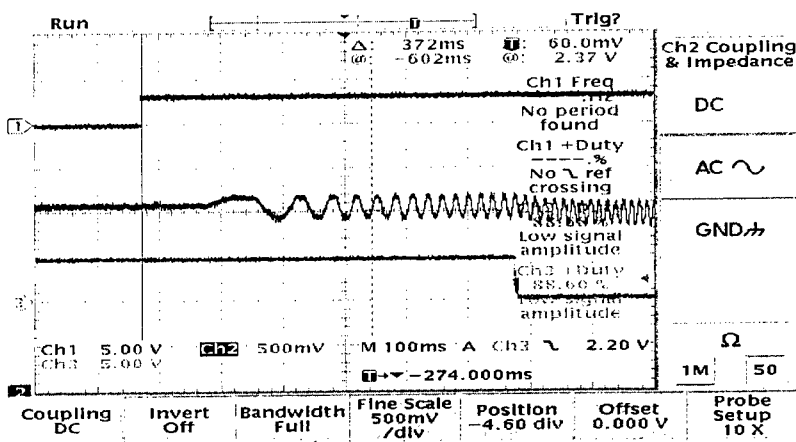
Fig. 6   Upper: Spindle motor power is enabled.
Middle: Hall sensor signals.
Lower: AC-coupled switch is enabled.

III. Conclusion

A practical solution of AC-couple Hall sensor in a spindle motor control loop to effectively eliminate the DC offset is proposed. This solution effectively removes the DC offset of Hall sensor and improved the stability of spindle-motor loop in a CD system.

Reference

[1] C.-C. Steve Lin, Cai-Gang Xu, W.-L. Tang, Wai. W. Wang, Y.-D. Hu, and K.-C. Cheng, "Thermal interference on a spindle motor and a method of correction in a CD-ROM system" Proceeding of the 13th Conference on Magnetism & Magnetic Technologies, pp. 213-215, July 1998.

Invited Paper

Liquid crystal aberration compensation devices

Sjoerd Stallinga[a], Joris Vrehen[b], Jeroen Wals[b], Henk Stapert[a], and Emile Verstegen[a]

[a]Philips Research Laboratories, Professor Holstlaan 4, 5656 AA Eindhoven, The Netherlands
[b]Philips Optical Storage, Glaslaan 1, 5600 JB Eindhoven, The Netherlands

ABSTRACT

The application of aberration compensation devices can support the trend to higher information densities in optical data storage. The information content of a disc may be increased while maintaining acceptable tolerance levels. For example, disc tilt dependence may require coma compensation, whereas double layer formats require spherical aberration compensation. Liquid crystals (LCs) can be successfully applied in such devices. The design of two practical implementations is discussed; a coma compensating LC-cell with special electrode-design for optimized tolerances w.r.t. decentering, and a lens made of photopolymerizable LC, which can be used to compensate for spherical aberration.

Keywords: aberration compensation, coma, spherical aberration, disc tilt, cover layer thickness, dual layer, liquid crystal, birefringent lens

1. INTRODUCTION

In the field of optical disc storage there is a continuous push to higher information densities. This is achieved by using a small wavelength λ and a high numerical aperture NA, as the spot size is roughly λ/NA. Table 1 shows that the NA increases from 0.45 for CD (Compact Disc) to 0.60 for DVD (Digital Versatile Disc), and even 0.85 for DVR (Digital Video Recorder),[1] while the wavelength decreases. The increase in NA and the decrease in λ lead to an increased sensitivity to aberrations. A measure for this sensitivity is the number $(d/\lambda)\text{NA}^k$, with d the cover layer thickness and $k = 2$ for defocus and astigmatism, $k = 3$ for coma, and $k = 4$ for spherical aberration. Clearly, a large NA and a small λ are disadvantageous from the point of view of aberrations. Important causes of aberrations are disc tilt, which gives rise to coma, and cover layer thickness variations, which give rise to spherical aberration. Table 1 shows the numbers $(d/\lambda)\text{NA}^k$ for CD, DVD, and DVR. As indicated by these numbers DVD has a coma problem, and DVD and DVR a spherical aberration problem. It turns out that the problem is slightly worse for DVR, because of higher order aberrations (with larger powers k).

Table 1. Aberration sensitivity of CD, DVD, and DVR.

format	NA	λ	d	$(d/\lambda)\text{NA}^2$	$(d/\lambda)\text{NA}^3$	$(d/\lambda)\text{NA}^4$
CD	0.45	780 nm	1.2 mm	0.31×10^3	0.14×10^3	0.06×10^3
DVD	0.60	650 nm	0.6 mm	0.33×10^3	0.20×10^3	0.12×10^3
DVR	0.85	400 nm	0.1 mm	0.18×10^3	0.15×10^3	0.13×10^3

Adaptive compensation of aberrations solves the increased aberration sensitivity in high NA optical storage formats. The widened design margins may be quite advantageous. An important type of aberration compensator uses liquid crystals (LCs). These birefingent liquids can be used to make an electrically controlable phase plate. This phase plate consists of an LC-cell with segmented (and transparant) electrodes. The voltage on each electrode translates into an angle ψ between the substrate normal and the director (the uniaxial symmetry axis of the liquid crystal). The extraordinary polarization mode has a refractive index depending on ψ:

$$n_{\text{eff}} = \frac{n_o n_e}{\sqrt{n_o^2 \sin^2 \psi + n_e^2 \cos^2 \psi}}, \tag{1}$$

Correspondence to Sjoerd Stallinga, E-mail: sjoerd.stallinga@philips.com

with n_o and n_e the ordinary and extraordinary refractive index, respectively. It follows that the refractive index for each electrode segment (and thereby the optical path length) can be varied between n_o and n_e by an electric signal. A suitable aberration compensator can be made by a proper choice of the shape and number of segments. An alternative method of making an LC aberration compensator uses a single non-segmented electrode and a non-flat substrate, leading to a non-constant LC layer thickness. The tilt angle ψ does not depend on the layer thickness, meaning that the single voltage gives rise to a uniform tilt angle ψ and thus to a uniform refractive index. The surface profile then reflects the aberration that is compensated, and the applied voltage is a measure for the amount of the compensation. For instance, when the thickness is $d_0 + d_1\rho^4$, with ρ the polar pupil coordinate, the cell can be used to compensate for spherical aberration.

Two examples of LC aberration compensators are discussed in this paper, a disc tilt compensator of the segmented electrode type for DVD, and a cover layer variation compensator of the surface profile type for DVR.

2. DISC TILT COMPENSATION

2.1. The Zernike Cell

Disc tilt causes a spot that is aberrated by coma. The compensating LC-cell must therefore add coma of the opposite sign. Coma has a phase profile in the pupil plane proportional to the Zernike polynomial:

$$Z_{31}(x,y) = \left[3(x^2 + y^2) - 2\right]x = \left(3\rho^3 - 2\rho\right)\cos\theta, \tag{2}$$

where x and y are the Cartesian pupil coordinates, and ρ and θ the polar pupil coordinates. Appropriate and simple electrode segments for the compensating LC-cell are given by the recipe:

- The pupil region for which $Z_{31}(x,y) > a$ is a segment, with voltage V_+.

- The pupil region for which $a \geq Z_{31}(x,y) \geq -a$ is a segment, with voltage V_0.

- The pupil region for which $-a > Z_{31}(x,y)$ is a segment, with voltage V_-.

The voltages satisfy $V_\pm = V_0 \pm \Delta$. If the voltage modulation Δ is sufficiently small, the phase modulation is linear in Δ. Note that the applied voltages are in fact AC-voltages, so V_0, V_+, and V_- are really the *amplitudes* of the voltage signals. Fig. 1, left figure, shows such a Zernike cell for $a = 0.21$. LC-cells of this type have already been proposed in the literature.[2]

The improvement that can be obtained can be estimated as follows. Suppose that the original comatic aberration due to disc tilt is $A_{31}Z_{31}(x,y,)$, where A_{31} is a constant proportional to the disc tilt α. The RMS wavefront aberration is then given by:

$$\mathrm{RMS}_0^2 = A_{31}^2 \int \mathrm{d}x\mathrm{d}y\, Z_{31}(x,y)^2, \tag{3}$$

where the integration range extends over the pupil (the unit circle), and where a multiplicative constant is ignored. The phase profile added by the LC-cell is $\Phi_{LC}(x,y) = B\Gamma_{LC}(x,y)$, where $\Gamma_{LC}(x,y)$ is the phase profile with unit modulation and B is a constant proportional to the voltage modulation Δ. The RMS wavefront aberration is now:

$$\mathrm{RMS}^2 = \int \mathrm{d}x\mathrm{d}y\, \left[A_{31}Z_{31}(x,y) + B\Gamma_{LC}(x,y)\right]^2, \tag{4}$$

and has a minimum when the constant B satisfies:

$$B = -A_{31}\frac{\int \mathrm{d}x\mathrm{d}y\, Z_{31}(x,y)\Gamma_{LC}(x,y)}{\int \mathrm{d}x\mathrm{d}y\, \Gamma_{LC}(x,y)^2}. \tag{5}$$

It follows that B is linear in A_{31}. As a consequence, the voltage modulation Δ is linear in the disc tilt α. This minimum RMS wavefront aberration can be obtained from the relative decrease in the square of the RMS wavefront aberration:

$$\frac{\mathrm{RMS}_0^2 - \mathrm{RMS}^2}{\mathrm{RMS}_0^2} = \frac{\left[\int \mathrm{d}x\mathrm{d}y\, Z_{31}(x,y)\Gamma_{LC}(x,y)\right]^2}{\int \mathrm{d}x\mathrm{d}y\, Z_{31}(x,y)^2 \int \mathrm{d}x\mathrm{d}y\, \Gamma_{LC}(x,y)^2}, \tag{6}$$

This quantity is a measure for the match between the Zernike coma and the LC phase profile. The parameter a is determined from the requirement that this measure is maximum. It turns out that the maximum is 0.85 and is obtained for $a = 0.21$. The remaining RMS is then $\sqrt{1 - 0.85} = 0.39$ of the original $\mathrm{RMS_0}$ due to disc tilt. This remaining RMS consists of higher order aberrations. Maximum improvement of the disc tilt margin is obtained when disc tilt is the only error. In that case the RMS is proportional to the tilt angle α. The spot on the disc is then still diffraction limited for a tilt angle that is 1/0.39=2.58 higher than without the LC-compensator. The improvement in tilt margin is 158%. In practice, there are other errors in the readout of the disc, and the improvement in tilt margin is not so large.
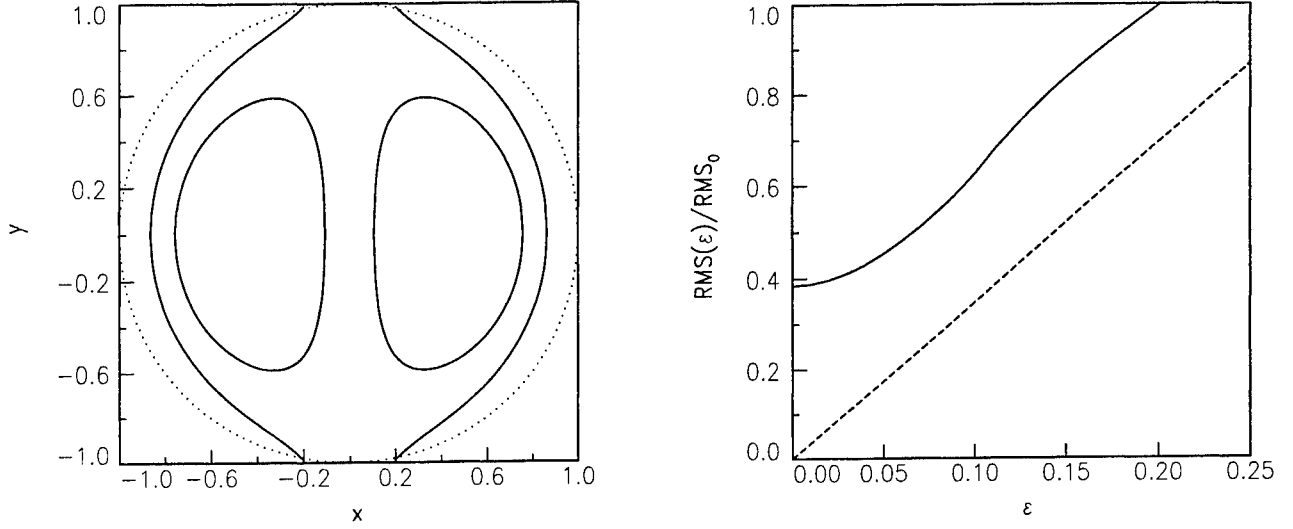

Figure 1. Left: Shape of the segmented electrode structure of the Zernike cell. Leads to the two inner segments pass through the central segment, but are not drawn in this figure. The pupil rim (for zero decentering) is indicated with a dotted line. Right: Ratio of the RMS wavefront aberration to the original comatic RMS wavefront aberration as a function of the decenter ε (full line), and the astigmatic approximation to this ratio (dashed line).

2.2. Decentering of the Objective Lens

The Zernike cell no longer works properly when the objective lens is decentered w.r.t. the fixed light path. The LC cell now generates a phase profile $B\Gamma_{\mathrm{LC}}(x - \varepsilon, y)$ instead of the original $B\Gamma_{\mathrm{LC}}(x, y)$. Here, ε is the objective lens displacement in units of the pupil radius. The RMS wavefront aberration as a function of ε can be obtained from:

$$\frac{\mathrm{RMS}_0^2 - \mathrm{RMS}(\varepsilon)^2}{\mathrm{RMS}_0^2} = \frac{\mathrm{RMS}_0^2 - \mathrm{RMS}(0)^2}{\mathrm{RMS}_0^2} \left\{ 2 \frac{\int dx dy\, Z_{31}(x,y)\Gamma_{\mathrm{LC}}(x - \varepsilon, y)}{\int dx dy\, Z_{31}(x,y)\Gamma_{\mathrm{LC}}(x,y)} - \frac{\int dx dy\, \Gamma_{\mathrm{LC}}(x - \varepsilon, y)^2}{\int dx dy\, \Gamma_{\mathrm{LC}}(x,y)^2} \right\}, \quad (7)$$

where $\mathrm{RMS}(0)$ follows from (6). Fig. 1, right figure, shows the ratio of $\mathrm{RMS}(\varepsilon)$ to the original comatic RMS_0 as a function of ε (full line). There is no net improvement when ε is larger than 0.20. For the fast seek feature in disc readout (a quick scan of the content of the tracks that are a few tracks ahead) it is necessary to have a margin of approximately 0.20. Consequently, the decentering margin and the tilt margin are incompatible.

The largest fraction of the aberrations generated by the decentering consists of astigmatism, as the phase profile of the LC-cell closely resembles a comatic phase profile. This can be seen using:

$$Z_{31}(x - \varepsilon, y) = \left[3(x^2 + y^2) - 2 \right] x - 3\varepsilon \left[x^2 - y^2 \right] - 3\varepsilon \left[2x^2 + 2y^2 - 1 \right] + 9\varepsilon^2 x - 3\varepsilon(1 + \varepsilon^2). \quad (8)$$

This equation implies that a decentered coma profile contains an additional amount of astigmatism (second term) proportional to the decentering ε. The remaining terms are defocus, wavefront tilt, and piston, which are not

important. The amount of astigmatism that is generated is $A_{22} = 3\varepsilon A_{31}$, leading to a relative increase in the square of the RMS wavefront aberration:

$$\frac{\Delta \text{RMS}^2}{\text{RMS}_0^2} = \frac{|A_{22}|^2/6}{|A_{31}|^2/8} = 12\varepsilon^2. \tag{9}$$

The astigmatic approximation of the numerically calculated curve in Fig. 1, right figure, is the line $\sqrt{12}\,\varepsilon$ (dashed line). Clearly, the slope of the curve agrees well with the numerical result. The difference between the two curves is nearly constant and is due to the higher order aberrations.

2.3. Solutions of the Decentering Problem

We have identified a number of different solutions to the decentering problem. The easiest one is fixing the LC-cell to the actuator. In that case there is simply no decentering of the objective lens w.r.t. the LC-cell. The disadvantage of this solution is that the weight of the actuator is increased substantially, and has therefore an adverse effect on the mechanical bandwidth.

A second solution is balancing of the coma that is compensated and the additional aberrations generated by decentering by making the coefficient B dependent on ε, instead of the fixed value given by (5). Minimum RMS is obtained when:

$$B(\varepsilon) = -A_{31}\frac{\int \mathrm{d}x\mathrm{d}y \, Z_{31}(x,y)\Gamma_{\text{LC}}(x-\varepsilon,y)}{\int \mathrm{d}x\mathrm{d}y \, \Gamma_{\text{LC}}(x-\varepsilon,y)^2}. \tag{10}$$

The remaining RMS is now given by a formula similar to (6):

$$\frac{\text{RMS}_0^2 - \text{RMS}(\varepsilon)^2}{\text{RMS}_0^2} = \frac{\left[\int \mathrm{d}x\mathrm{d}y \, Z_{31}(x,y)\Gamma_{\text{LC}}(x-\varepsilon,y)\right]^2}{\int \mathrm{d}x\mathrm{d}y \, Z_{31}(x,y)^2 \quad \int \mathrm{d}x\mathrm{d}y \, \Gamma_{\text{LC}}(x-\varepsilon,y)^2}. \tag{11}$$

Fig. 2 (left picture) shows the balanced ratio $\text{RMS}(\varepsilon)/\text{RMS}_0$ (full line), which clearly improves the unbalanced ratio (dotted line). The LC phase modulation $B(\varepsilon)$ relative to the original coefficient $B(0)$ is shown in the right picture of Fig. 2 (full line).
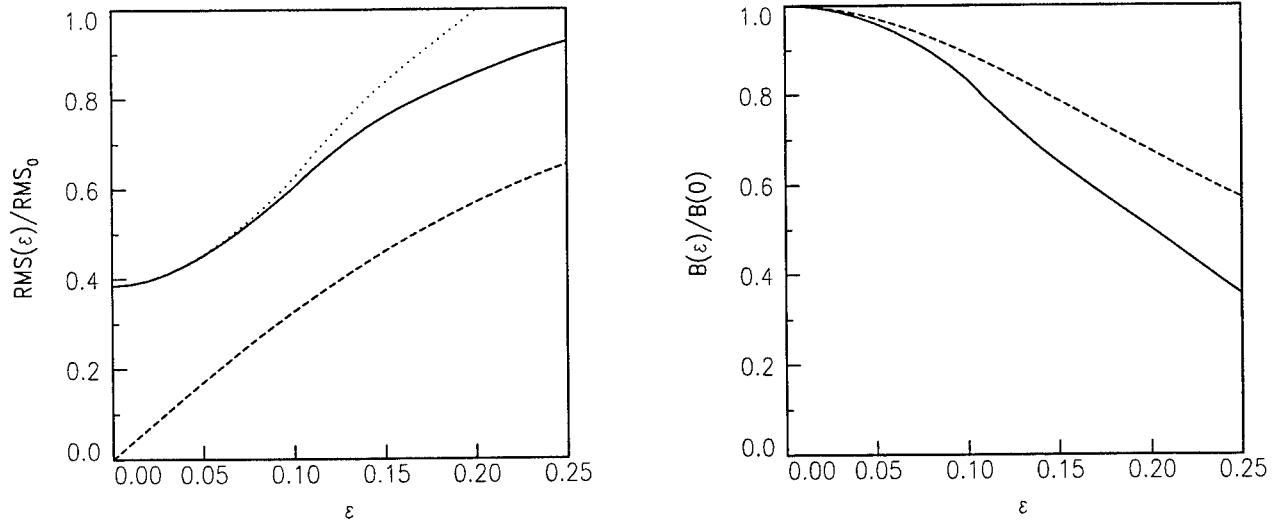
Figure 2. Left: Ratio of the balanced RMS wavefront aberration to the original comatic RMS wavefront aberration as a function of the decenter ε (full line), the astigmatic approximation to this ratio (dashed line), and the unbalanced ratio of the RMS wavefront aberration to the original comatic RMS wavefront aberration (dotted line). Right: Ratio of the LC phase modulation with balancing to the original Lc phase modulation (full line), and the astigmatic approximation (dashed line).

The balancing procedure can also be treated analytically with an approximation similar to the one described in the previous subsection. In this approximation the coma is balanced by the astigmatism that is generated. This means that only a fraction η of the coma caused by disc tilt is compensated, where η varies with the decentering ε. The remaining non-compensated coma is now $(1-\eta)A_{31}$, whereas the generated astigmatism is $A_{22} = 3\varepsilon\eta A_{31}$. This gives rise to an RMS^2 value:

$$\frac{\text{RMS}^2}{\text{RMS}_0^2} = (1-\eta)^2 + 12\varepsilon^2\eta^2 \,. \tag{12}$$

The minimum value is obtained when:

$$\eta = \frac{1}{1+12\varepsilon^2} \,, \tag{13}$$

and is equal to:

$$\frac{\text{RMS}^2}{\text{RMS}_0^2} = \frac{12\varepsilon^2}{1+12\varepsilon^2} \,. \tag{14}$$

Fig. 2 shows this minimum value (dashed line, left figure). Again, the slope of the curve agrees well with the numerical result, the nearly constant difference between the two curves being due to higher order aberrations. The LC phase modulation B is also shown in Fig. 2 (dashed line, right figure). Here, the agreement is only qualitative.

A third solution is having a second electrode structure on the opposite side of the LC-layer. On side 1 the segments are defined as:

- The pupil region for which $Z_{31}(x + \varepsilon_0, y) > a$ is one segment, with voltage $V_1 - \Delta_1$.

- The pupil region for which $a \geq Z_{31}(x + \varepsilon_0, y) \geq -a$ is one segment, with voltage V_1.

- The pupil region for which $-a > Z_{31}(x + \varepsilon_0, y)$ is one segment, with voltage $V_1 + \Delta_1$,

and on side 2:

- The pupil region for which $Z_{31}(x - \varepsilon_0, y) > a$ is one segment, with voltage $V_2 - \Delta_2$.

- The pupil region for which $a \geq Z_{31}(x - \varepsilon_0, y) \geq -a$ is one segment, with voltage V_2.

- The pupil region for which $-a > Z_{31}(x - \varepsilon_0, y)$ is one segment, with voltage $V_2 + \Delta_2$.

It follows that the electrodes on side 1 are displaced over a distance $-\varepsilon_0$ in the x direction, whereas the electrodes on side 2 are displaced over a distance $+\varepsilon_0$. This structure is schematically drawn in Fig. 3 (left figure). The voltages V_1, V_2, Δ_1 and Δ_2 are chosen such that:

$$V_1 - V_2 = V_0 \,, \tag{15}$$

$$\Delta_1 = \frac{\varepsilon_0 - \varepsilon}{2\varepsilon_0}\Delta \,, \tag{16}$$

$$\Delta_2 = \frac{\varepsilon_0 + \varepsilon}{2\varepsilon_0}\Delta \,, \tag{17}$$

When all the electric signals are in phase the amplitude at position (x, y) is the difference in the amplitude of the signals on the two sides of the LC. Consequently, the phase profile that is generated is a weighted sum of the two displaced coma profiles. For instance, if the decentering $\varepsilon = \varepsilon_0$, then $\Delta_1 = 0$ and all electrodes on side 1 have voltage V_1. On side 2, the modulation $\Delta_2 = \Delta$. This means that the original Zernike phase profile is recovered, but displaced over a distance ε, exactly what is required to compensate for the decentering of the objective lens. If $\varepsilon = -\varepsilon_0$ the roles of sides 1 and 2 are interchanged, and for other values of ε the phase profile is an interpolation between these two cases. By choosing ε_0 between 0 and the maximum objective displacement a good compensation for disc tilt can be achieved for all values of the decentering of the objective lens. Fig. 3, right figure, shows the ratio $\text{RMS}(\varepsilon)/\text{RMS}_0$ for $\varepsilon_0 = 0.15$. This ratio is in the range 0.40-0.45 for virtually the whole range of ε values. Finally, it is mentioned that it is also possible to have both electrode structures on the same side of the LC-cell. However, the increased number of electrodes requires additional leads to the inner segments. These additional leads pass through the other segments, thereby disturbing the phase profile.
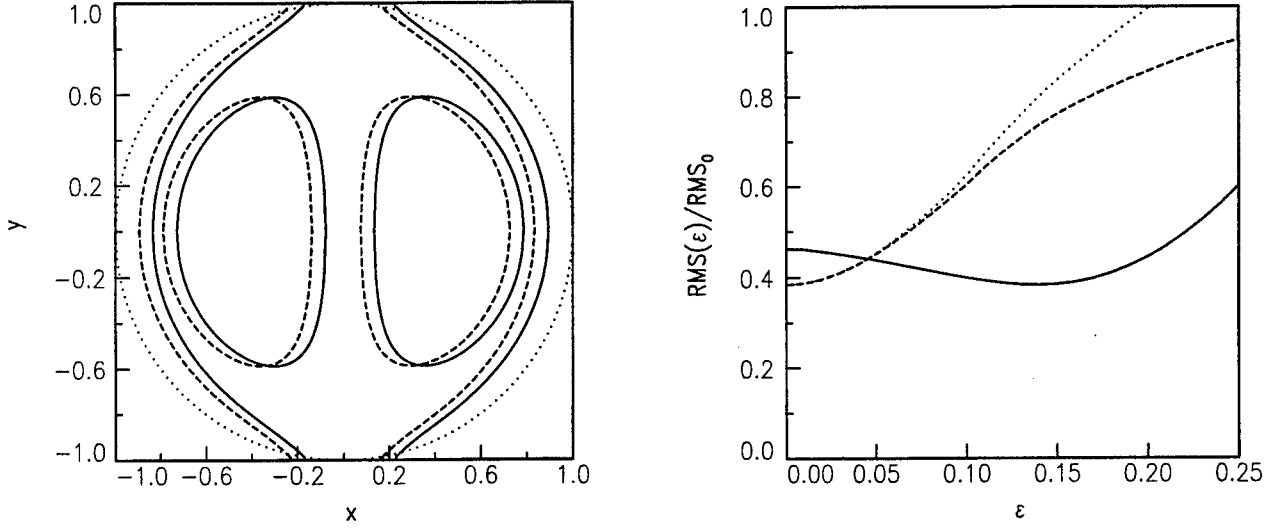
Figure 3. Left: Mutually displaced electrode segments on both sides of the doubled Zernike cell. The full lines refer to the segments on one side, the dashed lines to the segments on the other side. The pupil rim (for zero decentering) is indicated by the dotted line. Right: The ratio $\text{RMS}(\varepsilon)/\text{RMS}_0$ for the doubled Zernike cell with $\varepsilon_0 = 0.15$ (full line), the balanced single Zernike cell (dashed line) and the unbalanced single Zernike cell (dotted line).

2.4. The Seidel Cell

The disc tilt compensation with Zernike cells only reduces the RMS to around 40% of the original RMS because of the higher order aberrations. These aberrations are introduced by the large discontinuities in the phase profile at the edges of the electrode segments. This problem can be eliminated by increasing the number of electrode segments. However, not all segments are connected to the pupil rim, meaning that a large number of leads passing through other segments must be introduced in the design. In addition, a large number of leads from the driver IC to the LC-cell is required, which is highly unfavourable. These problems may be overcome with two changes in the design. First, we may take the Seidel coma $W_{31} = (x^2 + y^2)x$ as the basis of our compensator instead of the Zernike coma $Z_{31} = \left[3(x^2 + y^2) - 2\right]x$. The difference is a tilt term, meaning that the field of the objective lens is used. However, this effect can be neglected. For a Seidel cell the electrode segments are bent strips with varying width that are all connected to the pupil rim. Suppose the strips are numbered by an index taking values $-N, -N + 1, \ldots, 0, 1, \ldots, N$. Then there are $2N + 1$ strips. The strip with index j occupies the pupil region consisting of points (x, y) that satisfy:

$$\frac{2j - 1}{2N + 1} < W_{31}(x, y) < \frac{2j + 1}{2N + 1}. \tag{18}$$

Fig. 4 shows an example of such a cell with $N = 8$. The second problem is solved by making a resistor bench in the transparant conductor. The individual resistors are U-turns connecting strip j with strip $j + 1$. If a voltage is applied to only a limited number of strips than the voltage on the intermediate strips is found by linear interpolation between the voltages on the nearest strips with outside leads. For instance, if strips $-N$, 0, and N have these outside leads, with voltages $V_+ = V_0 + \Delta$, V_0, and $V_- = V_0 - \Delta$, respectively, then the voltage on strip j is:

$$V_j = V_0 - \frac{j}{N}\Delta. \tag{19}$$

The match between the LC phase profile and the Seidel coma can be calculated using an expression similar to (6). It turns out that the residual RMS wavefront aberration is smaller than 10% of the original Seidel coma if $N \geq 8$. Fig. 4 (right figure) shows the decentering performance of such a Seidel cell (dotted line). The decentering problem is reduced compared to the Zernike case, but is not eliminated alltogether. A further reduction can be obtained by balancing (dashed line) or by breaking the symmetry of the applied voltages, i.e. by choosing V_+ and V_-
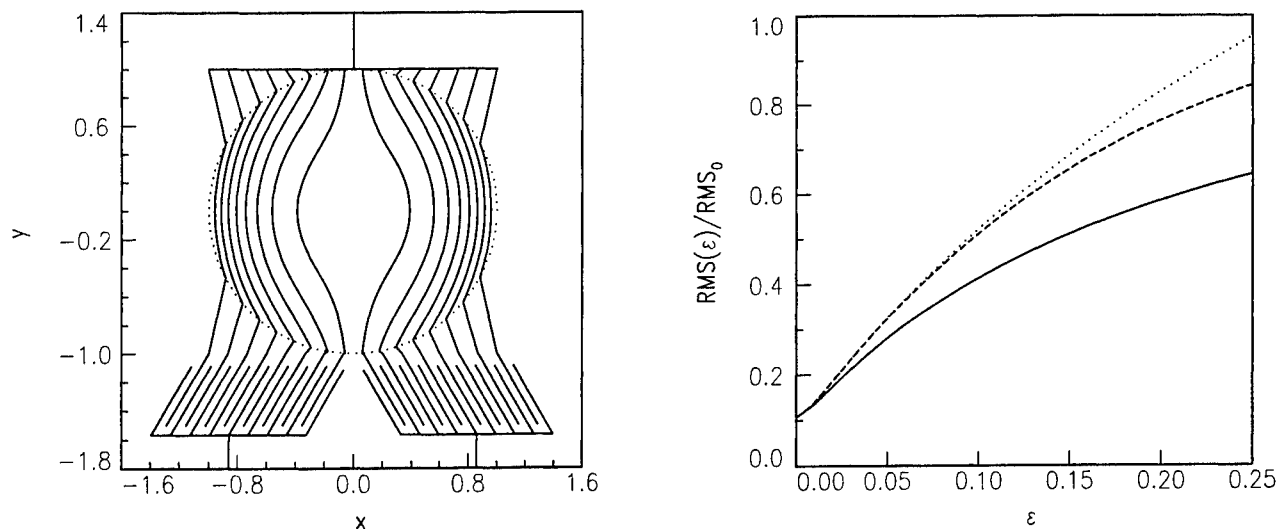
Figure 4. Left: Electrode segments for a Seidel coma cell with strip electrodes and resistor bench. The pupil rim is indicated with a dotted line. Right: The ratio of the RMS wavefront aberration to the original $\mathrm{RMS_0}$ for the unbalanced case (dotted line), the balanced case (dashed line), and the asymmetric case (full line).

asymmetrically, so that $(V_+ + V_-)/2 \neq V_0$ (full line). Averaged over the ε range the performance is similar to that of the double Zernike cell, for small ε it is better, for large ε worse.

3. COVER LAYER THICKNESS COMPENSATION

3.1. Liquid Crystal Lens and Spherical Aberration

There are two ways to compensate for spherical aberration. The first one is to introduce spherical aberration into the light path with an LC-cell with segmented electrodes similar to the coma LC-cell discussed in the previous section or with an LC-cell with a non-segmented electrode and a ρ^4 thickness profile. The second way is to introduce defocus into the light path. The objective lens is designed to compensate for the spherical aberration arising from focusing through a cover layer. The compensation is ideal when the illuminating beam is collimated. In case the incident beam is slightly convergent or divergent the compensation is non-ideal and a net amount of spherical aberration is generated. It follows that cover layer thickness variations can be compensated by varying the vergence of the illuminating beam. This can be done with an LC-cell with a single non-segmented electrode and a spherical pit in one of the substrates. Fortunately, the tilt angle ψ of the LC director only depends on the applied voltage, and not on the varying cell-gap. This means that the voltage controls the refractive index independent of the surface profile, whereas the surface profile determines the type of aberrration. A spherical pit gives rise to a ρ^2 thickness profile, implying that defocus is generated by the LC-cell. When the curvature radius of the spherical pit R is large compared to the LC layer thickness in the middle of the pit d and to the thickness of the substrate glass plates the focal length of the LC-lens is:

$$f_{\mathrm{lc}} = \frac{R}{n_{\mathrm{lc}} - n_{\mathrm{g}}}, \qquad (20)$$

with n_{lc} the refractive index of the LC, which is a function of the applied voltage, and with n_{g} the refractive index of the substrate glass.

3.2. Liquid Crystal Polymer Lens

An alternative type of LC-lens is made of photopolymerizable LC. Such a lens can be manufactured using more or less conventional LC-cell making, but without the transparant electrode layers. Instead of a conventional LC, a polymerizable LC in its monomer state is used. Alignment of the liquid crystal is possible because the monomer is a liquid. After cell making the LC is irradiated with UV-light, which initiates the formation of radicals that

56

start the polymerization reaction. The advantage of polymer LCs is the superfluousness of cell gap control. Also, it may be a birefringent lens that is easier and more cost-effective to manufacture than birefingent lenses made of conventional materials such as calcite.

Although such a type of lens is not continuously switchable it can be used for spherical aberration compensation by also using the ordinary polarization mode. For the extraordinary and ordinary modes we find focal lengths:

$$f_e = \frac{R}{n_e - n_g}, \tag{21}$$

$$f_o = \frac{R}{n_o - n_g}. \tag{22}$$

When the linear polarization can be rotated, for instance by a simple Twisted Nematic liquid crystal cell, the bifocal nature of the LC-lens can be used to compensate spherical aberration for two cover layer thickness values. This would be ideally suited for dual layer discs, i.e. discs that have two information layers at different depths.[3]

3.3. Aberrations of a Liquid Crystal Lens

It appears that LC-lenses suffer from astigmatism. This is due to the curvature of the pit region on one of the substrates, which causes a deformation of the liquid crystal director field, as drawn in Fig. 5. Due to the director tilt the refractive index of the extraordinary mode changes with x^2, whereas the spherical pit causes a thickness variation with $x^2 + y^2$. It follows that the lens must have astigmatism. A simple model can be used to estimate the amount of astigmatism. Consider a ray intersecting the lens at position (x, y). In the paraxial regime the ray is substantially parallel to the optical axis. Moreover, the lens thickness d is small compared to the curvature radius R. The optical path length for the ray traversing the pit is then given by:

$$\text{OPL} = n_g \frac{x^2 + y^2}{2R} + n_{lc} \left[d - \frac{x^2 + y^2}{2R} \right]. \tag{23}$$

The liquid crystal director makes an angle $x/R \ll 1$ with the x-axis on the curved substrate side and is parallel to the x-axis on the non-curved side, giving an average director tilt angle $\psi = \pi/2 - x/2R$. The refractive index of the extraordinary mode is then approximately:

$$n_{lc} = n_e - \Delta n \left(\frac{x}{2R} \right)^2, \tag{24}$$

with the birefringence $\Delta n = n_e - n_o$. This expression follows from the general expression (1) when Δn is sufficiently small. This small birefringence approximation is usually quite justified in practice. It leads to an OPL:

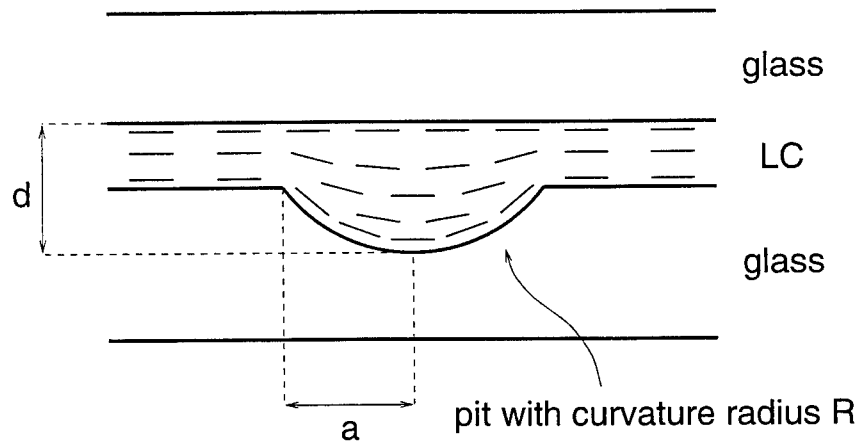$$\text{OPL} = n_e d - \frac{x^2}{2f_x} - \frac{y^2}{2f_y}, \tag{25}$$

Figure 5. Deformation of the LC director field in the spherical pit, causing astigmatism. The drawing is not on scale.

where the x and y focal lengths are given by:

$$\frac{1}{f_x} = \frac{n_e - n_g}{R} + \frac{d\Delta n}{2R^2} , \qquad (26)$$

$$\frac{1}{f_y} = \frac{n_e - n_g}{R} . \qquad (27)$$

The lens is clearly astigmatic. The ratio of astigmatism to defocus is constant, and given by:

$$\frac{A_{22}}{A_{20}} = \frac{f_y - f_x}{f_y + f_x} = \frac{d\Delta n/R}{4(n_e - n_g) + d\Delta n/R} . \qquad (28)$$

When the refractive index of the glass is matched to the ordinary refractive index of the LC ($n_g = n_o$), and using that $d \ll R$, we find the simple expression:

$$\frac{A_{22}}{A_{20}} = \frac{d}{4R} . \qquad (29)$$

The defocus coefficient is $A_{20} = \Delta n a^2/4R$ with a the pupil radius. It then follows that the astigmatism coefficient is below the 1 mλ level if $d\Delta n(a/R)^2/16\lambda$ is smaller than 1×10^{-3}. In practice Δn is approximately 0.10 leading to the criterion for sub-mλ astigmatism:

$$\frac{a}{R} \leq 0.4\sqrt{\frac{\lambda}{d}} . \qquad (30)$$

Clearly, a large radius of curvature (small NA) and/or a small thickness are advantageous from the point of view of aberrations.

The results may be generalized to the case with a director tilt due to the rubbing treatment or to an applied voltage. Defining ψ as the effective director tilt angle the LC refractive index is:

$$n_{lc} = n_e - \Delta n \sin^2\left(\pi/2 - \psi + \frac{x}{2R}\right) = n_e - \Delta n \cos^2\psi - \Delta n \sin(2\psi)\frac{x}{2R} + \Delta n \cos(2\psi)\left(\frac{x}{2R}\right)^2 + \dots . \qquad (31)$$

Clearly, the effective birefringence is reduced to $-\Delta n \cos(2\psi)$ and a wavefront tilt proportional to $\Delta n \sin(2\psi)$ is introduced. The resulting astigmatism is:

$$\frac{A_{22}}{A_{20}} = \frac{-d\Delta n \cos(2\psi)}{4R(n_e - \Delta n \cos^2\psi - n_g)} . \qquad (32)$$

Finally, it is mentioned that the case with two curved surfaces (with radii R_1 and R_2) can be described by replacing $1/R$ by $1/R_1 - 1/R_2$ in all previously derived formulas.

Astigmatism of birefringent lenses is first considered by Kikuta et. al..[4] They considered the case of a lens with a uniform uniaxial symmetry axis and found that there is astigmatism provided that both surfaces of the lens are curved. In the present case, the astigmatism is rooted in the liquid crystalline nature of the birefringent lens, causing a deformation of the uniaxial symmetry axis that is ultimateley responsible for the aberration. As opposed to the Kikuta type of astigmatism lenses with possibly one flat surface also suffer from astigmatism.

3.4. Experiment

Laboratory samples of polymer LC-lenses have been made by making a spherical pit with curvature radius of 100 mm in a flat 3 mm thick plate of glass. With a pit diameter of 3.5 mm, the depth of the pit in the centre is 15 μ. The overall thickness of the LC-layer was approximately 50 μ. For 632.8 nm light the resulting astigmatism is approximately 0.4 mλ, i.e. negligible. The other substrate was a flat, 1 mm thick plate of glass. Polyimide alignment layers were applied on both substrates by spincoating, and subsequently cured and rubbed in order to induce alignment of the LC molecules. Both substrates were squeezed together with a droplet of LC in between them. The LC-mixture was composed of 50% E7-diacrylate, 49% E7, and 1% photo-initiator. Domains in the LC alignment were eliminated by heating the LC above the clearing point and subsequently cooling down to room temperature. Finally, the mixture was polymerized using UV-light. The uniformity of the LC alignment was checked by polarization microscopy. The quality of the polymer LC lenses were measured for 632.8 nm laser light

polarized by a sheet polarizer with a shearing interferometer.[5] Focal lengths $f_e = 0.54$ m and $f_o = 12.4$ m (n_o and n_g are nearly matched) were obtained. The measured pupil was reduced to 90% of the pit diameter, i.e. the pupil diameter was 3.15 mm, leading to numerical apertures $NA_e = 2.9 \times 10^{-3}$ and $NA_o = 1.3 \times 10^{-4}$. Despite the small NA values aberration levels of $RMS_e=37$ mλ, and $RMS_o=13$ mλ (relative to the region surrounding the pit) were measured, mainly consisting of astigmatism. This is probably due to the assembly of the two glass plates, which turned out to be not sufficiently parallel for the measured sample. Improvement of the assembly may reduce the aberrations to a negligible level.

4. SUMMARY AND CONCLUSION

Liquid crystals can be applied in aberration compensation devices. Such devices can be quite beneficial for high NA optical recording formats.

The sensitivity to disc tilt can be decreased by a coma generating LC-cell. However, astigmatism is generated when the objective lens is decentered w.r.t this compensating LC-cell. Several solutions for this problem are discussed; attaching the compensator to the actuator, balancing the compensated coma and the generated astigmatism, using mutually displaced segmented electrodes on both sides of the cell, and correcting for Seidel coma instead of Zernike coma.

Liquid crystal lenses can be used to illuminate the objective lens with variable vergence thereby generating spherical aberration. This can be used to correct for cover layer thickness variations. A birefringent lens made of polymer LC is a viable alternative for lenses made of conventional birefringent materials such as calcite. The LC is aligned in its monomer state and subsequently cured by UV-irradiation. It appears that LC polymer lenses are always astigmatic. However, when the thickness and/or the NA of the lens is sufficiently small this aberration is negligible.

ACKNOWLEDGMENTS

REFERENCES

1. T. Narahara, S. Kobayashi, M. Hattori, Y. Shimpuku, G. van den Enden, J. Kahlman, M. van Dijk, and R. van Woudenberg, "Optical disc system for digital video recording," *Joint International Symposium on Optical Memory and Optical Data Storage, SPIE Vol.* **3864**, pp. 50–52, 1999.
2. N. Murao, M. Iwasaki, and S. Ohtaki, "Tilt servo using a liquid crystal device," *International Symposium on Optical Memory* , pp. 351–353, 1996.
3. K. Kurokawa, M. Naito, K. Yasuda, T. Kashiwagi, and O. Kawakubo, "A 16.8 GB double-decker phase change disc," *Joint International Symposium on Optical Memory and Optical Data Storage, SPIE Vol.* **3864**, pp. 197–199, 1999.
4. H. Kikuta, K. Iwata, and H. Shimomura, "First-order aberration of a double-focus lens made of a uniaxial crystal," *J. Opt. Soc. Am. A* **9**, pp. 814–819, 1992.
5. M. Mantravadi, "Lateral shearing interferometry," in *Optical Shop Testing*, D. Malacara, ed., pp. 123–172, John Wiley & Sons, New York, 1992.

Multi-level Recording in Erasable Phase-Change Media

by Light Intensity Modulation

Yen-Lin Chen and Han-Ping D. Shieh

Institute of Electro-Optical Engineering, National Chiao Tung University

Hsin-Chu, Taiwan, 30010, Rep. of China

Tel: 886-3-5720409   Fax: 886-3-5737681   Email: u8724501@cc.nctu.edu.tw

ABSTRACT

Multi-level recording has advantage of increasing the recording density without extensively altering the current optic configuration. In this paper, a new four-level recording phase-change disk using three-recording layers was demonstrated. By modulating the intensity of the laser pulse, marks were chosen to record in any of recording layers, to form four recording regions. Utilizing the property of the phase change media whose amorphous and crystalline states differ largely in refractive indices, each recording region corresponds to different reflectance. For the four-level recording disk, each recording region represents two-bit data, then the recording density of the four-level disk is a factor of two higher than that of a conventional disk recorded by adopting the pulse position modulation (PPM).

Keywords: light intensity modulation, multi-level recording optical disk, pulse position modulation, multi-layer

1. INTRODUCTION

Recording density of optical disks is limited by the optical diffraction limit. For a conventional disk whose marks are recorded by the pulse position modulation (PPM) method, each mark length corresponds to one bit. With the multi-level recording method, each recording region of the four-level disk corresponds to two-bit data. Therefore, the effective mark length for one bit is half of the actual mark length, and the recording density can be doubled without using the short wavelength diode laser or high numerical aperture (N.A) lens. Several multi-level recording methods have been reported. For example, the magnetic multi-valued (MMV) recording was realized in MO media, applying an exchange coupled bi-layer[1]. Using partial crystallization properties of phase-change optical disks to achieve multi-level recording was also reported[2]. In this paper, a new four-level recording technique on the three-recording layers disk was demonstrated.

2. PRINCIPLE AND DISK DESIGN

The four-level optical disk structure (Substrate /ZnS-SiO$_2$ /1st recording layer /ZnS-SiO$_2$ /2nd recording layer /ZnS-SiO$_2$ /3rd recording layer /ZnS-SiO$_2$ /Al) is composed of three recording layers. All of the recording layers are composed of phase-change material GeTeSb of the same composition, as shown in Fig. 1. Marks can be recorded in any of recording layers. The dielectric layers of ZnS-SiO$_2$ are used to control the reflectance and the thermal diffusion of the four-level disk. The Al reflective layer increases the cooling rate of the recording layers, and is as a reflector to optimize write/read properties.

The amorphous and crystalline states of the recording layer correspond to different refractive indices. The total reflectance of the disk is different when the recording layers are in the different phase. Four different reflectance, Rccc, Racc, Raac, Raaa of the four-level disk are produced, as shown in Fig. 2. For example, Racc denotes the reflectance when the upper recording layer is in the crystalline state, and the middle recording layer and lower recording layer are in the amorphous state, respectively.

Four recording regions, ccc, acc, aac, aaa are formed by using the different laser power to write marks in different recording layers. Each recording region represents two bits, as shown in Fig. 3(a). All recording layers should be initialized

60

In *Optical Storage and Optical Information Processing*, Han-Ping D. Shieh, Tom D. Milster, Editors, Proceedings of SPIE Vol. 4081 (2000) • 0277-786X/00/$15.00

to the crystalline state, as phase change disks, before to record amorphous marks. In the recording process, the laser beam is incident from the substrate. Most energy is absorbed by the 1st recording layer so that the temperature of the irradiated region of the 1st recording layer is higher than that of the 2nd and 3rd recording layers. The temperature of the 2nd recording layer is also higher than that of the 3rd recording layer. The amorphous state can be formed when the irradiated regions of the recording layer are heated over the melting point, then cool down rapidly. By controlling the laser power, the highest temperature of each recording layer is different, and the marks can be chosen to record in the different recording layers, as shown in Fig. 3(b). For example, in order to record marks only in the 1st recording layer, the irradiated region of the 1st recording layer is over melting point; meanwhile, the temperature of other two recording layers are lower than melting point. Thus, the amorphous marks are only recorded in the 1st recording layer.

The temperature difference between any two recording layers, which is controlled by the disk structure, should be high enough to avoid recording marks on the unexpected recording layers. By increasing the thickness of the dielectric layers between any two recording layers, the power margin of recording marks in different recording layers will be increased because of higher temperature difference. However, the mark size difference between any two recording layers will also be enlarged due to the effect of extensive heat diffusion. It will affect the quality of the readout signal. Therefore, there is a tradeoff between the power margin and the mark size.

The temperature profile of the recording layers need to be carefully controlled. By adopting single pulse writing, the highest temperature of the rear part of the recorded mark is higher than that of the front part of the same recorded mark due to the heat diffusion along the direction of the laser spot scanning. It may cause those marks be recorded in the unexpected recording layers. To decrease the effect of the thermal diffusion, a multi-pulse recording method[3] was utilized, as shown in Fig. 4.

When the focussed laser spot scans along the track, different recording regions produce different reflectance levels, as shown in Fig. 5. The C/N of the four-level disk is defined at the nearest interval of reflectance levels. The contrast of any two reflectance levels of the readout signal is determined by the reflectance of the disk and the recorded mark size. When the recording density increases, the reduced recorded mark size decreases, so does the readout signal. In order to achieve high signal quality, the reflectance contrast between each level needs as high as possible. With the optical simulation using the Jones matrix method[4], the reflectance was defined by controlling the thickness of each layer of the disk.

According to the optical and thermal simulations, the disk structure of (Substrate / 150nm ZnS-SiO$_2$ / 8nm 1st recording layer / 40nm ZnS-SiO$_2$ / 8nm 2nd recording layer / 12nm ZnS-SiO$_2$ / 7nm 3rd recording layer / 50nm ZnS-SiO$_2$ / 40nm Al) is designed for the experiments. The simulated reflectances of the four-level disk, Rccc, Racc, Raac, Raaa are 0.24, 0.03, 0.09, 0.18, respectively.

3. EXPERIMENT AND DISCUSSION

The optical and thermal designed four-level disk was measured by a dynamic tester. The wavelength is 660nm and N.A is 0.6. The linear velocity of the disk is about 4.8m/s.

When the recorded mark size of the four-level disk was about 0.8um, four recording regions were produced by different multi-pulse waveform, as shown in Fig. 6. The readout signal with the DC-read detection method was observed, as shown in Fig. 7. When the recording pattern was arranged as Fig. 7(b), the readout signal of four reflectance levels was no longer detectable.

The pulse-read detection method[5] to distinguish the four reflectance levels was adopted. The readout signal of the same recording pattern as shown in Fig. 7(b) was tested by the pulse-read method, as shown in Fig. 8. The four-level readout signal can be clearly differential. When the recorded marks became smaller than 0.6um, the readout signal was distorted and the reflectance level corresponding to each region no longer kept the original level, as shown in Fig. 9. Thus, the smallest recording region which was detectable in this four-level disk was about 0.6um using the above mentioned optical system, laser, and light intensity modulation writing method.

The C/N of the four-level disk is defined at the nearest interval of reflectance levels which is between the acc and aac regions in the experiment, as shown in Fig. 10. The C/N of the four-level disk for different effective mark size, half of the actual mark length, is compared to a conventional disk, as shown in Fig. 11. The C/N of the four-level disk for the actual mark size of 0.6um which corresponds to the effective mark size of 0.3um was about 36dB. It shows that the C/N of the

four-level disk for the small effective mark size was higher than that of the conventional disks. The C/N was not high enough for the large mark size because the contrast between the reflectance levels of acc and aac regions was small, and adjacent marks interfered with each other.

4. CONCLSION

Multi-level recording using the light intensity modulation method on the four-level disk of three erasable phase change recording layers was studied. Multi-level recording has advantage of increasing the recording density without altering the current optic configuration. At the laser wavelength of 660nm and N.A of 0.6, the C/N for the effective mark size of 0.3um on the four-level disk is above 36dB by light intensity modulation recording. The C/N can be increased further by optimizing the structure of the disk and the writing schemes.

5. ACKNOWLEDGEMENT

6. REFERENCES

[1] K.SHIMAZAKI. M. YOSHIHIRO. O. ISHIZAKI. S. OHNUKI and N. OHTA: Proc. MORIS '94 (1995). pp.429-430.
[2] L.P.SHI, T.C. CHONG, P.K. TAN, X.S. MIAO, Y.M. HUANG and R. ZHAO: Jpn. J. Appl. Phys. Vol. 38 (1999) pp.1645-1648.
[3] T. Ishida, M. Shoji, Y. Miyabata, Y. Shibata, E. Ohno, and S. Ohara, Proc. SPIE 2338, 121 (1994)
[4] Hecht, *Optics*, 2nd Edition, Addison-Wesley Publisher, U.S.A., 373 (1987).
[5] Gung-Chian YIN, Bing-Mau CHEN, Chia-Ping TAI and Han-Ping D. SHIEH: Jpn. J. Appl. Phys. Vol. 39 (2000) pp.830-3. Japan

Substrate
dielectric layer（ZnS-SiO$_2$）
1st recording layer (Ge$_{21}$Te$_{53}$Sb$_{26}$)
dielectric layer（ZnS-SiO$_2$）
2nd recording layer (Ge$_{21}$Te$_{53}$Sb$_{26}$)
dielectric layer（ZnS-SiO$_2$）
3rd recording layer (Ge$_{21}$Te$_{53}$Sb$_{26}$)
dielectric layer（ZnS-SiO$_2$）
reflective layer（Al-Cr）

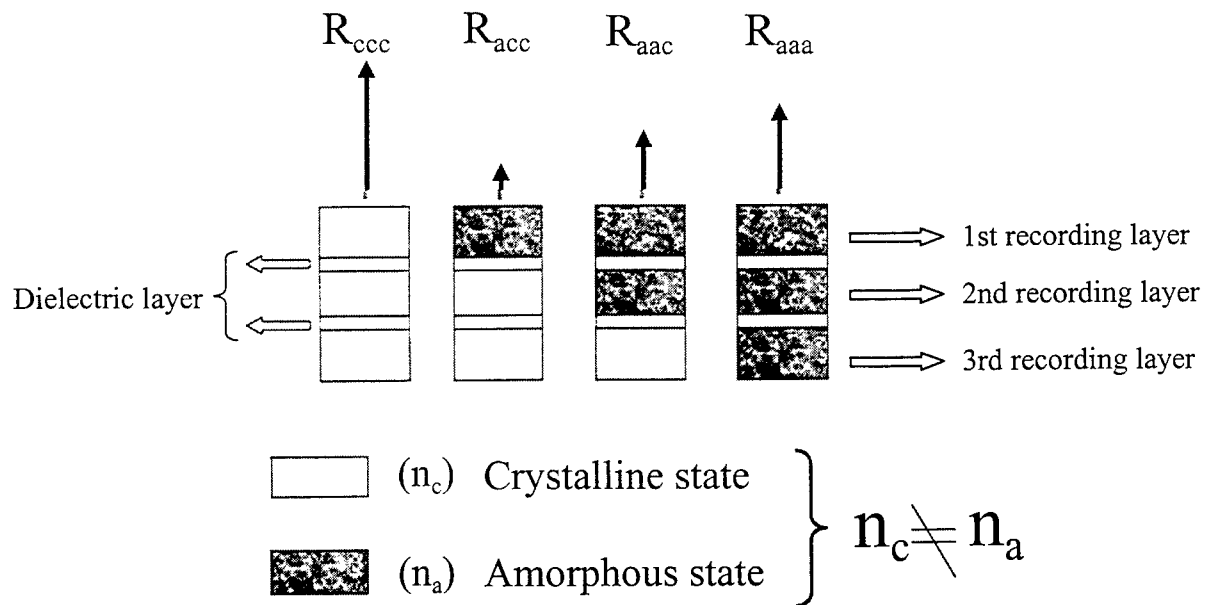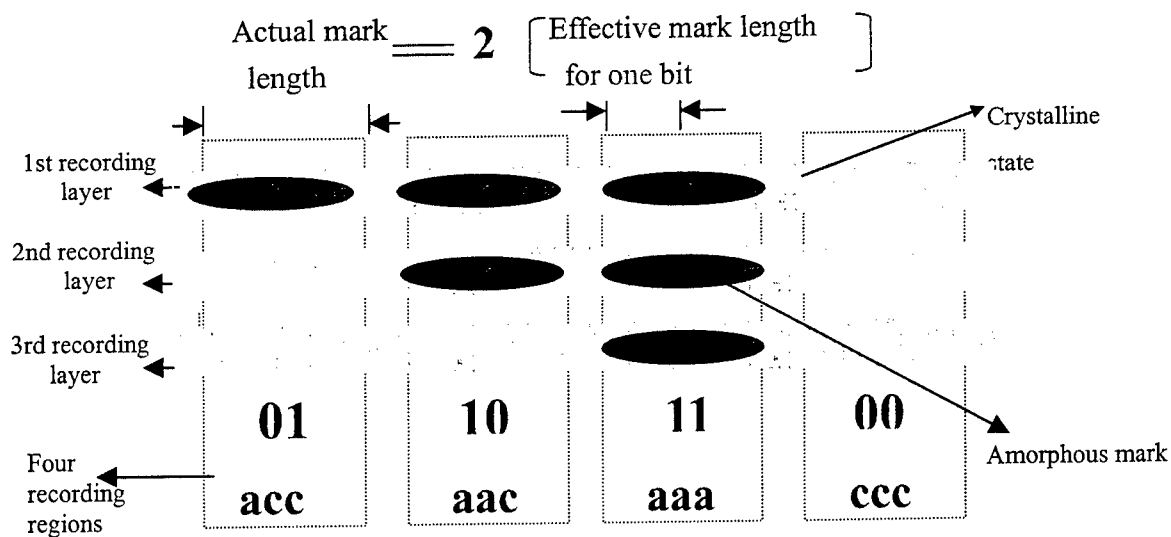Fig. 1 The structure of the four-level recording using erasable phase change media
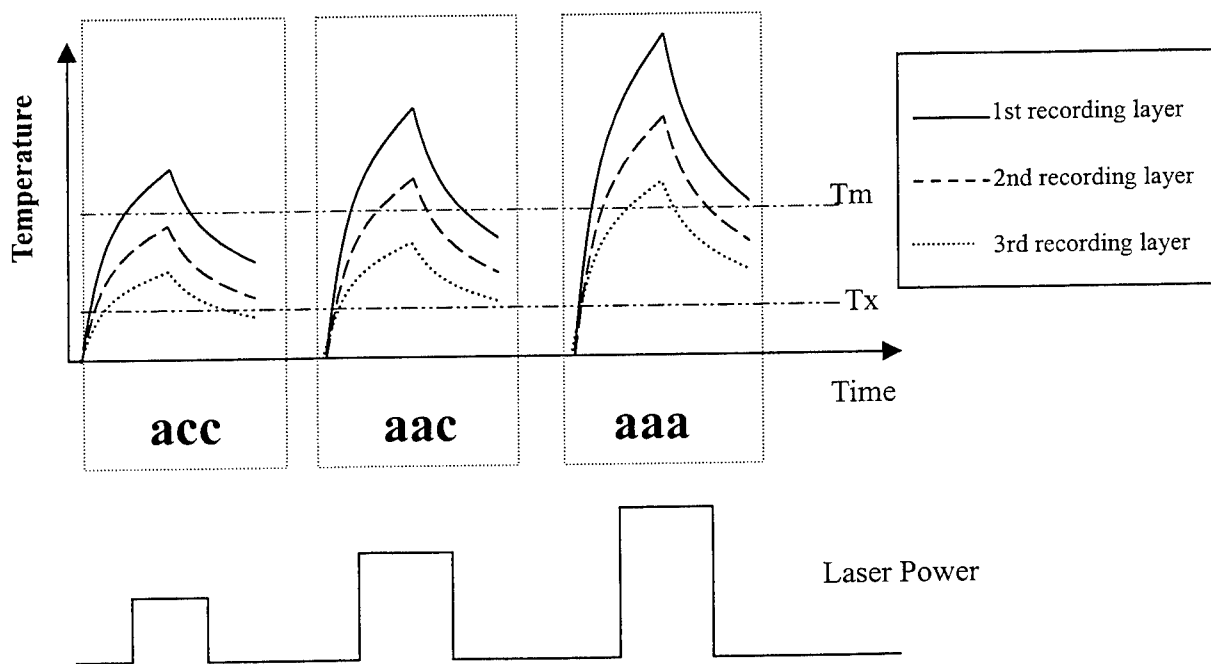

Fig. 2 Four different reflectances of the disk when both recording layers are in the different phase states.

Fig. 3 (a) Four different recording regions, acc, aac, aaa, ccc. (b) Temperature profiles on the recording layers at different recording power to produce different recording regions. Tx and Tm are the melting and crystallize temperature, respectively.
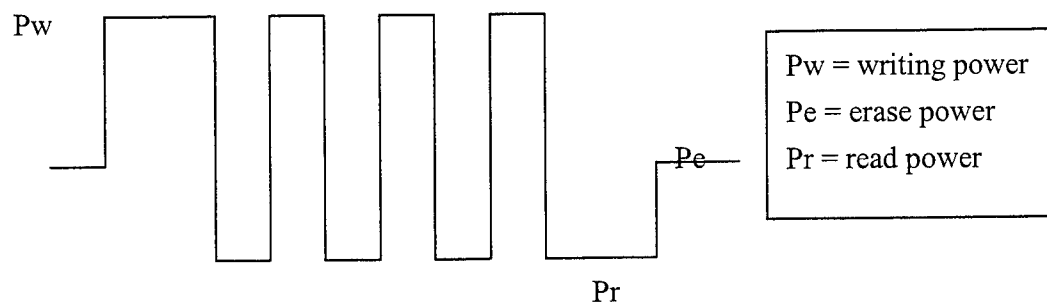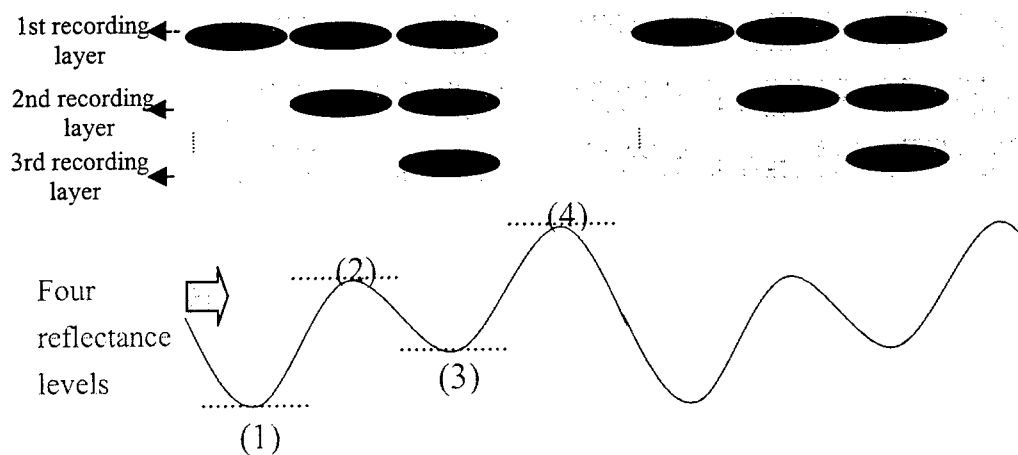
Pw

Pw = writing power
Pe = erase power
Pr = read power

Pe

Pr

Fig. 4 Multi-pulse recording waveform.

1st recording layer

2nd recording layer

3rd recording layer

Four reflectance levels

(1)

(2)

(3)

(4)

Fig. 5 The readout signal of the disk of four reflectance levels.

Pw1

Pw2

Pw3

Pe

Pw1= 9mW
Pw2= 11mW
Pw3= 14.5mW
Pe= 4mW

1st recording layer
2nd recording layer
3rd recording layer

0.8um

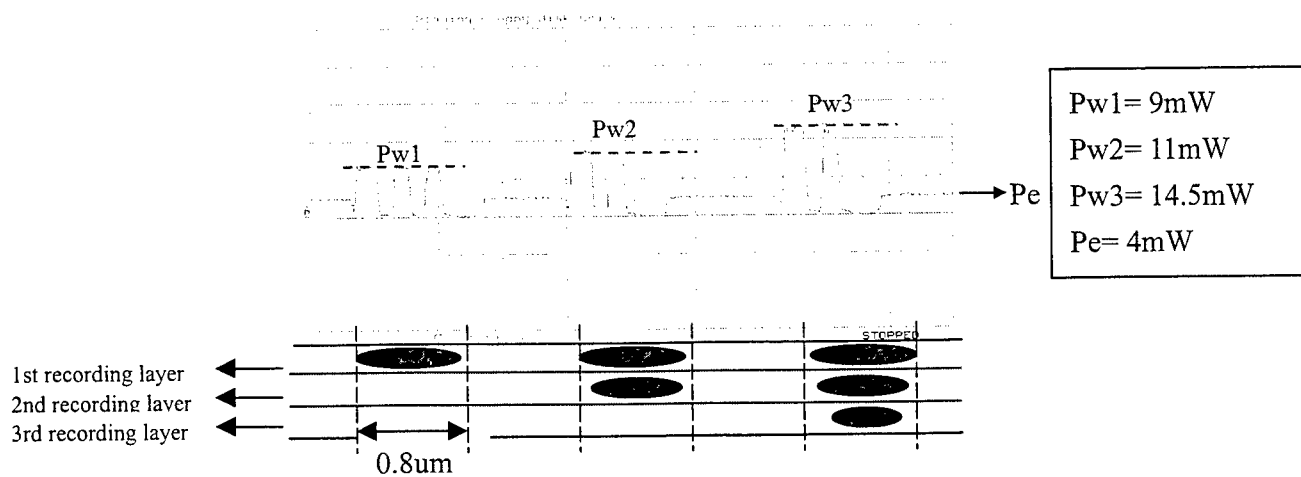Fig. 6 When the recorded mark size is about 0.8um, the different recording regions are produced by pulse readout method.
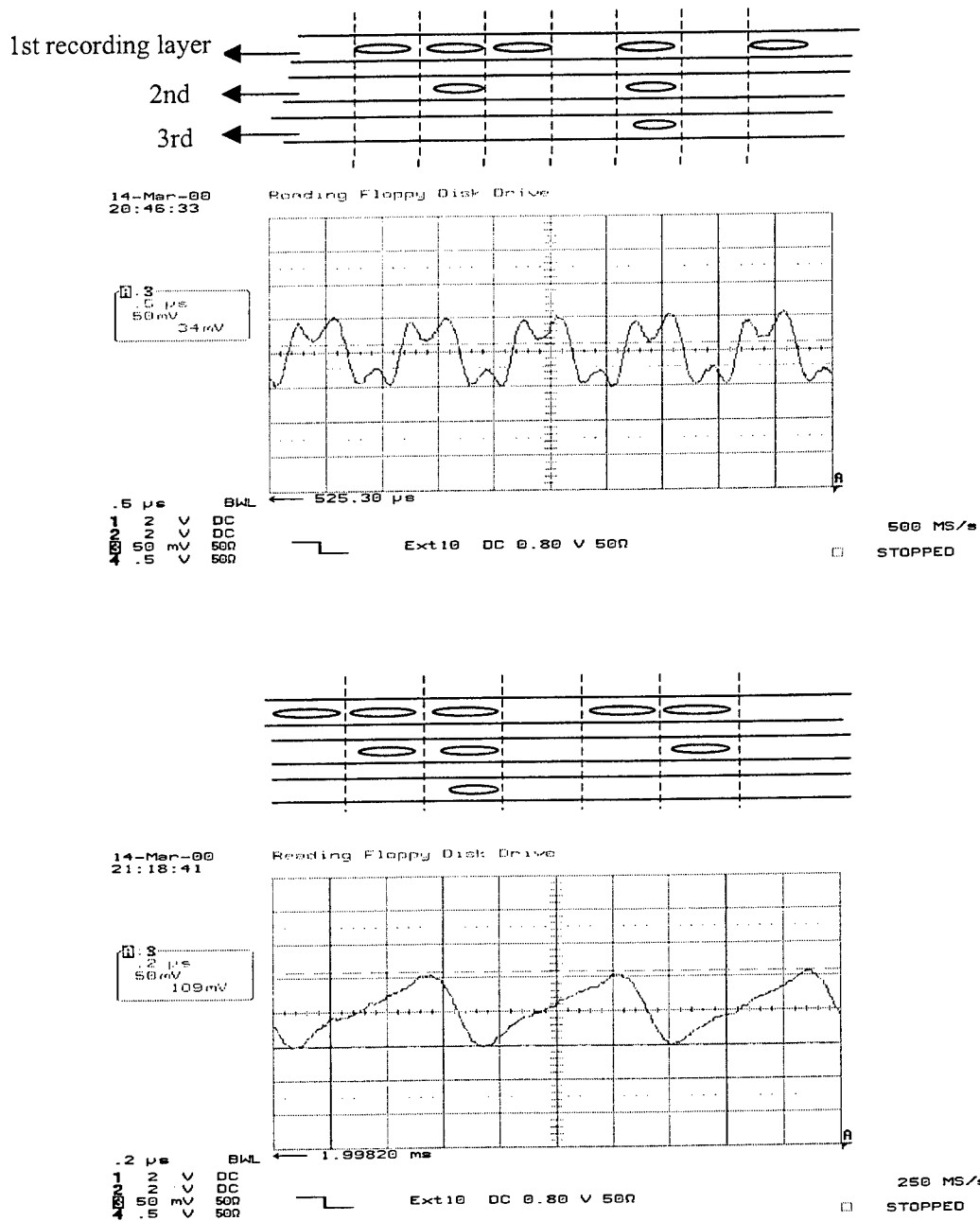
Fig. 7 (a) The readout signal of the repetitive recording regions with the DC-read detection when the mark size is about 0.8um. (b) The readout signal of the different recording pattern.
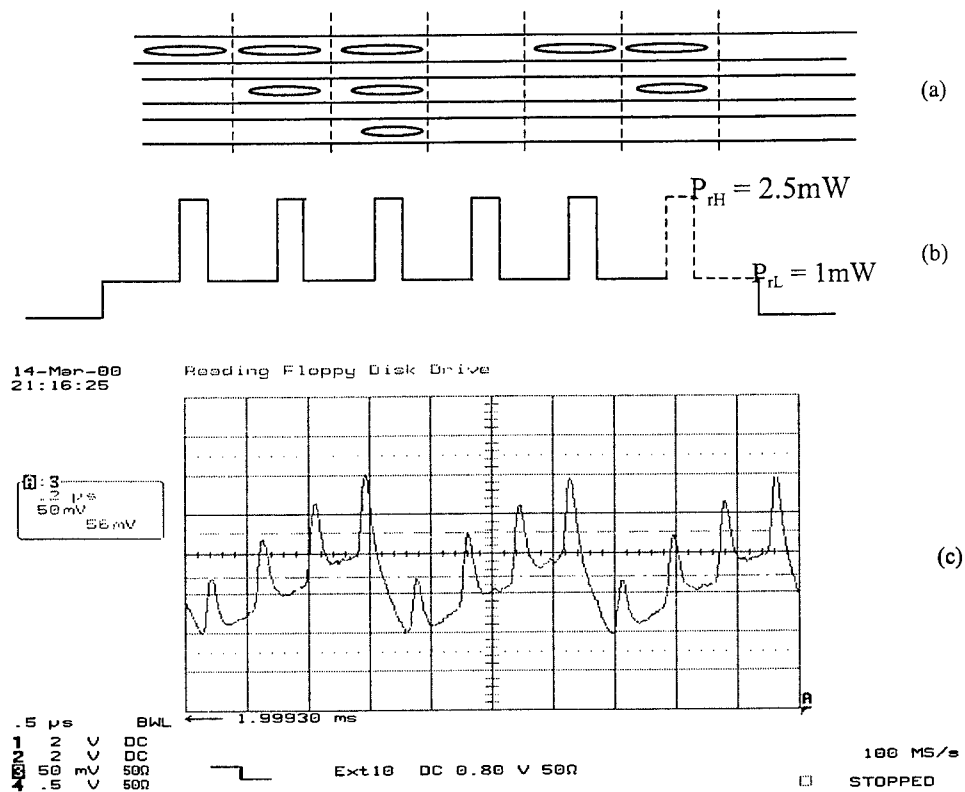
(a)

$P_{rH} = 2.5mW$

(b)

$P_{rL} = 1mW$

14-Mar-00
21:16:25

Reading Floppy Disk Drive

3
.2 µs
50 mV
56 mV

(c)

.5 µs   BWL   ← 1.99930 ms
1 2 V DC
2 2 V DC
3 50 mV 50Ω   Ext10 DC 0.80 V 50Ω
4 .5 V 50Ω

100 MS/s

STOPPED

Fig. 8 (c) The readout signalof the repetitive recording regions with (b) the pulse-read detection (a) when the mark size is about 0.8um.

16-Mar-00
11:41:23

Reading Floppy Disk Drive

3
.2 µs
25.0 mV
-23.9 mV

.2 µs   BWL   ← 1.70776 ms
1 2 V DC
2 1 V DC
3 50 mV 50Ω   Ext DC 240 mV 50Ω
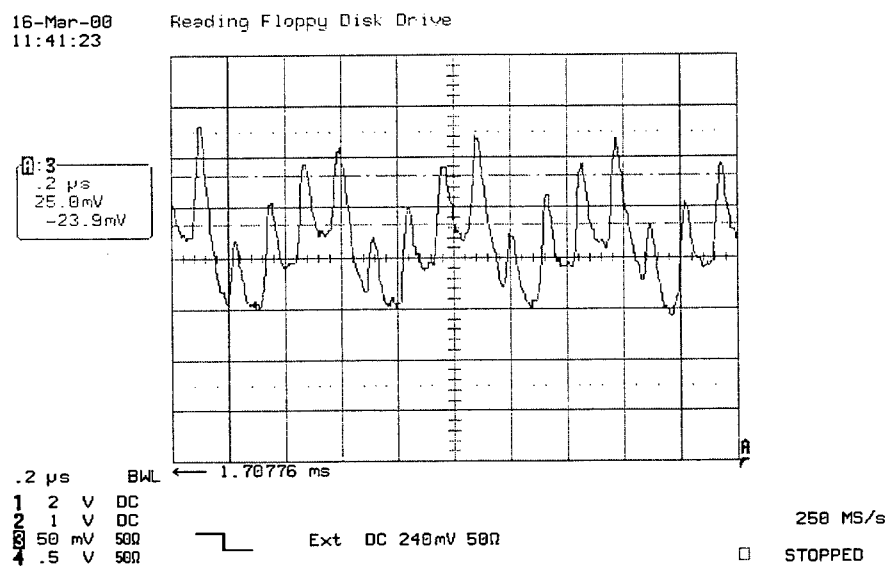4 .5 V 50Ω

250 MS/s

STOPPED

Fig. 9 The readout signal with the PULSE-read detection when the mark size is about 0.6um.
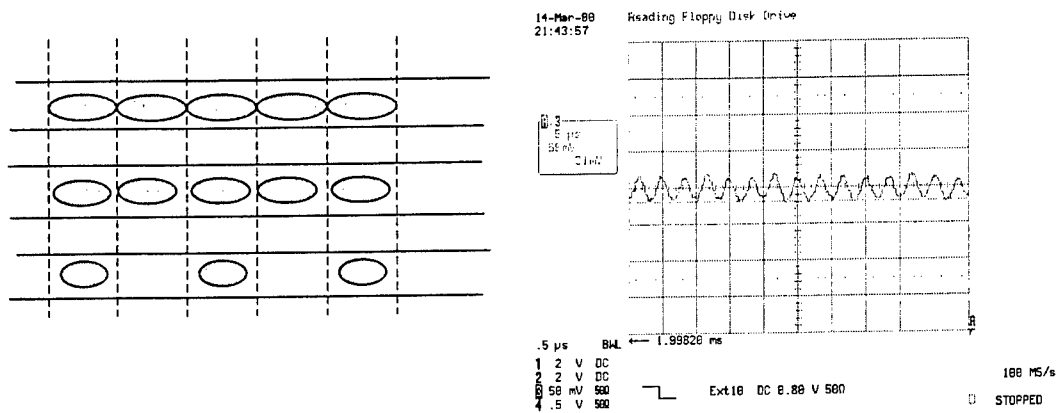
67

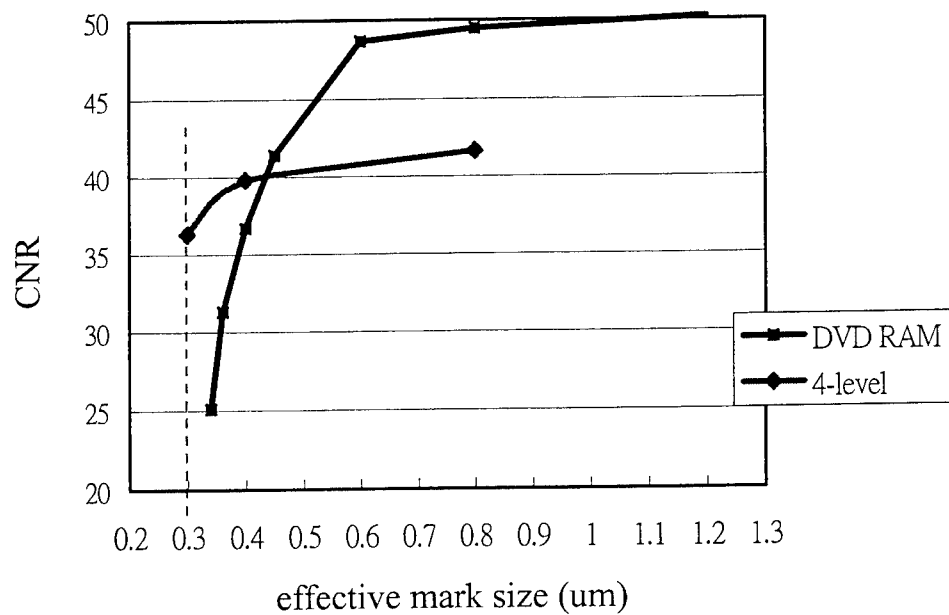Fig. 10 The C/N of the four-level disk is measured with this repetitive recording pattern.

Fig. 11 C/N as a function of the effective mark length in a four-level disk and a conventional disk.

Adaptive-Speed Quasi-CAV Algorithm In A CD-RW Drive

M.S. Mason Yen, Wai William Wang, C.H. Lester Chen, T.T. Chen

Storage Devices Division, Acer Peripherals, Inc.
157, San-Ying Road, Kwei-Shan, Taoyuan, Taiwan

I. Introduction

The performance of a CD-RW drive is evaluated mainly in terms of recording data rate, access time, and power consumption. Constant linear velocity (CLV) recording technology is broadly employed in almost all the commercially available CD-RW drives today. In the CLV mode, the spindle motor which is driven by the real-time linear velocity of the disc will always be braked while seeking outwards or accelerated for inward-oriented seeks. Since the motor driver is driven in saturation, additional power dissipation will occur. This is undesirable in a CD-RW drive especially during data recording and accessing and huge power consumption will thus take place.

When a long sequence of recording and seek actions are taking place, the spindle motor keeps braking and accelerating to result in excessive heat generated. Further, with even higher than 16X CD-RW drives on the horizon, the CLV would not only cause over heating but also induce larger vibration to distort the system. A feasible approach to avoid the excessive heat and vibration is to employ constant angular velocity (CAV) to record the data in a CD-RW drive. Since CAV recording would require the on-the-fly optical power calibration (OPC), this imposes a totally new generation of technology requirement on the chipset and system design which are not currently available yet to the mass market. A quasi-CAV recording technique is thus proposed in this paper. This quasi-CAV recording algorithm can not only effectively reduce the heat dissipation in a CD-RW drive during recording but also avoids the complicated interaction of on-the-fly write strategy adjustment.

In this paper, both experimental results and software implementation technique are presented.

II. Quasi-CAV recording algorithm and implementation

In order to realize the quasi-CAV recording in a CD-RW drive, a software technique is employed to arrange the data recording area into zones and stored in the drive firmware while the physical disc is no difference as compared to the regular CD-R disc. Within each speed zone, a corresponding recording speed is mapped.
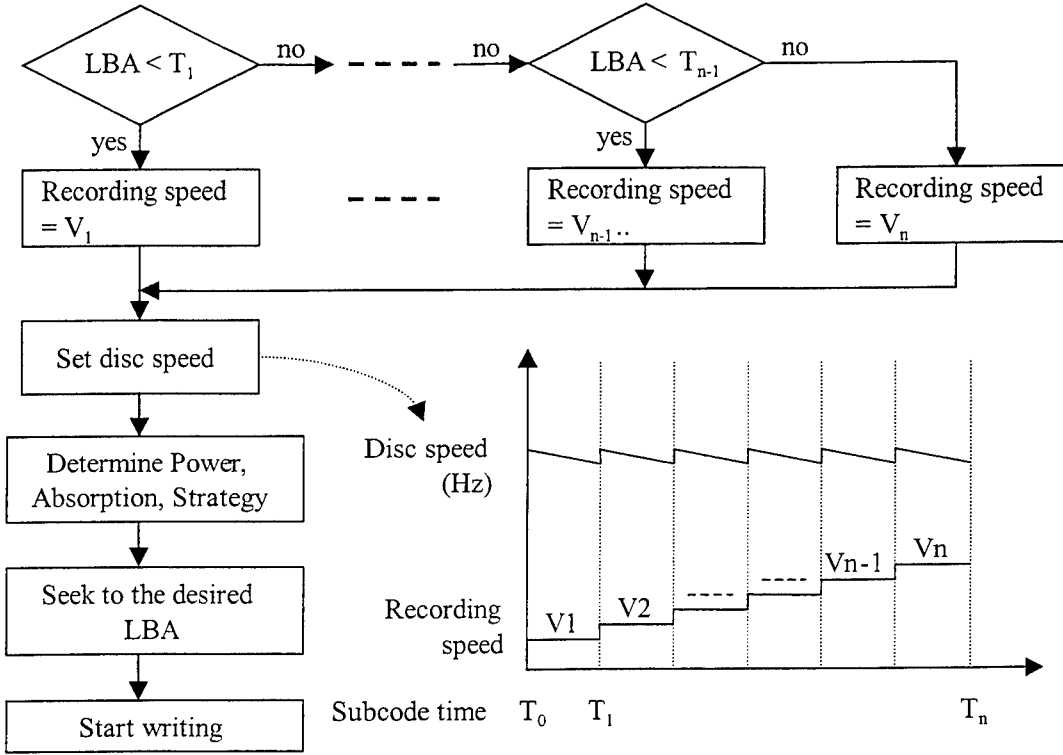

Figure 1. This figure shows the quasi-CAV firmware algorithm and conceptual zoning of the recording areas. V_n is the disc recording speed for zone n.

The each speed zone subcode address can be determined by

$$T_i = (R^2_i - R^2_0)/(V_a q) + T_0 \quad i = 1, 2, \dots, n \quad \text{Eq. (1)}$$
$$\text{where } R_0 = (N_1 V_1)/\omega_0 \quad \text{Eq. (2)}$$
$$R_i = (N_{i+1} V_1)/\omega_0 \quad \text{Eq. (3)}$$

where T_0 is the subcode location of the logic block address (LBA) where the data recording area starts on a disc, R_0 is the physical radius of T_0, T_i is the subcode location where the recording speed switches from V_i to V_{i+1}, n is the number of speed zones, R_i is the physical radius of T_i, V_i is the recording velocity of speed zone i where the subcode time starts at T_{i-1} and ends at T_i, N_i is the overspeed factor corresponding to the ith speed zone, V_a is the linear velocity of 1.3 m/s, ω_0 is the starting disc angular velocity of each speed zone, and q is the track pitch of 1.6 μm in a CD disc. To obtain the optimized

writing quality, the optical laser power calibration procedure is stored in EEPROM of a CD-RW drive to map the optimal laser power for each corresponding speed zone. The procedure of optimal power calibration (OPC) is executed through firmware implementation.
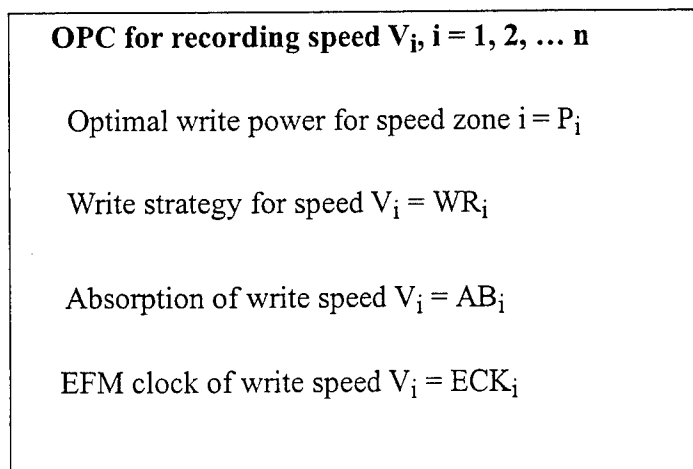
OPC for recording speed V_i, i = 1, 2, ... n

Optimal write power for speed zone $i = P_i$

Write strategy for speed $V_i = WR_i$

Absorption of write speed $V_i = AB_i$

EFM clock of write speed $V_i = ECK_i$

Figure 2 The procedure of optimal power calibration of each speed zone.

To execute a sequential writing with starting address at T_s and ending address at T_e on a disc, the function block of writing through firmware execution is shown in Figure 3. Packet writing methodology is implemented in this writing algorithm. For continuous random writing, this functional block can be recalled and executed repeatedly to complete the writing process. The starting and ending address for each writing cycle is not necessarily to be coincided with the starting and ending address of each speed zone but can be anywhere in the data recording area on a disc.
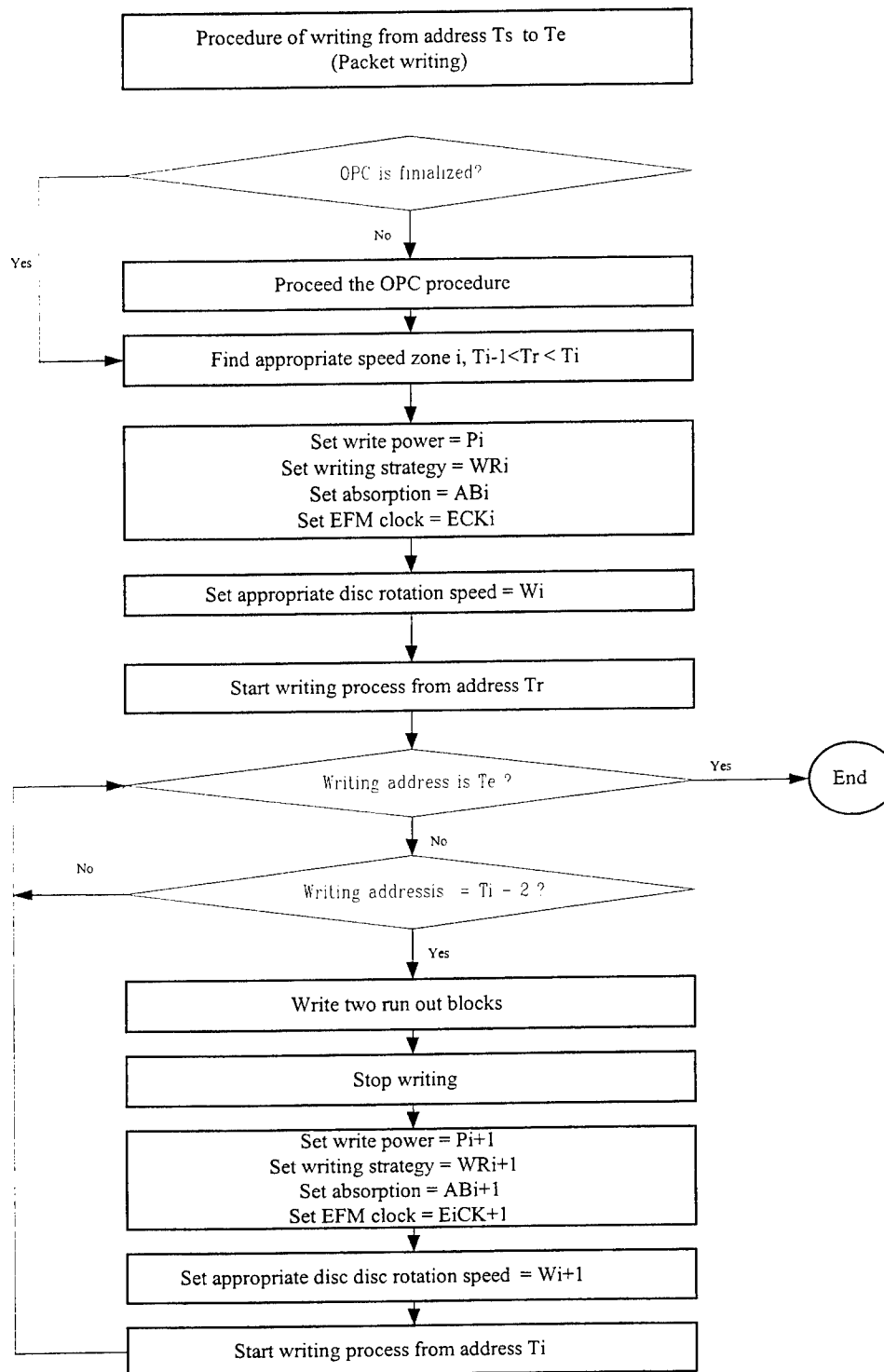
Figure 3 The functional flowchart of execution a sequential writing with a starting address at T_s and ending address at T_e.

III. Experiment and result

The CD-RW drive used in this experiment is a prototype of Acer CDRW1232A which employs this quasi-CAV recording algorithm. The speed zone of this CD-RW drive reported in this paper is defined as shown in figure 4. The power consumption of the spindle motor loop is significantly reduced when quasi-CAV recording is activated during continuous recording, as shown in figure 5.
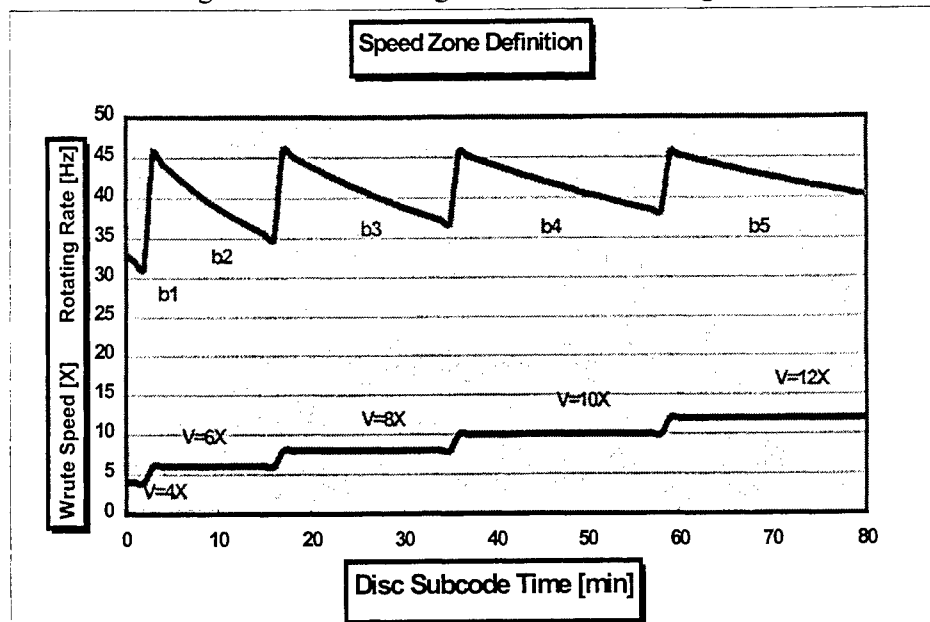

Figure 4 Speed zone definition in prototype of Acer 1232 CD-RW drive.

	CLV recording at 8X	Quasi_CAV recording at 12X
Spindle motor Temperature	60° C	41° C
Power consumption of motor driver	4.3W	1.8W

Figure 5 The power consumption comparison of CLV and quasi-CAV recording.

IV. Conclusion

A quasi-CAV recording algorithm in a CD-RW drive is proposed. This algorithm can greatly improve the power consumption in a CD-RW drive as compared to the commonly employed CLV recording algorithm. This quasi-CAV algorithm also relaxes the system design requirement as compared to the true CAV recording system.

Reference:
[1] S. G. Stan, H van Kempen, C.C. Steve Lin, M.S. Mason Yen, and Wai William Wang, "High Performance Adaptive-Speed/CAV CD-ROM Drive", Vol. 43, number 4, PP. 1034-1044, Consumer Electronics, Nov. 1997.

SESSION 3

High Density and Superresolution

Three-dimensional memory

Yoshimasa Kawata

Faculty of Engineering, Shizuoka University,

Johoku, Hamamatsu, 432-8561, Japan

ABSTRACT

Three-dimensional optical memory with photorefractive materials is discussed for ultra-high density/capacity memory exceeding the classical limit of a conventional optical recording system. Bit data are recorded as highly localized refractive index variations in three-dimensional volume using a focused laser beam. We show recording and reading results using various recording materials and optical configurations. A multi-structured optical recording medium using a photoisomerization polymer and a transparent films has been developed for reflection confocal reading. Two-photon recording is also demonstrated.

Keywords: optical memory, confocal microscopy, two-photon absorption, photopolymer, hologram memory

1. INTRODUCTION

Optical memories such as compact disks (CD) and magneto-optical disks (MO) are becoming essential in high technology products such as audio and visual disks, and the external computer memory disk. In these memory devices a laser beam is used to record and read information. Since the laser spot can be focused to within 1 μm scale, optical memory can attain higher density and capacity than those of magnetic memory.

Optical memory is ultimately limited by the diffraction of electro-magnetic waves. Present techniques have almost reached this limit in optical memories that are commercially sold as compact disks or magneto-optic disks. Even with an infinitely large objective lens, the best achievable bit-data resolution distance for recording and reading is never smaller than half the beam wavelength.

To overcome the density limitation, multilayered optical memories have been investigated by many researchers.[1-6] In the memories the z or longitudinal axis is utilized in addition to the surface dimension ($x - y$ space) of conventional optical memory. The data are thus written not on the material surface but within the three-dimensional (3D) thick volume.

This approach requires an optical reading system that is able to read the data from a particular layer without cross talk between adjacent layers. It is also required to a recording technique on which it is possible to write information at a particular layer without erasing or corrupting the data already written at neighboring layers.

In this paper we describe the 3D optics as recording and readout systems of the multilayered optical memories using photorefractive materials. Some configurations of readout system are discussed and the use of two-photon absorption to reduce the cross talk between adjacent layers is also demonstrated.

E-mail: kawata@eng.shizuoka.ac.jp

2. BIT-ORIENTED THREE-DIMENSIONAL MEMORY

Figure 1 shows a principle of bit-oriented three-dimensional (3D) optical memory. A laser beam is focused into a point in a recording medium. Chemical reactions of the medium should be induced at the spot because extremely high intensity is produced at the focus point. By 3D scanning of the focus spot in the medium we can record bit data in the medium in three dimensions.

Various materials such as photopolymers, photorefractive crystals, photochromic materials, polarization sensitive materials can store data. Among them, photorefractive recording mediums in which data are stored as refractive-index change are most promising materials in 3D memory because they have little absorption so the light penetrates in deep layer in the mediums.

Figure 2 shows a typical readout system of 3D memory. This is basically reflection confocal microscope configuration. Since the pinhole before a detector eliminated scattered light from out of focus region, so the system gives very good axial resolution and high contrast. The optical setup is very simple. We can also use other configurations, which are sensitive refractive-index variations, such as phase contrast microscope, differential phase contrast microscope, differential interference microscope, as readout system.[7,8]
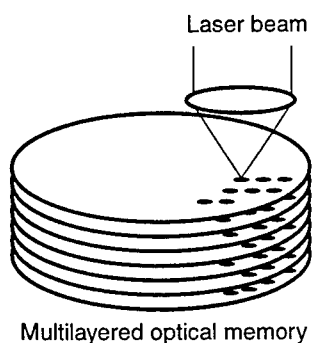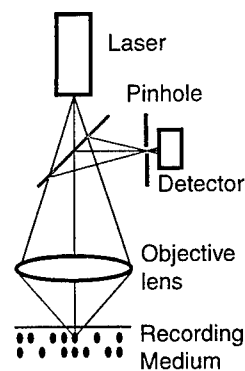
Figure 1. Principle of 3D memory

Figure 2. Reflection confocal readout system

3. PHASE-CONTRAST READOUT USING PHOTOPOLYMER MATERIALS

Figure 3 shows an example of 3D optical memory recording and reading using a photopolymer material. Bit data were written every 2 μm$\times$2 μm in a plane, and the longitudinal separation between the data planes was 10 μm. The total number of layers recorded for the optical memory shown in Fig. 3 was 30, which cover a total longitudinal length of 300 μm. The images were obtained using an ordinary phase-contrast microscope.

The photopolymer memory medium we used was monomer mixture composed of a methacryl compound and an allyl compound with benzil as an initiator and michler's ketone as a dye sensitizer.[9] The metacryl compound polymerizes faster than the allyl compound when illuminated with light. This causes the refractive index to increase from $n \simeq 1.5$ to $n \simeq 1.6$.

The photopolymerizable solution was sandwiched between a microscope slide and a microscope cover glass (thickness 170 μm) to prevent oxygenation of the photopolymer. The spacers between the slide and the cover glass was also made with cover slips of about 1 mm thickness.
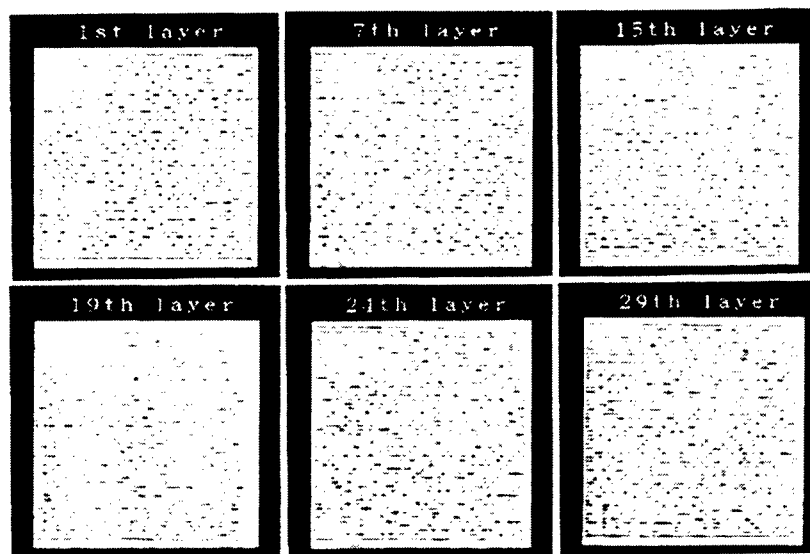
Figure 3. 30 layers recording and reading using photopolymer material

In order to write the data, the photopolymer is placed on a computer-controlled $x - y - z$ microscope stage. A 5 mW argon-ion laser, 488 nm wavelength, was used as the light source, which was focused onto the photopolymer by an objective lens (Carl Zeiss Axiophoto, NA=1.0, oil immersion, 40× magnification). An exposure time of 60 ms per point was used. At the focused spot, methacryl compounds photopolymerize because of their fast photopolymerization property. Allyl compounds, on the other hand, do not photopolymerize because the speed of photopolymerization of allyl compounds is slower than that of methacryle compounds.

As a result, only methacryl compounds are polymerized at the focused spot and the allyl compounds are pushed away, leaving a high-refractive-index region. We then record the data in the medium by scanning a focused spot in three dimensions with an exposure time of 60 ms at each data point.

We also developed a confocal type phase-contrast readout system. Figure 4 shows an optical setup of confocal configurations. This system is a laser-scanning confocal microscope appropriate for phase-contrast imaging. Point light source illumination reduces unnecessary scattered light because the point detector of a confocal microscope only detects the light intensity from a specific point of interest in the thick sample and rejects the scattered light produced from other non-focused points. High contrast images are therefore observed, and unwanted cross talk between planes is low. Better performance is obtained in comparison with the images produced using a conventional optical microscope. Spatial resolution is also improved because of the nonlinear frequency-response of the photorefractive materials.

Figure 5(a) presents an example of bit data which were read out using a confocal microscope, together with Carl-Zeiss Axiophoto. A He-Ne laser (632.8 nm) was used together with a phase-contrast objective and an annular pupil for phase-contrast (dark field) imaging. For comparison the same segment of the data was read using a conventional microscope with the same objective lens, and is shown in Fig. 5(b). The results demonstrate the advantages of confocal microscopy for high-contrast and high-resolution imaging of 3D structures. Since only the light intensity in the conjugate pair of the point of interest in the thick sample volume (or the focused point of the laser beam in the volume) is detected in a confocal microscope, scattered light produced by other non-focused points does not
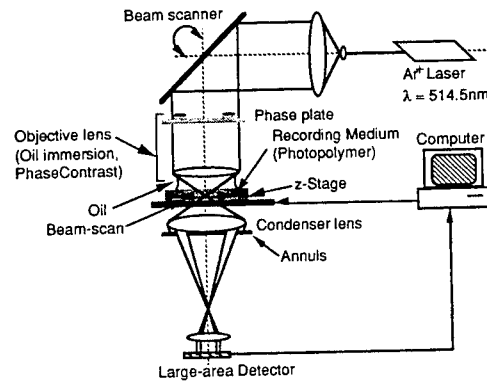
Figure 4. Optical setup of confocal type phase-contrast readout system.

contribute to the detected signal. Hence, the signal contrast of the images is excellent and the cross-talk between planes is negligible compared with images obtained using a non confocal microscope. Spatial resolution is also better because of the nonlinear spatial response (product of illumination point-spread functions and the detection amplitude point-spread function).
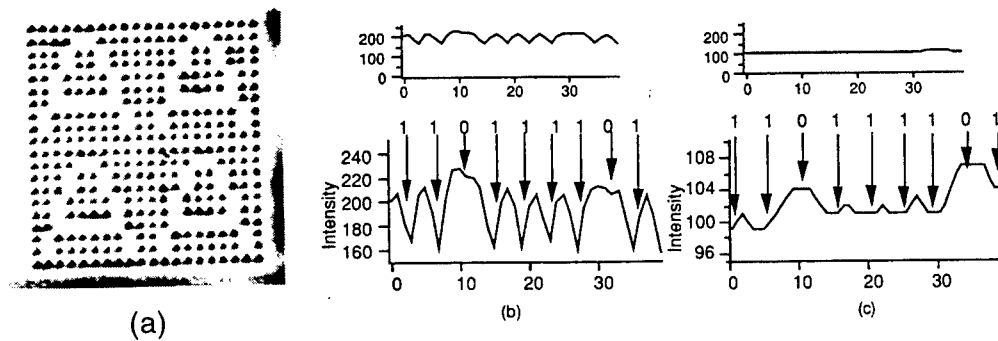

Figure 5. Readout result by using confocal phase-contrast microscope.

4. MULTI-STRUCTURED RECORDING MEDIUM
FOR READING WITH REFLECTION CONFOCAL MICROSCOPE

Reflection-type confocal microscope has very high axial resolution, so it is a very attractive configuration as the readout system of multilayered optical memories. However, it is difficult to use the reflection-type confocal configuration as the readout system, because an extremely high numerical aperture (NA) lens is required for recording and reading.[10]

Some techniques have been proposed in order to read out data in multilayered memories with the reflection confocal configuration. Wilson et al. proposed the recording with 4Pi confocal configuration,[10] while Toriumi et al. proposed the use of two-photon recording and reading with longer wavelength light.[11]

We achieved the reflection confocal readout by using a recording medium in which photosensitive thin films

and non-photosensitive films are piled up alternately.[12] We used urethane-urea copolymer film as the photosensitive material.

Figure 6 shows the spatial frequency distributions of bit-datum recorded with focused laser beam and coherent optical transfer function (CTF) of reflection type confocal microscope.[13,14] Figure 6(a) shows a spatial frequency distribution of bit datum recorded in very thick medium. This distribution coincides with the spatial frequency distribution of the focused light to record the bit data, because the bit is recorded with the focused beam. It is assumed that the NA of the objective lens is given by $n \sin \alpha$ and $k = 2\pi/\lambda$, where λ denotes the wavelength.

Figure 6(b) shows the spatial frequency distribution of bit-datum recorded in the thin layer of which thickness is same as the wavelength of recording light. Since the extension of the recorded bit in the axial direction is limited by the thickness of the photosensitive film, the spatial frequency distribution of the bit datum is much extended in the axial direction. The distribution is calculated by the convolution between the spatial frequency distribution of focused spot and the distribution of thin photosensitive film.

Figure 6(c) shows the CTF of reflection confocal microscope. As Wilson et al. pointed out,[10] the spatial distribution shown in Fig. 6(a) has no overlap with CTF of reflection confocal microscope unless we use extremely high NA lens.

The spatial distribution shown in Fig. 6(b) easily has overlapping area with the CTF, if we carefully select the thickness of the recording layer. As a conclusion, we can read the data with the reflection confocal configuration by using the medium piled up the thin recording layers and non-photosensitive transparent layers alternately.
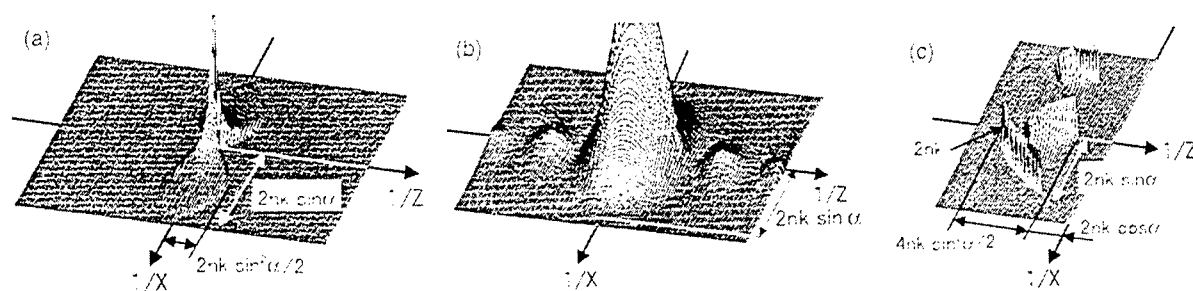

Figure 6. Spatial frequency distribution of the recorded bit datum recorded (a) in a thick medium and (b) in a thin layer. The thickness of the recording layer is the same as the wavelength of the recording light. (a) and (b) are truncated at an arbitrary value to show the structure in the high spatial frequency region. (c)CTF of the reflection confocal microscope.

We developed a recording medium in which photosensitive films and non-photosensitive films were coated on a

glass substrate alternately. Urethane-urea copolymer was selected for photosensitive layers and polyvinyl alcohol (PVA) was used for transparent layers.

Figure 7(a) shows the chemical structure of urethane-urea copolymer.[15,16] The urethane-urea copolymer was originally developed for nonlinear optical waveguide. The copolymer has comparatively high optical nonlinearity and its stability at the room temperature. The copolymer has a side chain structure to semi-fix chromophores as a photosensitizer for optical memory use.

The absorption spectrum of the copolymer shows a maximum at 476.3 nm and little absorption in the region longer than 600 nm. By illumination of blue light, the azo-dye induces cis-trans isomerization producing refractive-index change. The recording process is photon-mode, so the recording time is expected as very fast response.

In generally, it is difficult to pile up two organic films alternately without influence each other. We select PVA as non-photosensitive transparent film, because water and pyridine as solvents for PVA and the urethane-urea do not dissolve the urethane-urea film and the PVA film, respectively. Figure 7(b) shows the multilayered recording medium we developed. The process of making the medium is explained as follows. The urethane-urea copolymer was solved in pyridine and spin-coated on a glass substrate. The thickness was less than 1 μm. After evaporation of pyridine solvent in an oven the PVA film was also spin-coated on the urethane-urea copolymer film. The thickness of the PVA film was about 8 μm. The urethane-urea copolymer was spin-coated again on the PVA film.
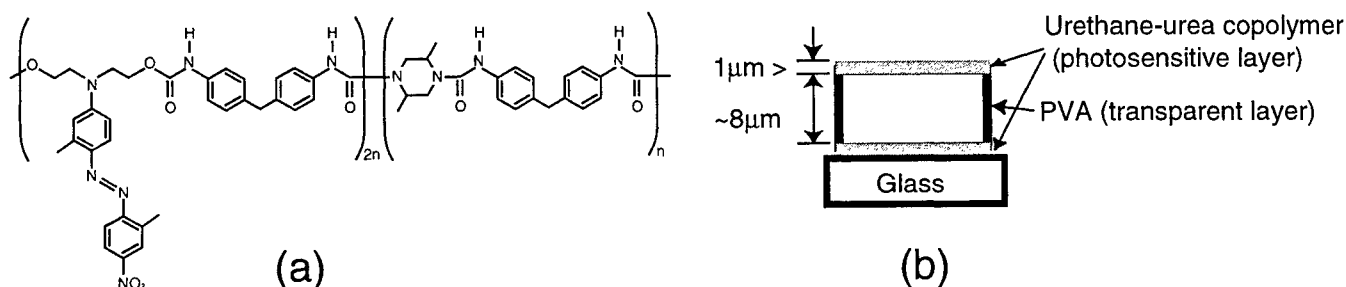

Figure 7. (a)Chemical structure of the urethane-urea copolymers and (b) the recording medium that we developed.

Figure 8 shows the optical configuration of recording and reading data system. An argon-ion laser (Ar^+) is used as a light source for recording. The wavelength of the laser is 488 nm and the output power is about 30 mW. The light is focused with an objective lens (NA: 0.65, 40×) into the recording medium. The medium is scanned with a computer-controlled three-axes stage. A shutter is also computer controlled in order to record the bit sequence in the medium. The power of laser light is adjusted with a neutral density filter. A white light source and a CCD camera is used to observe the recording process.

The readout system is a reflection-type confocal microscope. For reading a helium-neon (He-Ne) laser is used as a light source, because the urethane-urea copolymer has no absorption for red light. The scattered light at the recorded bit data is detected with a photo-multiplier tube (PMT). A pinhole of 30 μm diameter before the PMT eliminates the scattered light from the out of focus of the objective lens.

Figure 9 shows the axial distribution of the recorded data. The figure is reconstructed form a set of many images captured when the focus plane was changed. The three cross sections along the optical axis and along the first and second layers, respectively, are also shown in Fig. 9. The two recording layers are clearly detected. The bit data
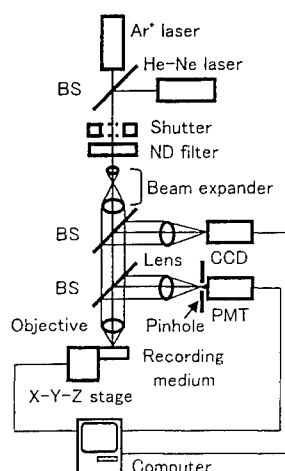
Figure 8. Optical system for recording and reading data of multilayered optical memory.

are also clearly recognized. The side-lobes in the cross-section along the optical axis is due to the aberrations of the objective. We may say that the reflection type confocal microscope configuration can be used as readout system of multilayered optical memory by using the recording medium in which the photosensitive thin films and transparent films are piled up alternately.
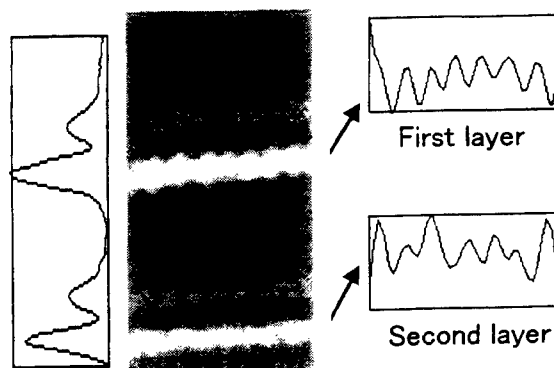

Figure 9. Axial distribution of the two-layer recorded data.

5. TWO-PHOTON RECORDING IN MULTI-STRUCTURED MEDIUM

Two-photon excitation is preferable in 3D optical memory because the crosstalk between adjacent layers is much reduced. Another advantage of two-photon excitation is reduction in multiple scattering. This reduction occurs because of the utilization of an illumination beam at infrared wavelength. A Ti:sapphire laser at 760 nm in mode-locked pulsed laser operation was employed as the recording light source. Since the probability of two-photon absorption is proportional to the squared intensity of the incident light,[17,18] photoisomerization can be induced only at the focal spot, where the intensity is very high. This technique is attractive for recording data in an erasable medium, because it is possible to write information onto a particular layer without erasing the data already written on neighboring layers.

Figure 10 shows a new type multi-structured recording medium. We have succeeded in developing four recording layers. This is very similar with the medium shown in Fig. 7(b) except for transparent layers. We used poly(methyl methacrylate) (PMMA) material with PVA as transparent layers, because it is difficult to coat thick (about 8 μm as shown in Fig. ??(b)) layer of PVA. PMMA is much easier to produce thick layer but it interferes with urethane-urea copolymer layer when it is spin-coated on the layer directly. To avoid such interfere we coated PVA thin film on urethane-urea copolymer layer in order to protect from PMMA.
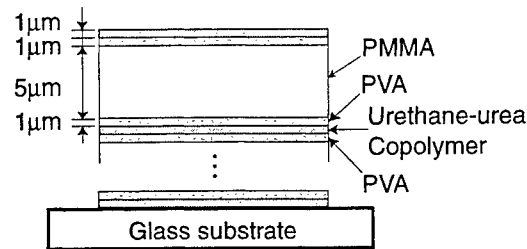

Figure 10. Multi-structured recording medium.

A Ti:sapphire laser was used for a light source of two-photon recording. The wavelength of laser light was 800 nm. Since urethane-urea copolymer has little absorption at the wavelength region longer than 600 nm, bit data should be recorded with two-photon process.

Figure 11 shows readout results of first, third, and fourth layers. Each layer were clearly read out with little crosstalk. In second layer, we failed to record data. We believe that the layer was damaged in the process of pile up other layers.
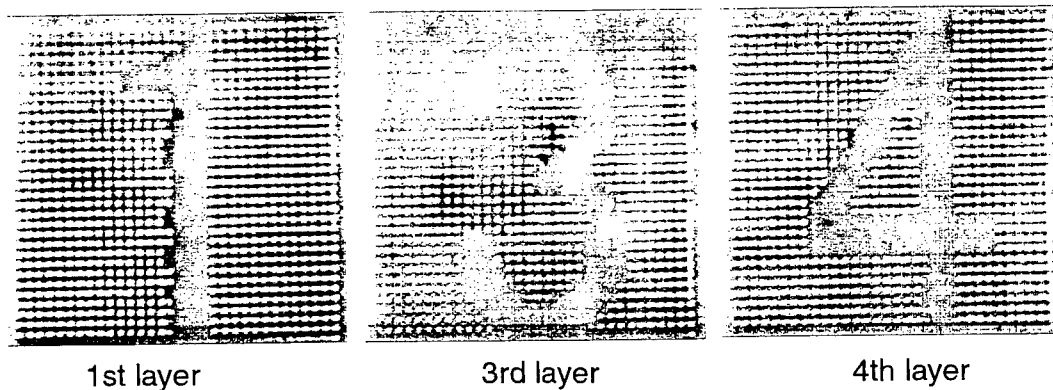

Figure 11. Recording results using two-photon absorption.

6. DISCUSSION AND CONCLUSION

We demonstrated multilayered optical memories in which three-dimensional optics was introduced into the readout system and writing system. The multilayered optical memories have clear advantages over holographic memory

recording.[19] In terms of the signal-to-noise ratio, holographic memory is not robust to speckle noise unlike multilayered memory recording by the focused-beam scanning which is essentially imaging using spatially-incoherent illumination. Moreover, signal contrast in images using confocal imaging is better than that obtained by the hologram read-out because pinhole detection eliminates the scattered light that causes background noise. Moreover, random access bit recording and reading is possible only when using scanning optics.

The high density memory using three-dimensional optics does not conflict with other techniques for achieve high density: they are combined with each other. The multilayered memory is a just extension of z-direction of conventional optical memories, so scanning, tracking, and auto-focusing techniques in the conventional memory systems can be useful with some modifications.

We also presented the confocal readout of multilayered optical memory. For this purpose, the recording medium piled up the thin urethane-urea copolymer films and non-photosensitive transparent films was developed. We need more discussion on the optimization of the thickness of the recording layers and the transparent layers. The thinner film of recording layer much extends the spatial frequency distribution of bit in the axial direction, but it reduces contrast of bit data.

REFERENCES

1. D. A. Parthenopoulos and P. M. Rentzepis, "Three-dimensional optical storage memory," *Science* **245**, pp. 843–845, 1989.
2. J. H. Strickler and W. W. Webb, "Three-dimensional optical data storage in refractive media by two-photon point excitation," *Opt. Lett.* **16**, pp. 1780–1782, 1992.
3. S. Kawata, T. Tanaka, Y. Hashimoto, and Y. Kawata, "Three-dimensional confocal optical memory sing photorefractive materials," *Photopolymers and Applications in Holography, Optical Data Storage, Optical Sensors, and Interconnects*, R. A. Lesard, ed., *Proc. SPIE* **2042**, pp. 314–325, 1993.
4. H. Ueki, Y. Kawata, and S. Kawata, "Three-dimensional optical bit-memory recording and reading with a photorefractive crystal: analysis and experiment," *Appl. Opt.* **35**, pp. 2457–2465, 1996.
5. S. Kawata and Y. Kawata, "Three-dimensional optical data storage using photochromic materials," *Chem. Rev.* (in press).
6. D. Day and M. Gu, "Effects of refractive-index mismatch on three-dimensional optical data-storage density in a two-photon bleaching polymer," *Appl. Opt.* **37**, pp. 6299–6304, 1998.
7. Y. Kawata, R. Juškaitis, T. Tanaka, T. Wilson, and S. Kawata, "Differential phase-contrast microscope with a split detector for the readout system of a multilayered optical memory," *Appl. Opt.* **35**, pp. 2466–2470, 1996.
8. Y. Kawata, T. Tanaka, and S. Kawata, "Multilayered optical memories using three-dimensional microscopy," *Optical Memory and Neural Network* **8**, pp. 1–7, 1999.
9. H. Tanigawa, T. Ichihashi, and A. Nagata, "Hologram recording on multicomponent monomer materials," *Kogaku* **20**, pp. 227–231, 1991.
10. T. Wilson, Y. Kawata, and S. Kawata, "Readout of three-dimensional optical memories," *Opt. Lett.* **21**, pp. 1003–1005, 1996.
11. A. Toriumi, S. Kawata, and M. Gu, "Reflection Confocal Microscope Readout System for Three-Dimensional Photochromic Optical Data Storage," *Opt. Lett.* **23**, pp. 1924–1926, 1998.
12. M. Ishikawa, Y. Kawata, C. Egami, O. Sugihara, N. Okamoto, M. Tsuchimori, and O. Watanabe, "Reflection confocal readout for multilayered optical memory," *Opt. Lett.* **23**, pp. 1781–1783, 1998.

13. N. Streibl, "Three-dimensional imaging by a microscope," *J. Opt. Soc. Am. A* **2**, pp. 121–127, 1985.

14. C. J. R. Sheppard, M. Gu, Y. Kawata, and S. Kawata, "Three-dimensional transfer functions for high-aperture systems," *J. Opt. Soc. Am. A* **11**, pp. 593–598, 1994.

15. Y. Kawata, Y. Aoshima, C. Egami, M. Ishikawa, O. Sugihara, N. Okamoto, M. Tsuchimori, and O. Watanabe, "Light-induced surface modification of urethane-urea copolymer film used as write-once optical memory," *Jpn. J. Appl. Phys.* **38**, pp. 1829–1831, 1999.

16. S. Alasfar, M. Ishikawa, Y. Kawata, C. Egami, O. Sugihara, N. Okamoto, M. Tsuchimori, and O. Watanabe, "Polarization-multiplexed optical memory with urethane-urea copolymers," *Appl. Opt.* **38**, pp. 6201–6204, 1999.

17. W. Denk, J. H. Strickler, and W. W. Webb, "Two-photon Laser Scanning Fluorescence Microscopy," *Science* **248**, pp. 73–76, 1990.

18. Y. Kawata, H. Ishitobi, and S. Kawata, "Use of two-photon absorption in a photorefractive crystal for three-dimensional optical memory," *Opt. Lett.* **23**, pp. 756–758, 1998.

19. L. Hesselink and M. C. Bashaw, "Optical memories implemented with photorefractive media," *Opt. Quantum Electron.* **25**, pp. 611–661, 1993.

Readout characteristics and mechanism of light-scattering-mode Super-RENS disks

Junji Tominaga, Dorothea Buechel, Takashi Nakano, *Hiroshi Fuji,
Toshio Fukaya and Nobufumi Atoda

Optical Memory Group
National Institute for Advanced Interdisciplinary Research
1-1-4 Higashi,Tsukuba 305-8562, JAPAN
*Advanced Technology Research Laboratories, Sharp Co.
2631-1 Ichinomoto-cho, Tenri 632-8567, JAPAN

ABSTRACT

Readout characteristics of light-scattering-mode super-resolution near-field structure (super-RENS) disks are described in detail. Readout intensities in reflected and transmitted signals are compared. Both signals showed mostly the same carrier-to-noise ratios (CNRs) using objective lenses with NA of 0.6. The formation mechanism of light scattering centers in the super-RENS disks is also described in comparison with several different disks. As increasing oxygen ratio during the deposition of silver oxide (AgOx) layers, two different chemical reactions were identified. It was found that the super-RENS disks with oxygen-rich AgOx films have both characteristics of transparent and light-scattering apertures in one disk. Further study also revealed that the AgOx dynamic nonlinearity is not so high and less than 6% by the film itself; however, it is enhanced to 12% in super-RENS. It is supposed that the imaginary refractive index k of the films is less than 0.1; therefore, it is hard to heat itself to the decomposition temperature without a heat source (GeSbTe film) underneath. This result would be a hint to further increase CNRs in a light-scattering-mode super-RENS disks

Keywords: optical memory, super-RENS, silver oxide, optical nonlinearity

1. INTRODUCTION

A gate of optical data storage with terabyte (TB) capacity has long been closed by the diffraction limit. However, Re-discovery of the importance of optical near-field and the development of scanning probe microscopes (SPMs) may make it realize such systems.[1,2] Since optical near-field recording (ONFR) was first carried out, a variety of ideas have been proposed and demonstrated theoretically and experimentally.[1-4] One of the difficulties to overcome is to control a space between a recording head and a medium surface carefully and precisely with few 10's nm at very high speeds. Up to date, specially designed optical fiber heads, planner flying heads with the same design as current hard disk heads, solid immersion lens (SILs) and mirrors (SIMs) have been developed.[5-8] One the other hand, our group proposed another idea to fabricate a near-field aperture into an optical disk, in order to avoid a contact or a head crash to the medium surface. We named the disk structure " super-resolution near-field structure (super-RENS)." The principle and characteristics of super-RENS were refereed elsewhere.[9-11] We have developed two different types of super-RENS disks: generating a transparent aperture (TA-super-RENS) with an Sb film and a light scattering center (LSC-super-RENS) with a silver oxide (AgOx) film.[10,11] The resolution of TA-super-RENS disks is superior to that of LSC-super-RENS disks; however, LSC-super-RENS is more attractive and more promising on the point of view of utilizing surface plasmon that further enhances signal intensity.[12] The mechanism of LSC-super-RENS, unfortunately, has not been well identified. The objectives of this paper are to reveal the reaction mechanism of AgOx films in LSC-super-RENS disks statically and dynamically. Especially, we carefully re-estimate the dynamic optical nonlinearities of the films, applying one-dc laser beams to LSC-super-RENS disks and estimating the output

reflections by a storage oscilloscope. We also describe the reflected and transmitted signal characteristics of LSC-super-RENS disks in detail.

2. EXPERIMENTAL

All AgOx films in this work were produced by r.f. reactive magnetron sputtering with a high purity Ag target and gas mixture of Ar and oxygen. The composition of the films can be controlled by changing the gas ratio, and the refractive index is also changed. [11] We used two different substrates: glass plates and polycarbonate disks. In some cases, ZnS-SiO_2 dielectric films were covered on the AgOx films. A $Ge_2Sb_2Te_5$ target was used as a recording film for LSC-super-RENS disks. The disk structures were refered in other papers. [11]

Optical transmission of the films was measured by LIMKAM LK-600PM micro-heating stage at a ramp rate of $30°C/min$ under an optical microscope, which is connected to a multichannel-photodetector (Hamamatsu Photonics, PMA-11) through an optical fiber.

The dynamic optical nonlinearities were estimate by DDU-1000 disk drive tester (Pulstech Indust. Co. Ltd.) with a laser wavelength of 635 nm, and an objective lens numerical aperture of 0.6. Dynamic optical nonlinearities of Sb and AgOx films have already been observed by our group. [11] However, the evaluation of the nonlinearities includes quite large errors because the nonlinearities are gradually increasing or decreasing during measurement in many cases. In order to avoid and evaluate more precisely, we applied one dc laser power on a disk during only one rotation. The reflection change was monitored with a storage oscilloscope synchronizing it to a tracking jump signal. The system configuration was depicted in Figs.1 and 2.
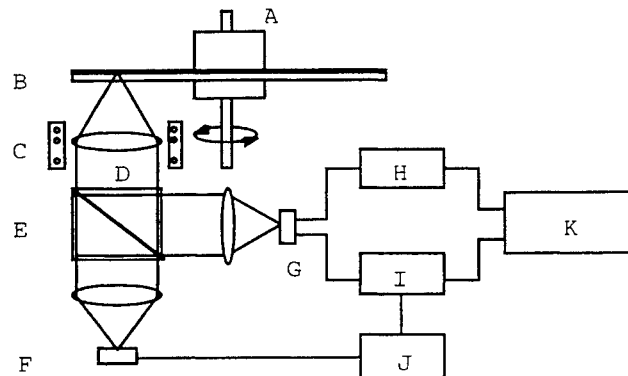

Fig. 1 Schematic diagram of synchronized dynamic disk tester.

A: Spindle motor, B: Test disk, C: voice control optical head,
D: focus lens (NA:0.6), E: beam spritter, F: semiconductor
laser (635 nm), G: photodetector, H: focusing unit, I:
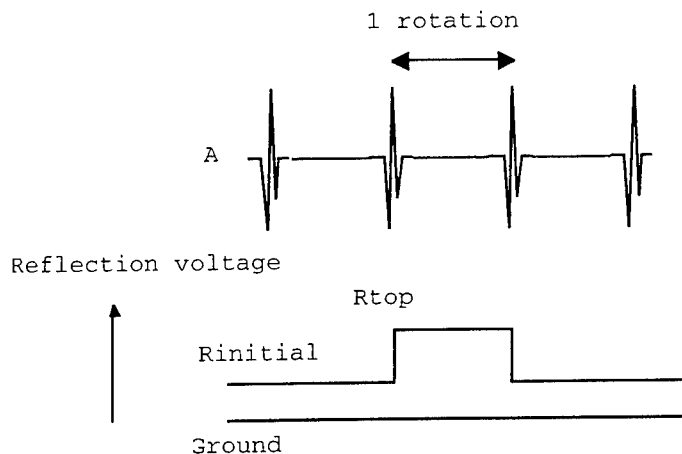tracking unit, J: frequency&laser power modulator and K:
storage oscilloscope.

Fig. 2 Evaluation method of dynamic optical nonlinearity.

A: Tracking-jump signals, Rtop: reflection output by a high readout power during one rotation of the disk, Rinitial: reflection of the initial readout power and G: ground level.

3. RESULTS AND DISCUSSION

3.1. Formation Mechanism and Dynamic Optical Nonlinearity of LSC-super-RENS Disks

It is well known that AgOx is easily decomposed into Ag and oxygen at temperatures of less than 200°C. Fig.3 shows optical transmission changes in three different AgOx films (thickness: 100 nm) deposited on glass plates under different mixture gas ratios. The film produced at a ratio of 0.35 shows that the transmittance gradually decreases as the temperature increases. The curve becomes steeper at temperatures of more than 150°C.The films produced with further high gas ratios: 0.5 and 0.6, on the other hand, show maximums at around the same temperature. Interestingly, the transmittance once increases, until the temperature reaches the maximum.   As a reference, the refractive indices depending on the gas mixture ratio are shown in Fig.4. In comparison with two figures, it is noticed that the high-transmitted region exists in the vicinity of the gas ratio of 0.4. The composition of the film was already determined as Ag_2O. [13] In higher temperature region in both cases, the transmission monotonically decreases. Therefore, it is supposed that as-deposited AgOx films usually do not exist as a single phase, but mixture phases with Ag_2O, AgO and Ag_2O_3.

The optical change or phase change from the as-deposited state to the stable state or phase was also confirmed under dynamical conditions. Fig.5 shows reflection outputs from the disk drive tester with the disk samples, whose structure is composed of /ZnS-SiO_2(170 nm)/AgOx (15 nm)/ZnS-SiO_2(20 nm). At the initial laser power (1.0 mW) to obtain a focus for readout, the reflection was 1.17 V. Applying dc laser powers to the disk, the reflection once drops and then is gradually recovered toward the initial. As increasing the dc power, the recovery speed becomes faster. This first reflection drops correspond to those observed in the static measurements. The initial reflection drop seems to appear even with powers of less than 1.5 mW, and at lower disk rotation speeds of less than 6 m/s. It is, therefore, supposed that the initial transition of AgOx films deposited by r.f. sputtering occurs by both thermal and photochemical mechanisms, and Ag_2O rich composition is produced.

It is interesting to confirm if the two different chemical states are actually identified in usual LSC-super-RENS disks. Fig.6 shows carrier to noise ratio (CNR) of 300-nm-sized marks against the increase of readout power. As increasing the power from 1.0 to 2.0 mW, the CNR once gradually increases. As further increasing the power, however, it suddenly drops to a

minimum (12.0 dB) and then it is rapidly improved at powers of more than 2.6 mW. The results are good in agreement with the static and the dynamic nonlinear characteristics.
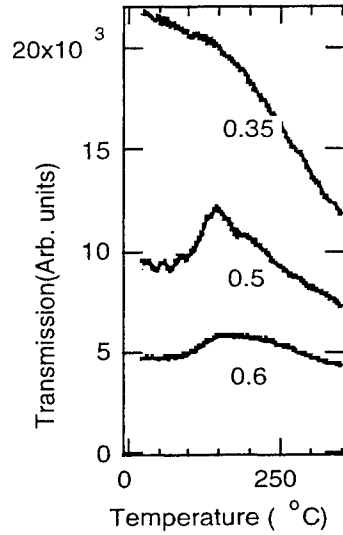

Fig.3 Optical transmission changes of AgOx films by temperature increasing. Each value marked on the lines shows a deposition gas mixture ratio (O_2/(Ar+O_2)). The AgOx films with a 100-nm thickness were all deposited on glass plate by r.f. magnetron sputtering.
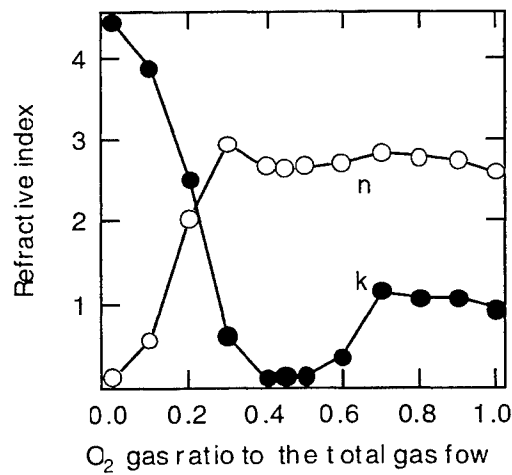

Fig.4 Refractive indices of AgOx sputtered films with different gas mixture ratios.
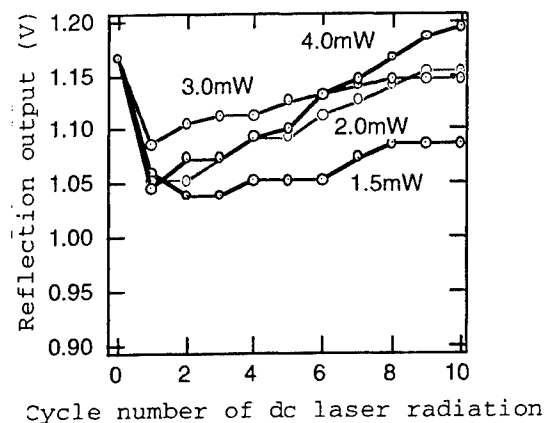n and k show real and imaginal refractive parts.

Fig.5 Dynamic reflection change by applying dc laser radiation.
The disk structure was composed of polycarbonate disk/ZnS-
SiO_2(170 nm)/AgOx (15 nm)/ZnS-SiO_2(20 nm). The disk was rotated
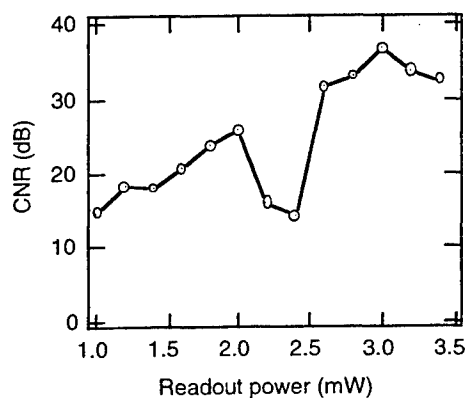at a constant linear velocity of 6.0 m/s.

Fig.6 CNR change of 300-nm sized marks of a LSC-super-RENS
disk against readout power.
The AgOx film was produced at O_2 gas ratio of 0.5.

Optical dynamic nonlinearity is one of the most important properties of super-RENS disks. However, the precise
evaluation is a very hard work because the nonlinearity gradually changes for the time being. In order to avoid the time-shift,
we synchronized one pulse dc laser radiation with a tracking jump signal during one disk rotation. The reflection output was
monitored by a storage oscilloscope. Fig. 7 shows a display of the monitor, when one pulse dc laser is irradiated on a sample

disk. The reflection output was measured against the ground level (G). As shown in Fig.7, the reflection after the laser radiation (C) slightly drops in comparison with that of the initial (A) in case of LSC-super-RENS disks. This is due to the thermally and photochemically produced Ag_2O rich phase, which was above mentioned. As increasing the dc laser power on the same track, One can draw a nonlinear curve at each disk rotation speed (here, we use a constant linear velocity (CLV)).
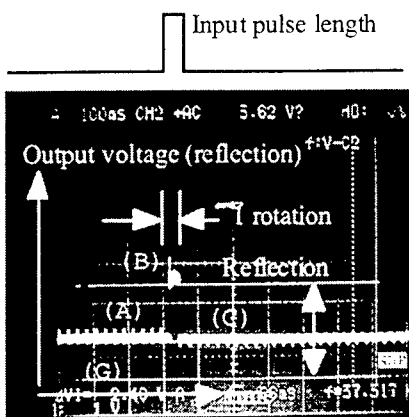

Fig.7 Synchronized one-rotation reflection measurement of dynamic optical nonlinearity.

Fig.8-(a) show the results. As it was already mentioned, the dynamic optical nonlinearity is gradually saturated to a linear relationship by increasing CLV.[14] This is because a special region generating a strong optical nonlinearity gradually shifts to the backward of the laser spot center by the time dulation. The nonlinear shifts in this work against reference values obtained at the highest CLV (9.0 m/s) were smaller than those observed previously by our group.[11] It is important to estimate nonlinear ratios against the reference observed at the highest speed because the magnitude of the nonlinearities may become big or small in aid of the optical interference in the multilayers. The nonlinear ratios at CLVs of 2.0 and 6.0 m/s was evaluated to the reference at 9.0 m/s. The results are shown in Fig.8-(b). The nonlinearity is only about 6% at a maximum of 2.5 mW. As further increasing the power, the nonlinearity gradually dorps. It is interesting to compare the results with the nonlinearities obtained from an actual LSC-super-RENS disk. The results are very intrigued and the nonlinear ratio is improved up to 12%. This is shown in Fig.9. The LSC-super-RENS disk has large nonlinearities at CLV = 6.0 m/s, on the other hand, a maximum appears at 2.0 m/s in the disk without the recording layer. The nonlinearity of the LSC-super-RENS disk at a slow speed (2.0 m/s) once increases: thus reflection increases, then rapidly drops, as increasing the dc power. The irreversible power corresponds to a dc power of 2.5 mW at the speed. As further increasing the power, therefore, AgOx cannot return to the stable phase. As increasing the disk rotation speed (6.0 m/s), on the other hand, such a property is improved up to powers around 3.5 mW. The initial drop that appears in the curve of 6.0 m/s is due to the generation of the stable phase mentioned previously.

In comparison with Figs. 8 and 9, we can reach a conclusion of the mechanism of LSC-super-RENS disks. The large nonlinear characteristics strongly depend on the recording layer deposited on the AgOx layer. As shown in Fig.4, the imaginary part of the refractive index k in normal LSC-super-RENS disks using a AgOx layer, which is deposited at the mixture gas ratio of 0.4 to 0.5, is very small and 0.08. Therefore, the 15-nm thick film does not sufficiently absorb an incident laser beam itself, and it can decompose into Ag and O_2 in aid of a light absorbing layer: that is the recording layer. As a result, it is thought that the mechanism generating a light scattering center in LSC-super-RENS disks is little due to a light-mode, but mostly heat-mode. Additionally, the chemical reaction in LSC-super-RENS disks is more complicate than what we thought previously. However, some important questions have not been revealed yet in this work. The condition of

decomposed oxygen atoms and how the oxygen and Ag return to AgOx again are our further studies. We are now engaging in the research and we will be able to make them clear in the near future.
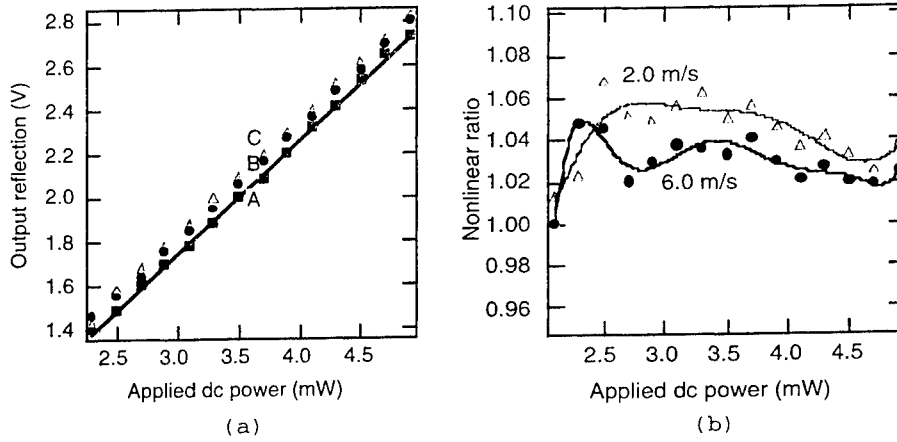

Fig.8 The dynamic optical nonlinearity and the ratios of a AgOx film.
(a):the actually observed nonlinearities. A: CLV=9.0 m/s,
B: 6.0 m/s and C: 2.0 m/s, and (b): the ratios against the data
obtained at CLV = 9.0 m/s.
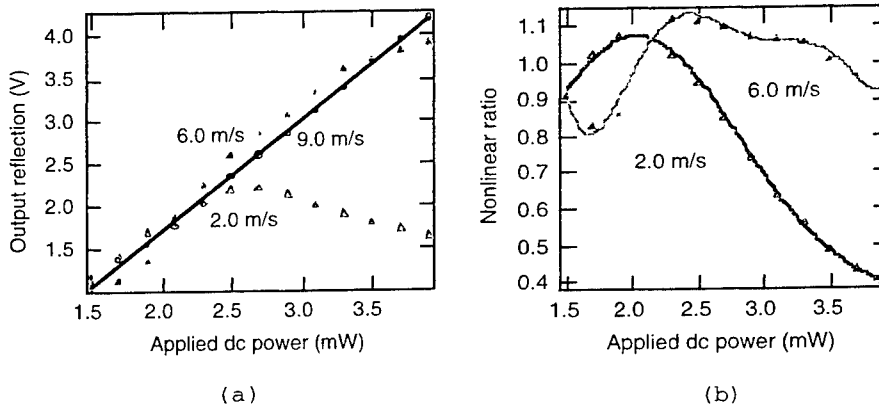The disk structure is PC.-sub/ZnS-SiO$_2$(170 nm)/AgOx(15 nm)
/ZnS-SiO$_2$(20 nm)

Fig.9 The dynamic optical nonlinearities of a LSC-super-RENS disk.
(a): observed nonlinearities, and (b): the ratios against
the data obtained at CLV = 9.0 m/s.
The disk structure is PC.-sub/ZnS-SiO$_2$(130 nm)/AgOx(15 nm)/
ZnS-SiO$_2$(40 nm)/Ge$_2$Sb$_2$Te$_5$(20 nm)/ZnS-SiO$_2$(20 nm).

3.2 Readout Characteristics of LSC-Super-RENS Disks

LSC-super-RENS disks are usually more transparent that TA-super-RENS disks. The transmitted near-field signals of a TA-super-RENS disk were already obtained. [14] It is also important to estimate transmitted signals from LSC-super-RENS disks. A sample disk was produced on a polycarbonate disk with the structure of ZnS-SiO$_2$(147 nm)/AgOx(15 nm)/ ZnS-SiO$_2$

(40 nm)/Ge$_2$Sb$_2$Te$_5$ (20 nm)/ ZnS-SiO$_2$ (20 nm). Fig. 10-(a) shows the readout intensities of both reflected and transmitted signals of 200-nm-sized marks. The recording was carried out on a land at a CLV of 6.0 m/s with the power of 10.0 mW. The system configuration for transmitted signal detection was the same as the previous work. [14] At a readout power of less than 2.0 mW, both signals are little detectable. As further increasing the power, the CNRs gradually increase and are saturated at around 2.4 mW. As shown in Fig. 10, the transmitted intensity is 5 dB higher than the reflected intensity. The tendency did not change in several different disks with different thicknesses. The resolutions are also compared in Fig. 10-(b).
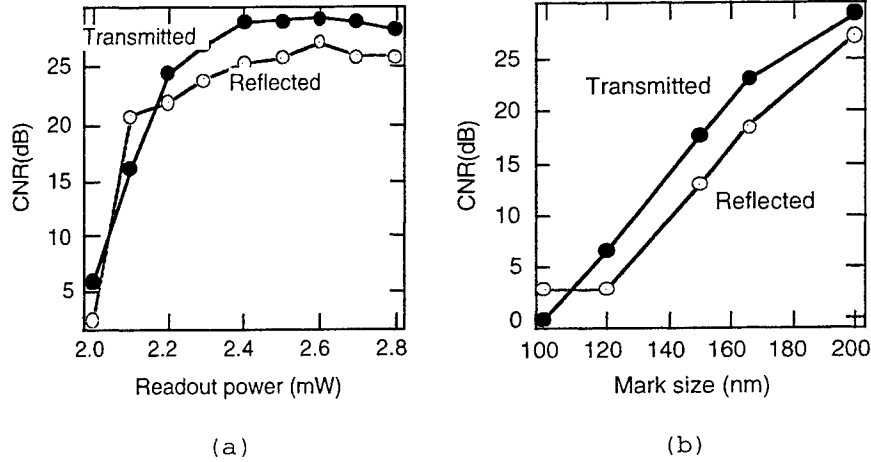

Fig. 10 Comparison of transmitted and reflected signals of 200-nm sized marks of a LSC-super-RENS disk.
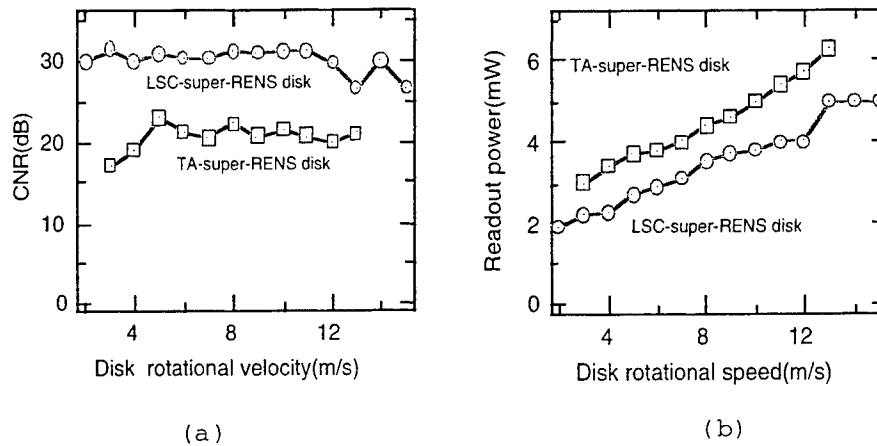(a):readout power dependence of CNR, and (b):mark resolution.

Fig. 11 CNR and optimum readout power dependence of disk rotation speed. (a): CNR, and (b):readout power.
Recorded mark size is 200 nm.

As decreasing mark size, the transmitted signal is higher than the reflected one until 120 nm. The limit was mostly the same and around 100 nm.

CNR dependence of disk rotation speed is also important characteristics in future data storage to increase data transfer rate. Fig. 11 shows the CNR change and the optimum readout power against disk rotation speed in comparison with a TA-super-RENS disk with a structure described in the reference.[9] As shown in Fig.11, CNR of 200-nm marks does not decrease in the LSC-super-RENS disk until CLV of 14.0 m/s, which is the limit of our disk drive tester. Additionally, the optimum readout power is less than 4 mW, even at 12.0 m/s. These characteristics are very important to further increase data transfer rate in future optical storage.

4. CONCLUSIONS

We described the formation mechanism of a light scattering center in LSC-super-RENS disks and some specific characteristics of the disks in detail. It is found that chemical reaction generated in the AgOx films are more complicated than what we have already described. By one-dc laser radiation method synchronized with the tracking jump signal, it was also revealed that the recording layer once absorbs the incident laser beam and produce heat; then it propagates to the AgOx film. The reaction is heat-mode process, rather than light-mode. Additionally, the transmitted signal is stronger than the reflected signal in LSC-super-RENS disks, and the disk can be readable even at a very high speed of more than 10 m/s. This will be very much important in the future optical data storage.

5. REFERENCES

1. E.Betzig, J.K.Trautman, "Near-field optics: Microscopy, spectroscopy, and surface modification beyond the diffraction limit", *Science,* **257**,pp.189-195,1992.
2. S.Hosaka, T.Shintani, M.Miyamoto, A.Hirotsune, M.Terao, M.Yoshida, K.Fujita, S.Kammer," Nanometer-Sized Phase Change Recording Using a Scanning Near-Field Optical Microscope with a Laser Diode", *Jpn. J. Appl. Phys.* **35B**, pp.443-447, 1996.
3. B.D.Terris, H.J.Mamin, D.Roger, W.R.Studenmund and G.S.Kino, "Near-field optical data storage using a solid immersion lens," *Appl. Phys. Lett.,* **65**, pp.388-390, 1994.
4. M. Ohtsu, "High speed near-field optical technology for ultrahigh density storage," *Tech. Digest of the joint MORIS/ISOM Symp.,* pp.180-181, 1997.
5. Y.Yatsui, M.Kourogi and M.Ohtsu, "Highly efficient exitation of optical near-field on an apertured fiber probe with an asymmetric structure," Appl. Phys. Lett., **71**, pp.1756-1758, 1997.
6. M.Kourogi, T.Yatsui, S.Ishimura, M.B.Lee, N.Atoda, K.Tsutsui and M.Ohtsu, "A Near-field planar apertured probe array for optical near-field memory," *Proc. SPIE, vol. 3467,* pp.258-267, 1998.
7. K.Kishima, I.Ichimura, K.Yamamoto, K.Osato, Y.Kuroda and K.Saito, "Near-field phase change optical recording over 1.2-numerical-aperture," *Tech. Digest of the joint ISOM/ODS Symp.,* pp.355-357, 1999.
8. C.W.Lee, S.T.Jung, J.E.Seo, Y.G.Kim and D.H.Shin, "Signal characteristics from a catadioptic system for near-field application," *Tech. Digest of the joint ISOM/ODS Symp.,* pp.367-369, 1999.
9. J.Tominaga, T.Nakano and N.Atoda, "Super-resolution structure for optical data storage by near-field optics," *Proc. SPIE,* vol. 3467, pp.282-286, 1998.
10. J.Tominaga, T.Nakano and N.Atoda, "An approach for recording and readout beyond the diffraction limit with an Sb thin film" *Appl. Phys. Lett.,* **73**, pp.2078-2080, 1998
11. J.Tominaga, H.Fuji, T.Nakano, L.Men and N.Atoda, " Reflection-mode super-resolution near-field structure (super-RENS) for super-density data storage," The 2nd. Asia-Pacific Workshop on Near-field Optics, Oct. 20-23, Peking, China, 1999.
12. D.P.Tsai, C.W.Yang, W.C.Lin, F.H.Ho and W.Y.Lin, "Super-resolution surface plasmon near-field optical data storage," The 2nd. Asia-Pacific Workshop on Near-field Optics, Oct. 20-23, Peking, China, 1999.
13. A.A.Schmidt, J.Offermann and R.Anton, "The role of nutral oxygen radials in the oxidation od AgO films," *Thin Solid Films,* **281-282**, pp.105-107, 1996.
14. J.Tominaga and T.Fukaya, "Thermal nano-phase change of an antimony thin films and the application for optical near-field data storage," *Adv. in Solid State Phys.,* **39**, pp.37-45, 1999.

Optical Disk Mastering Using Optical Super Resolution Effect

Shih-Yaon Tsai,Tsung-Eong Hsieh[a] and Han-Ping D. Shieh
Institute of Electric-Optical Engineering
[a]Department of Materials Science and Engineering
National Chiao Tung University, Hsinchu, Taiwan 300

ABSTRACT

We propose a new laser lithography technique using the effect of thermal-induced super resolution and demonstrate that the technique can effectively reduce the exposed spot size on the photoresist layer, thus allowing disk mastering toward higher density by using exiting light source and optics. A mask layer, whose nonlinear optical properties result in formation an aperture in high temperature area near to the center of the laser spot, is deposited on the top of the photoresist layer. Usually, the aperture size is much smaller than the laser spot, thus, achieving thermal-induced super resolution. The simulation and experimental results reveal that the line width on the photoresist layer could be shrunk by more than 40% .
KEYWORD: disk mastering, thermal-induced super resolution, lithography

1. INTORDUCTION

In the conventional laser lithography which is used to make optical master disks, the laser beam is directly illuminated on the surface of photoresist layer, so the resulted exposed area or spot size is limited by the optical diffraction limit. The spot size is approximated to $0.82\times \lambda/NA$, where λ is the free space wavelength of light source and NA is the numerical aperture of the object lens. There are two main approaches to reduce the spot size: reducing λ and increasing NA. However, the sensitivity of photoresist material depends on the wavelength of light source. NA of the commercial used object lens is 0.9, and the maximum value of NA is 1 in air. Thus, the two schemes in reducing focused spot size are either with some complication or limited performance. The aim of this paper is to demonstrate that using the effect of thermal induced super resolution[1,2] can effectively reduce the spot size on the photoresist layer, thus, allowing disk mastering toward higher density using existing light source and optics.

2. PRINCIPLE

Thermal-induced super resolution is caused by the nonlinear optical property of a metal film. [1,2] By illuminating a metal film with a laser beam, the metal film will melt and the index of refraction of the melting region will yield nonlinear variation locally. Thus, the transmittance of the melting area may be higher than that of other region. Because the Gaussian intensity distribution of the laser beam, so dose the temperature profile of the melting region on the metal film, thus melting region can be well controlled whose size can be much smaller than the focused laser spot size. The intensity distribution of the transmission light should become narrower than that of the incident light. A metal film of Indium is deposited on the photoresist layer, as shown in Fig. 1, the exposed area on the photoresist layer is reduced, thus, forming the finer definition of a line.

3. SIMULATION AND EXPERIMENT

Using Dill's exposure model[3] and Mack's development model[4], the thermal-induced super resolution effect caused by the metal layer on a photoresist layer was modeled. In the simulation, λ is 442 nm and NA is 0.5, and metal layer used in this work is GeTeSb, a DVD-RAM recording layer. Experimentally, a line is laterally exposed by a laser-exposing machine on a specimen with the structure shown in Fig. 1. Before development, the metal layer must be removed by some etching solution. After development, the exposed region was removed and formed a linear groove. The experimental parameters are listed in Table 1.

4. SIMULATION RESULTS

The simulated results of exposure and development of mastering process without and with the metal layer are shown in Figs. 2 and 3, respectively. After exposure, the distributions of the PAC (photoactive compound) concentration are shown in

In *Optical Storage and Optical Information Processing*, Han-Ping D. Shieh, Tom D. Milster, Editors, Proceedings of SPIE Vol. 4081 (2000) • 0277-786X/00/$15.00

95

Fig. 2. The PAC concentration is normalized so that 1 and 0 represents unexposed and completely exposed, respectively. Figs. 2(a) and 2(b) are the 2D and 3D distributions of the PAC concentration without the metal layer. Owing to the Gaussian intensity distribution of the laser beam and the standing wave effect, the distributions of the PAC concentration in the r and z direction are a Guassian distribution and sinusoidal profile, respectively. With the metal layer, the 2D and 3D distributions shown in Figs. 2(c) and 2(d) reveal that the standing wave effect still exits in the z direction, but the Guassian distribution in the r direction is distorted by the thermal-induced super resolution. After development, the cross-sectional views of the photoresist layer are shown in Fig. 3(a) without, Fig. 3(b) with 5 nm, and Fig. 3(c) with 10 nm metal layer, respectively. The black regions denote the residue photoresists. To simplify the description, we define the space at the bottom and the half depth of the groove as $W_{interface}$ and linewidth, respectively, as shown in Fig. 4. As shown in Fig. 3(a), $W_{interface}$ is about 2.1 nm without the metal layer, and the angle of the slope at the edge of the groove is about 30°. According to the simulation, 5 and 10 nm metal layers can form an aperture of the diameter of 0.7×spotsize and 0.5×spotsize respectively. The results imply that the metal layer yields optical super resolution effect. Consequently, as the thickness of mask layer increases from 0 to 10 nm, $W_{interface}$ shrinks from 2.1 to 1.3 um with the same angle at the edge of the groove, as shown in Figs. 4(b) and (c). As the angle does not vary with the shrinkage of $W_{interface}$, the linewith will decrease with $W_{interface}$. The experiment results demonstrate that thermal-induced super resolution effect can effectively shrink the linewidth of the groove.

However, it is very difficult to measure the size of aperture in real-time, so we examined influences of metal layer thickness and aperture size on the profile of photoresist layer in order to compare with the experimental results. The relations among the metal layer thickness, aperture size, $W_{interface}$, and the angle of the edge are depicted in Fig. 5. The three dashed lines represent the results of completely super resolution effect to result in the shrinkage of the $W_{interface}$ with same angle. The solid lines (a) and (b) represent the influences of the metal layer thickness and aperture size on the profile of the photoresist layer, respectively. From solid line (a), it is found that the decreasing of $W_{interface}$ mainly arises from the increasing of metal layer thickness. On the contrary, when the thickness of the metal layer is fixed, the variation of the aperture size can only result in altering the angle of the edge, as shown in solid line (b), implying that the optical super resolution is the combination of absorption effect, and shading effect.

5.EXPERIMENTAL RESULTS

Using the structure shown in Fig. 2, the shrinkage of the linewidth can be observed easily. In Fig. 6, the linewidth shrinks from 2.5 um, which is the limit of exposure machine, to 1.4 um as the thickness of Indium film increases form 0 to about 40 nm. To make sure the effect is caused by the super resolution, we further increase the thickness of Indium film. When the thickness is more than 40 nm, the linewidth does not shrink, but broaden, which may be caused mainly by absorption effect, as shown in Fig. 7 as the Indium film is too thick to be melted by laser beam. When laser beam passes through Indium film, the absorption effect no longer shrinks the spot size as optical super resolution. Experimental results demonstrate that the linewidth can only be reduced by the optical super resolution effect.

We then used SEM to make more detail observations on the microstructures of the groove. The top view is shown in Fig 8, where (a) without, (b) with 10 nm, and (c) with 30 nm Indium film, respectively. Most notably, the fluctuation of line edges gradually increase from 100 to 300 nm with the shrinkage of linewidth. Because the linewidth depends on the thickness of Indium film, the fluctuation must be influenced by the thickness of Indium film. As the thickness of Indium film increases from 15 to 36 nm, the grain size of the film will rapidly grow from 20 to about 100 nm, as shown in Fig. 9. In melting state, the larger the grain of film is, the rougher the edge of melting region is, as shown in Fig. 10. The sharpness of line is mainly determined by the grain size of Indium film.

In the previous simulation results, we used the cross-sectional profile of phototresist layer to observe the effect of super resolution. To compare with the results, we also used SEM to observe the cross-sectional profile of phototresist layer, as shown in Fig. 11. When $W_{interface}$ decreases from 2.1 to 1.7 um caused by the increase of the Indium film, the angle of the groove edge is almost the same. However, as $W_{interface}$ decreases from 1.7 to 1.368 um, the angle of the groove edge changes from 33° to 25°. From the simulation results shown in the curve c of Fig 3, we can extrapolate that the shrinkage of the linewidth is due to the absorption effect caused by the increase of Indium film and the change of the angle is the consequence of failing to form an aperture in the thick Indium film.

6. Conclusion

The effect of thermal-induced super resolution was applied the disk mastering process to greatly decrease the exposed area of photoresist using the existing optics. From simulation and experiment, the linewidth more than 40% less

than the diffraction limits defined by the laser-exposing machine limit was demonstrated. Further reductions of linewidths are feasible when shorter wavelength light source and higher NA optics are used in mastering system.

7. Reference

1) K. Yasuda, M. Ono, K. Aratani, A. Fukumoto, M. Kaneko: Jpn. Jap. Apl. Phys. 32, 5210(1993)
2) Jia-Reuy Liu and Hang-Ping David Shieh, Jpn. Jap. Apl. Phys. 37, 516(1998)
3) F. H. Dill et al., IEEE. Trans. Electron Device, ED-22, 445(1975)
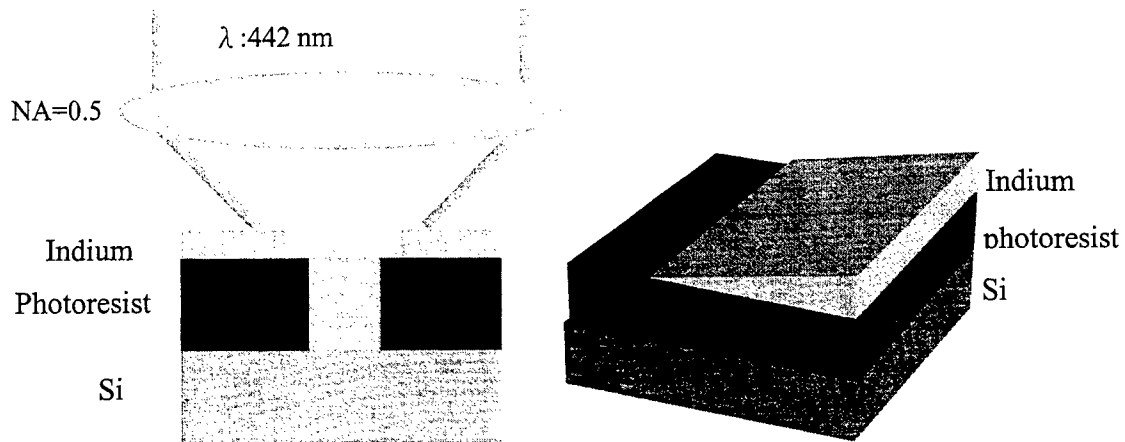4) C. A. Mark: Solid-state Science and Techol, 134 No. 1, 148 (1978)

Fig. 1. A metal layer (Indium) is deposited on the photoreisit layer

Table 1. The experimental parameters

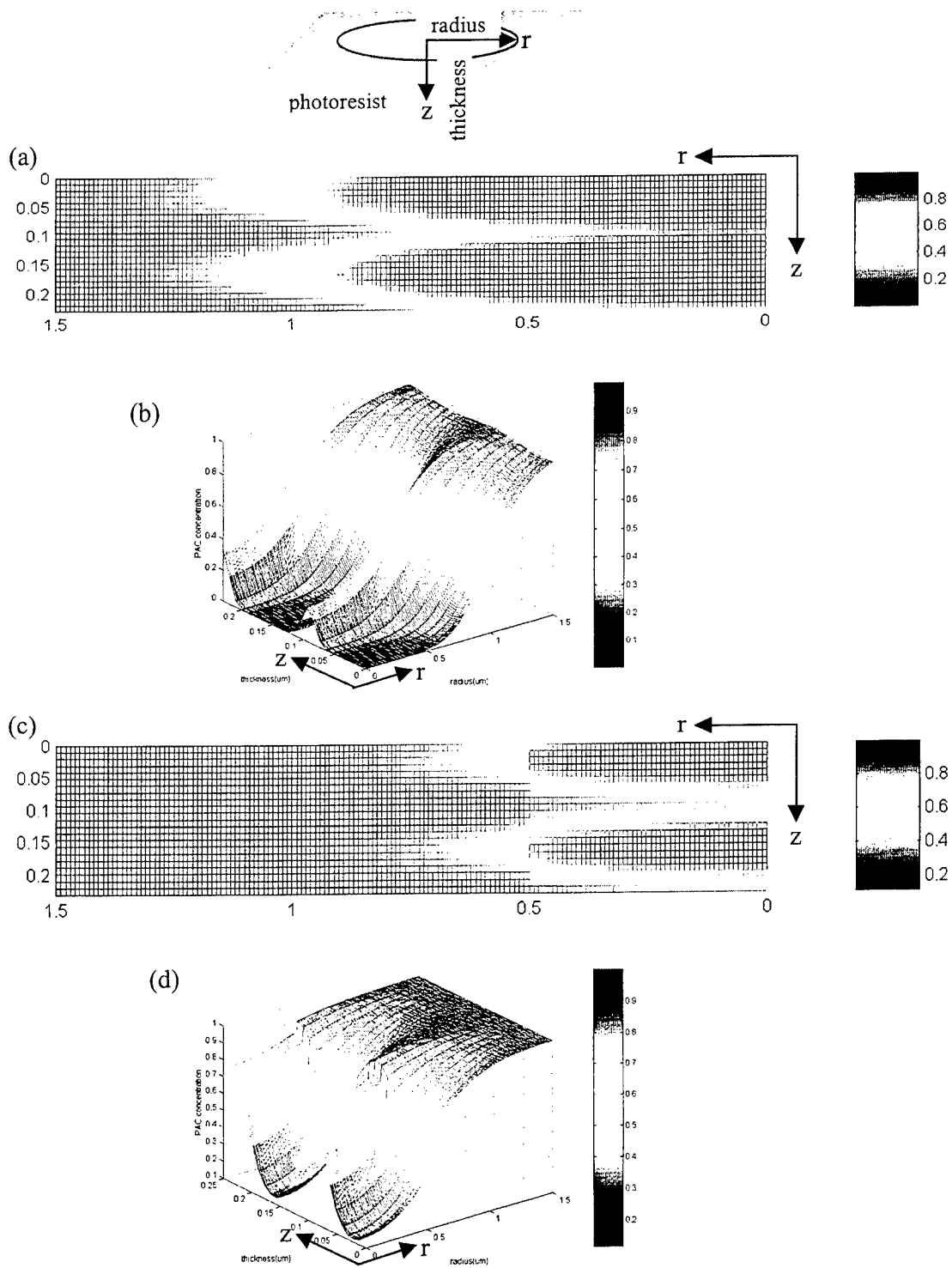| Materiel of the mask layer	Indium	
Thickness of the mask layer (nm)	0~30	
Photoresist	AZ 6112	
thickness of the photoresist layer (nm)	150-350	
development solution	AZ 300	
etching solution	$HF:H_2O_2:H_2O=4:1:1$	
Evaporation Condition		
Pressure (torr)	10^{-5}	
Current (A)	125	
Exposure Condition		
Wavelength (nm)	442	
NA	0.5	

Fig. 2 After exposure, the distribution of PAC concentration on the photoresist layer. (a) 、 (b) without the mask layer, (c) 、 (d) with the mask layer
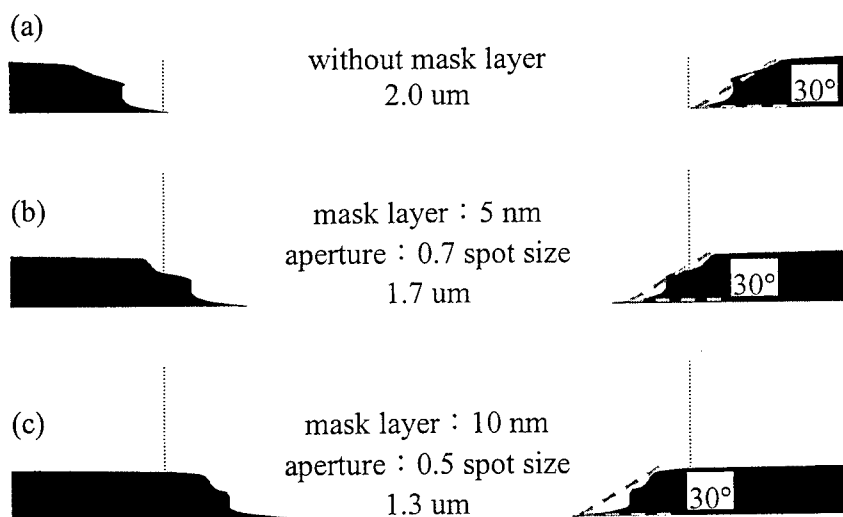
(a)

without mask layer
2.0 um

30°

(b)

mask layer : 5 nm
aperture : 0.7 spot size
1.7 um

30°

(c)

mask layer : 10 nm
aperture : 0.5 spot size
1.3 um

30°

Fig. 3 After development, the profile of photoresist layer. (a) without, (b) with 5 nm, and (c) with 10 nm mask layer

linewidth

angle

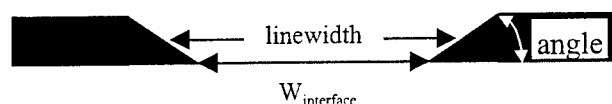$W_{interface}$

Fig. 4 Definition of $W_{interface}$, linewidth, and angle

: angle 30°

- - - : angle 27°

- - - : angle 24°

Linewidth

1.3 um

1.7 um

Thickness of metal layer

10 nm

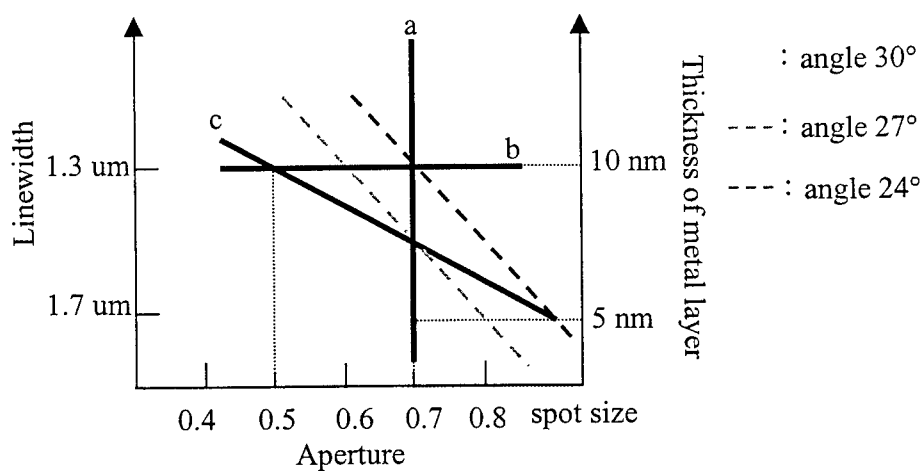5 nm

a

b

c

0.4   0.5   0.6   0.7   0.8   spot size

Aperture

Fig. 5 Relationship among the metal layer thickness, aperture size, $W_{interface}$ and the angle of the edge
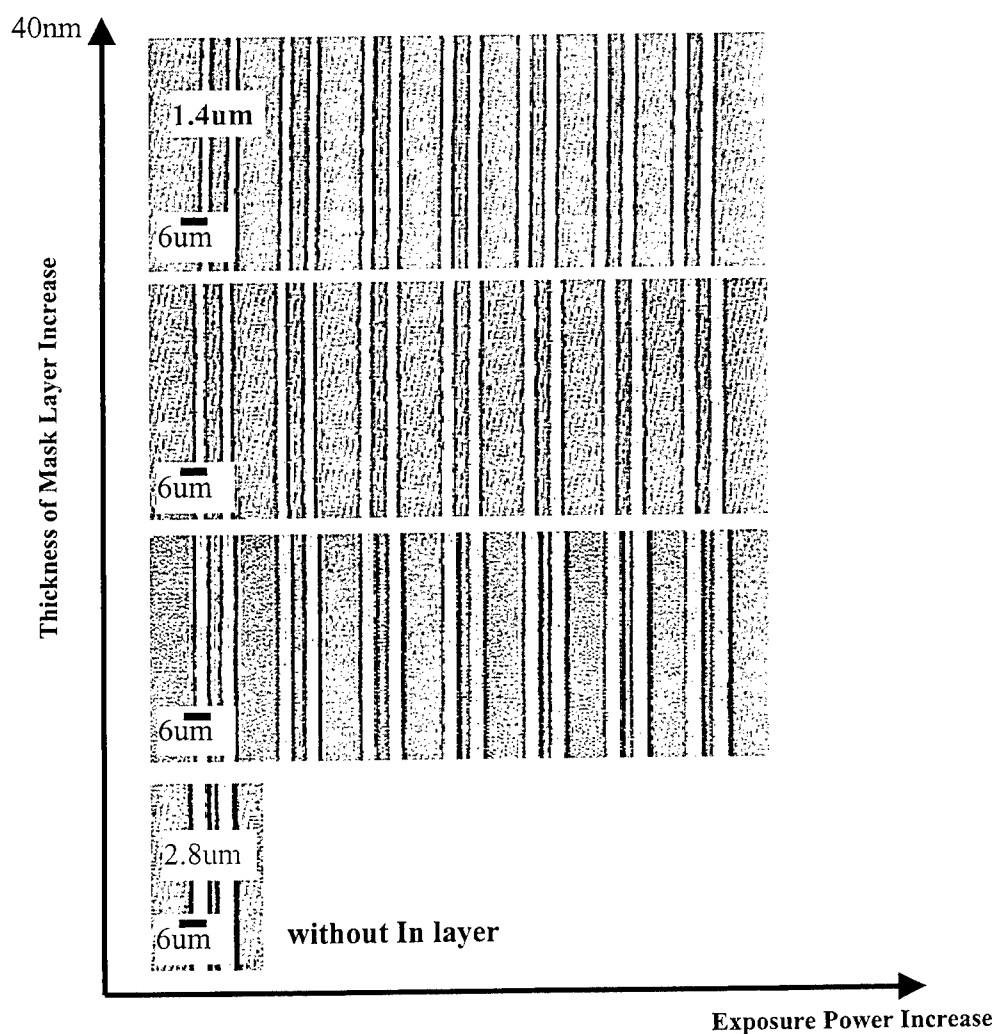
Fig. 6 Linwidth as functions of the thickness of Indium film and different exposure power
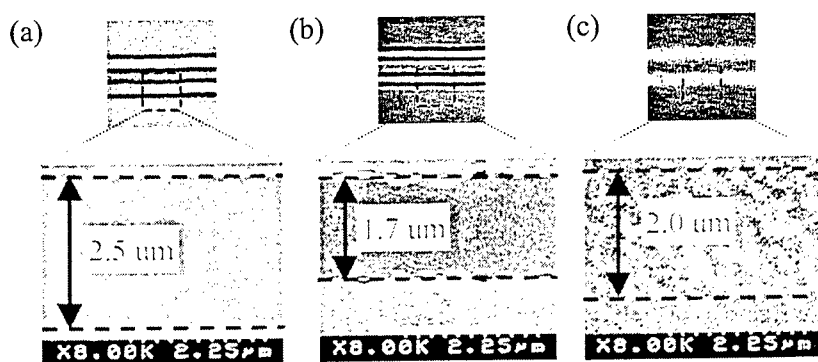

Fig. 7 The difference between super resolution effect and absorption effect. (a) without the Indium film, (b) result of super resolution, and (c) result of absorption effect
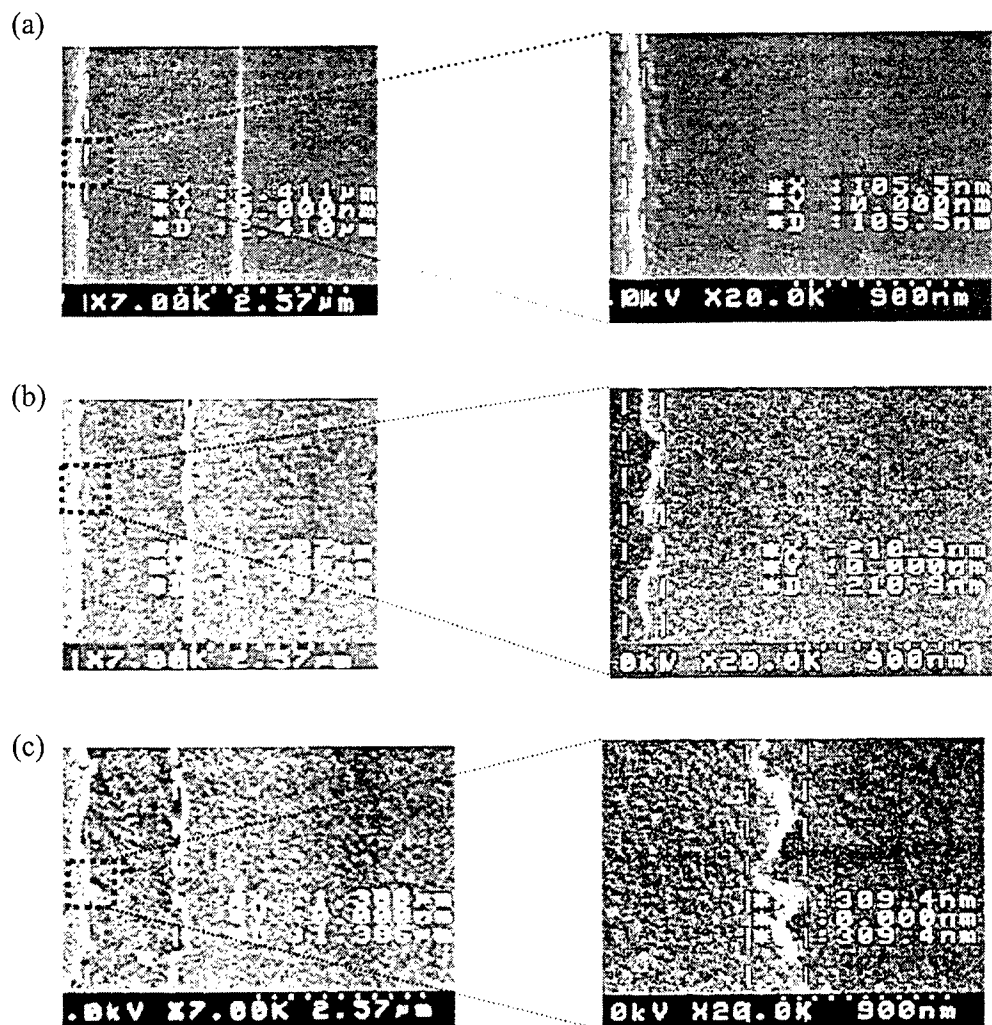
(a)

(b)

(c)

Fig. 8 The fluctuations of the line edge. (a) Without, (b) with 7nm, and (c) 30nm Indium film
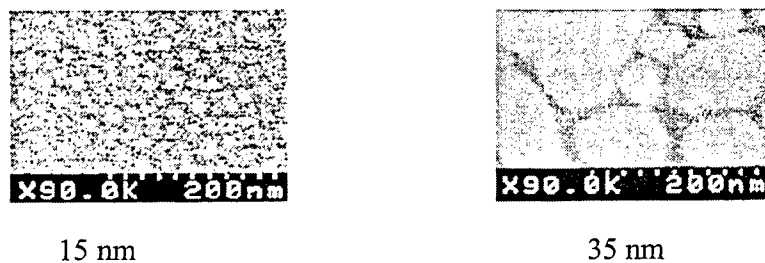

15 nm

35 nm

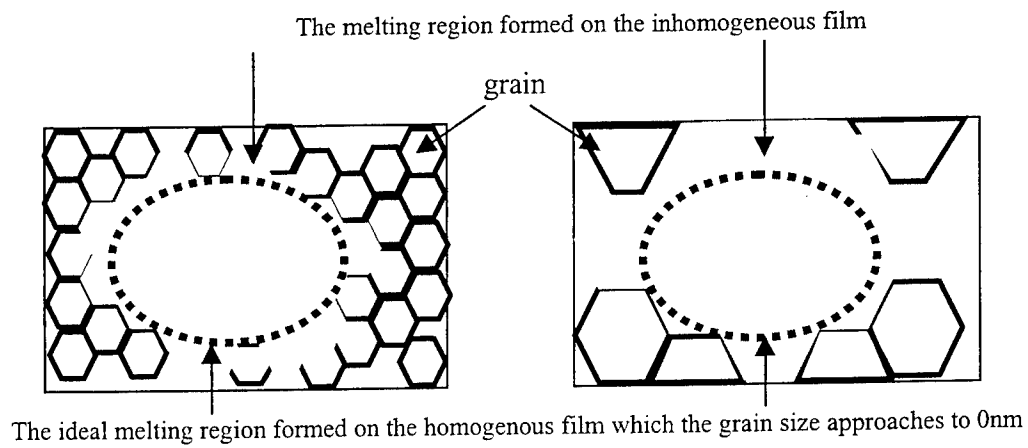Fig. 9 SEM micrographs showing different grain size of the Indium films of different thickness

The melting region formed on the inhomogeneous film

grain

The ideal melting region formed on the homogenous film which the grain size approaches to 0nm

Fig. 10 The influence of grain size on the area of melting region
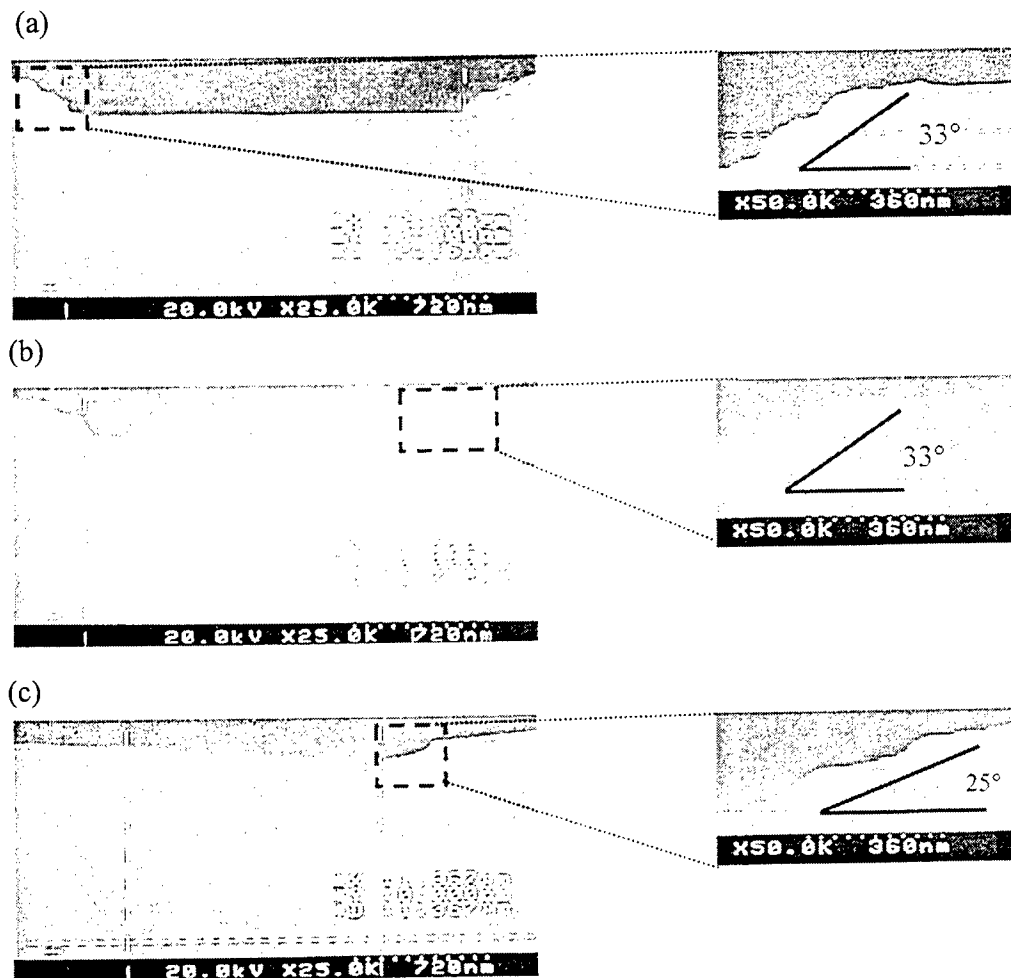
(a)

(b)

(c)

Fig. 11 After development, the cross section of photoresist layer. (a) without, (b) with 7 nm, and (c) with 30 nm Indium film

SESSION 4

Optical Information Processing I

Fabrication and Characterization of Thin Ferroelectric Interferometers for Light Modulation

Kewen K. Li[a*], Feiling Wang[a*], Jianjun Zheng[b] and Peter L. Pondillo[b†]

[a] NZ Applied Technologies, 14A Gill Street, Woburn, MA 01801, U.S.A.
[b] Electrooptics Center, Tufts University, Medford, MA 02155, U.S.A.

ABSTRACT

A thin ferroelectric interferometer (TFI) structure for light modulating devices is presented. It was fabricated entirely with thin film techniques on sapphire and silicon substrates. The ferroelectric layer in this structure was the lanthanum-modified lead zirconate titanate (PLZT) electrooptic material, deposited from a chemical precursor solution onto an ITO-coated dielectric mirror stack. Light intensity modulation in both transmission and reflection modes, and phase modulation in the reflection mode were demonstrated. Experimental and simulation data show that TFI devices can be fast switching with a low driving voltage. Variations of the basic TFI structure can be used for phase tunable spatial light modulators (SLM's) and laser beam steering devices. Design principles, fabrication procedure and the preliminary performance of the devices are described.

Keywords: Spatial light modulator, interferometer, thin film, PLZT

1. INTRODUCTION

High-speed optical modulators that can be integrated with microeletronic components are desirable for applications in optical signal processing and optical interconnects. The majority of the presently existing devices are based on liquid crystal technologies.[1,2] In spite of the technological maturity, liquid crystal materials suffer from slow responding speed, and therefore are unsuitable for systems where fast modulating speeds or large data rates are required. Among the high-speed devices, the best-known kind is the multiple quantum-well (MQW) devices.[3] So far, the MQW-based modulators are limited in usable wavelengths and are incompatible with silicon devices. Some success has been achieved in the integration of complex-oxide ferroelectric materials with silicon for applications in spatial light modulation, which was potentially high-speed.[4,5] Recently, a range of new devices based on the structure of the thin ferroelectric interferometer (TFI) have emerged as promising alternatives that can provide high modulating speed, wide usable wavelength range and ease of monolithic integration with silicon. The TFI structure is comprised of an oxide ferroelectric thin film material sandwiched between two conducting mirrors. A low finesse TFI intensity modulator was first demonstrated on silicon substrate.[6,7] Subsequently, TFI devices with higher finesse were fabricated on both sapphire and silicon substrates.[8-10] In terms of mirror configuration, two mirrors with equal reflectivity have been used to form Febry-Perot structure for optical intensity modulation. In order to apply the TFI device to optical phase modulation, two mirrors with substantially unequal reflectivities can be used. Optical cavities with unequal mirrors are known as Gires-Tournois etalon, from which nearly pure optical phase modulation can be achieved. In this paper, we describe the recent progress in the fabrication of the optical phase modulators based on the TFI structure.

2. FUNDAMENTALS OF TFI PHASE MODULATOR

Both the optical phase modulator array and the beam steering device share the same optical cavity structure shown in Fig. 1. In this structure, the bottom mirror is nearly a total reflection mirror and the top mirror is substantially less reflective, forming a Gires-Tournois etalon. To be used as an optical phase modulator, a light beam is incident on the device from the side of lower reflection mirror. If the wavelength of the light is near a resonance condition with the resonator, the reflected light

104

In *Optical Storage and Optical Information Processing*, Han-Ping D. Shieh, Tom D. Milster, Editors, Proceedings of SPIE Vol. 4081 (2000) • 0277-786X/00/$15.00

conserves its intensity while experiencing an optical phase shift sensitive to the change of cavity length. Explicitly, the optical phase of the reflected light can be expressed by the following equation:[11]

$$\Phi = -2\tan^{-1}\left(\frac{1+\sqrt{R}}{1-\sqrt{R}}\tan(\Delta\phi)\right),$$ (1)

where R is the reflectivity of the top mirror; $\Delta\phi$ is the deviation of optical length of the spacer (in unit of radian) from a resonance condition, i.e., an integer multiple of $\lambda/2$. In the TFI devices with the Gires-Tournois configuration the deviation $\Delta\phi$ is tunable for a monochromatic incident light. For some complex-oxide ferroelectric materials, a combination of the field-induced index change and the field-induced strain can provide up to 1- percent variation in their total optical path length. According to the above equation, a small field-induced $\Delta\phi$ is amplified by a factor of $(1+\sqrt{R})/(1-\sqrt{R})$ due to the light interference in the etalon, and therefore a large phase shift is obtained in the reflected beam.
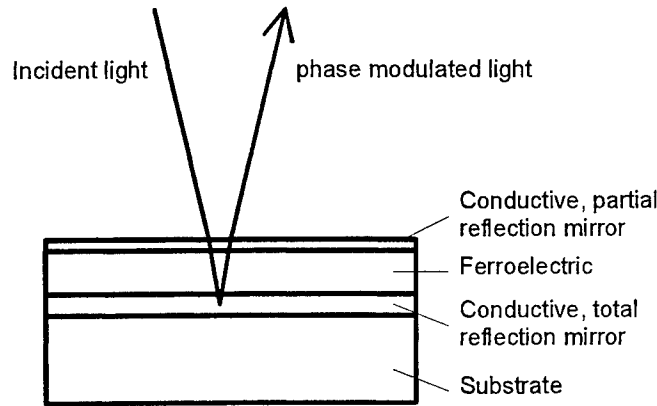

Figure 1. Structure of the TFI optical phase modulator. The two mirrors of unequal reflectivities and the electrooptic ferroelectric thin film form a Gires-Tournois etalon.

One can obtain continuous optical phase modulation in the range of $-\pi$ and π by tuning the Gires-Tournois etalon. With an appropriate reflectivity R for the top mirror, nearly the full 2π phase shift can be generated in the reflected light through the field-induced change in $\Delta\phi$. For example, a 1-μm thick ferroelectric film can create field-induced changes of $\Delta\phi$ in the range of -0.1 and 0.1 radian, which corresponds to an achievable field-induced index change of 0.02 for a visible wavelength. The optical phase modulation one can obtain is plotted in Fig. 2 for different reflectivities of the top mirror.

As shown in Fig. 2, within the attainable $\Delta\phi$, close to a 2π phase shift can be achieved using the ferroelectric thin film material in a Gires-Tournois etalon with top mirror reflectivity R=0.95. For a fixed $\Delta\phi$, the lower the R is the smaller the phase shift becomes. In practice, because of the imperfect bottom mirror (reflectivity close to but less than 100%), the higher the R the more energy loss the reflected light may suffer. Using a multilayer dielectric mirror as the bottom mirror, reflectivity above 99% can be easily obtained. With this bottom mirror, the intensity loss in the reflected light is insignificant even for R=0.95.

Several kinds of high-ε ferroelectric thin film materials have been studied for their use in the TFI devices. These materials include $BaTiO_3$, $(Pb,La)(Zr,Ti)O_3$ (PLZT) and $Pb(Mg,Nb)O_3$-$PbTiO_3$ (PMN-PT) solid solutions.[12-14] All these thin film materials can be formed by means of the metal-organic chemical liquid deposition (MOCLD) technique or other methods. These thin film materials are usually polycrystalline although quasi-single-crystal films can be formed on lattice-matched substrates. When properly produced, these materials possess high dielectric constant and broad phase transition temperature range, ideal for obtaining large electrooptic coefficients in wide usable temperature ranges. In Fig. 3 the quadratic electrooptic coefficients for most known ferroelectrics, bulk and thin films, are plotted against their dielectric constants in logarithm scales. As one can see, the quadratic electrooptic coefficients appear to be proportional to the dielectric constant squared, ε^2, which can be explained by a theory regarding the electrooptic effects in ferroelectrics.[15] The thin film ferroelectric materials produced in our laboratory typically possess dielectric constant in the range of 1000-3000 and the quadratic electrooptic coefficient in the range of 0.2-2×10^{-16} $(m/V)^2$. Although lower than some bulk materials, these electrooptical coefficients are remarkable for polycrystalline thin film materials.
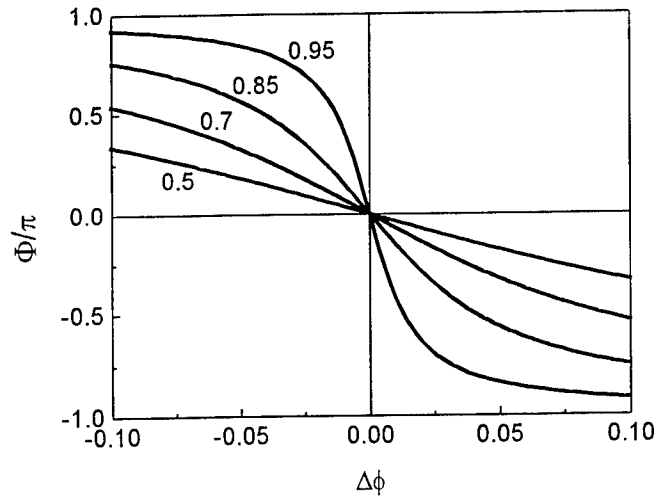
Figure 2. Optical phase of the light beam reflected from a Gires-Tournois etalon with different top mirror reflectivities, R's.

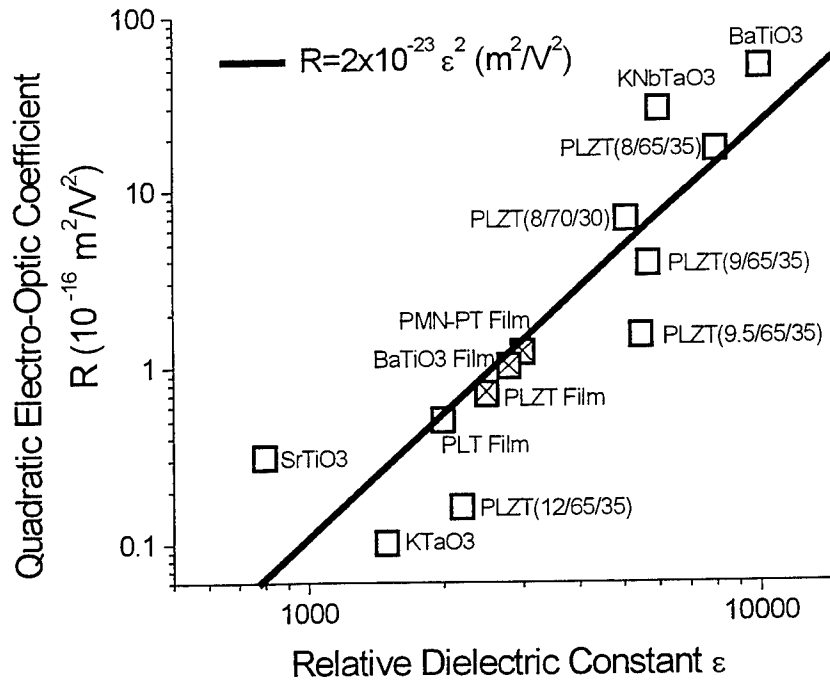**Figure 3.** Correlation between the quadratic electrooptic coefficient and the dielectric constant of various ferroelectric materials. The symbol "×" indicates thin film materials produced in our laboratory.

Most of the above mentioned thin film ferroelectric materials are transparent for the entire visible and a range of infrared wavelengths; an example is the PLZT material system with usable wavelength ranging from 400 nm to 6μm.[16] TFI phase modulators using the PLZT materials can be made to modulate laser lights in the wavelength range. The TFI phase modulators are polarization independent as long as the incident angle of the laser beam is small, which can be realized with an appropriate design.

3. FABRICATION OF PHASE MODULATOR

The TFI phase modulators have been successfully fabricated on sapphire substrates. Single-crystal, r-oriented sapphire wafers were used as substrates. The bottom conductive mirror consisted of a quarter-wave dielectric stack with an additional indium-tin oxide (ITO) layer. The top conductive mirror had a similar structure as the bottom mirror except that the ITO layer was deposited prior to the dielectric stack. Both dielectric mirrors were fabricated with the electron beam evaporation technique and the ITO layers were deposited by means of magnetron sputtering.

The ferroelectric in the TFI resonator was a lead lanthanum zirconate titanate (PLZT) thin film material deposited by means of the metal-organic chemical liquid deposition (MOCLD) technique. The photograph shown in Fig. 4 is a scanning electron microscopic (SEM) cross-sectional view of a TFI device fabricated with the described method. As shown in the picture, all the layers are well joined to form the optical resonator.

Figure 4. Scanning-electron-microscopic (SEM) photograph of the cross section of a TFI device fabricated on sapphire substrate.

Passive arrays of TFI phase modulators have been fabricated with the described technique. The sizes of the modulator pixels ranged from 10 μm × 10 μm to 200 μm × 200 μm. A 2×8 passive array on a sapphire substrate is shown in Fig. 5. The size of each pixel is 25 μm × 25 μm. The square pixels (at the center of the photograph) are connected to the fan-out metallic contacts shown in dark color. These arrays were packaged and wire bonded. Fig. 6 shows a packaged 2×8 modulator array sitting on its electronic controller box. Each individual pixel can be controlled by a modulating voltage independent of other pixels.
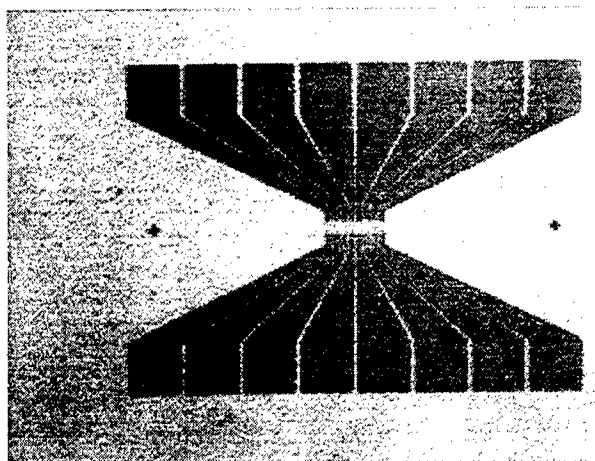
Figure 5. TFI phase modulator array fabricated on sapphire substrate. An array of 2×8 pixels is shown. The active area of each pixel is 25 μm ×25 μm. The metallic contacts are shown in dark color.

Figure 6. Packaged TFI phase modulator array with controller. Each individual pixel can be controlled by a modulating voltage independent of other pixels.

4. PERFORMANCE OF THE TFI PHASE MODULATOR

As the TFI modulators are fabricated on transparent substrates such as sapphire, some device characteristics can be measured easily from the transmitted light before packaging. As was discussed earlier, an ideal TFI phase modulator reflects all the light energy. Because of the imperfection of the bottom mirror, practical devices often pass a measurable amount of light, which can be used to characterize the device in terms of its optical quality, the finesse of the resonator and its tunability. Shown in Fig. 7 is the spectral transmission of a TFI phase modulator. For the measurement, a beam of while light was focused onto the device and the transmitted light was analyzed with a monochrometer. As shown by the data, the full width at half maximum (FWHM) of the transmitted peak is approximately 2.3 nm, which corresponds to a resonator finesse of 18. The peak transmission at the resonant wavelength is shown to be less than 5%, indicating that the reflected light may suffer approximately 5% light energy loss. The tunability of the device is clear demonstrated by the shift of the peak transmission wavelength under voltage. As shown, with 40 volts a shift of 0.7 nm was measured. A phase shift of approximately 0.5π is estimated in the reflected light under the voltage.
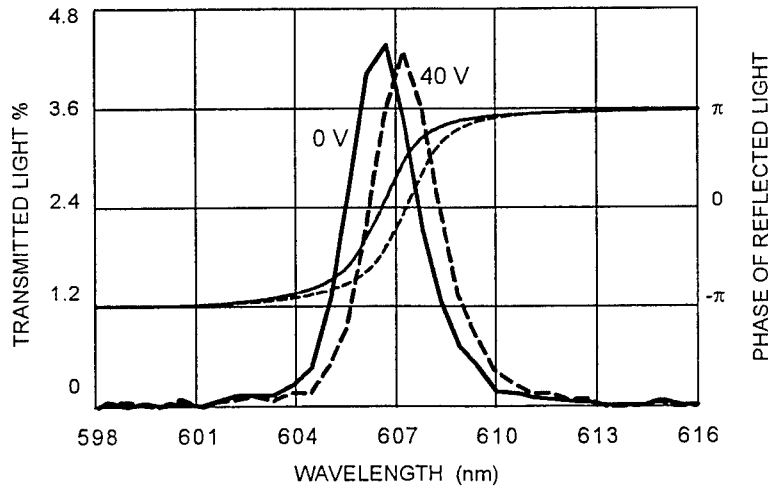
Figure 7. Characteristics of a TFI phase modulator, measured via its spectral transmission.

Direct characterization of the phase modulation from the fabricated TFI arrays was carried out with the Mach-Zehnder interferometer shown in Fig. 8. A He-Ne laser with 632.8-nm emission was used as the light source and focused onto one of the modulator pixels. The light reflected from the modulator was collimated and let interfere with the reference beam. With this arrangement the light intensity detected is proportional to $I_1 + I_2 + 2\sqrt{I_1 I_2} \cos\phi$, where I_1 and I_2 is the intensity of the reference beam and the modulated beam (reflected from the device), respectively; ϕ is the phase difference between the two light beams. For the convenience of measurements, the constant relative phase between the two beams was adjusted so that the modulation signal was proportional to $\sin\phi$. The system was calibrated by recording the intensity modulation corresponding to a full π phase shift introduced manually.
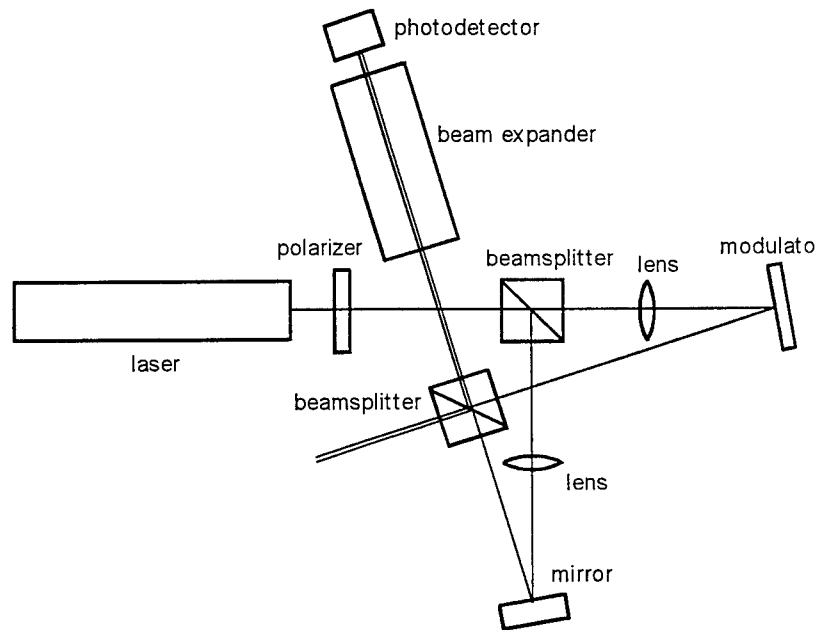

Figure 8. Experimental setup for characterizing the TFI reflective phase modulators.

The phase modulation from a TFI pixel was recorded when a sinusoidal voltage signal was applied to the modulator. Shown in Fig. 9 is the measured phase shift as a function of the applied voltage and phase modulation with time. The phase

shift as a function of the voltage, Fig. 8(a), shows an asymmetric hysteresis loop which is a manifestation of the asymmetric ferroelectric hysteresis loop, commonly observed from thin film ferroelectrics. As shown by the data, the modulator under an applied voltage of -45 volts produced a phase shift of 0.24 radians (or 13.7 degrees). This phase shift is small compared to a calculated value of 1.3π for a device with a ferroelectric layer that possesses a quadratic electrooptic coefficient of 0.5×10^{-16} $(m/V)^2$. We attribute the discrepancy to the imperfection of the fabricated Gires-Tournois resonator and the fact that the electrooptic coefficient for ferroelectric films in the cavity is often lower than that of materials grown on bare sapphire substrates.
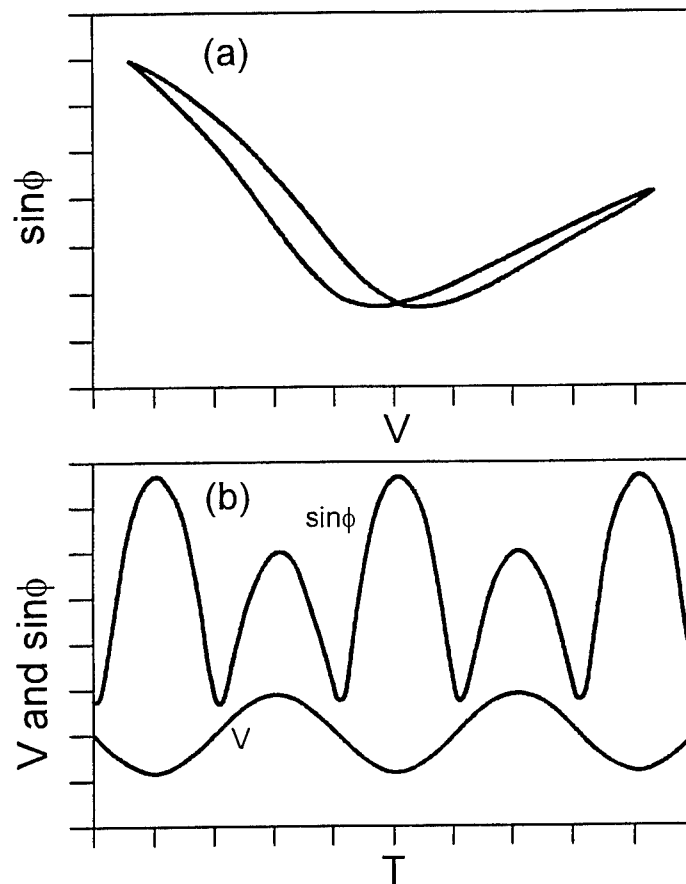

Figure 9. Phase modulation measured from a single pixel TFI phase modulator. (a): phase change as a function of the applied voltage; the x-axis is 10 volts per division and the y-axis is 0.045 per division. (b): phase modulation with time responding to the sinusoidal voltage signal; the x-axis is 250 μs per division and the y-axis is 0.045 per division for the phase shift and 50 volts per division for the voltage.

5. TFI LASER BEAM STEERING DEVICE

An application of the TFI optical phase modulator is laser beam steering. Two types of laser beam steering devices can be fabricated. The first type is based on modulator arrays similar to what is shown in Fig. 5. For laser beam steering modulator elements in the shape of long and narrow strips should be densely arranged. Since each individual element can provide a phase shift in the range of $-\pi$ and π, one can program the voltages applied to each individual element so that a quasi-linear phase variation is obtained across the diameter of a laser beam, thus the reflected beam is steered. As the TFI phase modulators are comprised of thin film structure, pitch length as small as 2 μm between pixels is possible. With small pitch length the device creates few diffraction side lobes.

Another type of laser beam steering device with TFI uses a single deflection element. The structure of the device is shown in Fig. 10. In the device, a sheet resistor is used in place of the top conductive layer for devices described in the preceding sections. This sheet resistor serves to create an electric field gradient inside the ferroelectric thin film material. The field

gradient in turn causes a variation of the phase deviation $\Delta\phi$ across the diameter of the laser beam. According to Eq. (1), a small spatial distribution of $\Delta\phi$ creates a optical phase distribution approximated by:

$$\Phi = -2\frac{1+\sqrt{R}}{1-\sqrt{R}}\Delta\phi . \tag{2}$$

If the sheet resistor generates a linear spatial distribution of $\Delta\phi$, the reflected laser beam will also possess a linear phase distribution governed by the above equation, the reflected beam is then deflected. Because the continuous phase variation in the device is limited to the range of $-\pi$ and π, substantial beam deflection angle can only be achieved for focused laser beam with the single element device, while the arrayed deflector is capable of steering unfocused laser beams with larger beam sizes.
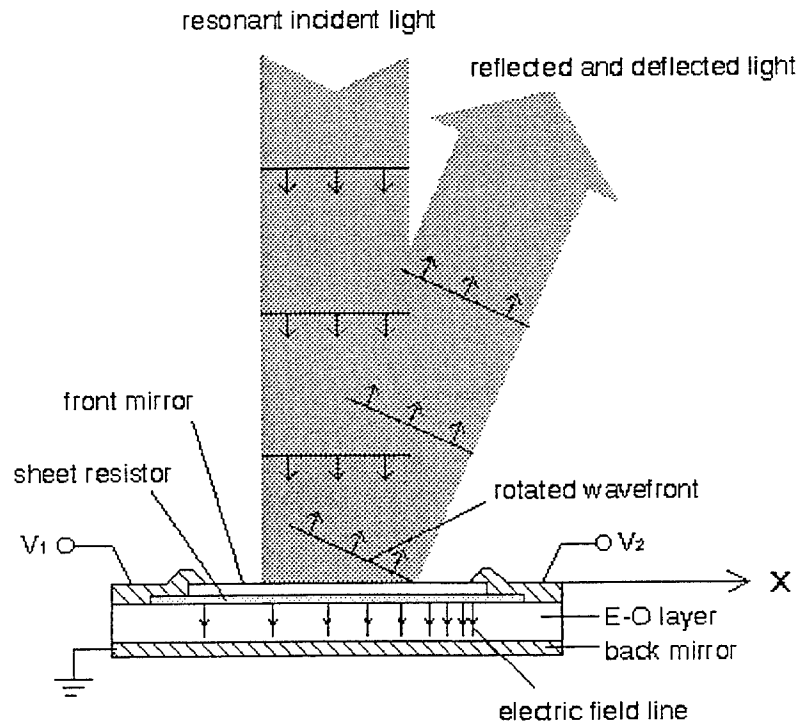

Figure 10. Structure of single-element TFI laser beam deflecting device. A sheet resistor is used in place of the conducting layer in the phase modulator. As differential voltages are applied to the two terminals of the sheet resister an electric field gradient is created inside the ferroelectric thin film material so that a wavefront rotation is achieved.

The single-element TFI beam steering devices have been fabricated using the techniques similar to what were used for the phase modulator arrays described previously. The sheet resistor was formed using a modified ITO thin film material with resistance of approximately 100 kΩ/$\square$. Shown in Fig. 11 is a microscopic photograph of a single-element TFI beam steering device on a sapphire substrate. The device has an active area of 50 μm $\times$ 50 μm. The triangle-shaped electrodes connect the sheet resistor to the two metallic contacts (one contact area is shown). The thickness of the PLZT thin film is approximately 1.2 μm, designed for deflecting He-Ne laser beam of 632.8-nm wavelength at an incident angle of 10 degrees.

In order to record the beam deflection, a charge-couple device (CCD) camera was set to intercept the laser beam reflected from the device. As a differential voltage was applied to the sheet resistor the position where the light impinged on the CCD camera was recorded. As shown in the lower portion of Fig. 11, the laser beam profile shifted for 4 mm as a differential voltage of 30 volts was applied to the device. The distance between the beam steering device and the CCD camera was 180 mm. The measured spatial shift corresponds to a deflection angle of 1.3 degrees.
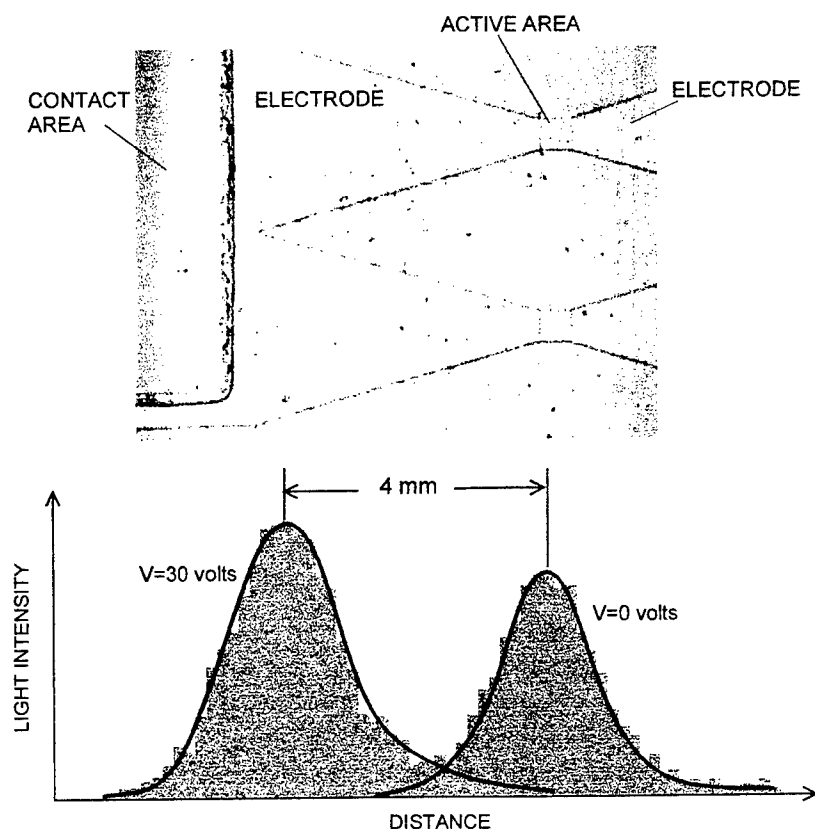
Figure 11. Single-element TFI laser beam steering device. The upper portion is a microscopic photograph of a device with 50 μm × 50 μm active area. The lower portion shows the deflection of the reflected light beam, recorded with a CCD camera intercepting the beam path.

6. CONCLUSION

The preliminary device types described in this paper show that the TFI devices represent a viable technology for laser light modulation and laser beam steering. The complex-oxide ferroelectric thin film materials, such as the PLZT materials, in the TFI resonator can produce large voltage-controlled refractive index change, second only to liquid crystal materials. The response speed of the complex-oxide ferroelectric materials is much faster than that of liquid crystals. The second attractive aspect of the TFI devices is that they can be integrated with silicon-based or wide band gap GaN-based microelectronic devices monolithically. It is therefore possible to fabricate high-density, high-speed, active-matrix-controlled SLMs on semiconductor substrates for various applications.

In this paper we demonstrated two applications of the TFI devices, i.e. the phase modulator and the single-element laser beam steering device, both fabricated on sapphire substrates with the thin film processing techniques. Both devices were based on the concept of tunable Gires-Tournois etalon, in which a thin film PLZT material was used as the tunable medium. Passive arrays of TFI phase modulators were fabricated and packaged. The phase modulators were characterized by means of their spectral transmission, and by the use of a Mach-Zehnder interferometer. Deflection of a He-Ne laser beam was demonstrated with the single-element TFI beam steering device. Substantial improvements in these devices are expected as the material and device processing techniques become more mature.

REFERENCES

1. K. M. Johnson, D. J. McKnight, and I. Underwood, "Smart spatial light modulators using liquid crystal on silicon," *IEEE J. Quantum Electron.* **29**, pp. 699-714, 1993.
2. D. J. McKnight, K. M. Johnson, and R. A. Serati, "256×256 liquid-crystal-on-silicon spatial light modulator," *Appl. Opt.* **33**, pp. 2775-2784, 1994.

3. P. Tayebati, C. Hantzis, and E. Canoglu, "An optically addressed modulator based on low-temperature-grown multiple quantum well GaAlAs," *Appl. Phys. Lett.* **71**, pp. 446-448, 1997.

4. T. H. Lin, A. Ersen, J. H. Wang, S. Dasgupta, S. Esener, and S. H. Lee, "Two-dimensional spatial light modulators fabricated in Si/PLZT," *Appl. Opt.* **29**, pp. 1595-1603, 1990.

5. M. S. Jin, J. H. Wang, V. Ozguz, and S. H. Lee, "Monolithic integration of a silicon driver circuit onto a lead lanthanum zirconate titanate substrate for smart spatial light modulator fabrication," *Appl. Opt.* **33**, pp. 2842-2848, 1994.

6. F. Wang and G. H. Haertling, "Large electrooptic modulation using ferroelectric thin films in a Fabry-Perot cavity," in *Proceedings of the Ninth IEEE International Symposium on Applications of Ferroelectrics*, pp. 683-686, 1994.

7. F. Wang and G. H. Haertling, "Integrated reflection light modulator using a ferroelectric thin film material on silicon," in *Conference on Lasers and Electro-Optics*, Vol. 15 of 1995 OSA Technical Digest Series (Optical Society of America, Washington, D. C., 1995), paper CThI22.

8. F. Wang, D. Tsang, H. Jiang, K. K. Li, and V. Fuflyigin, "Ferroelectric-on-silicon modulators for high density optical interconnects," in *Conference on Lasers and Electro-Op*tics, Vol. 6 of OSA Technical Digest (OSA, Washington, D.C. 1998), p. 141.

9. F. Wang, K. K. Li, V. Fuflyigin, H. Jiang, J. Zhao, P. Norris, and D. Goldstein, "Thin ferroelectric interferometer for spatial light modulation," *Appl. Optics* **37**, pp. 7490-7495, 1998.

10. P. L. Pondillo, K. K. Li, F. Wang, and M. Cronin-Golomb, "Spatial light modulation using a thin ferroelectric interferometer," *OSA Technical Digest on Spatial Light Modulators and Integrated Optoelectronic Arrays*, April 12-14, 1999, Aspen, Colorado, p. 103.

11. The fundamentals of Gires-Tournois etalon can be found in monographs such as A. Yariv and P. Yeh, *Optical Waves in Crystals* (Wiley, New York, 1984), pp. 290-293.

12. K. K. Li, G. H. Haertling, and W.-Y. Howng, "An automatic dip coating process for dielectric thin and thick films," *Integrated Ferroelectrics* **3**, pp. 81-91, 1993.

13. V. Fuflyigin, K. K. Li, F. Wang, H. Jiang, S. Liu, J. Zhao, P. Norris, and P. Yip, "Preparation of ferroelectric oxide films by sol-gel method," *High-Temperature Superconductors and Novel Inorganic Materials*, G. Van Tendeloo *et al.* Eds, (Kluwer Academic Publishers, Netherlands).

14. Y. Lu, G. H. Jin, M. Cronin-Golomb, S. W. Liu, H. Jiang, F. Wang, J. Zhao, S. Q. Wang, and A. J. Drehman, "Fabrication and Optical Characterization of $Pb(Mg_{1/3}Nb_{2/3})O_3$-$PbTiO_3$ Planar Thin Film Optical Waveguides," *Appl. Phys. Lett.* **72**, 2927-2929, 1998.

15. F. Wang, "Calculation of the Electro-Optical and Nonlinear Optical Coefficients of Ferroelectric Materials from Their Linear Properties," *Phys. Rev. B.* **59**, pp. 9733-9736, 1999.

16. G. H. Haertling, "PLZT electrooptic materials and applications — a review," *Ferroelectrics* **75**, pp. 25-55, 1987.

Stream cipher based on pseudo-random number generation using optical affine transformation

Toru Sasaki[a], Hiroyuki Togo[a], Jun Tanida[a] and Yoshiki Ichioka[b]

[a]Graduate School of Engineering, Osaka University, 2 - 1 Yamadaoka,
Suita, Osaka 565-0871, Japan
[b]NARA National College of Technology, 22 Yatamachi, Yamatokoriyama,
Nara 639-1080, Japan

ABSTRACT

We propose a new stream cipher technique for 2-D image data which can be implemented by iterative optical transformation. The stream cipher uses a pseudo-random number generator (PRNG) to generate pseudo-random bit sequence. The proposed method for the PRNG is composed of iterative operation of 2-D affine transformation achieved by optical components, and modulo-n addition of the transformed images. The method is expected to be executed efficiently by optical parallel processing. We verify performance of the proposed method in terms of security strength and clarify problems on optical implementation by the optical fractal synthesizer.

Keywords: pseudo-random number, stream cipher, fractal, parallel processing

1. INTRODUCTION

In recent years, various types of information from a simple message in an e-mail system to a personal identification code in electronic commerce are running over communication networks. Information leakage is a serious problem in such networks, and data encryption is considered as a key technique against the problem. As characteristics of current web technology, massive image data are frequently dealt with on the Internet. For such large amount of contents, large keys are required to guarantee a high level of security, which requires us long computational time for encryption and decryption.

Optical computing techniques are expected to be useful for encryption of massive information because of parallel optical processing.[1-10] Encryption using encoding masks with random phase distributions has been proposed.[2] This method utilizes two statistically independent phase masks at the input and the Fourier planes and the target message is encrypted into stationary white noise. By experimental demonstration, performance of the method has been studied.[3,4] As the application of the technique, an encrypted memory has been studied.[5-7] A method using a stream cipher technique has been also proposed.[8-10] In this method, XOR operations between a random bit sequence and the message are executed in parallel by optical techniques. The random bit sequence, which is used as a key for encryption, is generated by a pseudo-random number generator (PRNG). To generate a random bit sequence, optical parallel processing can be applied effectively.

In this paper, we propose a new method of pseudo-random number generation, which is based on an optical feedback operation with 2-D affine transformations. Affine transformation is a kind of linear transformation composed of rotation, scaling, and translation. This transformation can be implemented in parallel by optical components. For example, a series of imaging lens, dove prism, and deflection mirror achieve it efficiently. Although the proposed method also requires modulo-n addition of images, this operation is expected to be achieved in parallel by a spatial light modulator. With small number of parameters, such as the rotation angle and the scaling factor, we can generate pseudo-random intensity distribution on a 2-D image. We verify the performance of the proposed method in terms of security strength by computer simulations and evaluate randomness of the patterns generated by the proposed PRNG. Finally, the proposed PRNG is implemented by the optical fractal synthesizer[11] to clarify problems in optical implementation of this method.

Further author information (Send correspondence to T. Sasaki)
T. S.: E-mail: sasaki@gauss.ap.eng.osaka-u.ac.jp
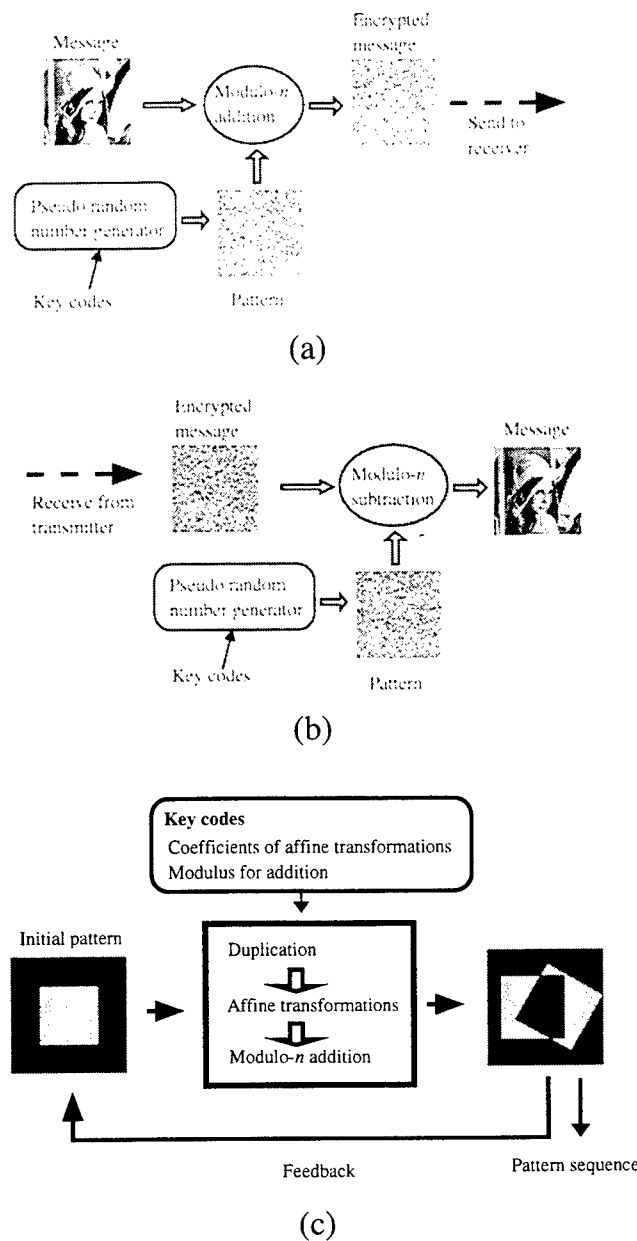J. T.: E-mail: tanida@mls.eng.osaka-u.ac.jp

Figure 1. Schematic diagram of the proposed method: (a) encoding and (b) decoding methods, and (c) PRNG.

2. STREAM CIPHER USING 2-D AFFINE TRANSFORMATION

Figures 1 (a) and (b) show the schematic diagrams of encryption and decryption based on the stream cipher. In these diagrams, messages and patterns are 2-D images whose intensity is represented by 256 levels. Although 1-D bit sequences are often employed in the stream cipher, we use 2-D bit sequences on an image due to suitability for optical implementation. In the encryption, a message and a key pattern generated by the PRNG for a set of key codes are added in modulo-n. The encrypted message has random intensity distribution, which does not show any structure of the original message. In the decryption, the message is retrieved by subtracting the key pattern from the encrypted message in modulo-n. The key pattern is generated by the PRNG using the same key codes as the encoding ones.

Figure 1 (c) shows the schematic diagram of the proposed PRNG. This method is composed of affine transformations and feedback operations. Affine transformation is expressed by a set of a deformation matrix and a translation vector as follows:

$$\mathbf{x}' = \left[\begin{array}{cc} a & b \\ c & d \end{array} \right] \mathbf{x} + \left(\begin{array}{c} e \\ f \end{array} \right),$$ (1)

where $\mathbf{x}$ and $\mathbf{x}'$ are 2-D vectors representing the points on the input and the output planes. Several number of affine transformations are used for the PRNG. The initial image is multiplicated, and each image is transformed by any one of the affine transformations. The transformed images are summed up by addition in modulo-n. The resultant image is used as the input of the next step to generate another 2-D bit sequence.

The matrix in Eq. (1) can be rewritten for optical implementation. 2-D rotation and scaling implemented by a dove prism and a lens system are written by the following equations.

$$R(\theta) = \left[\begin{array}{cc} \cos\theta & -\sin\theta \\ \sin\theta & \cos\theta \end{array} \right],$$ (2)

$$S(s) = \left[\begin{array}{cc} s & 0 \\ 0 & s \end{array} \right],$$ (3)

where θ is the rotation angle and s is the scaling factor. In this paper, we use a specific affine transformation for the proposed PRNG represented by Eq. (4).

$$\mathbf{x}' = S(s)R(\theta)\mathbf{x} + \mathbf{t},$$ (4)

where $\mathbf{t}$ is the translation vector representing image shift.

In this method, the key codes are assigned by the parameters of the affine transformations and the number of iterations. Space of the decoding key codes, which is expected to be large for high security strength, is determined by the possible combinatorial number of the parameters and the iteration. Although the space seems to be smaller than other implementations of the PRNG, high sensitivity on the parameter of the affine transformations enables us to increase available values for the parameter. Even if the number is insufficient, switching of several sets of affine transforms during iterations can be utilized to enlarge the key code space.

Figure 2 shows a sequence of 256×256 images generated by the PRNG with modulo 256 addition. A_i indicates the pattern generated by i times iteration. After 14 iterations, images with random intensity distribution are obtained.

Figures 3 (a) – (c) show the patterns generated by different parameter sets of the affine transformations and iterations. The parameter sets are shown in Table 1, where i is the identifier of affine transformation. Figures 3 (d) and (e) show the absolute value of intensity difference between Figs. 3 (a) and (b), and between (a) and (c), respectively. As seen from Figs. 3 (d) and (e), it is clear that these three patterns have different intensity distribution. Figure 3 (f) shows a specific case that random intensity distribution is localized into a fractal area. To use the proposed method for the stream cipher, the affine transformations and the iteration number must be selected to obtain a pattern where intensity is distributed randomly on the whole image. In this paper, to select the iteration number and the affine transformations, we calculate the autocorrelation function of the pattern, and verify if the autocorrelation function has only one peak on center of a plane like a delta function as described in the following section.

3. COMPUTER SIMULATION

To verify the effectiveness of the proposed method, we executed a computer simulation of data encryption and decryption. The message (the target image of cipher) is a 256×256 pixel image whose intensity is represented by 256 levels. Modulus for the image addition is 256. Figure 4 indicates (a) the message, (b) the key pattern, (c) the ciphered message, and (d) the decoded image. The key pattern is the same as the pattern in Fig. 3 (a). The ciphered message in Fig. 4 (c) has a pseudo-random intensity distribution in which the message content is not visible.

To verify security strength of the proposed method, we try to retrieve the message by slightly different key patterns. The key pattern is generated by the affine transformations whose parameters are modified from that of the encoding key. The encoding key pattern is the pattern in Fig. 4 (b). Table 2 indicates the modified parameters. Figures 4 (e), (f), and (g) show the decoded images by the key patterns with different scaling factor, rotation angle, and translation vector. The correct image can not be retrieved by these keys. Figure 4 (h) shows the decoded image
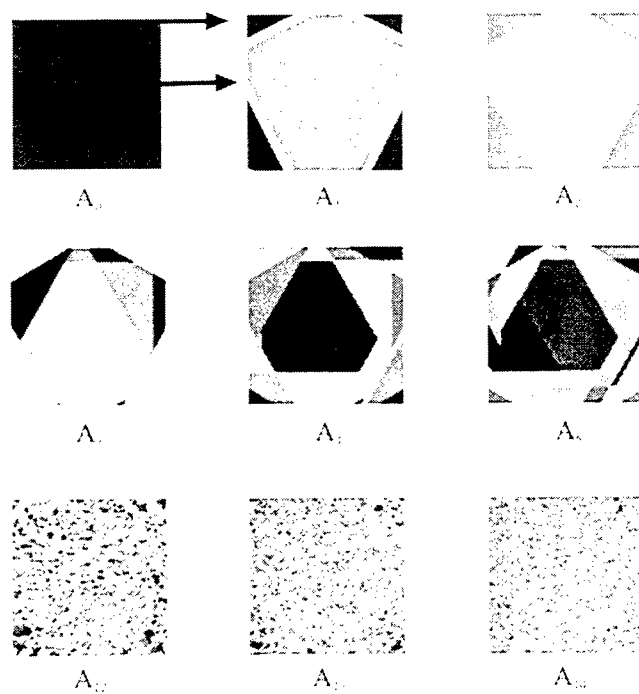
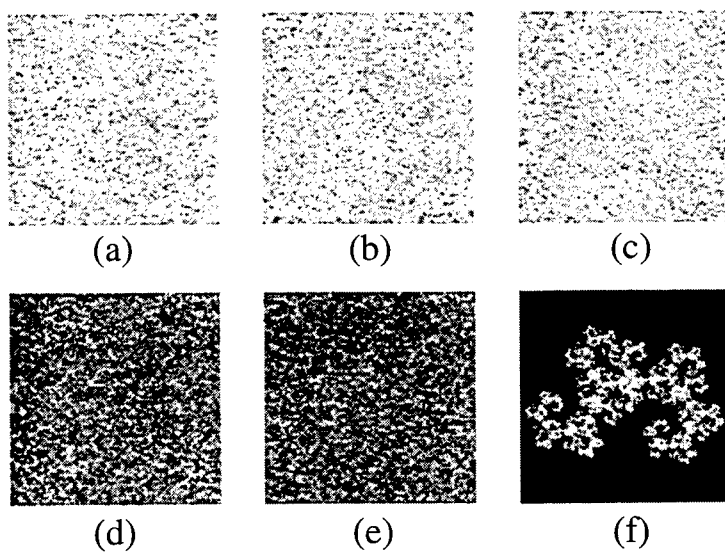**Figure 2.** Image sequence generated by the PRNG.

Figure 3. Patterns generated by different parameter sets of affine transformations.

Table 1. Coefficients of affine transformations for patterns of Figs. 3 (a), (b), (c), and (f).

Pattern	i	s_i	θ_i	$\mathbf{t}_i$	iteration
(a)	1	1.2	60	$(50,0)$	19
	2	1.2	120	$(-50,0)$	19
(b)	1	1.2	60	$(50,0)$	18
	2	1.2	120	$(-50,0)$	18
(c)	1	1.201	60	$(50,0)$	19
	2	1.201	120	$(-50,0)$	19
(f)	1	0.7	60	$(50,0)$	19
	2	0.7	120	$(-50,0)$	19

(a)   (b)   (c)   (d)
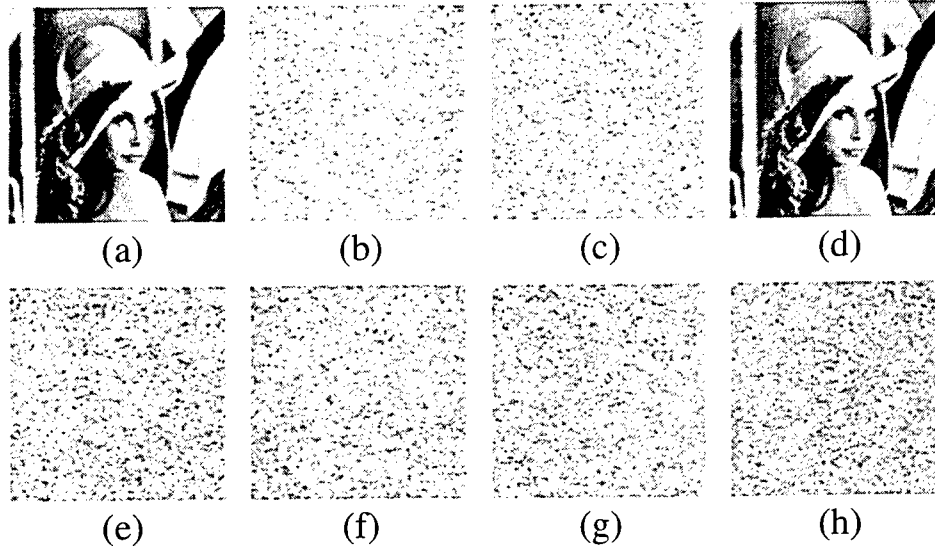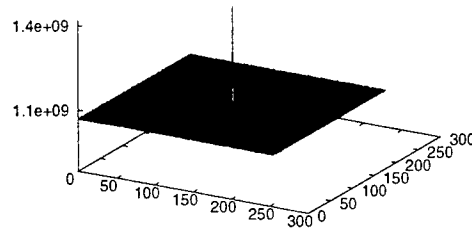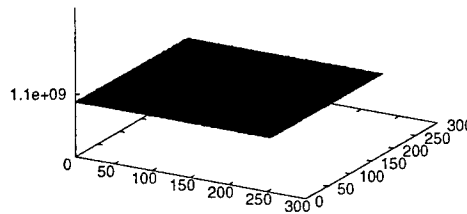
(e)   (f)   (g)   (h)

Figure 4. Verification of the proposed method: (a) message, (b) key pattern, (c) crypted message, and (d) encoded message. (e) – (h) are decoded image by slightly different key pattern, which are corresponding to Table 2.

Table 2. Modified parameters and variations.

Example	parameter	variation
(e)	s_1	$+0.01$
(f)	θ_1	$+0.1$
(g)	$\mathbf{t}_1$	$+(1,0)$
(h)	iteration	$+1$

(a)

(b)

Figure 5. Autocorrelation function of the generated patterns.

by the key pattern with the iteration number one time larger than that of the encoding key. Even in this case, the correct message can not be obtained. As seen from these results, it is very difficult to decrypt the message by the keys similar to the encoding ones.

Randomness of the intensity distribution is evaluated by statistical methods. In the case of a pattern with random intensity distribution, its autocorrelation function should be a delta function. Figure 5 (a) shows the autocorrelation function of the key pattern in Fig. 4 (b). It can be found that the autocorrelation function has only one peak on the center of pattern. As a consequence, the pattern is considered to have random intensity distribution.

It is expected that the patterns generated by different numbers of iterations has no correlation peak because they have different random distribution. Figure 5 (b) shows the correlation function between the patterns obtained by 18 and 19 iterations whose affine transformations are the same as in Fig. 4 (b). There is no peak on the correlation function. Therefore, we can verify that the patterns generated by the different number of iteration, even if the difference is just one, have different random distribution.

4. OPTICAL IMPLEMENTATION

To clarify problems on optical implementation of the proposed method, we constructed the PRNG on the optical fractal synthesizer.[11]   Optical setup of the optical fractal synthesizer is shown in Fig. 6. This system can generate a fractal pattern for given system parameters by optical feedback processing. The input image of the optical fractal synthesizer is displayed on the CRT, and duplicated by the beam splitter BS1. Each image is rotated and reflected by the dove prism and translated by the tilted mirror in each optical path. The images passing through the different paths are combined by the second beam splitter BS2. After scaling by the zoom lens, the images are captured by
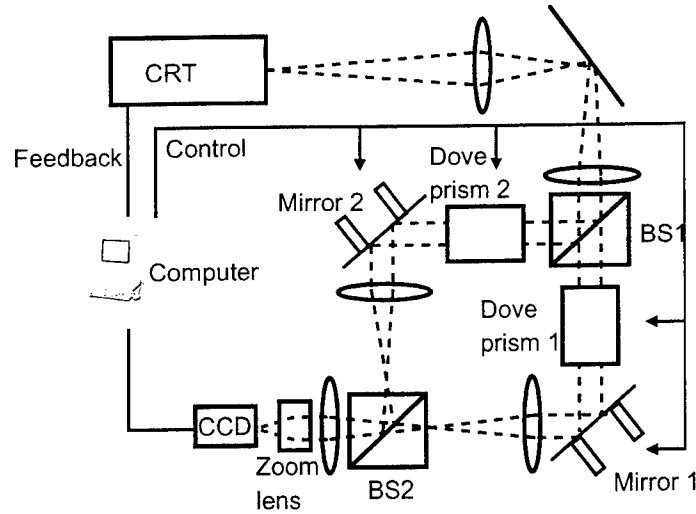
Figure 6. Optical setup of optical fractal synthesizer.

Table 3. Parameters of affine transformations used in optical implementation.

i	s_i	θ_i	$\mathbf{t}_i$
1	1.0	150	$(60, 0)$
2	1.0	30	$(-60, 0)$

the CCD camera. The captured image is displayed on the CRT again, and the same procedure is repeated. After a large number of iterations, the initial pattern is transformed into a complicated shape specified according to the system parameters.

To generate images with pseudo-random intensity distribution, the captured images through the different optical paths are added in modulo 2. XOR operation is used as modulo-2 addition, which is suitable for binary images. Figure 7 shows an example of pattern sequence generated by the optical system. Parameters of the affine transformation are shown in Table 3. The resolutional points of the image is 200×200 pixel. The overlapped area of two transformed patterns becomes dark by XOR operation executed by the computer. After 12 iterations, bright and dark pixels are spread over the image area.

Figures 8 (a)-(c) show results of message encryption and decryption using the optical PRNG, where the key pattern is the one obtained by 14 iterations shown in Fig. 7. In this case, the message is a binarized image to avoid effect of nonlinearity of the TV feedback system. As seen from Fig. 8 (c), the original message (Fig. 8 (a)) can not be retrieved. In addition, abstract structure of the message remains in the encrypted image of Fig. 8 (b). Difference between the key patterns independently generated by the same parameters is shown in Fig. 8 (d). As shown in this figure, the difference is relatively large. If we use the same key pattern as the encryption, the correct message is obtained as shown in Fig. 8 (e). It is clear that the obtained message is the same as the original.

We investigated the reason why the pattern can not be reproduced correctly. A histogram of an image captured by the CCD camera is shown in Fig. 9 (a), where the captured image is illustrated in Fig. 9 (b). The histogram has three peaks corresponding to the three areas (the black, dark, and white areas in Fig. 9 (b)). Note that there are many pixels whose intensity is between the peaks. To execute the XOR operation to the captured image, two threshold intensity values are set between the low and middle peaks, and between the middle and high peaks. We used 23 and 37 as the threshold values in this optical experiment. In the XOR operation, intensity values between the two threshold values are transformed to 255, the others are transformed to 0. In the case that intensity of the pixels on the CRT display fluctuates temporally, the pixels whose value is close to one of the threshold values become error sources.

Then we observed temporal transition of a pixel intensity in the captured image. In this experiment, a square
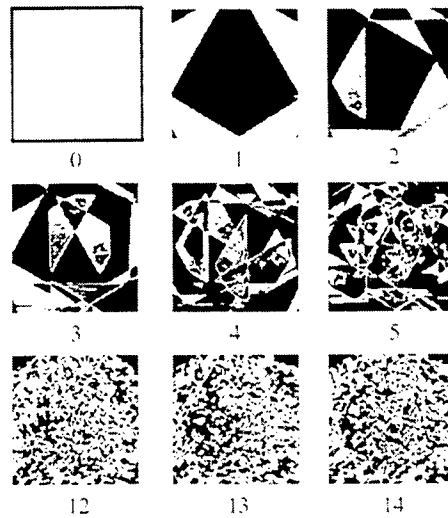
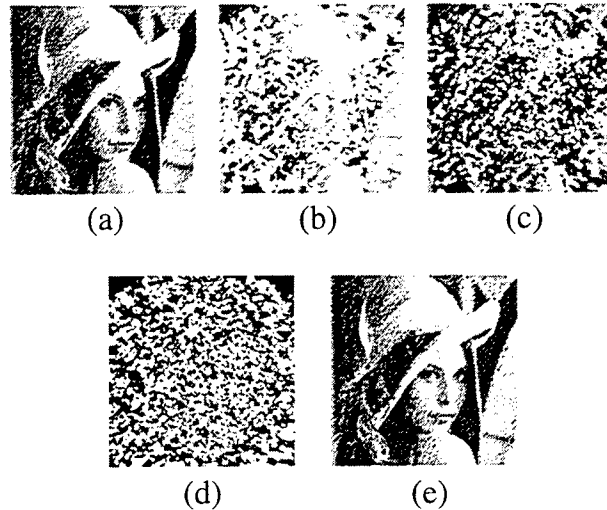**Figure 7.** Random pattern sequence generated by the optical system.

Figure 8. Result of optical implementation: (a) message, (b) data encrypted by a key generated optically, (c) message decoded by a key pattern generated independently, (d) intensity difference between the keys used for (b) and (c), and (e) message decoded by the key pattern used for (b).

pattern is displayed on the CRT at first step. Then the square pattern is transformed by the optical affine transformations shown in Table 3, and captured by the CCD camera. These processes are repeated 60 times. Finally, 60 images are obtained sequentially, and intensity transition of one pixel is measured from the images. Figure 10 shows the transition of the pixel whose location is $(30, 200)$, where the coordinate system (x, y) is indicated in Fig. 9 (b). During the 60 iterations, intensity of the pixel fluctuates between 36 and 38 frequently. As seen from these results, reproduction of the same patterns is very difficult in this experimental system. To solve the problem, we should reduce the fluctuation of the pixel values, or reproduce the same fluctuation.

Slow speed of the optical feedback operation is also an important problem. In the experimental system, speed of feedback operation is limited by the transfer frame rate from the CCD camera to the CRT, which is about 30 frames per second. A high speed optical feedback system based on the smart pixels with parallel optical input/output ports and free-space optics is expected to overcome the problem.
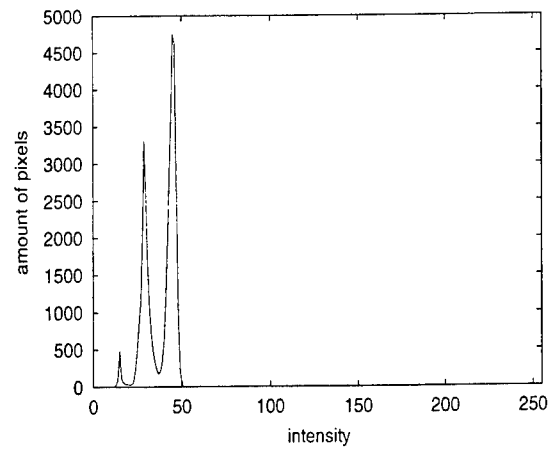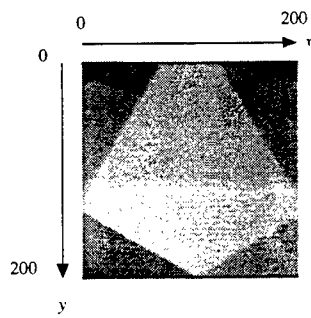
Figure 9. Histogram of an image captured by the CCD camera. (a) histogram and (b) captured image.
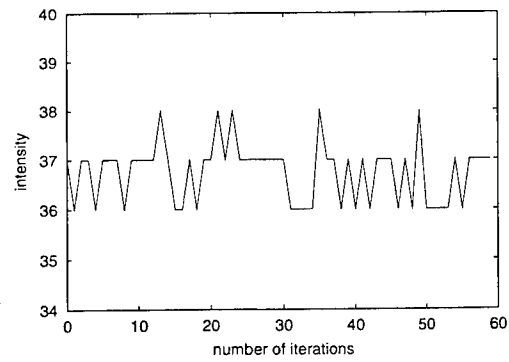

Figure 10. Temporal transition of pixel intensity.

5. CONCLUSION

We have proposed a method of stream cipher based on the PRNG using geometrical transformation, such as image rotation, scaling, and translations. The proposed method is suitable for optical implementation, and can generate 2-D pseudo-random intensity distribution by optical parallel affine transformations and optical feedback processing. Security strength of the method has been evaluated by computer simulations. It has been shown that different key pattern can not retrieve the ciphered image if sufficient number of iterations were done for random pattern generation. The proposed method was implemented on the optical fractal synthesizer, which suggests that uniformity of intensity distribution on the image plane is important for correct decoding.

REFERENCES

1. B. Javidi and J. L. Horner, "Optical pattern recognition for validation and security verification," *Opt. Eng.* **33**, pp. 1752–1756, 1994.
2. P. Refregier and B. Javidi, "Optical image encryption based on input plane and fourier plane random encoding," *Opt. Lett.* **20**, pp. 767–769, 1995.
3. B. Javidi, G. Zhang, and J. Li, "Experimental demonstration of the random phase encoding technique for image encryption and security verification," *Opt. Eng.* **35**, pp. 2506–2512, 1996.
4. B. Javidi, A. Sergent, and E. Ahouzi, "Performance of double phase encoding encryption technique using binarized encrypted images," *Opt. Eng.* **37**, pp. 565–569, 1998.
5. B. Javidi, G. Zhang, and J. Li, "Encrypted optical memory using double-random phase encoding," *Appl. Opt.* **36**, pp. 1054–1058, 1997.
6. G. Unnikrishnan, J. Joseph, and K. Singh, "Optical encryption system that uses phase conjugation in a photorefractive crystal," *Appl. Opt.* **37**, pp. 8181–8186, 1998.
7. O. Matoba and B. Javidi, "Encrypted optical memory system using three-dimensional keys in the fresnel domain," *Opt. Lett.* **24**, pp. 762–764, 1999.
8. M. Madjarova, M. Kakuta, M.Yamaguchi, and N. Ohyama, "Optical implementation of the stream cipher based on the irreversible cellular automata algorithm," *Opt. Lett.* **22**, pp. 1624–1626, 1997.
9. M. Kakuta, M. Madjarova, T. Obi, M. Yamaguchi, and N. Ohyama, "Vernam encryption using optical parallel processing," *Jpn. J. Opt. (KOGAKU)* **27**, pp. 104–109, 1998.
10. S. Zhang and M. Karim, "High-security optical integrated stream ciphers," *Opt. Eng.* **38**, pp. 20–24, 1999.
11. J. Tanida, A. Uemoto, and Y. Ichioka, "Optical fractal synthesizer: concept and experimental verification," *Appl. Opt.* **32**, pp. 653–658, 1993.

SESSION 5

Near-Field Recording

Near-field optical data storage:
Avenues for Improved Performance

Tom D. Milster
Optical Sciences Center / Optical Data Storage Center
University of Arizona, Tucson, Arizona 85721
milster@arizona.edu

Abstract

Because they produce small spot size, near-field techniques are applied to optical data storage systems in order to increase recording density. For data storage, the optical near field is defined in terms of evanescent coupling between the system used to read data and the recording layer. Two practical implementations that use evanescent energy are aperture probes and solid immersion lenses (SILs). In this paper, the basic characteristics of these systems are reviewed, and some considerations for improving performance are discussed. Combinations of SILs and apertures could produce data storage systems with ultra-fine resolution and good detection characteristics.

KEY WORDS: optical data storage, near-field optics, solid immersion lens, aperture probes, evanescent energy

1. Introduction

Both solid immersion lens (SIL)[1] systems and aperture[2] systems have been used to record on and retrieve data from optical media. SIL systems are attractive because they produce spots smaller than conventional optical systems and they have high throughput. Aperture systems are attractive because they offer the smallest spot size. In this paper, both systems are reviewed in terms of basic detection properties, and considerations for improving system performance are listed.

A typical arrangement for *near-field* optical recording using a SIL is shown in Figure 1. Light from a laser passes through a beam splitter and is focused onto a recording layer by an objective lens. The recording layer is on a disk that spins under the objective lens. The recording layer contains spiral tracks of mark patterns that differ in reflectivity from the area between marks. As the focused laser beam passes over a mark, the reflected light level changes. Changes in the reflected light level are sensed by using the beam splitter to direct a portion of the reflected light onto a silicon detector. The detector current, which is a representation of the mark pattern, is decoded to produce digital information. The fidelity of the detector signal determines the amount of data per unit length of track that can be decoded with high reliability.

There are several factors that influence the fidelity of the detector signal. The most important factor for closely-spaced marks is the focused *spot size s*. Large *s* blurs the reflected light signal, resulting in a loss of *contrast V* in the detector signal. Contrast is defined as $V = (I_{MAX} - I_{MIN})/(I_{MAX} + I_{MIN})$, where I_{MAX} and I_{MIN} are shown in Fig. 1. Conversely, if *s* is small, changes in the reflected signal are sharp as the marks traverse under the spot. Therefore, as *s* decreases, the contrast and fidelity increase. Increased fidelity and contrast lead to smaller detectable changes in the mark pattern, so smaller marks can be used and more data can be packed into each track. In systems that are limited by media noise, the signal-to-noise ratio is maximized by maximizing contrast.

Unfortunately, *s* cannot be made arbitrarily small. Due to the physics of diffraction, the minimum
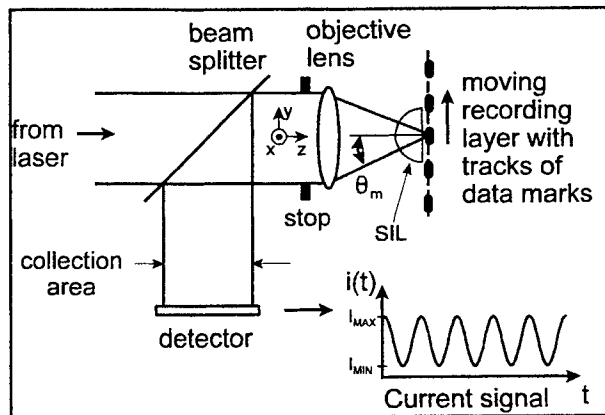
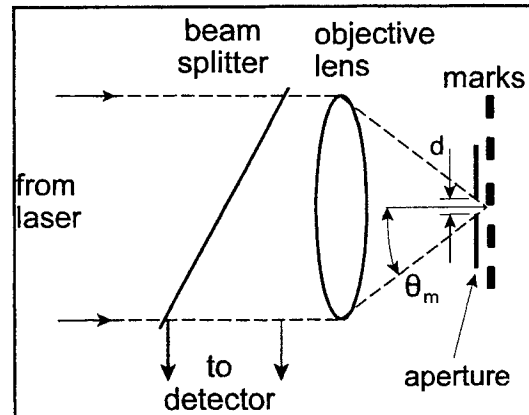**Figure 1.** System for near-field recording using a SIL.

Figure 2. System for near-field recoding using an aperture.

spot size s for SIL systems is a function of the wavelength of the laser λ, the focusing properties of the objective lens, system aberrations, and the thin-film structure used as the recording layer.[3] A simple relationship that is used to estimate the full-width-at-$1/e^2$ spot size for conventional gaussian illumination[4] at the stop is $s = \lambda / (n \sin\theta_m)$, where λ is the wavelength in air, θ_m is the marginal ray angle, and n is the refractive index of the SIL. The marginal ray passes just at the edge of the stop, which is the limiting aperture of the system. The value of $(n \sin\theta_m)$ is the effective numerical aperture NA_{EFF} of the system. As NA_{EFF} increases or λ decreases, the spot size s gets smaller, and mark density can increase. Given that new laser systems will be developed to reduce λ,[5] this paper describes how to increase NA_{EFF}.

A *near-field aperture system* is shown in Figure 2. An aperture of diameter $d < \lambda$ is placed in proximity to the recording layer, and the mark pattern is scanned. The illumination for the aperture can be from a fiber waveguide or a lens. The size of the light spot interacting with the marks is mainly determined by d. The reflected light collected by the objective lens is passed to the detectors, where the current signal is decoded to produce digital information. Like with the SIL system, smaller spots yield higher contrast and greater data density. This simplistic model can also be applied to superresolving systems, like SuperRENS media,[6] as a basic description of the device.

In the following sections, the basic detection principle of both systems is reviewed, and considerations for improved performance are listed. Section 2 briefly reviews how light scatters from near-field interfaces and how light is collected. Section 3 described the evanescent nature of near-field coupling. Section 4 describes how the scattered light produces modulation in the detector signal. Section 5 suggests avenues that may be useful for improving performance of near-field systems, and Section 7 presents conclusions form this work.

2. Scattering and collection of light energy

Light focused into the recording layers and scattered from them may be described in two ways. One way is in the *spatial domain*, where the physical distribution of light energy is determined as a function of the transverse dimensions at an observation plane inside the recording layers, as shown in Fig. 3. The spatial domain is easily understood and is useful to estimate spot size and other parameters. The second way is to describe the energy in the *frequency* (or *angular*) *domain*.[7,3]
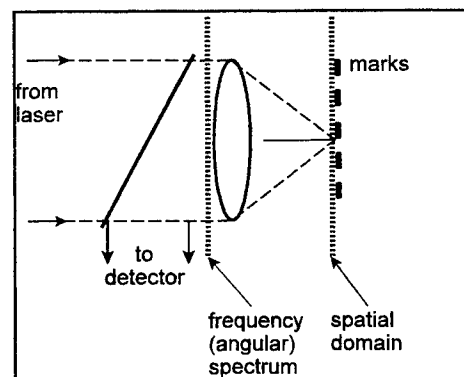

Figure 3. Spatial and Frequency Domains

The angular distribution of the focused spot is found by taking the Fourier transform of the spot amplitude distribution. The angular distribution of the focused spot inside homogeneous recording layers (no marks) is called the *illumination system transfer function* (ISTF), and is useful for understanding the roles of evanescent and propagating energy.(refs: milsters) The angular distribution of the reflected light is important, because it represents the distribution of reflected light collected by the objective lens and incident onto the detector. The reflected light distribution is often nonuniform, and it depends on the mark structure and medium parameters.

Figure 4. Several important parameters for a particular phase-change medium versus gap height.

Angular distributions are functions of direction cosines α and β, which correspond to the x and y axes, respectively, in the spatial domain. The ISTF is denoted by $H(\alpha,\beta; \Delta z)$, where Δz is the distance from the bottom of the near-field coupling surface to the observation plane. α_m is the direction cosine corresponding to the marginal ray angle, $\alpha_m = \sin \theta_m$.

The ISTF has also been shown to be a fundamental design tool for analyzing and optimizing SIL systems that use phase-change media.[8] For example, a plot of the peak energy, spot size, and contrast of a particular phase-change media geometry is shown in Fig. 4. For this system, the contrast is a more sensitive function of the gap between the bottom of a SIL and the recording surface than either the spot size or the peak irradiance in the recording layer. Shimura *et al.* in Reference 8 has shown a masking technique based on information obtained from ISTF calculations that improve contrast significantly for this system.
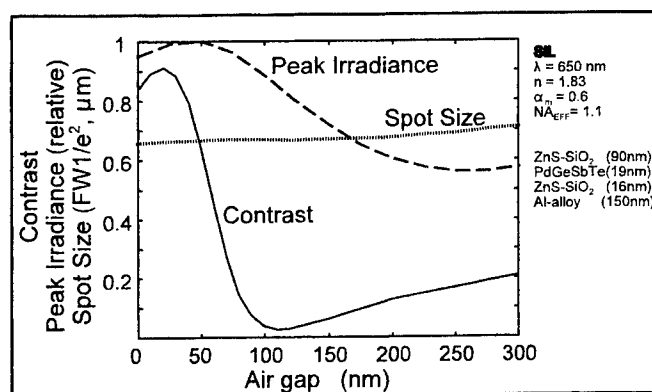
3. Evanescent characteristics of near-field devices

In aperture systems, a hole smaller than s is placed in an otherwise opaque mask near the recording layer. Hole-type apertures can be made with diameters much less than 0.5 μm. The angular specturm contains components that are well outside the range possible with a far field system, that is, without near-field apertures or SILs. For example, consider a 0.25μm diameter aperture illuminated by a $\lambda = 0.5$ μm laser beam with a uniform beam profile. The resulting angular spectrum $|H(\alpha,0; \Delta z =0)|$ in air is shown in Fig.5. A dashed line is included to indicate the boundary line where $\alpha_m = 1$. The energy outside the boundary line in Fig. 4 has special properties. It is called *evanescent energy* and does not propagate like the light inside the boundary line, which can be focused and imaged with a far-field system. Evanescent energy decays exponentially as the distance Δz between the aperture and the observation plane increases. The rate of evanescent decay depends on the radius $\rho = (\alpha^2 + \beta^2)^{1/2}$ for $\rho > 1$. A relationship that describes the evanescent decay is

$$|H(\alpha,\beta; \Delta z)| = |H(\alpha,\beta;0)| \exp\left\{-\frac{2\pi}{\lambda}\sqrt{\rho^2 - 1}\, \Delta z\right\} \qquad , \qquad (1)$$

where $|H(\alpha,\beta;\Delta z)|$ is the amplitude of the ISTF for a given Δz. For example, Fig. 6 shows $|H(\alpha,0; 50\text{nm})|$. It is apparent that energy in the range $\rho > 1$ is significantly reduced, even at a distance of only 0.1 λ from the aperture. The resulting spot profile $|h(x,0; 50 \text{ nm})|$ is much smoother than the spot profile $|h(x,0; 0)|$ shown in Fig.5, so the detected signal is not as sharp when the hole is away from the data. Therefore, apertures that pass a significant amount of evanescent energy must be used very close to the data layer to gain full advantage of the smaller spot size. The effective numerical aperture for aperture systems is $NA_{EFF} = \lambda/d$, which is the approximate limit to the angular spectrum of the ISTF.
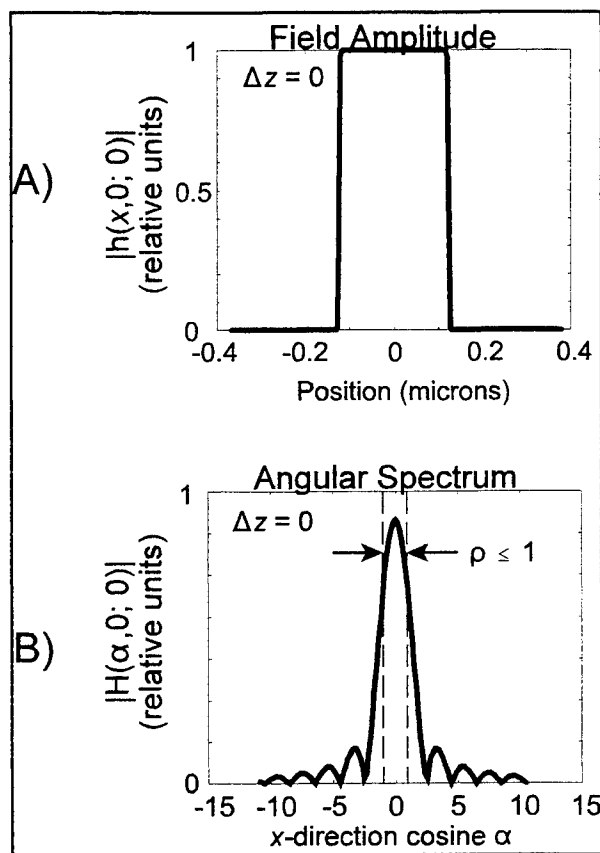
Figure 5. A) Field amplitude for a $\lambda/2$ diameter hole with the observation plane next to the aperture ($\Delta z = 0$); B) The angular spectrum corresponding to (A).
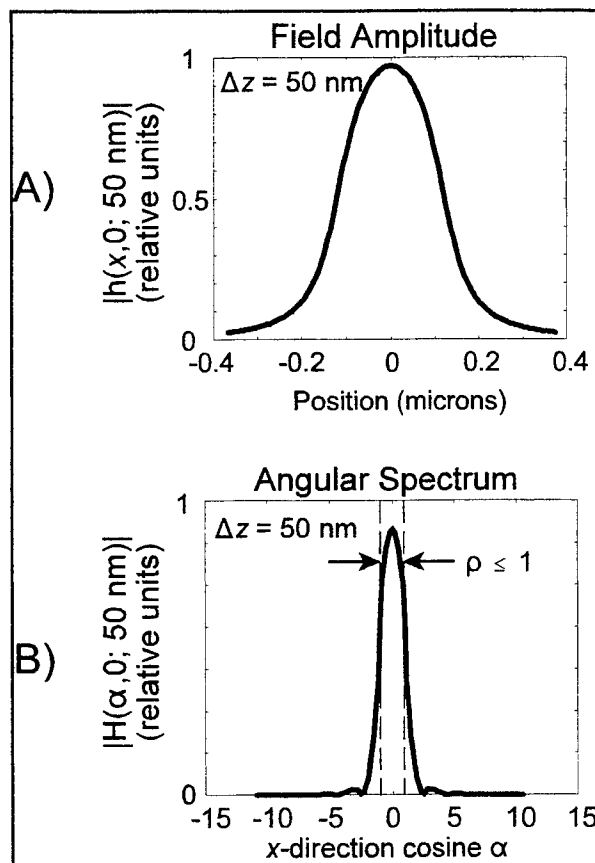
Figure 6. A) Field amplitude for a $\lambda/2$ diameter hole with the observation plane at a distance of 50 nm; B) The angular spectrum corresponding to (A).

The SIL system also exhibits evanescent energy as light propagates into the gap. With respect to Eq. (1), the SIL evanescent decay is characterized by replacing ρ by $\rho' = n\rho$. If the SIL is used in air, focused light with direction cosines greater than the critical angle $\rho_c = 1/n$ ($\rho' = 1$) undergo total internal reflection (TIR) back to the objective lens.[3] However, TIR light passes a short distance past the SIL interface where the light is evanescent, that is, exponentially decaying away from the interface. In fact, the evanescent decay is similar to decay of light from a hole-type aperture.

For both hole-type apertures and SIL systems, the recording layer must be in proximity to the coupling surface. For hole-type apertures, the coupling surface is the aperture. For SILs, the coupling surface is the flat surface of the SIL. Without close proximity, the spot size increases and the total energy available for coupling into the recording layer decreases due to evanescent decay. What differentiates near-field systems from far-field systems is the use of evanescent energy to project small spot sizes into the recording layers. The small spot sizes of near-field systems are otherwise impossible to obtain with far-field systems using the same laser wavelength.

Since a small air gap is present in both aperture systems and SILs, some decay of evanescent energy is always observed. If the energy in the gap has significant components beyond the $\rho = 1$ boundary, even very tiny gap changes can produce significant changes in the light spot. An important observation is that not all of the energy is evanescent. However, as performance is pushed to smaller spot sizes, the amount of evanescent energy increases, and the sensitivity to gap variations is increased.
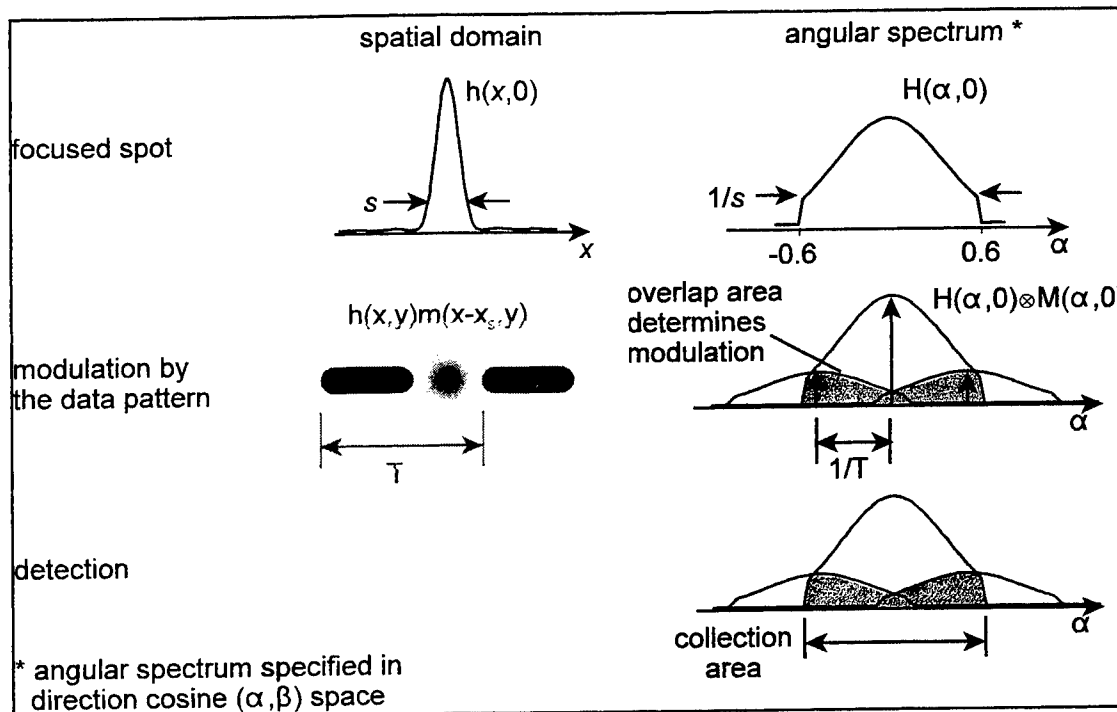
Figure 7. The basic process of detection for a DVD-type system with NA = 0.6.

4. Detection and Modulation

The basic process of detection is illustrated in Fig. 7 for a DVD-type far-field system. The focused spot $h(x,y)$ with size s scans the data pattern $m(x,y)$. The period of the mark pattern is $T = 2\lambda$. The reflected light is modulated according to $h(x,y)m(x-x_s,y)$, where x_s represents the scan coordinate of the disk. In frequency space, the Fourier transform of the mark pattern produces diffracted orders that, when convolved with H overlap within the collection area of the objective lens. Each diffracted order spans a range $|\alpha|$ < 0.6. As x_s increases, the phases of the diffracted orders change, and the resulting interference with the zero order creates light modulation in the overlap areas. The light modulation produces current modulation in the detectors, which is decoded to provide digital information. The larger the amount of overlap area, the larger the modulation. Large modulation produces high contrast in the detector current.

The modulation behavior of an aperture system and a SIL system scanning a mark pattern. Figure 8(a) displays the angular (frequency) spectrum of a near-field aperture system for $d = \lambda/2$ and $T = \lambda$. The collection area corresponds to a lens with NA = 0.6.
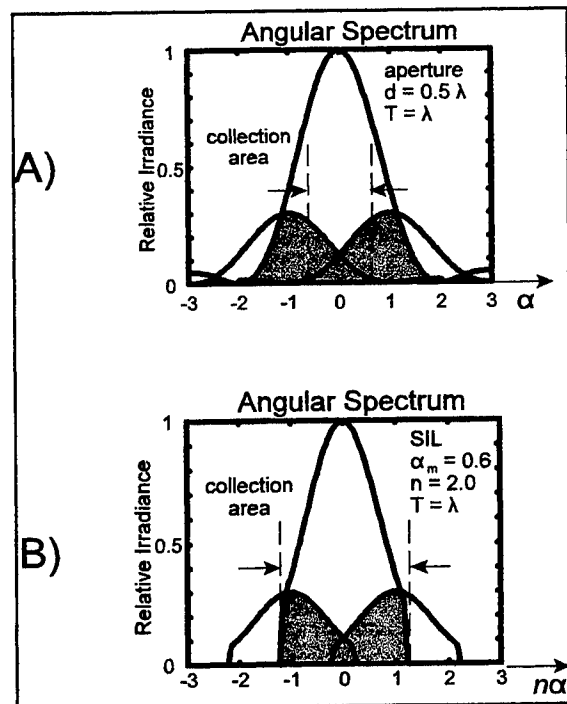

Figure 8. A) Angular spectrum for an aperture system; B) Angular spectrum for a SIL system.
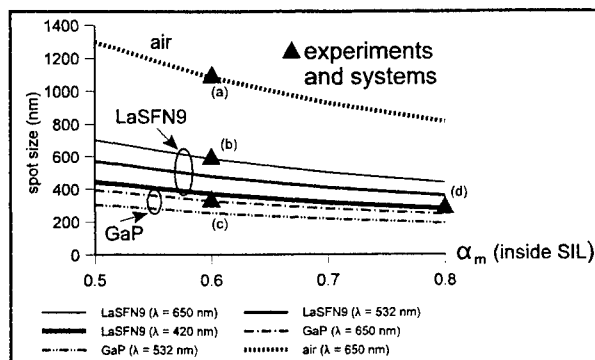
Figure 9. Spot size versus marginal-ray direction cosine (NA) for two SIL materials and three wavelengths. Triangles are experimental results or demonstrations. (a) DVD-type systems; (b) See Reference 8; (c) See Reference 9; (d) See Reference 10.
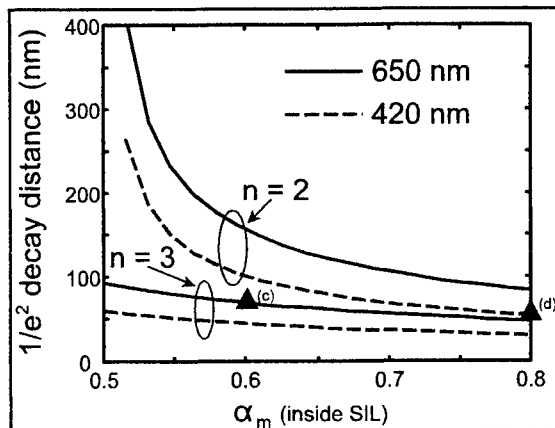

Figure 10. $1/e^2$ decay distance of the marginal-ray evanescent field for two SIL materials and two wavelengths. Triangles refer to experiements as described in Figure 9.

Notice that $NA_{EFF} \sim 2.0$. The overlap area is substantial, so a high contrast current signal should be expected. However, unlike the DVD system, substantial modulation exists outside the collection area. Figure 8(b) displays the angular spectrum of a SIL system for $\alpha_m = 0.6$, $n = 2.0$, $NA_{EFF} = 1.2$, and $T = \lambda$. Like the aperture system, the overlap area is large, and high contrast is expected. The collection area is larger than the aperture system due to the SIL's high index of refraction.

5. Avenues for Improving Performance

A simple calculation based on $s = \lambda/n\alpha_m$ yields the spot-size curves shown in Fig. 9 for SIL systems using LaSFN9 glass or GaP material. The curves are drawn as a function of α_m for three laser wavelengths, 650 nm, 532 nm, and 420 nm. No curve is drawn for GaP material at 420 nm because the material is highly absorbing at that wavelength. The triangles (▲) represent experimental data points or demonstrations. Dramatic improvement in spot size is obtained for all SIL systems. Beyond $\alpha_m = 0.6$, the spot-size reduction is not significantly improved by increasing α_m. The GaP system at a laser wavelength of 650nm exhibits smaller s than the LaSFN9 system at a wavelength of 420 nm for a given value of α_m.

Extending the performance of SIL systems beyond what has been demonstrated may be difficult due to the sensitivity of the gap height due to decay of the evanescent energy. Figure 10 shows the $1/e^2$ decay distance of the marginal ray versus the direction cosine of the marginal ray α_m. For low α_m and long wavelength, the decay length is large, and good tolerances are observed. However, this combination of parameters does not yield good spot size, as shown in Fig. 9. To achieve fine spot size, the wavelength must be short and n must be as high as possible. Figure 10 shows that with a laser wavelength of 420 nm and n = 2.0, the $1/e^2$ decay length for the Sony system described in Reference 10 (system (d) in Figure 10) was less than 100 nm, which was the upper limit of the gap height used in the experiment. The system used in Reference 9 (system (c) in Figure 10), which uses a GaP lens and a laser wavelength of 650 nm, has similar tolerances. The optimum operating conditions for these experiments includes operating the SIL at a much lower gap height, say 50 nm or less. Even with today's state-of-the-art equipment, it is difficult to maintain this gap tolerance. With more experience and development, the practical gap height and associated tolerances may be reduced, but, at this time, it does not appear that much improvement is practical. This consideration of the evanescent day is a first-order consideration in the design of SIL systems. However, other considerations, like the signal contrast shown in Fig. 4, may limit the gap height before spot size or evanescent decay is problematic.

Aperture systems are not fundamentally limited by spot-size constraints. Focused-ion beam techniques have proven that apertures can be fabricated in Al and Cr metallic layers down to 50 nm diameter. However, the practical consideration of gap height and power throughput are limiting factors. For example, Figure 11 illustrates the tradeoff between gap height and aperture size with respect to spot size. Small holes with diameters $\sim \lambda/10$ have low throughput and diverge rapidly in the gap. Larger holes with diameter $\sim \lambda/3$ have higher throughput and do not

Figure 11. When using apertures to obtain small spot size, the distance to the observation plane is important due to the rapid increase in spot size away from the aperture.

diverge as rapidly. Therefore, the spot size s in an observation plane a reasonable distance (~ 30 nm) from the aperture will be smaller for the large hole than for the small hole.

An additional practical consideration is the concentration of thermal energy near the coupling surface. SIL systems that focus light within a few hundred nanometers of the bottom surface of the SIL. The focused light spot creates an intense heat source that can damage material in the gap, like lubricants. The damaged material can produce obstructions to the beam path. One solution to this problem is to provide a high-index cover layer on top of the recording surface a few microns thick. With the coupling layer, the light is slightly defocused in the gap, and the energy density is dramatically reduced. Therefore, the heat is largely removed from the gap region. However, practical difficulties remain with respect to the manufacturing of the protective layers.

Combination of an aperture with a SIL can lead to improved detection. For example, Fig. 12 displays the angular spectra of two aperture systems scanning a mark pattern with $T = 0.5\lambda$. Fig 12(a) displays the result for an aperture system, where only a small fraction of the modulation is passed to the collection area. Fig. 12(b) displays the result when a SIL is used in conjunction with the aperture. The amount of overlap area is significantly improved, and a higher contrast signal will result. However, combinations of apertures with SILs presents a significant challenge with respect to the practical aspects of such a device. For example, the focused beam must remain centered over the aperture during recording and playback. On the other hand, the aperture could be used to compensate for some systematic errors, like mild aberrations, caused by component misalignments.

The very small aperture laser (VSAL)[11] uses a metallic aperture to form the light spot that interacts with the recording layer, so it suffers the same considerations as other near-field systems with respect
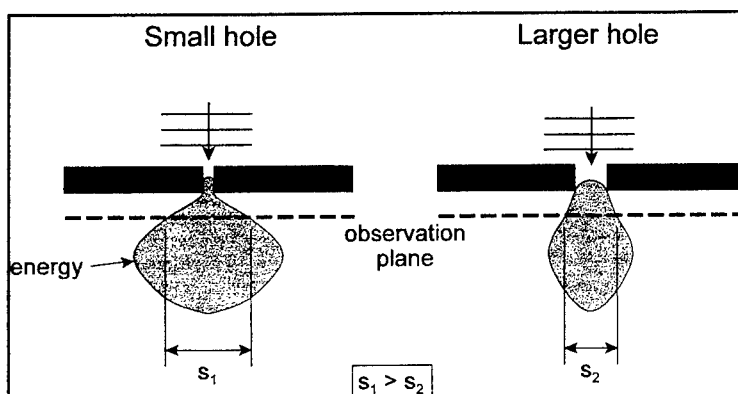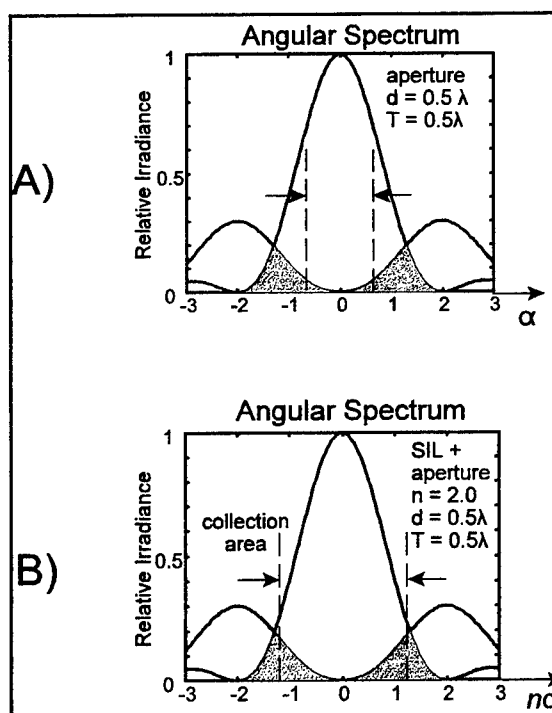

Figure 12. A) Angular spectrum of an aperture system with closely spaced marks; B) Angular spectrum of an aperture + SIL system with closely spaced marks.

to the decay of evanescent energy and contamination of the near-field interface. Therefore, the size of the VSAL aperture is limited as shown in Fig. 11. Too small of an aperture is not practical due to the rapidly increasing spot size. However, the detection process for the VSAL is different than other techniques because detection occurs inside the laser cavity, which is very close to the aperture. In order to get the maximum benefit, the VSAL cavity should be designed to propagate the high spatial frequency components during readout, as shown in Fig. 8(a).

6. Conclusions

The basic detection process of both SILs and apertures is well described using a frequency-space description. Modulation of the detector current is shown to be due to overlap of diffracted orders in frequency space. As the marks become more closely spaced, the diffracted orders move farther apart, and the overlap area decreases. Near-field systems make use of evanescent energy in the gap that is represented in frequency space where $\rho > 1$. Frequency components in the evanescent region decay exponentially as the gap increases. The contrast of the readout signal is shown to be more sensitive to gap variations than the spot size or peak irradiance when SILs are used with a phase-change media structure.

The performance of near-field systems can be improved to give smaller spot sizes. For SILs, the implementation of both high index SILs with red wavelength and lower index SILs with blue wavelengths have been shown. However, these systems use a very small gap (~ 50 nm) that may be near the practical limit. Aperture systems with very small holes can only be used with the medium impractically close to the aperture. Instead, slightly wider holes can be used to give small spot sizes with reasonable gap heights. The combination of a SIL lens and an aperture probe during readout can greatly improve the detectability. and contrast of the data signal.

7.0 Acknowledgments

8. References

1. S. M. Mansfield, W. R. Studenmund, G. S. Kino and K. Osato, "High numerical-aperture lens system for optical data storage," *Opt. Lett.* **18** (4), 305-307 (1993).
2. E. Betzig, J. K.Trautman, R. Wolfe, E. M. Gyorgy, P. L. Finn, M. H. Kryder, and C-H. Chang, "Near-field magneto-optics and high density data storage," *Appl. Phys. Lett.*, **61** (2) 142-144 (1992).
3. T. D. Milster, J. S. Jo, and K. Hirota, "Roles of propagating and evanescent waves in solid immersion lens systems," *Appl. Opt.*, **38** (23), 5046-5057 (1999).
4. H. M. Haskal, "Laser recording with truncated Gaussian beams," *Appl. Opt.* 18(13), pp. 2143-2146 (1979).
5. S. Nakamura, M. Senoh, S. Nagahama, N. Iwasa, T. Yamada, T. Matshushita, H. Kiyoku, Y. Sugimoto, T. Kozaki, H. Umemoto, M. Sano, and K. Chocho, "InGaN/GaN/AlGaN-based laser diodes with cleaved facets grown on GaN substrates," *Appl. Phys. Lett.*, **73** (6) 832-834 (1998).
6. J. Tominaga, F. Hiroshi, A. Sato, T. Nakano, T. Fukaya and N. Atoda, "The near-field super-resolution properties of an autimony thin film," Jpn. J. Appl. Phys. **37**, Part 2, No. 11 A, L323-L325 (1998).
7. D. G. Flagello, T. Milster, A. E. Rosenbluth, "Theory of high NA imaging in homogeneous thin films," JOSA A 13(1), pp. 53-64 (1996).

8. T. D. Milster, K. Shimura, J. S. Jo, K. Hirota, "Pupil-plane filtering for improved signal detection in an optical data storage system incorporating a solid immersion lens," *Opt. Lett.* 24(9), pp. 605-607 (1999).

9. K. Hirota, T. D. Milster, K. Shimura, Y. Zhang and J. S. Jo, " Near-field phase change recording using a GaP hemispherical lens," *Jpn. J. Appl. Phys.* 39(2000), Part 1, No. 2B, p. 968-972 (2000).

10. K. Kishima *et al.* "Near-field phase-change recording using a GaN laser diode," paper MC2 in Conference Digest of 2000 Optical Data Storage, 14-17 May, 2000, Whistler, British Columbia, Canada, sponsored by IEEE/Lasers and Electro-Optics Society, Piscataway, N. J., IEEE Catalog Nuber 00TH8491, pp. 33-35.

11. A. Partovi, D. Peale, M. Wuttig, C. A. Murray, G. Zydzik, L. Hopkins, K. Baldwin, W. S. Hobson, J. Wynn, J. Lopata, L. Dhar, R. Chichester, J. H. Yeh, "High power laser light source for near-field optics and its application to high-density optical data storage," *Appl. Phys. Lett.* 75 (11), 1515-1517 (1999).

Amplitude and phase apodization caused by focusing light through an evanescent gap in SIL recorders

Joshua S. Jo*, Tom D. Milster, and J. Kevin Erwin
Optical Data Storage Center/Optical Sciences Center
University of Arizona

ABSTRACT

High numerical aperture(NA) vector diffraction theory is used to analyze a near field optical system using a solid immersion lens (SIL). The amplitude and phase of the transmitted light through the system changes as a function of the air gap height as well as indices of refraction, incident angle, etc. We call these "amplitude apodization" and "phase apodization". The characteristics of those are done using supergaussian form. The effects of amplitude and phase apodization on irradiance are investigated for various index of refraction and air gap height.

Keywords: apodization, gap-induced aberration, evanescent coupling, characteristics, etc

1. Introduction

In optical systems the apodization of amplitude and phase degrades system performance. Phase apodization is called aberration. The focused spot-size in the recording media increases when aberrations are introduced. The peak intensity of the focused spot is also decreased by the aberrations. Amplitude apodization also decreases the peak intensity of the focused spot. Previously, we have shown the characteristics of phase apodization in solid immersion lens(SIL) systems and their effects on system performance.[1]
In this paper, we investigate the characteristics of amplitude apodization in SIL-systems. The origin and effect of the phase apodization is also studied in conjunction with amplitude apodization.

2. Theory

In SIL-systems, there is an air gap ($n_2 = 1$) between the SIL and the recording media, as shown in Fig. 1. The focused light wave is transmitted from the high index SIL to the low index air by evanescent coupling. The spot size is governed by λ/NA_{eff}, where NA_{eff} is,

$$NA_{eff} = n_{SIL} \sin \theta_m \qquad \text{(1),}$$

---

* Correspondence: 520) 621-8263 Fax : 520) 621-4358, Email : joshjo@optics.arizona.edu for Joshua S. Jo
milster@ arizona.edu for Tom D. Milster

135

where n_{SIL} is the index of the SIL and θ_m is the marginal ray angle emitted from the exit pupil. From Eq. (1) it can be seen that the spot size decreases with increasing SIL index as well as increasing marginal ray angle.

According to diffraction theory, the focused electro-magnetic field can be represented as a linear summation of electro-magnetic plane waves emitted from the exit pupil. By definition, the focused electro-magnetic field is the *amplitude point spread function* (APSF) of the system. Therefore the APSF can be represented as a linear sum of plane waves. In this model the plane waves making up the APSF do not just interact with the air. The plane waves interact with the air, the SIL, the disk substrate and the thin film stack on the substrate, which are together considered as thin film structure. This thin film structure is called "the system". Therefore the plane waves reflect and transmit through the system according to Fresnel's equations in p- and s- directions. Thus the effects of polarization and thin films are considered.

The direction cosine Fourier transform of the APSF, including the effects of the system, is the *"illumination system transfer function"* (ISTF). Therefore the ISTF at the exit pupil includes characteristics of the thin film.[2] The phase of ISTF is affected by the air gap height. This is called the phase apodization, or gap-induced aberration, due to the change of the phase by the air gap height. It is one kind of the instrumental aberration discussed by Chipman.[3] Here we extensively include the effects of gap induced aberration, even into the total internal reflection(TIR) region. The amplitude of the ISTF is also affected by the thin film character. This effect is called amplitude apodization.

The gap-induced aberration is also explained by the plane waves interacting with thin film structure as shown in Fig. 2. The initial phase of plane wave, ϕ_1 changes phase ϕ_3. The phase difference $\Delta\phi = \phi_3 - \phi_1$ is the aberration introduced by gap height. It is dependent upon the polarization state, index of refraction of materials (n), and the gap height(h). Mathematically, the complex phase of the transmission coefficient explains the phase apodization as shown in Eq. (2).

$$ t = \frac{E_t}{E_i} = \frac{E_o{}' e^{i\phi_3}}{E_o e^{i\phi_1}} = t(\alpha, \beta, n_1, n_2, n_3, h) \tag{2} $$

where E_t is the transmitted field and E_i is the input field. The transmitted field coefficient, t is dependent upon polarization state and the index of refraction of each layer, gap height, wavelength, etc.

The gap-induced aberration exits in the angular spectrum of the ISTF, not on the image plane. Figure 3 (a) explains that the electric field at the image plane is expressed as the form of A(x, y, z) exp [i × Φ(x, y, z)]. Here, the phase distribution, Φ(x, y, z) is not a gap-induced aberration. In Fig. 3 (b), the electric field of the ISTF is expressed as A'(α, β, γ) exp [i × Φ'(α, β, γ)], where Φ'(α, β, γ) is the gap-induced aberration, because of its dependency on angular space variables. The image distribution is found by convolution of Fourier transform of A'(α, β, γ) and the Fourier transform of exp [i × Φ'(α, β, γ)].

3. Characteristics of apodization

3.1. Characteristics of amplitude apodization

Changes in the amplitude of the ISTF due to system variables are called amplitude apodization. Each profile of amplitude apodization in p- and s- direction is shown for h = 100nm and n = 2.38 in Fig. 4. P-(solid line) and s-profile(dashed line) is shown. Profiles of the amplitude apodization in s-direction are investigated versus index of refraction and air gap width. S-profiles are fitted into a convenient mathematical form, called the "supergaussian", to within maximum rms error of 1.6 %. The rms is the difference value between the original amplitude apodization and

the fitted one. The supergaussian is explicitly,

$$f(\alpha, \beta) = A\exp[-(\alpha, \beta)/R]^{2N},$$

(3)

where A is the amplitude, R is the width, N is the shape factor. For example $N = 1$ results in $f(\alpha, \beta)$ having a gaussian shape in the pupil. α and β, represent the direction cosines in p-direction and s-direction of the pupil, respectively. In our example, NA_{air} is 0.7. Figure 5 displays the relevant relationship between R and A. The index of refraction varies from 1.5 (glass) to 3.1(GaP). The gap height varies from 0 to 300nm. The value of A ranges from 0.1 to 0.6 as shown in Fig. 6(a). The value of A increases as h increases for a given n. For values of n equal to or greater than 2.4 A increases linearly as h increases. The value of R ranges from 0.55 to 0.4, as shown in Fig. 6(b). The value of R decreases as h increases for a given n. For values of n equal to or greater than 2.4 R decreases linearly as h increases. The value of N ranges from 1.4 to 2.3 , as shown in Fig. 6(c). The value of N increases non-linearly for n less than 2.4. For values of n equal to or greater than 2.4, N decreases. The rms values for fitting errors are displayed in Fig.6(d). The rms value of the amplitude apodization fitting is less than 1.6%.

However, supergaussian is not good function for p-profile of amplitude apodization, as shown in Fig. 4, It behaves differently from supergaussian form.

3.2. Characteristics of phase apodization

Two dimensional distribution of the gap-induced aberration is also investigated versus n and h. Like the amplitude data, each phase profile is also fitted to the supergaussian form within maximum rms error of 2 % of λ. Therefore, the shape of the gap-induced aberration is well characterized by a supergaussian over a wide range of n and h. The A value has range of 0.1 to 0.6λ in p-profile and 0.1 to 0.4λ in s-profile, as shown in Fig 7. The A value increases as n or h increases. The A value is larger in p-direction than in s-direction. R and N values are well characterized.[1]

4. Spot width(FW1/e²) and peak irradiance

Figure 8 shows spot width(FW1/e²) in p- and s-direction. Amplitude-only apodization effects are displayed by dashed line. Amplitude and phase apodization are showed by solid line. The phase apodization affects significantly spot size in p-direction as shown in Fig. 8(a). Phase apodization does not affect the spot size in s-direction seriously. Maximum spot width is 0.6μm in p-direction for amplitude-only apodization case. Maximum spot width is 1.1μm in p-direction for amplitude and phase apodization.

Figure 9 shows comparison of peak irradiance for a range of 1.5 to 2.38 of n. Amplitude-only apodization gains larger peak irradiance than amplitude and phase apodization. Amplitude and phase apodization degrade peak irradiance of amplitude-only apodization. Therefore, the phase apodization reduces the peak irradiance of amplitude-only apodization. The difference between peak irradiances decreases as n increases. For n equal to 2.38, there is small difference between peak irradiances.

5. Conclusion

The air gap induces the amplitude and phase apodization in SIL systems due to vector diffraction effect. Amplitude apodization in s-direction is well characterized in SIL systems in terms of magnitude, width, and shape factor. The phase apodization affect the spot width significantly in p-direction. It also reduces peak irradiance.

REFERENCES

1. Joshua S. Jo, Tom D. Milster, and Kevin Erwin, "Characteristics of gap-induced aberration in solid immersion lens systems," in Optical Data Storage. 2000.
2. T. D. Milster, J. S. Jo, K. Hirota, "Roles of Propagating and Evanescent Waves in Solid Immersion Lens Systems", vol. 38, No. 23, pp. 5046, Applied optics (1999).
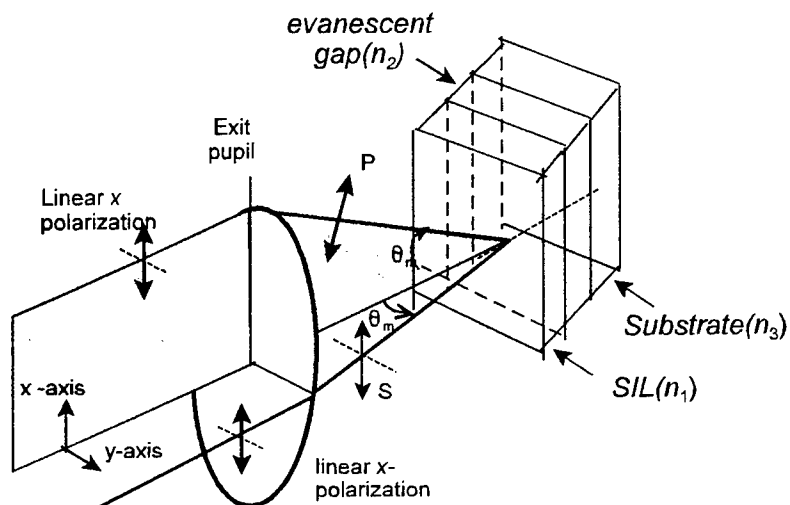3. R. A. Chipman, " Polarization aberrations", Ph.D. dissertation (University of Arizona, Tucson, Ariz., 1987).

Figure 1. A diagram of the system configuration. Collimated electro-magnetic waves are focused by a lens placed in the exit pupil. The focusing electro-magnetic waves propagate to the SIL, which focuses the light to form a spot. The focused electro-magnetic wave can be described by a linear summation of plane waves.
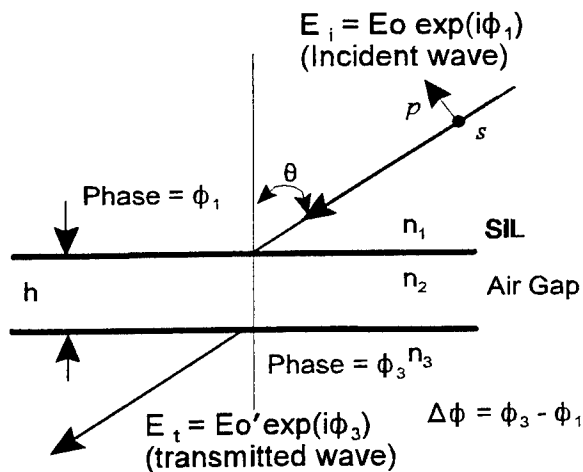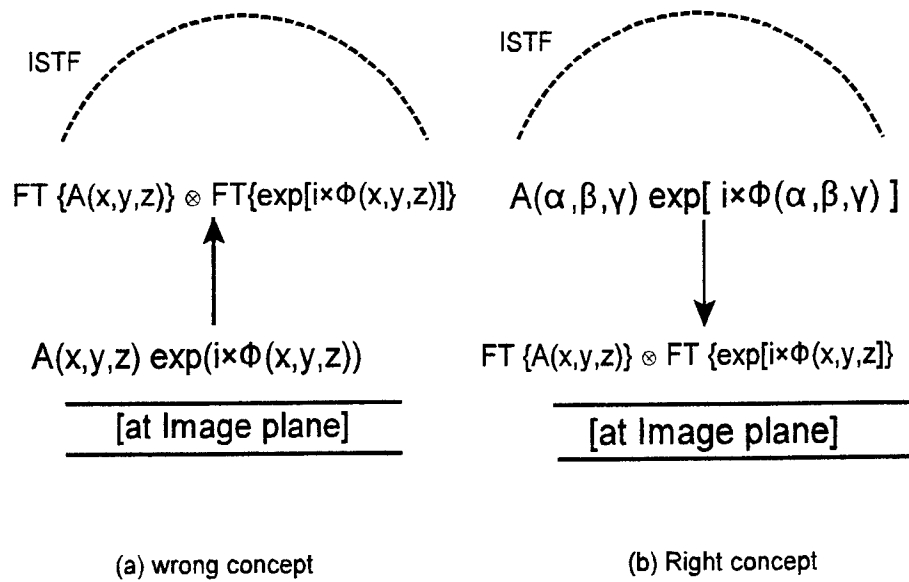

Figure 2. Explanation for the phase change

ISTF

$FT\{A(x,y,z)\} \otimes FT\{exp[i \times \Phi(x,y,z)]\}$

$A(\alpha,\beta,\gamma) \, exp[\, i \times \Phi(\alpha,\beta,\gamma)\,]$

$A(x,y,z) \, exp(i \times \Phi(x,y,z))$

$FT\{A(x,y,z)\} \otimes FT\{exp[i \times \Phi(x,y,z)]\}$

[at Image plane]

[at Image plane]

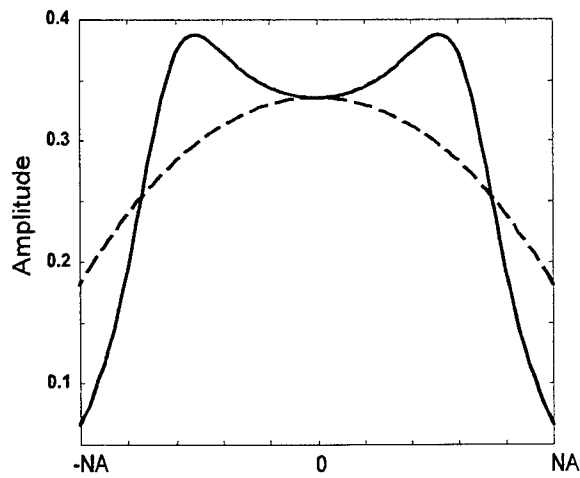(a) wrong concept

(b) Right concept

Figure 3. Right understanding for the gap-induced aberration

Figure 4. P-and s-profile of amplitude apodization in SIL system.
n1/n2/n3 = 2.38/1/2.38. NA (air) = 0.7. P-profile is represented by solid line. S-profile is represented by dashed line.
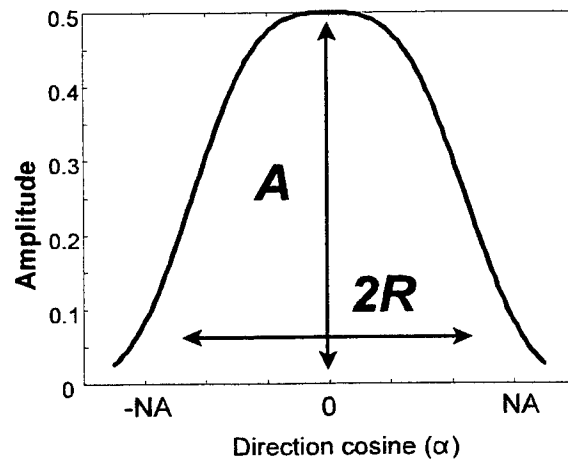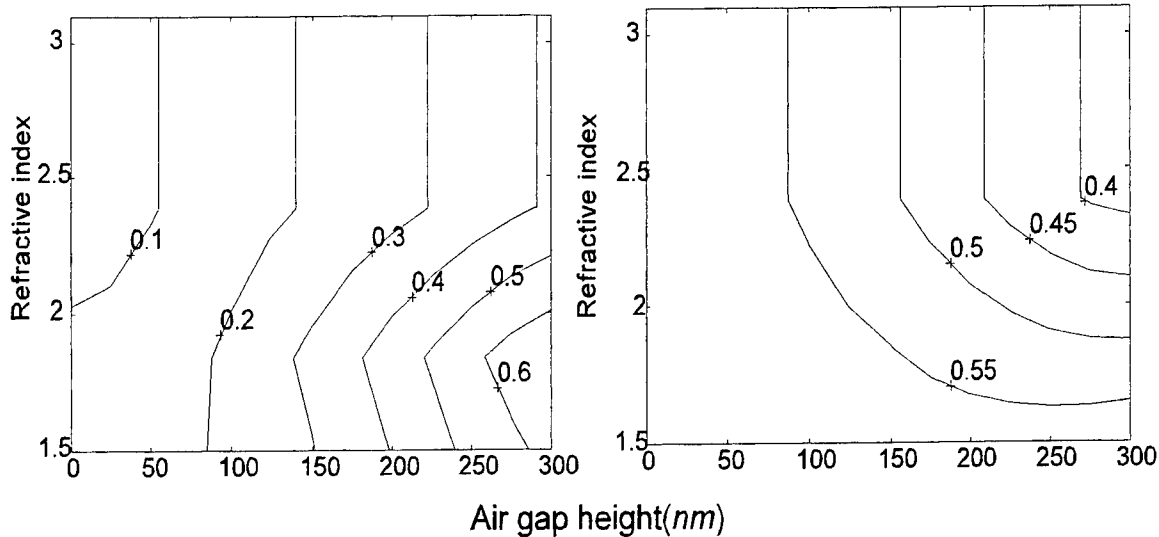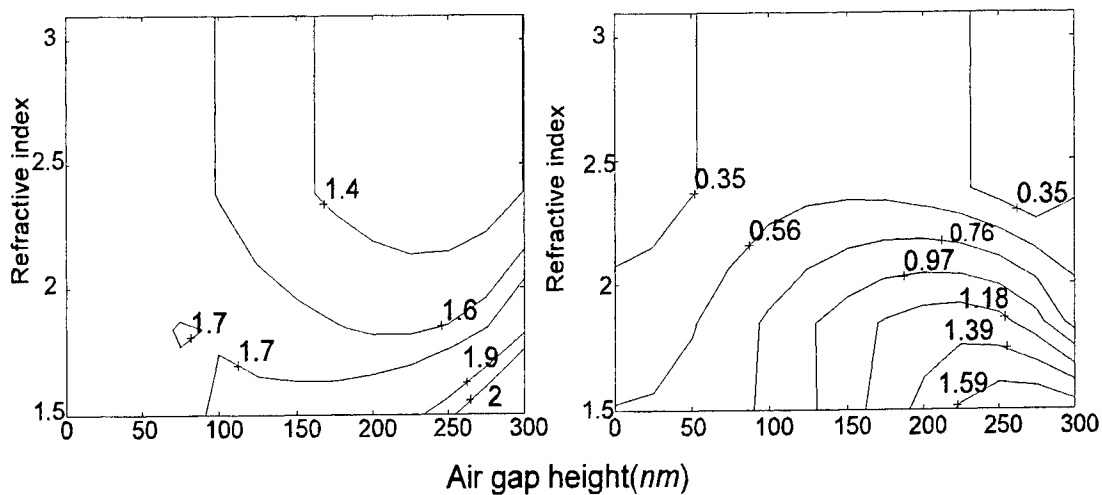

Figure 5. Supergaussian form. A represent amount of amplitude, R shows the width.

(a) The value of A vs n and h

(b) The value of R vs n and h

(c) N value vs n and h

(d) Rms value(%) vs n and h

Figure 6. (a) The value of A of amplitude apodization in s-direction vs n and h (b) the value of R of amplitude apodization in s-direction vs n and h. (c) The value of N of amplitude apodization in s-direction vs n and h (d) Rms value of amplitude apodization fitting errors in s-direction vs n and h
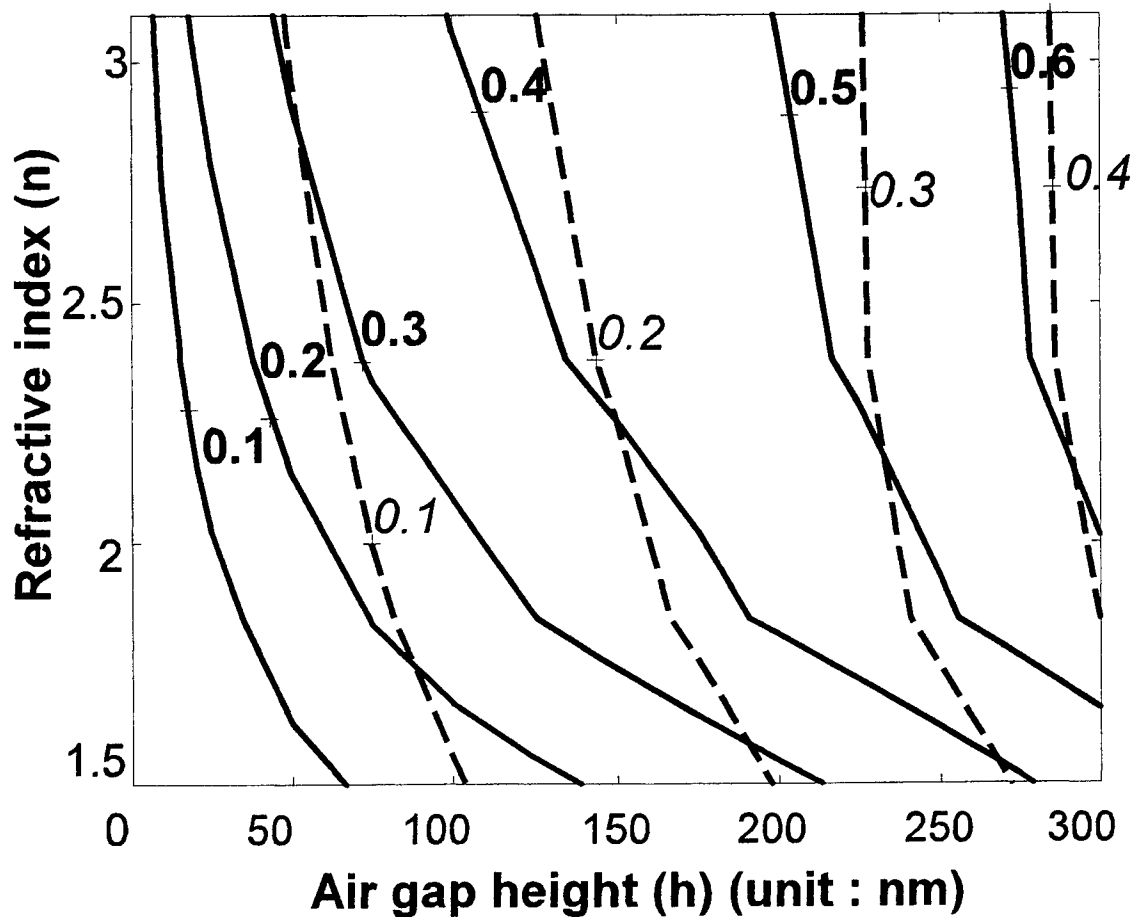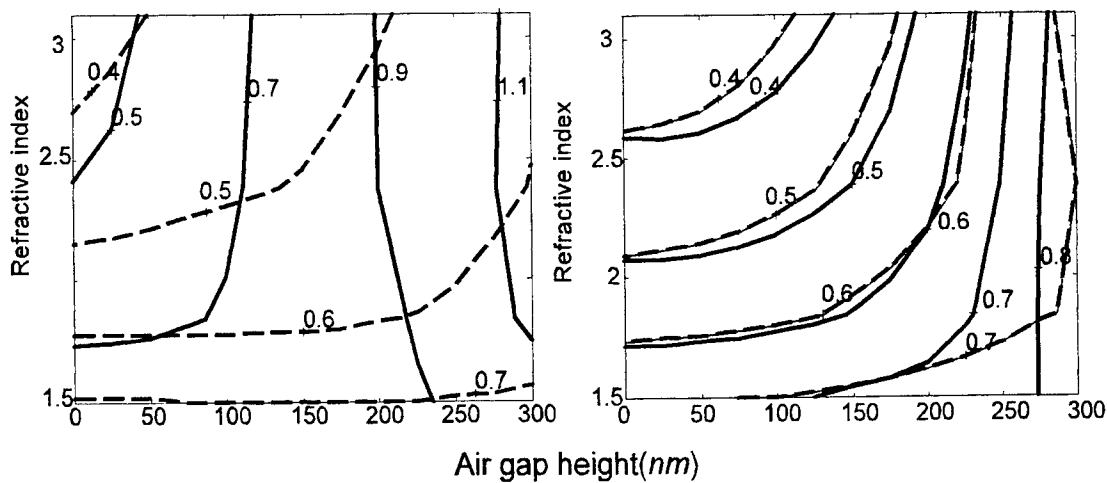
Figure 7. The A value of phase apodization vs n and h. Solid line represent p-direction, while dashed line does s-direction in the pupil

(a) Spot width(μm) in p-direction vs n and h.

(b) spot width(μm) in s-direction vs n and h.

Figure 8. (a) Spot width in p-direction vs n and h. (b) Spot width in s-direction vs n and h. Solid line represent the both amplitude and phase apodization case. Dashed line represent amplitude-only apodization.
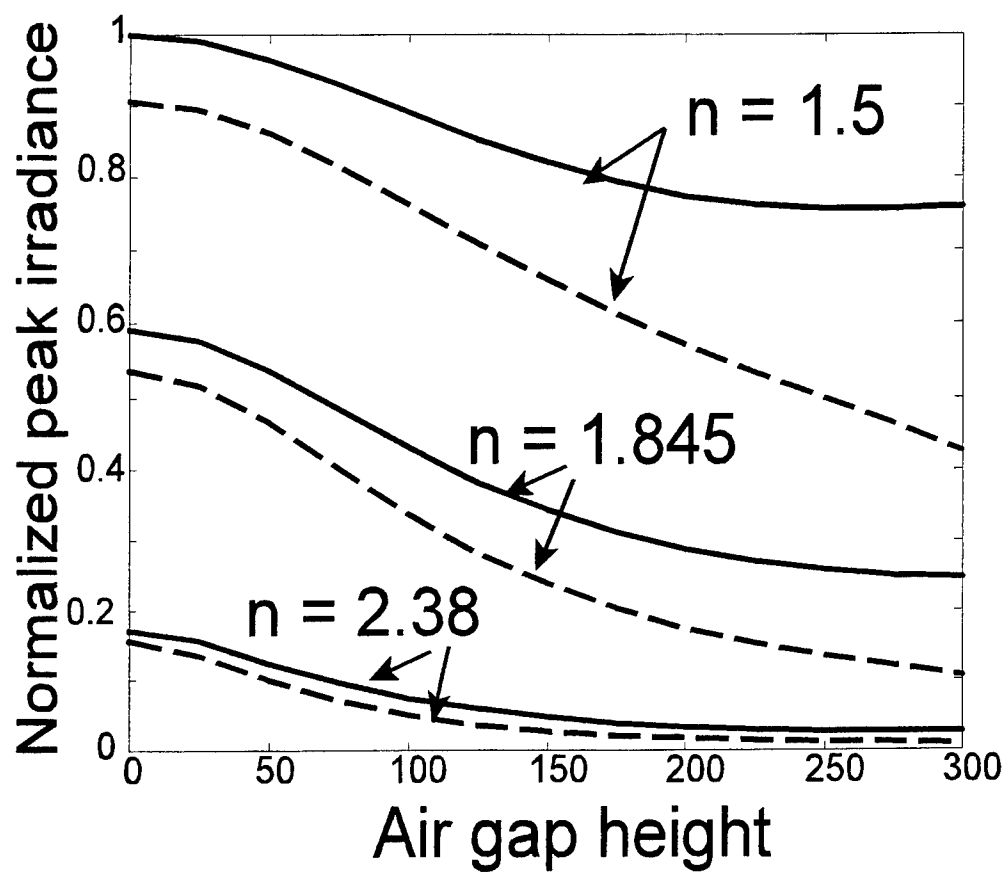
Figure 9. Comparison of peak irradiance for a range of 1.5 to 2.38 of n. Solid line represent peak irradiance for amplitude-only apodization. Dashed line represent peak irradiance for amplitude and phase apodization.

Exit Pupil Patterns from Optical Disks

Robert S. Upton and Tom D. Milster

Optical Sciences Center, University of Arizona, Tucson, AZ, USA, 85721

ABSTRACT

The modulation of the irradiance in the exit pupil of an optical data storage scanning system is described by analyzing the behavior of scan-dependent interference fringes. These fringes are grouped into three independent irradiance components. The variation of the exit pupil irradiance pattern as a function of groove depth is discussed.

Keywords: Diffraction, Interference, Pupil Irradiance Modulation, Scanning Optical Microscope

1. INTRODUCTION

Optical data storage scanning systems are a sub-class of optical microscopes that use a coherent laser source. The laser light is focused onto semi-periodic marks recorded on the data layer of a rotating optical disk. The semi-periodic property of the marks the marks to be well represented by a Fourier series. The laser light field scattered from the optical disk is collected by a high numerical aperture (high-NA) collection lens. The electronic readout signal is generated by a detector placed in the exit pupil. In this paper, the effects of the phase depth of the pre-grooves on the disk on the exit pupil irradiance modulation are discussed. The exit pupil irradiance modulation with varying groove depth is simulated using Optiscan,[1] which is a Matlab[2] based diffraction code.

Section 2.1 presents a high-NA scalar diffraction model that is used to describe the propgation of the light fields from the optical disk to the exit pupil.[3] Section 2.2 also presents a technique that describes the reflected light field from the optical disk as a linear summation of component disk fields by Babinet's principle.[4] Section 3 presents the simulation parameters and optical disk model used in the computer simulations. Section 4 presents the simulated exit pupil irradiance modulations.

2. DIFFRACTION MODEL

In this section a high-NA scalar diffraction theory is outlined and the linear decomposition of the light field reflected from the optical disk is discussed.

2.1. High NA Scalar Diffraction Theory

Figure 1 shows a simplified layout of the optical data storage scanning system. Light from the laser source is collimated and then focused onto the optical disk where it interacts with the data marks. The data marks scatter the incident laser light, which is collected by the collection lens. The scanning system can be represented by the illumination pupil, disk and collection pupil, as shown in Fig. 1(b).

The light field in the illumination pupil is denoted by $\tilde{O}_{ILL}(\alpha, \beta)$. α and β are direction cosines, which are also the coordinates of the pupils. The focused light field on the optical disk is denoted by $O_{DISK}(\hat{x}, \hat{y})$. $\hat{x}$ and $\hat{y}$ are wavelength-normalized spatial variables. The relationship between the direction cosines and the wavelength-normalized variables is described by a propagating plane wave,

$$U(\hat{x}, \hat{y}) = A(\hat{x}, \hat{y}) \exp[2\pi i(\hat{x}\alpha + \hat{y}\beta)]. \tag{1}$$

α and β are also Fourier transform conjugate[5,6] variables with $\hat{x}$ and $\hat{y}$, respectively.

The relationship between $\tilde{O}_{ILL}(\alpha, \beta)$ and $O_{DISK}(\hat{x}, \hat{y})$ is,

$$O_{DISK}(\hat{x}, \hat{y}) = \exp\left[-\pi i \left(\frac{\hat{x}^2 + \hat{y}^2}{\hat{r}}\right)\right] \int_{\infty}^{\infty} \int_{\infty}^{\infty} \tilde{O}_{ILL}(\alpha, \beta) \frac{\hat{r} \exp(-i2\pi\hat{r})}{i\gamma} \exp[2\pi i(\alpha\hat{x} + \beta\hat{y})] d\alpha d\beta, \tag{2}$$

Further author information: (Send correspondence to Tom D. Milster)
Robert S. Upton: E-mail: rsupton@u.arizona.edu
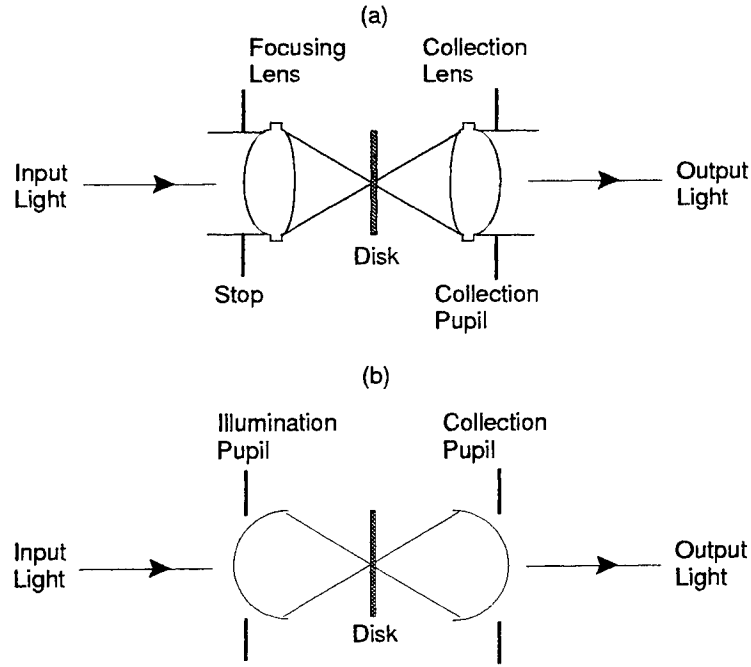Tom D. Milster: E-mail: milster@arizona.edu

In *Optical Storage and Optical Information Processing*, Han-Ping D. Shieh, Tom D. Milster, Editors, Proceedings of SPIE Vol. 4081 (2000) • 0277-786X/00/$15.00

143

Figure 1. A schematic showing the geometry of an optical data storage scanning system. (a) The optical data storage scanning system is shown unfolded. (b) The scanning system can be represented as an illumination pupil, optical disk and collection pupil. The fields in the pupils reside on a surface called the reference sphere. The radius of the reference sphere in the illumination pupil equal to the radius of the focusing light field and the radius of the reference sphere in the collection pupil equal to the radius of the diffracted light field.

where $\hat{r}$ is the wavelength-normalized radius of the illumination pupil illustrated in Fig 1(b).

$O_{DISK}(\hat{x}, \hat{y})$ is modified upon reflection by the data marks, which are represented by the mark reflectivity function $C_R(\hat{x}, \hat{y})$. The field reflected from the disk is,

$$U_{DISK} = C_R(\hat{x}, \hat{y})O_{DISK}(\hat{x}, \hat{y}). \tag{3}$$

The form of the reflected field in the collection pupil, $\tilde{O}_{COLL}(\alpha, \beta)$ is,

$$\tilde{O}_{COLL}(\alpha, \beta) = \int_{\infty}^{\infty} \int_{\infty}^{\infty} U_{DISK}(\hat{x}, \hat{y}) \left[\frac{i\gamma \exp(i2\pi\hat{r})}{\hat{r}} \exp\left[\pi i \left(\frac{\hat{x}^2 + \hat{y}^2}{\hat{r}}\right)\right] \right] \exp[-2\pi i(\alpha\hat{x} + \beta\hat{y})]d\alpha d\beta. \tag{4}$$

Substitution of Eq. (4) into Eq. (2) and use of the convolution theorem for Fourier transforms[7] results in a simple analytical expression for $\tilde{O}_{COLL}(\alpha, \beta)$, which is,

$$\tilde{O}_{COLL}(\alpha, \beta) = \int_{\infty}^{\infty} \int_{\infty}^{\infty} \tilde{O}_{ILL}(\alpha', \beta')\tilde{C}_R(\alpha - \alpha', \beta - \beta')d\alpha' d\beta'. \tag{5}$$

$\tilde{C}_R(\alpha, \beta)$ is the Fourier transform of the mark reflectivity function. Therefore, the field in the collection pupil is the two-dimensional convolution between the Fourier transform of the disk reflectivity function and the field in the illumination pupil.

The irradiance in the collection pupil, $\tilde{E}_{COLL}(\alpha, \beta)$ is

$$\tilde{E}_{COLL}(\alpha, \beta) = \tilde{O}_{COLL}(\alpha', \beta')^* \tilde{O}_{COLL}(\alpha, \beta). \tag{6}$$

2.2. Linear Decomposition of the Optical Disk Light Field

This section is a mathematical description of the exit pupil irradiance modulation using the scalar diffraction model developed in section 2.1.
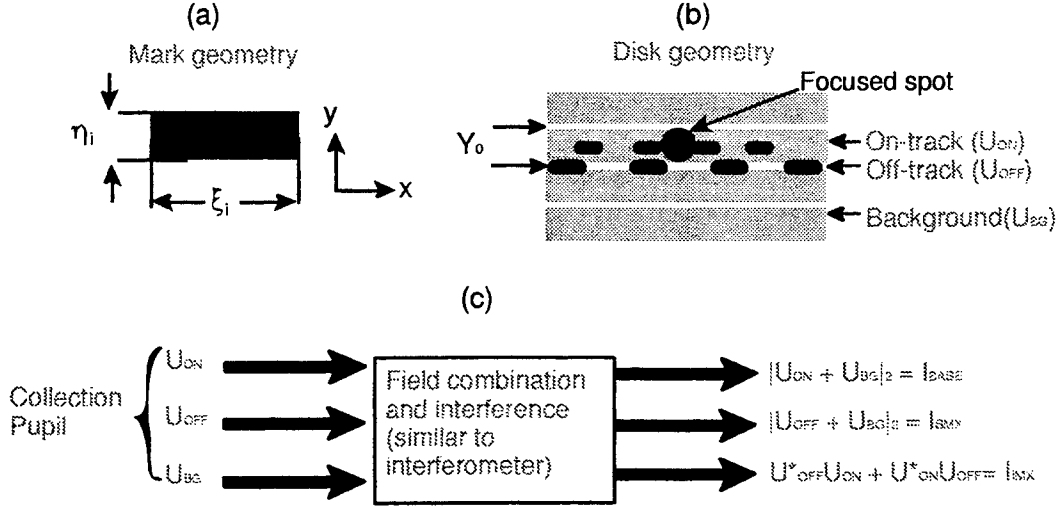

Figure 2. A schematic showing the disk model used in the formation of the exit pupil irradiance. (a) The mark geometry and shape simulated. ξ_i and η_i are the length and width of the data mark on the i'th data track. (b) The disk geometry and disk component fields for on-track, U_{ON}, off-track, U_{OFF}, and background, U_{BG}, are shown. (c) The fields in the pupil combine and form the pupil irradiance. The total pupil irradiance is decomposed into three signal groups. The first group is BASE, which is the combination of U_{ON} and U_{BG}. The second signal group is SMX, which is the combination of U_{OFF} and U_{BG}. The third group is IMX, which the interference between U_{ON} and U_{OFF}.

In this section the total field reflected from the disk, $U_{DISK}(\hat{x},\hat{y})$, is re-expressed as a linear combination of disk component fields by use of Babinet's principle.[4,8] The disk component fields are also known as the Babinet fields. Figure 2 is a schematic of the disk model used in the description of the diffraction from the optical disk to the collection pupil. The total field reflected from the optical disk is rewritten as,

$$U_{DISK}(\hat{x},\hat{y}) = [r_L u_{BG}(\hat{x},\hat{y}) + (r_M - r_L)u_{ON}(\hat{x},\hat{y}) + \exp(i\phi_G)(r_M - r_L)u_{OFF}(\hat{x},\hat{y})]\, O_{DISK}(\hat{x},\hat{y}). \tag{7}$$

$|r_L|$ is the scalar reflectivity of the disk without data marks, $|r_M|$ is the scalar reflectivity of the data marks and ϕ_G is the phase depth of the pre-grooves on the disk. ϕ_G is related to the physical groove depth d by,

$$\phi_G = \frac{4\pi d}{\lambda}, \tag{8}$$

where λ is the vacuum wavelength of the light source. The off-track data marks are located in a groove, therefore the phase of $u_{OFF}(\hat{x},\hat{y})$ is modified by ϕ_G.

One of the properties of optical data storage scanning systems are semi-periodic data marks. The semi-periodic property of the data marks allows the Babinet fields, $u_{ON}(\hat{x},\hat{y})$, $u_{OFF}(\hat{x},\hat{y})$ and $u_{BG}(\hat{x},\hat{y})$, to be expressed as a Fourier series.[5,9,7] Therefore, using the parameters defined in Fig. 2(a) and (b), $u_{ON}(\hat{x},\hat{y})$, $u_{OFF}(\hat{x},\hat{y})$ and $u_{BG}(\hat{x},\hat{y})$ are

$$u_{ON}(\hat{x},\hat{y}) = f_1(\hat{y}) \sum_{m=-M}^{M} R_m \exp\left[-2\pi i m \left(\frac{\hat{x}_0 - \hat{x}}{T_1}\right)\right] \star \delta(\hat{y}), \tag{9}$$

145

$$u_{OFF}(\hat{x}, \hat{y}) = f_2(\hat{y}) \sum_{m=-M}^{M} S_m \exp[-2\pi i m \left(\frac{\hat{x}_0' - \hat{x}}{T_2} \right)] \star \delta(\hat{y} - \hat{Y}_0), \tag{10}$$

$$u_{BG}(\hat{x}, \hat{y}) = \sum_{n=-N}^{N} A_n \exp[2\pi i n \left(\frac{\hat{y}}{Y_0} \right)]. \tag{11}$$

In our analysis, the data marks are separable functions of x and y, which allows the pupil fields associated with the marks to be represented as separable functions of α and β. The delta functions $\delta(\hat{y})$ and $\delta(\hat{y} - \hat{y}_0)$ in Eqs. 9 and 10 locate the y center of the data tracks. Therefore u_{ON} and u_{OFF} have their y centers located at $y = 0$ and $y = y_0$, respectively. The functions $f_1(\hat{y})$ and $f_2(\hat{y})$ describe the variation of $u_{ON}(\hat{x}, \hat{y})$ and $u_{OFF}(\hat{x}, \hat{y})$ along the y direction. The $\star$ describes a one dimensional convolution operation. R_m, S_m and A_n are the Fourier weighting coefficients. The coefficients are dependent upon the mark shape and size.

The corresponding Babinet fields in the collection pupil are calculated by taking the Fourier transforms of Eqs. 9, 10 and 11, and then applying Eq. 5. The result is,

$$\tilde{O}_{ON}(\alpha, \beta) = \sum_{m=-M}^{M} R_m \exp[-2\pi i m \left(\frac{\hat{x}_0}{T_1} \right)][F_1(\beta) \star \tilde{O}_{ILL}(\alpha - \frac{m}{T_1}, \beta)], \tag{12}$$

$$\tilde{O}_{OFF}(\alpha, \beta) = \sum_{m=-M}^{M} S_m \exp[-2\pi i m \left(\frac{\hat{x}_0' - \hat{x}}{T_2} \right)][F_2(\beta) \exp(-2\pi i \beta \hat{y}_0) \star \tilde{O}_{ILL}(\alpha - \frac{m}{T_1}, \beta)], \tag{13}$$

$$\tilde{O}_{BG}(\alpha, \beta) = \tilde{O}_{ILL}(\alpha, \beta) + [\exp(i\phi_G) - 1] \sum_{n=-N}^{N} A_n \tilde{O}_{ILL}(\alpha, \beta - \frac{n}{\hat{y}_0}). \tag{14}$$

$\tilde{O}_{OFF}(\alpha, \beta)$ in Eq. 13 contains a linear phase in the beta direction of the pupil due to the off-set of $u_{OFF}(\hat{x}, \hat{y})$ from the on-track. The functions $F_1(\beta)$ and $F_2(\beta)$ are Fourier transforms of the functions $f_1(\hat{y})$ and $f_2(\hat{y})$, respectively. The one-dimensional convolution functions in Eqs. 12 and 13 can be represented as a single function, κ_m,

$$[F_1(\beta) \star \tilde{O}_{ILL}(\alpha - \frac{m}{\hat{T}_1}, \beta)] = \kappa_m(\beta, 0) \tag{15}$$

$$[F_2(\beta) \exp(-2\pi i \beta \hat{y}_0) \star \tilde{O}_{ILL}(\alpha - \frac{m}{\hat{T}_1}, \beta)] = \kappa_m(\beta, \hat{y}_0). \tag{16}$$

$\kappa_m(\beta, \hat{y}_0)$ is a complex number and $\kappa_m(\beta, 0)$ corresponds to the case $\hat{y}_0 = 0$. Figure 3 shows the amplitude and phase variation of κ_m along the β direction of the pupil for the on-track case and the off-track case. In Fig. 3(a) the amplitude of the off-track field in the pupil is smaller than the on-track amplitude as a consequence of the linear phase component of $\kappa_m(\beta, \hat{y}_0)$ in Eq. 16. In Fig. 3(b) the linear phase in Eq. 16 results in a linearly varying phase along the β direction for the off-track scanning case. From Eqs. 12, 13 and 14 the Babinet fields in the pupil are distributed into a summation of diffraction orders. The diffraction orders in Eqs. 12 and 13 are distributed in the α direction, which is in the scan-direction of the pupil. This distribution occurs because $u_{ON}(\alpha, \beta)$ and $u_{OFF}(\alpha, \beta)$ are arranged in the scan direction of the disk. This distribution is illustrated in Fig. 4.

The total field in the collection pupil, $\tilde{O}_{COLL}$ is written as,

$$\tilde{O}_{COLL} = r_L \tilde{O}_{BG} + (r_M - r_L) \exp(i\phi_G) \tilde{O}_{ON} + (r_M - r_L) \tilde{O}_{OFF}. \tag{17}$$

The irradiance in the pupil is calculated by means of Eq. 6. The irradiance in the pupil is described by a summation of interference fringes, some of which modulate the irradiance pattern as the marks are scanned. The modulating fringes in the pupil are grouped into the three signal groups, $E_{BASE}(\alpha, \beta; \hat{x}_0)$, $E_{SMX}(\alpha, \beta; \hat{x}_0)$ and $E_{IMX}(\alpha, \beta; \hat{x}_0)$, as described in Fig. 2. The explicit form of the BASE signal group is,

$$E_{BASE}(\alpha, \beta; \hat{x}_0) = 2\Delta r^2 \sum_m R_m^2 |\kappa(\beta; 0)|^2 \left[\cos \left(2\pi m \frac{\hat{x}_0}{\hat{T}_1} \right) + \sin \left(2\pi m \frac{\hat{x}_0}{\hat{T}_1} \right) \right] \tag{18}$$

$$+ 2r_L \Delta r \sum_m R_m \kappa_m(\beta; 0) \tilde{O}_{ILL}(\alpha, \beta) \cos \left(2\pi m \frac{\hat{x}_0}{\hat{T}_1} \right)$$

$$+ 2r_L \Delta r \sum_m \sum_n R_m A_n \kappa_m(\beta; 0) \left[\cos \left(2\pi m \frac{\hat{x}_0}{\hat{T}_1} + \phi_G \right) - \cos \left(2\pi m \frac{\hat{x}_0}{\hat{T}_1} \right) \right] \tilde{O}_{ILL}(\alpha, \beta - \frac{n}{\hat{y}_0}).$$
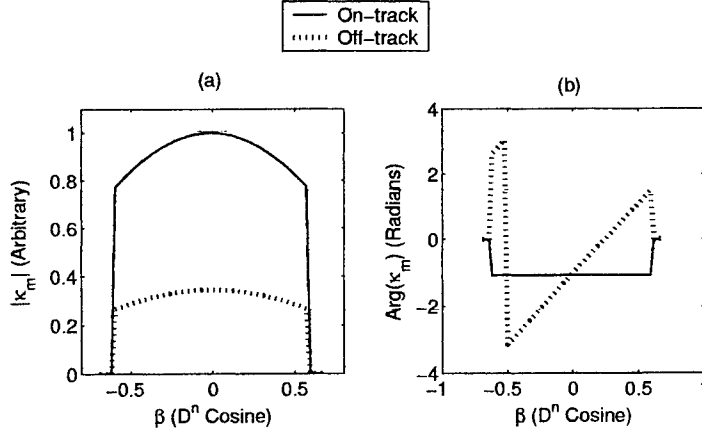
Figure 3. The variation of the **(a)** amplitude and **(b)** phase of the one-dimensional convolution along β for on-track and off-track scanning that is represented by $|\kappa_m|$ and $Arg(\kappa_m)$, respectively.
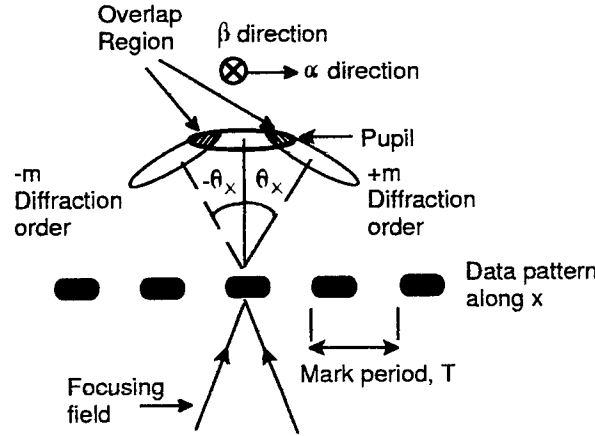

Figure 4. For periodic marks arranged along the x direction of the disk the diffraction orders are arranged along α in the pupil. The modulation of the irradiance in the pupil occurs in the overlap regions between the different scan-track higher diffraction orders ($\tilde{O}_{ON}$ and $\tilde{O}_{OFF}$), and the diffraction orders of $\tilde{O}_{BG}(\alpha, \beta)$.

$E_{BASE}(\alpha, \beta; \hat{x}_0)$ consists of three distinct sets of interference fringes. The first set is the interference of the higher m on-track diffraction orders. The phase of the modulation of this fringe has cos and sin components, which are in quadrature with respect to each other.

The explicit form of the SMX signal group is,

$$
\begin{aligned}
E_{SMX}(\alpha, \beta; \hat{x}_0) \;=\; & 2\Delta r^2 \sum_m S_m^2 |\kappa(\beta; \hat{y}_0)|^2 \left[\cos\left(2\pi m \frac{\hat{x}_0'}{\hat{T}_2} + Arg(\kappa_m) \right) + \sin\left(2\pi m \frac{\hat{x}_0'}{\hat{T}_2} + Arg(\kappa_m) \right) \right] \quad (19) \\
+ \; & 2r_L \Delta r \sum_m S_m \kappa_m(\beta; \hat{y}_0) \tilde{O}_{ILL}(\alpha, \beta) \cos\left(2\pi m \frac{\hat{x}_0'}{\hat{T}_2} + Arg(\kappa_m) - \phi_G \right) \\
+ \; & 2r_L \Delta r \sum_m \sum_n S_m A_n \kappa_m(\beta; \hat{y}_0) \cos\left(2\pi m \frac{\hat{x}_0'}{\hat{T}_2} + Arg(\kappa_m) \right) \tilde{O}_{ILL}(\alpha, \beta - \frac{n}{\hat{y}_0})
\end{aligned}
$$

$$- \quad 2r_L \Delta r \sum_m \sum_n S_m A_n \kappa_m(\beta; \hat{y}_0) \cos\left(2\pi m \frac{\hat{x}_0'}{\hat{T}_2} + Arg(\kappa_m) - \phi_G\right) \tilde{O}_{ILL}\left(\alpha, \beta - \frac{n}{\hat{y}_0}\right).$$

Like $E_{BASE}(\alpha, \beta, \hat{x}_0)$, $E_{SMX}(\alpha, \beta, \hat{x}_0)$ has three distinct sets of interference fringes. The first set is a result of the interference between the off-track pupil fields. From Fig.3(b) $Arg(\kappa_m)$ is a linearly varying phase function with respect to β. $Arg(\kappa) < 0$ for $-NA < \beta < 0$ and $Arg(\kappa) > 0$ for $0 < \beta < NA$. The effect of $Arg(\kappa_m)$ combined with the scan phase, $2\pi m \hat{x}_0/T_2$, is described with the aid of Fig. 5. The phases in the four quadrants are,

$$\phi_A \quad = \quad Arg(\kappa_m) - 2\pi m \frac{\hat{x}_0}{\hat{T}_2}, \tag{20}$$

$$\phi_B \quad = \quad -Arg(\kappa_m) - 2\pi m \frac{\hat{x}_0}{\hat{T}_2}, \tag{21}$$

$$\phi_C \quad = \quad -Arg(\kappa_m) + 2\pi m \frac{\hat{x}_0}{\hat{T}_2}, \tag{22}$$

$$\phi_D \quad = \quad Arg(\kappa_m) + 2\pi m \frac{\hat{x}_0}{\hat{T}_2}. \tag{23}$$

Taking the cos and sin values of the phases describes the modulation between the four quadrants that is rotational. The modulation of the remaining sets of fringes is also rotational due to a similar phase variation between the four quadrants. The presence of ϕ_G in the phases of these fringes results in a shift of these fringes along the β direction of the pupil. The shift of these fringes affects the overall rotation modulation of $E_{SMX}(\alpha, \beta, \hat{x}_0)$ in the pupil. This is further described in sections 4.2 and 4.3. The rotational characteristic of the exit pupil irradiance as off-track marks are scanned is the basis of segmented pupil detection schemes for tracking[10] and crosstalk cancellation[11,12] in optical data storage. The rotation of the exit pupil irradiance for off-track scanning can be quantified by quadrant pupil detection,[10,11] in which the detector in the exit pupil is divided into quadrants, as in Fig. 5. Taking the sums of the integrated irradiance along the two diagonals and then taking their difference results in the QPD signal $i_{QPD}(t)$. Mathematically this is
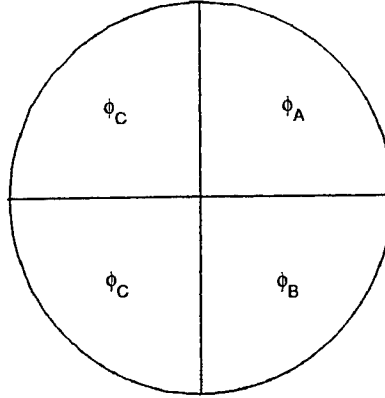
$$i_{QPD} = i_A + i_C - i_B - i_D. \tag{24}$$

Figure 5. The modulation of $E_{SMX}(\alpha, \beta, \hat{x}_0)$ in the pupil can be described by considering the phase of the cos and sin modulation in four quadrants of the pupil. The phases of the modulations in the four quadrants is denoted by ϕ_A, ϕ_B, ϕ_C and ϕ_D, respectively. The rotational modulation of $E_{SMX}(\alpha, \beta, \hat{x}_0)$ is quantified by the quadrant pupil detection signal, which is $i_{QPD} = i_A + i_C - i_B - i_D$.

The form of the $E_{IMX}(\alpha, \beta, \hat{x}_0)$ is,

$$E_{IMX}(\alpha, \beta; t) = 2\Delta r^2 \sum_m R_m S_m |\kappa_m(\beta; 0)\kappa_m(\beta; \hat{y}_0)| \cos\left[2\pi m \left(\frac{\hat{x}_0'}{\hat{T}_2} - \frac{\hat{x}_0}{\hat{T}_1}\right) - Arg(\kappa_m) - \phi_G\right]. \tag{25}$$

$E_{IMX}(\alpha, \beta, \hat{x}_0)$ consists of a single set of fringes. As with $E_{SMX}(\alpha, \beta, \hat{x}_0)$ in Eq. 19 the IMX interference fringe has rotational characteristics due to the linear property of $Arg(\kappa_m)$ in the phase of the fringe modulation. The presence of ϕ_G in the interference fringe causes the IMX fringe to be shifted in the pupil for different groove depths.

3. DISK MODEL AND SIMULATION PARAMETERS

Table 1 lists the simulation parameters for the quantities described in Fig. 2. The simulation parameters also include the the disk reflectivities and the variation of groove depth. These parameters are programed in Optiscan and the signal groups are calculated according to the linear decomposition model developed in section 2.2.

Table 1. The simulation parameters for the disk model. The quantities listed refer to the parameters given in Fig 2.

λ	$0.65\mu m$
NA	0.6
y_0	$0.5\mu m$
Groove Depths	0, $\lambda/40$, $\lambda/20$ $3\lambda/40$, $\lambda/10$, $\lambda/8$, $6\lambda/40$, $7\lambda/40$, $\lambda/5$, $9\lambda/40$, $\lambda/4$
η	$0.4\mu m$
ξ_1	$1.08\mu m$
ξ_2	$1.08\mu m$
r_M	0.006
r_L	0.2

4. THE IRRADIANCE MODULATION IN THE COLLECTION PUPIL

This section presents simulated exit pupil irradiance modulation results. The results are separated into three sections containing the BASE, SMX and IMX pupil irradiances, respectively. The pupil irradiances for each signal group are shown for the four scan locations, I, II, III, IV, which are shown in Fig. 6.
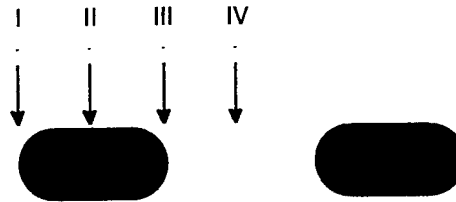

Figure 6. The scan locations, I, II, III, IV on the disk corresponding to the pupil irradiances shown in sections 4.1, 4.2 and 4.3.

4.1. The On-track Data Irradiance Modulation (BASE)

Figure 7 shows the the on-track scanning pupil irradiances for for the scan positions and groove depths indicated. The diffraction orders introduced by the grooved background are clearly seen lying along the β direction of the pupil for groove depths greater than zero.

The modulation of the fringes is along the α direction of the pupil. The data marks being scanned lie along the x direction of the disk, introducing the higher on-track diffraction orders in the α direction of the pupil, which is illustrated in Fig. 4. The modulation along α occurs from the overlap of the higher on-track diffraction orders with the on-track zero'th order and background fields. The symmetry of the fringe modulation along α is determined by

the groove depth. This can be seen from the variation of the pupil irradiance patterns for changing groove depths for scan position I. The effect of groove depth on the pupil irradiances leads to the conclusion that the modulating fringe that contains the phase of the groove in the cosine dominates the BASE signal group modulation for groove depths greater than zero. The fringe in question is described by the third term in Eq. 18, which is,

$$2r_L \Delta r \sum_m \sum_n R_m A_n \kappa_m(\beta; 0) \left[\cos\left(2\pi m \frac{\hat{x}_0}{\hat{T}_1} + \phi_G\right) - \cos\left(2\pi m \frac{\hat{x}_0}{\hat{T}_1}\right) \right] \tilde{O}_{ILL}\left(\alpha, \beta - \frac{n}{\hat{y}_0}\right). \qquad (26)$$
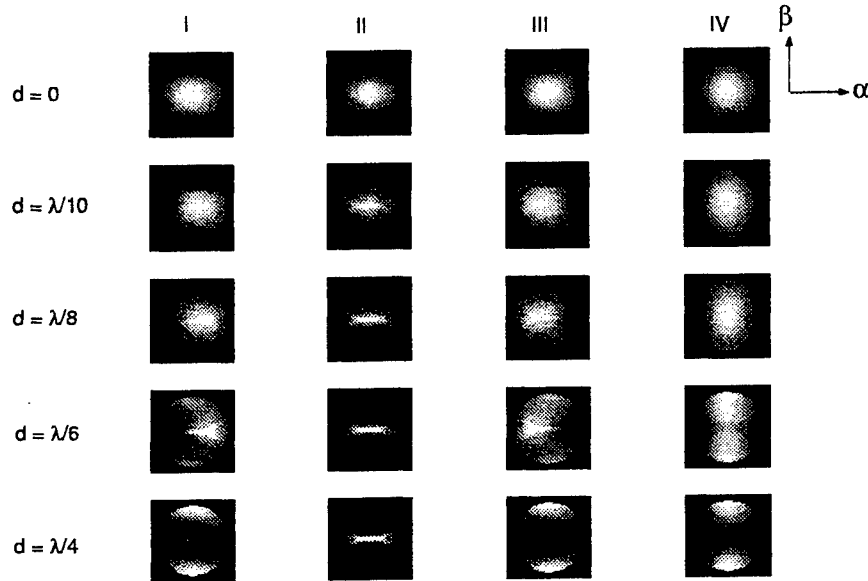

Figure 7. The pupil irradiance modulation for the BASE signal group. The pupil patterns are arranged for the groove depths indicated in rows and in columns for the scan positions I, II, III and IV. The bright portions of the pupil are positive contributions to the pupil irradiance and the dark portions are zero.

The form of Eq. 26 can be used to predict the symmetry of the fringe movement along the α direction of the pupil. Fig. 8 is a cosine function describing the BASE irradiance modulation between the $\alpha > 0$ and $\alpha < 0$ portions of the pupil. For $\phi_G = 0$, which corresponds to position A on the cosine function in Fig. 8, the modulation of the fringe in the pupil, described by Eq. 26, is the same for $\alpha > 0$ and $\alpha < 0$. For $\lambda/8$ groove depth, which corresponds to position B on the cosine function, the modulation of the fringe in the pupil for $\alpha > 0$ has opposite phase to the modulation of the fringe in the $\alpha < 0$ portion of the pupil. Therefore, according to Eq. 26 the difference of the integrated irradiance between the $\alpha > 0$ portion and the $\alpha < 0$ portion is a maximum for groove depth of $\lambda/8$. This is confirmed by the results of the computer simulation, as shown in Fig. 9.

4.2. The Off-track Data Irradiance Modulation (SMX)

Figure 10 shows the off-track scanning pupil irradiances for the groove depths and scan locations indicated. The scan locations, I, II, III and IV are shown in Fig. 6. The bright portions of the pupil are positive contributions to the irradiance and the dark portions are zero. The modulation of the irradiance in the pupil is highly dependent upon groove depth. This is seen from the plots in Fig. 11(a) and (b).

All the modulating fringes in Eq. 19 rotate as the off-track data marks on the disk are scanned. For the groove depth of zero the modulation of the irradiance is determined by one set of fringes, which is highly rotational, as can be seen by the large QPD amplitude in Fig. 11(a). By introducing a grooved substrate, more interference fringes are introduced into the pupil. This effect is seen from Eq. 19. Each of the fringes has a rotational modulation in the pupil, but the groove dependent fringes are shifted in the pupil by an amount that is determined by the value of ϕ_G.
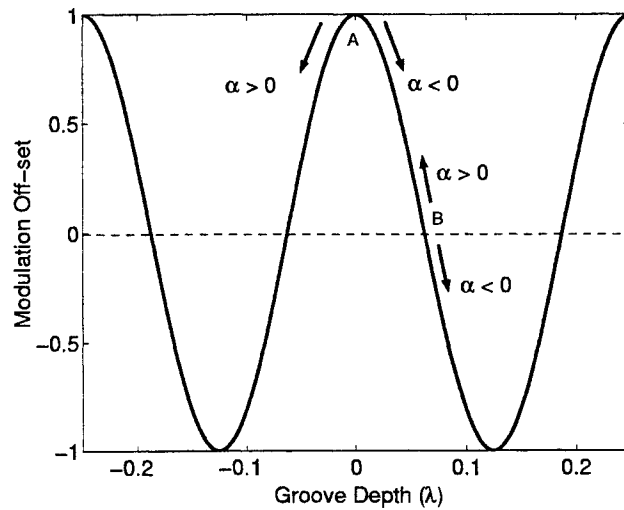
Figure 8. The modulation of the BASE signal group fringe can be described by considering the fringe modulation off-set values, which are dependent upon the groove depth. Positions A and B on the cosine function correspond to groove depths 0 and $\lambda/8$, respectively. The arrows correspond to modulation of the fringe for the $\alpha > 0$ and $\alpha < 0$ portions of the pupil.
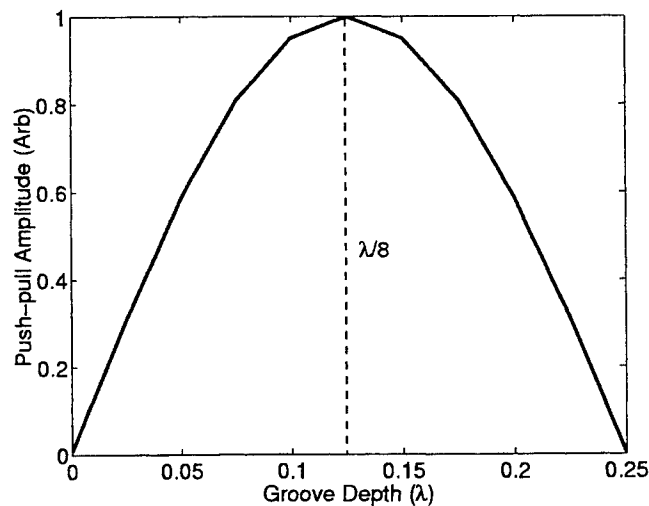

Figure 9. The amplitude of the integrated irradiance modulation for the BASE signal group between the $\alpha > 0$ and $\alpha < 0$ portions of the pupil.

This shift has the effect of reducing the overall rotation of the total irradiance, and increasing the modulation along the β direction of the pupil. The amplitude of the modulation of the fringes along the β direction of the pupil for different groove depths can be seen in Fig. 11(b). For the range of groove depths $\lambda/10 < d < \lambda/6$ the modulation of fringes is almost exclusively along the β direction of the pupil, with very little rotation.

4.3. The Irradiance Modulation of the Interference between On-track and Off-track (IMX)

Figure 12 shows pupil irradiances for the interference between the on-track and off-track fields. The bright regions are positive contributions to the irradiance and the dark regions of are negative contributions to the irradiance. This
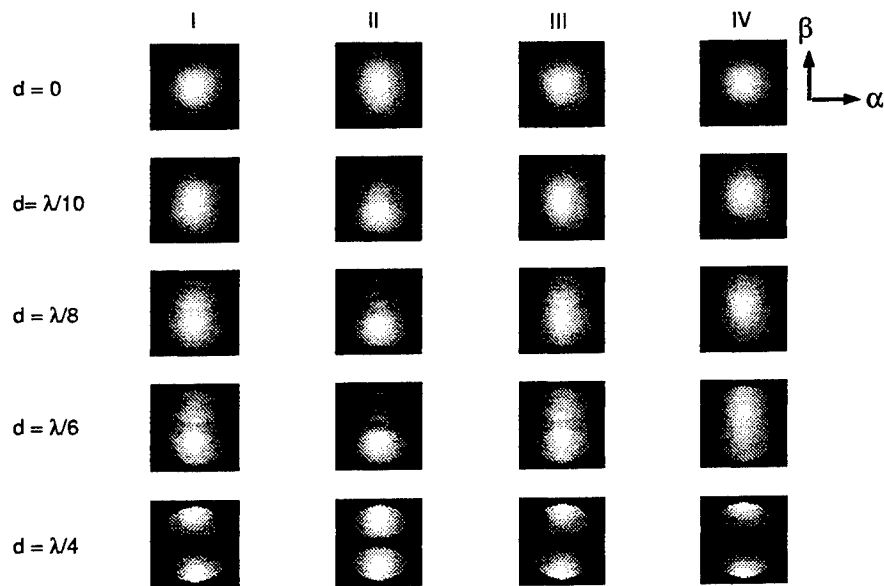
Figure 10. The pupil irradiance modulation for the SMX signal group. The pupil patterns are arranged for the groove depths indicated in rows and in columns for the scan positions I, II, III and IV. The bright portions of the pupil are positive contributions to the irradiance and the dark portions of the pupil are zero.
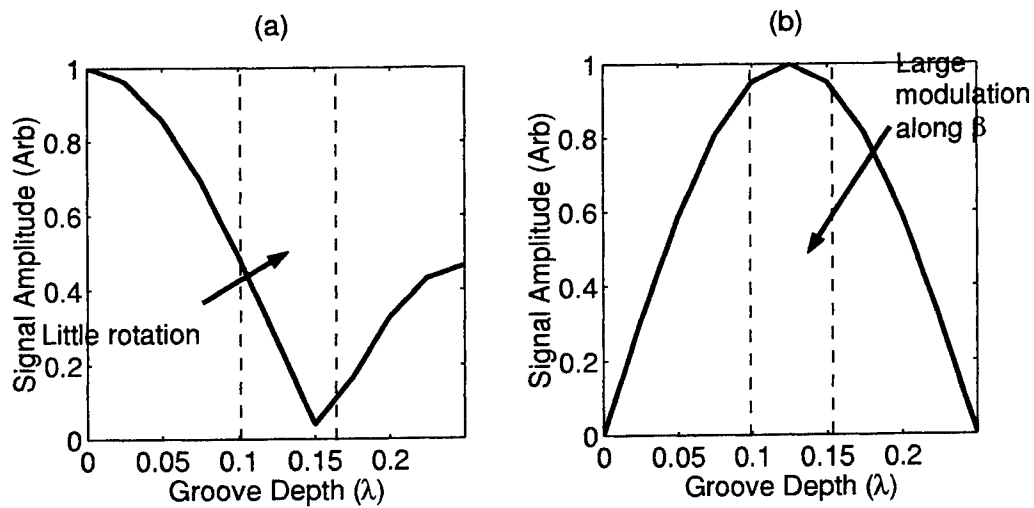

Figure 11. For the SMX signal group. (a) The amplitude of the QPD signal as a function of groove depth. (b) The amplitude of the integrated irradiance between the $\beta > 0$ and $\beta < 0$ portions of the pupil.

is a result of the IMX signal group being a cross modulation between the on-track and off-track fields. Eq. 25 shows that the IMX pupil irradiance consists of a single set of fringes. The modulation of the IMX fringe in the pupil is highly rotational. IMX is more rotational for all groove depths compared with SMX because IMX consists of a single interference fringe.

The IMX fringe shifts along the β direction of the pupil for differing groove depths. The rotation of the fringe is unaffected by the groove depth. However, the shifting IMX fringe affects the integrated readout signal. This is due
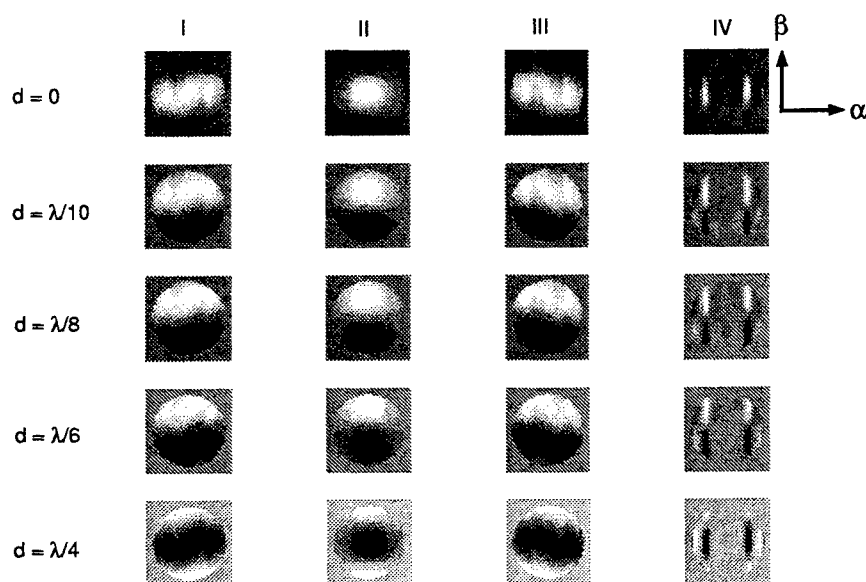
Figure 12. The pupil irradiance modulation for the IMX signal group. The pupil patterns are arranged for the groove depths indicated in rows and in columns for the scan positions I, II, III and IV. The bright portions of the pupil are positive contributions to IMX irradiance and the dark portions of the pupil are negative contributions.

to the distribution of the IMX fringe in the pupil. For groove depth $\lambda/8$ there are equal amounts of positive and negative irradiance contributions in the pupil, which gives an integrated signal of zero. The same occurs for forming the QPD signal, as shown in Fig. 13.

5. CONCLUSIONS

The total field reflected from the optical disk is described as a linear summation of fields reflected from the on-track data marks, off-track data marks and the background, respectively. The fields are propagated to the exit pupil of the optical data storage scanning system where they combine and interfere to form the total exit pupil irradiance pattern. The total exit pupil irradiance is grouped into three meaningful terms, BASE, SMX and IMX. The BASE irradiance results from the combination of the on-track field with the background field. The SMX irradiance results from the combination of the off-track fields with the background fields. The IMX irradiance occurs as a result of the interference between the on-track fields and the off-track fields. The modulating components of BASE, SMX and IMX are termed the BASE, SMX and IMX signal groups.

The modulation of the pupil irradiances for the signal groups is described by the modulation of interference fringes. The BASE and SMX signal groups consist of three groups of interference fringes. The IMX signal group consists of a single group of interference fringes. The BASE signal group modulates along the α direction of the pupil, which is also the scan-track direction. The symmetry of the movement along α is affected by the interference fringes whose modulation is explicitly dependent upon the groove depth.

The modulation of the SMX and IMX signal groups is largely rotational. The rotation of the irradiance is a consequence of the linear dependence in phase along the β direction of the pupil of the fields diffracted from the off-track marks combined with the phase of the higher diffraction orders along the α direction of the pupil changing linearly with scan location. However, for the SMX signal group, the groove depth explicit fringes are shifted in the β direction of the pupil for increasing groove depth. This has the effect of masking the overall rotational modulation of the SMX signal group and increasing the net modulation along the β direction of the pupil. The point of minimum rotation in the pupil is for groove depth of $\lambda/6$ and the point of maximum modulation along the β direction of the pupil is for groove depth of $\lambda/8$. The modulation of the IMX signal group is rotational due to the single group of interference fringes. The IMX fringes shift in the pupil for changing groove depth, which determines the amplitude
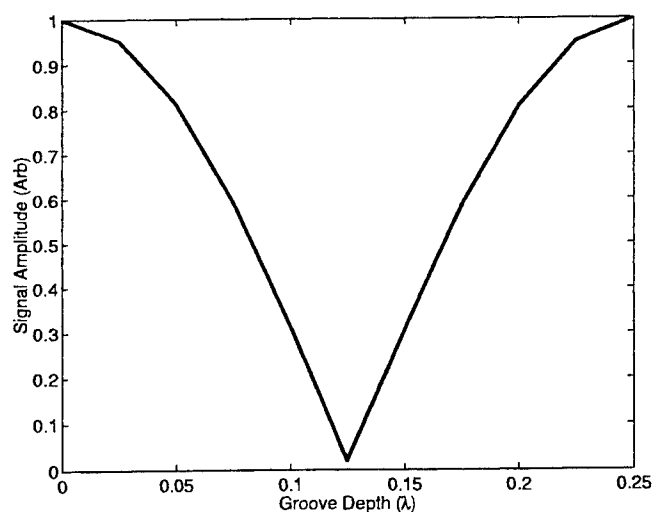
Figure 13. For the IMX signal group. The amplitude of the QPD signal as a function of groove depth. The variation of the QPD signal amplitude with groove depth is due to the positive and negative contributions of irradiance in the pupil.

of the integrated IMX signal. The rotational modulation in the pupil is unaffected by the variation of groove depth because IMX consists of a single set of interference fringes.

REFERENCES

1. T. D. Milster *Conference digest of the optical data storage meeting* **60**, 1997.
2. "Matlab is a registered product of mathworks inc.."
3. D. Flagello, T. D. Milster, and A. E. Rosenbluth, "Theory of high-na imaging in homogeneous thin films," *Journal of the Optical Society of America* **13**(1), 1996.
4. T. D. Milster, "New way to describe diffraction from optical disks," *Appl. Opt.* **37**(29), 1998.
5. H. H. Hopkins, "Diffraction theory of laser read-out systems for optical disks," *Journal of the Optical Society of America* **69**(1), 1979.
6. J. E. Harvey, "Fourier treatment of near-field scalar diffraction theory," *American Journal of Physics* **47**(11), 1979.
7. R. N. Bracewell, *The Fourier Transform and it's Applications*, McGraw-Hill, second ed., 1986.
8. T. D. Milster and R. S. Upton, "Fundamental principles of crosstalk in optical data storage," *Jpn. J. Appl. Phys.* **38 Part1**(3B), pp. 1608–1613, 1999.
9. G. Bouwhuis, *Principles of optical disk systems*, Adam Hilger, 1986.
10. T. D. Milster, Z. Chen, E. P. Walker, M. T. Tuell, and E. Gage, "Optical data storage readout with quadrant pupil detection," *Appl. Opt.* **35**(14), pp. 2471 – 2476, 1996.
11. R. S. Upton, F. Akhavan, T. D. Milster, W. Bletscher, J. K. Erwin, M. Schweisguth, and A. M. Nichol, "Electronic crosstalk cancellation using a quadrant cell detector," *Jpn. J. Appl. Phys.* **39**(Part 1, No. 2), 2000.
12. C. S. Chung, T. K. Kim, S. T. Jung, C. W. Lee, S. S. Joo, and I. S. Park, "New method of the readout signal generation to reduce the adjacent track crosstalk," *SPIE Conf. Proc. International Symposium on Optical Memory* **3864**, pp. 237 – 239, 1999.

Polarization Analyses of Readout Signals in Phase Change Material Incorporating a Solid Immersion Lens (SIL)

Chung-Hao Tien, Yin-Chieh Lai, Han-Ping D. Shieh

Institute of Electro-Optical Engineering, National Chiao Tung University

Hsin-Chu, Taiwan, 30010, Rep. of China

Tel: 886-3-5726111-59211 Fax: 886-3-5737681 Email: u8624503@cc.nctu.edu.tw

ABSTRACT

Comprehensive analyses based on rigorous vector diffraction theory have been presented to simulate the readout signal contrast using SIL in reading phase change recording disk. De-polarized reflected light (y-polarized from x-polarized incident beam) results in the reduction of total signal contrast, and becomes more obvious for high numerical aperture (NA) systems. Due to the signal degradation from de-polarized reflected light, filtering de-polarized light is applied to signal detection. The x-polarized contrast is a factor 1.0 to 1.35 higher than the conventional detection contrast (x+y polarized) at different gap widths, at a cost of 0 to 25 percent total intensity reduction.

Keywords: Solid Immersion Lens (SIL), near-field recording, NA (numerical aperture), polarization, vector diffraction.

INTRODUCTION

Areal density of optical recording is limited by the laws of diffraction to be about $0.6\lambda/NA$, where λ is the wavelength of the laser and NA is the numerical aperture of the focusing lens. A solid immersion lens (SIL) attached to an objective with effective NA higher than 1 is a feasible scheme to produce an ultra-small focus laser spot to read/write in optical recording[1-4]. The principle of the SIL-based near field optics is that by focusing light inside a high refraction index lens without another refraction, the wavelength of light is shrunk by a factor n, where n is the refraction index of the lens. Based on vector diffraction theory using plane-wave expansion, the spectrum within the critical angle of SIL-air interface will diffract like a focus wave with NA=1 (region1), the other part will decay exponentially away from the bottom of SIL (region2). When the SIL was positioned closely enough to the disk, optical tunneling effect of region2 results in increasing the effective numerical aperture (NA) above theoretical upper limit of 1 in air[5]. Through evanescent coupling into the recording medium, the reduced marks can be readout using SIL, promising substantial increase in the storage density. For SIL systems with $NA_{eff} > 1$, the air gap spacing between SIL lens and recording medium dramatically affects the signal contrast. Moreover, in such high NA systems, the incident angle is so large that the readout signal will be affected by de-

In *Optical Storage and Optical Information Processing*, Han-Ping D. Shieh, Tom D. Milster, Editors, Proceedings of SPIE Vol. 4081 (2000) • 0277-786X/00/$15.00

155

polarization effect. Here we examine the effect of de-polarization on readout signal contrast in phase change disks using SIL.

SYSTEM LAYOUT

The SIL-based system and disk structures are shown in Fig. 1. We adopt the linearly x-polarized Gaussian beam with a 1/e radius of r_0=RA (the objective radius), resulting in an effective NA_{eff}=1.1 and 1.48 for 0.6-NA and 0.8-NA objective lens with SIL (n=2.0), respectively. Reflected beam is collimated, separated into the x and y-polarized electric field by a PBS and then detected denoted by S_1 and S_2, respectively. The full vectorial character of light is considered in this simulation. Here reflective crystalline and amorphous state in x-polarized is denoted as S_{1X} and S_{1A}, respectively, while S_{2X} and S_{2A} for y-polarized, respectively. The readout signal contrast is defined as $(S_{1X}-S_{1A})/(S_{1X}+S_{1A})$.

SIMULATION METHODS

Our approach to vector diffraction is based on Mansuripur's[6,7]. Wavefront is decomposed into a set of plane waves that propagate independently through the SIL system. Then each plane wave propagation in θ and ϕ directions has associated with its two orthogonal electric fields in the input pupil plane, E_p^0 and E_s^0, which are aligned in the radial and azimuthal directions, respectively. After reflected from the layered media, the two independent electric fields become E_p and E_s. The reflection matrix of the phase-change disk can be written as follows:

$$\begin{bmatrix} E_p \\ E_s \end{bmatrix} = \begin{bmatrix} R_{pp} & R_{ps} \\ R_{sp} & R_{ss} \end{bmatrix} \begin{bmatrix} E_p^0 \\ E_s^0 \end{bmatrix} \quad (1)$$

$$\theta = \tan^{-1}\left(\frac{\sqrt{E_x^2 + E_y^2}}{E_z}\right) \qquad \phi = \tan^{-1}\frac{E_y}{E_x}$$

The reflection coefficient given by thin-film matrix techniques is adopted for reflected field at the medium. In phase change material, s and p-polarized waves are independent as the cross terms R_{ps} and R_{sp} are zero. After coordinate transformation, the polarization of a refracted beam can be expressed in terms of that of the incident beams in Cartesian coordinates:

$$\begin{bmatrix} E_x \\ E_y \\ E_z \end{bmatrix} = \begin{bmatrix} \Psi_{xx} & \Psi_{xy} \\ \Psi_{yx} & \Psi_{yy} \\ \Psi_{zx} & \Psi_{zy} \end{bmatrix} \begin{bmatrix} E_x^0 \\ E_y^0 \end{bmatrix} \quad (2)$$

where

156

$$\Psi'_{xx} = \frac{1}{2}\left\{(R_{ss} + R_{pp}\cos\theta) - (R_{ss} - R_{pp}\cos\theta)\cos 2\phi - (R_{sp} + R_{ps}\cos\theta)\sin 2\phi\right\}$$

$$\Psi'_{xy} = \frac{1}{2}\left\{-\left[(R_{sp} - R_{ps}\cos\theta) - (R_{sp} + R_{ps}\cos\theta)\cos 2\phi + (R_{ss} - R_{pp}\cos\theta)\sin 2\phi\right]\right\}$$

$$\Psi'_{yx} = \frac{1}{2}\left\{(R_{sp} - R_{ps}\cos\theta) + (R_{sp} + R_{ps}\cos\theta)\cos 2\phi - (R_{ss} - R_{pp}\cos\theta)\sin 2\phi\right\}$$

$$\Psi'_{yy} = \frac{1}{2}\left\{(R_{ss} + R_{pp}\cos\theta) + (R_{ss} - R_{pp}\cos\theta)\cos 2\phi + (R_{sp} + R_{ps}\cos\theta)\sin 2\phi\right\}$$

$$\Psi'_{zx} = (R_{pp}\cos\phi - R_{ps}\sin\phi)\sin\theta$$

$$\Psi'_{zy} = (R_{ps}\cos\phi + R_{pp}\sin\phi)\sin\theta$$

At a focal length from the SIL bottom along the z axis, the electric field distribution in exit pupil is obtained by superimposing each plane waves, taking into account their different propagation paths and polarization vectors. The integral of the overall electric field can be computed efficiently by fast-Fourier-transform (FFT) algorithm. Finally, the reflected electric field components of x and y polarized (z is too small to be included) separated by PBS are detected individually.

SIMULATION RESULTS

The difference and DC values of reflected wave in x and y-polarized for $NA_{eff}=1.1$ are shown in Fig. 2(a). DC values of x-polarized $S_{1x}+S_{1A}$ change extensively as the gap width increases, which mainly determine the signal contrast, as shown in Fig. 2(b). On the other hand, the y-polarized $S_{2x}+S_{2A}$ is so weak that the signal contrast degradation due to y-polarized can be neglected. Moreover, the contrast of y-polarized is even reversed at gap width ≈ 0 nm because of interference effects.

Then we use an annular aperture, shown in Fig. 1, to block the rays below the critical total reflection angle (TIR) angle to concentrate on the readout contrast of evanescent wave, as shown in Figs. 3(a) and (b), respectively. The ratio of block radius to full aperture radius is 0.77. As shown in Fig. 3(a), the DC values of both x $(S_{1x}+S_{1A})$ and y-polarized $(S_{2x}+S_{2A})$ increase as air-gap increases because of the total reflection effect. As the air-gap exceeds about 400 nm, the incident beam is all reflected by TIR so that the signal contrast in both x and y-polarized approach to zero, as shown in Fig. 3(b).

De-polarization resulted from large incident angle becomes more significant in higher NA systems. Then, we used a $NA_{eff}=1.48$ to examine the relationship between polarized readout contrast and gap width compared to $NA_{eff}=1.1$. As Fig. 4(a) shows, DC values of y-polarized $(S_{2x}+S_{2A})$ increase compared to $NA_{eff}=1.1$, shown in Fig. 2(a), result in apparent degradation of total contrast due to y-polarized, as shown in Fig. 4(b).

We also observed the annular aperture of $NA_{eff}=1.48$, compared with $NA_{eff}=1.1$, to observe whether more evanescent components have influence on readout signal contrast. The ratio of block radius to full aperture radius is 0.44. As Fig. 5(a) shows, the signal and DC values both increase compared to $NA_{eff}=1.1$. Consequently, the total readout contrast will not been

improved by more evanescent components, as shown in Fig. 5(b). Moreover, the faster decay of evanescent wave results in contrast margin shrunk when gap is below 400 nm for 1.1-NA_{eff} to approximate 150 nm for 1.48-NA_{eff}, respectively.

The calculated results above show that the conventional detection of phase change medium (total intensity of x+y polarized) is from individual contribution of x and y polarization, respectively. Moreover, readout contrast in x and y-polarized are different functions of gap width. Since readout signal contrast from x-polarized is always higher than the sum, the readout signal contrast can be improved by filtering y-polarized. Taking NA_{eff}=1.48 full aperture objective for example, the intensity and contrast ratio of x-polarized/sum reveals a trade-off between signal improvement and detected intensity, as shown in Fig. 6. The x-polarized contrast is a factor 1.0 to 1.35 higher than the sum contrast at different air gap, at a cost of 0 to 25 percent total intensity reduction.

CONCLUSIONS

Comprehensive analyses based on rigorous vector diffraction theory have been presented to simulate the readout signal contrast using SIL optics in reading phase change recording disks. The readout signals of SIL-based systems are affected not only by evanescent coupling but also de-polarization effect in such high NA system. We noticed that the de-polarized reflected light (y-polarized from x-polarized incident beam) resulted in the reduction of total contrast, and became more seriously for high NA system. Moreover, more evanescent coupling will not contribute to signal contrast. Due to the signal degradation from de-polarized reflected light, a filtering de-polarized light is applied to signal detection. The reflected x-polarized contrast is a factor 1.0 to 1.35 times higher than the sum contrast (x+y polarized) at different air-gap, at the cost of 0 to 25 percent total intensity reduction.

Acknowledgement

Reference

1. E. Betzig, J. K. Trautman, R. Wolfe, E. M. Gyorgy, P. L. Finn, M. H. Kryder and   C.-H. Chang, "Near-field magneto-optics and high density data storage," Appl. Phys. Lett. **61**, 142-144 (1992).
2. S. M. Mansfield, W. R. Studenmund, G. S. Kino and K. Osato, "High numerical aperture lens system for optical storage,"Opt. Lett. **18**, 305-307 (1993).
3. B. D. Terris, H. J. Mamin, D. Rugar, W. R. Studenmund, and G. S. Kino,"Near-field optical data storage using a solid immersion lens,"Appl. Phys. Lett. **65**, 388-390 (1994).
4. I. Ichimura, S. Hayashi, and G. S. Kino, "High- density optical recording using a solid immersion lens," Appl. Opt. **36**,

4339-4348 (1997).

5. Tom D. Milster, Joshua S. Jo and Kusato Hirota, "Roles of propagating and evanescent waves in solid immersion lens systems," Appl. Opt. 38, 5046-5057(1999).

6. M. Mansuripur, "Certain computational aspects of vector diffraction problems," J. Opt. Soc. Am. A., 6, 786-805(1989).

7. Wei-Hung Yeh and M. Mansuripur, "Evanescent coupling in magneto-optical and phase-change disk systems based on the solid immersion lens," Appl. Opt. 39, 302-315 (2000).
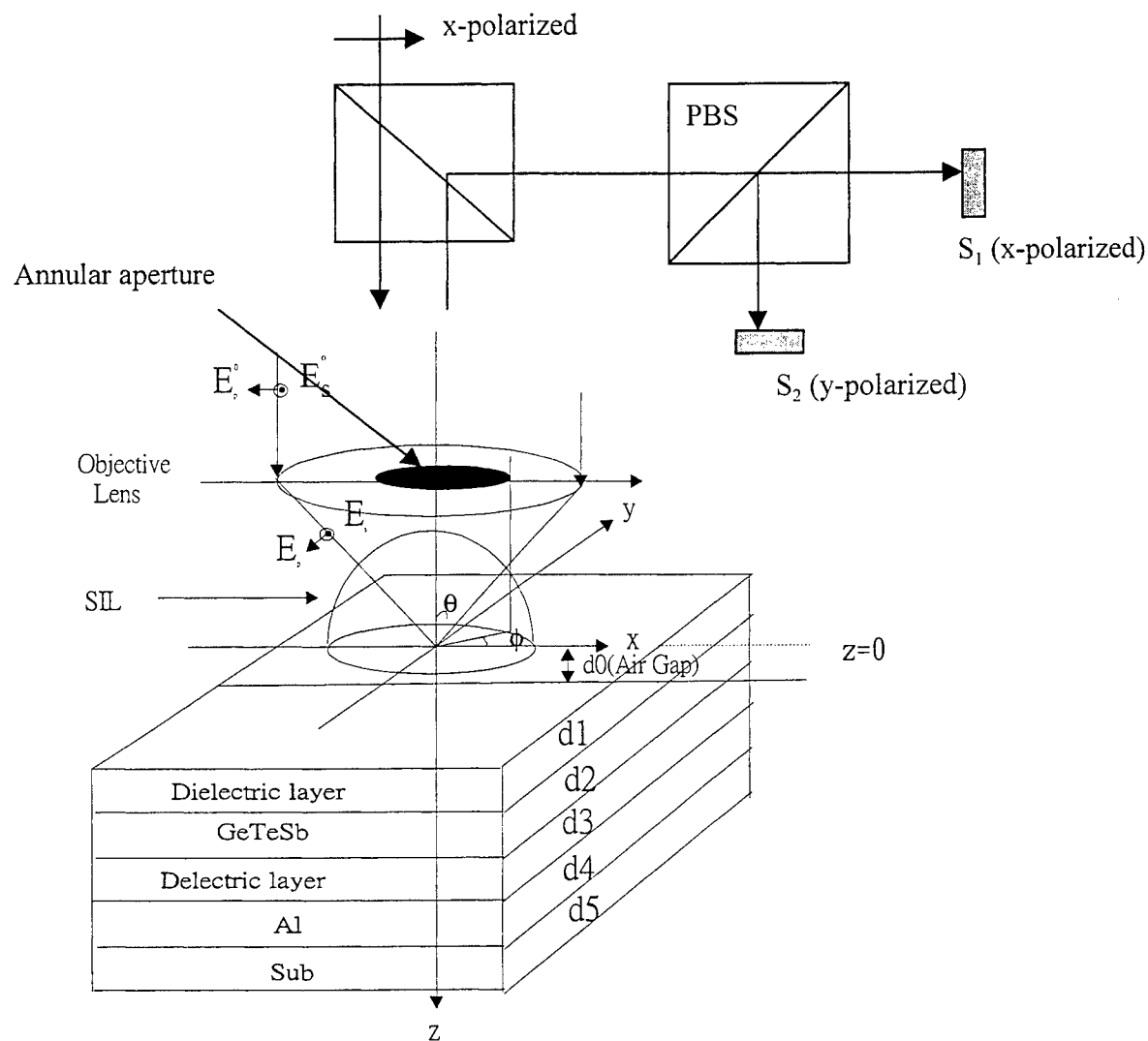
Fig. 1 Schematic of SIL-based system and disk structure.

(λ=650nm, Focal length=6000λ

d1=110 nm, d2=26 nm, d3=32 nm, d4=100 nm)

159
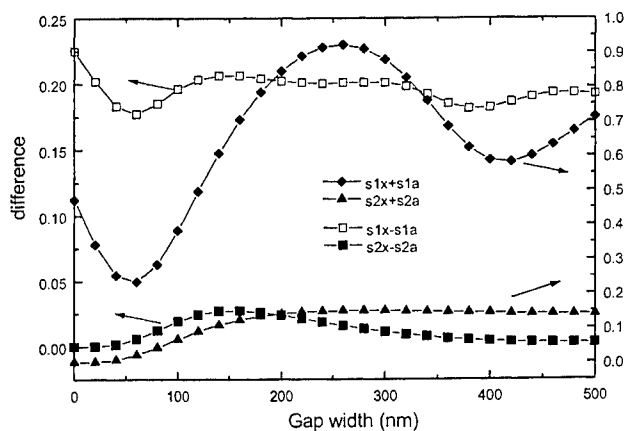
Fig. 2(a) Difference and DC values of x and y-polarized for the system of $NA_{eff}=1.1$, respectively. DC value of x-polarized $(S_{1x}+S_{1A})$ changes extensively as the gap width increases, which mainly determines the sum signal contrast $((S_{1x}-S_{1A})+ (S_{2x}-S_{2A}))/ ((S_{1x}+S_{1A})+ (S_{2x}+S_{2A}))$, as shown in Fig. 2(b).
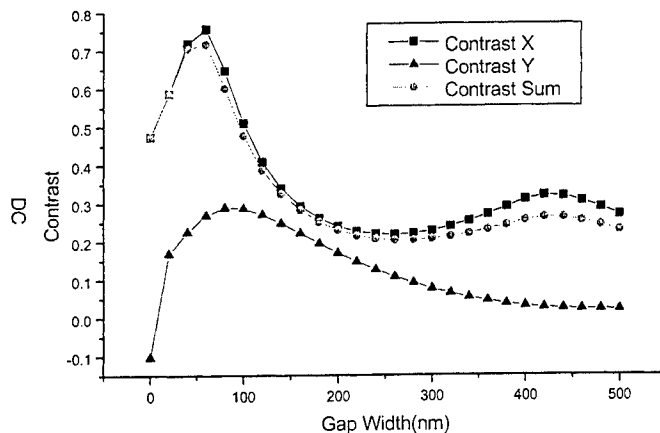

Fig. 2(b) The signal contrast in x, y, and sum (x+y polarized), respectively. The y-polarized reverses sign near gap width ≈ 0 nm, which result in total signal contrast reduction.
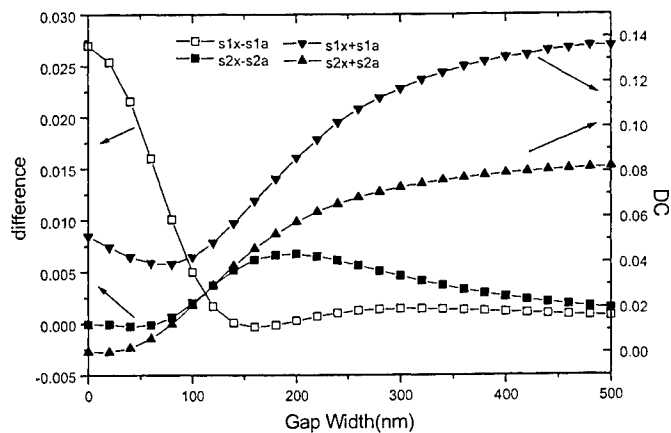
Fig. 3(a) Difference and DC values for the system of $NA_{eff=1.1}$ with an annular aperture blocking the rays below the critical TIR angle (evanescent wave). Both DC values of x and y-polarized increase as gap width increases because of total reflection effect.
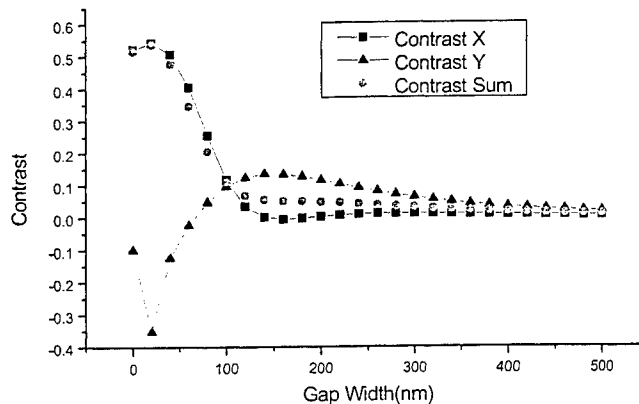

Fig. 3(b) The signal contrast with annular aperture in x, y and sum (x+y polarized), respectively. The contrast in y-polarized will make the total signal contrast enhanced or deteriorated. The contrast margin in sum is below 400 nm.
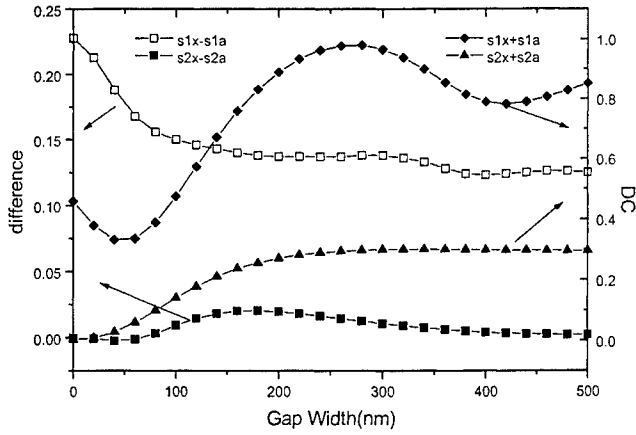
Fig. 4(a) Difference and DC values of x and y-polarized for the system of NA_{eff}=1.48, respectively. DC values in y-polarized increase compared to NA_{eff}=1.1 (Fig. 2(a)), result in apparent separation between sum signal contrast and x-polarized, as shown in Fig. 4(b).
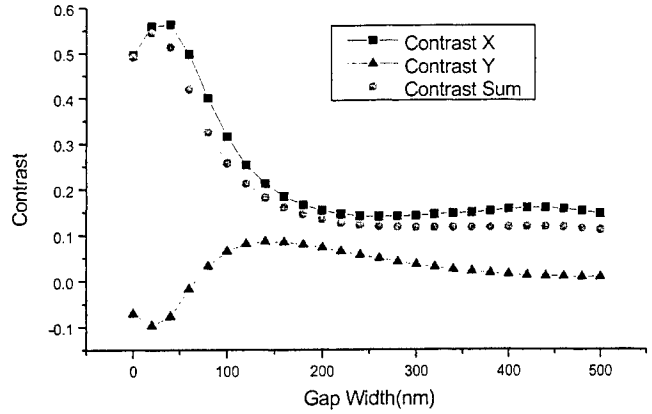
Fig. 4(b) The signal contrast in x, y, and sum (x+y polarized) for the system of NA_{eff}=1.48, respectively. The sum signal contrast is departed from x-polarized due to increased y-polarized.
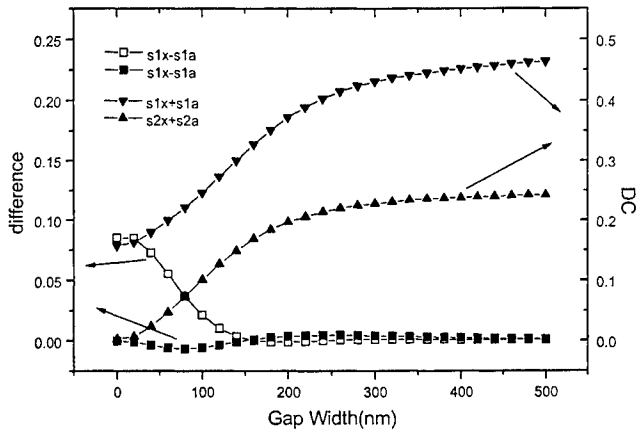

Fig. 5(a) Difference and DC values for the system of NA_{eff}=1.48 with an annular aperture blocking the ray below the critical TIR angle. Both DC and difference in x and y-polarized increase compare to NA_{eff}=1.1 (Fig. 3(a)).
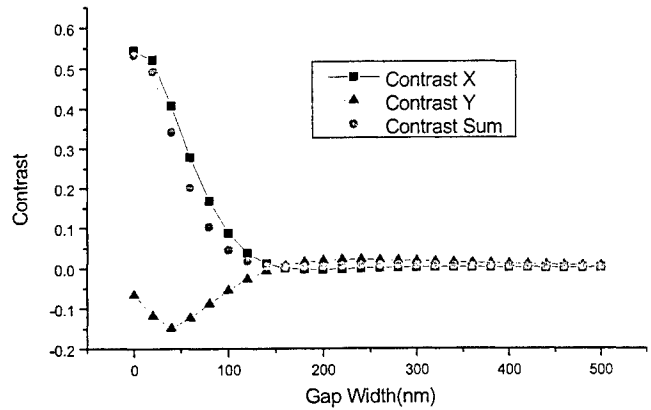
Fig. 5(b) The signal contrast of annular aperture in x, y and sum (x+y polarized), respectively. Signal drops more sharply than that of NA_{eff}=1.1 (Fig. 3(b)). Moreover, the contrast margin shrunk as gap is less than 400 nm in NA_{eff}=1.1 to approximate 150 nm.
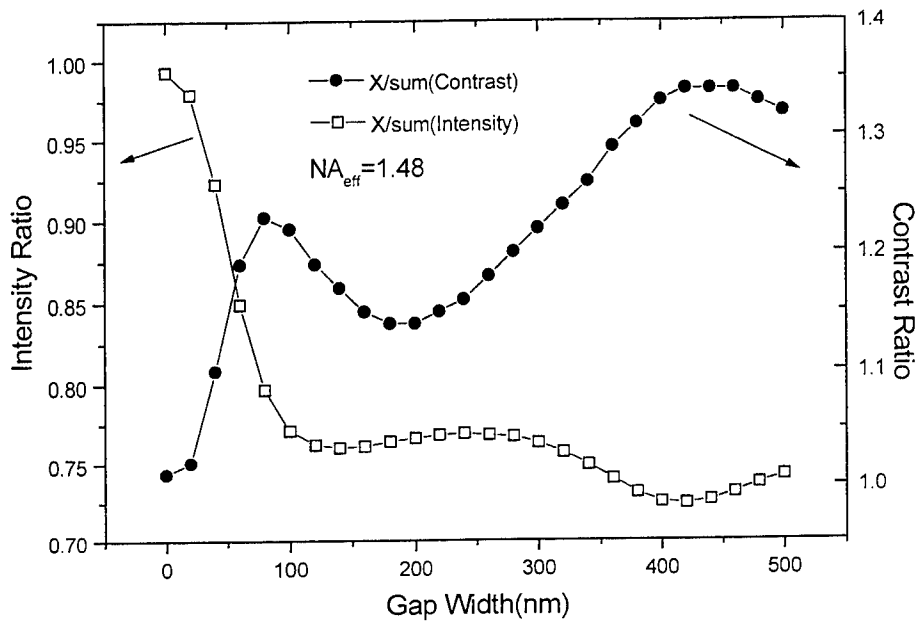
Fig. 6 Intensity and contrast ratio of x-polarized to sum (x+y polarized) for the system of $NA_{eff}=1.48$ with full aperture. There is a tradeoff between signal contrast and detected intensity.

A high Speed Finger-Print Optical Scanning Method

Warren W. C. Liu[a], H. C. Lin, C. S. Lin[b], and H. L. Wang[b]

[a]WELON TECH INC.

[b]Chunghwa Telecommunication Laboratories

ABSTRACT

An optical scanning technique of dactylogram (fingerprint) has been developed by using plural LED's with different wavelength as emitting elements and a color CCD or CMOS area image sensor as receiving element. Owing to the R/G/B filters built in that color area image sensor, if the above LED's have wave lengths corresponding to those peak sensing wavelengths of the R/G/B outputs of that color area image sensor, and if the above mentioned LED's are installed to emit light on the surface of finger from different directions, then it will be effective to get a 3D picture by using a single color area image sensor. Moreover, the time needed to obtain a 3D picture is only that for single exposure.

Thanks to the inherent nature of 3D picture, the sharpness of border of the ridges of a fingerprint in the picture is greatly enhanced. This simplifies the data transmission. Besides, by a simple signal processing of those output waveforms of the color area image sensor, the security against counterfeiting in fingerprint identification can be easily ensured. These features are essential for fingerprint authentication in INTERNET environment and E-Commerce environments.

Keywords: fingerprint, optical scanning, plural LED, identification, E-commerce

1. INTRODUCTION

Recently the biometrics revolution is coming to life. For the past years, those biometric technologies which are used to identify people through fingerprints, facial, voice pattern and other physical characteristics has existed for years, in view of those requirements in INTERNET environment where many users are on line simultaneously, the demand of technological breakthroughs always exists for quicker response, greater convenience and higher security.

Among those biometrics technologies for authentication, from the view point of convenience and higher security, dactyloscopy is by far the best, much better than the current system like keycard, passwords and personal identification numbers (PIN).

And among those various methods for reading fingerprints, by using sensing technologies using static capacitance, thermal or optical detection, the optical detection is by far with the most potential to meet the requirements in INTERNET environment owing to the recently fast progress in E/O device such as LED and color CCD/CMOS image sensor.

In the following we will propose a newly developed optical scanning method[1] to take the full benefit of the recently plurality of high luminesce LED's with different wavelengths corresponding to those peak sensing wavelengths of the R/G/B outputs of the detecting device (the color area image sensor), a 3D-like image pattern can be obtained by using a single receiving element within a single exposure time period. These two or three output signals are stored in analog form in the color area image sensor; these output signals can be simultaneously processed to give a very clear fingerprint pattern by using very simple circuitry. Besides, these analog signals can also be used for the detection of counterfeiting of fingerprint.

With the method no additional semiconductor memory is required during signal processing of these outputs, and prevention of counterfeiting can be manipulated by using only simple explains the high speed sensing nature of fingerprint pattern of this design.

Correspondence: Warren W. C. Liu; Email: wclon@tpts8.sccd.net.tw C. S. Lin; Email: smartlin@ms.chttl.com.tw H. L. Wang; Email: hanlan@ms.chttl.com.tw

2. SOME WAYS FOR FINGERPRINT SENSING

As the background for the evaluation of that high speed sensing method of fingerprint pattern, the currently used methods to get fingerprint pattern for subsequent matching and identification use will be briefly described below; these methods can be classified into four categories[2-4]:

2.1 Ink-based fingerprint (paper based fingerprint)

This is the conventional way commonly used by governments and public agencies for years. This conventional fingerprint matching method is quite time-consuming. And this kind of paper based fingerprint data is not easy to use.

2.2 Heat based sensing

This is not so widely accepted at the present time due to the low resolution of the inherent nature of thermal imaging technique. Besides, this method is easily influenced by environmental changes such as temperature changes.

2.3 Static capacitance sensing

In this method the static capacitance between the electrode plate and the surface of finger is detected. Since the surface of finger is structured with ridges and valleys over the whole region, thus the difference in height of the top of ridges and the bottom of valleys are used for the distinguish of fingerprint pattern.

The advantage of static capacitance detection is easy to use and simple in hardware structure. However, it suffers the disadvantage that the static capacitance is very sensitive to moisture. Therefore, this method will encounter some difficulties in case of sweated hands or in high moisture conditions. Another disadvantage of the dactyloscopy by capacitance detection is its limited resolution and poor edge sharpness of the pattern due to the fact that the electric field in the vicinity of the micro pads of a capacitor may diverge.

2.4 Optical scanning method

This method senses difference of the intensity of reflected light from the ridges and valleys. The reflected light from the ridges of surface of finger is higher than that from the valleys.

Three basic units are required to construct an optical scanning module, namely (1) light source, (2) lens system and (3) B/W area image sensor. Fig.1 illustrates this method.
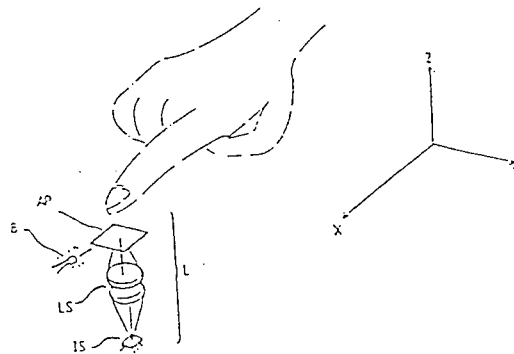

Figure 1. Schematic of an optical scanning method

For the purpose of area image sensor to receive the reflected light from surface of a finger, light should be emitted from below (vertically or obliquely) upon the surface of the finger, as be seen in Fig.1. Two signal processing methods are commonly used as explained as below:

2.4.1 2D image scanning

Since the whole area of the surface of the finger is illuminated by lights from all directions, each side (for example the left side) of bottom of a "valley" which is scarcely illuminated by the light from the corresponding (i.e. left) side will be exposed to the light from another (i.e. right) side. Thus the darkness of the margin decreases. This means the contrast between the darkness/brightness is weakened. Thus the sharpness of the border lines of the ridges and valleys is poor, as depicted in Fig. 2.
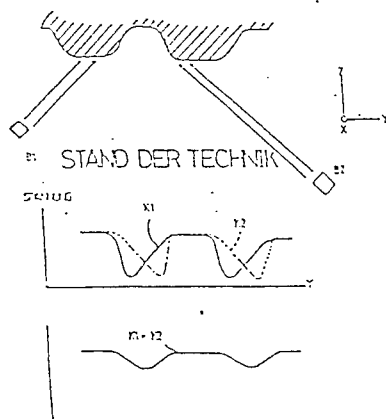

Figure 2. Standard technique of 2D image scanning where the sharpness of the border lines of ridges and ridges is poor

2.4.2 3D image scanning

If the light sources at the left side and at the right side are turned on separately in sequence and the image pictures are taken two times respectively by the two sequences, then it is a way for obtaining the 3D image pattern, For example, one image pattern will show the pattern as lighted from left direction, and the other image pattern shows those as lighted from right direction. The darker area of these two image patterns are not alike, thus defining a 3D picture.

However for the processing of these two image patterns, a memory with enough capacity is needed; one of the image patterns that is taken at first should be stored in the memory. Then this information will be retrieved out and be processed together with information of that second image pattern. This is illustrated in Fig.3.
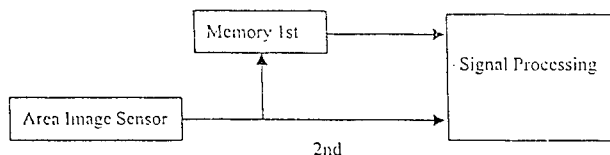

Figure 3. The processing of 3D image scanning, where an additional memory is needed for the storage of the first image pattern

3. IMPROVED 3D OPTICAL SENSING METHOD

Fig.4 shows an improved method for fingerprint pattern scanning, wherein a color area image sensor and LED's of different primary colors are used. This color area image sensor will has three outputs (here we call R/G/B outputs, with built-in R/G/B optical filters in their receiving pixels.) The LED's used to respectively light the surface of finger from different directions have different colors (and therefore wavelengths) corresponding to the peak sensing wavelength of the R/G/B

output of the above mentioned color area image sensor. This is shown in Fig. 4.

By employing this hardware structure, if all these LED's light simultaneously, this means the color area sensor will receive the reflected light from all these LED's. For example, if only two kinds of LED's namely RED and GREEN are used, they emit RED and GREEN light respectively with peak wavelengths matching the peak sensing wavelength of the R output and G output of that color area image sensor, respectively.

Then the R output and G output will show the separate image patterns which are produced only by RED LED's or GREEN LED's, respectively. Since the RED LED's and GREEN LED's are installed to emit light out from different directions, the 3D image pattern can be obtained with a single exposure. Moreover, no memory is needed in this hardware structure. This is shown in Fig.5.
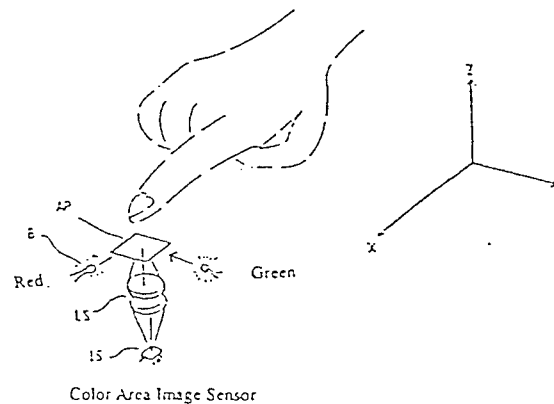

Figure 4. An improve method for fingerprint pattern scanning by using color area image sensor and LED's of different primary color
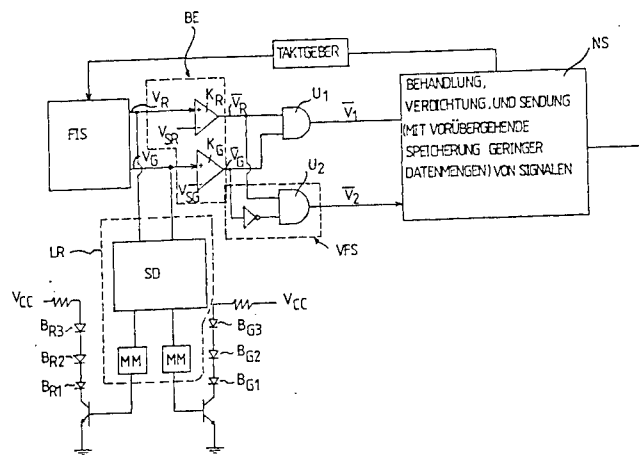

Figure 5. Hardware structure of this improved 3D optical sensing method, where RED and GREEN LED's are lighted by monostable multivibrators

166

4. 3D ANALOG SIGNALS PROCESSING

The output signals from R/G/B output ports of the color area image sensor are further processed to obtain those valuable information we want. Since the output signals are stored in the form of analog signal in the color area image sensor, much flexibility will be attained in the subsequent data processing.

For the simplicity in explanation, if only two kinds of LED's are used namely RED and GREEN are used, the same assumption as described in Sec.3, then we will find the R and G output will show s steep slope just corresponding to the both sides of ridges of the surface of finger, respectively. When these signals are converted into digital waveforms Vrd and Vgd by voltage compartors, respectively, it is found that the actual locations of both sides of ridges are not sensitive to the change of reference voltage used with voltage comparator. This unique feature will be further explained below. This can be seen in Fig. 6.
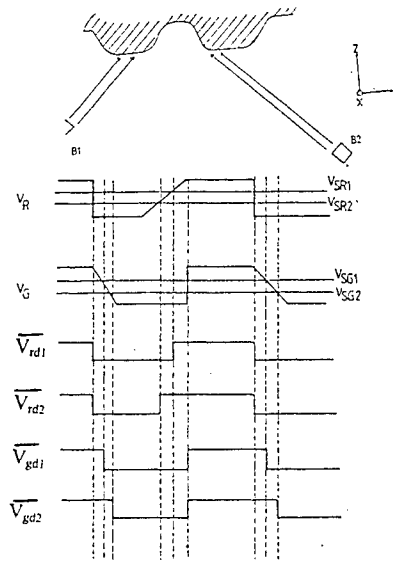

Figure 6. R and G output signals are converted into digital waveforms V_{rd1} and V_{gd1}, V_{rd2} and V_{gd2} means the waveform by using different reference voltage for compartor

4.1 Binary-like fingerprint pattern

The digital waveforms Vrd and Vgd related to R and G output signals can be used together with simple digital logic circuitry to obtain a signal binary-like fingerprint pattern as shown in Fig. 7. The locations in the change of digital signal waveforms Vrd and Vgd corresponds exactly to the both sides of the border of fingerprint. Moreover, these two locations are not sensitive to the changes of the reference voltage used in the voltage comparator as explained previously.

Since the reference voltage used to convert analog output signal of area image sensor may be influenced by many factors such as changes in environmental conditions, tolerance in assembly procedure and etc., therefore we have found that the signal binary-like fingerprint scanning techniques.

4.2 Prevention of counterfeiting

In case of a copied fingerprint pattern is used to replace the real finger for fingerprint optical scanning, then the R and G output will be the same owing the fact that is the image of a planar pattern and not the image of a surface with ridges and valleys. Consequently, the digital waveforms Vrd and Vgd can be used together with simple digital circuitry such as XOR gate to obtain a digital waveform Vcd which directly indicates whether the signals Vrd and Vgd are the same.

In this manner, the detection of counterfeiting is very easily to be achieved. Moreover, the counterfeiting by using a

chemical etched processed fingerprint pattern will also be detected owing to the fact that the etched pattern will be with a nearly vertical edge shape, and the borders of this kind of edge are clearly defined and digital signals Vrd and Vgd will be in a similar wave shape. As depicted in Fig. 8.
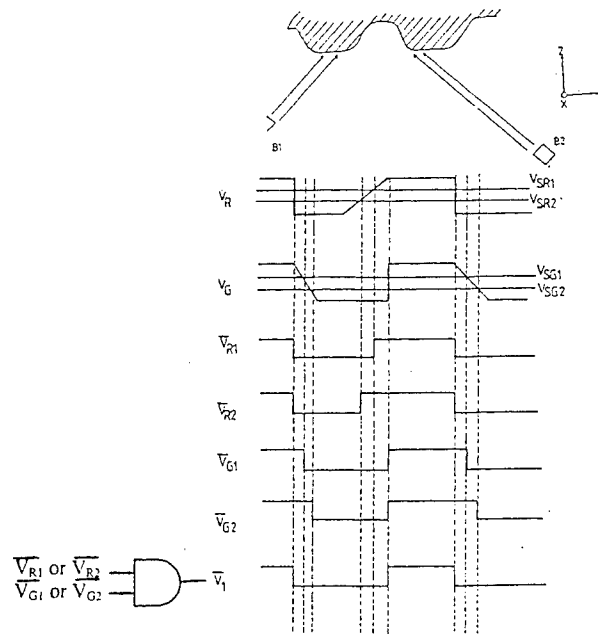

Figure 7. A binary-like fingerprint pattern can be obtained by AND of V_{rd} and V_{gd}
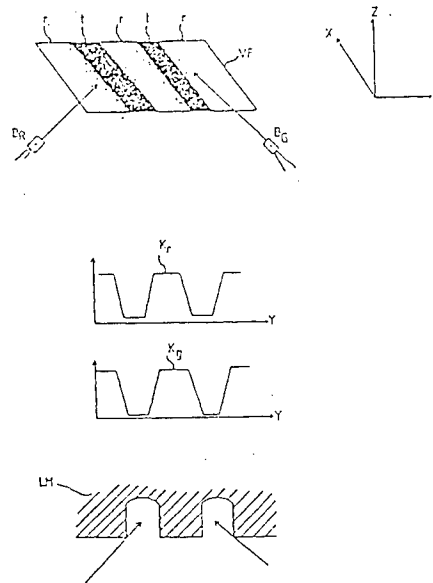

Figure 8. Prevention of counterfeiting for this improve method

5. TOTAL TIME FOR IDENTIFICATION PROCESS

The evaluation standard for fingerprint verifying techniques are FAR (False Accept Rate) and FRR (False Reject Rate). For the optimum expectation, the value of FAR and FRR should be low. Besides, for efficiently consideration, the time needed for authentication should be kept as low as possible. Total is the time needed for a complete cycle of authentication process, it consists of all the following time factors:

T1: time needed for picture imaging
T2: time needed for counterfeiting prevention
T3: time needed for data compression
T4: time needed for data encryption and transmission
T5: time needed for data decompression
T6: time needed for fingerprint verification

In our improved optical scanning method, those time factors T1, T2, T3, and T4 will be reduced.

Regarding the time factor T6, because a binary-like image pattern can be obtained by using the above mentioned improved optical scanning method, thus the time T6 needed for fingerprint verification may be reduced to a great extend owing to high quality fingerprint pattern if identified by a host computer in remote location.

6. DATA COMPRESSION AND TRANSMISSION OF FINGERPRINT PATTERN

The fingerprint pattern as obtained by using the above mentioned improved 3D optical scanning method will be much like a binary image pattern, this kind of image pattern is more suitable to the data compression than those image pattern as obtained by using other sensing method. Because a binary-like image pattern will have higher percentage of redundancies in its image pattern, and the aim of data compression is to reduce the number of bits required to represent the image pattern by removing these redundancies, thus a large portion of redundancies can be removed. In this manner, it is possible to develop a more efficient data compression scheme by using information theory concepts to process this binary-like image pattern.

Moreover, although the data compression can be categorized into two fundamental groups as lossless and lossy[5], where lossy compression scheme is more efficient for data transmission. Because the major purpose of the decompressed data of the above mentioned compressed data is for the characteristic extraction of minutia of the fingerprint to be used for identification in the remote host computer, in this case, a complete data recovery is not absolutely necessary. Besides, considering the total time required for identification is important in INTERNE environment, therefore the more efficient lossy compression scheme is more suitable to be used in this application. The general framework for a lossy compression scheme is shown in Fig.9.
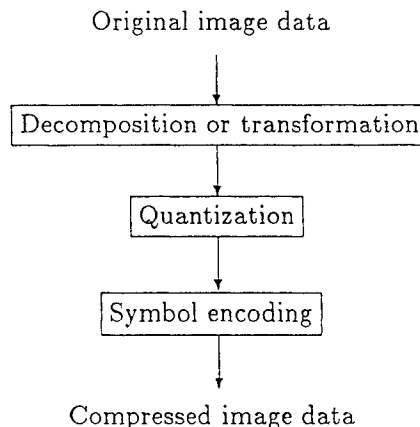
Original image data

| Decomposition or transformation |

| Quantization |

| Symbol encoding |

Compressed image data

Figure 9. Lossy compression framework

7. CONCLUSIONS

The fingerprint optical scanning method as designed to take the full benefit of the recently developed E/O components, and characterized by using a plurality of high illuminance LED's with different wavelengths corresponding to the peak sensing wavelengths of the R/G/B output of the color CCD/CMOS area image sensor, a 3D-like image pattern can be easily obtained within a single exposure time period.

Moreover, by simple signal processing of those R/G/B outputs together, a binary-like fingerprint pattern can be obtained, this binary-like pattern is not sensitive to environmental conditions changes, this means the reliability of this fingerprint optical scanning method is greatly improved. Moreover, by another simple processing of R/G/B outputs together, the prevention of counterfeiting can be achieved to a greater extent.

Finally due to the high quality of the binary-like fingerprint pattern as mentioned above, the total time needed for authentication will be greatly reduced under the condition that the identification of fingerprint be processed by a host computer through communication links in remote location.

REFERENCES

1. Lesegerät zum klaren Lesen von Figerabdrücken Germany Patent No. 200 01 814.00 by WELON TECH INC.
2. J. Rudy van de Plassche, Johan H. Huijsing, and Willy M. C. Sansen, *Analog Circuit Design: RF analog-to-digital converters; sensor and actuator interfaces; low-noise oscillators, PLLs and synthesizers*, Kluwer Academic Publishers, Boston, 1997.
3. Ljubisa Ristic, *Sensor technology and devices*, Artech House, Boston, 1994.
4. Larry K. Baxter, *Capacitive sensors: design and applications*, IEEE, New York, 1997.
5. Majid Rabbani & Paul W. Jones, *Digital image compression techniques*, SPIE Optical Engineering Press, Bellingham, 1991.
6. C. A. Jan van der Lubbe, *Basic Methods of Cryptography*, Cambridge University Press, Cambridge, 1998.

SESSION 6

Optical Information Processing II

Chinese Seal Recognition Using Hybrid Electro-Optical Filter

Jian-Shuen Fang, Chulung Chen, Sway Wang

Department of Electrical Engineering
Yuan Ze University
Chung-Li, Taiwan, R.O.C

ABSTRACT

We present a new technique for Chinese seal recognition using constrained energy minimization joint transform correlator (CEMJTC). Either optical or digital correlation is one of the most powerful operations for detecting the presence/absence of the seal image. The CEMJTC is proposed to improve the discrimination capability for shift-invariance and rotational-invariant seal recognition. By minimizing the average correlation energy with respect to all training seal images, while constraining the correlation peak value to a constant, a filter function is constructed. The main emphasis is to design a filter for good discriminate ability. Numerical results are presented to demonstrate the improvements. Furthermore, experimental results show the sharp correlation output profile when the seal image is correct, otherwise the correlation peak will be obviously reduced. The new technique for seal recognition shows a significant increase in high speed and detection ability.

Key words: CEMJTC; Pattern recognition; Optical correlation; Optical filter

1. INTRODUCTION

For the purpose of person identification, seal are used in Chinese society in stead of signatures on many types of articles such as paintings, documents, checks, receipts, money withdrawing lists, etc. A problem encountered in seal pattern recognition is the nearly infinite variation of seal imprints even if the imprints are all produced from the same seal, such as nonuniformly stained paints, different stroke widths, rotation, spot noises, a broken edge, blurred parts, double setting, etc. The variation results from many factors. For example, the force a person uses in setting a seal on paper is almost always different and often nonuniform or the seal may be stained on the seal head [1,2]. In contrast to other methods, seal imprint recognition can be achieved with the optical correlator, for which two widely used schemes have been the VanderLugt optical correlator [3,4] and the joint transform correlator (JTC) [5]. Since its introduction by Vanderlugt, optical correlation has been one of the most effective methods for optical pattern recognition [6,7]. Optical recognition methods based on the Fourier transform, such as the Vanderlugt correlator, or the joint transform correlator offer advantages such as parallel

processing and large-volume databases [8]. Since the optical information processing system works at the speed of light and is a parallel process, it is a good for image recognition system [9]. During the past decade, optical signal processing has been used in a wide variety of applications, e.g., optical pattern recognition, image subtraction for machine vision, and optical computing. Although optical processing relies on general holographic filtering techniques, the concept of programmability in signal processing will be introduced [10]. This is primarily due to the advance in sophisticated spatial light modulators and photorefractive crystals that allow us to construct various types of near real-time hybrid optical information system [11,12].

A 2D input signal (i.e., an image) is processing in correlator, the description for the correlator is representatively (but not always) given in the frequency domain. Correlation can be implemented optically by the frequency plane correlator. The specialized filter suggests a system that passes certain frequency components and attenuates others. Optical correlation has been one of the most powerful operations for detecting the presence of a target in noise and clutter [13]. The correlation operation is attractive because of its shift-invariance, i.e., the output correlation distribution shifts directly proportional to the moving distance of the input target. As a result, the output correlator can not only detect the presence or not of the target image, but it can also track these images as they shift in the input plane, e.g., targets in different position [14,15]. The optical correlator at the speed of light makes it more attractive than electronic version for the pattern recognition. But, obviously, a purely optical processor has some drawbacks, which make certain tasks difficult or impossible to implement. The first is that an optical system is difficult to program as general-purpose electronic computers. Although an optical system can be designed to perform specific tasks, it cannot be used where more adaptability is required. A second drawback is that optical systems by themselves can not be used to make decisions as some electronic counter parts can [16,17]. To overcome the problem, optical system and electronic system can cooperate together. For instance, controllability and programmability are the advantage of the digital computer. Therefore we introduce an optical pattern recognition technique with assisting of the electronic computer. The CEMJTC setup offers clear advantages in practical implementations with respect to a VanderLugt correlator using a frequency domain MACE filter, where position match between filter and transform is critical to obtain a good correlation signal. The proposed system has the ability to recognize seal imprints regardless of the orientation and blurring.

2. Theoretical analysis

The implementation of hybrid optical setup is to use a conventional optical configuration, as shown in Fig. 1.
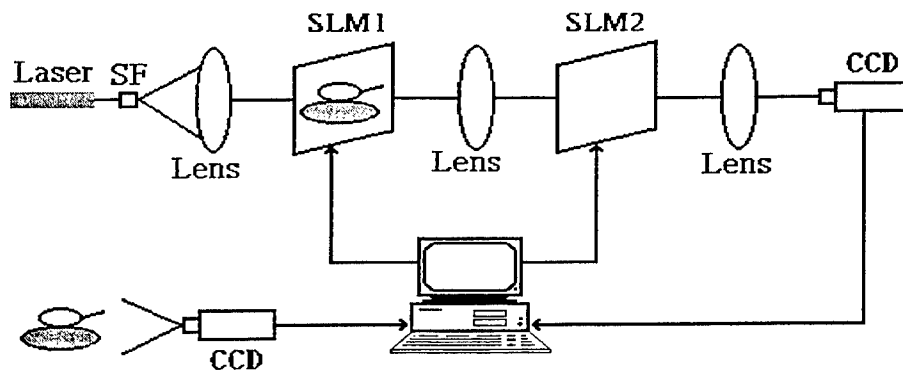
Fig. 1 VanderLugt optical configuration

Spatial light modulators (SLM1) contains input image pattern in the input plane, and the Fourier transform of the reference pattern is generated with the SLM2, through which cross-correlation (convolution) between the input object and the reference pattern can be detected by a charge coupled device (CCD) array detector. The detected signal can be fed back to the computer for display and for decision-making. That is, we can appropriately control the hybrid signal optical processor by a computer. An analog system diagram of the optical architecture appears in Fig. 3. The corresponded optical signal processor, is depicted in Fig. 4.
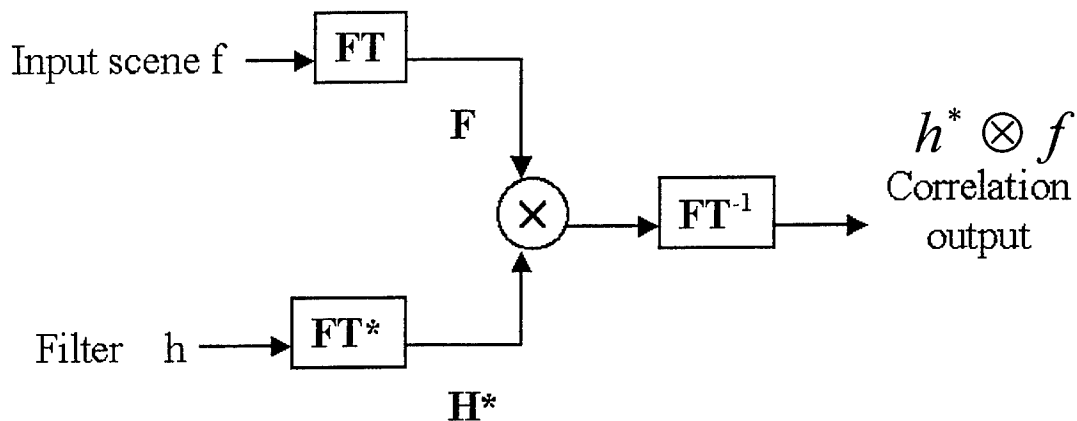

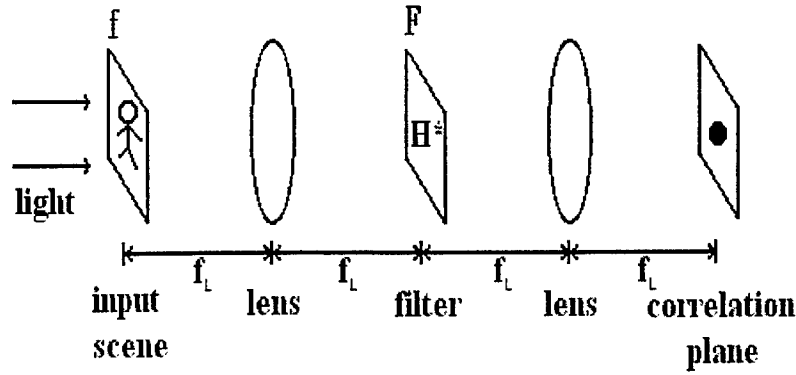
Fig. 3 Analog system diagram

Fig. 4 An optical signal processor

Now we design the CEM filter. The basic idea of CEM filter is to constrain the central correlation amplitudes for training images and to minimize the average output correlation plane energy. Let us denote the training images by $f_i(x, y)$. Let $F_i(u, v)$ represent the Fourier transform of $f_i(x, y)$, and let $H^*(u, v)$ represent the filter function in the Fourier frequency domain. We first constrain the filter to satisfy the desired correlation response as below.

$$\iint F_i(u,v)H^*(u,v)dudv = c_i \qquad i = 1,2,...,N,$$
(1)

where c_i is the pre specified constant, the subscript i refers to the i-th training image, and N is the number of training images. The CEM filter is designed to minimize the average correlation plane energy (which is related to the sharpness of the correlation peak) given by

$$E_{ave} = \frac{1}{N}\sum_{i=1}^{N}\iint |F_i(u,v)|^2 |H(u,v)|^2 dudv,$$
(2)

where Parsecal-Rayleigh's energy theory has been used to derive the above equation for the average correlation plane energy. To minimize E_{avg} it is much convenient and powerful to use the vector/matrix notation. Then Eq. (1) can be rewritten as

$$F^T H^* = C,$$
(3)

where C is a column vector of size N with c_i as entries, H^* is a column vector with discrete spatial variables obtained by scanning the filter from left to right and from top to the bottom, F is a matrix with each column vector corresponding to the sampled Fourier transform of each training image. For convenience, we define a matrix A (which is average power spectrum

over all training images), whose elements are

$$A(u,v) = \frac{1}{N} \sum_{i=1}^{N} |F_i(u,v)|^2 .$$

(4)

Using vector notation, the E_{ave} in Eq. (2) can be rewritten as

$$E_{ave} = H^+ A H ,$$

(5)

where + denotes complex conjugate transpose and A is a diagonal matrix with its diagonal elements corresponding to the average power spectrum.

By using the Lagrange functional method, minimizing E_{ave} in Eq. (5) under the constraints in Eq. (3) leads to the following filter function in the frequency domain.

$$H^* = A^{-1} F^* \left[F^T A^{-1} F^* \right]^{-1} C ,$$

(6)

where * refers to complex conjugate. Since A is a diagonal matrix, its inverse is trivial. The only non-trivial matrix inversion needed is that of $\left[F^T A^{-1} F^* \right]$, which is a N by N matrix.

Since the adjustment of Fourier plane correlator is hard to achieve. The joint transform correlator has been found to improve the drawback. The main advantages of JTC are that the reference image can be updated in real time, it does not require filter fabrication beforehand, and it avoids the precise the position of the filter otherwise required in Vanderlugt-type correlators. Fig. 5 shows the joint transform correlator.
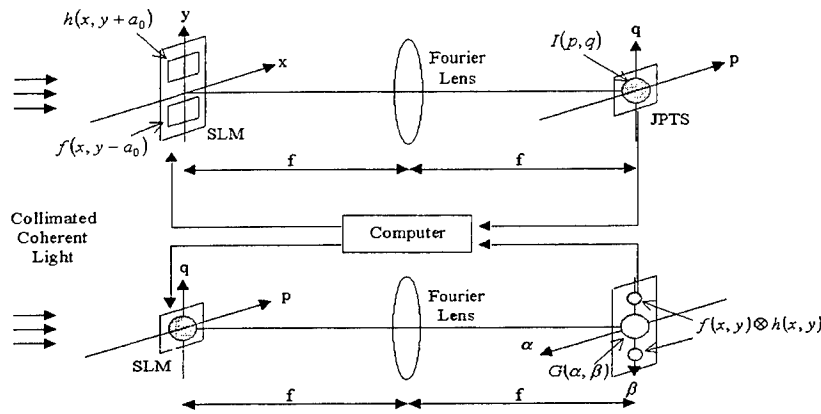

Fig. 5 The joint transform correlator.

176

Nevertheless, the JTC suffers from poor detection efficiency, particularly for multi-target and high-background noise environments. This disadvantage is primarily due to the existence of the zero-order spectra. The power spectrum subtraction technique can be used to remove the zero-order diffraction [18,19] and the output of JTC can be shown as [6,17]

$$g(\alpha,\beta) = h(x,y) \otimes f^*(x,y) * \delta(y - 2a_0) + h^*(x,y) \otimes f(x,y) * \delta(y + 2a_0),$$ (7)

where

$$h = \mathcal{F}^{-1}\{H\}$$ (8)

and $2a_0$ is the separation distance between the reference function h and the test image f.

3. Numerical Results

The numerical analysis of the proposed technique using CEM filter in JTC was investigated. For the reference and input objects, we used a 64×64-pixel image. The reference function has been designed on a Pentium III 450MHz computer. It took approximately 2 minutes of CPU time to run the computer program for the synthesis of the reference function. The JTC input is composed of two parts: the upper part is the input test scene, and the lower part is the synthesized reference image. Fig. 6 shows the input test scene of JTC. There are six input test images for correlation, 5 are for the legitimate user (each seal images has different rotation angle) and 1 is for similar but invalid user (the lower middle one). The magnitude of the reference image is depicted in Fig. 7. The joint transform correlation output is shown in Fig. 8(a). A three-dimensional profile of the output correlation is plotted in Fig. 8(b). Sharp correlation peaks corresponding to the authorized seal pattern are quite distinguishable and indicate the successful detection of the technique. The position measurement of the correlation can be computed as the location of the valid image. As anticipated, no strong correlation peak is observed for wrong image. Since the correlation output is symmetric, we can show only one cross correlation result. Fig. 9(a) illustrates the test for noise but valid patterns such as smeared and lined images. Fig. 9(b) reveals that the sharp correlation profile offers high detection efficiency.
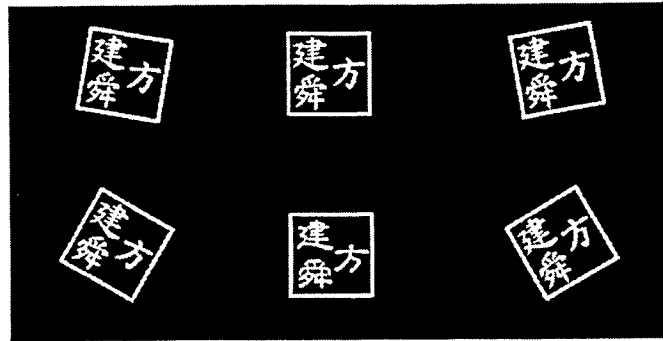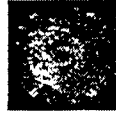

Fig. 6 An input test scene

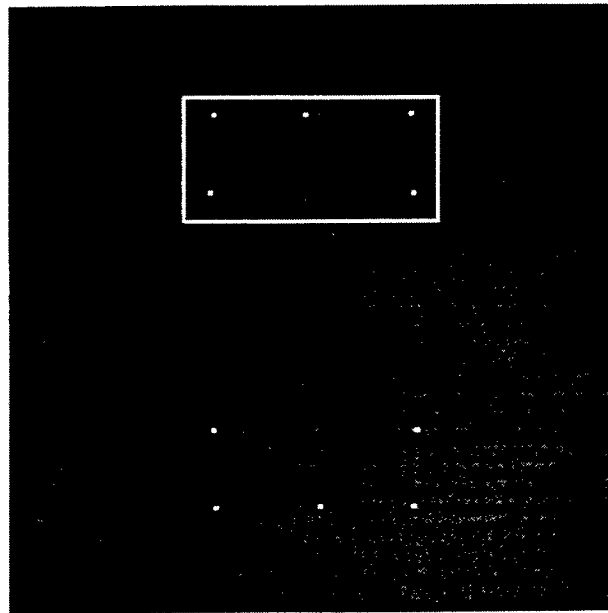Fig. 7 The magnitude of the reference image

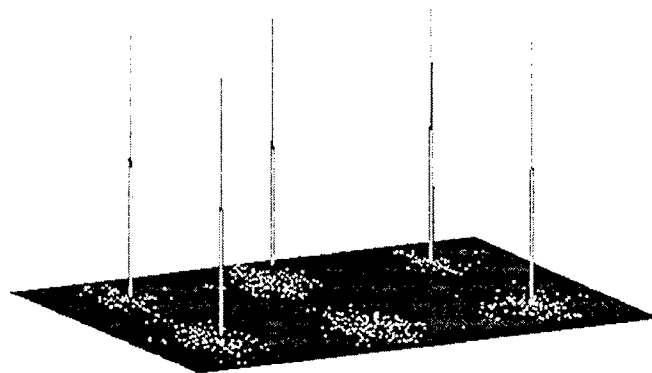Fig. 8(a) The symmetric cross correlation output

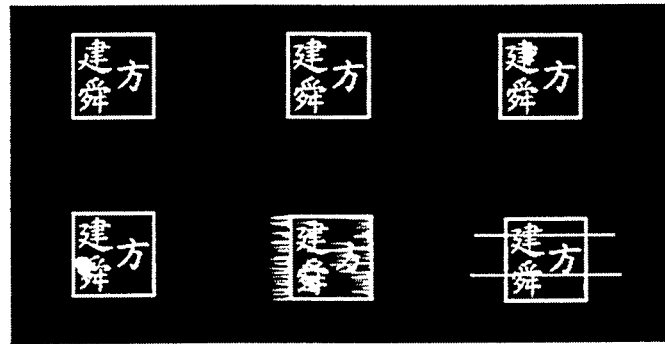Fig. 8(b) The three-dimensional profile in the rectangular area

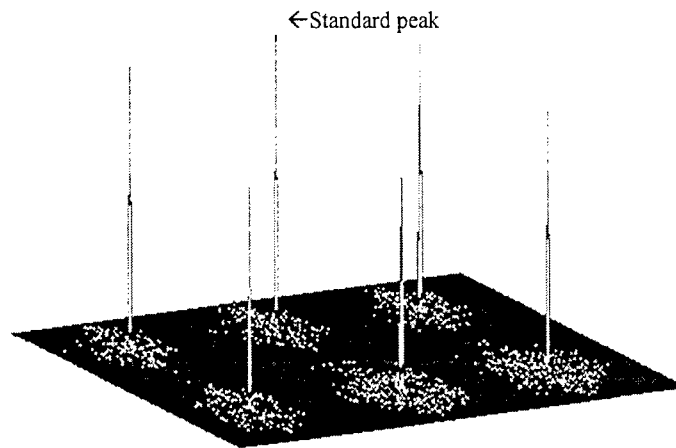Fig. 9(a) An input test scene (smeared and lined images).

←Standard peak

Fig. 9(b) The three-dimensional profile of cross correlation

4. Experimental Results

Now we are going to describe real tests. Satisfactory results have been obtained. An example of a Chinese money-withdrawing list, which includes a seal imprint, is shown in Fig. 10. A prototype Chinese seal recognition system is illustrated in Fig. 11. Fig. 12 shows the valid seal pattern. Recognition tests for rotational images are shown in Fig. 13(a) and Fig. 14(a), respectively. The corresponding output correlation profiles are shown in Fig. 13(b) and Fig. 14(b), respectively. Fig. 15(a) shows the invalid seal pattern, and the 3D profile is shown in Fig. 15(b). As anticipated, no strong and sharp correlation peak is observed for wrong image. Therefore, we can make a decision by giving a global threshold value of correlation peak, above which the image can be treated as a legitimate seal pattern and below which it is a illegitimate seal pattern.

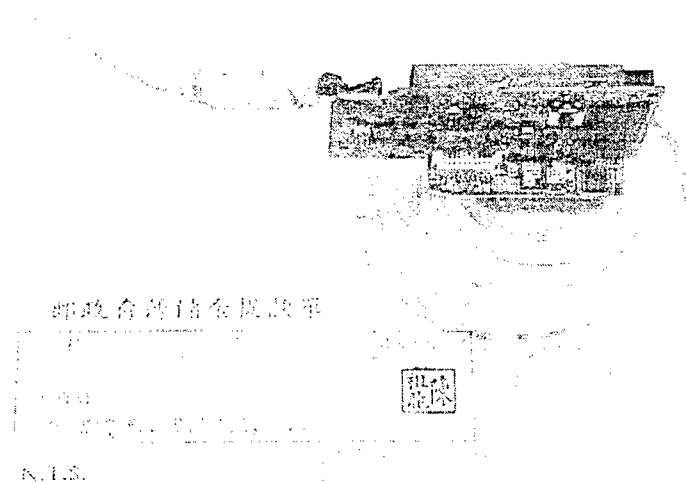Fig. 10 A binary image of a Chinese money withdrawing list

Fig. 11 A prototype Chinese seal recognition system
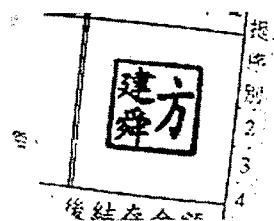

Fig. 12 The valid seal pattern

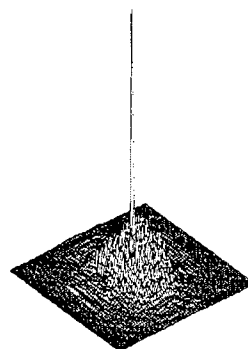Fig. 13(a) A right-rotated correct image

Fig. 13(b) The 3D Profile of cross correlation
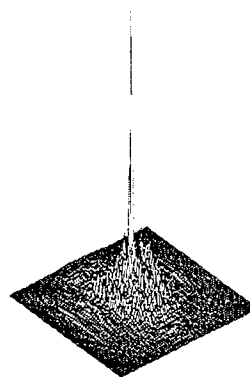

Fig. 14(a) A left-rotated correct image
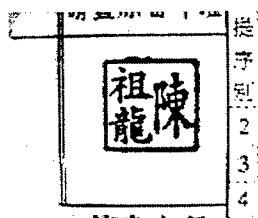

Fig. 14(b) The 3D Profile of cross correlation

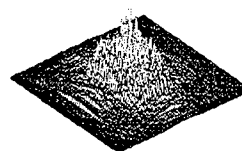Fig. 15(a) An invalid seal pattern under test

Fig. 15(b) The 3D Profile

5. Conclusion

We have describe a new scheme for Chinese seal pattern verification that combines the advantage of electronics and optics. The CEM filter designed for optical correlator has the desirable property of the sharp peak with low sidelobes levels in the output correlation plane. The major advantages of the system are alignment simplicity, rotation invariant capability, high discrimination capability, and suitability for hybrid optical signal processing. The test result indicates that the correlator produces reasonably good and impressive sharp correlation peak intensity at the valid seal location. With the choice of proper threshold in the output correlation, the proposed technique is shown to result in highly robust and discriminating detection.

ACKNOWLEDGMENT

REFERENCE

1. T. J. Fan and W. H. Tsai, "Automatic Chinese Seal Identification," *Computer Vision, Graphics, and Image Processing,* **25**, 311-330 (1984).

2. S. Lee and J. H. Kim, "Attributed stroke graph matching for seal imprint verification," *Pattern Recognition Letters,* **9**, 137-145 (1989).

3. A. VanderLugt, "Signal detection by complex spatial filtering," *IEEE Trans. Inf. Theory* **IT-10**, 139-146 (1964).

4. Y. S. Chen, "Automatic identification for a Chinese seal image," *Pattern Recognition,* **29**, 1807-1820 (1996).

5. C. S. Weaver and J. W. Goodman, "A technique for optically convolving two functions," *Appl. Opt.* **5**, 1248-1249 (1966).

6. C. Chen, J. Fang, "Cross- correlation optimization on joint transform correlators," *Optics Communications.* (in press)

7. C. Chen, J. Fang, "Chinese seal pattern recognition with nonzero order joint transform correlators," *Optical Engineering.* (submitted)

8. J. W. Goodman , Introduction to Fourier Optics, McGraw- Hill, New York, (1968).

9. F. T. S. Yu and S. Jutamulia, Optical Signal Processing, Computing and Neural Network, Wiley-Interscience, New York, (1992).

10. F. T. S. Yu, Q. W. Song, Y. S. Cheng, and D. A. Gregory. "Comparison of detection efficiencies for Vander Lugt and joint transform correlators," *Appl. Opt* .**29**,225-232 (1990).

11. J. Fang, C. Chen and S. Wang, 1999, "Joint transform correlator with a new zero order reduction technique," *1999 12th*

IPPR Conference on Computer Vision, Graphics and Image Processing, pp. 151-157.

12. C. Chen, S. Wang and J. Fang, 1999, "Military target recognition with a power spectrum subtracted joint transform correlators," *Eighth National Conference on Science and Technology of National Defense,* pp. 4.

13. B. V. K. Vijaya Kumar, "Tutorial survey of composite filter designs for optical correlators, "*Appl. Opt.* **31**, 4773-4801 (1992).

14. J. Fang, C. Chen and S. Wang, "Hybrid Electro-Optical Filter Design for Chinese Seal Image Recognition," *Optic and Photonics Taiwan'99,* pp. 981-984.

15. C. Chen, J. Fang, S. Wang, "Correlation Filter Designs for Military Target Recognition," *Optic and Photonics Taiwan'99,* pp. 989-992.

16. C. Chen, "Mimimum average correlation energy nonzero order joint transform correlator," *Applied Optics.* (submitted the revised paper)

17. C. Chen, J. Fang, "Equal correlation peak optimization on ideal joint transform correlators," *Optical Memory and Neural network.* (in press)

18. S. Wang, C. Chen, J. Fang, "Correlation Energy Minimization (CEM) Filter Designs for Different Size Image Recognition," *Optic and Photonics Taiwan'99,* pp. 977-980.

19. C. Li, S. Yin and F. T. S. Yu, "Nonzero order joint transform correlator," *Opt.Eng.,* **37**, 58-65 (1998).

Effect of Grating Detuning on Volume Holographic Memory using Photopolymer Storage Media : Reflection holograms

Mei-Li Hsieh, Ken Y. Hsu, and Pochi Yeh*
Institute of Electro-Optical Engineering
National Chiao Tung University
Hsin-Chu, Taiwan
R. O. C.
FAX: 886-3-571-6631
E-Mail: ken@cc.nctu.edu.tw
*Department of Electrical and Computer Engineering
University of California at Santa Barbara
Santa Barbara, California 93106
U. S. A.

Abstract

We present a study of the grating detuning effect on the volume holographic data storage using photopolymer recording material. By using the Bragg matching condition, the angle shift and the decay of the diffraction efficiency of the reconstructed beam is obtained. Then the distortion of the readout page is described. And a method for pre-compensation of the incident angles of the reading beam is presented.

Keywords: Bragg Detuning; Holographic memory; Volume holograms

I. Introduction:

Holographic data storage has been considered as one of the next generation information storage technologies because of its distinct advantages of large storage capacity and fast data access rate [1-3]. The development of suitable recording material remains one of the central challenges in the area of holographic data storage. So far, the most popular materials for volume holographic storage are photorefractive crystals and photopolymers. Photorefractive crystals have been the traditional experimental choice because of its excellent dimensional stability and optical quality. However, it suffers from small dynamic range and low photosensitivity. Photopolymer materials are especially interested because these materials with different compositions are relatively easy to be synthesized. Also, they can be designed to have large index contrasts ($\Delta n \sim 0.01$) and high photosensitivity ($10 \sim 10^4 J/m^2$)[4]. However, these materials have a disadvantage, which is called the shrinkage (or expansion) effect. These are the dimensional changes induced by the chemical reactions during the holographic recording procedure such that the recorded refractive index grating has different grating spacing from that of the light interference fringes. As a result, the Bragg condition for volume holograms is lost and the recorded information cannot be readout completely.

In this paper, we present a study of the grating detuning effect on the volume holographic data storage using photopolymer recording material. By using the Bragg matching condition, the angle shift and the decay of the diffraction efficiency of the reconstructed beam is obtained. Then we discuss the distortion of the readout data page. Finally, a method for pre-compensation by deviating the incident angles of the reading beam from the original writing beam will be proposed.

II. Theoretical Analysis :

1. Angle shift of the reconstructed beam and the degrading of the diffraction efficiency:

Firstly, we consider the shift of Bragg angle due to the changes in the refractive index and the shrinkage of the recording material for the reflection hologram. The schematic diagram of the geometry for the reflection holographic recording is shown in Figure 1. In the figure, the angles θ_{1a} and θ_{2a} are the angle between beam 1 and beam 2 measured outside the medium with respect to the surface of the sample, respectively. Hence, beam 1 is the reference beam and beam 2

is the object beam. Let the original thickness of the recording medium be d and the lateral dimensions be 1. λ is the wavelength for recording and reading lights, and n is the refractive index of sample before recording. Two recording beams were incident into the medium and form an interference pattern. The interference pattern can be stored in the medium and the grating wave vector can be written as:

$$\vec{K} = \frac{2\pi}{\Lambda}\left(\sin\theta_0 \hat{x} + \cos\theta_0 \hat{z}\right) \tag{1}$$

where $\theta_0 = \left(\theta_1 - \theta_2\right)/2$, Λ is the grating spacing and is given by

$$\Lambda = \frac{\lambda}{2n\sin\left(\dfrac{\theta_1 + \theta_2}{2}\right)} \tag{2}$$

where θ_1 and θ_2 are the incident angles of the recording beam 1 and beam 2 inside the medium, respectively. According to the Snell's law, they can be written as $\theta_1 = \cos^{-1}\left(\cos(\theta_{1a})/n\right)$ and $\theta_2 = \cos^{-1}\left(\cos(\theta_{2a})/n\right)$.

Assume that after the holographic grating has been recorded, because of the shrinkage effect, the material dimensions have changed to $\left(1 + \alpha_d\right)\cdot d$ and $\left(1 + \alpha_l\right)\cdot l$, and the refractive index of the material has changed to $\left(1 + \alpha_n\right)\cdot n$, where α_d, α_l and α_n are the dimensional shrinkage and index change rate of the material, respectively. Then, the grating vector will be changed to

$$\vec{K}' = \frac{2\pi}{\Lambda}\left(\frac{1}{1+\alpha_l}\sin\theta_0 \hat{x} + \frac{1}{1+\alpha_d}\cos\theta_0 \hat{z}\right) \tag{3}$$

Thus, the Bragg matching condition has been changed. If we consider the reading beam being incident at the angle identical with that of the original reference beam 1, then there is a phase mismatch ΔK, which can be written as:

$$\Delta K = \frac{2\pi}{\lambda}\left\{-\sqrt{\left[(1+\alpha_n)n\right]^2 - \cos^2\theta_{1a}} - \frac{n}{1+\alpha_d}\left[\sin\theta_1 + \sin\theta_2\right] - \sqrt{\left[(1+\alpha_n)n\right]^2 - \left[\cos\theta_{1a} + \frac{1}{1+\alpha_l}\left(\cos\theta_{2a} - \cos\theta_{1a}\right)\right]^2}\right\} \tag{4}$$

As a result, the diffracted angle will be shift from the Bragg matched case, and diffraction efficiency of the reconstructed beam will also be degraded. The shift of the diffracted angle and its diffraction efficiency can be derived as following:

$$\eta = \frac{|\kappa|^2 \sinh^2(s\cdot t)}{s^2 \cosh^2(s\cdot t) + \left(\dfrac{\Delta K}{2}\right)^2 \sinh^2(s\cdot t)} \tag{5}$$

$$\Delta\theta_d = \cos^{-1}\left(\cos\theta_{1a} + \frac{1}{1+\alpha_l}\left(\cos\theta_{2a} - \cos\theta_{1a}\right)\right) - \theta_{2a} \tag{6}$$

where $s = \sqrt{|\kappa|^2 - \left(\dfrac{\Delta K}{2}\right)^2}$ and $|\kappa| = \dfrac{\pi\Delta n}{2\lambda\sin\theta_1}$.

By Eq.(6), it is seen that the diffracted angle is only dependent on α_l. Assume that the shrinkage parameters of the material are the following : $\alpha_l = 0$, $\alpha_d = -1\%$ and $\alpha_n = 1\%$. Also, the thickness of the material is assumed to be 100μm. According to Eq.(6), the shift of the diffracted angle is equal to zero, which means that the diffracted angle remains not changed if there is no shrinkage along the transverse dimension of the recording material. However, the diffraction efficiency will be degraded and it depends on the recording angles θ_{1a} and θ_{2a}. The simulation results are shown in Figure 2. This figure shows that the diffraction efficiency is degraded significantly for the ranger of $\theta_{1a} = 0 \sim 90^o$ and $\theta_{2a} = 0 \sim 90^o$. Hence, in order to obtain high and uniform diffraction efficiency, we should choose the appropriate recording angles for the hologram.

On the other hand, if there is shrinkage along the transverse dimension of the recording material, i.e. $\alpha_l \neq 0$, then both the diffracted angle and diffraction efficiency are changed. Assume $\alpha_l = -1\%$, then the computer simulation results are shown in Figure 3. Figure 3a shows the relationship between the diffraction efficiency and the incident angles of the recording beams. Figure 3b represents the diffracted angle as a function of the recording angles. It is seen that the diffracted angle shifts significantly and the value of angular shift is from −7.15° to 0.58°, especially when the writing angle of beam 2 is small. In this case, if the position of CCD did not shift with respect to the shift of the diffracted angle, then the diffracted

pattern can not be detected accurately. In other words, the error of output data from CCD detector can be produced by the shrinkage effect of the storage medium. Therefore, for the given parameters of the material, we should calculate the diffraction efficiency and the shift of the diffracted angle. Another way of improving the detuning effect is that we can select the appropriate incident angles of the recording beams to provide a pre-compensation for the reading condition.

2. Shift of the Bragg angle:

Due to the shrinkage effect during the recording procedure, there is a phase mismatch if we read the grating with the incident angle of the original recording beam 1. In order to reconstruct the volume grating with the Bragg matching condition, we should adjust the incident angle of the reading beam. The shift of the incident angle for the reading beam from the reference beam can be derived by using the conservation of grating momentum, and is given as

$$\Delta\theta_r = \cos^{-1}\left(\alpha_n n \cdot \cos\left(\sin^{-1}\left(\frac{\lambda}{2(1+\alpha_n)n\Lambda'}\right) + \tan^{-1}\left(\frac{1+\alpha_d}{1+\alpha_l}\tan\theta_0\right)\right)\right) - \theta_{1a} \tag{7}$$

where Λ' is the new grating spacing after shrinkage and it can be given by

$$\Lambda' = \frac{\Lambda}{\sqrt{\left(\frac{1}{1+\alpha_l}\sin\theta_0\right)^2 + \left(\frac{1}{1+\alpha_d}\cos\theta_0\right)^2}} \tag{8}$$

Now the reading beam satisfies the Bragg condition, and thus the diffraction efficiency can be maintained. But the diffracted angle is changed due to the angle shift of the reading beam, and the shift of the diffracted angle can be derived as

$$\Delta\theta_d = \cos^{-1}\left(\alpha_n n \cdot \cos\left(\sin^{-1}\left(\frac{\lambda}{2(1+\alpha_n)n\Lambda'}\right) - \tan^{-1}\left(\frac{1+\alpha_d}{1+\alpha_l}\tan\theta_0\right)\right)\right) - \theta_{2a} \tag{9}$$

From Eq. (7), it is seen that changes in either the refractive index or the dimension of the recording material will lead to a shift in the Bragg angle. Assume that the parameters of the material are as same as that used for obtaining Fig. 3, the incident angle of the reading beam can be plotted as the function of the incident angles of the recording beams, which is shown in Figure 4a. It shows that the quantity of the Bragg shift is increased with the decreasing incident angle θ_{2a} of the object beam. Figure 4b represents the shift of the diffracted angle as the function of the incident angles of the recording beams. In Figure 4b, it is seen that the shift of the diffracted angle is only dependent on the incident angle of the object beam. For the angular multiplexing technique, the incident angle of the object beam is fixed and we record multiple holograms with the different incident angle of the reference beams. Then, the shift of the diffracted angle for the different angle of writing beams all are same and it also can be predicted according to Eq.(9). Thus in advance we can arrange CCD on the accurate position to detect the diffracted pattern by using the different incident angle of reading beams. Incidentally, a method for pre-compensation by deviating the incident angles of the reading beam from the original recording beam is discussed.

III. Optical Experiments :

The optical setup for measuring the shift of the Bragg angle is shown in Figure 5. An Argon laser beam is expanded and split into two beams. One passes through 4f system as the reference beam and other one is directly incident into the recording material as the object beam. Two beams interfere in the medium and the hologram is record. After the recording procedure, the object beam is blocked and reference beam illuminated the material for reconstructing the hologram. By using the 4f system, we can adjust the incident angle of the reading beam to find the Bragg angle. A detector is arranged in the output plane and measures the diffraction efficiency of the reconstructed beam. When the incident angle of the reading beam is equal to the Bragg angle, then we can obtain the maximum diffraction efficiency from the linear detector. Here, we use DuPont HRF-800-71 photopolymer as the storage medium and we only consider the shrinkage effect of the material along the z-axis and the refractive index change. The parameters of the photopolymer are the following : $n = 1.5285$, $\alpha_n = 0.27\%$, $d = 20\mu m$ and $\alpha_d = -1.5\%$. We recorded the reflection grating with the symmetric incident geometry to minimum the shrinkage effect of the material along the lateral dimension. After recording a grating in the photopolymer, we adjust the incident angle of the reading beam and measured the shift of the Bragg angle.

The computer simulation and optical experimental results are shown in Figure 6. The solid line is the computer simulation result by using Eq.(9) and the circle points are the optical experimental results. It is seen that the result of the optical experiment matches with the computer simulation. In other words, we can predict the shift of Bragg angle according

to Eq.(9). Hence, we can pre-compensate the shift of the diffracted pattern by deviating the incident angle of the reading beam from the original recording beam.

IV. Conclusions :

In summary, we have derived the equations for the detuning effect on the Bragg angle and the diffraction efficiency of the reconstructed image for reflection holograms. A useful guide for selecting appropriate recording beam conditions for reducing the grating detuning effect has been obtained. And a method for compensation by detuning the reading beam from the original recording beam has been proposed. Also, optical experimental demonstration of the detuning effects have been performed using the photo-polymer materials as the recording medium.

Acknowledgements:

References :

[1]. G. T. Sincerbox, ed., *Selected Papers on Holographic Storage*, SPIE Milestone Series, Volume MS 95, The Society of Photo-Optical Instrumentation Engineers, 1994.

[2]. H. Y. Li and D. Psaltis, "Three-dimensional holographic disks", Appl. Opt., Vol. 33, pp. 3764-3774, 1994.

[3]. D. Psaltis and F. Mok, "Holographic memories", Scientific American, Vol. 273, No. 5, pp. 70-76, 1995.

[4]. P. Hariharan, *Optical Holography*, Cambridge University Press, Cambridge, 1991.

[5]. L. Dhar, M. G. Schnoes, T. L. Wysocki, H. Bair M. Schilling and C. Boyd, "Temperature-induced changes in photopolymer volume holograms", Appl. Phys. Lett., Vol. 73, No. 10, pp. 1337-1339, 1998.

[6]. M. G. Schnoes, L. Dhar, M. L. Schilling, S. S. Patel, and P. Wiltzius, "Photopolymer-filled nanoporous glass as a dimensionally stable holographic recording medium", Opt. Lett., Vol. 24, No. 10, pp. 658-660, 1999.

[7]. P. Yeh, *Introduction to photorefractive nonlinear optics*, Chap. 2, Wiley, New York, 1993.
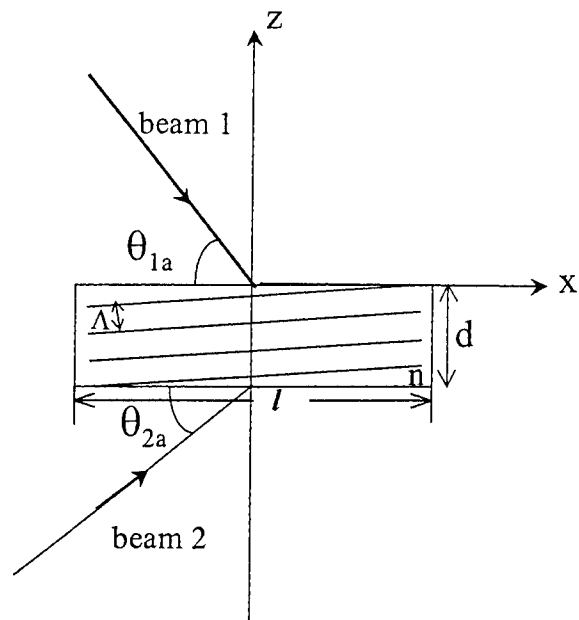
Figure 1 The schematic diagram of the geometry for the reflection hologram.
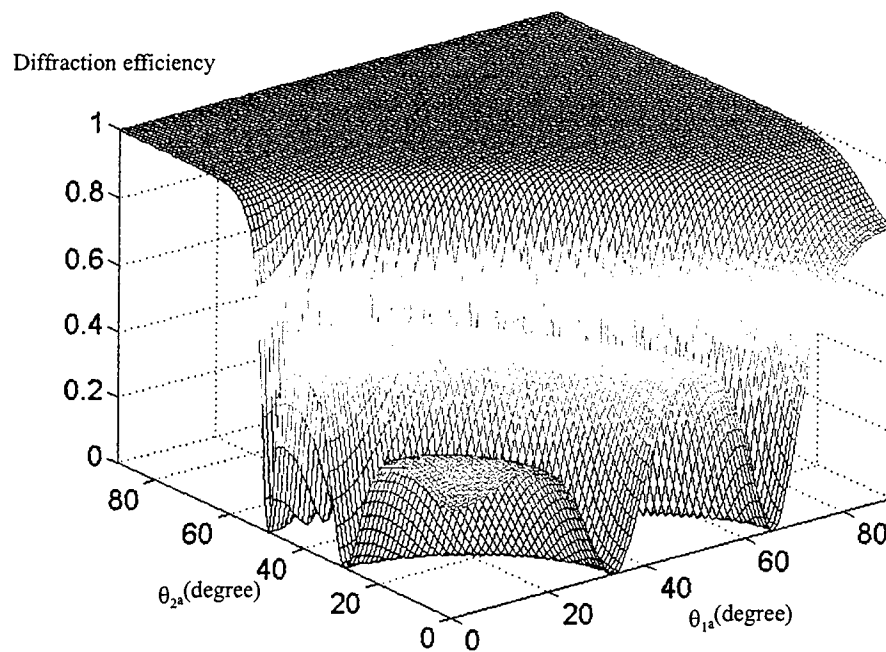
Figure 2 The relationship of the diffraction efficiency and the incident angles of the recording beams.
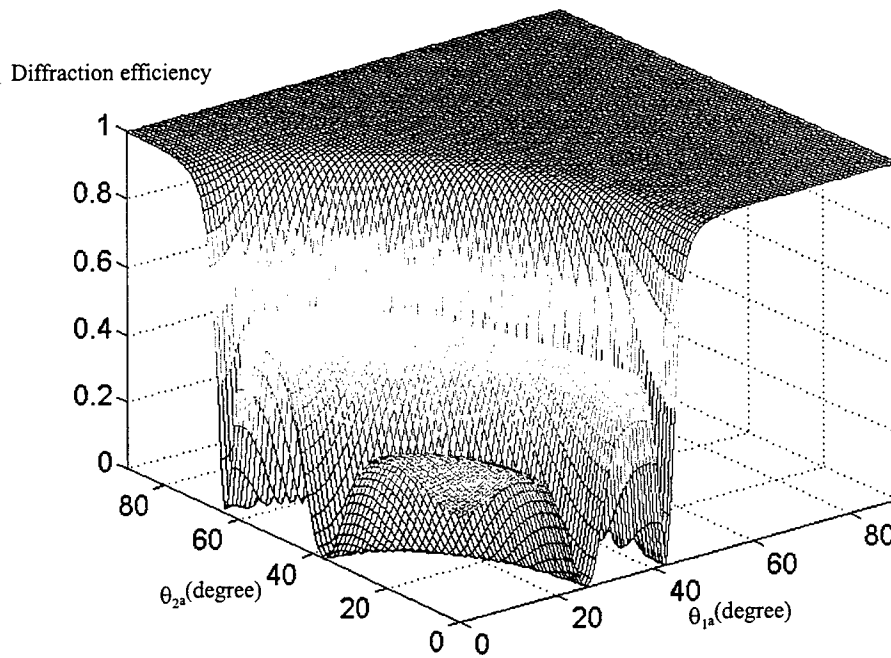
Figure 3a The relationship of the diffraction efficiency and the incident angles of the recording beams.
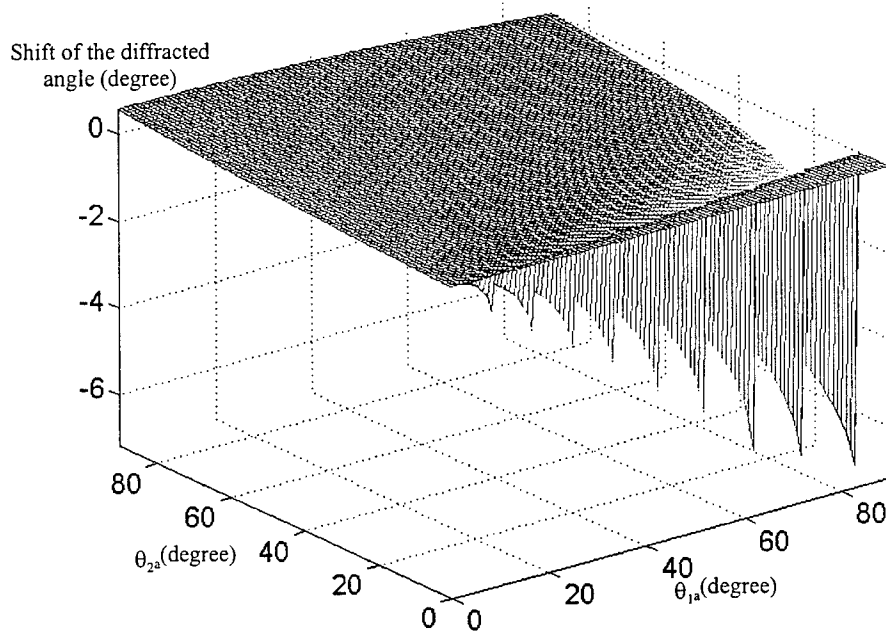
Figure 3b The shift of the diffracted angle as the function of the incident angles of the recording beams.
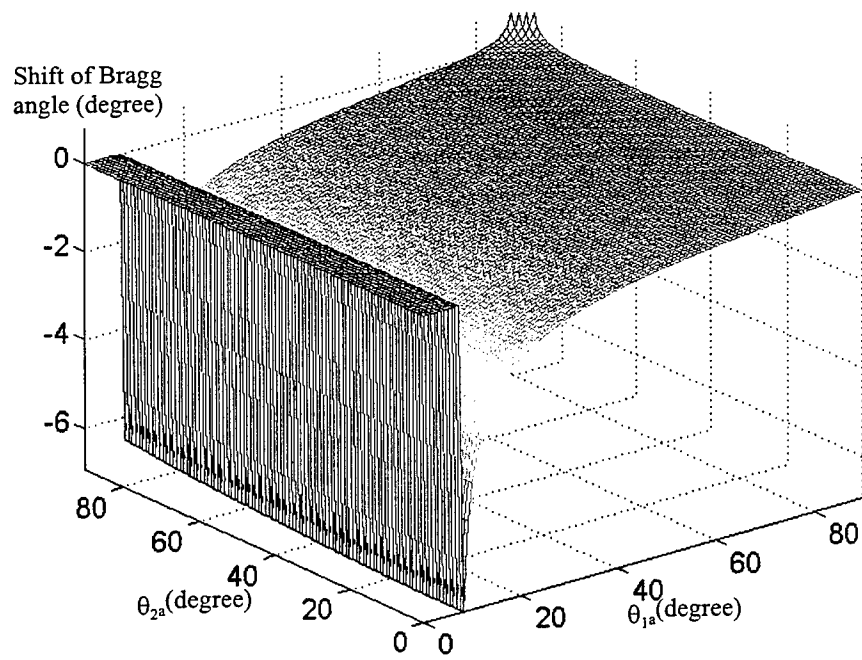
Figure 4a The shift of Bragg angle as the function of the incident angles of the recording beams.
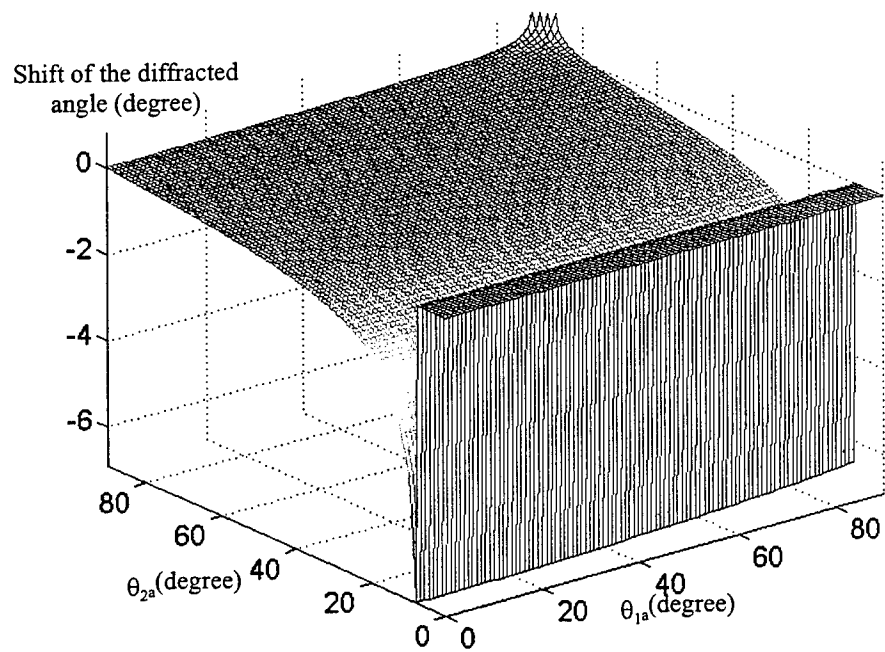
Figure 4b The shift of the diffracted angle as the function of the incident angles of the recording beams.
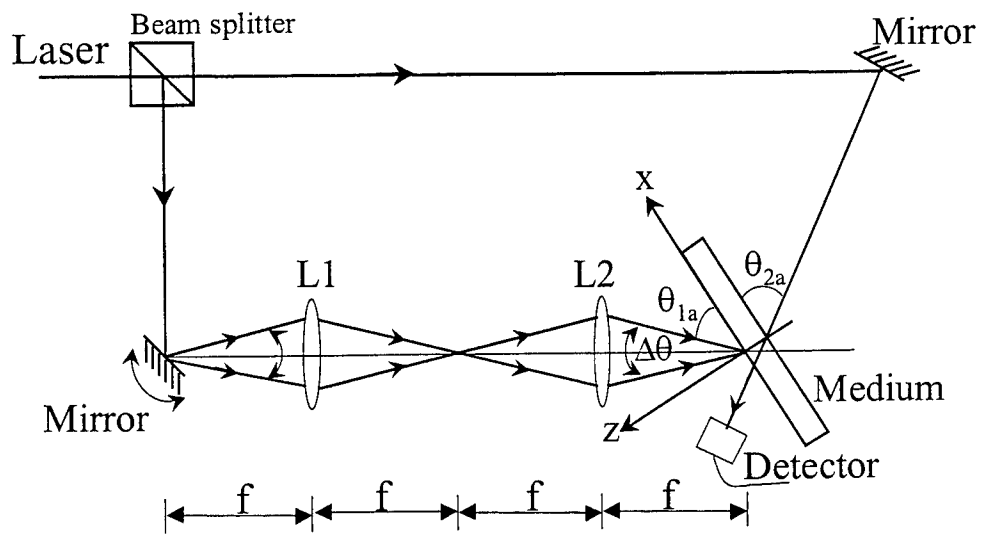
Figure 5 The optical experimental setup of the reflection hologram.
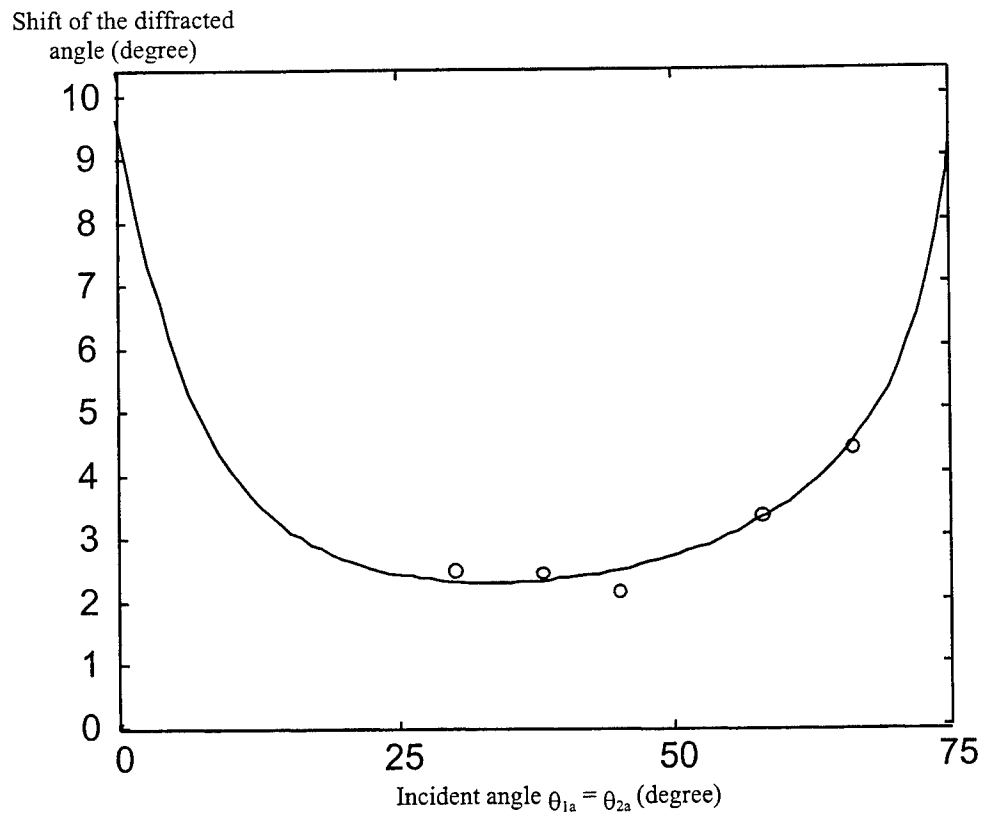
Figure 6 The shift of Bragg angle as the function of the incident angles of the recording beams.

All-optical logic device using bent nonlinear waveguide structure

Yaw-Dong Wu[*][a], Mao-Hsiung Chen[b]
Wuu-Wen Lin[b], Chin-Hsuan Chu[b]

[a] Electronic Engineering of National Kaohsiung Institute of Technology,
Taiwan, R. O. C.

[b] Institute of Electrical Engineering National Sun Yat-Sen University,
Taiwan, R. O. C.

ABSTRACT

We propose an all-optical logic device made of a bent waveguide with a Kerr-like nonlinear interface. It could provide an OR gate, exclusive-OR (XOR) gate and AND gate. We could obtain different transmission results by modifying the bending angle. The numerical simulation results show that the device functions as OR, XOR and AND gates.

Keywords : All-optical logic device, bent nonlinear Y-junction waveguide, Kerr-like nonlinear interface, nonlinear medium, spatial soliton.

1.INTRODUCTION

The interest in nonlinear waveguide designs and their applications has been growing rapidly in recent years. It has been well displayed that all-optical switching and logic gates have potential applications in optical communication and ultrafast signal processing.[1~3] For logic functions, many novel optical devices using nonlinear waveguide technologies have been discussed extensively.[4~8] In 1991, Ogusu[9] and Chang et al.[10] studied the evolution of the TE waves propagating along the nonlinear dielectric interfaces. The numerical results are related to the spatial structure of dielectric interface. Their structures are potentially useful for digital applications such as optical threshold devices.

In this paper, we design an all-optical logic device using a bent nonlinear waveguide structure. The

[*] Correspondence: E-mail : ydwu@cc.nkit.edu.tw

proposed device is based on the propagating characteristics of the nonlinear waveguide. This device could implement three all-optical logic functions (AND, OR and XOR) by adjusting the structure parameters. The numerical results appeared in this paper are calculated by using the beam propagation method (BPM).[11]

2.NUMERICAL METHOD

The proposed structure is shown in Figure 1. The branching angle between the waveguide is 2ϕ in the input section, and the bending angle is θ in the output section. The two input ports A and B must be adequately separated so that the fields in each port do not overlap. Separation distance between input ports A and B is s and the film thickness is 2d.

We consider the case of TE waves as $\varepsilon(x,z,t) = E(x,z)\exp[\ j(\beta k_0 z - wt)]$, where β is the effective index of refraction , k_0 is the wave number in the free space. We have taken the field to be homogeneous in the y direction. Taking into account the slowly varying envelope approximation, we obtain the following equation for E(x,z):

$$2j\beta k_0 \frac{\partial E}{\partial z} + \frac{\partial^2 E}{\partial x^2} + k_0^2[n^2(x,z,|E|^2) - \beta^2]E = 0 \quad , \tag{1}$$

The square of the refractive index for the Kerr-like nonlinear medium is expressed as

$$n_I^2(x,z,|E|^2) = n_{IL}^2 + \alpha_I |E|^2 \qquad \text{I=s,c} \quad , \tag{2}$$

where n_{IL} is the linear refractive index of the nonlinear medium and α_I is the nonlinear coefficient. The subscripts s and c in Eq.(2) are used to denote the substrate and cladding, respectively. For the linear medium in the film, the refractive index n_f is constant.

3.RESULTS AND DISCUSSIONS

All numerical results presented here were calculated with the values: refractive index n_f=2.2888, $n_{sL} = n_{cL} = 2.2885$, d=3 μm, s=24 μm, ϕ =0.275°, $\alpha_I = 1 \times 10^{-8} m^2/V^2$, free space wavelength λ =0.6 μm, waveguide length l_1=2500 μm 、 l_2=1500 μm 、 l_3=2000 μm 、, input power $P_{in} = 25mw/mm$. P_0 is defined as the normalized output power when only one input port is excited. Figure 2 shows the propagating condition of the wave along the nonlinear waveguide for the bending angle θ =0.3°. When only port A is excited, the result is shown in Fig.2(a). The waves propagating along the waveguide are almost well confind in the output port C. With only port B excited, the result is shown in Fig.2(b). It is similar to that of Fig.2(a). Figure 2(c) shows the propagation results when both ports A and B are excited. The optical waves propagating along the waveguide are also well enclosed in the output port C.

Figure 3 shows the propagating condition of the wave along the nonlinear waveguide for the bending angle $\theta = 0.7°$. With either port A or B excited, the results are shown in Figs.3(a) and 3(b), respectively. Those are resembling to that of Figs.2(a) and 2(b) for the bending angle $\theta = 0.3°$. Figure 3(c) shows that the spatial soliton is producing in the nonlinear medium and propagates in the output port D when two input ports A and B are excited simultaneously.

4.CONCLUSIONS

We have designed an all-optical logic device using a bent nonlinear waveguide and the numerical results show that the device functions as AND, OR and XOR gates by simply modifying the bending angle. The proposed device has potential application in all-optical signal processing systems.

REFERENCES

1. J. P. Sabini, N. Finlayson, and G. I. Stegeman, "All optical switching in nonlinear X junctions," *Appl. Phys. Lett.* **55**, pp. 1176-1182, 1992.

2. Y. Silberberg, and B. G. Sfez, "All optical phase and power controlled switching in nonlinear waveguide junctions," *Opt. Lett.* **13**, pp. 1132-1134, 1988.

3. D. R. Heatley, E. M. Wright, and G. I. Stegeman, "Soliton coupler," *Appl. Phys. Lett.* **53**, pp. 172-174, 1988.

4. N. J. Doran, and D. Wood, "Soliton processing element for all-optical switching and logic," *J. Opt. Soc. Am. B* **4**, pp. 1843-1846, 1987.

5. C. C. Yang, "All-optical ultrafast logic gates that use asymmetric nonlinear directional couplers," *Opt. Lett.* **16**, pp. 1641-1643, 1991.

6. L. S. Tamil, and A. K. Jordan, "Synthesis of optical interconnects and logic gates," *Guided-Wave Optoelectronics* 1st, pp. 177-186, 1995.

7. J. M. Jeong, and M. E. Marhic, "All-optical logic gates based on cross-phase modulation in a nonlinear fiber interferometer," *Opt. Commun.* **85**, pp. 430-436, 1991.

8. C. K. Kim, J. M. Jeong, and H. Chang, "All-optical logic functions in a bent nonlinear Y-junction waveguide," *Jpn. J. Appl. Phys.* **37**, pp. 832-836, 1998.

9. K. Ogusu, "Nonlinear wave propagation along a bent nonlinear dielectric interface," *Opt. Lett.* **16**, pp. 312-314, 1991.

10. W. C. Chang, S. F. Liu, and W. S. Wang, "Novel photonic device using nonlinear corner-bend structure," *Electron. Lett.* **27**, pp. 2190-2192, 1991.

11. Y. Chung, and N. Dagli, "Assessment of finite difference beam propagation method," *IEEE J. Quantum Electron.* **26**, pp. 1335-1339, 1990.
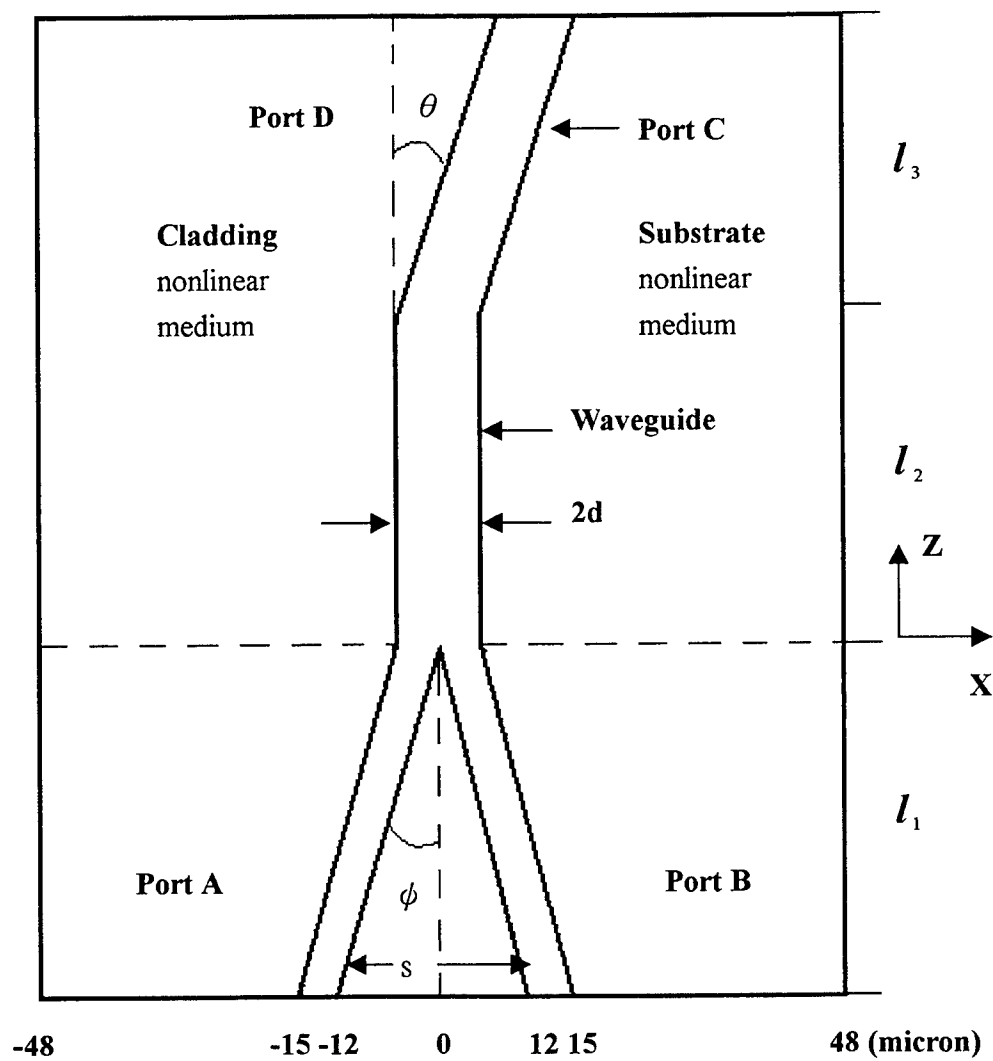
Figure 1. The schematic of the proposed bent nonlinear
waveguide structure.
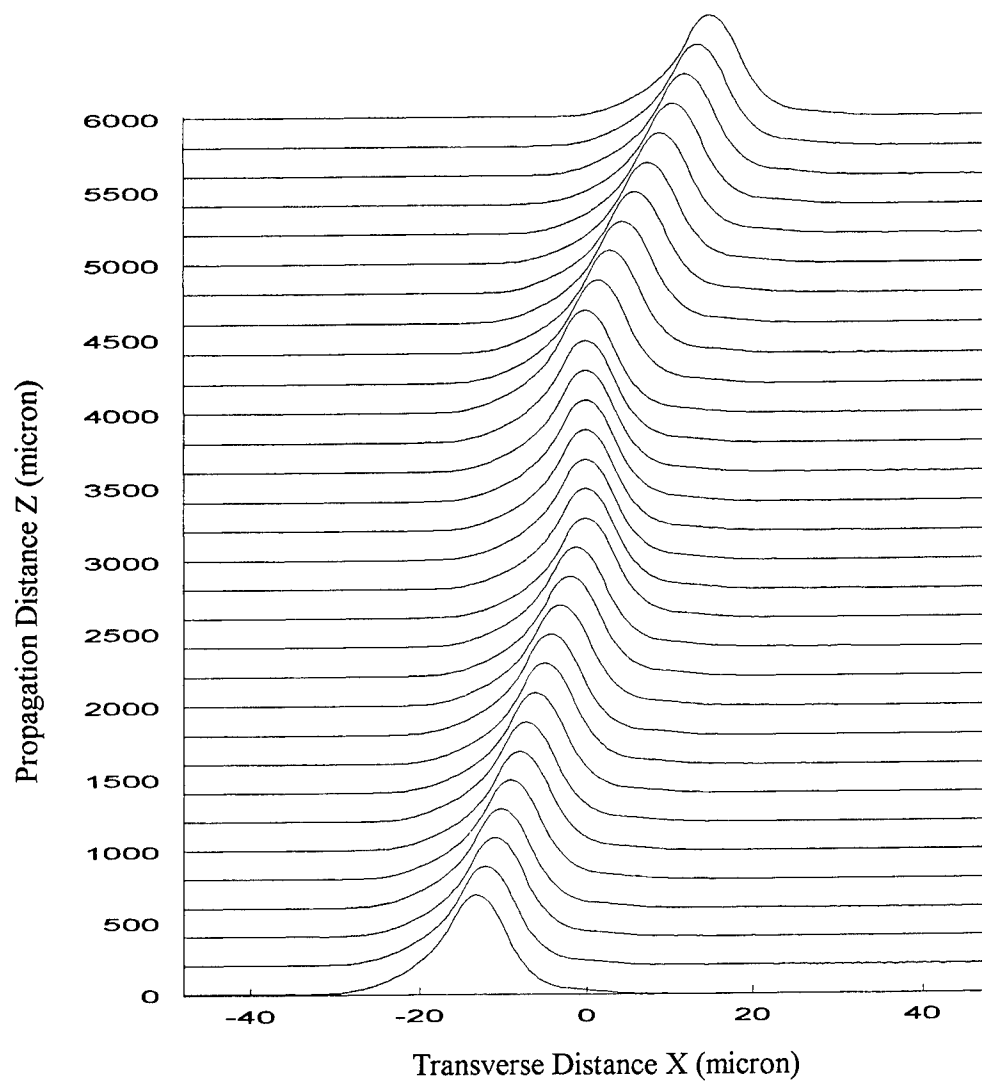
(a)

Figure 2. The typical evolution of the wave along the nonlinear
waveguide for the bending angle θ =0.3°(a)Input：A,
(b)Input：B, (c)Input：A and B.

Transverse Distance X (micron)

(b)

Propagation Distance Z (micron)

Transverse Distance X (micron)
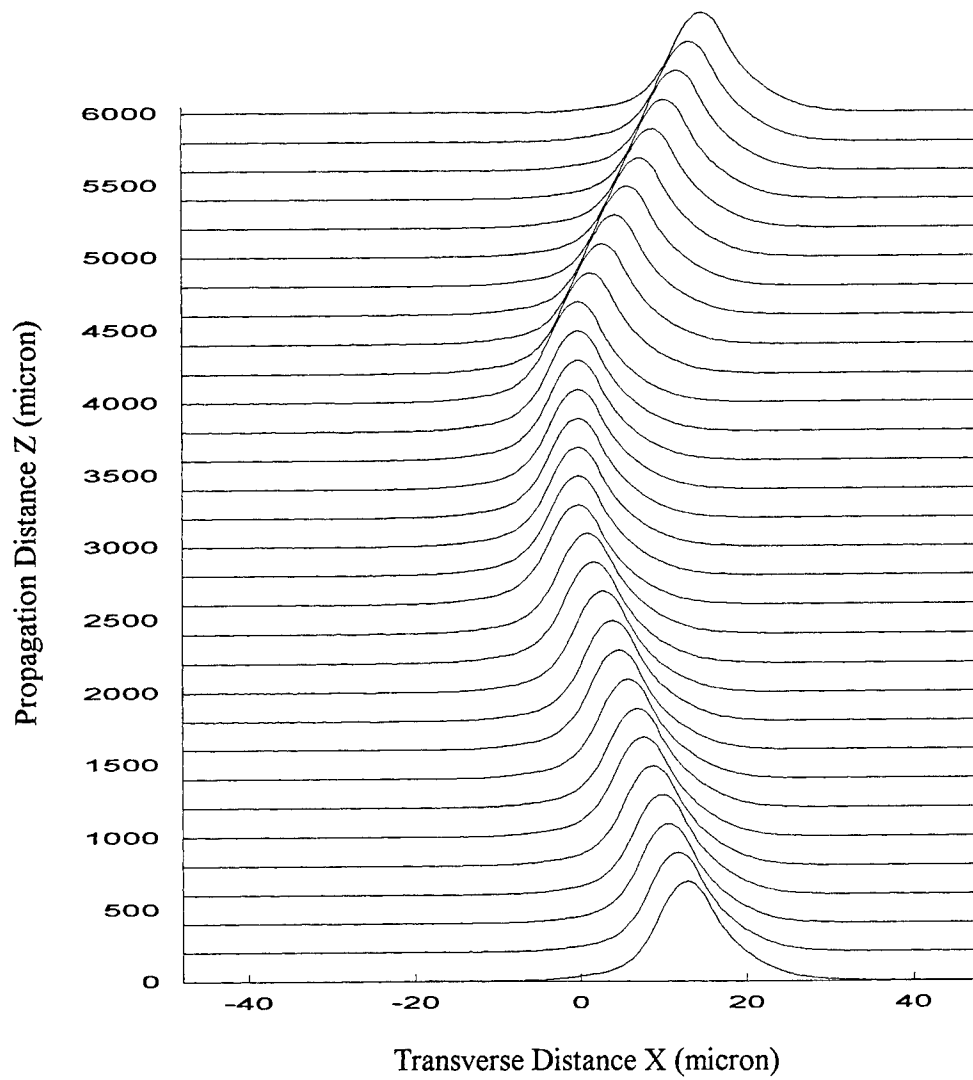
(c)

(a)

Figure 3. The typical evolution of the wave along the nonlinear

waveguide for the bending angle θ =0.7˚(a)Input：A,

(b)Input：B, (c)Input：A and B.
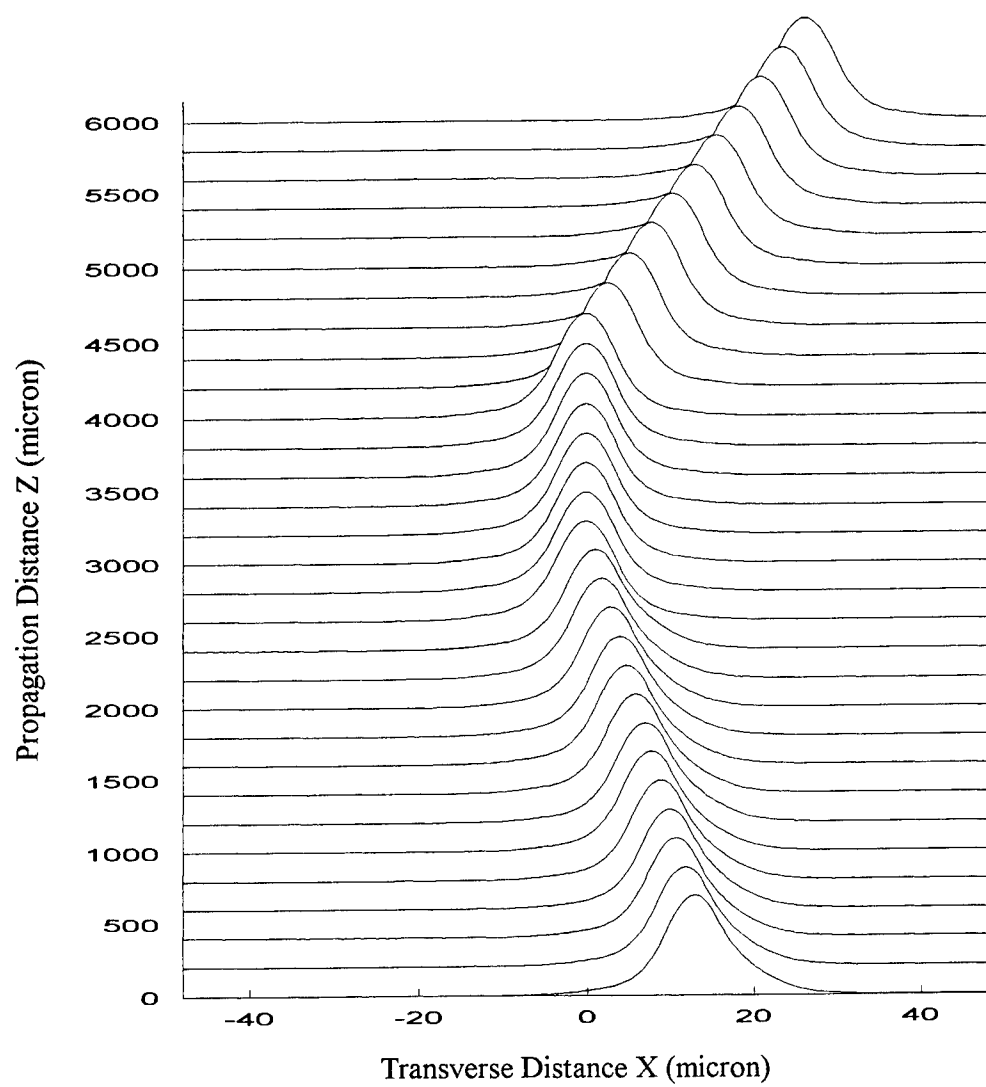
(b)
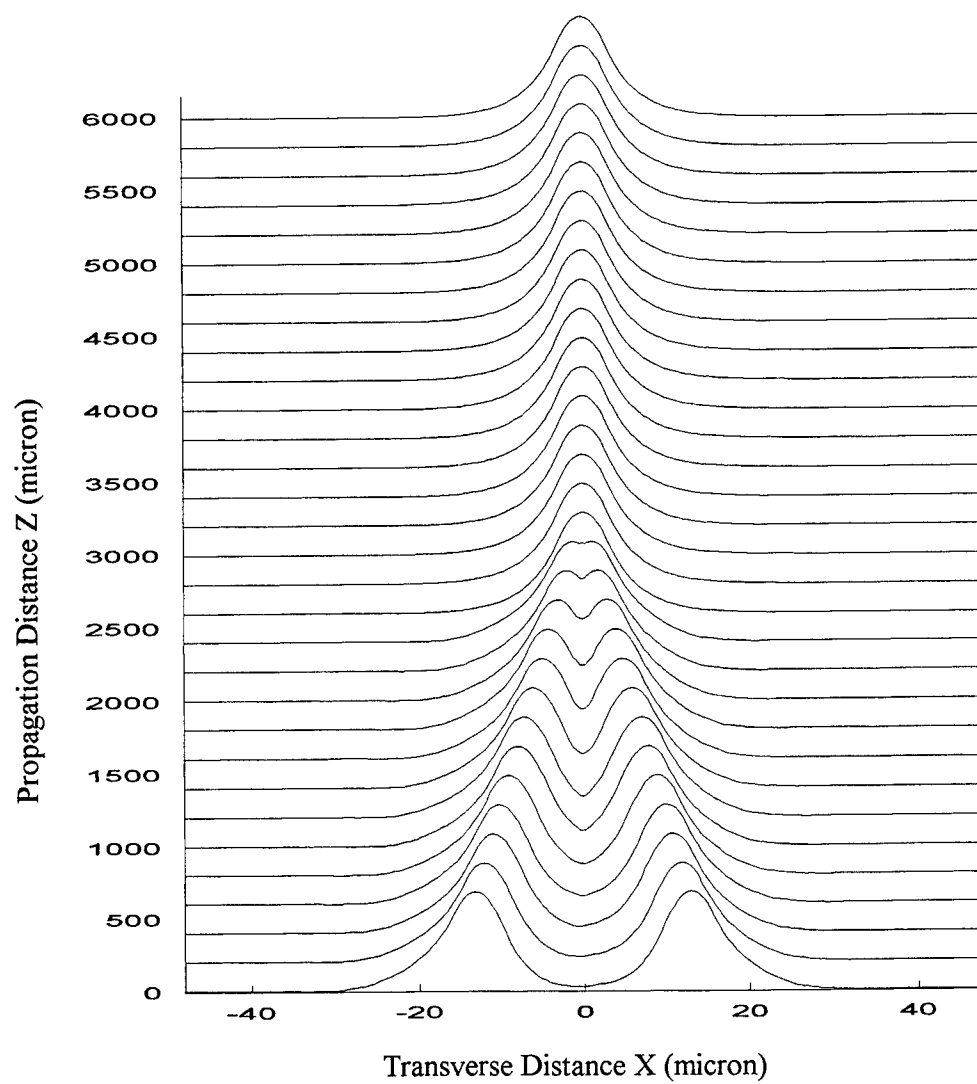
(c)

Nonuniform Quantization for Diffractive Optical Elements design

Chung J. Kuo, Hung C. Chien, Ni Y. Chang & Chia H. Yeh
Signal and Media (SAM) Laboratory
Graduate Institute of Communications Engineering
National Chung Cheng University
Chiayi, Taiwan 62107
Tel:+886-5-2720411-5350
Fax:+886-5-2722702

e-mail:kuo@ee.ccu.edu.tw

ABSTRACT

Recently, the applications of diffractive dptical element (DOE) for commerce and research have become more and more popular. DOE itself has a lot of advantages like small volume, low weight, ease of reproduce and low cost. A DOE actually can be considered as a wavefront modulator, and its performance can also be described as a complex amplitude transmittance. In the past, we usually design a DOE by quantizing the phase of DOE from Gerchberg-Saxton algorithm or other methods with equal etching-depth and etching-width because of the ease of process. In this paper, we present a novel approach for design DOE. We change the element's etching-depth and etching-width nonuniformly. The reason why we strike out this approach is that one who can control the timing within the etching process can make any depth and width after all. Therefore, we have more components of etching-depth and etching-width that can be produced to reach the better diffractive efficiency on output diffraction plane than the conventional etching method. In terms of our proposed method, the conventional method of DOE design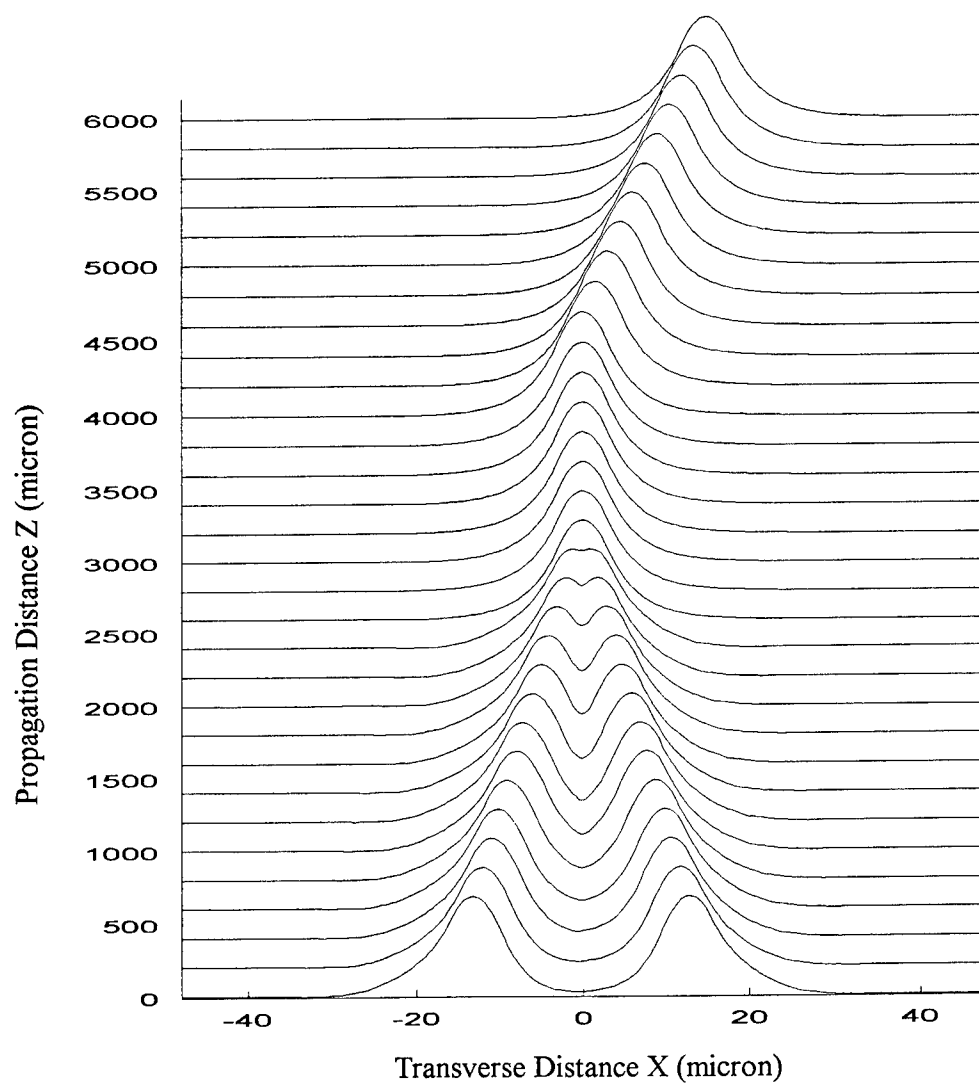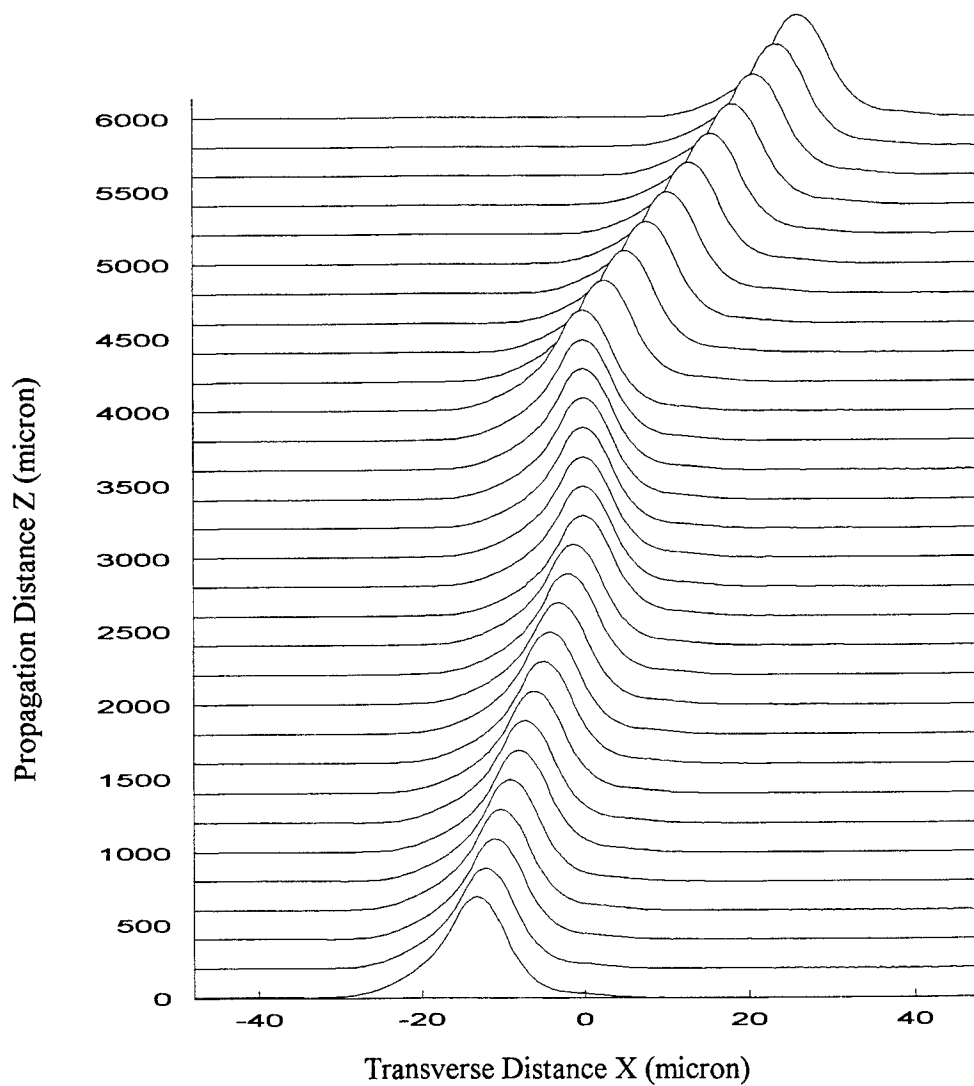 will become a special case of our new approach. According to the minimum etching-depth, we try all possible combinations to find a set of DOEs phases that have better diffractive efficiency than the conventional method can achieve. The DOE design with the proposed method has higher efficiency on output diffraction plane than those achieved by the conventional method

Please correspond with Dr. Chung J. Kuo, Email: kuo@ee.ccu.edu.tw

May 1, 2000

1. INTRODUCTION

In recent years, optical element for diffracting its input light to any desired output position, named as diffraction optical element (DOE), has a lot of advantages like small volume, low weight, ease of reproduce and low cost. The applications of Diffractive Optical Element (DOE) have become more and more popular in optical communications, optical interconnect, integrated optics and optical sensing.

Various methods for DOE design consider only the problem of the DOE with arbitrary phase and use Fourier transform to calculate the approximate light distribution of the DOE. Because the optical system for the DOE design has enormous complexity, there exist a number of mathematical problem that do not yield to analytical solutions. In order to design DOE with high efficiency most methods for DOE design are based on the theory of projection onto convex set (POCS)[1] and far field assumption. In addition, the amplitude transmittance of the designed DOE is set to be a constant. The most-known technique is the iterative Gerchberg-Saxton (G-S) algorithm.[2] In G-S algorithm, the Fourier transform is used to calculate the light field distribution at the output plane of the DOE. The transmittance of a DOE and its output light distribution must satisfy both the input and output domain constraints.

In order to fabricate the DOE with binary grating the constraints of input domain in the G-S algorithm are the corresponding phase of the DOE that procedure of the fabrication can provide. Conventional procedure of DOE fabrication are using uniform etching depth to match the phase function of designed DOE. By the advance technology etching depth of the DOE can be accurate fabricated and more corresponding phase of DOE can be implemented. For this advantage we proposed a new method for DOE design that quantized the phase of DOE nonuniformly. The reason why we strike out this approach is that one who can control the timing within the etching process can make

any depth and width after all. Therefore, we have more components of etching-depth and etching-width that can be produced to reach the better diffractive efficiency on output diffraction plane than the conventional etching method.

The organization of this paper is as follows: Section 2 reviews the theory of G-S algorithm firstly and determines the phase using nonuniform quantization method. Section 3 shows the results (from simulation) of the proposed nonuniform method and compares the results with uniform case. Finally, a conclusion is given in Section 4.

2. THEORY

The schematic of a typical optical system being considered is shown in Figure 1. This optical system is composed of one DOE, an input plane P_1, and an output plane P_2 is placed behind the DOE at distance L. The wave functions at input plane P_1 and output plane P_2 are denoted by U_1 and U_2, respectively, and expressed as

$$U_1(x,y) = A_1(x,y)\exp[j\phi_1(x,y)] \tag{1}$$
$$U_2(f_x,f_y) = A_2(f_x,f_y)\exp[j\phi_2(f_x,f_y)] \tag{2}$$

The z axis is chosen as the optical propagation axis of the system, and the coordinates of the input and output planes are (x,y) and (f_x,f_y), respectively.

We consider the Fourier transformation as the mathematical model for the light propagation and the relation between U_1 and U_2 are

$$U_2(f_x,f_y) = \int\int U_1(x,y)\exp[\frac{j2\pi}{\lambda z}(xf_x+yf_y)]dxdy \tag{3}$$

$$U_1(x,y) = \int\int U_2(f_x,f_y)\exp[\frac{-j2\pi}{\lambda z}(xf_x+yf_y)]df_xdf_y \tag{4}$$

where z is the propagation distance, and λ is the wavelength.

The synthesis problem arise when the Fourier transform[3] of a DOE has certain desirable properties as its output diffraction pattern itself must satisfy certaion constraints. However, it is not easy to find a Fourier transform pair[4] (or the pair does not exist) that satisfies all the constraints in both input and output planes. The iteration method is shown to be very powerful in solving the problems above mentioned. There are many variations in the iterative method and not limited to single fixed algorithm. The most known algorithm is the G-S algorithm. The block diagram of the G-S algorithm is shown in Figure 2. The G-S algorithm is an effective method for recovering the phase. It involves iterative Fourier transformations back and forward between input and output domains and is performed as follows:

1. Given the desired output diffraction pattern and found the phase function of DOE in input plane.

2. Match the constraints of the input domain and get the new phase function of DOE in input plane.

3. Fourier transform the phase function of DOE in step 2 and get the output diffraction pattern in output plane.

4. Match the constraints of output domain.

5. Repeat the Steps 1 to 4 until satisfies all constraints in the input and output domains.

The quantized phase method for DOE design is a significant problem. It determines the performance of DOE. Figures 3 and 4 show the uniform and nonuniform quantization cases. We find that the nonuniform case that can provide the phase function that is similar to the phase function without quantization.

3. SIMULATION

In this section, we first compare the results of our proposed method with those in the past. Then we show the far-field patterns of each methods and compare the difference. Summaries of the optical system parameter are shown below:

1. Light beam : uniform beam

2. Index of reflection : 1.5

3. Incident wavelength : 0.85nm

4. DOE size : 64 × 64 pixel

The simulation result shows in Table 1. It's well known that G-S algorithm is very sensitive to the initial guess, so we experimented with ten different random phases in order to find the global optimum. We see that the improvements between proposed and conventional under 8 phase levels are relatively small and the average improvement is 0.77%. On the other hand, we can get much more improvements in 4 phase levels and the improvement is 10.30%.

Figure 5 shows the far-field patterns. (a) far-field pattern after 4 uniform phase levels. (b) far-field pattern after 8 uniform phase levels. (c) far-field pattern after 4 non-uniform phase levels. (d) far-field pattern after 8 non-uniform phase levels. We see that (b) and (d) are almost the same because their efficiency are close, while in (a) and (c), the differences are so obvious especially in the four corners and sidelobs.

Figure 6 shows the difference of phase functions. (a) difference of phase function between uniform and non-uniform quantized phase in 4 level case. (b) difference of phase function between uniform and non-uniform quantized phase in 8 level case. The phases in many pixels are changed in (a), while in (b), there are just several pixel changes. It implies that the ranges we can improve the DOE efficiency under 4 phase levels using non-uniform quantization are larger than that under 8 phase levels using non-uniform quantization.

4. CONCLUSION

Based on the POCS technique and Fourier transformation, the G-S algorithm is proposed to design DOE. We use the nonuniform quantized method to quantize the phase of DOE and the design DOE that can better achieve the desired pattern compared to the uniform quantized method. For microlens design, 10.3% light energy increase is obtained at the desired output position by our method compared with the uniform quantized method.

REFERENCES

1. G. Strang, *Introduction to Applied Mathematics* , Wellesley, 1986
2. R. W. Gerchberg and W. O. Saxton, "A Particaular algorithm for the determination of phase from image plane picture," *Optik 35*, pp. 237–246, 1972
3. F. Wyrowski and O. Bryngdahl, "Iterative Fourier-Transform Algorithm Applied to Computer Holograms," *J. Opt. Soc. Am. A 5*, pp. 1058–1065, 1988
4. J. W. Goodman,*Introduction to Fourier Optics*, McGraw-Hill, New York, 1968

	G-S Algorithm without quantization	Proposed 4 Level	Conventional 4 Level	Improved Efficiency	Proposed 8 Level	Conventional 8 Level	Improved Efficiency
	Efficiency	Efficiency	Efficiency	%	Efficiency	Efficiency	%
Phase1	0.8927	0.7016	0.6421	9.27	0.8383	0.8322	0.73
Phase2	0.8929	0.7093	0.6514	8.89	0.8386	0.8309	0.93
Phase3	0.8924	0.7016	0.6421	9.27	0.8383	0.8322	0.73
Phase4	0.8863	0.7148	0.6355	12.48	0.8321	0.8281	0.48
Phase5	0.8929	0.7093	0.6514	8.89	0.8368	0.8309	0.71
Phase6	0.8929	0.7093	0.6514	8.89	0.8368	0.8309	0.71
Phase7	0.8863	0.7148	0.6355	12.48	0.8321	0.8281	0.48
Phase8	0.8861	0.7107	0.6347	11.97	0.8302	0.8275	0.33
Phase9	0.8861	0.7107	0.6347	11.97	0.8302	0.8275	0.33
Phase10	0.8902	0.7011	0.6437	8.92	0.8418	0.8228	2.31
Average	0.8899	0.7083	0.6423	10.30	0.8355	0.8291	0.77
Maximum	0.8929	0.7148	0.6514	12.48	0.8418	0.8322	0.93

Table 1. simulation results.

P_1

P_2

DOE

L
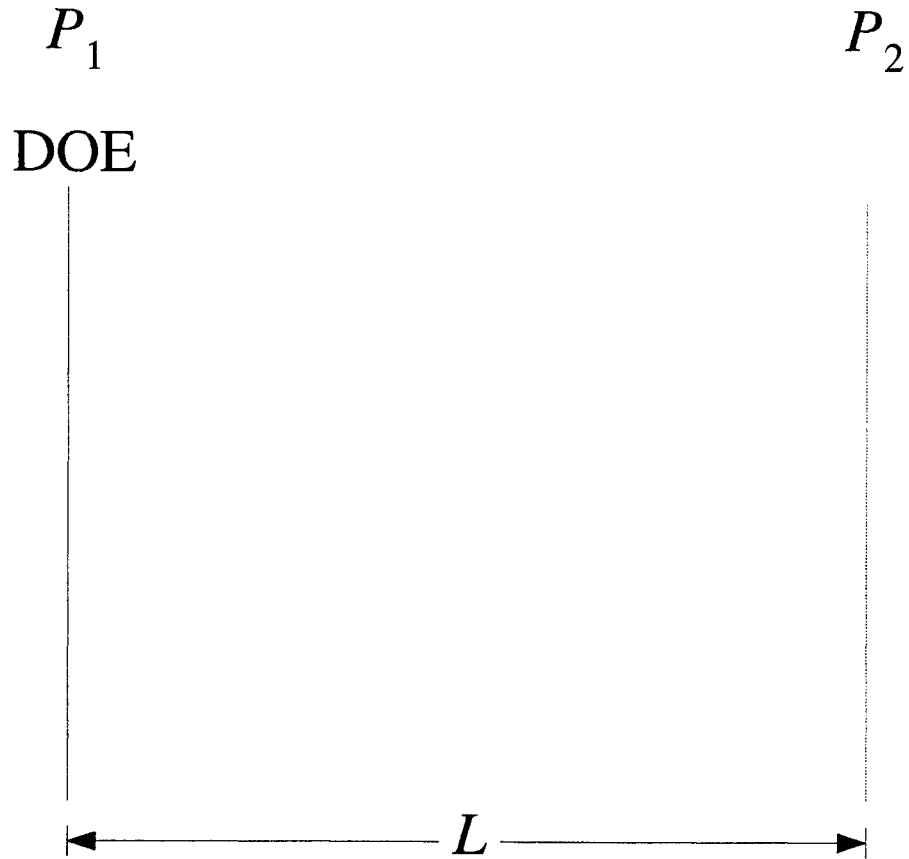
Figure 1. optical system
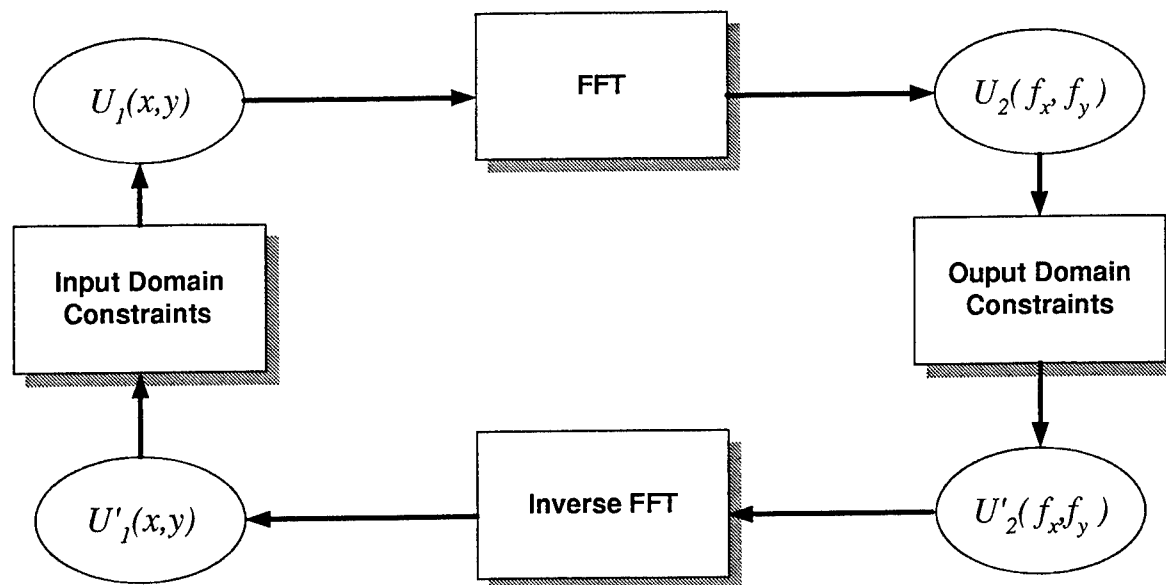
$U_1(x,y)$: wave function at input plane
$U'_1(x,y)$: wave function at input plane before adding constraints
$U_2(f_x,f_y)$: wave function at output plane
$U'_2(f_x,f_y)$: wave function at output plane with constraints

Figure 2. G-S algorithm
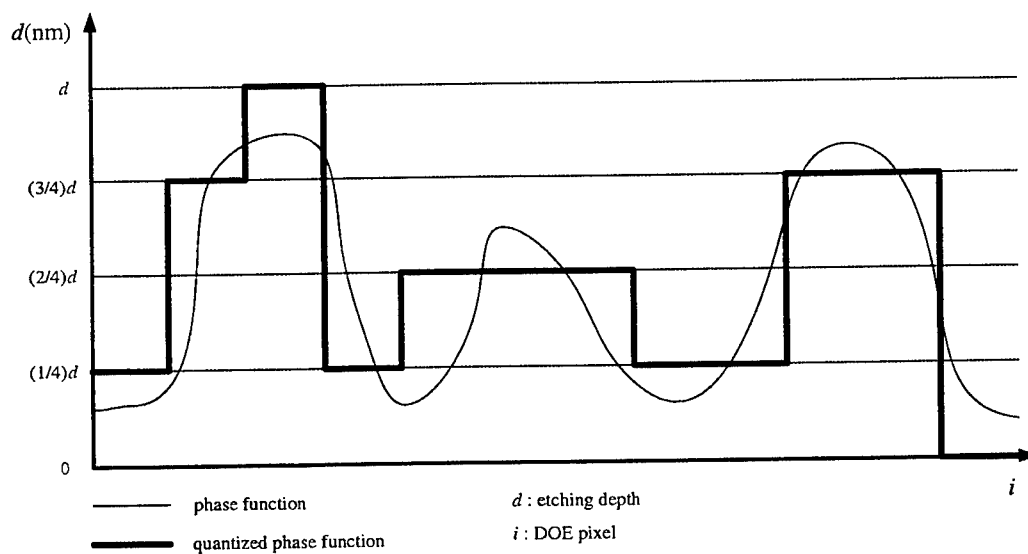
Figure 3. uniform quantization
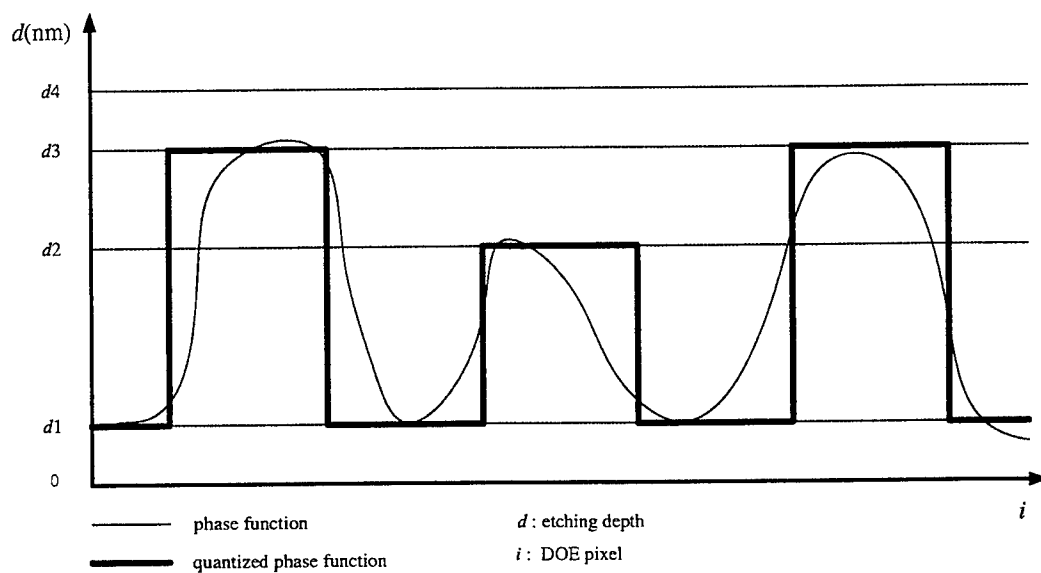
Figure 4. nonuniform quantization

(a)

(b)

(c)

(d)
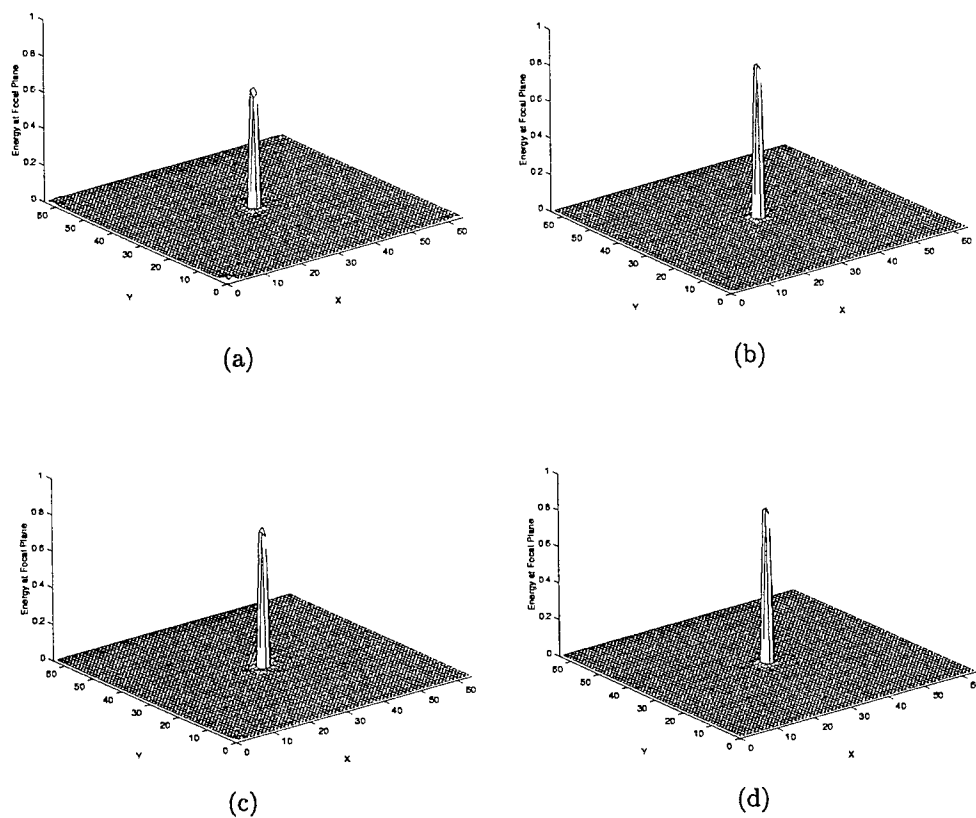
Figure 5. (a) far-field pattern after 4 uniform phase levels. (b) far-field pattern after 8 uniform phase levels. (c) far-field pattern after 4 nonuniform phase levels. (d)far-field pattern after 8 nonuniform phase levels

(a)

(b)
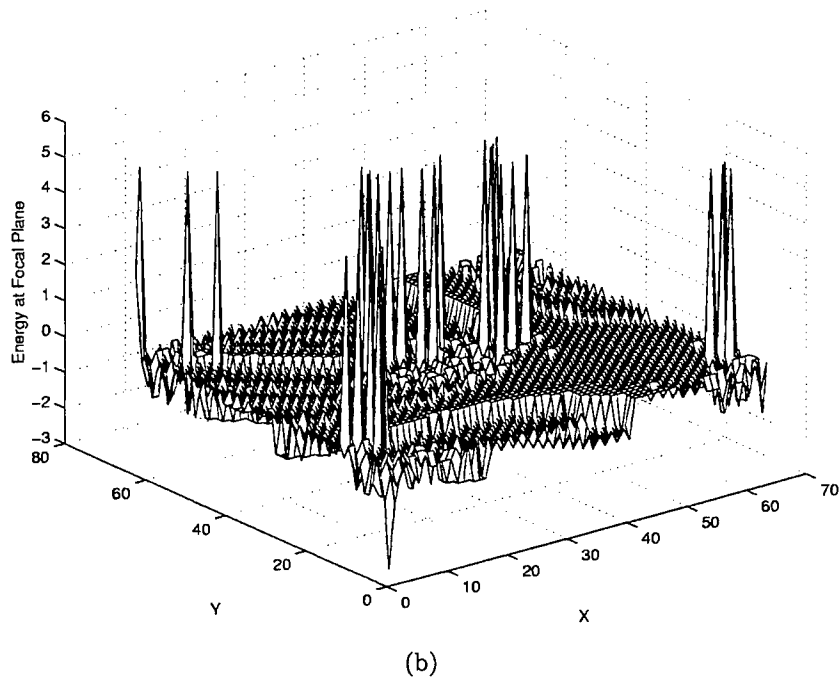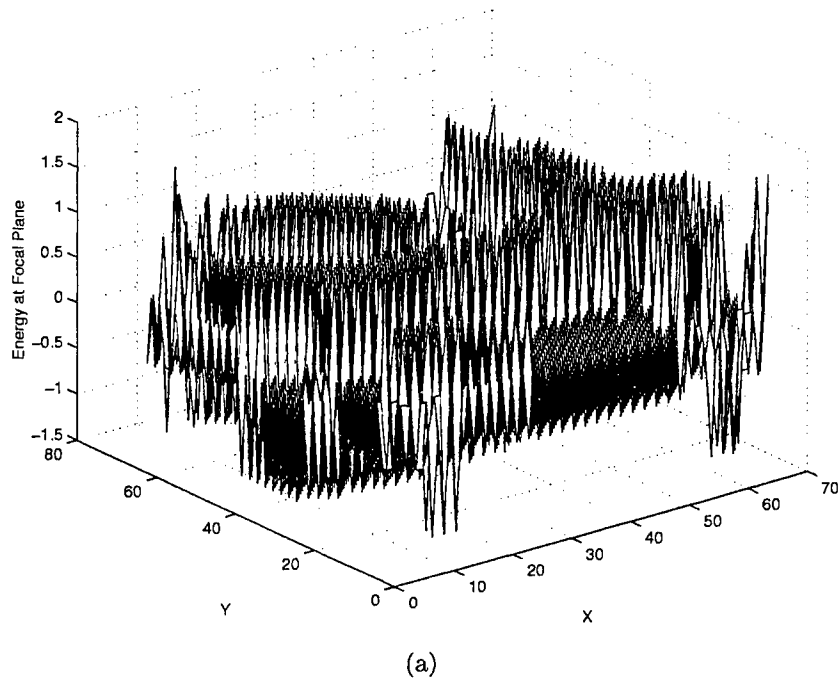
Figure 6. (a) difference of phase function between uniform and nonuniform quantized phase in 4 levels case. (b) difference of phase function between uniform and nonuniform quantized phase in 8 levels case.

Poster Session

Comparison of Two 1550 nm Ultra Narrow-Band Optical Infinite Impulse Response Filters for High-Speed Optical Signal Processing

Shyh-Lin Tsao* and Te-Yu Chen

Department of Electrical Engineering, Yuan Ze University

Chung-Li,Taiwan, R.O.C.

ABSTRACT

Comparison of the frequency responses of two high-speed optical fiber processing elements is reported. The two filters we considered are a two-loops optical infinite impulse response (IIR) filter and a three-loops optical IIR filter. The theoretical models of these two kinds of optical IIR band pass filters are built up. Some suitable coupling coefficients are searched for simulating the narrow band-pass filters. The frequency responses under different conditions are analyzed. The theoretical models can provide parameter evaluation for experimental design. A higher design flexibility can be given by the three-loops optical IIR filter. These filters can be implemented with PIC (photonic IC) techniques and applied for optical data signal processing.

Keywords : Optical Data Storage, Optical Signal Processing, Optical IIR filter, Optical Fiber Communication

1.INTRODUCTION

In the next generation memory system, high capacity optical data storage will be the future trend. Many methods, such as hologram, CD-R, DVD, are studied for high capacity data storage above Giga-byte[1-3]. In recent years, some fast data access and optical signal processing methods are extensively reported[4-8]. Especially reading optically storaged data by fiber, then using time-space-conversion optical signal processing attract a lot of attentions[5].

Promising progress is shown in high speed optical communication systems developments recently[9-18]. The fiber optic recirculating delay line is one of the basic optical signal elements generally being studied. We also reported some various designs and applications for high speed signal processing[19-21]. Ultra fast signal processing over 100 Gbps is difficult to do by traditional electric signal processing circuit. This optical digital signal processor (OPSP) may be applied in high-speed DVD data storage systems as shown in Fig.1. In this paper, we design and analyze two ultra narrow-band optical infinite impulse response IIR filters for high-speed optical signal processing. Those two designed narrow-band optical IIR filters are operating at wavelength of 1550nm. The center of the narrowband filter is located at 100GHz. We use Z-transform to analyze the frequency responses of these two IIR filters: two-loops optical IIR filter and three-loops optical IIR filter. The two theoretical models for comparing their frequency responses are built up. Optimal coupling coefficients are sorted for simulating narrow bandwidth optical band pass filters.

Correspondence : Email : jimmy@saturn.yzu.edu.tw ; Telephone : 886-3-4638800-424 ; Fax : 886-3-4638355

2. THEORETICAL MODELS

We use Z-transform techniques to build up the theoretical model of a two-loops optical IIR filter and a three-loops optical IIR filter, respectively in this section. Assume these two kinds filters are linearly time-invariant systems and no temperature fluctuation effect, we derive the transfer functions as following.

2.1 *Two-Loops Optical IIR Filter*

The schematic diagram of two-loops optical IIR filter with two 3×3 optical couplers and four optical delay lines is shown in Fig.2. In Fig.3, we modeled the equivalent theoretical model by signal flow diagram. The signal can be represented as Eq. (1) to Eq. (6)

$$X_1(Z) = K_3[I_1(Z) + r_{X_4} Z^{-X_4} X_4(Z) + r_{X_3} Z^{-X_3} X_3(Z)] \tag{1}$$

$$X_2(Z) = K_2[I_1(Z) + r_{X_4} Z^{-X_4} X_4(Z) + r_{X_3} Z^{-X_3} X_3(Z)] \tag{2}$$

$$X_3(Z) = K_6[I_2(Z) + r_{X_2} Z^{-X_2} X_2(Z) + r_{X_1} Z^{-X_1} X_1(Z)] \tag{3}$$

$$X_4(Z) = K_5[I_2(Z) + r_{X_2} Z^{-X_2} X_2(Z) + r_{X_1} Z^{-X_1} X_1(Z)] \tag{4}$$

$$O_1(Z) = K_1[I_1(Z) + r_{X_4} Z^{-X_4} X_4(Z) + r_{X_3} Z^{-X_3} X_3(Z)] \tag{5}$$

$$O_2(Z) = K_4[I_2(Z) + r_{X_2} Z^{-X_2} X_2(Z) + r_{X_1} Z^{-X_1} X_1(Z)] \tag{6}$$

$I_1(Z)$ and $I_2(Z)$ are the input signals at the input ports. $O_1(Z)$ and $O_2(Z)$ are the output signals at two ports. $X_1(Z)$, $X_2(Z)$, $X_3(Z)$, $X_4(Z)$ represent the input signals of delays Z^{-X_1}, Z^{-X_2}, Z^{-X_3}, Z^{-X_4}, respectively. The coupling coefficients and path transmittive coefficients for each optical output are represented as $K_{j(j=1\sim6)}$ and $r_{Xj(j=1\sim6)}=1$, respectively.

The relationship of the above six equations can be simplified as

$$X_1(Z) = K_3[I_1(Z) + \frac{K_5}{K_6} r_{X_4} Z^{-X_4} X_3(Z) + r_{X3} Z^{-X_3} X_3(Z)] \tag{7}$$

$$X_3(Z) = K_3[I_2(Z) + \frac{K_2}{K_3} r_{X_2} Z^{-X_2} X_1(Z) + r_{X1} Z^{-X_1} X_1(Z)] \tag{8}$$

Substitute Eq. (8) into Eq. (7), we find

$$X_1(Z) = \frac{K_3[I_1(Z) + (K_5 r_{X_4} Z^{-X_4} + K_6 r_{X_3} Z^{-X_3}) I_2(Z)]}{\Delta} \tag{9}$$

and

$$\Delta = 1 - K_3 K_6 r_{X_1} r_{X_3} Z^{-(X_1+X_3)} - K_3 K_5 r_{X_1} r_{X_4} Z^{-(X_1+X_4)} - K_2 K_6 r_{X_2} r_{X_3} Z^{-(X_2+X_3)} - K_2 K_5 r_{X_2} r_{X_4} Z^{-(X_2+X_4)} \tag{10}$$

Similarly, we can write $X_3(Z)$ as

211

$$X_3(Z) = \frac{K_6\left[I_2(Z) + \left(K_3 r_{X_1} Z^{-X_1} + K_2 r_{X_2} Z^{-X_2}\right)I_1(Z)\right]}{\Delta} \tag{11}$$

Then the output signals can be represented as

$$O_1(Z) = \frac{K_1\left[I_1(Z) + \left(K_5 r_{X_4} Z^{-X_4} + K_6 r_{X_3} Z^{-X_3}\right)I_2(Z)\right]}{\Delta} \tag{12}$$

$$O_2(Z) = \frac{K_4\left[I_2(Z) + \left(K_3 r_{X_1} Z^{-X_1} + K_2 r_{X_2} Z^{-X_2}\right)I_1(Z)\right]}{\Delta} \tag{13}$$

In this paper, we assume no input signal launched to port I_2. Therefore, the above two transfer funtions can be simplified as

$$H_{11}(Z) = \frac{O_1(Z)}{I_1(Z)} = \frac{K_1}{\Delta} \tag{14}$$

$$H_{12}(Z) = \frac{O_2(Z)}{I_1(Z)} = \frac{K_4\left(K_3 r_{X_1} Z^{-X_1} + K_2 r_{X_2} Z^{-X_2}\right)}{\Delta} \tag{15}$$

2.2 Three-Loops Optical IIR Filter

The schematic diagram of a three-loops optical IIR filter is shown in Fig.4. This filter includes two 4×4 optical couplers and six optical delay lines. The schematic diagram of theoretical model of this filter is illustrated in Fig.5. Similarly, we consider the nodal signals $X_1(Z)$, $X_2(Z)$, $X_3(Z)$, $X_4(Z)$, $X_5(Z)$, and $X_6(Z)$, represent the input signals of the phase delays Z^{-X_1}, Z^{-X_2}, Z^{-X_3}, Z^{-X_4}, Z^{-X_5}, Z^{-X_6}, respectively. The transmittive coefficient of each delay path $r_{X_{j(j=1\sim8)}}$ is set to be 1. The coupling coefficient of each optical output is represented as $K_{j(j=1\sim8)}$ which is a positive real number. Because of energy conservation, the signal in each coupler should satisfy $K_1+K_2+K_3+K_4+K_5+K_6+K_7+K_8$ = (1-L), and L means the intrinsic loss of optical couplers. In this paper, we assume the intrinsic loss is small enough that can be neglected. According to Fig.5, the transfer functions can be derived according to the following equations as

$$X_1(Z) = K_4[I_1(Z) + r_{X_4} Z^{-X_4} X_4(Z) + r_{X_5} Z^{-X_5} X_5(Z) + r_{X_6} Z^{-X_6} X_6(Z)] \tag{16}$$

$$X_2(Z) = K_3[I_1(Z) + r_{X_4} Z^{-X_4} X_4(Z) + r_{X_5} Z^{-X_5} X_5(Z) + r_{X_6} Z^{-X_6} X_6(Z)] \tag{17}$$

$$X_3(Z) = K_2[I_1(Z) + r_{X_4} Z^{-X_4} X_4(Z) + r_{X_5} Z^{-X_5} X_5(Z) + r_{X_6} Z^{-X_6} X_6(Z)] \tag{18}$$

$$X_4(Z) = K_8[I_2(Z) + r_{X_1} Z^{-X_1} X_1(Z) + r_{X_2} Z^{-X_2} X_2(Z) + r_{X_3} Z^{-X_3} X_3(Z)] \tag{19}$$

$$X_5(Z) = K_7[I_2(Z) + r_{X_1} Z^{-X_1} X_1(Z) + r_{X_2} Z^{-X_2} X_2(Z) + r_{X_3} Z^{-X_3} X_3(Z)] \tag{20}$$

$$X_6(Z) = K_6[I_2(Z) + r_{X_1} Z^{-X_1} X_1(Z) + r_{X_2} Z^{-X_2} X_2(Z) + r_{X_3} Z^{-X_3} X_3(Z)] \tag{21}$$

$$O_1(Z) = K_1[I_1(Z) + r_{X_4} Z^{-X_4} X_4(Z) + r_{X_5} Z^{-X_5} X_5(Z) + r_{X_6} Z^{-X_6} X_6(Z)] \tag{22}$$

$$O_2(Z) = K_5[I_2(Z) + r_{X_1}Z^{-X_1}X_1(Z) + r_{X_2}Z^{-X_2}X_2(Z) + r_{X_3}Z^{-X_3}X_3(Z)] \tag{23}$$

Similarity, we deduce the above equations and find that

$$X_1(Z) = K_4[I_1(Z) + r_{X_4}Z^{-X_4}X_4(Z) + r_{X_5}\frac{K_7}{K_8}Z^{-X_4}X_5(Z) + r_{X6}\frac{K_6}{K_8}Z^{-X_4}X_6(Z)] \tag{24}$$

$$X_4(Z) = K_8[I_2(Z) + r_{X1}Z^{-X_1}X_1(Z) + r_{X_2}\frac{K_3}{K_4}Z^{-X_1}X_2(Z) + r_{X3}\frac{K_2}{K_4}Z^{-X_1}X_3(Z)] \tag{25}$$

From the above two equations, $X_1(Z)$ can be derived as

$$X_1(Z) = \frac{K_4\left[I_1(Z) + \left(K_8 r_{X_4}Z^{-X_4} + K_7 r_{X_5}Z^{-X_5} + K_6 r_{X_6}Z^{-X_6}\right)I_2(Z)\right]}{\Delta'} \tag{26}$$

and

$$\begin{aligned}
\Delta' = 1 &- K_4 K_8 r_{X_1} r_{X_4}Z^{-(X_1+X_4)} - K_4 K_7 r_{X1} r_{X_5}Z^{-(X_1+X_5)} - K_4 K_6 r_{X_1} r_{X_6}Z^{-(X_1+X_6)} - K_3 K_8 r_{X_2} r_{X_4}Z^{-(X_2+X_4)} \\
&- K_3 K_7 r_{X_2} r_{X_5}Z^{-(X_2+X_5)} - K_3 K_6 r_{X_2} r_{X_6}Z^{-(X_2+X_6)} - K_2 K_8 r_{X_3} r_{X_4}Z^{-(X_3+X_4)} - K_2 K_7 r_{X_3} r_{X_5}Z^{-(X_3+X_5)} \\
&- K_2 K_6 r_{X_3} r_{X_6}Z^{-(X_3+X_6)} \tag{27}
\end{aligned}$$

The $X_4(Z)$ can also be derived as

$$X_4(Z) = \frac{K_8\left[I_2(Z) + \left(K_4 r_{X_1}Z^{-X_1} + K_3 r_{X_2}Z^{-X_2} + K_2 r_{X_3}Z^{-X_3}\right)I_1(Z)\right]}{\Delta'} \tag{28}$$

After a lot of reductions , we can find the transfer functions of the three-loops IIR optical filter as

$$H_{11}(Z) = \frac{O_1(Z)}{I_1(Z)} = \frac{K_1}{\Delta'} \tag{29}$$

$$H_{12}(Z) = \frac{O_2(Z)}{I_1(Z)} = \frac{K_5\left(K_4 r_{X_1}Z^{-X_1} + K_3 r_{X_2}Z^{-X_2} + K_2 r_{X_3}Z^{-X_3}\right)}{\Delta'} \tag{30}$$

3. SIMULATION RESULTS AND COMPARISONS

Here we use the theoretical model derived in the above section, the frequency responses of these two optical IIR filters are simulated. The simulation results can be applied for practical realizing various filters. Taken narrow bandwidth optical band pass filters as example, the optimal parameters searching work is performed.

Table 1 shows three set of searched parameters corresponding to the simulated three examples of frequency responses of the two-loops optical IIR filter. According to the theoretical model we derived in subsection 2.1, three examples of frequency responses of two-loops IIR filters are shown in Fig.6. Example I is the best result we found. If the parameter K_4 increases, the sidelobe will arise as shown in the curveture of example II. The delay coefficients X_1, X_2, X_3, X_4 can be adjusted for designing higher order filters. The simulation result example III shown in Fig.6 give a general scope of view of higher order filter.

The parameters we used for simulating three-loops IIR filters in Fig.7 are listed in Table 2. Similarily, the numerical results are shown as example I, II and III for comparing the results of Fig.6. The optimal result of narrowband filter is

shown in example I. When K_4 increases, the sidelobe will grow up as shown in example II like the two loops IIR filters. Increasing the order of this filter, the ripple of this filter will increased as shown in example III. We found the ripple is larger then the two loops IIR filters if the parameter is not well choosen.

Comparison of the optical two numerical results in Fig.6 and Fig.7, we zoom in the two cases of example I and show the spectra details in Fig.8. We can find that the three-loops IIR filter has a narrower optical frequency bandwidth than the two-loops IIR filter. The narrowest bandwidths of the two-loops IIR filter and the three-loops IIR filter we found are 0.00012 Hz and 0.00007 Hz, respectively. The narrow linewidth can provide pure filtering effect for extracting the phase lock loop carrier signal in DVD control systems.

4. CONCLUSIONS

The access data rate of optical storage systems increases rapidly in the last five years. Therefore, the signal processing will follow the trend, increasing the processing speed in the future. Accompany with the age of optical data storage above Tera byte, studying all-optical fiber high speed signal processing elements is important. The research results in this paper are very helpful for practical realizing various optical signal processing filters. The narrow band filter at 100GHz can be applied for clock recovery in high speed data-accessed DVD systems accompany some fiber pick up heads.

ACKNOWLEDGEMENT

REFERENCE

1. L. Hesselink (Chairman), *International Workshop on Holographic Data Storage*, Nice, France, March, 1999.

2. K. Goto and K. Kurihara, "High speed VCSEL array head for Tera byte optical disk", *Proceeding of CLEO/Pacific Rim '99*, PP.1113-1114, 1999.

3. K. Goto, "High bit rate and Tera bytes optical memory in a disk system", *SPIE*, **3109**, pp. 192-195, 1997.

4. J. Ma, J. Chang, S. Choi, J. Hong, "Digital holographic data storage with fast access" *proceeding of CLEO/Pacific Rim '99*, pp. 1241-1242, 1999.

5. T. Kurokawa, H. Takenouchi, H. Tsuda, "Time-Space-Conversion optical processing using arrayed-wavegnide grating", *Proceeding of CLEO/Pacific Rim '99*, pp. 809-810, 1999.

6. K.P.Jackson ,J.E. Bowers.S.A. Newton, and C.C.Cutler, "Microbend optical fiber tapped delay line for gigahertz signal processing". *Appl. Phys. Lett*, **41**, pp. 139-141,1982.

7. K.P., Jackson ,S.A. Newton, B.Moslehi, M. Tur, C.C.Cutler, J.W.Goodman, and H.J.Shaw, "Optical fiber delay-line signal processing", *IEEE Trans. on Microwave Theory and Techniques,* **33**, pp. 193-210,1985.

8. J, Capmany., "Time domain analysis of direct coupled fiber ring resonator " , *Opt.Comm.* **192**, pp. 283-290,1992.

9. W.Pieper, "4-channel × 40 Gbps unrepeated TDM transmission over 100Km standard fiber", *IEEE Photonic Technology Letter* **10**, pp. 451-453,1998.

10. E.A.Varvarigos, "Control protocols for multigigabit-per-second networks", *IEICE Transactioons on Communications*, E81-B, 2, pp. 440-448 ,1998.

11. G.D.Bartoliini, D.K.Serkland, P.Kumar, "All-optical storage of a picosecond- pulse packet using parametric amplification: Demonstration of single-shot loading", *Technical Digest of Conference on Optical Fiber Communication*, pp. 201-202, 1998.

12. J.-H.Han, S. K.Taejon, J.-W.Ko, J.-S. Lee, "0.1-nm slim bandwidth transmission of a 2.5-Gbit/s spectrum-sliced incoherent channel using an all-optical bandwidth expansion technique at the recceiver", *Technical Digest of conference on Optical Fiber Communication*, pp. 127-128, 1998.

13. A.K.Dutta, H.Kosaka, K.Kurihara, Y.Sugimoto, K.Kasahara, "High-speed VCSEL of modulation bandwidth over 7.0 GHz and its application to 100m PCF datalink", *IEEE Journal of Lightwave Technology*, 16, pp. 870-875, 1998.

14. J.Manchester, J.Anderson, B.Doshi, S.Dravida, "IP over SONET", *IEEE Communications Magazine*, 36, pp. 136-142, 1998 .

15. R.K. Butler, M.L. Jones, W.C. Szeto, "OC-48/STC-480 IP direct on wavelength application", *Technical digest of Conference on Optical Filber Communication*, pp. 153~155, 1999.

16. H.Suzuki, N. Takachio, Y.Hamazumii, H.Masuda, S.Kawai, K.Arays, "Seamless 32×10G bit/s transmission over 320km of 1.55μm dispersion-shifted fiber using wavelengths ranging from 1546 nm to 1587 nm ",Technical dugest of *Conference on Optical Fiber Communication*, pp. 221-223,1999.

17. I.Morita, M.Suzuki, N.Edagawa, "20 Gbit/s single-channel soliton transmission over 9000km without inline filters", *First Optoelectronics and Commmunications Conference*, pp. 30-31,1996.

18. T.Ido, S.Tonaka, M.Suzulci, M.Koizumi and H.Znoue, "Ultra-high speed multiple-quantum well electro-absorption modulators with integrated wawegnides", *First Optoelectronics and Communication Conference*, pp. 172-173, 1996.

19. S.-L. Tsao, H.-W. Tsao And Y.-H. Lee, "Design of a self-routing frequency division multiple access (SR-FDMA) network using an optical ring filter with or without gain as a router", IEEE Journal of Lightwave Technology, 13, pp. 2168-2182, 1995.

20. S.-L. Tsao.Y.-T. Chen, H.-W. Tsao and J. Wu , "Active optical two-coupler fiber ring filter", *International Symposium on Communications*(ISCOM'93), 2, pp. 15-22, 1995.

21. S.-L. Tsao, J. Wu. C.-F. Tsai, "Filter response of a third-order masterslave fiber-optic recirculating delay lines", *Chinese Journal of Radio Science, Proceedings of ICRS'95*, pp. 448-451, 1995.

Table 1

	K_1	K_2	K_3	K_4	K_5	K_6	X_1	X_2	X_3	X_4
I	0.0001	0.49995	0.49995	0.001	0.4995	0.4995	1	2	1	2
II	2	4	4	2	4	4	1	2	1	2
III	0.0001	0.49995	0.49995	0.9	0.05	0.05	3	4	5	6

Table 2

	K_1	K_2	K_3	K_4	K_5	K_6	K_7	K_8	X_1	X_2	X_3	X_4	X_5	X_6
I	0.0001	0.3333	0.3333	0.3333	0.001	0.25	0.499	0.25	1	2	3	1	2	3
II	2.5	2.5	2.5	2.5	2.5	2.5	2.5	2.5	1	2	3	1	2	3
III	0.0001	0.3333	0.3333	0.3333	0.91	0.03	0.03	0.03	4	7	1	7	4	1
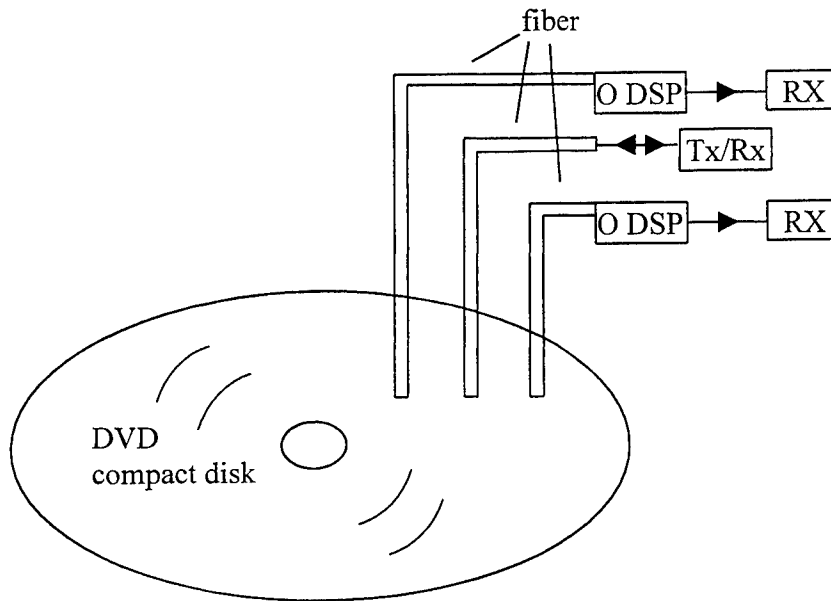
Fig.1 The schematic diagram of application of high speed optical digital signal processing (ODSP) elements
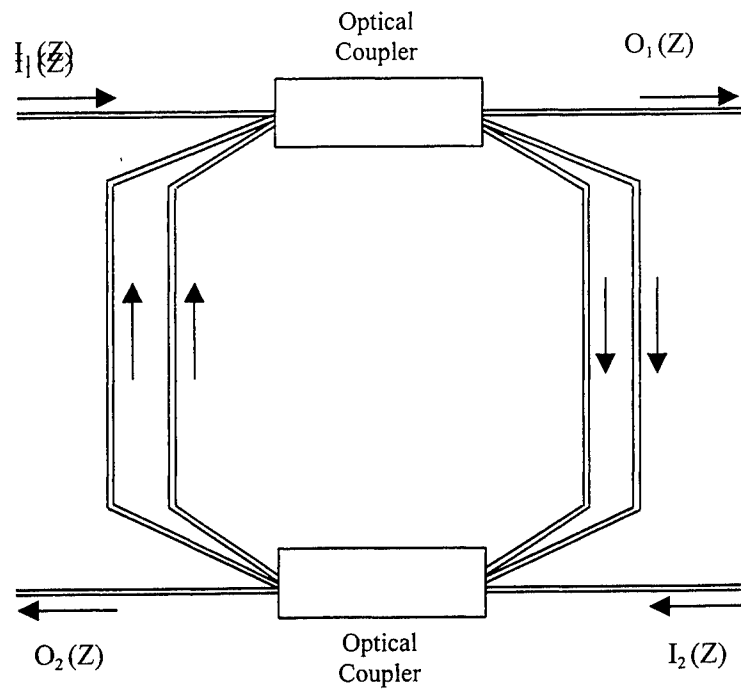
Fig.2 The schematic diagram of a two-loops optical IIR band-pass filter

216
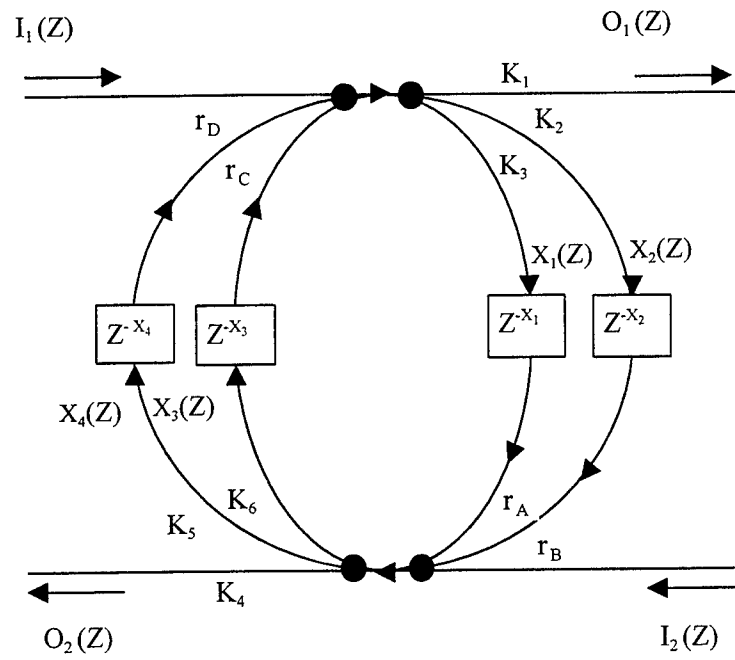
Fig.3 Two-loops optical IIR band-pass filter signal flow chart
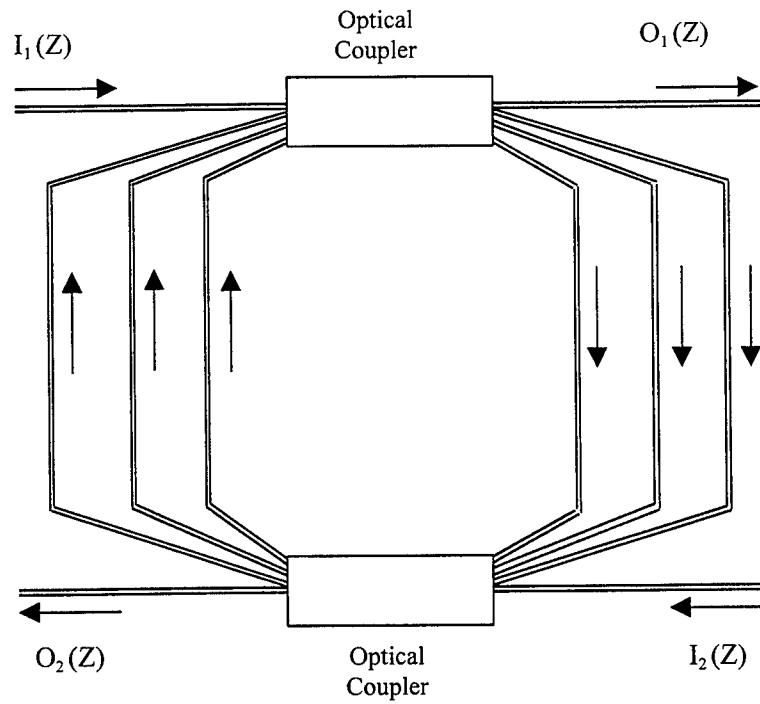
Fig.4 The schematic diagram of a three-loops optical IIR band-pass filter
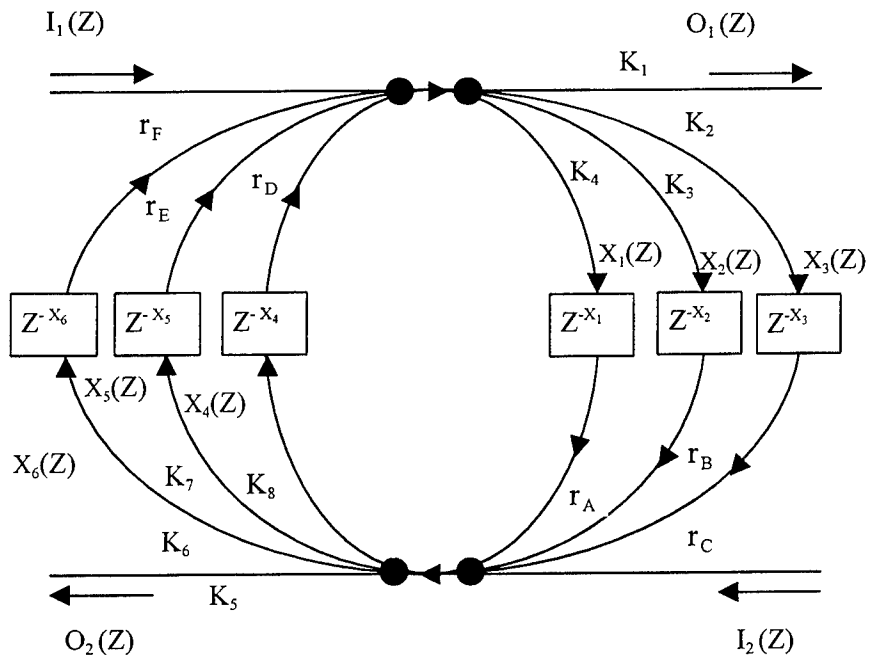
Fig.5 Three-loops optical IIR band-pass filter signal flow chart
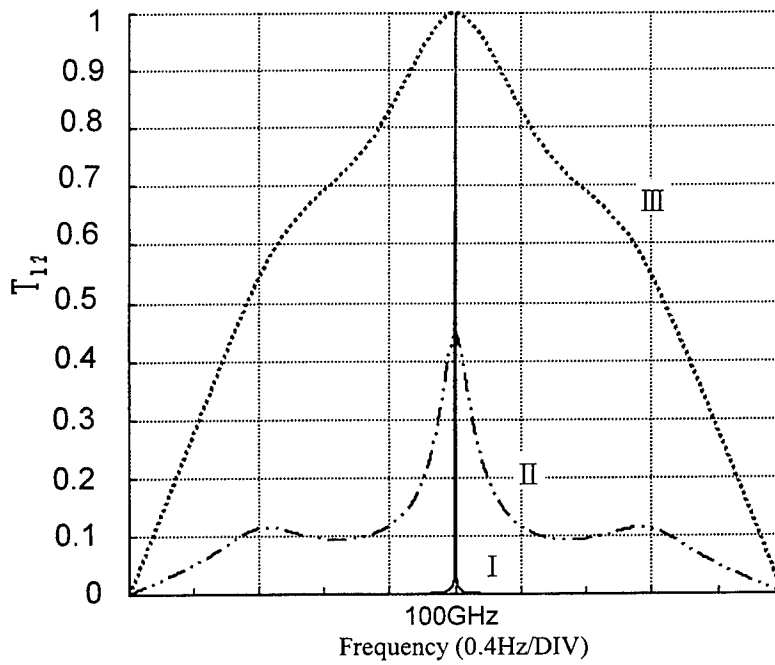
Fig.6 Frequency response T_{12} of two- loops optical IIR band-pass filter
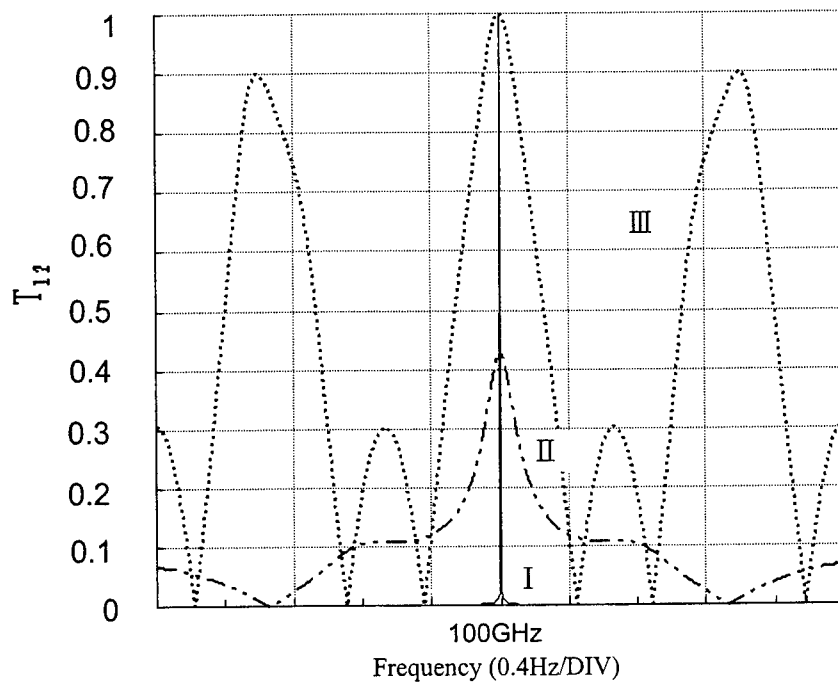
Fig.7 Frequency response T_{12} of three- loops optical IIR band-pass filter

Fig.8 Comparison of Two and Three-loops optical IIR narrow band-pass filter frequency responses

Polarized diffractive optical element design for a multiple-beam optical pickup head

Hsi-Fu Shih, Mark O. Freeman, Jau-Jiu Ju, Tzu-Ping Yang, Yuan-Chin Lee

Opto-Electronics & Systems Labs, Industrial Technology Research Institute, Hsinchu, Taiwan

ABSTRACT

This paper addresses the design and construction of an interesting polarization-switched diffractive optical element (DOE) that generates multiple beams incident on the disk and acts as a beamsplitter and servo-generating element f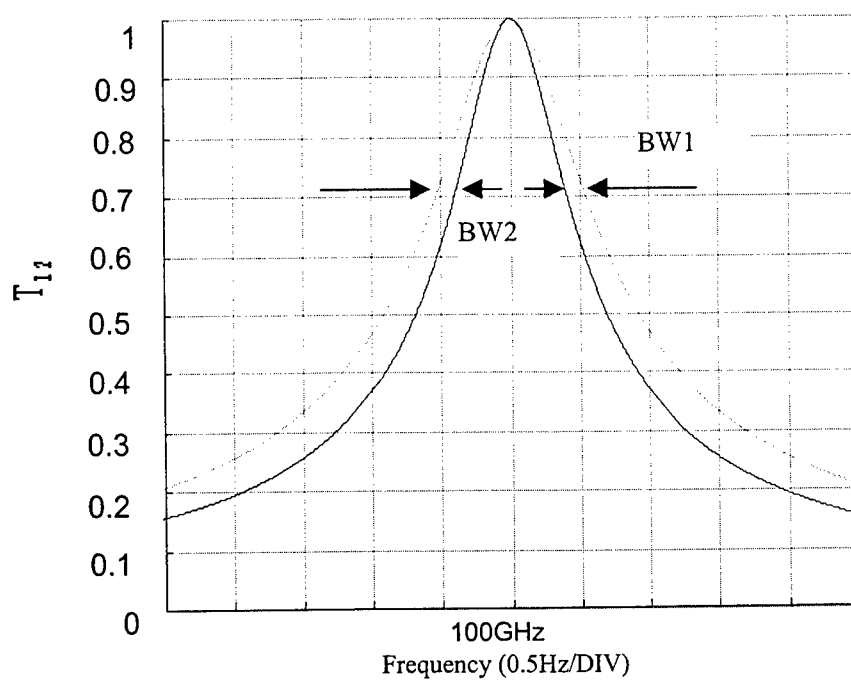or light returning from the disk. In this way, data speed is increased proportional to the number of beams on the disk, and, by combining three functions into a single optical element, allows a more compact and lightweight pickup to be realized. The polarization-switched DOE is constructed as a sandwich of two pieces of some birefringent material, with one rotated by 90 degrees relative to the other so that the ordinary and extraordinary axes are interchanged, and with a common index-match layer between them. A diffractive pattern is etched into each of the two birefringent pieces. Linearly polarized light travelling from the laser towards the disk is diffracted into multiple beams by one of the diffractive patterns while experiencing no diffraction from the other. Travelling the roundtrip from the DOE to the disk and back to the DOE, the light traverses a quarter-wave retarder two times thereby rotating its polarization direction by 90 degrees. It now experiences no diffraction from the multiple beam diffraction layer, but is diffracted by the second diffraction layer, which steers it onto the photodetectors and alters the beam to create useful focus and tracking error signals. This design is important in that it provides a way for two diffractive surfaces, each acting independently with high efficiency on orthogonal polarizations of light, to be combined into a single element. Implementation and application to a multiple-beam holographic pickup head module are presented.

Keywords: Diffractive Optical Element, Holographic Optical Element, Optical Pickup Head, Multiple-Beam Pickup Head

1. INTRODUCTION

In these years, optical drive market has prosperously grown. CD-ROMs have become standard peripheral equipment for computer hardware. With each new generation of disk drives, optical storage system designers face tougher challenges to cut margin, reduce size and weight, and increase data speeds. The challenges, translated to the pickup-head level, lead the designer to multiplex several functions into a single optical element and devise techniques to increase data speed.

CD-ROM drive data transfer rates increased phenomenally from 1X in 1991 to 50X in 1999. The CD-ROM drive market today allows for a maximum speed of 50X under constant angular velocity (CAV) motor control, but only on the outermost tracks. Data read from the inner tracks of a disk is only read at a mere 20-25X. High speed CD-ROM drives make noisy vibration induced from high speed spindle motor operation and run the risk of ruining the disks. There has been a significant amount of negative performance for these high-speed drives.

Most CD-ROM drives use an optical head with a single laser beam for sequential data access. The laser beam is directed at a single track of information that forms a continuous spiral on the disc. The disk drive rotates the tracks under the laser and the result is a stream of serial data that can be transferred to a processor for interpretation.

ZEN proposed multibeam technology[1] to increase the performance of an optical drive. Multibeam technology provides for reading and processing multiple data tracks simultaneously. It multiplies the data transfer rate by the number of beams in use compared to single-beam technology under the same motor rotation speed. Combined with constant linear velocity (CLV) rotation system for constant rates across the whole disc, a multibeam drive is a so-called TrueX drive.

Rather than directing a single laser beam at a single track of serial data on a disc, a multiple beam optical head creates multiple focus points that illuminate multiple tracks and reads their data in parallel. Other than the multiple beam optical head and controller electronics, there is no substantial change in a multibeam system. The mechanical elements and disc media are identical with standard drives. Fig. 1 shows the conceptual drawing of two kinds of optical heads. It is seen that the only differences between a conventional single-beam optical head (Fig. 1(a).) and a multiple-beam optical head (Fig. 1(b).), are that a multiple-beam grating[2] is placed in front of the laser for splitting the laser light into multiple diffracted beams and a multiple-beam detector array is positioned in the returning optical path for generating servo and data signals. The diffracted multiple beams pass through a beam splitter to the objective lens and are focused into multiple spots on the disk. The spots are uniformly spaced and illuminate multiple tracks. Focus and tracking are accomplished with the central beam with the same techniques used for a single-beam optical head. The beams reflected from the data tracks via the same optical path are directed to the multiple detecting regions that are spaced to align with multiple reflected tracks. A conventional central detecting region, e.g. a quad detector, is also provided for focus and tracking.

Holographic optical head modules combine the source, photodetectors, beamsplitter, and servo generating optical element(s) into a single package[3]. Many examples of holographic pickup-head modules have been developed. Besides the advantages of cost reduction in packaging the components and the compactness of the unit, one of the biggest advantages is modularity. Pickup heads can be flexibly designed to meet the mechanical and system needs of a variety of drive designs and the holographic module, which contains a significant portion of the optical system, can be plugged in almost as an afterthought. It's quite common in current commercialized single-beam optical head designs to plug in a holographic module to comprise the bulk of the optical system. Fig. 2 shows the basic construction of a holographic single-beam optical head. It can be easily extended to a holographic multiple-beam optical head.

Despite the advantages stated above, there are some drawbacks to using a holographic module in existing pickup-heads. The biggest problem is the low light utilization. The returning power incident on the photodetectors of a holographic module is around 1/3 - 1/12 that of a conventional pickup-head. This increases the loading of the current-to-voltage preamplifiers and can reduce the signal-to-noise ratio. Moreover, using a holographic module for a multiple-beam pickup-head increases the severity of the efficiency problem since a multiple-beam grating and holographic optical element (HOE) split the laser power into an even greater number of diffraction orders, many of which go unused in either the forward or returning light paths. In this paper, we avoid the efficiency problem of the holographic pickup head by using a polarization-selective diffractive optical element (DOE)[4,5]. An interesting polarization-selective DOE design is proposed that both increases the round-trip light efficiency and, at the same time, combines three functions (beamsplitter, servo signal generating, and multiple-beam grating) into a single optical element. With this design, a more compact, lightweight and high performance holographic multiple-beam pickup can be realized.

2. DESIGN CONCEPT

Fig. 3 shows the physical operation of a polarization diffractive element. The pattern is etched on a birefringent substrate with the indices n_o and n_e corresponding to ordinary and extraordinary waves respectively. The etched surface of the birefringent substrate is refilled with an isotropic material having index equal to n_o (or n_e). Consider the case of incident light with polarization aligned perpendicular to ordinary wave. The incident light will be phase modulated due to the difference between the extraordinary index of the birefringent material and the index of the isotropic backfill material and be diffracted by the etched pattern. In the other case, with the incident light polarization aligned along the ordinary index of the birefringent material, the light will experience no diffraction since the backfill material and is index-matched to the ordinary index and therefore the light doesn't see the grating.

The key idea of our polarization-selective DOE design uses two pieces of polarization elements. One element is designed as a multiple beam grating and the other is designed to function as a beamsplitter and servo-generating element. These two pieces are designed to diffract light of orthogonal polarizations. This can be implemented by rotating one piece of the polarization element by 90 degrees relative to the other and therefore interchanging the ordinary and extraordinary axes of the birefringent material in both elements. As shown in Fig. 4, by proper orientation of the diffractive patterns on two polarization elements, linearly polarized light travelling from the laser towards the disc is diffracted into multiple beams by the first grating surface, while experiencing no diffraction from the second. Travelling the roundtrip from the DOE to the disc and back to the DOE, the light traverses a quarter-wave retarder two times so that the return-trip light incident on the DOE is now linearly polarized perpendicular to that of the light coming from the laser. This light is now polarized such that it will be diffracted by the beamsplitter/servo-generating diffractive surface and experiences no diffraction from

the multibeam grating surface. The light is steered onto the photodetectors and, at the same time, conditioned to create useful focus and tracking error signals.

In a holographic multiple-beam pickup-head, the multiple-beam grating is used only on the forward light path, while the beamsplitter/servo-generating element is used only on the returning path. With this polarization-selective DOE design, the two polarization elements are orthogonally oriented. Whether on the forward or the returning path, the laser beam will be diffracted by only one of the two elements. In this way, this design avoids wasting laser power in unwanted diffraction orders thereby increasing the light utilization efficiency. This is necessary to make a holographic multiple-beam pickup head feasible.

Fig. 5 compares various types of optical system designs with regards to the losses of grating and beamsplitter for multiple-beam optical heads. The efficiency calculation shown in Fig. 5(a) and Fig. 5(b) is for conventional type pickup-head design. Fig. 5(a) uses a common beamsplitter and has 50% of the light is lost in each direction. The multiple-beam grating is usually designed to evenly distribute 90% of incident light into the useful diffracted beams. This grating can be designed according to Dammann's method[6]. Fig. 5(b) uses a comparatively expensive polarization beamsplitter combined with a quarter wave plate and gains the highest roundtrip efficiency of 90%. It is four times the efficiency of Fig. 5(a). Fig. 5(c) and Fig. 5(d) are optical designs with holographic beamsplitters. Fig. 5(c) adapts the general structure common to holographic pickup heads to the multibeam case. It is seen to be the least efficient with only 2.2% roundtrip efficiency. This is why a standard holographic module for multibeam is impractical. Fig5d shows the design utilizing the proposed polarization-selective DOE element. The beamsplitter/servo-generating diffractive surface can be etched with either binary or blazed shape giving efficiencies of 40% or 96% respectively. The total roundtrip efficiency in Fig. 5(d) is estimated to be around 36~86%. It is better than Fig. 5(a) and Fig. 5(c).

The polarization-switched DOE can be constructed as a sandwich of two pieces of some birefringent material, as shown in Fig. 6, with one rotated by 90 degrees relative to the other so that the ordinary and extraordinary axes are interchanged, and with a common index-match layer between them. The index-match layer is a kind of isotropic material with index equal to that of either ordinary wave or extraordinay wave in the two birefringent pieces. Multiple-beam grating and HOE patterns are etched into each of the two birefringent pieces. This sandwich structure provides the same functions as that described in Fig. 4, combines two diffractive elements into a single piece and furthermost reduces the size of holographic optical module. An alternative method is to attach the quarter-wave plate on the sandwich polarization-switched DOE and make the system even more simplified. These compound polarization selective DOEs should be manufacturable at low cost with simultaneous fabrication of many pieces on a single substrate as is characteristic of DOEs.

3. CONCLUSION

In conclusion, we have introduced a method for constructing a holographic multiple-beam optical head. A polarization-switched DOE is proposed for avoiding the severe power losses in a holographic pickup head. The efficiency analysis gives a promising result. A sandwich-like structure is implemented for this polarization-switched DOE. With these designs, a high performance, compact size and lightweight multiple-beam optical pickup head can be achieved.

REFERENCES

1. ZEN Research Co., http://www.zenresearch.com.
2. W. H. Lee, "High Efficiency Multiple Beam Gratings", *Applied Optics*, Vol. 18, No. 13, pp.2152-2158, 1979.
3. W. H. Lee, U. S. Patent, Patent No. 4731772, Mar. 15, 1988.
4. J. C. Lehureau, B. Mourey, and H. Magana, U. S. Patent, Patent No. 5168485, Dec. 1, 1992.
5. J. E. Ford, F. Xu, K. Urquhart, and Y. Fainman, "Polarization-Selective Computer-Generated Hologram", *Optics Letters*, Vol. 18, No. 6, March 15, pp456-458, 1993.
6. H. Dammann, and K. Gortler, *Opt. Commun.* 3, 312, 1971.

Single Focus Spot and
2 Tracking Spots

Disc

Objective Lens

Cylindrical Lens

Photodetector

Collimating Lens

Beamsplliter

3-Beam
Grating

Laser Diode

(a) Single-beam type

Multiple Focus Spots

Disc

Objective Lens

Cylindrical Lens

Multiple Element
Photodetector

Collimating Lens

Beamsplliter

Multiple-Beam
Grating

Laser Diode

(b) Multiple-beam type
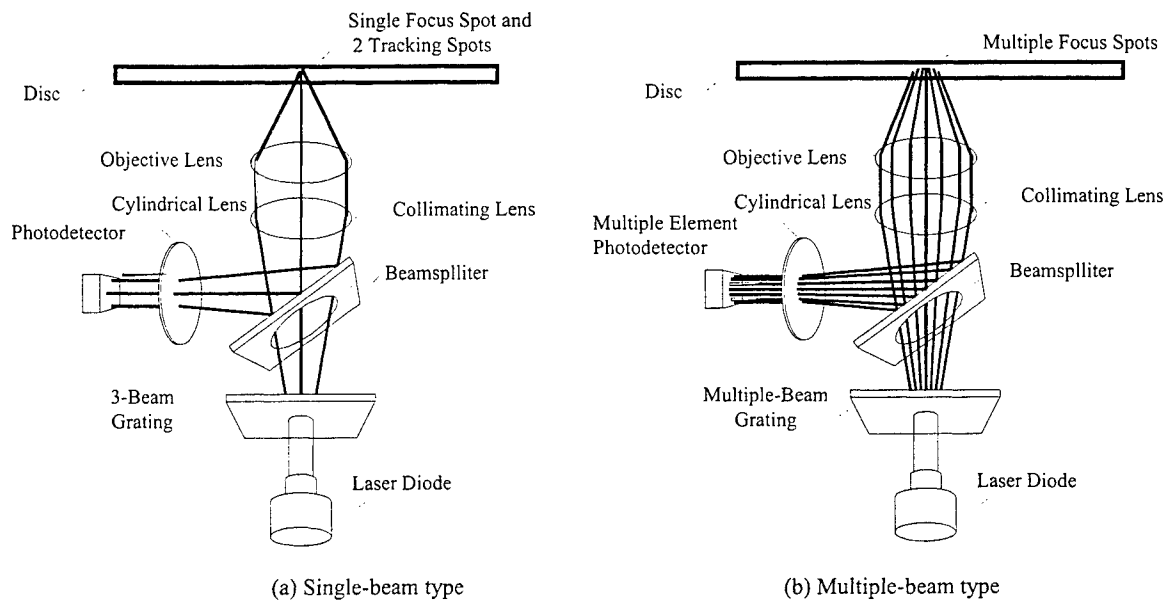
Fig. 1: Conventional optical pickup-head structure

Disc

Objective
Lens

Collimating
Lens

Holographic Optical Element
(HOE)

Photodetector

Laser Diode

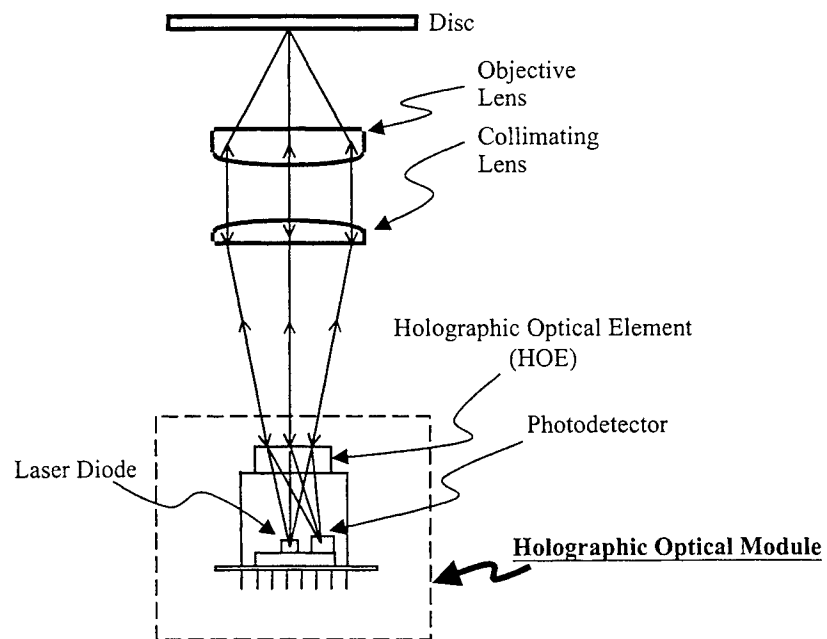**Holographic Optical Module**

Fig. 2: Structure of a common holographic optical pickup-head
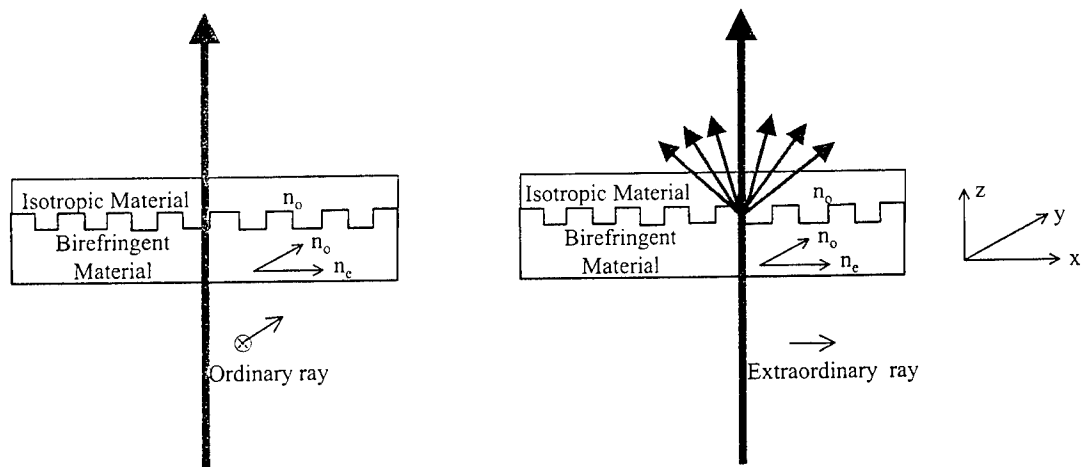
Fig. 3: The operation of a polarization-selective diffractive element

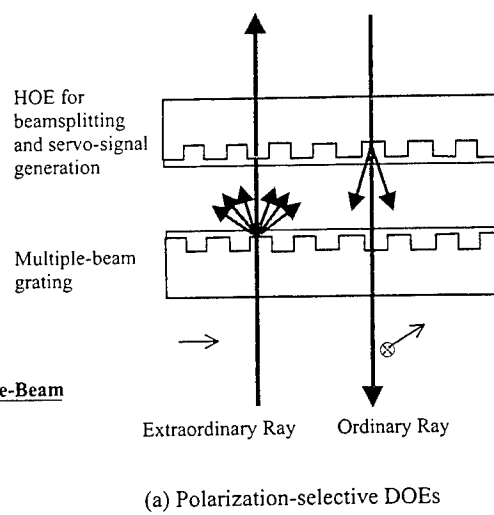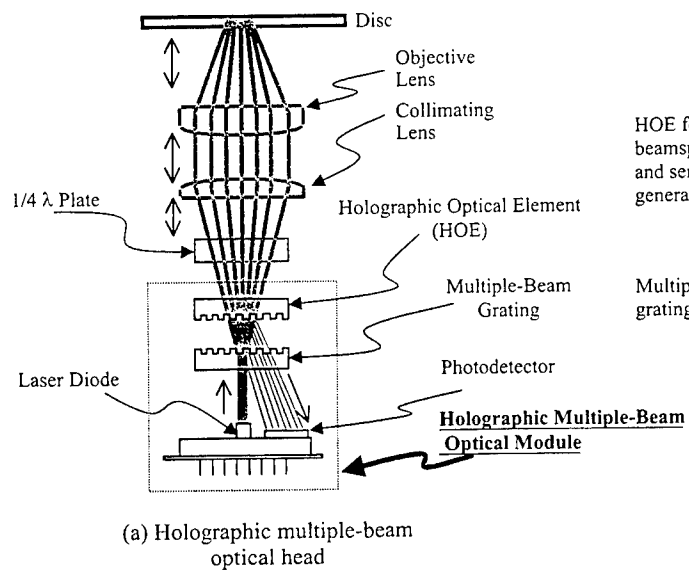(a) Holographic multiple-beam
optical head

(a) Polarization-selective DOEs

Fig. 4: The structure of a holographic multiple-beam optical head and polarized-switched DOE

Common Beamsplitter
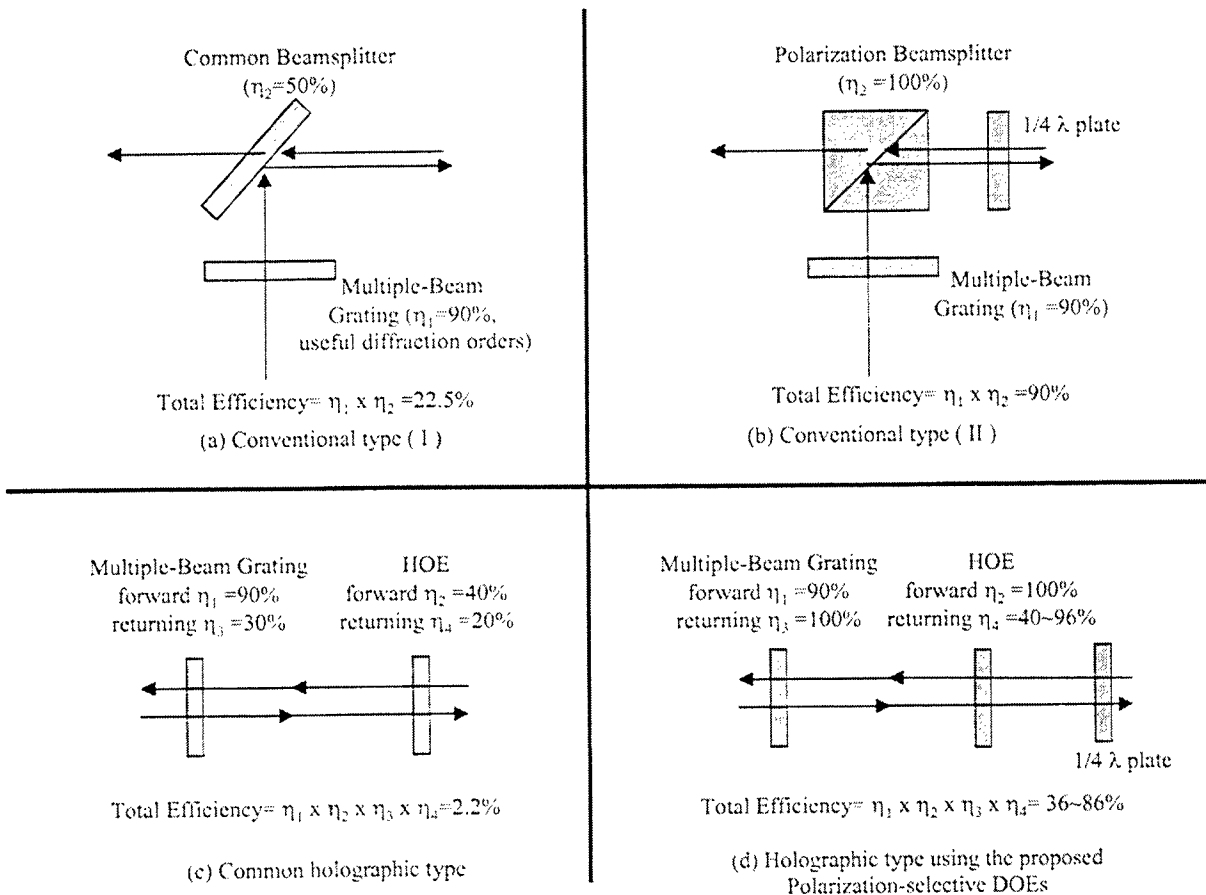($\eta_2 = 50\%$)

Multiple-Beam
Grating ($\eta_1 = 90\%$,
useful diffraction orders)

Total Efficiency= $\eta_1 \times \eta_2 = 22.5\%$

(a) Conventional type (I)

Polarization Beamsplitter
($\eta_2 = 100\%$)

1/4 λ plate

Multiple-Beam
Grating ($\eta_1 = 90\%$)

Total Efficiency= $\eta_1 \times \eta_2 = 90\%$

(b) Conventional type (II)

Multiple-Beam Grating   HOE
forward $\eta_1 = 90\%$ forward $\eta_2 = 40\%$
returning $\eta_3 = 30\%$ returning $\eta_4 = 20\%$

Total Efficiency= $\eta_1 \times \eta_2 \times \eta_3 \times \eta_4 = 2.2\%$

(c) Common holographic type

Multiple-Beam Grating   HOE
forward $\eta_1 = 90\%$ forward $\eta_2 = 100\%$
returning $\eta_3 = 100\%$ returning $\eta_4 = 40\sim96\%$

1/4 λ plate

Total Efficiency= $\eta_1 \times \eta_2 \times \eta_3 \times \eta_4 = 36\sim86\%$

(d) Holographic type using the proposed
Polarization-selective DOEs

Fig. 5: Efficiency considerations for various types of multiple-beam optical head.

Disc

Objective
Lens

Collimating
Lens

1/4 λ Plate

Holographic Optical Element
(HOE)

Fill-in Material

Multiple-Beam
Grating

Laser Diode

Photodetector

Holographic Multiple-Beam
Optical Module

(a) Holographic multiple-beam
optical head with sandwich DOE

HOE
(birefringent material)

Fill-in Material
(isotropic material)

Multiple-Beam
Grating
(birefringent material)

Extraordinary Ray   Ordinary Ray

(a) Sandwich-like Polarization-
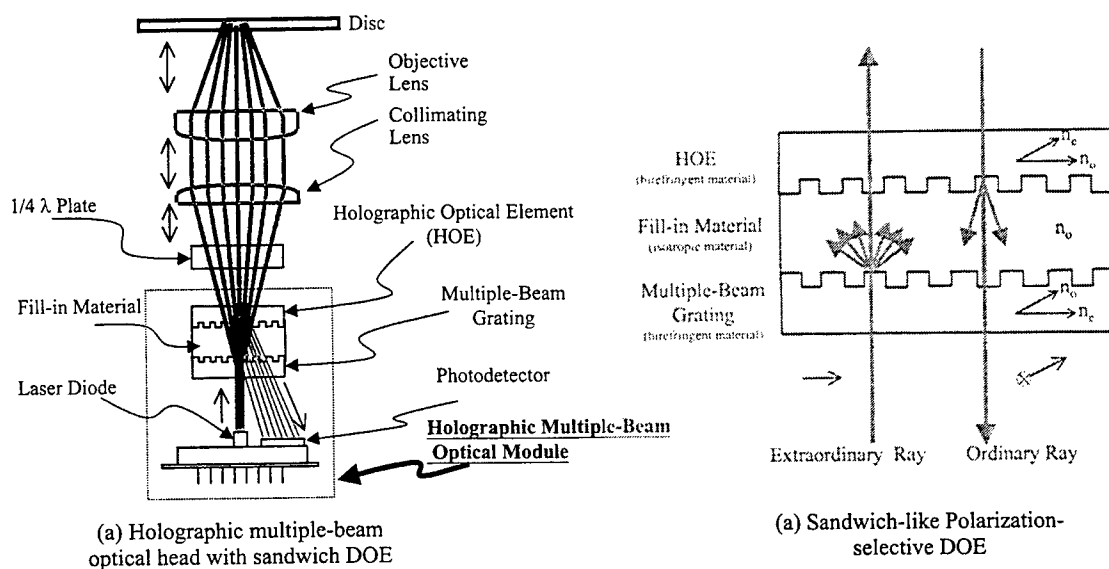selective DOE

Fig. 6: The structure of a holographic multiple-beam optical head that uses a compact sandwich-like
polarized-switched DOE

225

Diffractive phase element for reducing a diameter of main-lobe of a focal spot

Yusuke Ogura[a], Jun Tanida[a], Yoshiki Ichioka[b], Yoshiaki Mokuno[c], and Katsunori Matsuoka[c]

[a]Graduate School of Engineering, Osaka University,
2-1 Yamadaoka, Suita, Osaka, 565-0871 Japan
[b]Nara National College of Technology,
22 Yata-cho, Yamatokoriyama, Nara, 639-1080 Japan
[c]Department of Optical Materials, Osaka National Research Institute,
1-8-31 Midorigaoka, Ikeda, Osaka, 563-8577 Japan

ABSTRACT

A diffractive phase element (DPE) reducing the diameter of main-lobe of a focal light spot has been developed. A light spot focused by an optical system spreads due to the light diffraction from a limited aperture of lens. The developed DPE reduces the main-lobe diameter by modulating the incident wave-front of the focusing lens. Although the DPE increases the side-lobe intensity of the focal spot, appropriate design can reduce its magnitude enough not to affect the photoresist in lithography process. An iterative method based on the Gerchberg-Saxton algorithm combined with new constraints was applied to design a DPE. A rotation symmetrical binary DPE was designed, which reduces the main-lobe diameter to 74% and makes the side-lobe intensity under 2.7% of the main-lobe. The designed DPE was fabricated with the laser beam lithography system developed by the authors, and its performance was measured by mounting it on this system. The minimum line width obtained with the DPE becomes 1.0μm while it is 1.2μm without the DPE. It is also shown by a computer simulation that the focal depth of the focusing system with the DPE becomes wider than that without the DPE when both systems produce the same focal spot size.

Keywords: diffractive phase element, focusing system, focal depth, focal spot pattern, laser beam lithography

1. INTRODUCTION

Diffractive phase elements (DPEs) have considerably extended their applications according as the development of microfabrication technology, which enables us to realize various optical functions, an optical integration of numerous optical systems, or a easy replication for optical elements. Especially, DPEs have ability to create distinctive optical functions designed by a computer with high efficiency of light usage in a thin element. So DPEs have been applied as special optical elements such as optical interconnections,[1] beam shaping,[2] mode formers[3] and so on.

In order to obtain the desired functions of a DPE, it is important to design a proper surface relief of a element. The Simulated Annealing method (SA)[4] and an iterative method based on the Gerchberg-Saxton algorithm (GSA)[5] are well-known methods for designing DPEs. The SA method can design DPEs with high accuracy, but needs heavy computational load than the GSA. On the other hand, the GSA leads a desirable answer in a short time but it needs a proper constraints to converge in many cases. For example, it was reported that the GSA produced the DPE in only 20 iterations, which converts a Gaussian beam profile to a uniform intensity distribution.[6]

DPEs are usually fabricated by using lithography and etching processes. The functions of DPEs are often restricted by a fabrication limit, that is, finer structures than the spot size determined by diffraction limit of the focusing lens can not be achieved. We attempt to make finer structures than the spot size determined by diffraction limit by using a DPE. The DPE, we used, is designed by the GSA with special constraints. It modulates a wave-front of the incident light to the focusing lens of a photolithography system as illustrated in Fig. 1, and generates a smaller spot size than diffraction limit but it allows a little increase of side-lobe intensity. This technique looks similar to an apodization technique, that is well-known to obtain wider focal depth in an imaging system.[7-9] But an apodization technique usually spreads a focal spot pattern for concentrating light energy of side-lobes to main-lobe. For our purpose, it is more important to make a light spot sharp than to concentrate light energy to main-lobe, even if a

---

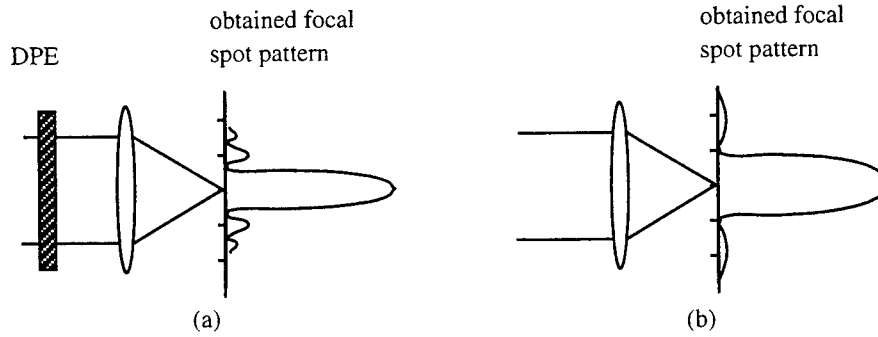Correspondence: E-mail: ogura@mls.eng.osaka-u.ac.jp

Figure 1. Scheme of a focusing system for reducing spot size; (a) with the DPE, and (b) without a DPE (a conventional system).

side-lobe intensity might increase. In the lithography process, an effect of the side-lobe intensity to pattern drawing can be eliminated because of the nonlinear sensitivity of a photoresist material.

In this paper, we describe the design method for the DPE, its implementation, and its evaluation by optical experiments. The DPE is designed by a modified GSA with new constraints. The designed DPE is fabricated by using the laser beam lithography system we developed, and it is mounted on the system for evaluation. The drawing resolution is evaluated from experimental results. We also discuss on the focal depth of the focusing system with or without the DPE, and performance of the DPE is evaluated.

2. DESIGN OF THE DPE

2.1. Design Method

Design of a DPE is performed by two steps. The first step is to calculate the continuous phase distribution of a DPE, and the second step is to quantize the calculated phase distribution. In this paper, the GSA is basically applied in the first step and the stepwise quantization method (SQM) proposed by Wyronski[10] is used in the second step. The design procedure for the GSA is described as the following six steps, in which l denotes the iteration number and an observation plane means a focal plane of a focusing lens:

1. An initial phase distribution ψ_0 of a wave-front on the observation plane is chosen at random.

2. The wave-front on the DPE plane is calculated by inverse Fourier transform of the wave-front $\sqrt{\bar{I}_l}e^{i\psi_l}$ on the observation plane, where $\sqrt{\bar{I}_l}$ denotes an ideal amplitude of wave-front on the observation plane. It is expressed as $A_l e^{i\phi_l}(= F^{-1}[\sqrt{\bar{I}_l}e^{i\psi_l}])$, where F^{-1} is an operator for the inverse Fourier transform. The details of the ideal amplitude $\sqrt{\bar{I}_l}$ at lth iteration are described in Sec. 2.2.

3. The amplitude A_l of the wave-front on the DPE plane is replaced with the amplitude W_0 of the illuminating light source. (This is the DPE plane constraint.) The phase ϕ_l is maintained to be unchanged.

4. The wave-front on the observation plane is calculated by Fourier transform of the wave-front $W_0 e^{i\phi_l}$ on the DPE plane. It is expressed as $\sqrt{I_l}e^{i\psi_l}(= F[W_0 e^{i\phi_l}])$, where F is an operator for the Fourier transform.

5. The calculated amplitude $\sqrt{I_l}$ of the wave-front on the observation plane is replaced with the $(l+1)$th ideal amplitude $\sqrt{\bar{I}_{l+1}}$. (This is the observation plane constraint.) The phase ψ_l is maintained.

6. If the iteration number reaches at the prescribed number or $I_{err} \leq 0.01$ is satisfied, the iteration is stopped. Here, I_{err} is determined as $\sqrt{\frac{\iint (I_0 - I_l)^2 \, dS}{\iint I_0^2 \, dS}}$ which is the root mean square error of I_l and I_0, where I_l and I_0 are an obtained intensity distribution and an ideal intensity distribution on the observation plane, individually. If the condition is not fulfilled, return to the step 2.

The phase distribution obtained by the above algorithm is quantized by the SQM in the second step. The procedure of SQM is same as that of GSA except for adding the quantization of the phase ϕ_l to the DPE plane constraint in step 3. The SQM leads a quantized phase distribution gradually by extending the quantization area as the iteration process proceeding.[10] In the design procedure for DPEs, we used the same parameters for SQM as described in Ref. 10; that is, $Q=5$, $P=10$, and $\epsilon^{(1)} = 0.3$, $\epsilon^{(2)} = 0.5$, $\epsilon^{(3)} = 0.6$, $\epsilon^{(4)} = 0.7$, $\epsilon^{(5)} = 0.75$, $\epsilon^{(6)} = 0.8$, $\epsilon^{(7)} = 0.85$, $\epsilon^{(8)} = 0.9$, $\epsilon^{(9)} = 0.95$, and $\epsilon^{(10)} = 1.0$, where Q is the number of iteration in each subdivided cycle in which the quantization area is fixed, P is the total number of subdivided iteration cycles, and $\epsilon^{(p)}$ indicates ratio of a quantization area to the total area in the pth subdivided iteration cycle.

In the case of design for DPEs to generate a rotation symmetrical focal spot pattern, it is convenient to use the one dimensional Hankel transform instead of the two dimensional Fourier transform. The complex-amplitude distribution $T_s(\rho)$ of the focal spot pattern is expressed as the Hankel transform of the transmittance distribution $t_s(r)$ of the DPE as follows.

$$T_s(\rho) = \frac{2\pi}{\lambda f} \int_0^\infty t_s(r) J_0\left(\frac{2\pi}{\lambda f}\rho r\right) r\, dr, \tag{1}$$

where λ denotes a wavelength, f is a focal length of a focusing lens, r and ρ are radial coordinates in a DPE plane and a spot pattern plane, respectively, J_0 is the first kind zeroth order Bessel function. The inverse Hankel transform is expressed with the same mathematical expression of Eq. (1). In actual design, the discrete Hankel transform can be calculated by using the quasifast Hankel transform algorithm in a computer.[11]

2.2. Design of DPE for Generating a Small Light Spot

As a preparation before designing a DPE based on the procedure described in Sec. 2.1, the profile of an incident beam on to the DPE has to be measured. The intensity distribution $I_{\text{inc}}(r)$ for a laser beam can be expressed with a gaussian profile by introducing a parameter w_s as follows,

$$I_{\text{inc}}(r) \propto \exp\left(-\frac{r^2}{w_s^2}\right). \tag{2}$$

The beam profile in our system was measured experimentally by using the knife edge method, and we obtained $w_s = 1.47\mu$m. From this result, W_0 in design process 3 is set to $\sqrt{I_{\text{inc}}(r)}$ with $w_s = 1.47$.

As the observation plane constraint in the design procedure, the rules of Eq. (3) which is based on an adaptive-additive algorithm[12] is utilized.

$$\bar{I}_{l+1}(\rho) = \begin{cases} \alpha I_0(\rho) + (1-\alpha)I_l(\rho) & (\rho \geq \frac{1}{2}\rho_{1/e^2}), \\ I_0(\rho) & (\rho < \frac{1}{2}\rho_{1/e^2}), \end{cases} \tag{3}$$

where $I_0(\rho)$ is a target spot intensity pattern, $I_l(\rho)$ is a spot intensity pattern calculated in lth iteration, $\bar{I}_{l+1}(\rho)$ is a constrained pattern, ρ is a radial variable, and ρ_{1/e^2} is the radius at which the intensity $I(\rho_{1/e^2})$ becomes $1/e^2 I(0)$, where $I(\rho)$ is the spot pattern obtained without the DPE. The parameter α in Eq. (3) controls the strength of constraints.

For the design of the DPE to reduce a spot diameter, a target intensity distribution I_0 was given by

$$I_0 = \begin{cases} 1 & (\rho < \frac{1}{2}\rho_{1/e^2}), \\ 0.003 & (\rho \geq \frac{1}{2}\rho_{1/e^2}), \end{cases} \tag{4}$$

and the parameter α in Eq. (3) is selected as follows:

$$\alpha = \begin{cases} 1 & (l \leq 50), \\ 0.02 \times l & (51 \leq l \leq 100), \\ 2 & (101 \leq l \leq 150). \end{cases} \tag{5}$$

The total iteration number is set to 100 for the first step and to 50 for the second step, sampling number in each plane is 4096 on a radial axis by using the Hankel transform, and the number of the phase levels of the DPE is 2. The design results are shown in Fig. 2. Figure 2(a) is the amplitude profile of the incident beam, (b) is the phase
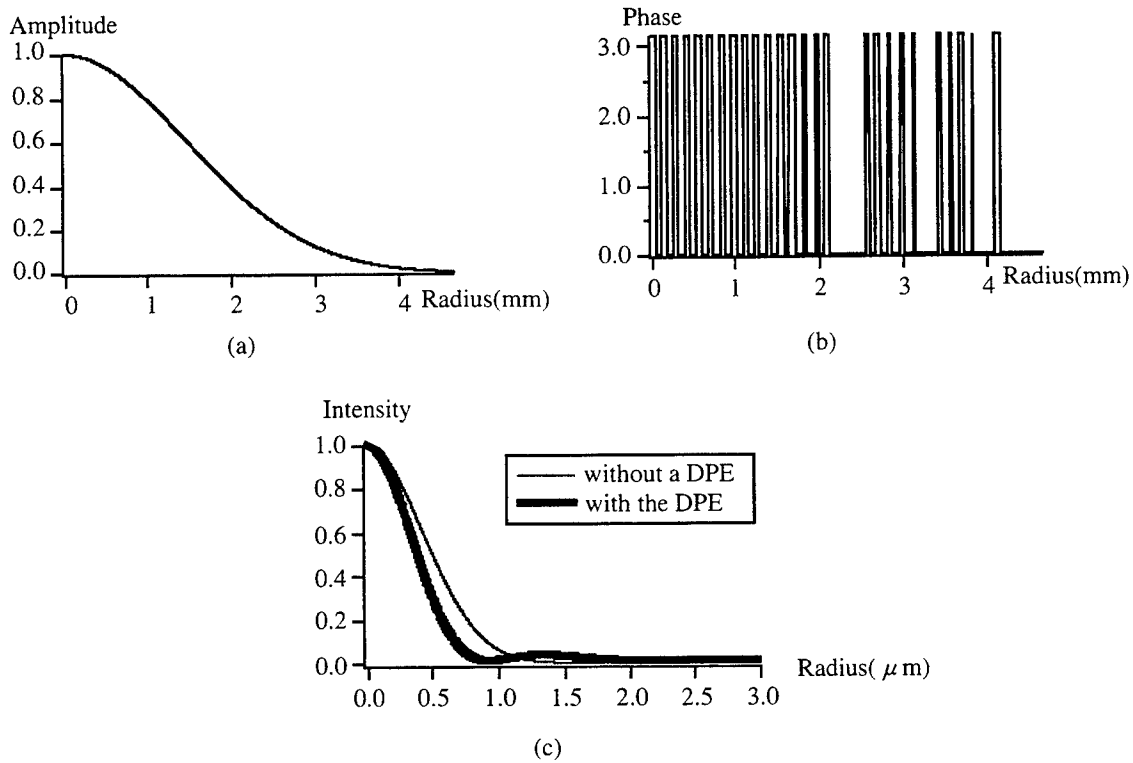
Figure 2. Design of the DPE; (a) amplitude profile of the incident beam, (b) phase distribution of the DPE, and (c) calculated focal spot pattern.
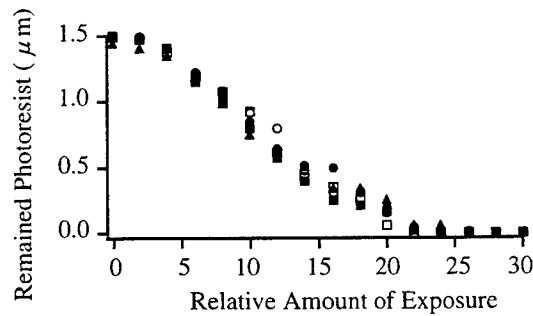

Figure 3. The relationship between the thickness of photoresist and exposure. Each marker denotes different measurements.

distribution of the designed DPE, and (c) is the calculated focal spot pattern obtained by using the designed DPE. The designed DPE reduces the spot radius from 0.85μm to 0.63μm, that is about 74% reduction, where we define a spot radius as a radius at which the spot intensity decreases to $1/e^2$ of main-lobe. On the contrary, the maximum side-lobe intensity increases to 2.7% of the main-lobe intensity. For an application of the laser beam lithography, side-lobe intensity should become small and not affect to the exposure. Figure 3 shows the relationship between the thickness of the remained photoresist after exposure and an amount of exposure, which we measured for the photoresist AZ1500 (Hoechst Industry Limited). This relationship shows that the side-lobe intensity less than 10% of the central intensity does not act on the exposure to the photoresist. Therefore, the DPE designed here can be utilized to improve the resolution of patterns drawn by a laser beam lithography system.
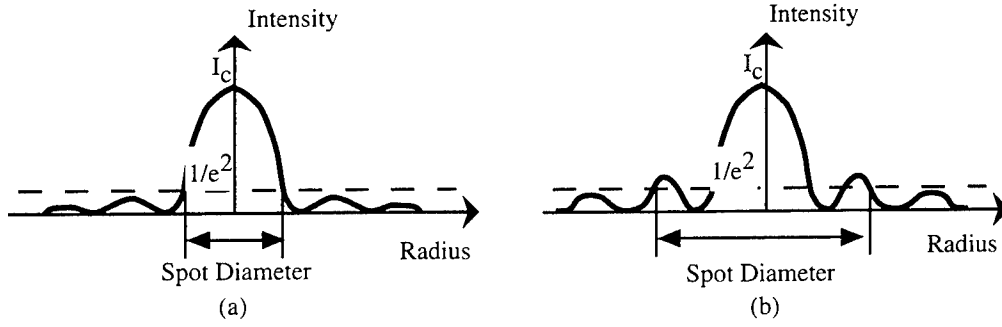
Figure 4. Definition of spot diameter. (a) Maximum side-lobe intensity is less than $1/e^2$ of main-lobe intensity and (b) more than $1/e^2$.

3. DISCUSSION ON FOCAL DEPTH OF FOCUSING SYSTEM WITH DPE

In a laser beam lithography process, a focused laser beam is scanned and exposes the photoresist coated on the glass substrate. The coated photoresist usually has thickness of sub micron meter or a few micron meter. So it is important not only to make a laser spot small but also to make the focal depth deep enough to obtain high resolution. In this section, we discuss on the focal depth of a focusing system with the DPE by comparing to other systems without the DPE.

3.1. Defocused Spot Pattern in a Focusing System

Let us consider a focusing system shown in Fig. 1(a). The spot pattern defocused by the amount of δd in the focusing system has the intensity distribution $I_\delta(\rho)$ of

$$I_\delta(\rho) \propto \left| \int t_s(r) \exp\left(ik\omega_{20}r^2\right) J_0\left(\frac{k}{f}\rho r\right) r\, dr \right|^2, \tag{6}$$

where $k = 2\pi/\lambda$, and

$$\omega_{20} = \frac{\delta d}{2}\mathrm{NA}^2, \tag{7}$$

in which NA is the numerical aperture of the optical system.[7,9] The other variables have same meanings as in Eq. (1).

Now we evaluate the focal depth for the three focusing systems as follows;

(i) Using a objective lens of NA=0.46 alone,

(ii) Using a objective lens of NA=0.46 with the DPE designed in Sec. 2.2,

(iii) Using a objective lens of NA=0.58 alone.

The number of NA in case (iii) is selected to get a same focal spot diameter as in case (ii). Now we define a spot diameter and a defocus distance for the following discussion. A spot diameter is defined as the twice of maximum value of ρ satisfying the condition of $I_\delta(\rho) = 1/e^2 \times I_c$, where I_c is the main-lobe intensity as shown in Fig. 4. We call δd in Eq. (7) a defocus distance.

3.2. Evaluation of the Focal Depth of Focusing Systems

To evaluate the focal depth of three focusing systems (i), (ii), and (iii), we calculated the spot diameters and maximum side-lobe intensities at each defocus distance by using Eq. (6). The calculated results are shown in Fig. 5. Figure 5(a) denotes that the system of case(ii) generates the smallest spot diameter in the area of defocus distance less than $\pm 3\mu m$. But the spot diameter of case(ii) enlarges discontinuously at the defocus distance of $\pm 3\mu m$ because the first side-lobe intensity becomes more than $1/e^2$ of main-lobe.
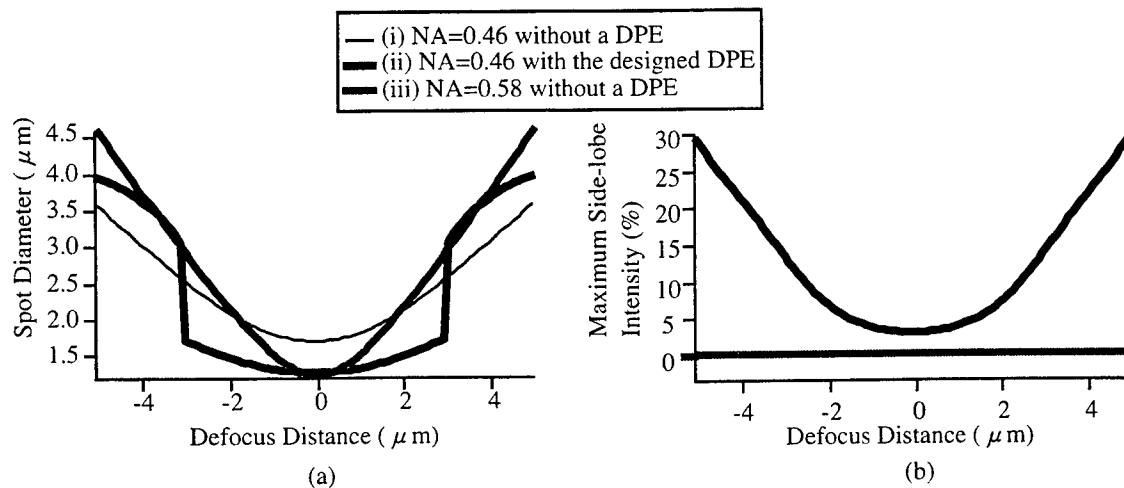
Figure 5. Changes of (a) spot diameters and (b) maximum side-lobe intensity versus defocus distance in three configurations of focusing systems.
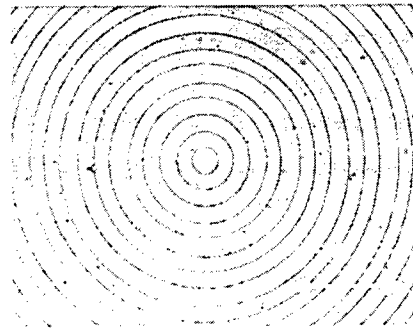

Figure 6. The microscopic picture of the fabricated DPE.

Now let us consider the case of the photoresist with 1.5μm thickness, which is a maximum thickness we usually use. When the defocus distance is 1.5μm, the spot diameter increases about 1.1 times of the focal spot size in case(ii), while 1.5 times in case(iii). On the other hand, the maximum side-lobe intensity is almost zero constantly in cases(i) and (iii), while it reaches to 4.6% of main-lobe intensity in case(ii) when the defocus distance is 1.5μm. However this side-lobe is too weak to affect pattern drawing because of nonlinear sensitivity of the photoresist material.

From above consideration, it is shown that the focusing system with the DPE has a wider focal depth with a small spot than the system without a DPE. So the focusing system with the designed DPE is useful to achieve higher resolution of pattern drawing, and more efficient than using a focusing lens with larger NA alone.

4. EXPERIMENTAL RESULTS

The designed DPE was fabricated by using a photolithography and reactive ion etching processes. In a lithography process, the laser beam lithography system developed in our laboratory and AZ1500 of photoresist (Hoechst Industry Limited) were utilized. And a compact ECR ion shower system (EIS-200ER; Elionix Inc.) was used in etching process. Figure 6 shows the microscopic picture of the fabricated DPE. The ring patterns were drawn as multiple concentric circles by changing their radii with 0.5μm pitch. The etching depth was 491nm corresponding to π phase modulation for wavelength 422nm of a He-Cd laser, which is the light source of the lithography system we use.

The fabricated DPE was mounted on the laser beam lithography system to evaluate its effectiveness. In this section, the function of the DPE is verified by measuring the spot diameters obtained in the laser beam system and
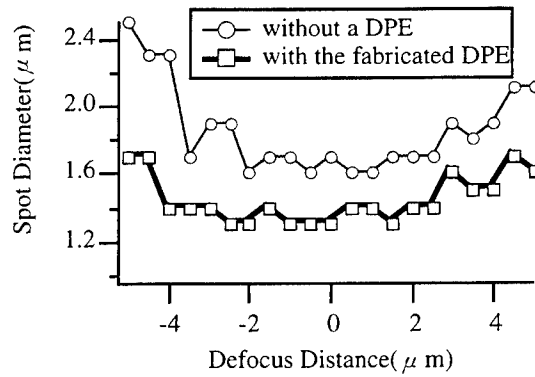
Figure 7. The measured spot diameters of the focusing system with or without the DPE.

its performance is evaluated by drawing some basic patterns.

4.1. Measurement of the Spot Diameters by Knife Edge Method

The diameters of focal and defocused spot patterns were measured by the scanning knife edge method. The scanning interval of knife edge is 0.1μm and a defocus interval was set as 0.5μm in the direction of optical axis by the control of a piezo-actuator. The positional repeatability of a x-stage used for scanning the knife edge is about 0.2μm. To reduce noise, the measured data were filtered with Savitzky-Golay filter[13] and fitted to two dimensional gaussian profile. The measured spot diameters by changing the defocus distance within $\pm5\mu$m are shown in Fig. 7. Although it is difficult to specify the focal plane precisely in the measured data, the minimum diameters can be estimated as 1.6μm for the system without a DPE and as 1.3μm for the system with the DPE. By this result, it is confirmed that the diameter is reduced by using the DPE. The spot diameter obtained with the DPE varies a little at the range of defocus distance from -4μm to 2μm and increases gradually at outside of this range. The case without a DPE also shows same characteristics. These results agree with the simulation results of Fig. 5(a).

4.2. Evaluation of the Resolution by Pattern Drawing

Firstly, in order to verify the effect of the side-lobes of a focal spot, the point spread patterns were drawn. Figure 8 shows the microscopic pictures of these patterns drawn on the photoresist; (a) is obtained without a DPE, and (b) with the DPE. For the comparison, we tested another DPE generating strong side-lobes, whose intensity is over 20% of main-lobe intensity. Figure 9(a) shows the calculated spot pattern by using the DPE with strong side-lobes and (b) is the picture of the obtained point spread patterns on the photoresist. The ring patterns generated by side-lobes appear around each central spot in Fig. 9. On the other hand, the effect of side-lobes is not presented in Fig. 8(b). These results demonstrate that the side-lobes produced by the DPE designed adequately do not make adverse effects on the pattern drawing. This is because that the side-lobe intensity is small enough (about 2.7% in design) and the photoresist have weak sensitivity to such small intensity.

In the next, line and space patterns were drawn on a photoresist and line width was measured. Straight lines with 3μm period were drawn by scanning laster beam. The photoresist images obtained by the scanning electronic microscopy (SEM) are shown in Fig. 10; (a) shows the pattern obtained without a DPE, and (b) shows the pattern with the DPE. It is verified from Fig. 10 that the width of drawn lines are reduced from 1.2μm in (a) to 1.0μm in (b). While the side-lobe area for each adjacent line is overlapped in Fig. 10(b), undesirable patterns do not appear. From these results, the drawing resolution is surely improved by the DPE developed by us. The reducing rate for a spot diameter was measured as about 83% in the experiment whereas the computer simulation predicted it as 74%. The reason of this difference mainly depends on the difference of threshold level for the focal spot. The line width obtained in the experiment depends on the sensitivity of the photoresist material, while the spot diameter is defined by the spot area with $1/e^2$ intensity of main-lobe in the computer simulation. The fabrication error in etching depth also affects the line width.
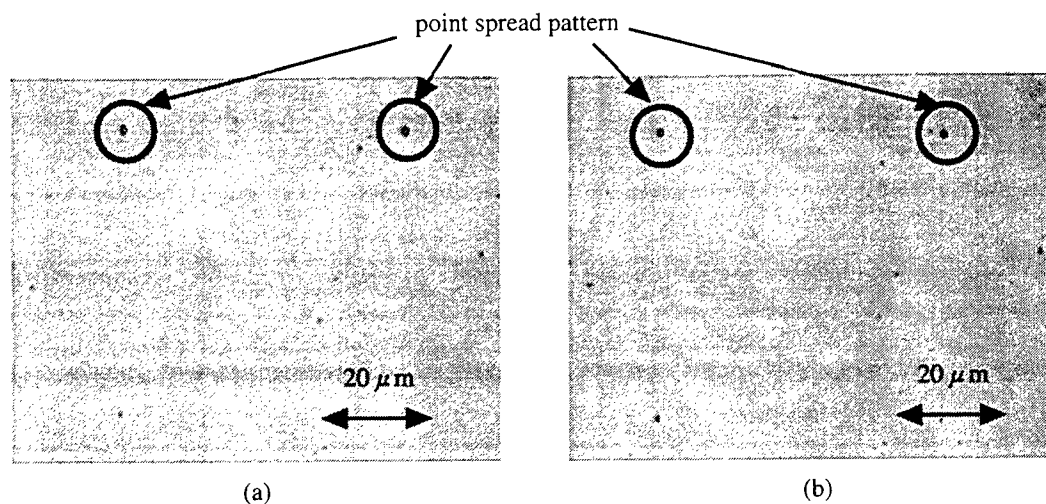
Figure 8. The microscopic pictures of point spread patterns on the photoresist material obtained (a) without a DPE and (b) with the fabricated DPE.
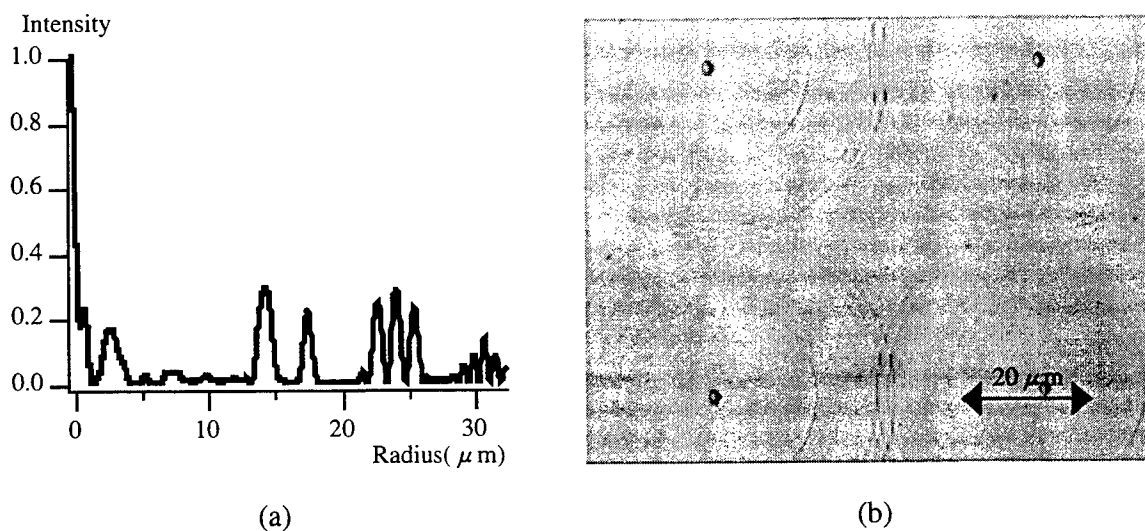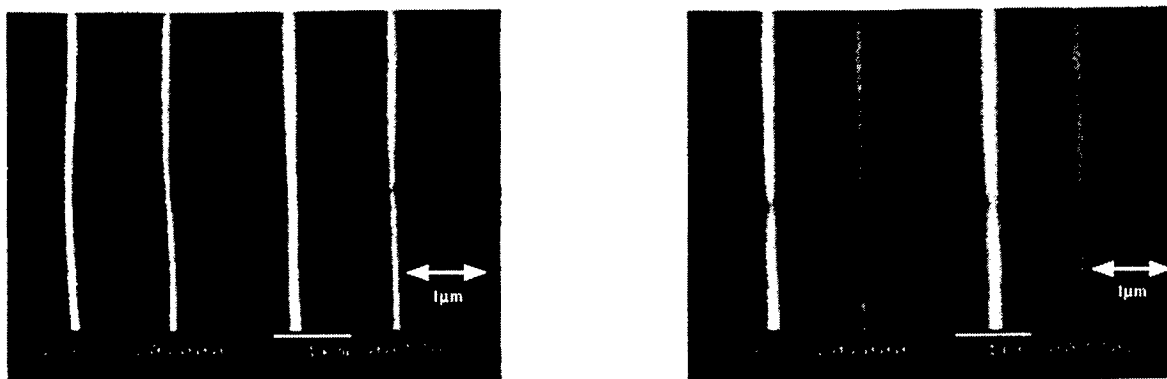

Figure 9. The experimental results for the DPE generating the strong side-lobes. (a) The calculated focal spot pattern and (b) point spread patterns drawn on a photoresist material by using the DPE.

(a) without a DPE   (b) with the DPE

Figure 10. SEM images of line and space patterns.

5. CONCLUSION

In this paper, we presented about the design, fabrication, and evaluation of the DPE to reduce the focal spot diameter, and to improve the resolution of the laser beam lithography system. By using iterative method with new constraints, we designed the rotation symmetrical DPE that can reduce the spot diameter to 74% in the cost of increase of side-lobe intensity to 2.7%. The DPE was fabricated by a lithography process and was mounted on the laser beam lithography system to evaluate the effectiveness of the DPE. We confirmed experimentally that the minimum line width of drawn pattern is reduced from $1.2\mu m$ to $1.0\mu m$ by using the fabricated DPE. It was also verified that the focal depth of the system with the DPE is wider than that of the system without the DPE when both systems produce the same focal spot size. Thus, it can be shown that the developed DPE is useful for a laser beam lithography process to obtain finer structures than the conventional system with a focusing lens alone. For improving the resolution of the focusing system, it is well-known to use a focusing lens with large NA or a short wavelength of light. Utilization of the DPE described in this paper is another approach and it would be expected to improve the density of an optical memory system, the resolution of a laser beam printer, or other focusing systems.

REFERENCES

1. D. Prongué, H. P. Herzig, R. Dändliker, and M. T. Gale, "Optimized kinoform structures for highly efficient fan-out elements," *Appl. Opt.* **31**, pp. 5706–5711, 1992.

2. T. Dresel, M. Beyerlein, and J. Schwider, "Design of computer-generated beam-shaping holograms by iterative finite-element mesh adaption," *Appl. Opt* **35**, pp. 6865–6874, 1996.

3. A. Vasara, J. Turunen, and A. T. Friberg, "Realization of general nondiffracting beams with computer-generated holograms," *J. Opt Soc. Am. A* **6**, pp. 1748–1754, 1989.

4. M. S. Kim and C. C. Guest, "Simulated annealing algorithm for binary phase only filters in pattern classification," *Appl. Opt.* **29**, pp. 1203–1208, 1990.

5. R. W. Gerchberg and W. O. Saxton, "A practical algorithm for the determinaion of phase from image and diffraction plane pictures," *Optik* **35**, pp. 237–246, 1972.

6. V. V. Kotlyar, I. V. Nikolski, and V. A. Soifer, "Adaptive iterative algorithm for focusators synthesis," *Optik* **88**, pp. 17–19, 1991.

7. J. Ojeda-Castañeda, L. R. Berriel-Valdos, and E. Montes, "Bessel annular apodezers: imaging characteristics," *Appl. Opt.* **26**, pp. 2770–2772, 1987.

8. J. Ojeda-Castañeda, R. Ramos, and A. Noyola-Isgleas, "High focal depth by apodization and digital restoration," *Appl. Opt.* **27**, pp. 2583–2586, 1988.

9. M. Mino and Y.Okano, "Improvement in the OTF of a defocused optical system through the use of shaded apertures," *Appl. Opt.* **10**, pp. 2219–2223, 1971.

10. F. Wyrowski, "Diffractive optical elements: iterative calculation of quantized blazed phase structures," *J. Opt. Soc Am. A* **7**, pp. 961 – 969, 1990.

11. A. E. Siegman, "Quasifast hankel transform," *Opt. Lett.* **1**, pp. 13–15, 1977.

12. V. V. Kotlyar, P. G. Seraphimovich, and V. Soifer, "An iterative weight-based method for calculating kinoforms," *Proc. SPIE Image Processing and Cmmputer Optics* **2363**, pp. 175–183, 1994.

13. A. Savitzky and M. J. E. Golay, "Smoothing and differentiation of data by simplified least squares procedures," *Anal. Chem.* **36**, pp. 1627–1639, 1964.

A novel speckle angular-shift multiplexing for high-density holographic storage

Peikun Zhang, Qingsheng He, Guofan Jin, Minxian Wu, Yingbai Yan, Fengtao Wang

State Key Laboratory of Precision Measurement Technology and Instruments

Department of Precision Instruments, Tsinghua University, Beijing, 100084, P.R.China

E-mail: pkzhang@pim.tsinghua.edu.cn

ABSTRACT

The volume holographic optical data storage has been an important and exciting area of research. Recently the more interested study for a high-density holographic memory is focused on the speckle wave used as the coded reference wave in various multiplexing techniques. In this paper, a novel speckle holographic storage scheme is proposed, which a random phase diffuser is added in the front of storage medium along the reference optical path of the original 90 degree storage geometry. In this scheme the incident angle of the reference beam and the place of the random phase diffuser illuminated by the reference beam can be changed simultaneously. The joint action of these changes generated a dynamic speckle wave for the reference beam in holographic storage. A theoretical model has been derived to describe the storage properties of this scheme based on the cross-correlation of dynamic speckle and the diffractive theory. The storage density influenced by the properties of the speckle patterns has been analyzed and experimentally confirmed. The results indicate that this scheme allows an increase in the data storage density with simple storage-retrieval architecture.

Keywords: Holographic storage, dynamic speckle, high-density, angular-shift multiplexing.

1. INTRODUCTION

Volume holographic data storage and processing offer the potential for high capacity inherent in bulk media, fast access owing to optical addressing, and fast transfer rates owing to their parallel nature[1]. Multiple holograms may be stored in the same volume by use of, i.e., wavelength[2], angular[3], shift[4], and phase encoding[5], typically in a volume Fourier holographic arrangement[6]. These multiplexing methods of volume holograms are based on the selective reconstruction of specific holograms out of an entire ensemble of holograms stored in the medium. Although all these methods permit high-density storage of the holograms, the longitudinal shift component of the volume-recording medium has not been considered for coding the individual pages of information. Recently V.Markov et al.[7,8] used speckle encoded reference beam to demonstrate a single volume, multilayer holographic optical memory based on the features of three-dimensional spatial-shift selectivity in a volume hologram. Their recording method permits more efficient use of the recording medium and yields greater storage density than the spherical or plane-wave reference beams.

According to V.Markov's method, a novel scheme is adopted to realize the same storage performance by using the dynamic speckle rather than the static speckle. It is convenient to use this scheme in the general system of holographic storage by use of angular multiplexing. A random phase diffuser is placed in front of the storage medium and the reference beam transmitted through it with different incident angle into the storage medium. Along with the incident angle change, the illuminated part of diffuser shifted simultaneously. The joint action of these two kinds of variations will transform the original collimated reference beam into a dynamic speckle, as illustrated in Fig.1.
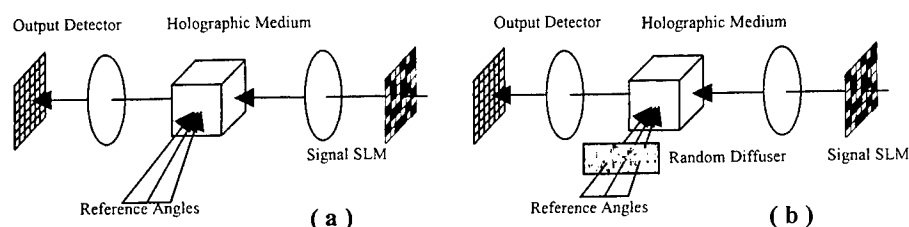

Fig.1. (a) General schematic for holographic storage by angular multiplexing. A signal is generated by an illuminated amplitude spatial light modulator (SLM), and reference beams are incident at different angles. (b) The reference beams are generated by illuminating an random phase diffuser with different incident angles and positions simultaneously.

In this paper, a theoretical model has been derived to describe the storage properties of this system based on the cross-correlation of dynamic speckle and the diffractive theory. The numerical calculation of the model indicates that the angular selectivity for angular multiplexing has been improved by adjusting the speckle size and so the storage density has been increased. The function of dynamic speckle reference beam is showed to be the same as the static speckle reported by V.Markov. The experiment results farther confirm that the model is competent for describing the holographic storage with dynamic speckle reference beam.

2. THEORY

Let us consider a volume phase hologram recorded with reference speckle wave (writing wave) $R_W(\vec{r})$ and plane wave (signal wave) $S_0(\vec{r}) = A \exp(i\vec{k}_{S_0} \cdot \vec{r})$ of the amplitude A using a 90 degree storage geometry. We assume that after exposure the permittivity $\varepsilon(\vec{r})$ of the recording material will exhibit local changes $\varepsilon(\vec{r}) = \varepsilon_0 + \delta\varepsilon(\vec{r})$ and $\delta\varepsilon(\vec{r})$ is the modulated component of the permittivity. The value of $\delta\varepsilon(\vec{r})$ is supposed to be proportional to the square of the electric field of the interacting waves, i.e.

$$\delta\varepsilon(\vec{r}) \propto |E|^2 = |\vec{S}_0(\vec{r}) + \vec{R}_W(\vec{r})|^2 \propto S_0(\vec{r})R_W^*(\vec{r}) \tag{1}$$

Now we consider the reconstruction of the hologram influenced by the reading speckle wave $R_R(\vec{r})$. Propagation of transmitted $R_R(\vec{r})$ and diffracted $S(\vec{r})$ waves in the volume of the hologram can be described through the system of Maxwell's equations[9]. For the monochromatic waves of identical polarization in an isotropic media, the system can be reduced to a scalar wave equation

$$\Delta E(\vec{r}) + [\varepsilon_0 + \delta\varepsilon(\vec{r})]k_0^2 E(\vec{r}) = 0 \tag{2}$$

In the first Born approximation, the total field $E(\vec{r})$ in the hologram be presented as an incident reference wave $R_R(\vec{r})$ plus a result of diffracting, $S(\vec{r})$, i.e.

$$E(\vec{r}) = R_R(\vec{r}) + S(\vec{r}) \tag{3}$$

Substituting the total field (3) into the Helmholtz equation (2) and considering that $S(\vec{r})$ is of the first order with respect to the perturbation parameter $\delta\varepsilon(\vec{r})$, then the diffracting field $S(\vec{r})$ satisfies the equation

$$\Delta S(\vec{r}) + k_0^2 \varepsilon_0 S(\vec{r}) = -\delta\varepsilon(\vec{r})k_0^2 R_R(\vec{r}) \tag{4}$$

the solution of (4) can be presented as

$$S(\vec{r}) = -k_0^2 \int_{-\infty}^{\infty} \delta\varepsilon(\vec{r})R_R(\vec{r})G(\vec{r},\vec{r}')dV'$$

$$\cong -A k_0^2 \exp(i\vec{k}_{S_0} \cdot \vec{r}) \int_{-\infty}^{\infty} R_W^*(\vec{r}')R_R(\vec{r}')G(\vec{r},\vec{r}')dV' \tag{5}$$

where

$$G(\vec{r},\vec{r}') = -\frac{1}{4\pi} \frac{\exp[ik_0|\vec{r} - \vec{r}'|]}{|\vec{r} - \vec{r}'|}$$

is Green's function.

In the novel scheme for speckle holographic storage, the variation of reference wave includes both changes of incidence angle and shift of illuminating part on the random phase diffuser simultaneously. For the sake of simplification, we assume that the central direction of propagation for the writing wave $R_W(\vec{r})$ is normal to the hologram front surface and the reading wave $R_R(\vec{r})$ has a small angle θ of deviation with respect to the writing wave, as shown in Fig.2.

By using the Fresnel-Kirchhoff diffraction integral[10], the writing and reading reference waves in this system can be expressed as

$$R_W(\vec{r}) = \int_{-\infty}^{\infty} P(\vec{r}_0)A_W(\vec{r}_0)h_W(\vec{r},\vec{r}_0)d\vec{r}_0 \tag{6}$$
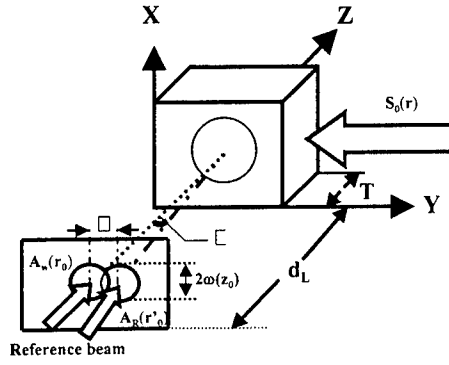
Fig.2. Geometry of the hologram recording by signal plane wave $S_0(r)$ and dynamical speckle reference wave $R_W(r)$ and reading wave $R_R(r)$. Here T is the diameter of signal beam, d_L is the distance from the hologram front surface to random-phase diffuser, Δ is the shift of the illuminated part of the diffuser and θ is an angle between writing beam and reading beam.

$$R_R(\vec{r}') = \int P(\vec{r}_0')A_R(\vec{r}_0')h_R(\vec{r}',\vec{r}_0')d\vec{r}_0' \tag{7}$$

where $\vec{r}$ and $\vec{r}'$ denote the vector coordinate of the diffuse plane, $A_W(\vec{r}_0)$, $A_R(\vec{r}_0')$ are the complex amplitude transmittance of the diffuser with respect to writing and reading waves, respectively. The following relationship is satisfied

$$\left\langle A_W^*(\vec{r}_0)A_R(\vec{r}_0')\right\rangle = \delta(\vec{r}_0 - \vec{r}_0' - \vec{\Delta}) \tag{8}$$

in which $\delta(\ )$ represents a Dirac delta function, $\langle\cdots\rangle$ standing for an ensemble average and $\vec{\Delta}$ is the shift of the illuminated part of the diffuser arising from the change of incidence angle of illuminating beam.

The transfer functions of the optical system for writing and reading waves can be written

$$h_W(\vec{r},\vec{r}_0) = \frac{1}{i\lambda z}\exp\left(i\frac{2\pi}{\lambda}z\right)\exp\left(i\frac{\pi}{\lambda z}|\vec{r} - \vec{r}_0|^2\right) \tag{9}$$

$$h_R(\vec{r}',\vec{r}_0') = \frac{\cos\theta}{i\lambda z}\exp\left(i\frac{2\pi}{\lambda}z\right)\exp\left(i\frac{\pi}{\lambda z}|\vec{r}' - \vec{r}_0'|^2\right) \tag{10}$$

When a Gaussian beam with a waist width ω_0 is employed to illuminate the diffuser, the illumination function of diffuser can be written[11]

$$P(\vec{r}) = \frac{\omega_0}{\omega(z_0)}\exp\left(i\frac{2\pi z_0}{\lambda}\right)\exp\left(-\frac{|\vec{r}|^2}{\omega^2(z_0)}\right)\exp\left(i\pi\frac{|\vec{r}|^2}{\lambda\rho(z_0)}\right) \tag{11}$$

where $\omega(z)$ and $\rho(z)$ are the width and wave front curvature radius of the illuminating beam at the diffuser and are given by

$$\omega(z) = \omega_0(1 + z^2/a^2)^{1/2} \tag{12}$$

$$\rho(z) = z(1 + a^2/z^2) \tag{13}$$

and

$$a = \pi\omega_0^2/\lambda \tag{14}$$

Substitution of Eqs (6)-(11) into Eq.(5) leads to

$$S(\vec{r}) = Ak_0^2 \exp(i\vec{k}_{S_0}\cdot\vec{r})\frac{\exp(ikr)}{4\pi r}\int_{-\infty}^{\infty}\Gamma(\vec{r},\vec{r}')dV' \tag{15}$$

where $\Gamma(\vec{r},\vec{r}')$ is the cross-correlation function of the speckle reference beams, given by

238

$$\Gamma(\vec{r},\vec{r}') = \left\langle R_W^*(\vec{r})R_R(\vec{r}') \right\rangle = \frac{\omega_0^2 \cos\theta}{\omega^2(z_0)\lambda^2 z^2} \exp\left(-\frac{\left|\vec{\Delta}\right|^2}{2\omega^2(z_0)}\right)$$

$$\times \exp\left(-\frac{\pi^2 \omega^2(z_0)}{2\lambda^2 z^2}\left|\sigma\vec{\Delta}-\vec{r}+\vec{r}'\right|^2\right) \times \exp\left\{i\frac{\pi}{\lambda z}\left[\left|\vec{r}\right|^2 - \left|\vec{r}'\right|^2 + \vec{\Delta}\cdot(\vec{r}+\vec{r}')\right]\right\} \qquad (16)$$

where $\sigma = 1 + \dfrac{z}{\rho(z_0)}$, $\left|\vec{\Delta}\right| = d_L tg\theta$.

As the experimentally measured value is the diffracted beam intensity $I_D = |S|^2$, it is convenient to introduce the parameter of relative diffracted beam intensity $I_{DN}(\theta) = I_D(\theta)/I_D(\theta=0)$, where $I_D(\theta=0)$ is the diffracted beam intensity at zero angle deviation. Then we can express the $I_{DN}(\theta)$ as

$$I_{DN}(\theta) = \cos^2\theta \exp\left(\frac{d_L^2 tg^2\theta}{\omega^2(z_0)}\right) \frac{\left|\iiint_\cdot H(\vec{r},\vec{r}')\exp[M(\vec{r},\vec{r}')]\exp[iN(\vec{r},\vec{r}')]dx'dy'dz\right|^2}{\left|\iiint_\cdot H(\vec{r},\vec{r}')dx'dy'dz\right|^2} \qquad (17)$$

where

$$H(\vec{r},\vec{r}') = \frac{1}{z^2}\exp\left\{-\frac{\pi^2\omega^2(z_0)}{2\lambda^2 z^2}\left[x'^2+(y-y')^2\right]\right\}\exp\left\{i\frac{\pi}{\lambda z}\left[-x'^2+(y^2-y'^2)\right]\right\}$$

$$M(\vec{r},\vec{r}') = -\frac{\pi^2\omega^2(z_0)}{2\lambda^2 z^2}\left[\sigma^2 d_L^2 tg^2\theta + 2\sigma d_L tg\theta(y-y')\right]$$

$$N(\vec{r},\vec{r}') = \frac{\pi}{\lambda z}d_L tg\theta(y+y')$$

The equation (17) can be used to discuss the storage properties of our novel system, such as, the influence of speckle size on the data storage density. From this equation the speckle size is determined by the $\omega(z_0)$ and d_L, i.e. the correlation length of dynamic speckle $\delta = \dfrac{\lambda z}{\pi\omega(z_0)}$.
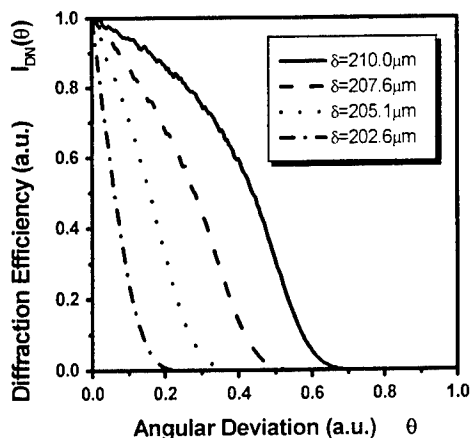
3. EXPERIMENTAL RESULTS

We have calculated numerically the dependence of diffracted beam intensity $I_{DN}(\theta)$ on incident angular deviation at reconstruction with different speckle sizes according to Eq.(17). The speckle size varied with the distance from the front surface of the hologram to random phase diffuser and the diameter of illuminated part on the diffuser. The sensitivity of the diffracted beam $I_{DN}(\theta)$ has a monotonic character and smoothly falls down with increase of the angular deviation around the hologram writing beam, as shown in Fig.3.

Obviously, the bigger the speckle size δ is, the more slowly the diffractive intensity attenuates along with the angular deviation increasing. The angular selectivity of the storage arrangement, as shown in Fig.1b, by using the joint action of the angular-shift variation of the illuminating beam that produce a dynamic speckle on the storage medium, can be more sensitive if an appropriate diffuser be used. The characteristics of selectivity become mainly dependent on the properties of the speckle pattern of the reference beam, that is, speckle size. In comparison with the selectivity determined by cross-correlation between recording and retrieving speckle structures the Bragg selectivity of the original angular multiplexing becomes subsidiary.

A standard 90 degree storage geometry for angular multiplexing was used in the experiment to demonstrate the multiple holograms stored in a same volume with dynamic speckle reference beams with simply an addition of diffuser in the reference optical path. As the angle scanning, a collimated light beam will firstly illuminate the diffuser with different incident angle and position and then transmit through diffuser to form a speckle pattern on the surface of the lithium niobite crystal. The central locations of all speckle patterns are almost at the same point during scanning as in the original angular multiplexing system (Fig.1a). A diode pumped YAG laser (λ=532nm, P~200mW) was used as a coherent light source to

record volume holograms with a block of $LiNbO_3$: Fe crystal. A ground glass is used as the diffuser in our experiment and the speckle sizes are changed through adjusting the distance from crystal surface to diffuser d_L.

As seen from Fig.4, the angular selectivity is monotonically increasing with the increasing of d_L. The dependence of selectivity on speckle properties showed in Fig.4 corresponds to the theoretical analysis. This consistency shows that our theoretical model is suitable for describing the characteristic of dynamic speckle holographic storage.

Fig. 3. Calculated dependence of the normalized diffracted beam intensity $I_{DN}(\theta)$ on incident angular deviation θ at reconstruction with different speckle sizes δ. In this case, the parameters of $\omega_0=370\mu m$, $d_L=500mm$, and T=8mm are chosen.
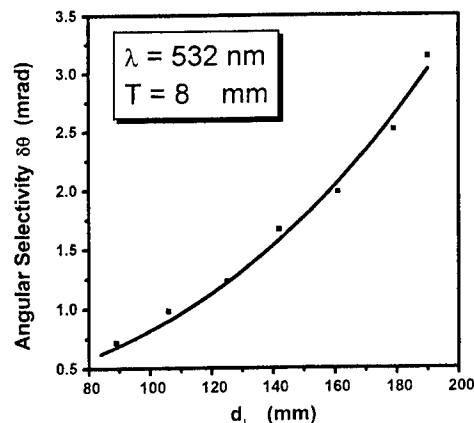
Fig. 4. The incident angular selectivity $\delta\theta$ as a function of the distance d_L from the hologram front surface to random phase diffuser.

4. CONCLUSION

We have proposed a novel scheme that introduces a dynamic speckle in the original angular multiplexing arrangement by means of an appending a random phase diffuser in the front of storage medium along the reference optical path. We have also derived an expression for new angular-shift multiplexing mechanism by applying the perturbation technique and cross-correlation of dynamic speckle as well as the diffractive theory. That calculated results coincide with experimental ones indicates our theoretical model being able to analyze this novel scheme rightly.

The selectivity of holographic storage with dynamic speckle is mainly limited by the speckle size. Reducing the speckle size on the surface of storage medium can unceasingly increase the data storage density as long as the scan resolution meets the needs of retrieval. We can place the diffuser close to the storage medium or change illuminating condition to obtain high-density storage. In addition, the dynamic speckle has ability to achieve 3D holographic storage based on the features of three-dimensional spatial-shift selectivity that leads to get more high-density of holographic storage.

ACKNOWLEDGMENTS

REFERENCES

1. J. F. Heanue, M. C. Bashaw, and L. Hesselink, "Volume holographic storage and retrieval of digital data", *Science*, **256**, pp. 749-752, 1994.
2. G. A. Rakuljic, V. Leyva, and A. Yariv, "Optical data storage by using orthogonal wavelength-multiplexed volume holograms", *Opt. Lett.*, **17**, pp. 1471-1473, 1992.
3. F. H. Mok, "Angle-multiplexed storage of 5000 holograms in lithium niobate", *Opt. Lett.*, **18**, pp. 915-917, 1993.
4. D. Psaltis, M. Levene, A. Pu, and G. Barbastathis, "Holographic storage using shift multiplexing", *Opt. Lett.*, **20**, pp. 782-784, 1995.
5. J. E. Ford, Y. Fainman, and S. H. Lee, "Array interconnection by phase-coded optical correlation", *Opt. Lett.*, **15**, pp. 1088-1090, 1990.
6. L. Hesselink and M. C. Bashaw, "Optical memories implemented with photorefractive media", *Opt. Quantum Electron.*, **25**, pp. S611-S661, 1993.

7. V. Markov, J. Millerd, J. Trolinger, and M. Norrie, "Multilayer volume holographic optical memory", *Opt. Lett.*, **24**, pp. 265-267, 1999.
8. V. Markov, "Spatial-angular selectivity of 3-D speckle-wave holograms", *Journal of Imaging Science and Technology*, **41**, pp. 383-388, 1997.
9. L. Solimar and D. J. Cooke, *Volume Holography and Volume Gratings,* Academic Press, New York, 1981.
10. M. Born and E. Wolf, *Principles of Optics,* Pergamon Press, Oxford, 1980.
11. T. Iwai, N. Takai, and T. Asakura, "Dynamic statistical properties of laser speckle produced by a moving diffuse boject under illumination of a Gaussian beam", J. Opt. Soc. Am., **72**, pp. 460-467, 1982.

Design and Implementation of A New Two-Way Opto-Electronic Probe

for Optical Information Processing Components Analysis

Shyh-Lin Tsao[*] and Thi-Chi Liou

Department of Electrical Engineering

Yuan Ze University

Chung-Li, Taiwan, R.O.C

ABSTRACT

In this paper, a new two-way measurement method of optical signal processing elements is presented. The proposed method can decrease testing time and reduce human errors induced by disconnection in conventional one-way testing method. We can measure the scattering parameters of optical devices with fast two-way measurement when applying the new probes in conventional network analyzers. We demonstrated using our designed opto-electronic probes can measure the frequency responses of S_{21} and S_{12} of optical information processing component simultaneously. No reverse connections are needed for transfer functions measurement. In the future, this system can be applied to measure the characteristics of broadband optical signal processing elements for system applications. The theoretical model we built is very match to the experimental results.

Key words: Opto-electronic Probe , Optical signal processing , Measurement , Fiber optics, Optical filter

1. INTRODUCTION

High speed optical signal transmission above Gbps in fiber communications show promising results recently[1~8] . Using lightwave technology for measuring S parameters of optical signal processing components has becoming an important issue. The application of a microwave network analyzer tailored an opto-electronic probe for analyzing fiber-optic signal processing components has been reported [9]. But, the human errors induced by disconnections are introduced with using full two ports S parameter measurement with changing direction of element. The purpose of "through" calibration is to correct errors in transmission coefficients in both the forward and reverse direction for the measurement of device with many ports [10]. But no equipment can achieve a two-way "through" calibration for optical signal processing elements until now. The use of lightwave technology for measuring S parameters of optical component is becoming important. Development of an optical component 100Gbps laser diode were reported recently[11]. The microwave photonic component characteristics measurement is obviously urgent now. Some calibrations of prototype true time delay optical signal processing applications, such as optical beam-forming circuit networks, array antennas and matched filters applications, are reported [12].

[*] Correspondence: E-mail:jimmy@saturn.yzu.edu.tw, Telephone: 886-3-4638800-424, Fax: 886-3-4639355

In this paper, we propose and demonstrate a new probe for applying in optical component network analyzer. A two-way fast measurement can be achieved by using the new method to reduce testing time and human errors.

2.SYSTEM STRUCTURE AND RESULTS

2.1 Description of the system

The schematic diagram of the new method of testing two-port optical signal elements is shown in Fig.1. We designed a new two-way optoelectronic probe including an electrical circulator, an optical circulator, an optical transmitter and an optical receiver as the dashline block shown in Fig.1 .The device under test (DUT) is inserted in the middle of the two probes.   We use two designed probes to set up the optical component S parameters measurement testbed. In this paper, we use a fiber ring as a DUT. The parameters of the DUT are G (coupling coefficient) = 0.9 , L(length) =154 cm and ρ (intrinsic loss of coupler)= 0.85, as shown in Fig.2.

When the system function of the network analyzer operates at the S_{21} mode and S_{12} mode, the network analyzer can output electronic frequency sweeping signal to the optical transmitter, then through the optical circulator to the DUT. After the signal go through the DUT, the optical signal received by the second probe. The optical signal will be converted to the electrical signal by the optical receiver. Because of the electrical circulators and optical circulators in these two probes can provide two-way signal bypassing function, the measurement system we setup can provide a two-way fast S-parameter measurement. In the following section, we use this system to measure a single fiber resonator notch filter.

.

2.2 Theory and Experimental Results

The theorretical model of a single fiber ring resonator notch filter used as the DUT shown in Fig.2 is derived in this subsection. The signal flow chart of the DUT is shown in Fig.3. We define the transfer function of the first path as $H_1(z)$ and the second path as $H_2(z)$.

Output $O_F(z)$ of the feedback path can be written as

$$O_F(Z) = H_F(z)I_F = \frac{LZ^{-1}I_F}{1 - LGZ^{-1}\rho} \tag{1}$$

where G is the coupling coefficient, ρ is the intrinsic loss of coupler, L is the loop transmittance of the fiber loop line.

The output O_1 of   the first path can be described as

$$O_1(Z) = H_1(z)I = G\rho I \tag{2}$$

The output O_2 (z) at the second path output is

$$O_2(Z) = H_2(z)I_2 = \left(1 - G\rho\right)^2 H_F(Z)I_2 = \frac{(1 - G\rho)^2 LZ^{-1}I_2}{1 - LGZ^{-1}\rho} \tag{3}$$

Combining the above three equations, we find the transfer function can be represented as

$$H(Z) = \frac{O}{I} = G\rho + \frac{(1-G\rho)^2 L Z^{-1}}{1 - LGZ^{-1}\rho} \qquad (4)$$

From the above derived theoretical model of the DUT, we simulate the frequency responses of S_{21} and S_{12}. The simulation results of S_{21} and S_{12} are shown in Fig.4 and Fig.5, respectively. The measured results are shown in Fig.6 and Fig.7, respectively. Using the experimental setup shown in Fig.1, we can measure the frequency responses of S_{21} and S_{12}. Comparing the numerical and experimental results, we find these two results have good coincidence. This results shows our designed two-way opto-electric probe is very helpful for measuring the optical fiber information components.

3. CONCLUSION

In this paper, we made and design a new two-way optoelectronic probe for application in S parameters measurement of optical information processing components. Measuring a fiber ring notch filter as a DUT, we find the numerical results and the experimental results matched very well. Therefore, this two-way optoelectronic probe can be studied in the future for microwave-photonic information processing devices measurement.

ACKNOWLEDGMENT

REFERENCE

1. H. Izadpanch, D. Chen, C.Lin, M. A. Saifi, . I. Way, A. Yiyan, J. L. Gimlett," Distortion- free amplification of high-speed test patterns up to 100 Gbps with erbium- droped fiber amplifiers", Electronic.Letters, vol.27,no.3, pp.196 ~ 198,1991.

2. G.J.Pondock, M. J. L. Cahill and D.D Sampson, "Multi-gigabit per second demonstration of photonic code-division multiplexing", Electronic.Letters,vol.31,no.10,pp.819~820,1995.

3. M.Nakazawa,K.Suzuki,Y.Kimura,"3.2-5 Gbps,100km error-free soliton transmission with erbium amplifiers and repenters", IEEE photonics Tech Lett.,vol.23,no.2,pp.216~219,1990.

4. K.iwatsuki, K. Suzuki, S.Nishi and M.Saruwatari,"20Gbps optical soliton data transmission over Tokim using distributed fiber Raman amplifiers", paper PDP4 of proceeding of optical amplifiers and their applications, Monteretey, California, August,1990.

5. I.D. Garber, D.P. Michal, "Performace of shot-noise limited optical communications in presence of intersymbol interference", Electronics Letters, ,Vol.24, pp.1008-1010,1988. Microwave Photonics, International Topical Meeting ,pp.55-58,1998.

6. H. Taga , S. Yamamoto , N. Edagawa , Y. Yoshida , S. Akiba , H. Wakabayashi," Fiber chromatic dispersion equalization at the receiving terminal of IM-dd ultra-long distance optical communication systems", Lightwave

Technology, vol.26,no.5,pp.1042~1046,1994.

7. V. Pruneri, F.Samoggia, G. Bonfrate, H.Takebe, P.G.Kazansky, "Poled glass optical communication devices", Integrated Optics and Optical Fibre Communications, 11th International Conference, Vol.2, pp.103-106,1997..

8. F.S.Yang , M.E. Marhic, X.Y. Zou, L.G. Kazovsky,"Cancellation of SRS cross talk in an analog WDM optical communication system by a parallel technique", Technical Digest ,pp.86-87,1998.

9. David Curtls and Elizabeth E.Ames, "Characterization of high speed optical components", IEEE Transaction Microwave Theory and Techniques,vol.38,no.5,pp.552~559,1990..

10. Balasundaram Elamaran,Roger D. Pollard , Stavros Iezekiel," Tax calibration of optcial scattering parameter test set".

11. Takada, A., and Sarawatari, M.,"100 Gbps optical signal peneration by time-division multiplication of modulated and compressed pulses from gain-switched DFB laser diode", Electron.   Lett.,Vol.24,No.23,pp.1406-1408,1998.

12. Atsushi Ishihara, "Method for calibrating circuit network measurement devices", United States Patent number 5,646,536,1997.
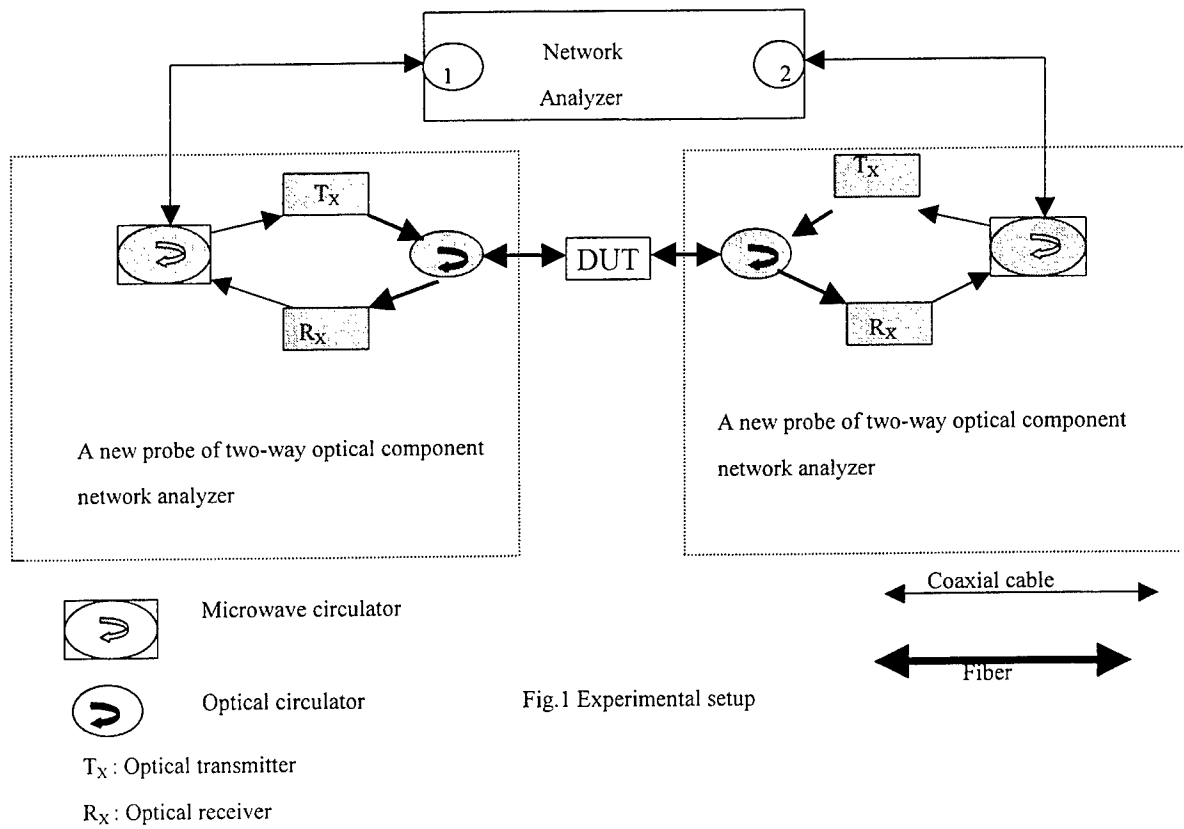
Microwave circulator

Optical circulator

Fig.1 Experimental setup

T_X : Optical transmitter
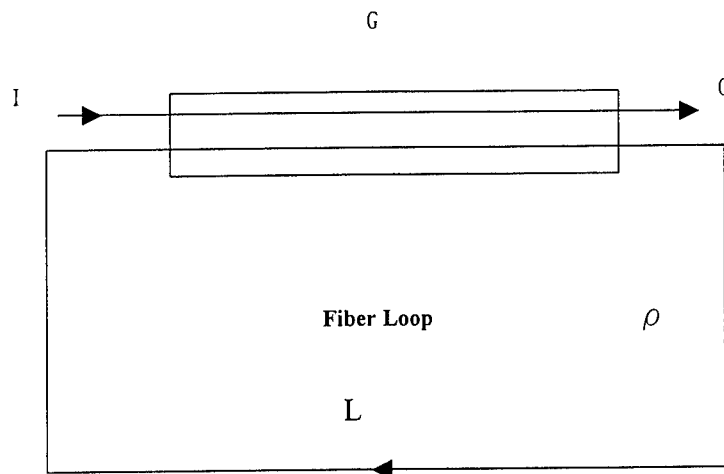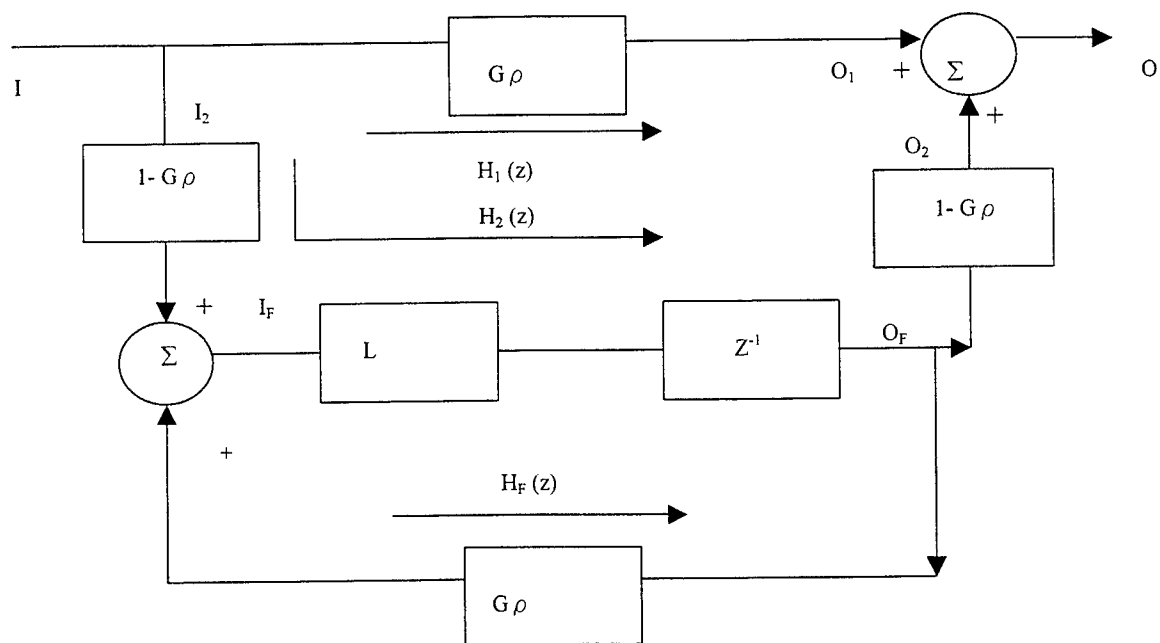
R_X : Optical receiver

Fig.2 Schematic diagram of an SFRRF

Fig.3 The singal flow chart of the fiber ring resonator notch filter as a DUT

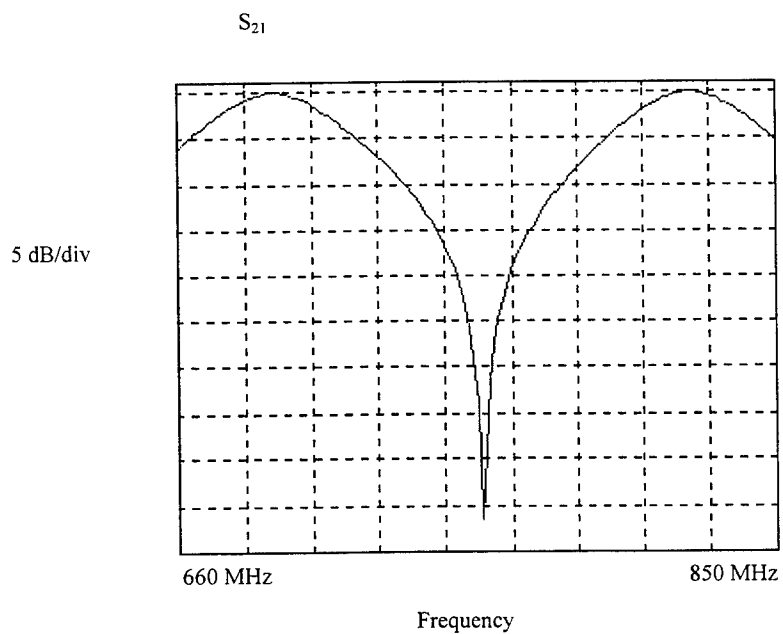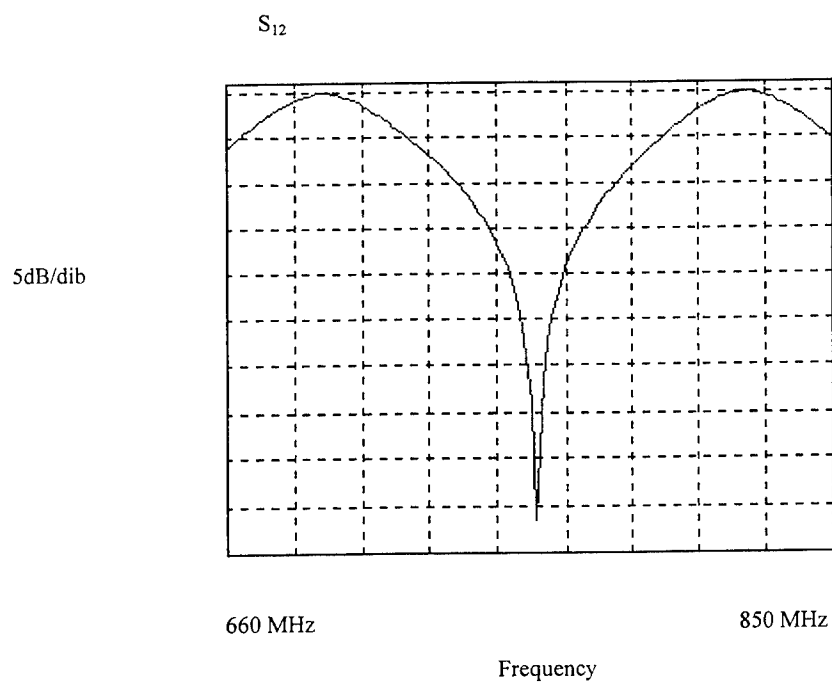Fig.4 Simulated frequency response of S_{21} of the DUT

S_{12}

5dB/dib

660 MHz   850 MHz

Frequency

Fig.5 Simulated frequency response of S_{12} of the DUT

S_{21}

5 dB/div

660 MHz   850 MHz

Frequency

Fig.6 Measured frequency response of S_{21} of the DUT

248

S_{12}

5 dB/div

600 MHz   850 MHz
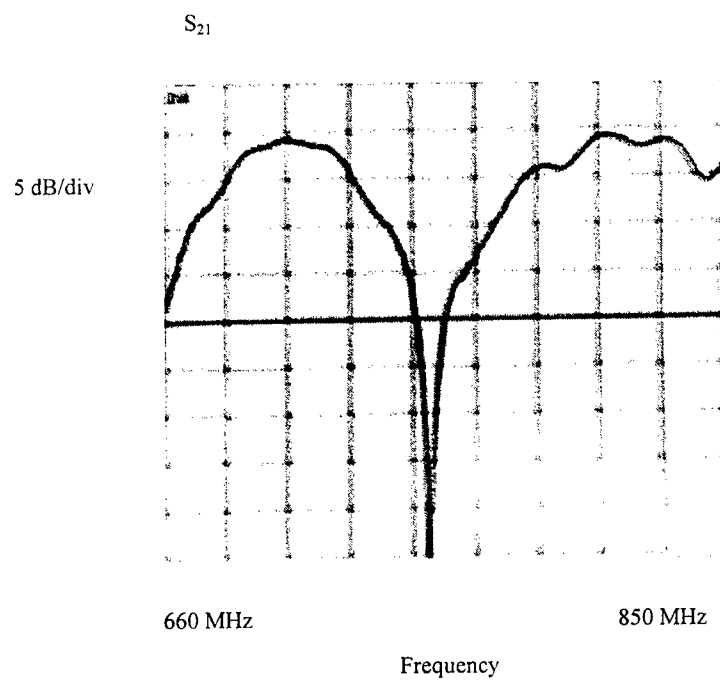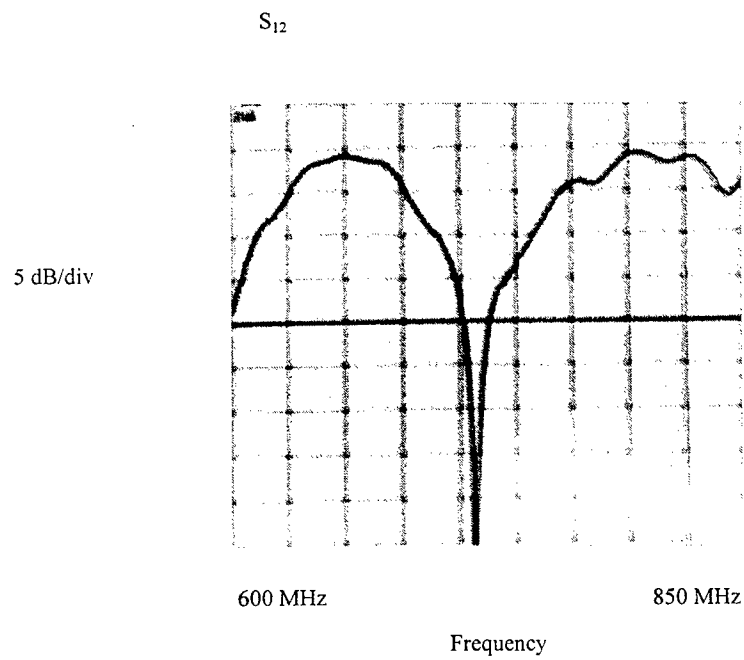
Frequency

Fig.7 Measured frequency response of S_{12} of the DUT

Development of Rewritable Dual-layer Phase-change Optical Disks

Feng-Hsu Wu, Tsung-Eong Hsieh[1], Han-Ping D. Shieh
Institute of Electro-Optical Engineering,
[1]Department of materials Science and Engineering,
National Chiao Tung Univ., Hsin-Chu, Taiwan, 300
E-mail: u8724528@cc.nctu.edu.tw

Abstract

Dual-layer optical disks comprised of two data layers were developed to study readout/write/erase characteristics. This disk was composed of recording layer 1and 2, of high transmittance and high reflectivity, respectively. Layer 1 and 2 of 15 and 20 nm increase transmittance and reduce writing power for recording. Only 1.5 mW laser power was sufficient for readout, 9 and 16 mW was required for recording on recording layer 1 and 2, respectively. Thse dual-layer disk can double data capacity on a disk substrate.

1. Introduction

Digital versatile disks (DVD) are now emerging in the market. Many advanced recording technologies, such as mark-edge recording and land/groove recording, have already been proposed for DVD-RAM disks in increasing their recording density and capacity. Volumetric optical disks can increase the storage capacity by using multiple data layers for storage where the data are recorded on each layer of a multi-layer stack[1,2], respectively. In this paper, we present the study of write/erase/read performance of a dual-layer erasable optical disks using phase change recording media.

2. Design of disk structure and thermal simulation

The dual-layer optical disk was composed of two polycarbonate substrates[3], which were coated with layer 1 and layer 2, as shown in Fig. 1, respectively. Layer 1 is the first data layer impinged by laser beam while layer 2 is the second layer. The data layers of the disk were spaced from each other by an UV resin layer of 40 μm in thickness.

The transmittance of the layer 1 must be sufficiently large in order to focus, track and record on the layer 2 through the layer 1. Thus, the disk structure with no metallic reflective for the layer 1, which is in a "High-to-Low" structure, where the reflectivity decreases in accordance with recording process (crystalline to amorphous state). Since metallic cooling layer accelerates phase change material in temperature descending during recording process, recording performance of layer 1 of no metallic cooling layer will be lower.

For the layer 2, reflectivity must be high, because the incident laser beam is inevitably reduced by the light absorption and reflection from the layer 1. In order to increase the optical efficiency, the transmittance is set to zero. Thus, a "Low-to-High" structure is adopted. Besides, owing to write power of laser pulse is proportional to thickness of recording media, proper thickness of recording media is necessary. Therefore, schemes to meet the write power limit of commercial disk drive (less than 20 mW) by using thin active layer are necessary.

By thin-film theorem and metric optics, the reflectivity, transitivity, and absorption coefficient of the two recording layers were calculated. A very simple 3 and 4 layers disk structure for recording layer 1 and 2 that meets the condition mentioned above was selected. Optical design of reflection, absorption and transmittance of recording layer 1 and 2 is shown in Fig. 2.
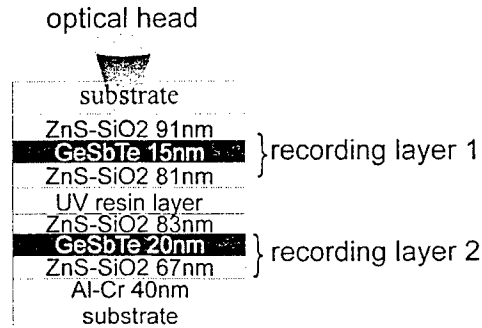
optical head

substrate
ZnS-SiO2 91nm
GeSbTe 15nm
ZnS-SiO2 81nm } recording layer 1
UV resin layer
ZnS-SiO2 83nm
GeSbTe 20nm
ZnS-SiO2 67nm } recording layer 2
Al-Cr 40nm
substrate

Fig. 1 Schematics of a dual layer optical disk structure

crystalline state

| 21% | 49% | 30% |

crystalline state

| 35% | 65% |

amorphous state

| 6% | 37% | 61% |

amorphous state

| 55% | 45% |

recording layer 1

recording layer 2

— reflection ⬜ absorption ▓ transmittance
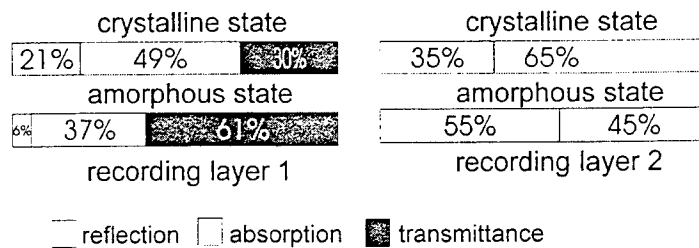
Fig. 2 Reflection, absorption and transmittance of layer 1 and 2 of a dual-layer optical disk

A gaussian-distributed diffraction limited spot impinged perpendicular on a disk of a multi-layered thin film structure was then analyzed by thermal simulation. When the light penetrates the multi-layer structure, its energy is absorbed by the recording layer, and converted into heat. The heat diffuses to neighbor area and the other layers. The temperature distributions was calculated by a thermal simulation program "Temprofile"[4] to ensure that quench rate was high enough for writing by simulation. The quench rate of layer 1 and 2 is 6 and 9 °C/ns, respectively, as shown in Figs. 3, which can meet the writing requirement[5].
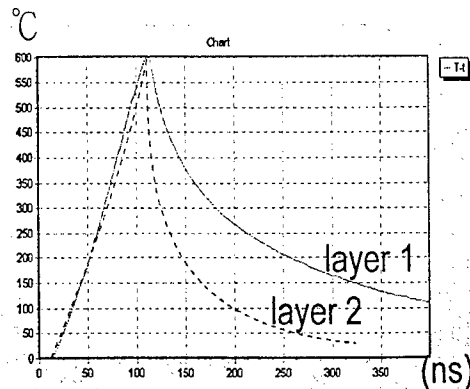

Fig. 3 Simulated quench rate of layer 1 and 2 of dual layer optical disk

3. Experiment

Disks of recording layers 1 and 2, were deposited on a u-grooved 120-mm diameter polaycarbonate substrate separately, then glued together by an ultraviolet-light-cured resin. The parameters of the read and write measurement are listed in Table 1. Write pulse patterns shown in Fig. 4 were frequency-modulated between 3 and 9 MHz; peak laser power was modulated between 0 and 20 mW.
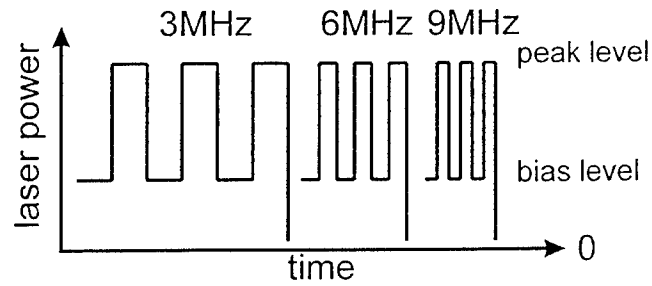

Fig. 4 Write pulse waveform used in this experiment

Table 1 Read/write parameters

Linear velocity	7.33m/s
Laser wave length	660 nm
Numerical Aperture (NA)	0.6
Read power	1.5 mW
Recording waveform	as shown in Fig. 4

4. Results and discussions

CNR as a function of laser peak power for layer 1 and 2 was shown in Fig. 5. At writing frequency of 3 MHz, corresponding to 1.2 µm in mark length, the peak power giving a CNR of 45 dB was 9 mW for layer 1 and 13 mW for the layer 2. The eraseability better than 35 dB was obtained at erase laser power of 6 and 9 mW for layer 1 and 2, respectively.
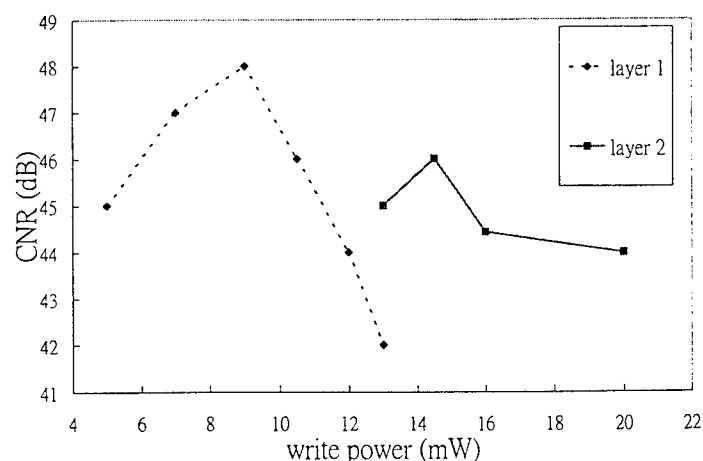
Fig. 5 CNR as a function of write power for layer 1 and 2 at recording frequency of 3 MHz

CNR as a function of laser peak power for layer 1 and 2 is shown in Fig. 6. The peak CNR is at power of 9 mW for layer 1 and at 13 mW for the layer 2 at recording frequency of 7 MHz, corresponding to 0.52 µm in mark length. Thin recording layers were adopted in dual-layer optical disk recording in, to increase write power sensitivity, i.e. too low a write power won't be adequate for phase change media and too high write power will destroy the phase change material or disk track. Therefore, optimized write power can achieve higher CNR on this dual-layer disk.
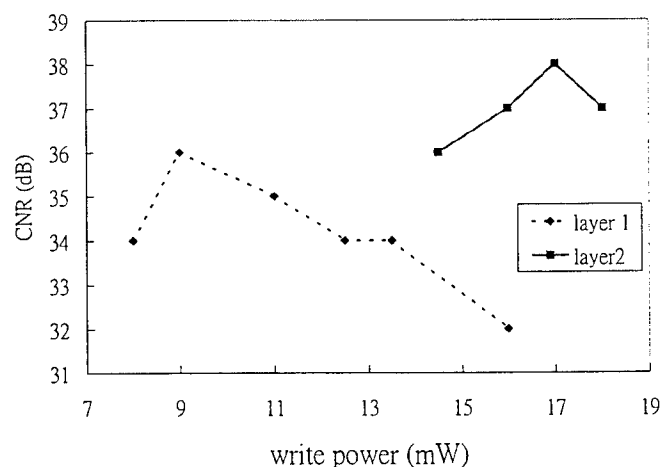

Fig. 6 CNR as a function of write power for layer 1 and 2 at recording frequency of 7 MHz

CNR as a function of mark size of layers 1 and 2 and a commercial DVD-RAM disk is shown in Fig 7. CNR at mark size of 0.6 µm higher than 43 dB is obtained on both layers. CNR of the dual-layer disks is very close to that of single layer DVD-RAM disks.
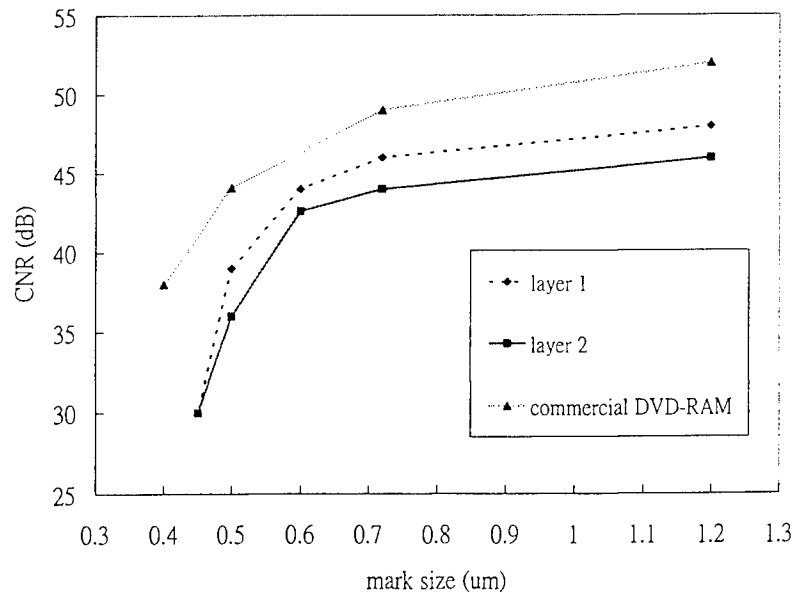
Fig. 7 CNR as a function of mark size of layers 1, layer 2, and a commercial DVD-RAM disk

To examine the effect of layer 1 on the writing performance of layer 2, a single layer disk, "a comparison disk" with the same disk structure as layer 2, was prepared. CNR as a function of write power for comparison disk and layer 2 was shown in Fig. 8. The peak CNR is at power of 8 mW for comparison disk and at 15 mW for the layer 2 of dual-layer disk at recording frequency of 3 MHz, implying that writing power is about double to compensate the optical energy lose in transmitting through the layer. Dependence of the CNR on the mark size for comparison disk and layer 2 of dual-layer disk as shown in Fig. 9, where CNR write power of 10 and 16 mW are almost the same. According to the simulation, transmittance of layer 1 approximate 60%, which agrees with peak power requirement (10 and 16 mW) measured experimentally.
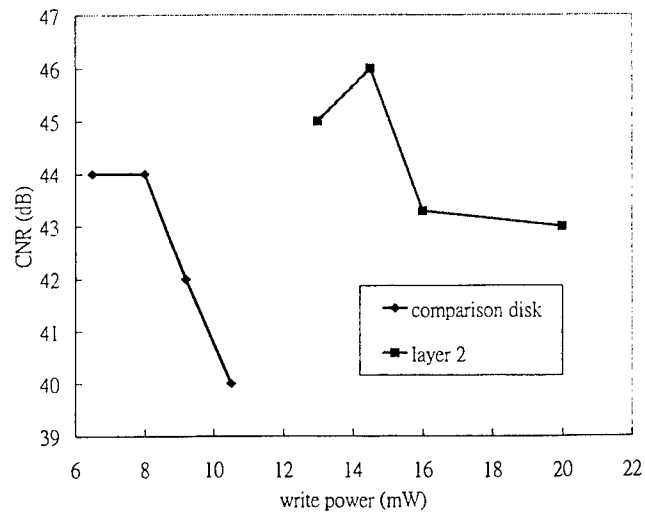

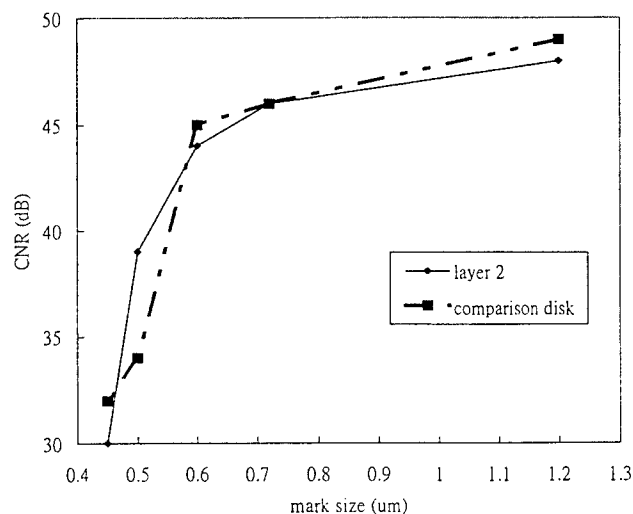Fig. 8 CNR as a function of write power for comparison disk and layer 2

Fig. 9 CNR as a function of the mark size for comparison disk and the layer 2 of dual-layer disk

5. Conclusion

The thermal and optical simulations facilitate the design of dual-layer erasable optical disks using phase change recording media with high transmittance and high reflectivity recording layers, respectively. CNR of 0.6 μm mark size on both layers was better than 45 dB at read power of 1.5 mW. The results suggest that dual-layer disks can be promising for double data capacity on a disk substrate.

Acknowledgement

Reference

1 Bor-Wen Yang, Han-Ping D Shieh, "*Interlayer cross talk in dual-layer read-only optical disks*", Applied Optics, 38, 333 (1999)

2 Bor-Wen Yang, Han-Ping D Shieh, "*The characteristics of a dual-layer optical disk with read-only and erasable functions*", IEEE Journal of Selected Topics in Quantum Electronics, 4, 821 (1998)

3 Kenichi Nagata, Noboru Yamada, Kenichi Nishiuchi, Shigeaki Furukawa and Nobuo Akahira, "Rewritable dual-layer phase change optical disk", Jpn. J. Appl. Phys. Vol. 38(1998) pp. 1679-1686

4 Temprofile, MM research, Inc.

5 Nai-yuan Tang, "Design and Fabrication of Erasable Phase-Change Superresolution Optical disk",National Chiao Tung Univ.,Thesis, 1998

LCD DIFFRACTIVE ELEMENT DESIGN TO HANDLE MULTIPLE DISK THICKNESSES

Mark O. Freeman, Hsi-Fu Shih, Yuan-Chin Lee, Jau-Jiu Ju

Opto-Electronics & Systems Labs, Industrial Technology Research Institute, Hsinchu, Taiwan

1. ABSTRACT

We describe the design of a single diffractive LCD element placed adjacent to the objective lens that can be addressed to provide the required spherical aberration (SA) compensation for a plurality of disk substrate thicknesses. It is now commonplace that optical disk drives must be able to handle disks of more than one substrate thickness. The major problem is compensating for the SA introduced when the highly corrected objective lens is used with a disk substrate thickness other than that which it was specifically designed for. An abundance of methods for solving this problem in the specific case of CD/DVD backward compatibility exist in the literature; we use an active device to extend this to include HD-DVD as well.

The LCD element acts as a switchable diffractive optical element. A set of electrodes defines the circular grating features that can be switched on or off to create diffractive lenses of the desired set of focal lengths. The liquid crystal modulates the phase and amplitude of the transmitted light according to the electrode pattern. We examine various approaches for the electrode layout that can implement 2-level, multi-level and continuous phase gratings in the LCD element. Two designs for the LCD wavefront compensator are presented that provide backward compatibility with DVD and CD formats from an HD-DVD system.

Keywords: multilayer disks, optical pickup head, CD/DVD, HD-DVD, LCD, diffractive optical element, optical disk storage

1. INTRODUCTION

With each new generation of optical disk storage, the optical system parameters, laser wavelength, disk thickness and the numerical aperture of the objective lens in particular, change to accommodate the increased information density on the disk. Backward compatibility with earlier formats is necessary to produce a commercially acceptable product. A major problem to solve is the compensation of spherical aberration (SA) introduced when the highly corrected objective lens is used with a disk substrate thickness and/or wavelength other than that for which it was specifically designed. An abundance of methods for solving this problem in the specific case of CD/DVD backward compatibility exist in the literature. Although the format is not yet fixed, the next generation of HD-DVD will use a blue laser, and likely also increase the lens NA and decrease the thickness of the disk substrate. At the same time, there is widespread interest in using multiple information layers, beyond the current two layers included in the DVD standard, for future disk systems. These new systems further complicate the problem of full compatibility.

Low voltage operation and low cost are two features that make liquid crystal devices (LCD) particularly attractive as optical modulators. Researchers have been investigating their application to amplitude and phase modulation in optical processing systems for more than a decade[1,2]. . LCDs have been used previously for wavefront correction and beamsteering[3,4] and have also been applied to optical disk systems. An early DVD pickup design by researchers at Sanyo used an LCD amplitude modulator to stop down the beam aperture giving a lower NA for reading CD disks[5]. In a different application, researchers at Pioneer utilized an LC panel to correct for aberrations caused by disk tilt[6].

This paper investigates the feasibility of using a diffractive LCD element placed adjacent to the objective lens that can be addressed to provide the required SA compensation for compatibility with HD-DVD, DVD, and CD disks. In the next section, we examine various types of LC devices and electrode structures and discuss their application to the present problem. In Sec. 3, we look at two specific design examples for LCD diffractive wavefront compensation devices that permit reading disks of

any of the three formats, the first using the same wavelength for all three formats and the second using a separate wavelength for each format.

2. BACKGROUND AND DEVICE LAYOUT OPTIONS

The basic system layout being addressed is shown below in Fig. 1. An electrically addressable LCD modulator is placed in front of the objective lens. We assume that the objective lens has been optimized for an HD-DVD system using a 415nm laser source, 0.1mm disk substrate thickness and an NA of 0.8. The LCD modulator must provide amplitude modulation to stop down the NA of the lens and phase modulation to compensate for the spherical aberration induced by the DVD and CD disk thickness'.

2.1 LC Selection

Twisted nematic (TN) liquid crystals, such as those commonly used in display devices, produce amplitude modulation in a straightforward manner. The twist of the LC through the volume of the cell rotates the polarization of incident light by the amount of the twist. Placing the TN LC cell between crossed polarizers makes a simple amplitude modulator. The same device can also be used as a phase modulator, however Lu and Saleh[1] show that the phase and amplitude are coupled. This makes the TN cell a poor choice for wavefront correction.

Ferroelectric liquid crystals (FLC) can also be used for amplitude and phase modulation and have orders of magnitude faster switching times than nematic or twisted nematic cells.. Typically, an FLC cell is constructed as a half-wave retarder and an applied voltage rotates the birefringence axis. The specific FLC material determines the range of rotation. Amplitude modulation is accomplished by placing the cell between crossed polarizers. Phase modulation, on the other hand, uses circularly polarized light[2]. The amount of phase delay introduced is equal to twice the rotation angle of the FLC axis. Currently FLC materials are available that provide close to 90 degrees of rotation or a phase modulation range of roughly 180 degrees. As discussed in more detail below, binary 0° , 180° modulation can be used for a diffractive wavefront modulation device but the efficiency is poor compared to devices where 360° or more phase modulation is available. This range can be increased by cascading multiple FLC cells or by making two or more passes through the same cell. However, creating a diffractive lens with phase modulation distributed between multiple cells physically separated on the order of a millimeter is a design problem beyond the scope of this paper. Unlike TN cells, the phase modulation is pure with no associated amplitude modulation. Independent control of amplitude and phase modulation is most easily accomplished by cascading two FLC cells, using one for amplitude control and one for phase.

Homogeneously aligned nematic (HAN) liquid crystals also provide pure phase modulation. In the off state, the long (extraordinary) axis of the (uniaxial birefringent) LC molecules is typically parallel to the glass plates enclosing the cell, all molecules pointing in the same direction throughout the volume of the cell. When a voltage is applied between the two plates, the LC molecules tilt towards the direction of the applied electric field, the tilt amount being roughly proportional to the applied voltage. Phase modulation is accomplished using light polarized along the extraordinary axis. As the LC molecules tilt under applied voltage, the polarized light sees an index of refraction that varies continuously from n_e to n_o. The phase modulation is equal to $2\pi T\Delta n/\lambda$ where λ is the wavelength of the light, T is the LC cell thickness and Δn is the change in the index of refraction. Therefore the amount of phase modulation available from HAN LCDs can be set to multiple-π radians by controlling the thickness of the device. However, HAN LCD's are not configurable to provide amplitude modulation.

Therefore, for this application, a cascade of two LC layers is the most suitable arrangement, consisting of an amplitude modulator layer for stopping down the aperture, and a phase modulation layer to compensate for the SA due to differing substrate thickness. HAN LC is chosen for the phase modulation because it permits greater than 2π radians modulation range with a single LC layer. The amplitude modulator could be either TN or FLC, TN probably being the better choice since the same nematic LC material could be used for both phase and amplitude modulating layers by simply adding a 90° twist to the TN cell. The structure of the resulting LCD wavefront compensator is shown in Fig. 2.

2.2 Electrode layout

The electrodes determine the phase modulation profile. A significant range of modulation, many tens of π radians, is required to provide the necessary SA compensation. For this reason, direct refractive wavefront modification is not possible

with a single thin LC layer. Instead, the standard diffractive optics approach is used whereby the desired phase profile is 'folded' by introducing discontinuities of 2π to keep the maximum phase range on the order of just a few π or less. Three candidate electrode styles are illustrated in Fig. 3. In the figure, the density of E-field lines in the LC indicates the relative strength of the E-field. The simplest type, a two-level phase grating, is shown in Fig. 3a. Transparent electrodes are deposited over the regions where an odd number of π modulation is desired. This is equivalent to a staircase approximation to the desired phase profile with each step having a phase height of π radians. While this gives a very simple form to the electrodes, it places a severe limitation on the light efficiency. It is well known from diffraction theory that a rectangular grating of this type can, at best, achieve 41% diffraction efficiency into the desired +1 order. Furthermore, since the light passes through this element twice, once on the way to the disk and a second time after reflection from the disk, this element utilizes only about 16% of the light, the rest going into unused diffraction orders.

A better option in terms of efficiency is shown in Fig. 3b. In this arrangement, each 2π phase range is divided into multiple steps, with a separate electrode for each step. Using four steps as shown in Fig. 3b, the efficiency is doubled compared to the 2-level grating of Fig. 3a. This quadruples the efficiency of the element when the double pass through the element is taken into account giving an overall efficiency on the order of 64%. Further increasing the number of phase steps will increase the efficiency but at a diminishing rate. For example, increasing from four to eight phase steps will boost the single pass theoretical efficiency only by a factor of approximately 1.1. Therefore, four steps seems to an optimum compromise between efficiency gain and increased electrode complexity. The number of steps that are practical is limited by the minimum electrode width that can be implemented. Since two addressable gratings are to be multiplexed within the electrode pattern for this application, one for DVD compatibility and one for CD compatibility, this will further impact the required minimum electrode width. Klaus et. al.[4] describe a wavefront modulator using a nematic LC supplied by Merck Japan Ltd. that has a birefringence of 0.29. With this LC, a phase modulation range of 2π requires an LC thickness of >1.5 microns @λ=415nm and an LC thickness of >2.7microns @λ=780nm. A minimum electrode zone width on the order of 5 microns should be sufficient to clearly define the distinct E-field regions within the LC.

A third alternative is shown in Fig. 3c. Klaus et. al.[4] introduced the concept of "superelectrodes" for an LC wavefront modulator where they applied it to beamsteering and adaptive microlenses for a Shack-Hartmann wavefront sensor. The superelectrode consists of a number of thin discrete transparent electrodes deposited at uniform positions across a region or zone of the LC device. The discrete electrodes are joined outside of the active optical area by a distributed resistive divider (e.g. opaque thin metal) into groups that form the superelectrodes. When a voltage is applied at each side of the superelectrode, a linear voltage gradient is created impressed across the corresponding LC region creating a continuous phase grating. This is equivalent to increasing the number of phase steps in the arrangement of Fig. 3b but, in some cases, results in a simpler driver. Since the discrete electrodes making up the superelectrode are intended to act together to create a phase gradient, the minimum electrode width can be reduced to whatever is lithographically feasible. Klaus et. al. used 2 micron electrode widths and reported that, if the separation between two discrete electrodes in a superelectrode bundle was π/5 or less in phase, then there was no significant difference with a continuous grating. In an actual device, they were able to achieve efficiencies greater than 90%.

The final question to be addressed is that of multiplexing two or more application-specific sets of electrodes onto a single device. In general, the desired electrode patterns are unrelated. While there is some freedom to scale the phase response when the superelectrode approach is used (see the first example below), even for functionally related phase profiles, the diffractive element approach creates 2π phase zones that overlap in an irregular manner. Therefore, the electrodes must be deposited in such a way that each application can be addressed independently. The basic approach is shown in Fig. 4. The electrode patterns for each application are computed separately. When electrodes from two applications overlap, a third set of electrodes is created in the overlap areas. In Fig. 4a, electrodes from application X and application Y are seen to overlap. Electrode "w" is created in the overlap area and shared by the two applications applying power to electrodes X' and w for application X (Fig. 4b), and applying power to electrodes Y' and w for application Y (Fig. 4c).

3. DESIGN EXAMPLES

3.1 *Example 1: HD-DVD, DVD, CD compatibility using same wavelength*

We first designed an NA 0.8 system at λ=415nm wavelength with a lens radius of 2.45mm, working distance of 1.51mm and disk substrate thickness of 0.1mm to represent the HD-DVD system. The lens design was performed with Zemax optical design software[7]. For this first example, we assume that the same laser source will be used for all disk formats and designed the LCD element to provide wavefront compensation to give the same spot size on the disk as in standard DVD and CD

systems. Since spot size is proportional to λ/NA, the effective NA for the DVD and CD systems are small due to the use of the blue wavelength. Direct scaling by wavelength gives NA=0.38 for the DVD system and NA=0.24 for the CD system. As a result, the compensated lens radii were 1.1mm for DVD and 0.7 mm for CD. These apertures are straightforward to implement using either the TN or FLC amplitude modulator methods described in the previous section. Standard disk thickness of 0.6mm for DVD and 1.2mm for CD were assumed and the working distances of the two systems are 1.25mm for DVD and 1.0mm for CD. The calculated phase profiles to produce diffraction-limited spots on the disks are shown in Fig. 5a.

The steeper phase profile of the CD system means that the mod 2π phase zones will be narrower for this system. The minimum zone width is calculated to be 30 microns. This is large enough that both the multi-level grating approach of Fig. 3b and the superelectrode approach of Fig. 3c can be considered. It turns out that the phase profiles for the NA 0.38 DVD system and the NA 0.24 CD system are scaled versions of eachother to within $\lambda/15$ peak variation using a scale factor of 3.61226. (i.e., max[(3.61226 x phase (0.38 system) – phase (0.24 system)] < $\lambda/15$.) This relationship makes the use of the superelectrode approach attractive.

The superelectrodes are designed to fit the 2π phase zones of the CD system. One side of the superelectrode is attached to ground and the other to the voltage that corresponds to 2π phase. The DVD system will use the same superelectrodes within the CD system aperture augmented by a set of superelectrodes to fill out the DVD system aperture that fit the 2π phase zones of the DVD system. Since the phase profiles are related by scale, one might at first be tempted to directly scale the CD voltages for the DVD system. This wouldn't work since the phase discontinuities would no longer be 2π multiples. Instead, the modulator must be made thick enough to support up to 4π phase range (in general) and the applied voltages take on analog values such that the phase discontinuities are multiples of 2π. The following table shows the positions and the necessary phase levels for this example. The diffractive 'folded' phase profile for the CD and DVD systems when the same set of superelctrodes are used is shown in Fig. 6. The phase curvatures of the individual zones, particularly the first superelectrode zone can be implemented with a slightly nonuniform spacing of the discrete electrodes making up the superelectrode. The DVD phase profile is no longer the customary uniform sawtooth associated with most diffractive optical elements. It becomes apparent that the simplification offered by directly using the same set of superelectrodes for both DVD and CD systems comes at the cost of a more complicated electronic driver requiring a rather large set of analog voltages.

Table 1: positions and phase levels for the superelectrodes for example # 1

Superelectrode #	Superelectrode position (µm)	NA0.24 Amplitude/Phase	NA0.38 Amplitude/Phase
1	0 - 185	1.0 / 0 - 2π	1.0/ 0 - 1.77338
2	186 - 263	1.0 / 0 - 2π	1.0/ 1.77338 - 3.54799
3	264 - 323	1.0 / 0 - 2π	1.0/ 3.54799 - 5.30709
4	324 - 374	1.0 / 0 - 2π	1.0/ 5.30709 – 7.05990
5	375 - 420	1.0 / 0 - 2π	1.0/ 0.776717 - 2.55161
6	421 - 461	1.0 / 0 - 2π	1.0/ 2.55161 - 4.28146
7	462 - 500	1.0 / 0 - 2π	1.0/ 4.28146 - 6.05007
8	501- 536	1.0 / 0 - 2π	1.0/ 6.05007 – 7.78391
9	537 - 570	1.0 / 0 - 2π	1.0/ 1.50072 - 3.22288
10	571 - 603	1.0 / 0 - 2π	1.0/ 3.22288 - 4.96875
11	604 - 634	1.0 / 0 - 2π	1.0/ 4.96875 – 6.67176
12	635 - 664	1.0 / 0 - 2π	1.0/ 0.388576 - 2.09123
13	665 - 694	1.0 / 0 - 2π	1.0/ 2.09123 - 3.78494
14	695 - 735	0.0 / --	1.0 / 3.78494 - 2π
15	736 - 834	0.0 / --	1.0 / 0 - 2π
16	835 - 929	0.0 / --	1.0 / 0 - 2π
17	930 - 1021	0.0 / --	1.0 / 0 - 2π
18	1022 - 1114	0.0 / --	1.0 / 0 - 2π

3.2 Example 2: HD-DVD, DVD, CD compatibility using customary wavelengths for the media

In this example, the same system parameters as the first example are used with the exception that we now assume the customary wavelengths for each medium, i.e., 415nm for HD-DVD, 650nm for DVD, and 780nm for CD. This may be required, for example, in a HD-DVD drive that supports backward compatibility with DVD-R and CD-R media. In this case, the system NA's also assume the customary values of 0.6 for the DVD system and 0.45 for the CD system. Again the aperture stops are implemented using either TN or FLC amplitude modulation as indicated in Fig. 2. The desired phase profiles are shown in Fig. 5b. In this case, the phase profiles are not proportional to each other, as can easily be seen. For contrast with the first example, we look at the feasibility of implementing the multiplexed LCD compensator using a four-level grating approach. The mod 2π diffractive phase profiles are shown in Fig. 7. The profile for the NA 0.6 system has been reflected across the origin in the figure to make viewing and comparison simpler.

We wish to implement these two profiles with four-level step approximations. The minimum 2π phase zone occurs in the CD system compensator and is equal to approximately 40 microns, easily sufficient to split into four levels. Table 2 shows the data for where the phase steps should be when the two systems are considered independently. (The electrodes for the two systems multiplexed on one device must include a third set of shared electrodes for the overlap regions. From the table, it can be seen that these shared electrodes may need to be switched between any of the four phase levels. It can also be seen that some of the shared electrodes will be as narrow as 2 microns. This poses no challenge to modern lithography. The step widths, on the other hand, will be much wider – 10 microns minimum – since the shared electrodes are never used alone.

Table 2: Positions of the phase steps for a four-level grating wavefront compensator for the NA 0.45 and NA 0.6 systems of example #2. A third set of shared electrodes must be fabricated in the areas where the two systems overlap. All units are in microns. (Blank rows in the NA 0.6 system are simply for convenience in comparing the positions with the NA 0.45 system.)

NA 0.45 level 0	NA 0.45 level π/2	NA 0.45 level π	NA 0.45 level 3π/2	NA 0.60 level 0	NA 0.60 level π/2	NA 0.60 level π	NA 0.60 level 3π/2
0-119	119-168	168-206	206-238	0-165	165-234	234-287	287-333
238-267	267-293	293-317	317-339				
339-360	360-380	380-399	399-417	333-373	373-409	409-443	443-475
417-435	435-452	452-468	468-484				
484-500	500-515	515-530	530-545	475-505	505-534	534-562	562-589
545-559	559-573	573-586	586-600				
600-613	613-626	626-639	639-652	589-614	614-639	639-664	664-688
652-664	664-676	676-689	689-701				
701-713	713-724	724-736	736-747	688-711	711-734	734-756	756-779
747-759	759-770	770-781	781-793				
793-804	804-815	815-825	825-836	779-800	800-822	822-843	843-864
836-847	847-858	858-868	868-879				
879-889	889-899	899-910	910-920	864-885	885-906	906-926	926-947
920-930	930-941	941-951	951-961				
961-971	971-981	981-991	991-1001	947-967	967-987	987-1007	1007-1027
1001-1011	1011-1021	1021-1031	1031-1040				
1040-1050	1050-1060	1060-1070	1070-1080	1027-1047	1047-1067	1067-1087	1087-1107
1080-1089	1089-1099	1099-1109	1109-1118				
1118-1128	1128-1138	1138-1148	1148-1157	1107-1128	1128-1148	1148-1168	1168-1188
1157-1167	1167-1177	1177-1186	1186-1196				
1196-1205	1205-1215	1215-1225	1225-1234	1188-1209	1209-1229	1229-1250	1250-1271
1234-1244	1244-1254	1254-1264	1264-1273				
1273-1283	1283-1293	1293-1302	1302-1312	1271-1292	1292-1314	1314-1336	1336-1358
1312-1322	1322-1332	1332-1342	1342-1352				
1352-1361	1361-1371	1371-1381	1381-1391	1358-1380	1380-1403	1403-1427	1427-1451
				1451-1476	1476-1501	1501-1528	1528-1555
				1555-1584	1584-1615	1615-1647	1647-1683
				1683-1722	1722-1767	1767-1823	1823-1840

4. CONCLUSION

We have demonstrated that it is feasible to design an active LCD wavefront compensation device that can enable a disk drive to handle many different disk formats with the same objective lens. The paper lays out the basic design concepts in terms of type of liquid crystal and options for laying out the electrodes. Two examples were presented of full designs for the LCD element that will compensate the wavefront of a system designed for HD-DVD so that it can also be used for DVD and CD disk formats. The first example assumed the same wavelength was used for all three systems. The wavefront compensator was designed using the superelctrode concept introduced in [Ref. 4] and shown in Fig. 3c. The second example used a different wavelength for each HD-DVD, DVD and CD. A 4-level grating design was described. Both appear to be viable design approaches, however testing needs to be done to verify that these systems can achieve the necessary wavefront accuracy for this application. Other applications can also be considered such as an active compensation device that greatly increases the number of disk layers that can be read.

.

5. REFERENCES

1. K. Lu and B. Saleh, "Theory and design of the liquid crystal TV as an optical spatial phase modulator", Optical Eng. 29, No. 3, pp.240-246, 1990

2. M. O. Freeman, T. A. Brown, and D. M. Walba, "Quantized complex ferroelectric liquid crystal spatial light modulators", Appl. Optics 31, No. 20, pp. 3917-3929, 1992

3. F. Naumov et. al., "Liquid crystal wavefront correctors of new type", Proc. SPIE vol. 3688, pp.485-491

4. W. Klaus et. al, "Efficient liquid crystal wavefront modulator", Proc. SPIE vol. 3015, pp. 84-92, 1997

5. Y. Tsuchiya et. al., " Digital video disk/ compact disk compatible pick-up with liquid crystal shutter", Jap. Journal of Appl. Physics 36, No. 1B, pp. 481-485, 1997

6. N. Murao et.al., "Tilt servo using liquid crystal device", Tech. Digest ISOM '97, pp. 351-353, 1997

7. Zemax Optical Design Program is a product of Focus Software Inc. , P.O.Box 18228, Tucson, AZ, 85731, USA
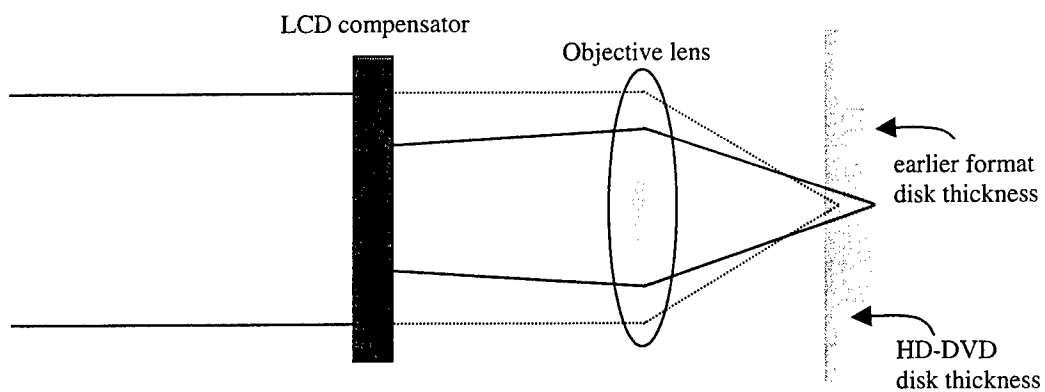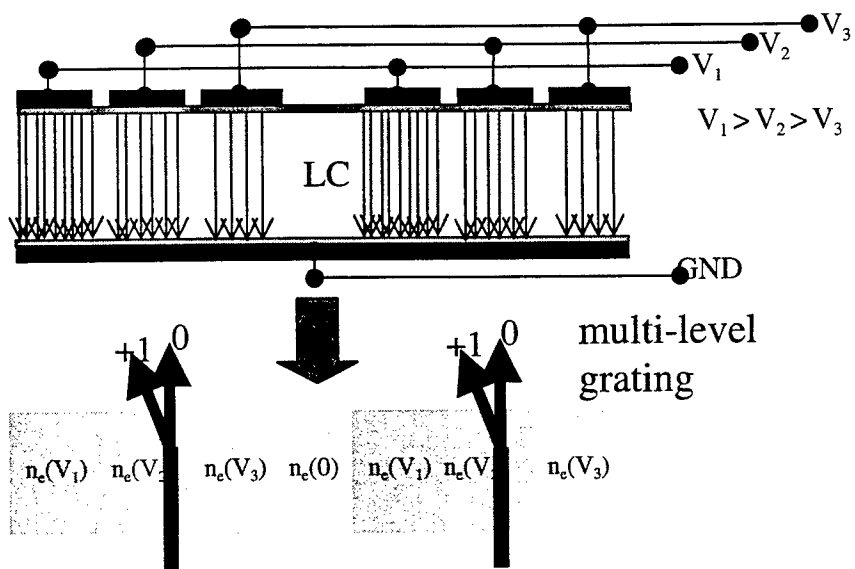
Fig. 1: Basic system configuration
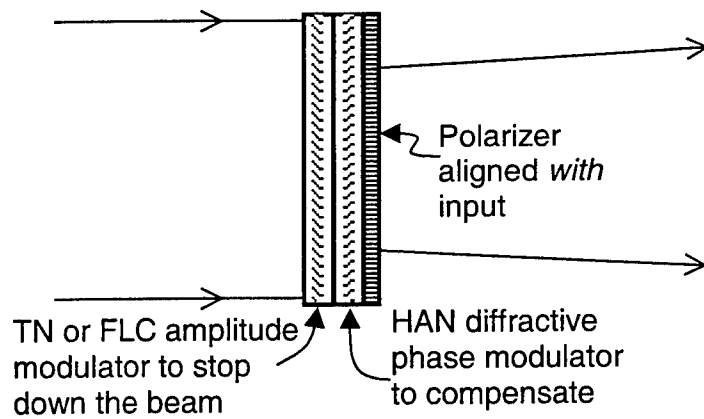
Fig. 2: Structure of the LCD wavefront compensator

LC

+1   0   -1

$n_e(V)$ $n_e(0)$ $n_e(V)$

2-level grating

(3a)

$V_1 > V_2 > V_3$

LC

+1   0   +1   0

multi-level grating

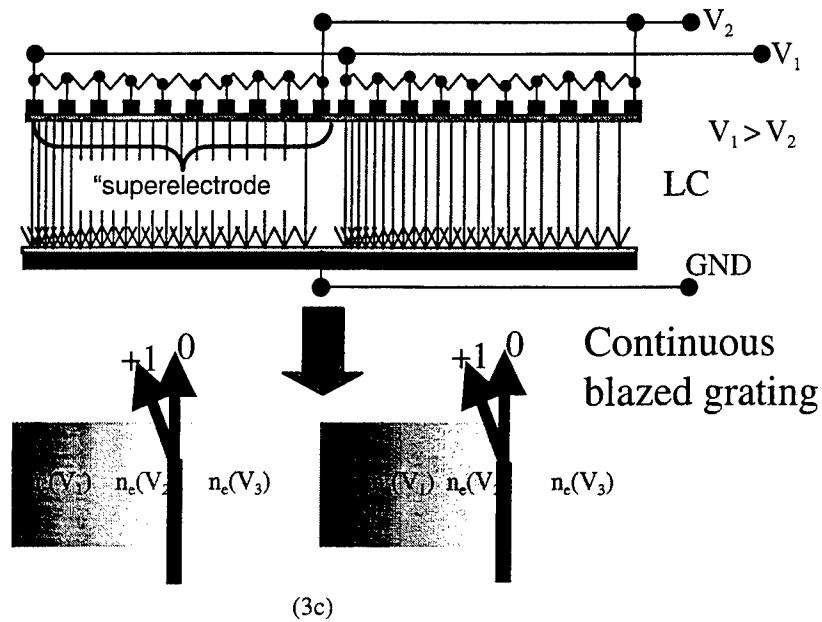$n_e(V_1)$ $n_e(V_2)$ $n_e(V_3)$ $n_e(0)$ $n_e(V_1)$ $n_e(V_2)$ $n_e(V_3)$

(3b)

(3c)
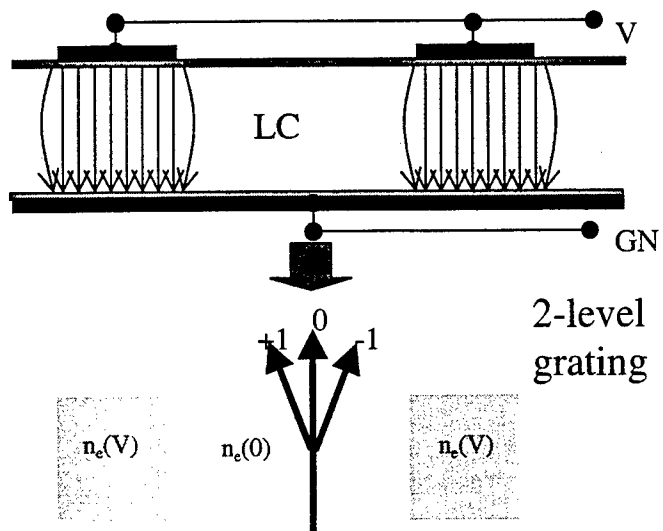
Fig. 3: Three types of electrode layout to implement diffractive LCD element. (a) 2-level binary grating (b) multilevel binary grating, (c) continuous blazed grating using "superelectrodes"
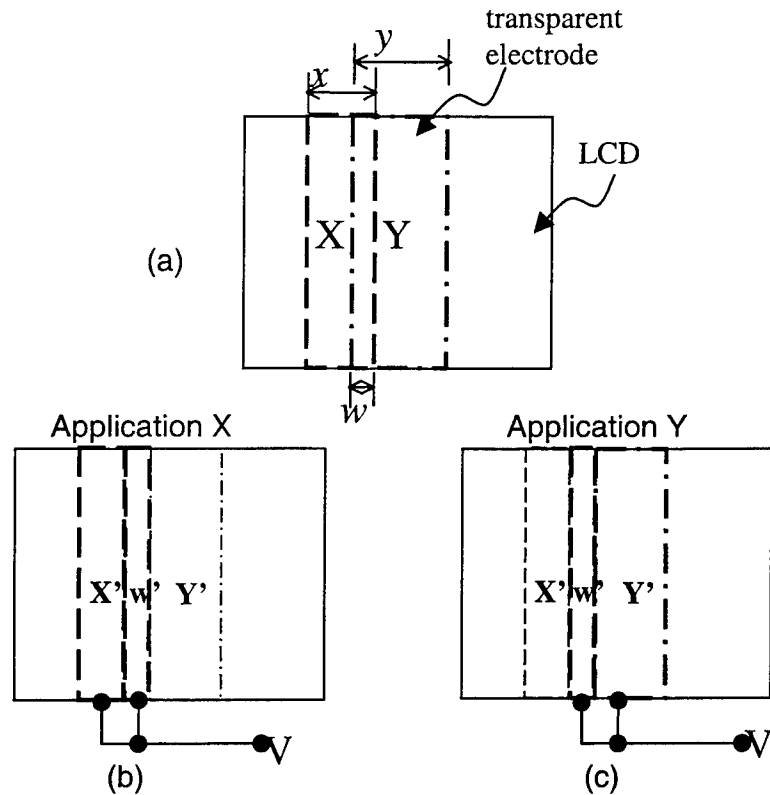
Fig. 4: Multiplexing two or more applications onto the same LC device. Separate electrodes are required for each application. (a) An extra set of electrodes is created where electrodes from two applications overlap. The two applications share this extra electrode and the particular application is selected by applying correct application of the driving voltage.

264
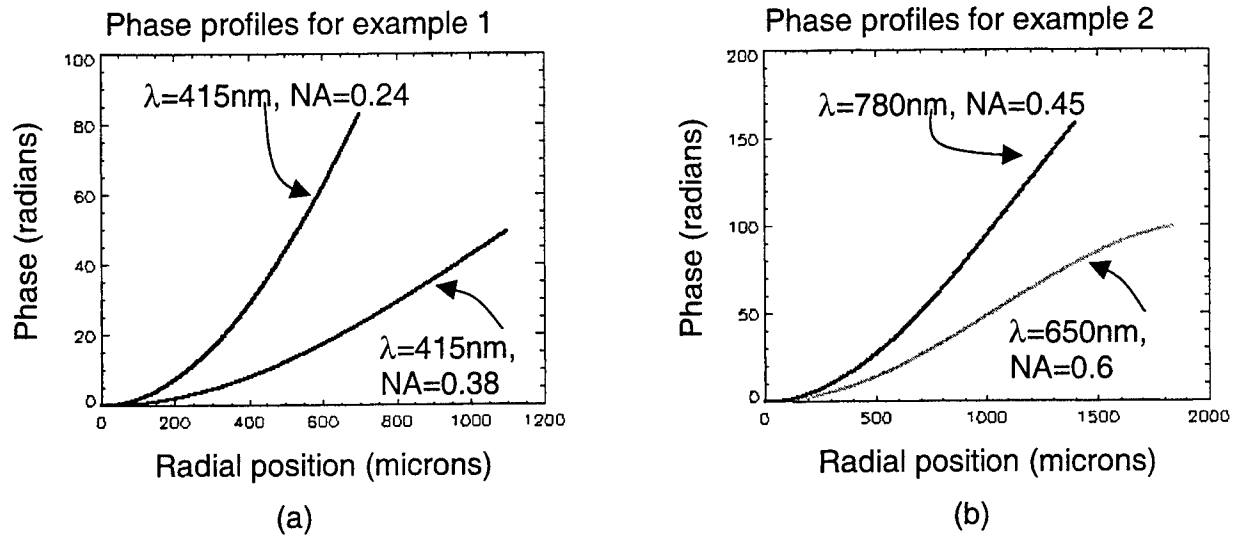
Fig. 5: Desired phase profiles for the LCD diffractive compensator. (a) Example 1 – same wavelength for HD-DVD, DVD, and CD, (b) Example 2 – HD-DVD uses λ=415nm, DVD uses λ=650nm, CD uses λ=780nm
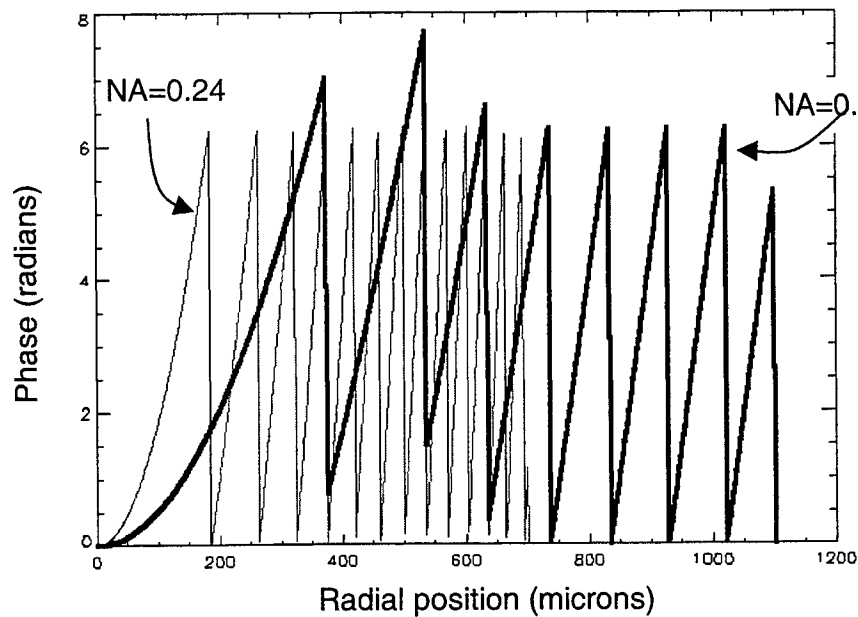
Fig.6: Diffractive phase profile for NA 0.38 compensator when the superelectrode pattern from the NA 0.24 system is directly used.
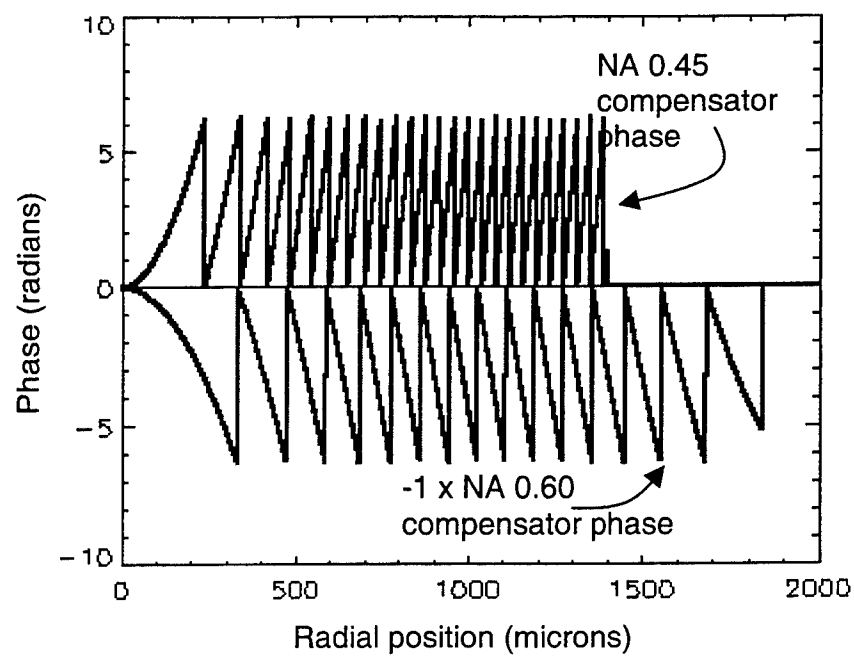
Fig. 7: Ideal diffractive phase profiles for the NA 0.45 and NA 0.6 wavefront compensator devices. The phase profile for the NA 0.6 compensator has been multiplied by -1 to make it more easy to view.

Realization of Infrared Wireless Local Area Network

Chen xiaojuan, Chen haiqing[*]

Dept. of Optoelectronics Eng. ,HUST, Wuhan 430074,China.

ABSTRACT

The technology of Infrared wireless local area network is one branch of the IEEE802.11 protocol's access network technology. As a medium for short-range or indoor communication, infrared radiation offers several significant advantages over radio. Infrared emitters and detector capable of high-speed operation are available at low cost. The Infrared spectral region offers a virtually unlimited bandwidth that is unregulated worldwide.

Keyword: Infrared NIC , IEEE802.11, DFE, PPM, IrDA

1. INTRODUCTION

As the increasing developments of the mobile communication, such as portable computer , PDA. The demands for wireless access technology is increasing rapidly. Today the medium for wireless digital communication include microwave, infrared and radio. As a medium for short-range, indoor communication infrared link offers several significant advantages over others. The infrared spectral region offers an unlimited bandwidth that is unregulated worldwide. And the infrared can not penetrate through walls or other opaque barriers, so that the signal is confined in the room which makes it easy to secure. The infrared has other several advantages as that Infrared emitters and detector capable of high-speed operation are available at low cost.

1.1 PPM(pulse position modulation) technology

In the infrared wireless communication system we employ encode and modulation technology, such as OOK,ASK,QPSK,PPM. The analysis shows that PPM has the best compromise of power and bandwidth efficiency. So the IEEE802.11 recommends the PPM for Infrared wireless communication. PPM is the technology which use the pulse position to modulate data, different position stands for different data. Using the PPM technology, we can reduce the proportion of the high level pulse and decrease code streams duty ratio. And that we can increase the efficiency of transmitter. The PPM modulation decrease the power consumption. And this is important to the Infrared communication systems. PPM is been used like X-PPM, 2-PPM stand one pulse represent 1 bit message. In the 4-PPM one pulse denotes 2 bit message. And 16-PPM is 4 bit message.

1.2 IrDA(Infrared Data Associate Protocol) and IEEE802.11 Standard

IrDA is an International Organization that creates and promotes interoperable, low cost infrared data interconnection

---

[*] E-mail:chenxjj@263.net   Tel: 086-027-8753655

In *Optical Storage and Optical Information Processing*, Han-Ping D. Shieh, Tom D. Milster, Editors, Proceedings of SPIE Vol. 4081 (2000) • 0277-786X/00/$15.00

267

standards that support a walk-up, point-to-point user model. The standards support a broad range of appliances, computing and communications devices. Today the IrDA is the widely accepted wireless transmission standard. It is a half duplex technology. IrDA Data is recommended for high speed short range, line of sight, point-to-point cordless data transfer - suitable for HPCs, digital cameras, handheld data collection devices, etc. If IrDA is supported, it must be targeted at the 4 Mb/s components. IrDA Data Protocols consist of a mandatory set of protocols and a set of optional protocols. The mandatory protocols are: PHY (Physical Signaling Layer) , IrLAP (Link Access Protocol) , IrLMP (Link Management Protocol and Information Access Service (IAS)). IEEE802.11 standard specifies a single Medium Access Control (MAC) sub layer and three kinds of Physical Layer media. The standard provides 2 Physical layer specifications for radio, operating in the 2 400 - 2 483.5 MHz band (depends on local regulations) and one for infrared. In our system, we will use infrared as the physical medium.

1.3 ANTI-NOISE AND DFE (decision-feedback equalization) technology

There are two configurations for indoor wireless infrared links. The transmitter and receiver may have a narrow field of view or a wide field of view, producing a directed or a non-directed systems. Systems may also be classified into line-of-sight (LOS) or non line-of-sight (non-LOS), depending on whether there is directed path between transmitter and receiver. We will choose non-directed, non-LOS, or diffuse links because they combine ease of use with robustness against shadowing. Infrared links are also impaired by noise due to background illumination. This comes in two forms. Sunlight and incandescent lights sources whose intensity varies slowly with time. It will produce shot noise at the receiver. So it can be modeled as a stationary, Gaussian, white noise with a power spectral density proportional to the total detected optical power. On the other hand, fluorescent lights flicker in a nearly deterministic periodic fashion at the drive frequency. A low-pass filter is employed to limit shot noise and receiver thermal noise. In addition, to reduce the impact of near-dc fluorescent-light interference, we employ a high-pass filter. So when the ambient illumination is sufficiently weak, the signal-to-noise (SNR) of direct-detection links is limited by thermal noise of the receiver front-end preamplifier. In this system there are multi-path effects. It lead to distortion that produces significant inter-symbol interference (ISI) when the symbol rate is over 1Mbaud. A decision-feedback equalizer (DFE) is introduced to mitigate inter-symbol interference (ISI). The DFE reduces the impact of ISI arising form multi-path distortion. The forward filter consists of four taps that are spaced one-half baud apart, and the reverse filter consists of four taps that are spaced one baud apart. There filters are constructed using analog tapped delay lines and manually controlled tap gains.

2. PRINCIPLE OF INFRARED NETWORK INTERFACE CARD (NIC)

Infrared communication is the technology which employ infrared ray as the signal carrier. It is made up of infrared transmitter, infrared receiver and network interface card. The infrared transceiver accomplish the signal's transfer. In the sending part the digital data is encoded. Through the electric-opto transfer circuit, it will drive the infrared LED and transmit infrared light pulse to the air. In the receiving part the receiver gets the infrared light pulse from the air and converts the light pulse into electric signal. Then the signal gate through equalization, judgement and decoding. The original data signal is be recovered. The infrared network interface card (NIC) accomplish function of connecting with the computer.

2.1 Infrared transmitter

Infrared transmitter is the device that can convert the electric signal into optical signal. It transmits infrared pulse in the form of IrDA style. The key components of the infrared transmitter are infrared LED and corresponding drive circuit. The

wavelength is between 850nm and 910nm.The infrared LED's light power should be high enough. The analysis shows that the system's signal-to-noise(SNR) is proportion to the square of the transmitter's light power. So increasing the power of the transmitter can reduce the bit-error rate(BER), and increase the communication quality. But the large power infrared LED will is relatively expensive and the high infrared light is harmful to our eyes. So the IrDA has specified the light power of infrared data communication in a limited field.

2.2 Infrared receiver

Infrared receiver receives the infrared pulse from the space and convert the optical signal into electric signal. Then handle the signal in the following ways: demodulation, threshold judgement and decoding. In the infrared communication system the transmitter light power is low and the signal is transmitted through air. So it is easily affected by the environment. And the signal received is very weak. So the key part of the receiver is low noise preamplifier and self-adapting code element judgement. We choose the large input resistance transconductance amplifier as the preamplifier which has large dynamic range and wide bandwidth. Self adapting code element judgement can automatically trace the input signal electric level and judge the threshold electric level according to the signal and change the signal into digital level. Because the inter-symbol interference(ISI) is the obvious when the data transfer rate is high, we will employ a block decision-feedback equalization(DFE) strategies to mitigate the effect of multipath-induced ISI. We use the time domain equalizer because it is easily to realize.

2.3 Infrared network interface card

Infrared NIC include two parts. One part is the computer communication module. The other part is infrared transceiver part. The IEEE has defined the IEEE802.11 as the standard of infrared links. The IEEE802.11 has specified that base-band range is 0~10Mbit/s and recommended the pulse position modulation (PPM) technology. The* IEEE802.11 employed the Carrier Sense Multiple Access with Collision Avoidance (CSMA/CA) collision detection system. In our system, our infrared network interface card (NIC) is based on ethernet card. By adding a infrared transceiver and properly to the ethernet NIC, we can realize the infrared links. Using this kind of NIC we can utilize current network resource. The signal of the ethernet NIC port rj45 is the difference TTL level. And the code element rate is 10Mbit/s. The infrared transceiver get this signal and change it to single-level signal. We employed is the same communication agreement as current ethernet, such as TCP/IP, IEEE802.11. The infrared NIC can not work automatically with the computer, so we use some tool software, such as vtool for windows to drive the hardware to work compatibly with computer.

3.DEVICE CONFIGUTION

3.1 Infrared network interface card (NIC)

The infrared transceiver is one important part of the device. It is made up of universal asynchronous receiver transmitter(UART), microcomputer and integrated IrDA element. In our device, we use MAX3100 as the UART. The MAX3100's IrDA mode can be used to communicate with other IrDA SIR-compatible devices. In IrDA mode, a bit period is shortened to 3/16 of a baud period (1.6μs at 115,200 baud). A data zero is transmitted as a pulse of light (TX pin = logic low, RX pin = logic high). The integrated IrDA element we use the Rohm Electronics RPM-801CB. This module include a infrared LED, PIN opto-electronic diode and wave form shaping IC. It supports IrDA 1.0 SIR standard. In the following I will draw the simplified schematic:
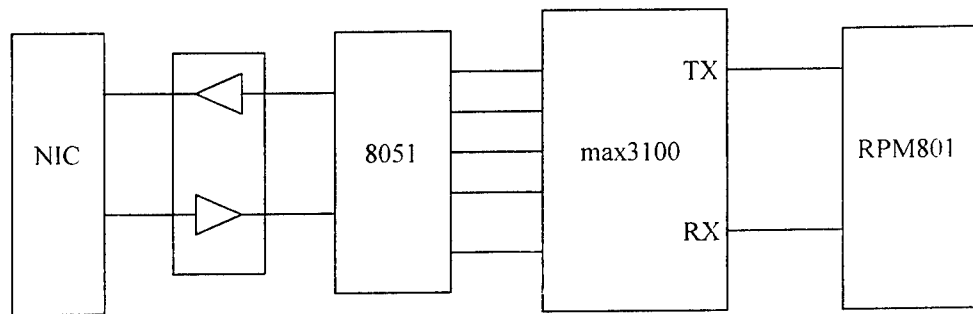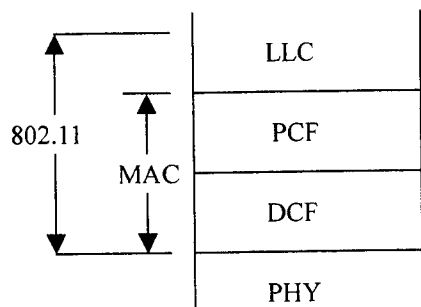
Infrared network interface card schematic

3.2 Infrared wireless local area network
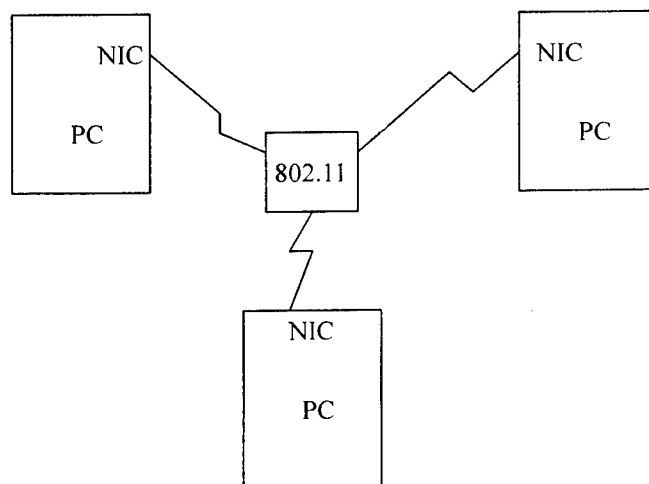
Infrared local area network configuration

The infrared wireless local area network (WLAN) is consists of three sets of PC and NIC. The WLAN is built according to IEEE802.11. Its hierarchy structure is described as follow.

The infrared transceiver accomplish the physical layer function. We use 850nm infrared light to transfer data in the room. And the access rate is 4Mbit/s. The Medium Access Control(MAC) includes Distributed Coordination Function(DCF) sub-layer and Point Coordination Function(PCF) sub-layer. These two sub-layers function is realized with software routine. Many software such as C, Visual C and visual Basic can do this work. In our system we use turbo c. Sub-layer DCF use CSMA/CA to let every PC complete the chance of sending. Sub-layer PCF provide a service of non-completion. It is suitable to time-sensitive service, such as packed voice service should choose PCF. The 802.11 has three kinds of inter-frame space (IFS). They are SIFS(short IFS), PIFS(PCF IFS) and DIFS(DCF IFS). The SIFS is the shortest and has the highest priority. Using these IFS, we can easily avoid collision. The layer LLC ensures accurate link. Using software we can programmed the user communication interface. Such as chat, ftp, http universal program. So it is easily to realize the resource sharing and form a local wireless infrared area network.

4. CONCLUSION

In our system we realize three PCs' communication and resource sharing. Its operation mode is diffuse links. The communication distance is 5 m in a room and code element rate is 10Mbit/s. This paper gives the details about infrared wireless communication and the configurations of the infrared wireless local area network. The protocols of IrDA and their components have been introduced. A Infrared network interface card (NIC) has been designed which can realize the wireless connection. The wireless local area network is made up of three sets of PC and Infrared network interface card. PC is used to form the local area network and control data communication. The Infrared network interface card is responsible for establishing the infrared link, detecting transmission errors, compensating for speed changes and obtaining the required quality of service. The design of the Infrared link must take into account a number of factors to obtain the best compromise for the indoor environment. As for the average-power efficiency and bandwidth efficiency, we employ the pulse-position modulation(PPM) ,using block decision-feedback equalization(DFE) strategies to mitigate the effect of multi-path induced inter-symbol interference(ISI).The key technology in developing this system consists of designing a high performance Infrared network interface card which can work compatibly with the computer and an Infrared link channel with high anti-interference characters.

ACKNOWLEDGMENTS

REFERENCES

1. Barry J.R Wireless Infrared Communication. Boston:Kluwer Academic Publisher 1994.
2. Gene W.Marsh, Joseph M.Kahn Performance evaluation of experimental 50-Mb/s diffuse   infrared wireless link using OOK with decision-feedback equalization. IEEE Transactions On Communications. Vol.4   No.11   1996.
3. Audeh M D, Kahn J M . Performance evaluation on basebaud OOK for wireless indoor infrared LAN's operating at 100Mbit/s. IEEE Transactions on Communications. Vol.43 No.6   1995.
4. Travis B. Ease file transfers with IrDA-protocol wireless infrared. EDN, Vol.40 No.7, 1995.
5. Roviras D, et al. Wireless infrared factory network for hand-held terminals. European Transactions and Telecommunications and Related Technology. Vol.6 No.2 1995.
6. JmcCullagh M, Wisely D R. 155Mbit/s optical wireless link using bootstrapped silicon APD receiver. Electronics Letters, 1994, Vol.30 No.5 1994.
7. Jimemez P et al. Improved PPM schemes for infrared wireless LAN. Electronics Letters. Vol. 32   No.10 1996.
8. Tajnai J., et al., Serial Infrared Physical Layer Link Specification, Version 1.2, Infrared Data Association, 1997 *
9. Seaborne, A., et al., Link Management Protocol(IrLMP), Version 1.1, Infrared Data Association, 1996.
10.   Williams T., et al. Serial Infrared Link Access Protocol(IrLAP), Version 1.1, Infrared Data Association, 1995.
11.   IEEE 802.11 Standard.

The servo characteristics of single-phase spindle motor in DVD-ROM

King-Yin Wang Ching-Ping Kuei   Sung-San Chang Yao-Yu Lee Yu-Hung Kuo

Optic-Electronic & System
Industrial Technology Research Institute
Hsinchu, Taiwan, R.O.C

ABSTRACT

The single-phase DC motor has the low-cost advantage over 3-phase DC motor owing to its easy-assembling and high yield-rate, however, it has larger torque ripple and cogging torque. Single-phase DC motor is currently applied to low profit margin products such as cooling fan. In order to utilize single-phase DC motor to high precision system, for instance, DVD (Digital Versatile Disk), the vibration caused by torque ripple and cogging torque needs to be solved. In this paper, focusing error, tracking error, seeking ability and some velocity control performances are studied when single-phase DC motor is used in DVD related products.

Keywords: single-phase spindle motor , focusing servo, tracking servo, sled seeking

1. INTRODUCTION

In terms of the widespread use of multi-media devices and the remarkably demanding in high-density memory storage devices, there is a tendency that CD-ROM is being replaced by DVD-ROM. Because the prices of computer peripheral products are tending downward, DVD is no exception. As the maker's prices are approaches the cost, the cost-down of component parts becomes an important issue for the makers. The single-phase DC motor has the low-cost advantage over 3-phase DC motor owing to its easy-assembling and high yield-rate. If the single-phase DC motor can be applied to the DVD-ROM, it will become more competitive in the market.

Currently, a large portion of DVD-ROM is made in Taiwan. However, the key components like spindle motor, chip set and pick-up head rely on the supply from Japan. Taiwanese makers can only make little profit from assemble. In order to stop the long-term control from Japan, ITRI and SUNON developed the single-phase spindle motor to replace the traditional 3-phase 9-slot 12 pole design. SUNON has already had its single-phase DC motor patent, with SUNON's experience in making single-phase motor, the low-cost single-phase spindle motor will step into the DVD market. Figure. 1 shows the mechanical structures of the 3-phase and single-phase motor.

The DVD system was constituted with Toshiba's servo DSP TC9453F, pre-amplifier TA1293F, Sankyo's Mecha SF-HD2R, disk loader, single-phase motor and servo circuit developed by OES. This paper discusses a traditional three-phase spindle motor that is replaced by a single-phase motor applied in DVD-ROM. In Section 2, we describe the servo systems of focusing, tracking, sled and spindle. In Section 3, we show the implementation results of these servo systems. In Section 4, the experimental results are discussed.

2. DVD SERVO SYSTEM DESCRIPTION

Figure 2 shows the data are stored on the disk with uniform density so that the DVD-ROM system must rotate with constant linear velocity (CLV) for reading out the data. For reading out the data, the DVD servo system includes the focusing, tracking, sled and spindle servos [1], as shown in figure 2. The focusing and tracking servos adjust the vertical and radial positions of the pick-up head so that the data can be continuously and reliably read from the disc. The sled servo functions when the pick-up head is required to move with a significant distance radially. The spindle servo controls the disc angular velocity according to the position of the pick-up head so as to maintain CLV of the focusing spot on the disc.

2-1 Focusing servo system

In *Optical Storage and Optical Information Processing*, Han-Ping D. Shieh, Tom D. Milster,
Editors, Proceedings of SPIE Vol. 4081 (2000) ● 0277-786X/00/$15.00

273

When the disc is rotating, it may exhibit wobble up to ± 300 μm and the allowable focusing error is ± 0.23 μm. It is impossible to maintain focus point on the disc without proper servo control. Thus, the focusing system is a closed loop control system. It consists of the focusing actuator, the optical system, a photo detector, a focusing error signal amplifier and a dynamic compensator. Figure 3 shows the block diagram of the DVD-ROM focusing servo system.

An astigmatism method [2][3] is used to sense the focusing error signal from the reflected laser beam. The focusing error signal is amplified before it is fed to the focusing servo control. The servo controller contains control algorithms that can generate control signals to drive the actuator drive the lens up and down to adjust the focusing spot. In most system configurations, the actuator is a voice coil motor and can be modeled by a second order dynamic system within the frequency bandwidth of interest. The servo controller is a phase lead/lag type compensator to compensate the actuator's dynamics. The servo controller is designed so that the desired closed loop system performance can be obtained.

2-2 Track following servo system
In order to read data from the DVD disc, the DVD-ROM has to keep the pick up head following the spiral track on the disc. As specified in the DVD Book, the track pitch on a DVD disc is 0.74 um. The tracking servo system has to perform track following within the precision requirement, while subjecting to disturbances and noises. Due to the disc run-out in rotation, the track of the disc will oscillate back and forth if viewed from a steady pick-up head. Without proper tracking error detection methods and servo designs, satisfactory track following can not be maintained.

The tracking servo system is quite similar to the focusing servo system. The major difference is that the tracking servo system has two actuators[4][5]. As shown in Figure 4, Actuator 1 is the fine actuator and Actuator 2 is the coarse actuator. The coarse actuator is usually a sled motor on which the fine actuator is installed.

The frequently used method for DVD tracking error sensing is Differential Phase Detection (DPD). The DPD method utilizes the fact that the tracks on the disc behave as a diffraction grating and generate multiple diffraction orders in the reflected light spot. Analyzing the laser light reflected from the disc, we can get a phase difference varies while the spot is at different place of the track.

In general, the closed loop system with the fine actuator has bandwidth much larger than the one with the coarse actuator. This is because the fine actuator is designed mainly for high precision track following, while the coarse actuator is used to "zero" the reaction force from the suspension of the fine actuator and to perform long distance track seeking. However, in most system configurations, the fine actuator is suspended by springs and can only move the pick-up head within a small radial distance (about $\pm$ 0.6 mm).

2-3 Track seeking servo system
The access time is one of the most important DVD-ROM performance indices, and the seeking time represents the most significant part of the access time. For accessing data quickly from the disc, reliable and efficient seeking servo system is major concern. The seeking servo design is strongly related to software control and hardware function of the DVD_ROM chip set and pick-up head design.

Figure 5 shows the block diagram of a seeking servo system. We see that the system shares the dual actuators with the tracking servo system. The seeking servo system is to drive the pick-up head to a desired track location specified by the host or system controller. When the DVD_ROM performs seeking control, the system CPU calculates the direction and number of tracks to be "jumped" to get to the target address. Based on the number of tracks to be crossed, the CPU determines a seeking mode to move the pick-up head.

For short distance track jumps, the system might have to use only the fine actuator. For long distance track jumps, the sled motor will be used to swiftly move the pick-up head. Since the sled motor can only bring the pick-up head to a location near the target address, it provides only "rough seek". Usually, the CPU will provide a sled velocity profile for sled motor to follow. The velocity profile depends on the number of tracks to be crossed, and the acceleration/braking capability of the sled motor. This velocity profile can be converted into a voltage versus track number profile. For better sled control, some pick-up heads are equipped with photo sensor to provide sled velocity and position feedback. This allows the sled motor to better follow the desired velocity profile under the framework of feedback control.

2.4 Spindle servo system

The DVD-ROM system needs to read data from the disc with constant bit rate regardless of the disc constant linear velocity (CLV) values. One robust approach to maintain constant data rate is to use the on-line sync pattern for spindle CLV control. In Figure 6, a crystal oscillator is used as the reference of channel bit rate (26.16 MHz/sec. at single speed). The rate of the RF signal from the optical system depends on the spindle angular velocity. After channeling and demodulation process, one can obtain the synchronized data pattern. The difference in frequency and phase between the reference clock and the synchronized data rate is used to drive the CLV controller, usually a phase-locked loop (PLL) circuit. From the system-control point of view, we have a closed loop system that follows the reference signal (frequency in our case). By properly designing the PLL circuit, CLV control can be achieved. For DVD-ROM players that can operate in multi-speed modes, one needs to adjust the reference clock rate to accommodate the desired data bit rates.

3. IMPLEMENTATION AND RESULTS

DVD-ROM system needs to read out the data fast, stably and accurately from the disk, so the cross frequency of the tracking and focusing system is up to several KHz, the rotation speed of the spindle is also within this bandwidth. Due to the larger torque ripple of the single-phase spindle motor than the 3-phase one, the system bandwidth is required to increase in order to overcome the vibration. DVD servo systems are quite complicated, although the internal control loops can be designed separately, the integration of these systems for data read-out is required. The setting of parameters for focusing, tracking, sled and spindle and control strategy will influence the performance. It is hard to judge the whole servo system by individual servo system.

Figure 7 shows the open-loop gain of focusing loop under the rotation of single-phase spindle motor. The cross frequency of focusing loop is 2.4 kHz which is larger than the standard cross frequency 2 kHz in the DVD-ROM specification book. Due to the higher cross frequency of focusing loop, the focusing error can be reduced to the 0.23 um. Similarly, Figure 8 shows the open-loop gain of tracking loop. The cross frequency of tracking loop is 4.5 kHz which is larger than the standard cross frequency 2.4 kHz in the specification book. The tracking error can reach the standard value in the DVD-ROM specification book.

In general, there are 2 indices for DVD performance: (1) data read-out jitter. (2) time for pick-up head to read out data from target track. Figure 9 shows the jitter value of read-out data is 4.09 ns. It is larger than the standard jitter 3.8 ns in the specification book. Figure 10 shows the pick-up head crossing 25,000 tracks to the target track will takes 0.32 s and the maximum track-crossing velocity is 240 kHz.

4. CONCLUSION

In this paper, single-phase spindle motor is used to replace the traditional 3-phase spindle motor. Although the single-phase spindle motor will cause larger torque ripple than the 3-phase motor, we can increase the focusing and tracking bandwidth to overcome the vibration caused by torque ripple. From above experiments, jitter value of read-out data and pick-up head crossing 25,000 tracks show that the single-phase spindle motor has the same performance as the 3-phase motor.

5. REFERENCES

1. DVD Specifications for Read-Only Disc / Part 1. Physical Specifications Version 1.0 August 1996.
2. G. Bouwhuis, J. Bratt, A. Huijser, J . Pasman, G. van Rosmalen, and K. Schouhamer Immink. *Principles of Optical Disc System*. Adam Hilger Ltd, Bristol and Boston, 1985
3. Sony Corp. and N. V. Philips. *Compact Disc Digital audio* - System Description, 1985.
4. Gene F. Franklin, J. David Powell, and Abbas Emami-Naeini. *Feedback Control of Dynamic System*. Addison-Wesley-, New York, 1986.
5. Jordan Isailovic. Videodisc and Optical Memorial Systems. 1985.

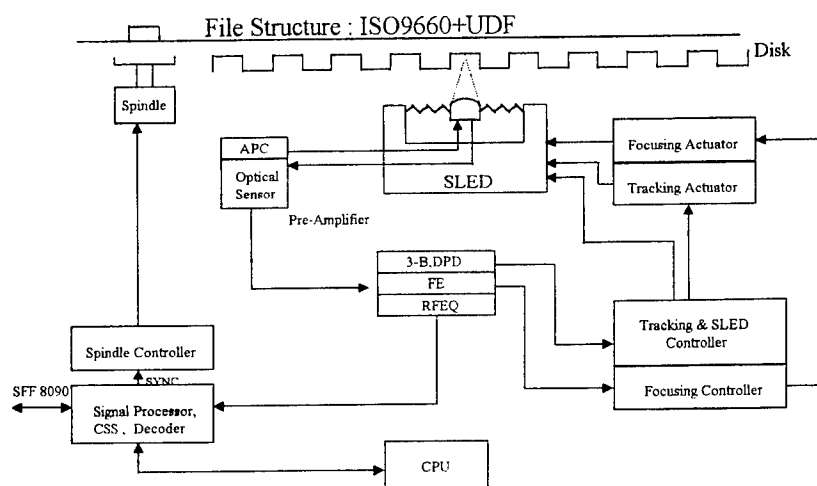Figure 1 Mechanical structures of the 3-Phase and 1-Phase motor.
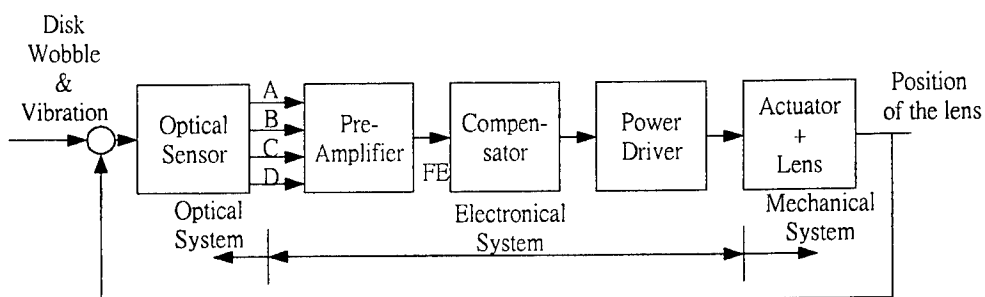

Figure 2. DVD-ROM servo system structure.

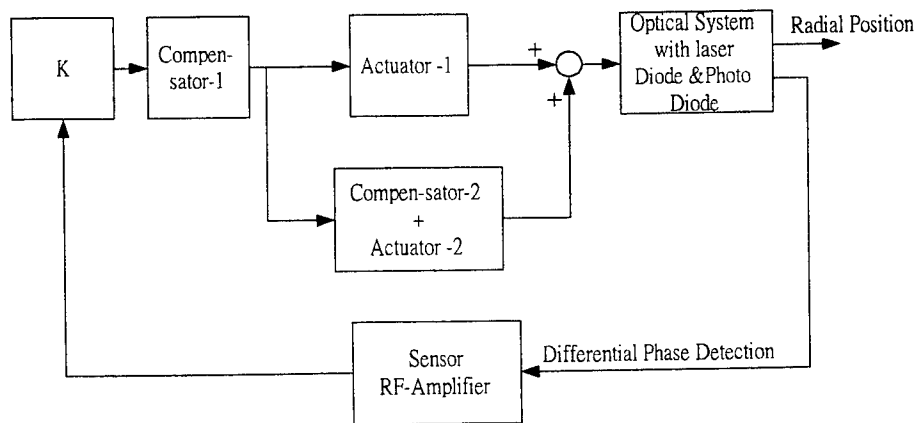Figure 3. Block diagram of DVD-ROM focusing servo system.

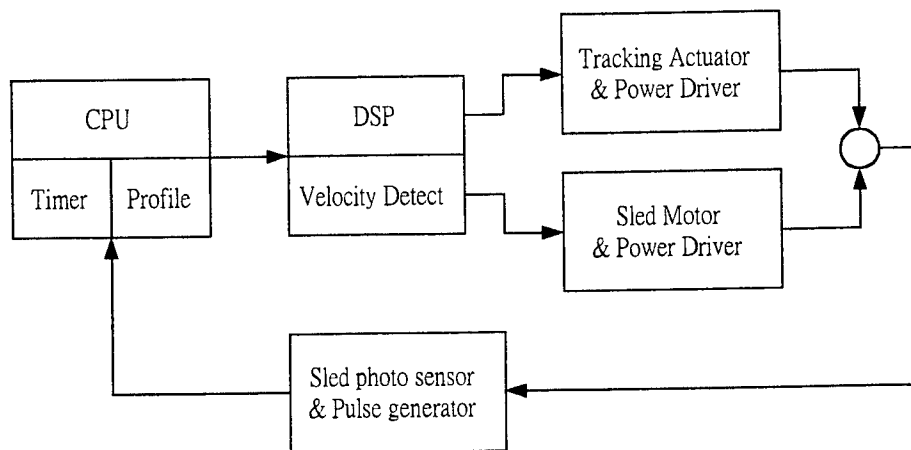Figure 4. Block diagram of DVD-ROM track following system.

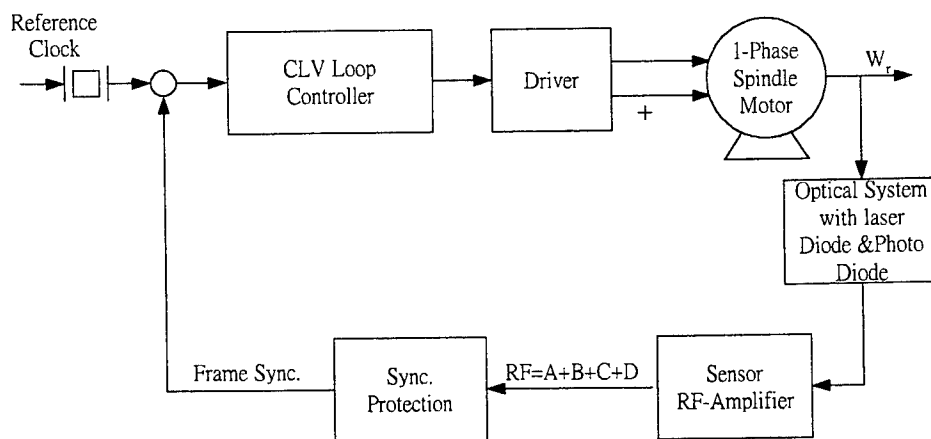Figure 5. Block diagram of seeking servo system.

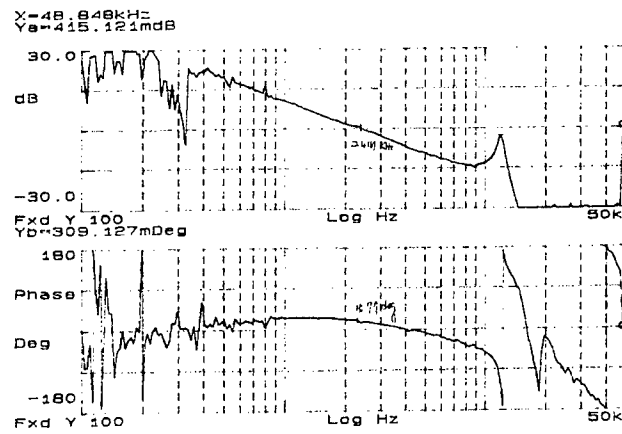Figure 6. The block diagram of the spindle servo system.
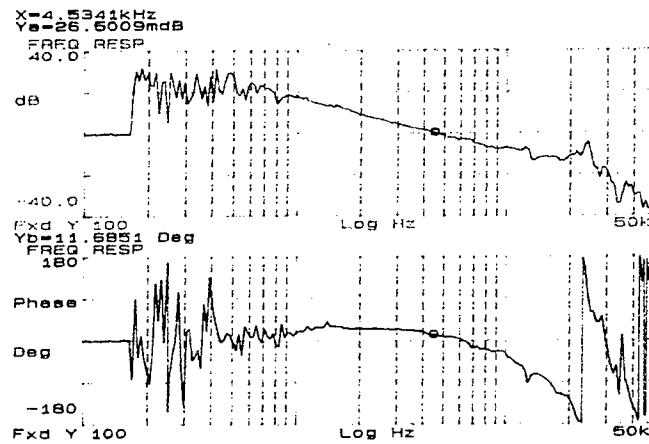
Figure 7. The open-loop gain of focusing loop

Figure 8. The open-loop gain of tracking loop.

Hist: Hist TI AB   29 Aug 1999 14:26:46
Min: 4.0 ns   Mean: 22.3081 ns
Max: 42.8 ns   Std Dev: 4.0962 ns

1E+05
meas

1
meas
View 2:1   0   s   50.0 ns
                               400 ps/disp bin
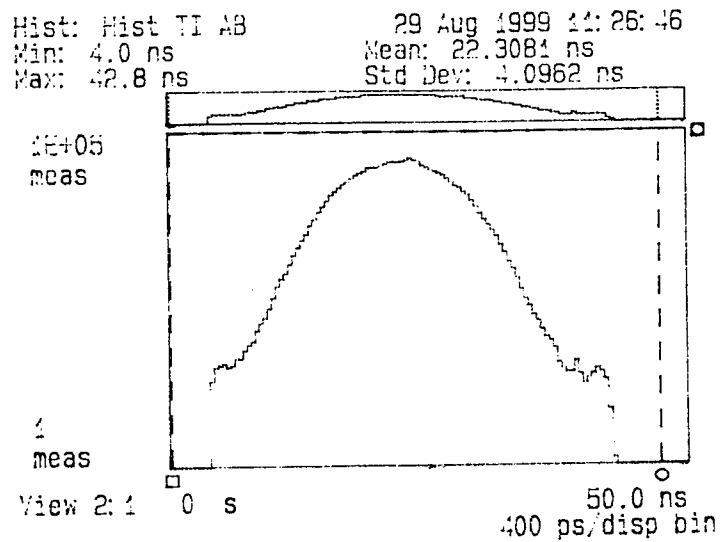
Figure 9. Data read-out jitter signal.
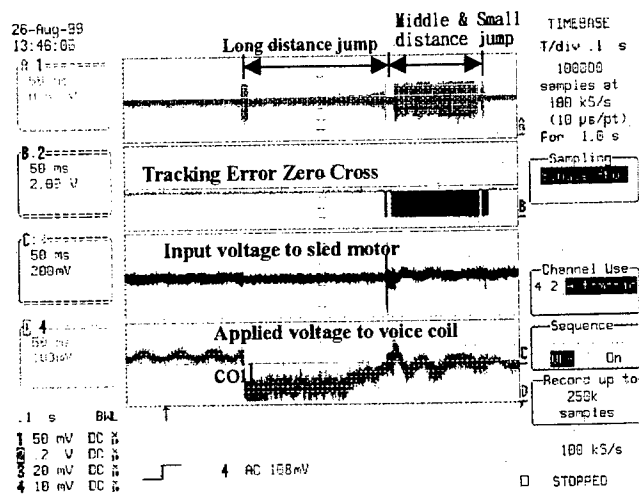
Figure 10. The long-distance seeking profile

279

Author Index